Scattering Analysis and Ultra-Wideband Radar for High-Throughput Phenotyping of Wheat Canopies

BY

Daniel Gomez Garcia Alvestegui

M.S.E.E., University of Kansas, 2011

B.S.E.E., University of Kansas, 2008

Submitted to the graduate degree program in Electrical Engineering

and the Graduate Faculty of the University of Kansas

in partial fulfillment of the requirements for the degree of Doctor of Philosophy

_____

Chair: Dr. Carl Leuschen

_____

Dr. Fernando Rodriguez-Morales

_____

Dr. Ron Hui

_____

Dr. Chris Allen

_____

Dr. David Braaten

Date Defended: February 4th, 2019

The dissertation committee for Daniel Gomez Garcia Alvestegui certifies that this is the approved version of the following dissertation:

Scattering Analysis and Ultra-Wideband Radar for High-Throughput Phenotyping of Wheat Canopies

_____

Chair: Dr. Carl Leuschen

Date Approved: February 4th, 2019

Abstract

Rising the yield of wheat crops is essential to meet the projected demands of future consumption and it is expected that most yield increases will be associated to improvements in biomass accumulation. Cultivars with canopy architectures that focus the light interception where photosynthetic-capacity is greater achieve larger biomass accumulation rates. Identifying varieties with improved traits could be performed with modern breeding methods, such as genomic-selection, which depend on genotype-phenotype mappings. Developing a non-destructive sensor with the capability of efficiently phenotyping wheat-canopy architecture parameters, such as height and vertical distribution of projected-leaf-area-density, would be useful for developing architecture-related genotype-phenotype maps of wheat cultivars. In this dissertation, new scattering analysis tools and a new 2-18 GHz radar system are presented for efficiently phenotyping the architecture of wheat canopies.

The radar system presented was designed with the objective to measure the RCS profile of wheat canopies at close range. The frequency range (2-18 GHz), topology (Frequency-modulated-continuous-wave) and other radar parameters were chosen to meet that goal. Phase noise of self-interference signals is the main source of coherent and incoherent noise in FMCW radars. A new comprehensive noise analysis is presented, which predicts the power-spectral-density of the noise at the output of FMCW radars, including those related to phase noise. The new 2-18 GHz chirp generator is based on a phase-locked-loop that was designed with large loop bandwidth to suppress the phase noise of the chirp. Additionally, the radar RF front-end was designed to achieve low levels of LO-leakage and antenna feed-through, which are the main self-interference signals of FMCW radars.

In addition to the radar system, a new efficient radar simulator was developed to predict the RCS waveforms collected from wheat canopies over the 2-18 GHz frequency range. The coherent radar simulator is based on novel geometric and fully-polarimetric scattering models of wheat canopies. The scattering models of wheat canopies, leaves with arbitrary orientation and curvature, stems and heads were validated using a full-wave commercial simulator and measurements. The radar simulator was used to derive retrieval algorithms of canopy height and projected-leaf-area-density from RCS profiles, which were tested with field-collected measurements. The retrieved heights and projected-leaf-area densities compare well against ruler measurements and image-based retrievals, respectively.

Acknowledgements

I would like to acknowledge all the people who have helped me throughout my Ph.D. studies and the development of this dissertation. First, I would like to thank my advisor Dr. Leuschen for giving me the opportunity to re-join his research team and work on this exciting topic. He has helped me stay focus on practical research while allowing me to build my own ideas. He is always quick to point out where something may be wrong in my work and I appreciate that. He has been a great mentor, helping me both within and outside my research.

I would like to thank Dr. Rodriguez-Morales for all his advice and insights on radar development. He has also helped me review this document and navigate through its development, always patient and willing to answer questions about it. I appreciate all the long hours he took to listen to me and provide advice and encouragement.

I would like to express my sincere appreciation to Dr. Hui, Dr. Allen and Dr. Braaten for agreeing to participate as the committee members and for taking the time to read this document.

I would like to acknowledge Dr. Stephen Welch from the Kansas State University for answering all my questions about wheat physiology and phenotyping.

Last but not least, I thank Kevin Carr, Aaron Paden, Hara Madhav, Teja Karidi, Brian Macharia and Shravan Kaundinya for participating in the field experiments.

List of Figures

List of Tables

Table of Contents

1. Introduction

1.1. Motivation for Phenotyping the Architecture of Wheat Canopies

1.1.1. Opportunities for Increasing Wheat Yield

Wheat is a staple crop consumed worldwide and its production plays an important role in global food supply and security [1, 2]. More than 200 million hectares of land are used to grow wheat globally. Moreover, about a fifth of total calorific intake comes from wheat grains [3].The current rate of yield increase per year for wheat is 0.9% and the estimated rate of yield increase per year should be greater than about 2.4% by 2050 to meet the projected demand [3, 4].

During the Green revolution of the 20th century, the wheat yield was increased through improved agricultural management practices and breeding [5, 6]. Potential yield is the maximum achievable yield for a given wheat variety, under no stress conditions. Potential yield has primarily been improved since the 1950s by rising the harvest index, which is the portion of the biomass that is partitioned for grain production. The rate of harvest index, which has been raised to 0.6, is unlikely to increase significantly in the future [6]. Most of the yield increases in the future will come from higher efficiencies related to the biomass accumulation [6].

In the absence of nutritional stresses, biomass accumulation is primarily dependent on the ability of the canopy to capture light and the efficiency of the plant organs (e.g. leaves) to use light for biomass production [6].

1.1.2. Importance of Canopy Architecture Parameters: Height and Projected Leaf Area Density

Monitoring canopy height is important for both management and breeding. For a wheat plant variety with a known relationship between the growth stages and height, monitoring height could help farmers assess the developmental performance of wheat crops.

The yield potential of wheat was significantly increased by the introgression of genes of semi-dwarf varieties [6]. Because of a genetically related inhibition of the stem elongation before anthesis, these varieties have a larger amount of biomass available for grain filling. As more cultivar varieties are developed, stem elongation during anthesis remains an important feature to monitor.

Canopy height is also related to the lodging of wheat plants. Tall plants are more prone to lodge than shorter ones.

The total projected leaf area density of a canopy defines how much light it captures. Moreover, the vertical distribution of the projected leaf area density in a canopy establishes where most of the light is captured. At high concentrations of light, the radiation use efficiency is determined by the photosynthetic capacity. The photosynthetic capacity is dependent on the level of CO_2, nitrogen content within the plants, chlorophyll content, among other factors. Thus, the efficiency of converting light to biomass by a canopy is largest at the vertical level where these compounds concentrate. Cultivars with canopy architectures that focus the light interception where photosynthetic-capacity is greater achieve larger biomass accumulation rates.

Identifying varieties with improved traits could be performed with modern breeding methods, such as genomic-selection, which depend on genotype-phenotype mappings. Developing a

non-destructive sensor with the capability of efficiently phenotyping wheat-canopy architecture parameters, such as height and vertical distribution of projected-leaf-area-density, would be useful for developing architecture-related genotype-phenotype maps of wheat cultivars.

1.2. Summary of Research Approach and Contributions

The main objectives of this work were to (i) develop a radar sensor capable of measuring the vertical profile of the radar-cross-section (RCS) of wheat canopies; and (ii) develop an efficient coherent radar simulator to predict the RCS profiles of wheat canopies for a given set of plant parameters. The radar simulator is an analysis tool that can be used to derive canopy parameters from RCS profiles under a given set of constraints. In this investigation, the radar simulator is used to develop retrieval algorithms for the canopy height and the profile of the projected leaf area density. The combination of the radar sensor and the coherent radar simulator permit the non-destructive and efficient phenotyping of the mentioned wheat canopy architecture parameters.

1.2.1. UWB FMCW Radar Design and Analysis

Motivation

As discussed in chapter 2, canopy height is an important parameter related to growth and biomass. Moreover, the vertical distribution of projected leaf area density defines the height

distribution of light interception, as explained in chapter 2. A non-destructive sensor for efficiently collecting measurements of the canopy height and vertical distribution of projected leaf area density would be useful for breeding activities.

Most of the electromagnetic wave sensors used for crop phenotyping operate at near infrared and the visible region of the spectrum. These sensors can only detect the leaves at the top of the canopy, since only a small amount of the signal penetrates the lower layers of the canopy at these spectral bands. In contrast, electromagnetic signals at microwave frequencies propagate through wheat canopies with little attenuation.

A coherent ultra-wideband radar (UWB) operating in near-nadir mode is able to measure a profile of the radar cross section from the ground to the top of the canopy. Developing such as system along with a scattering simulator, which relates the RCS profile to internal canopy architecture parameters, would be of great value for crop phenotyping.

The frequency-modulated-continuous-wave (FMCW) radar system topology was chosen for the UWB radar. The shape and amplitude of the noise floor at the output of FMCW radars is not well understood. Phase noise due to self-interference signals is usually the largest contributor to the noise floor of these radars, but it is often ignored in receiver design. A comprehensive model for the noise floor of FMCW radars would be beneficial to accurately predict the noise level and understand how to improve it.

Approach

A new comprehensive noise model for FMCW radar is presented in chapter 5. This model was compared against numerical simulations. It was also successfully used to predict the amplitude

and shape of the total noise of the designed FMCW radar. This model accounts for both coherent and incoherent noise sources.

A new 2-18 GHz FMCW radar system was designed and built for this application. The design of the system leveraged previous work on airborne radar for snow probing applications [9-14]. The radar is described in detail in chapter 5. In the radar design, special attention was given to the chirp generator, which is the main source of phase noise. This sub-system is based on a phase-locked-loop that synthesizes an intermediate chirp (11-19 GHz), which gets frequency-multiplied up to millimeter-waves (22-38 GHz) and down-converted to the desired 2-18 GHz band. The phase noise of the chirp generator is kept low by designing the PLL with a wide loop bandwidth (4.6 MHz). The total (maximum) phase noise of this waveform generator is less than -42 dBc. This magnitude translates to a (maximum) phase noise in the FMCW radar output of less than -45 dBc. A full description of the PLL and performance measurements are shown in chapter 5. The receiver is designed with a high gain (47.3 dB), since the noise floor of FMCW radars is (usually) phase noise limited, not thermal noise limited. Without coherent integrations, the equivalent RCS of the incoherent noise floor is -43 dB and a maximum RCS of +13.4 dB.

Contributions

- Formulation of a new analytic model of the effect of coherent and incoherent phase noise in FMCW radars to the noise floor of the radar output signal.
- Development of a new 2-18 GHz FMCW radar optimized for medium-range applications. The radar is built upon a highly-linear PLL-based chirp generator with 4 MHz loop bandwidth. This chirp generator sweeps a signal from 2 GHz to 18 GHz with a chirp

length of 240 μs. Emphasis was put in minimizing phase noise from coherent and incoherent sources to maximize sensitivity. Design considerations are thoroughly documented to serve as reference for future work.

1.2.2. Scattering Analysis

Motivation

Scattering models and simulations of targets of interest are analytic tools that are useful for the prediction of radar-received signals and for the development of parameter retrieval algorithms. Coherent scattering models in the frequency-domain can be used to find time-domain radar responses and RCS waveforms. In this work, it was sought to find coherent scattering models of wheat plant constituents and canopies, and develop a Monte Carlo simulator. The type of scattering models sought after had to be valid in the 2-18 GHz frequency range; be valid for canopies with leaves, heads, considering all arbitrary shapes, size and orientations seen in real crops; and be sufficiently fast to be able to run Monte Carlo simulations of 60+ realizations in a reasonable amount of time.

Coherent scattering models of leaves with arbitrary location, orientation and distributed curvature were not available before this work. For instance, the model in [7] is inaccurate for axial incidence and assumes that leaves are very thin with respect to the wavelength, which would not be valid in the frequency range considered by this work. In [8], the scattering model of a parabolic shaped leaf is given using the Physical Optics approach. This is a scattering model for a curved leaf, but it is constrained to a specific shape (parabola) and it is not accurate for axial incidence.

On the other hand, full-wave simulations, such as the Method of Moments or Finite-Difference-Time-Domain, are exact, as long as sufficient numerical resolution is used. However, these methods are very time consuming. Computing Monte Carlo simulations with 60 realizations of wheat canopies with 100s of plants would not be possible with these methods.

Since current scattering models using analytic approximations are inaccurate and restrictive in the allowed shapes, new analytic approximations of scattering models are required to compute the Monte Carlo simulations desired.

Approach

First, a new scattering analysis method, the constructive-geometry-method, was developed. This method computes the coherent scattering models and radar responses due to complex targets and it is only valid for targets with smooth surfaces, such as leaves, and sparse media, such as wheat canopies. This method relies on the (modeled) scattering dyads of primitive shapes (i.e. solids), such as thin flat sheets. It combines the scattering dyads of multiple primitives by linearly transforming the incident and scattered vector fields and the incident and scattered wave-vectors, depending on the position and orientation of the primitives. This method is described in chapter 3.

Secondly, we developed accurate scattering dyad models of dielectric cylinders and thin sheets. The models are derived from first principles. The derivation of the models, including the approximations made, are specified in chapter 3. The scattering dyad model of the thin sheet is accurate for any orientation or any angle of incidence, including axial incidence. The scattering dyad model of the dielectric cylinder is more accurate than reported models.

Thirdly, the geometric models of leaves, heads, stems, plants and canopies are developed. A script was developed to translate the model to STL format to visualize the geometric models.

Forth, using the constructive-geometry-method, the scattering models of leaves with arbitrary orientations and curvatures were formulated. These models rely on the geometric models of the leaves and the scattering model of the primitives. In a similar manner, scattering models of heads, stems, plants and canopies were formulated.

The geometric models, which are a set of parametric equations that mathematically describe the targets, are used to calculate the parameters of the targets, such as their position and orientation. These parameters are computed numerically. Similarly, the scattering dyads of the complex targets and their radar responses are computed using a personal computer, or server. For these reason, we refer to the computation of the scattering dyads and radar responses as simulations.

Finally, the radar simulations/modeling was validated by comparing the simulation/modeling results against full-wave simulations and measurements. The radar simulation results from individual plant components, at multiple physical configurations, and whole wheat plants were used for the comparisons.

Contributions

- Scattering modeling of curved thin sheets and curved cylinders.
- Scattering modeling of wheat canopy, plants and their constituents:
    - Scattering of wheat leaves with arbitrary curvature
    - Scattering of wheat heads

    - Scattering of wheat stem
    - Scattering of wheat plant and canopies for single realization and Monte-Carlo simulations.
- Geometric modeling of wheat plants

1.2.3. Canopy Architecture Parameter Retrieval: Height and Projected Leaf Area Density

Coherent Monte-Carlo radar simulations are used to derive the simple relationships between the amplitude of the range-domain RCS and the canopy parameters. This relationship is used to formulate a simplified incoherent scattering model due to wheat canopies. Base on this model, we define a simple expression to solve the vertical distribution of the projected leaf area density.

Likewise, Monte-Carlo simulation are used to find a relationship between the range-domain RCS waveform and the height level (i.e. average height of plants in the canopy). The definition of the height of the plant and canopy are given in chapter 2.

Both retrieval procedures were applied to radar measurements collected in a field experiment, conducted in the wheat fields of Tom Pauly Seed (Conway Springs, KS). The radar and the mobile platform used for the experiment are described in chapter 5. The results of the height retrievals of some wheat plots were compared against in-situ measurements. The results of the retrievals of projected leaf area density were compared against those derived from a image-based method.

The retrieval procedures and results are given in chapter 6.

Contributions

- Retrieval method of canopy height and projected leaf area density from range-domain RCS waveforms measured with a 2-18 GHz radar.

1.3. Dissertation Outline

This document is organized in seven chapters, including this introduction. A brief summary of the content of each chapter is given below.

Chapter 2 provides some background on the influence of the canopy architecture to the canopy's biomass accumulation rate. This chapter provides the definitions of the main efficiencies that account for biomass production by a canopy in the absence of nutrient stresses. This chapter also provides an example of how some canopy architectures have advantages over others regarding production efficiencies.

Chapter 3 details background concepts regarding scattering analysis. This chapter derives a coherent equation to compute the coherent radar response due to a target with known scattering dyad. This chapter also provides the derivation of improved scattering models for a dielectric cylinder and dielectric thin sheet. In the second part of this chapter, the constructive-geometry-method is defined for coherent scattering analysis of complex targets.

Chapter 4 describes a novel coherent radar simulator for wheat canopies. The scattering models of leaves, heads, stems, plants and canopies are specified. This radar simulator is based on the constructive-geometry-method. Geometric models for the canopy and its constituents is given. Both full-wave simulations and measurements are used to validate the radar simulator.

In Chapter 5, a 2-18 GHz ultra-wideband radar is described. The chirp generator, which severely influences the performance of the radar, is described in detail. This chapter presents an analysis of the effects of the coherent and incoherent phase noise on the FMCW radar output.

Chapter 6 presents a summary of the relationship of the amplitude of the range-domain RCS waveform and leaf-related canopy parameters. Procedures for the retrieval of canopy architecture parameters are given based on the results of Monte-Carlo radar simulations. These procedures are used to derive canopy parameters from radar measurements collected in a field experiment.

Chapter 7 summarizes the main contributions of this work and provides recommendations for future studies.

1.4. References

[1] T. Fischer, D. Byerlee, G. Edmeades, “Crop yields and global food security: will yield increase continue to feed the world?” Camberra: Australian Center for International Agricultural Research, 2014.

[2] D. Tilman, C. Balzer, J. Hill, B. Befort, “Global food demand and the sustainable intensification of agriculture,” Proc. Of National Academy of Sciences of the U.S.A., vol. 108 no. 50, pp 20260-20264, Aug. 2011.

[3] N. Alexandratos, J. Bruinsma, “World agriculture towards 2030/2050. The 2012 Revision. ESA Working paper No. 12-03,” Rome: Food and Agriculture Organization of the United Nations, April 2012.

[4] D. Ray, N. Mueller, P. West, J. Foley, “Yield trends are insufficient to double global crop production by 2050,” PLoS ONE 8 e66428, 2013.

[5] P. L. Pingali, “Green Revolution: Impacts, limits, and the path ahead,” PNAS, vol. 109 no.31, 12302-12308, July 2012.

[6] M. Reynolds, M. Foulkes, G. Slafer, P. Berry, M. Parry, J. Snape, W. Angus, “Railing yield potential,” Journal of experimental Botany, vol. 60, no. 7, pp. 1899-1918, April 2009.

[7] T. B. A. Senior, K. Sarabandi and F. T. Ulaby, "Measuring and modeling the backscattering cross section of a leaf," in Radio Science, vol. 22, no. 06, pp. 1109-1116, Nov. 1987.

[8] L. Liu et al., "Modeling Microwave Backscattering From Parabolic Rice Leaves," in IEEE Transactions on Geoscience and Remote Sensing, vol. 55, no. 11, pp. 6044-6053, Nov. 2017.

[9] F. Rodriguez-Morales, S. Gogineni, C. Leuschen, J. Paden, J. Li, C. Lewis, B. Panzer, D. Gomez-Garcia , A. Patel, K. Byers, R. Crowe, K. Player, R. Hale, E. Arnold, L. Smith, C. Gifford, D. Braaten, and C. Panton, "Advanced Multifrequency Radar Instrumentation for Polar Research," in IEEE Transactions on Geoscience and Remote Sensing, vol. 52, no. 5, pp. 2824-2842, May 2014.

[10] Panzer, B., D. Gomez-Garcia, A. Patel, C. Leuschen, J. Paden, T. Markus, and S. Gogineni, “Development of an ultra-wideband radar for measuring snow thickness on sea ice,” Journal of Glaciology Instruments and Methods, vol. 59, no. 214, pp. 244-254, April 2013.

[11] Daniel Gomez-Garcia , Fernando Rodriguez-Morales, Carlton Leuschen, Prasad Gogineni, "KU-Band radar altimeter for surface elevation measurements in polar regions using a wideband chirp generator with improved linearity," 2012 IEEE International Geoscience and Remote Sensing Symposium, Munich, 2012, pp. 4617-4620.

[12] Daniel Gomez-Garcia, “Linearization Method for a UWB VCO-based chirp generator using dual compensation,” M.S. Thesis Defense, Nov. 2011, Lawrence KS.

[13] D. Gomez-Garcia, C. Leuschen, F. Rodriguez-Morales, Jie-Bang Yan and P. Gogineni, "Linear chirp generator based on direct digital synthesis and frequency multiplication for airborne FMCW snow probing radar," 2014 IEEE MTT-S International Microwave Symposium (IMS2014), Tampa, FL, 2014, pp. 1-4.

[14] J. B. Yan, D. Gomez-Garcia, J. McDaniels, Y. Li, S. Gogineni, F. Rodriguez-Morales, J. Brozena, C. Leuschen, "Ultrawideband FMCW Radar for Airborne Measurements of Snow Over Sea Ice and Land," in IEEE Transactions on Geoscience and Remote Sensing, vol. 55, no. 2, pp. 834-843, Feb. 2017.

2. Wheat Canopy Architecture: Influence on Biomass Accumulation

2.1. Introduction

2.1.1. Wheat Yield Potential

Yield is the amount of grain production defined in mass or weight per unit area. The yield potential of a given wheat variety is the yield that is achieved under optimal environmental conditions. In contrast, farm yield, which is a fraction of yield potential, is the actual crop yield of a producing farm field. Wheat accounts for one fifth of the global caloric intake. Increasing the yield potential of wheat is important to help crop production keep up with the doubling of demand projected for the next half-century [1-2]. During the Green Revolution of the 20th century, breeders doubled the yield potential of wheat [3]. During this time, varieties more tolerant to biotic and abiotic stresses were developed.

Yield potential (Y_P) is the product of the net primary production (P_n) and the harvest index (ε_{HI}), given in (2.1.1) [4]. The primary production is the amount of chemical energy generated by the plant or canopy and stored as biomass. The harvest index is a parameter that indicates the efficiency of partitioning biomass into harvested product (i.e. grain).

$$Y_P = \varepsilon_{HI}\, P_n \tag{2.1.1}$$

Since the 1950s, increases in yield potential have been primarily achieved by improving the harvest index [3, 5]. In contrast, improvements in biomass accumulation have been marginal [5]. The most significant improvements in harvest index are attributed to the introgression of semi-dwarf genes, such as those derived from the Norin 10 cultivar (Rht1 and Rht2) [5]. These types of varieties have a genetic restriction of the stem growth right before anthesis, which increases the amount of biomass available for translocation to spikes at an important time of its development. Because of the larger amount of assimilates are available for the spike than those related to the stem growth, these semi-dwarf genes result in a larger number of grains and spike dry mass.

Improved wheat cultivars achieve harvest indices of 0.6 [5, 6]. Substantial increases in harvest index are unlikely to occur [5, 6]. Some amount of the produced biomass by the plant must remain in its body to maintain other physiological functions. Most of the future yield potential increases will come from improvements in the biomass accumulation [5, 6]. Under no stresses due to lack of irrigation or nutrients, the production of biomass in a plant depends on its efficiency to capture and use light for photosynthesis. Therefore, enhacing these efficiencies would be beneficial for future improvement of the wheat yield-potential.

2.1.2. Accumulated Biomass

Under no environmental stresses, the primary production (P_n) or accumulated biomass is determined by the relationship given in (2.1.2) [4, 6]. In (2.1.2), the term S_R represents the power or radiant flux density of light illuminating the top of the canopy. The unit-less parameter ε_e is the effective efficiency of the canopy of capturing and using the light power density S_R into

a biomass accumulation rate per unit area. The term k_c represents the energy content of vegetation mass, which is 17.5 MJ/g for vegetative biomass [7]. The biomass accumulation rate per unit area is integrated over time to find the total biomass per unit area.

$$P_n = \int_{\Delta t} {k_c}^{-1}\, \varepsilon_e\, S_R\, dt \tag{2.1.2}$$

Rising the production of biomass by the canopy requires an improvement in the effective efficiency ε_e. This parameter depends on the canopy's efficiency for capturing light and the efficiency of converting the captured light in to biomass. These two topics are covered in sections 2.3 and 2.4.

2.1.3. Effect of Canopy Architecture on Effective Efficiency

Compounds related to photosynthesis, such as CO_2 and chlorophyll, vary in concetration at different vertical levels within the canopy, thereby increasing the photosynthetic capacity at vertical regions in the canopy.

The vertical distribution of the projected leaf area density in a canopy establishes the areas in which most of the light is captured. In other words, the canopy architecture dictates where most of the photosynthesis takes place. Therefore, the biomass of a canopy is improved if it focuses its photosynthetic production near the vertical region where the photosynthetic capacity is the largest (e.g. a region with large concentration of chlorophyll or CO_2). Section 2.3 provides some

basic definitions regarding the canopy architecture parameters. Section 2.5 provides simulation examples of canopies with improved production.

Modifying the canopy architecture to improve the biomass production efficiency is one of the approaches being investigated by breeders and plant scientists [6, 8].

2.2. Canopy Architecture: Height and Projected Leaf Area Density

The plant architecture is the three dimensional organization of its parts [9]. In other words, plant architecture refers to the position, orientation and shape of all the organs in a plant, including branches, leaves, flowers and fruits. Similarly, the canopy architecture is the organization of all the plants in a canopy and their constituents.

Canopy architecture is an important feature in crop breeding for improved yields [8]. Modifying the canopy architecture of wheat crops has great potential to help improve biomass production efficiencies [8].

In this section, we introduce some of the canopy architecture parameters related to plant growth and light interception by the canopy.

2.2.1. Plant and Canopy Height

The plant's height is defined as the shortest distance between the ground level and the top boundary of the plant's photosynthetic tissues [10]. In the case of wheat plants, the highest point of photosynthetic tissue is either the top of a leaf or the top of the head, whichever is taller. The canopy height is the average of the height of the plants that belong to it.

Plant height is highly dependent on the plant variety. For a given variety, for which the relationship of the height and the growth stage is known, the height becomes an indicator of plant growth. Height is also related to the biomass allocation in a plant. For instance, plant that allocates significant amount of biomass for stem elongation becomes a tall variety. In contrast, shorter wheat plants with genes that restrict stem growth before anthesis, allocate more biomass for spike development.

2.2.2. Leaf and Projected Leaf Area

The leaf area is the one sided area of a leaf lamina. The magnitude of the leaf area affects the transpiration, respiration and photosynthesis functions of a plant.

The projected leaf area of a leaf is the extend of the projection of the leaf onto the plane that is perpendicular to the illuminating beam of light. If the illumination comes from above the canopy in the nadir direction, this parameter is the area of the leaf projected onto the horizontal plane.

2.2.3. Leaf Density, Leaf Area Density and Projected Leaf Area Density

Plant density is the number of plants per unit area. The volumetric leaf density is the density of leaves per unit volume in a canopy. This is also known as the volumetric number density of leaves.

The leaf area surface-density is the ratio of the total leaf area within a surface area of the canopy to the magnitude of the surface area. Likewise, the leaf area volume-density is the ratio of the total leaf area within a volume of the canopy to the magnitude of the volume being considered. The projected leaf area surface-density and projected leaf area volume-density are defined in the same manner, replacing the leaf area by the projected leaf area.

The projected leaf area is used to calculate the light propagation losses through the canopy using radiative transfer theory. The projected leaf area density also defines the efficiency of light-interception within a canopy. These topics are further discussed in section 2.3.

2.2.4. Leaf Orientation and Curvature

The leaf orientation refers to all the related leaf angles. Since leaves usually are uniformly distributed in the azimuth direction, the main angle of interest is the elevation angle. The elevation or tilt angle is the angle measured with respect to the vertical axis.

The curvature of the main axis of a leaf is the inverse of the radius of curvature at every point in the pathlength. This curvature may also be defined as the rate of change of the elevation angle with respect to the pathlengh. The patlength is the arc that runs along the main axis of the leaf.

If the leaf is perfectly straight, its curvature is zero and its radius of curvature is infinity. A curved leaf is one with non-zero curvature at some region along its length-path. A wheat plant may have straight leaves only, all curved leaves, or a combination of curved and straight leaves. A curved leaf can be defined by its minimum radius of curvature, initial and final elevation angles.

Both the elevation angle and the leaf curvature affect the projected leaf area.

2.3. Light Interception by a Wheat Canopy

2.3.1. Power and Power Density of Light Captured by a Leaf

Considering a beam of light, illuminating a single leaf, with power density S_{Ro}, the amount of power captured P_C by the leaf is determined by its projected leaf area A_P, as given by equation (2.3.1). The projected leaf area is the fraction of the area that is projected onto a plane perpendicular to direction of illumination. In this context, the power captured by a leaf refers to the amount of power illuminated onto a leaf. The power captured by the leaf may be reflected and/or absorbed by the leaf. The fraction of the power that is absorbed and used by the leaf is accounted for by the radiation use efficiency, defined in section 2.4.

$$P_C = A_P \, S_{Ro} \tag{2.3.1}$$

The ratio of the power captured by a leaf and a given area illuminated by light (e.g. ground area) is the power density of light captured by a leaf S_C. In (2.3.2), the term $\rho_{s,P}$ is the leaf area surface-density and it is defined in (2.3.3) as the ratio of the projected leaf area over a given

ground area. The leaf area surface-density is also known as the projected leaf-area-index (PLAI).

$$S_{PAR,C} = \frac{P_{PAR,C}}{A_G} = \rho_{s,P}\, S_{PAR,R} \tag{2.3.2}$$

$$\rho_{s,P} = \frac{A_{P,L}}{A_G} \tag{2.3.3}$$

2.3.2. Power Density of Light Captured by a Canopy

2.3.2.1. Power Density of Light Captured by Non-Overlapping Leaves

Equation (2.3.2), describes the power density of light captured by a single leaf. If numerous non-overlapping leaves, distributed over a surface with area A_G, the power density captured by them is given by (2.3.4), which is equivalent to (2.3.3). In (2.3.4), the leaf area surface-density is given by (2.3.5) in terms of the projected leaf area of every leaf A_{P,i_L}. The expression (2.3.5), is also given in terms of the average projected-leaf-area $\bar{A}_{P,L}$ and the surface number density $n_{o,s}$.

$$S_{PAR,C} = \rho_{s,P}\, S_{PAR,R} \tag{2.3.4}$$

$$\rho_{s,P} = \frac{1}{A_G}\sum_{i_L}^{N_L} A_{P,i_L} = n_{o,s}\, \bar{A}_{P,L} \tag{2.3.5}$$

2.3.2.2. Power Density of Light Illuminating Leaves in a Canopy

A canopy is usually composed of leaves overlapping each other. As light propagates through a canopy, it is attenuated by the absorption and reflection of the canopy constituents (e.g. leaves). The canopy is a sparse inhomogeneous medium, for which the extinction of light may be calculated using the simplified form of the radiative transfer equation, given in (2.3.6). In (2.3.6), $\kappa_e(r)$ is the extinction coefficient and r is the pathlength of the light beam.

$$\frac{dS_R(r)}{dr} = -\kappa_e(r)\, S_R(r) \tag{2.3.6}$$

The extinction coefficient is equal to the (volumetric) projected leaf area density $\rho_{v,P}(r)$ (2.3.7). This is shown in section 2.3.3.

$$\kappa_e(r) = \rho_{v,P}(r) \tag{2.3.7}$$

For the special case where the projected leaf area density is constant or uniformly distributed within the canopy, the power density of the illuminating source within the canopy takes the form given in (2.3.8). In (2.3.8), we use the condition $S_{Ro} = S_R(-r_{tc})$ was used, where $-r_{tc}$ represents the point in the pathlength at the top of the canopy.

$$S_R(r) = S_{Ro}\, e^{-\kappa_e\,(r+r_{tc})} = S_{Ro}\, e^{-\rho_{v,P}\,(r+r_{tc})} \tag{2.3.8}$$

2.3.2.3. Power Density of Light Captured by a Canopy

The power density captured by the entire canopy is expressed by (2.3.9), where $\rho_{v,P}(r)$ is the projected leaf area volume-density. Using a change of variable, the power density captured by the canopy may be written in terms of the vertical axis variable 'z', as given in (2.3.10).

$$S_C = \int_{-r_{tc}}^{0} \rho_{v,P}(r)\, S_R(r)\, dr \tag{2.3.9}$$

$$S_C = \int_{-h_{tc}}^{0} \rho_{v,P}(z)\, S_R(z)\, dz \tag{2.3.10}$$

2.3.2.4. Light-Interception Efficiency

The light-interception efficiency of the canopy is defined as the ratio of the power density of the total captured light to the power density of the illuminated light onto the top of the canopy, as shown in (2.3.11).

$$\varepsilon_i = \frac{S_C}{S_{Ro}} = \frac{1}{S_{Ro}} \int_{-r_{tc}}^{0} \rho_{v,P}(r)\, S_R(r)\, dr \tag{2.3.11}$$

2.3.2.5. Special Case: Captured Power Density of Light in a Canopy with Uniform $\rho_{v,P}$

In the special case, where the projected leaf area density $\rho_{v,P}(r)$ is uniformly distributed, the integral in (2.3.9) results in (2.3.12), where θ_i is the elevation angle of illumination.

$$S_C = S_{Ro}(1 - e^{-\rho_{v,P}\, r_{tc}}) = S_{Ro}\left(1 - e^{-\rho_{v,P}\, h_{tc}/\cos(\theta_i)}\right) \quad (2.3.12)$$

From (2.3.12), the light-interception efficiency ε_i when the projected leaf area is distributed uniformly is then given by (2.3.13).

$$\varepsilon_i = \left(1 - e^{-\rho_{v,P}\, h_{tc}/\cos(\theta_i)}\right) \quad (2.3.13)$$

2.3.2.6. Monsi-Saeki Theory

Monsi and Saeki [11] empirically found the relations in (2.3.12) and (2.3.13). The Monsi-Saeki equations are the most common expressions used to find the light intercepted by a canopy. In the literature, the Monsi-Saeki equations are sometimes referred to as the Beer's law for light propagation through a canopy. The Monsi-Saeki equation for the power density captured by the canopy is given by (2.3.14), which is equivalent to (2.3.13).

$$S_C = S_{Ro}\left(1 - e^{-PLAI/\cos(\theta_i)}\right) = S_{Ro}\left(1 - e^{-G \cdot LAI/\cos(\theta_i)}\right) \quad (2.3.14)$$

In the Monsi-Saeki equations, the projected leaf area surface-density ($\rho_{s,P}$) is known as the projected leaf area index (PLAI) (2.3.15). Alternatively, the Monsi-Saeki equations may be written in terms of the total leaf area index (LAI), which is the total leaf area per unit of ground area, and a projection function (G), as shown in (2.3.14). The projection function (*G*), also known as the gap function, is a factor that accounts for the projection of the leaf area (2.3.16). A term known as the "extinction coefficient" K_{MS} is sometimes used to represent the expression in (2.3.17). This "extinction coefficient" is not related to the extinction coefficient from radiative transfer theory, so we will refer to it in this document as the Monsi-Saeki extinction coefficient.

$$PLAI = \rho_{s,P} \tag{2.3.15}$$

$$PLAI = G \cdot LAI \tag{2.3.16}$$

$$K_{MS} = G\ /\cos(\theta_i) \tag{2.3.17}$$

Monsi-Saeki equations provide a useful and fast method to find the light-interception efficiency of a canopy for a given LAI, G and light incident angle. The limitations of this equation is that it is only valid for uniformly distributed projected leaf area densities.

For projected leaf area densities that are not uniformly distributed, we may use (2.3.9) to find the power density captured by the canopy and (2.3.11) to find the light-intercepted efficiency.

2.3.3. Extinction Coefficient

The extinction coefficient (κ_e) is the double of the imaginary component of the effective propagation coefficient (k_e) (2.3.18).

$$\kappa_e = 2\ Im\{k_e\} \tag{2.3.18}$$

The coherent component of a wave propagating in inhomogeneous media can be readily solved using Dyson's equation. If the inhomogeneous medium is sufficiently sparse, the contributions due to the scattering of the particles to the wavefront are statistically independent. Under this approximation, the effective propagation can be obtained by solving Dyson's equation under Foldy's approximation. Ignoring depolarization, the effective propagation constant results in

(2.3.19). In (2.3.19), (k_o) is the wavenumber of free space, (n_o) is the volumetric number density and (f_f) is the forward scattering amplitude.

$$k_e \approx k_o + \frac{2\pi n_o f_f}{k_o} \tag{2.3.19}$$

By the optical theorem, the extinction cross section can be expressed in terms of the imaginary component of the forward scattering amplitude, as shown in (2.3.20). The extinction cross section is the sum of the scattering and absorption cross sections.

$$\sigma_e = \frac{4\pi}{k_o} Im\{f_f\} \tag{2.3.20}$$

By combining (2.3.18-2.3.20), we obtain the expression (2.3.21) for the extinction coefficient in terms of the extinction cross section and the volumetric number density. In the geometric limit, the extinction cross section is equal to twice the projected area of a single particle (i.e. leaf). However, experimental tests [11] on leaves showed that the extinction coefficient is equal to half of that. The extinction coefficient κ_e is then equal to the projected leaf area volume-density $\rho_{v,P}$.

$$\kappa_e = 2\, Im\{k_e\} \approx n_o \sigma_e \tag{2.3.21}$$

2.4. The Light Response Curve and Radiation Use Efficiency

Radiation use efficiency (RUE) is the efficiency of the plant organs (e.g. leaves), capable of photosynthesis, to convert the intercepted light into biomass. Similar to the light-interception efficiency, described in section 2.3, the RUE is a unit-less parameter.

The RUE is the rate of change of the light-intensity curve, which relates the power density (irradiance flux density) of the intercepted light to photosynthesis. Figure 2.4.1 shows a sample light-response curve for leaves of wheat. As the amount of intercepted-light increases, the curve saturates approaching the photosynthetic capacity (A_{max}). The photosynthetic capacity of wheat leaves depends on the type of variety and reported values range from about 17 μmol m^{-2} s^{-1} to 25 μmol m^{-2} s^{-1} [13-14].

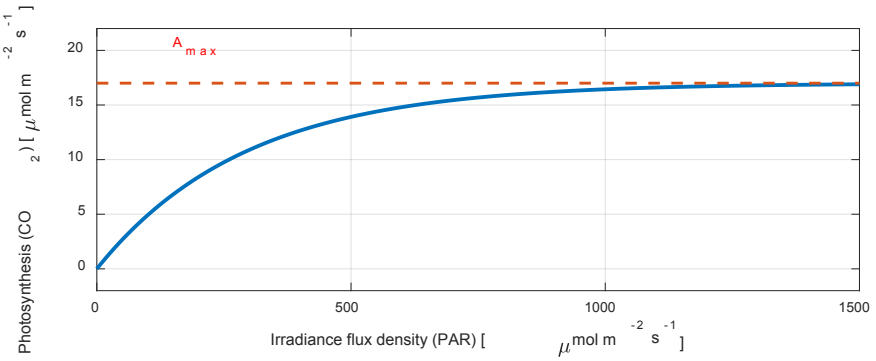

Figure 2.4.1 – Sample Light-Response Curve

Figure 2.4.2 shows a sample RUE for wheat leaves. The RUE decays exponentially with the power density of the intercepted light. A typical value for RUE of wheat at low irradiance levels

is 0.024 [6]. In [15], the reported $\varepsilon_P \; {k_c}^{-1}$ values for wheat are 1.65 to 1.59 [g/MJ], which is equivalent to about 0.026 to 0.029 values of RUE (ε_P) at an energy density of 17.5 MJ/kg.

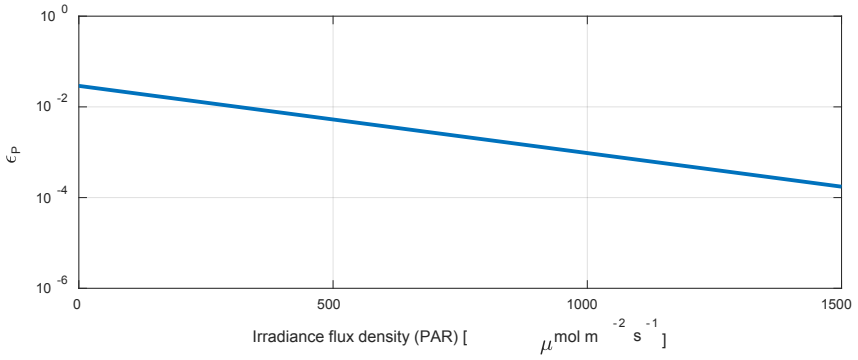

Figure 2.4.2 - Sample radiation-use-efficiency vs irradiance-flux-density curve for wheat leaves

Photosynthesis is a complex process and the RUE depends on many factors. The environmental factors that affect the RUE are the intercepted light power density, the ambient temperature, the content of carbon dioxide within and above the canopy and the amount of water content available to the plant. Other factors that affect the RUE include the amount of nitrogen and chlorophyll in the leaves.

Photosynthetic rates have been reported to increase with larger amounts of CO_2 within the canopy [13]. Similarly, increased levels of nitrogen [16] and chlorophyll [17] are reported to correlate positively with RUE. Measurements indicate that the concentration of these compounds is focused at specific heights in the canopy. Reported measurements of the vertical distribution of CO_2 within the canopy indicate that there is a higher concentration of the gas at the bottom layer [18-20]. In contrast, higher concentrations of chlorophyll are found at the top and medium vertical layers [21]. Similarly, Nitrogen is also found in the top layers of the canopy

[22]. This vertical tendency of these compounds in the canopy creates a vertical profile of the photosynthetic rate or the photosynthetic capacity.

2.5. Canopy Architectures with Improved Overall Efficiency

The vertical distribution of the captured light by a canopy is influenced by its architecture, which may be defined by the profile of the projected leaf area density. As mentioned in the previous section, the concentrations of compounds such as CO_2 or chlorophyll vary with the height of the canopy, varying the RUE or the photosynthetic capacity A_{max} as a function of height. A canopy architecture that focuses the captured light in the region where RUE is greater will have a larger overall efficiency than one that focuses the captured light elsewhere.

In this section, the light interception, radiation use efficiency and biomass accumulation rate are simulated for three different cases of canopies. These simulations are performed to show how the overall efficiency is improved when the light interception by the canopy is focused where the photosynthetic capacity is larger.

We consider three canopy cases with projected leaf area densities as shown in figure 2.5.1. The first canopy has constant projected leaf area density. In the second and third canopies, the projected leaf area density increases and decreases, respectively, with increasing depth. All canopies have the same average projected leaf area. The height of the canopies is 0.5m and the top is shown in the figures at a depth of -0.5 m.

For this example, we assume that the canopy is illuminated by sunlight with a power density of 800 W/m^2 out of which 50% is within the PAR spectral region. The plant density is 1500 pt/m^2, with an average of three leaves for each plant. This results in average number density of the leaves of 9000 leaves/m^3. The average projected leaf area is 2 m^3. The average projected leaf area (volumetric) density is 18 m^2/m^3.

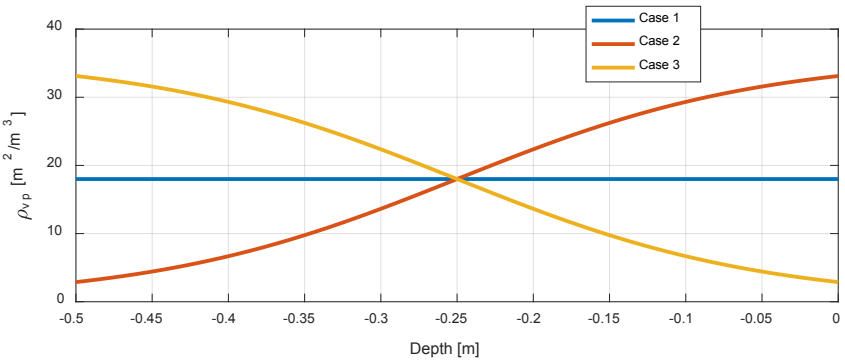

Figure 2.5.1 – Vertical Profile of Projected Leaf Area Density ($\rho_{v,P}(z)$) [m^2/m^3]

The profiles of the power density of the light propagated through the canopy for three different cases are shown in figure 2.5.2. This figure shows how the radiated light decays faster for the case where the projected leaf area density is larger at the top and slower for the one with the lowest density at the top. Figure 2.5.3 shows the profile of the power density of the captured light by the canopies. Because of the different canopy architectures, the amount of captured light is focused at different vertical regions in the three different canopies. For instance, canopy 2 captures more light near the center region, whereas canopy 3 captures most of the light at the top.

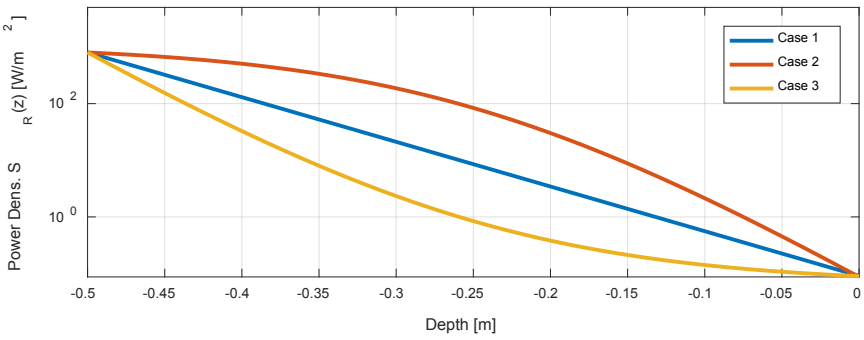

Figure 2.5.2 – Power Density of Light through the Canopy ($S_R(z)$) [W/m^2]

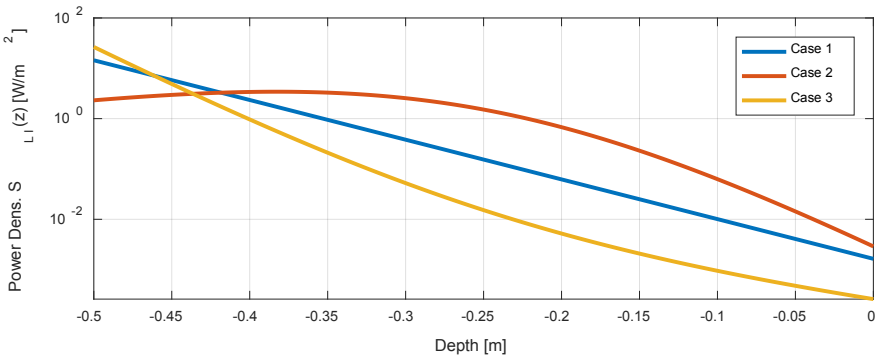

Figure 2.5.3 – Profile of Power Density of Light Intercepted by Canopy ($S_{LI}(z)$) [W/m^2]

Constant Photosynthetic Capacity

In this first example, the photosynthetic capacity is assumed constant within the canopy. In order to simulate the biomass accumulation rate, we consider the light-interception curve shown in figure 2.5.4. This curve has a maximum rate (RUE) $\varepsilon_{p,max}$ of 0.026 and a photosynthetic capacity A_{max} of 20 $\left[\frac{\mu mol}{m^2 s}\right]$.

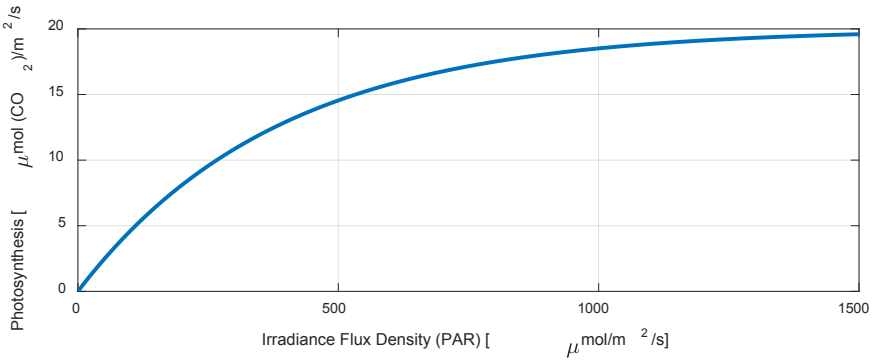

Figure 2.5.4 – Photosynthetic Rate ($A(S_{PAR,R})$). ($A_{max} = 20\left[\frac{\mu mol}{m^2 s}\right]$; $\varepsilon_{p,max} = 0.026$)

Figure 2.5.5 shows the resulting RUE profile for the three canopy cases. At the vertical regions where the radiated light is greater, the photosynthetic rate saturates and the efficiency (RUE) decreases.

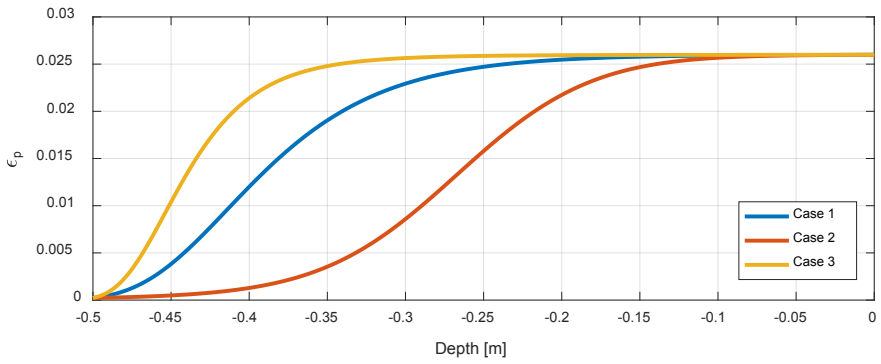

Figure 2.5.5 – Profile of RUE ($\varepsilon_p(z)$). Constant $A_{max} = 20\left[\frac{\mu mol}{m^2 s}\right]$.

Figure 2.5.6 shows the profiles of the simulated rates of biomass accumulation for the three cases. These profiles show that the canopies focus the production of biomass at different vertical regions in the canopy. Canopy 3, which has a larger density of projected leaf area near the top, focused most of the biomass production in that region. In contrast, canopy 2, which as a low density of projected leaf area near the top, concentrates its biomass production near the center of its profile.

In all the three cases considered, almost 100% of the radiated light is captured by the canopy, due to the large values of projected leaf area chosen. Because of this and the fact that the A_{max} is constant within the canopy, the total biomass accumulation rate is equal for the three canopy cases, as shown in figure 2.5.6. In actual canopies, the photosynthetic capacity varies within the vertical profile. In the following example, the biomass accumulation rate of the three canopies is

calculated for a photosynthetic capacity that varies with depth. The overall efficiencies for all these canopies is 0.534%.

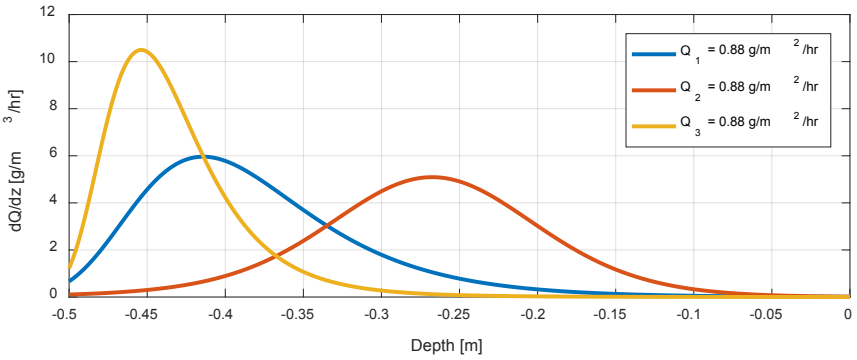

Figure 2.5.6 – Profile of Biomass Accumulation Rate $(dQ(z)/dz)$ [g/m^2/hr]. Constant A_{max}.Total Biomass Accumulated for Case 1, 2 and 3 is 0.88 g/m^2/hr.

Distributed Photosynthetic Capacity

In this example, the photosynthetic capacity is considered to vary within the vertical profile of the canopies. The photosynthetic capacity profile shown in figure 2.5.7 is considered in this example for the simulations of biomass accumulation rate. This example has a larger photosynthetic capacity near the center of the profile.

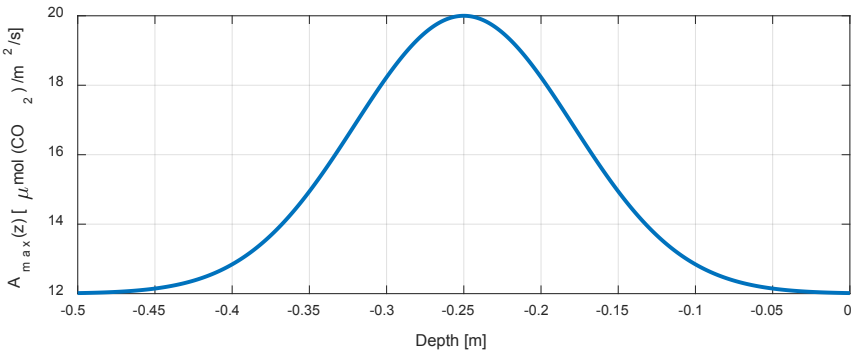

Figure 2.5.7 – Profile of Photosynthetic Capacity $A_{max}(z)$.

In this example, the RUE has a lower value for canopies 1 and 3 compared to canopy 2 at regions where the radiated light is largest. Since canopy 2 has a higher density of projected leaf area near the bottom, it allowed a larger amount of radiated light to penetrate to the center of the canopy, where A_{max} is larger. This translates in a larger RUE for canopy 2 at the center of its vertical profile, where it intercepts a large fraction of its total amount of light captured.

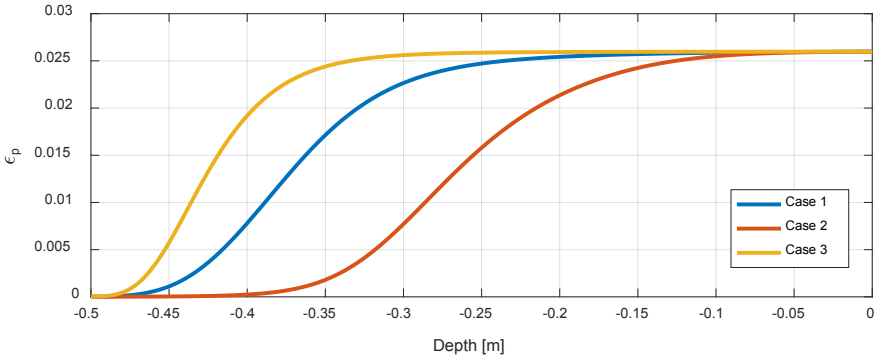

Figure 2.5.8 – Profile of RUE ($\varepsilon_p(z)$). $A_{max}(z)$.

Figure 2.5.9 shows the profile of the simulated biomass accumulation rate for the three canopies. In this example, the second canopy has the largest total biomass accumulation rate. This is because this canopy focuses the biomass production near the center through its architecture (i.e. distribution of projected leaf area density).

The overall efficiency of the canopies 1, 2 and 3 is 0.352%, 0.452% and 0.328%, respectively.

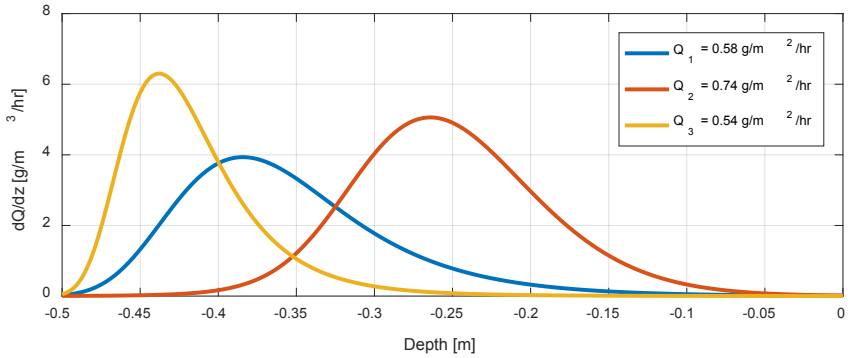

Figure 2.5.9 – Profile of Biomass Accumulation Rate $(dQ(z)/dz)$ [g/m^3/hr]. Distributed $A_{max}(z)$. Total Biomass Accumulated for Case 1, 2 and 3 is 0.58 g/m^2/hr, **0.74 g/m^2/hr** and 0.54 g/m^2/hr.

The above simulation examples showed that the canopy architecture could be used to focus the biomass production in a vertical region of the canopy where the photosynthetic rate is largest.

2.6. References

[1] D. Tilman, C. Balzer, J. Hill, B. Befort, “Global food demand and the sustainable intensification of agriculture,” Proc. Natl. Acad. Sci. USA, vol. 108, pp 2020– 2026, 2011.

[2] D. Tilman, C. Balzer, J. Hill, B. Befort, “Global food demand and the sustainable intensification of agriculture,” Proc. Of National Academy of Sciences of the U.S.A., vol. 108 no. 50, pp 20260-20264, Aug. 2011.

[3] P. L. Pingali, “Green Revolution: Impacts, limits, and the path ahead,” PNAS, vol. 109 no.31, 12302-12308, July 2012.

[4] J. Monteith, “Climate and the efficiency of crop production in Britain,” Phil. Trans. R. Soc. Lond. B. vol. 281, pp. 277-294, 1977.

[5] M. Reynolds, M. Foulkes, G. Slafer, P. Berry, M. Parry, J. Snape, W. Angus, “Railing yield potential,” Journal of experimental Botany, vol. 60, no. 7, pp. 1899-1918, April 2009.

[6] S. Long, X. Zhu, S. Naidu, D. Ort, “Can improvement in photosynthesis increase crop yields,” Plant, cell and environment, vol 29, pp 315-330, 2006.

[7] Bharat P. Singh, Biofuel Crops: Production, Physiology and Genetics.

[8] P. Horton, “Prospects for crop improvement through the genetic manipulation of photosynthesis morphological and biochemical aspects of light capture,” Journal of Experimental Botany, vol. 51, no. suppl. 1, pp. 475-485, Feb., 2000.

[9] D. Reinhardt, C. Kuhlemeier, “Plant Architecture,” EMBO reports vol. 3, no. 9, pp 846-851, 2002.

[10] N. Pérez-Harguindeguy A Y , S. Díaz A , E. Garnier B , S. Lavorel C , H. Poorter D , P. Jaureguiberry A , M. S. Bret-Harte E , W. K. Cornwell F , J. M. Craine G , D. E. Gurvich A , C. Urcelay A , E. J. Veneklaas H , P. B. Reich I , L. Poorter J , I. J. Wright K , P. Ray L , L. Enrico A , J. G. Pausas M , A. C. de Vos F , N. Buchmann N , G. Funes A , F. Quétier A C , J. G. Hodgson O , K. Thompson P , H. D. Morgan Q , H. ter Steege R , M. G. A. van der Heijden S , L. Sack T , B. Blonder U , P. Poschlod V , M. V. Vaieretti A , G. Conti A , A. C. Staver W , S. Aquino X and J. H. C. Cornelissen F, "New handbook for standardised measurement of plant functional traits worldwide," Australian Journal of Botany, vol 61 no 3, pp 167-234, April, 2013.

[11] M. Monsi, T. Saeki, "On the factor light in plant communities and its importance for mater production," Annals of Botany, vol. 95, pp. 549-567, 2005.

[12] L. Taiz, E. Zeiger. *Plant Physiology 3rd Edition*. Sunderland, MA: Sinauer Associates, 2002, pp. 111-143.

[13] D. Biswas, H. Xu, Y. Li, B. Ma, G. Jiang, "Modification of photosynthesis and growth responses to elevated CO_2 by ozone in two cultivars of winter wheat with different years of release," Journal of Experimental Botany, vol. 64, no. 6, pp. 1485-1496, 2013.

[14] C. Chytyk, P. Hucl, G. Gray, "Leaf photosynthetic properties and biomass accumulation of selected western Canadian spring wheat cultivars," Can. J. Plant Sci., vol 91, pp. 305-314, 2011.

[15] P. Sandana, M. Ramirez, D. Pnochet, "Radiation interception and radiation use efficiency of wheat and pea under different P availabilities," Field Crops Research, vol. 127, pp. 44.50, 2012.

[16] S. Peng, K. Cassman, M. Kropff, "Relationship between leaf photosynthesis and nitrogen content of filed-grown rice in tropics," Crop Science, vol .35, pp. 1627-1630, 1995.

[17] R. Emerson, “The relation between the maximum rate of photosynthesis and the concentration of chlorophyll,” Journal of Gen. Physiol. vol. 12, no. 5, pp 609-622, May, 1929.

[18] A. Al-Saidi, Y. Fukuzawa, N. Furukawa, M. Ueno, S. Baba, Y. Kawamitsu, “A system for the measurement of vertical gradients of CO_2, H_2O and air termperature within and above the canopy of plant,” Plant Production Science, vol. 12, no. 2, 139-149, 2009.

[19] R. Moriwaki, M. Kanda, “Vertical profiles of carbon dioxide, temperature and water vapor within and above a suburban canopy layer in winter,” 86th AMS Annual Meeting, 2006.

[20] R. Brooks, L. Flanagan, G. Varney, J. Ehleringer, “Vertical gradient in photosynthetic gas exchange characteristics refixation of respired CO_2 within boreal forest canopies,” Tree Physiology, vol. 17, pp. 1-12, 1997.

[21] W. Huang, Z. Wang, Z. Ma, J. Zhang, J. Want, C. Zhao, “Inversion of vertical distribution of chlorophyll concentration by canopy reflectance spectrum in winter wheat,” Precision Agriculture, vol. 12, pp. 165-178, 2011

[22] W. Huang, W. Yang, R. Pu, S. Yang, “Estimation of nitrogen vertical distribution by bi-directional canopy reflectance in winter wheat,” Sensors, vol. 14, pp. 20347-20359, 2014.

3. Coherent Scattering Analysis and the Constructive-Geometry-Method

This chapter presents a review of coherent electromagnetic scattering analysis, a new coherent radar equation and a new analysis method for coherent scattering analysis, the Constructive-Geometry-Method (CGM).

Coherent radars systems capture both the amplitude and phase of the reflected signal from a target over a span of frequencies. Using the inverse Fourier transform, the time-domain received signal can be obtained from these frequency-domain received signals. The frequency- and time- domain waveforms of the received signals provide different and potentially useful information about the target. Coherent scattering methods aim at relating the coherent transmit and receive signals. The goal of forward coherent-scattering methods is to predict the amplitude and phase of the frequency-domain received signals, from which the time- and frequency-domain waveforms may be found.

Section 3.1 provides an overview of the concepts of coherent scattering analysis. This section also defines and shows a derivation of the coherent radar equation, which relates the transmitted to the received signals of a radar system. The radar response is defined as the ratio of the coherent received to transmitted signals. The dyadic operator that relates the scattered to the incident field is defined as the ‘scattering dyad’, which serves as a coherent dyadic version of the RCS. The scattering response, which is the scalar coherent version of the RCS, is defined as the projection of the scattering dyad onto the transmitted and received polarizations. This section also defines a useful rotation function for the rotation of scattering dyads.

In section 3.2, we derive the scattering dyad for three simple shapes: a facet, a thin dielectric sheet and a finite dielectric cylinder. The solutions found for the scattering dyads of the thin dielectric sheet and dielectric cylinder are compared against full-wave numerical simulations.

Full-wave numerical simulations provide exact solutions to coherent scattering simulations of complex targets. However, these methods have high computational cost, rendering them impractical for Monte Carlo simulations of large complex targets using multiple (60+) realizations. Section 3.3 describes a new scattering analysis method, the Constructive-Geometry-Method (CGM). This is a fast method to compute the radar response and the scattering dyad of complex targets. This is the method used by the radar simulator of wheat canopies, described in chapter 4.

3.1. Coherent Electromagnetic Scattering Analysis

3.1.1. Electromagnetic Wave Theory Fundamentals

The behavior of electromagnetic waves is governed by Maxwell's equations. The propagation and scattering of electromagnetic waves are described by Ampere's and Faraday's laws, which in differential-phasor form are written as shown in (3.1.1) and (3.1.2), respectively. In these equations, $\mathbf{E}(\mathbf{r})$ and $\mathbf{H}(\mathbf{r})$ are the electric and magnetic field intensities, $\mathbf{B}(\mathbf{r})$ and $\mathbf{D}(\mathbf{r})$ are the magnetic and electric flux densities, $\mathbf{J_e}(\mathbf{r})$ and $\mathbf{J_m}(\mathbf{r})$ are the electric and magnetic current density sources.

$$\nabla \times \mathbf{E}(\mathbf{r}) = -j\omega\mathbf{B}(\mathbf{r}) - \mathbf{J_m}(\mathbf{r}) \tag{3.1.1}$$

$$\nabla \times \mathbf{H}(\mathbf{r}) = +j\omega\mathbf{D}(\mathbf{r}) + \mathbf{J_e}(\mathbf{r}) \tag{3.1.2}$$

In an isotropic medium, these two equations may be re-written as shown in (3.1.3-3.1.4), where k and η are the wave number and intrinsic impedance of the medium, respectively. The wave number and intrinsic impedance parameters can be expressed in terms of the relative permittivity, relative permeability, permittivity of free-space and permeability of free-space, as given in (3.1.5-3.1.6).

$$\nabla \times \mathbf{E}(\mathbf{r}) = -jk\eta \quad \mathbf{H}(\mathbf{r}) - \mathbf{J_m}(\mathbf{r}) \tag{3.1.3}$$

$$\nabla \times \mathbf{H}(\mathbf{r}) = +jk\eta^{-1}\,\mathbf{E}(\mathbf{r}) + \mathbf{J_e}(\mathbf{r}) \tag{3.1.4}$$

$$k = \sqrt{\varepsilon_r \mu_r} k_0 = \sqrt{\varepsilon_r \mu_r} \sqrt{\varepsilon_0 \mu_0} \omega \tag{3.1.5}$$

$$\eta = \sqrt{\mu_r / \varepsilon_r} \eta_0 = \sqrt{\mu_r / \varepsilon_r} \sqrt{\mu_0 / \varepsilon_0} \tag{3.1.6}$$

Combining equations (3.1.3) and (3.1.4) results in the differential form of the inhomogeneous Helmholtz wave equation, shown in (3.1.7). In (3.1.7), $\mathbf{Q}(\mathbf{r})$ represents a vector source field and it is described in equation (3.1.8).

$$\nabla \times \nabla \times \mathbf{E}(\mathbf{r}) - k^2 \mathbf{E}(\mathbf{r}) = \mathbf{Q}(\mathbf{r}) \tag{3.1.7}$$

$$\mathbf{Q}(\mathbf{r}) = -jk\eta \mathbf{J_e}(\mathbf{r}) - \nabla \times \mathbf{J_m}(\mathbf{r}) \tag{3.1.8}$$

The wave equation (3.1.9) describes the propagation of a vector field $\mathbf{E}(\mathbf{r})$ due to an input source vector field $\mathbf{Q}(\mathbf{r})$**.** This vector-field input-output system can be characterized by a dyadic function $\overline{\overline{\mathbf{G}}}$**,** known as the dyadic Green's function (DGF) of the Helmholtz wave equation. The electric vector-field can then be written as the convolution of the DGF and the source vector field, as given in (3.1.9). This form of the Helmholtz wave equation is known as the integral Helmholtz equation.

$$\mathbf{E}(\mathbf{r}) = \int d\mathbf{r}' \, \overline{\overline{\mathbf{G}}}(\mathbf{r}, \mathbf{r}') \cdot \mathbf{Q}(\mathbf{r}') = \int d\mathbf{r}' \left[(-jk\eta) \overline{\overline{\mathbf{G}}}(\mathbf{r}, \mathbf{r}') \cdot \mathbf{J_e}(\mathbf{r}') - \nabla \times \overline{\overline{\mathbf{G}}}(\mathbf{r}, \mathbf{r}') \cdot \mathbf{J_m}(\mathbf{r}') \right] \tag{3.1.9}$$

The DGF for a medium with wavenumber k is given by (3.1.10). In (3.1.10), $\mathbf{r}$ is the output or observation position vector and $\mathbf{r}'$ is the input or source position vector. The DGF can also be defined as the solution of the differential equation shown in (3.1.7).

$$\overline{\overline{\mathbf{G}}} = \overline{\overline{\mathbf{G}}}(\mathbf{r}, \mathbf{r}') = \left(\mathbf{I} - \frac{\nabla\nabla}{k^2}\right)\frac{e^{jk|\mathbf{r}-\mathbf{r}'|}}{4\pi|\mathbf{r}-\mathbf{r}'|} \tag{3.1.10}$$

$$\nabla \times \nabla \times \overline{\overline{\mathbf{G}}}(\mathbf{r}, \mathbf{r}') - k^2\overline{\overline{\mathbf{G}}}(\mathbf{r}, \mathbf{r}') = \mathbf{I}\delta(\mathbf{r}-\mathbf{r}') \tag{3.1.11}$$

If the source is located at the origin, and the observation point ($\mathbf{r}$) is in the far-field region, we can make the far-field approximations in (3.1.12-3.1.13), where (3.1.12) is applied to the amplitude and (3.2.13) to the phase term. This DGF far-field approximation is shown in (3.1.14), when the source is at the origin. In (3.1.14), the wave-vector $\mathbf{k}$ and unit wave-vector were used, which are defined in (3.1.15-3.1.16).

$$|\mathbf{r}-\mathbf{r}'| \approx r \tag{3.1.12}$$

$$|\mathbf{r}-\mathbf{r}'| \approx r - \hat{\mathbf{r}}\cdot\mathbf{r}' \tag{3.1.13}$$

$$\overline{\overline{\mathbf{G}}} = \overline{\overline{\mathbf{G}}}(\mathbf{r}, \mathbf{r}') \approx \left(\mathbf{I} - \hat{k}\hat{k}\right)\frac{e^{jkr}}{4\pi r}e^{-j\mathbf{k}\cdot\mathbf{r}'} \tag{3.1.14}$$

$$\mathbf{k} = k\frac{\mathbf{r}}{|\mathbf{r}|} = k\hat{\mathbf{r}} \tag{3.1.15}$$

$$\hat{k} = \hat{r} \tag{3.1.16}$$

In case the source is at a location other than the origin or its distance from the origin cannot be neglected, the far-field approximation of the distance from the source ($\mathbf{r_o}$) to the observation ($\mathbf{r}$) is given by (3.1.17). The DGF far-field approximation is given by (3.1.18), when the source is not at the origin. In this case, the wave-vector and unit wave-vector have the form shown in (3.1.19-3.1.20).

$$|\mathbf{r}-(\mathbf{r_o}+\mathbf{r}')| \approx |\mathbf{r}-\mathbf{r_o}| \;\;,\;\; |\mathbf{r}-(\mathbf{r_o}+\mathbf{r}')| \approx |\mathbf{r}-\mathbf{r_o}| - \frac{\mathbf{r}-\mathbf{r_o}}{|\mathbf{r}-\mathbf{r_o}|}\cdot(\mathbf{r}'-\mathbf{r_o}) \tag{3.1.17}$$

$$\overline{\overline{\mathbf{G}}}(\mathbf{r},\mathbf{r}') \approx \left(\mathbf{I}-\hat{k}\hat{k}\right)\frac{e^{jk|\mathbf{r}-\mathbf{r}_o|}}{4\pi|\mathbf{r}-\mathbf{r}_o|}e^{-j\mathbf{k}\cdot(\mathbf{r}'-\mathbf{r}_o)} \tag{3.1.18}$$

$$\mathbf{k} = k\frac{\mathbf{r}-\mathbf{r_o}}{|\mathbf{r}-\mathbf{r_o}|} \tag{3.1.19}$$

$$\hat{k} = \frac{\mathbf{r}-\mathbf{r_o}}{|\mathbf{r}-\mathbf{r_o}|} \tag{3.1.20}$$

We can define a horizontal $\hat{h}$ and a vertical $\hat{v}$ unit vectors, with respect to a surface normal unit vector $\hat{z}$ and the unit wave-vector (3.1.21-3.1-22).

$$\hat{h}_q = \frac{\hat{z}\times\hat{k}_q}{\left|\hat{z}\times\hat{k}_q\right|} \tag{3.1.21}$$

$$\hat{v}_q = \hat{h}_q \times \hat{k}_q \tag{3.1.22}$$

The horizontal, vertical unit vectors along with the unit wave-vector form a vector basis. Since the electric and magnetic fields are orthogonal to the direction of propagation, defined by $\hat{k}$, they can be fully described in terms of $\hat{h}$ and $\hat{v}$.

In terms of the vertical and horizontal unit vectors, the far-field approximated DGF acquires the form shown in (3.1.23).

$$\overline{\overline{\mathbf{G}}}(\mathbf{r},\mathbf{r}') \approx \left(\hat{v}\hat{v}+\hat{h}\hat{h}\right)\frac{e^{jk|\mathbf{r}-\mathbf{r}_o|}}{4\pi|\mathbf{r}-\mathbf{r}_o|}e^{-j\mathbf{k}\cdot(\mathbf{r}'-\mathbf{r}_o)} \tag{3.1.23}$$

The electric field at a point in the far-field region, with a source at some arbitrary position, is given by the integral for of the Helmholtz equation (3.1.24) or (3.1.25). In (3.1.24-3.1.25), we used the term $\Phi(\mathbf{r}, \mathbf{r}_o)$, which we define as the propagation function (3.1.26).

$$\mathbf{E}(\mathbf{r}) = \Phi(\mathbf{r}, \mathbf{r}_o)\left(\mathbf{I} - \hat{k}\hat{k}\right) \cdot \int d\mathbf{r}' \mathbf{Q}(\mathbf{r}')\ e^{-j\mathbf{k}\cdot(\mathbf{r}'-\mathbf{r}_o)} \tag{3.1.24}$$

$$\mathbf{E}(\mathbf{r}) = \Phi(\mathbf{r}, \mathbf{r}_o)\left(\hat{v}\hat{v} + \hat{h}\hat{h}\right) \cdot \int d\mathbf{r}' \mathbf{Q}(\mathbf{r}')\ e^{-j\mathbf{k}\cdot(\mathbf{r}'-\mathbf{r}_o)} \tag{3.1.25}$$

$$\Phi(\mathbf{r}, \mathbf{r}_o) = \frac{e^{jk|\mathbf{r}-\mathbf{r}_o|}}{4\pi|\mathbf{r} - \mathbf{r}_o|} \tag{3.1.26}$$

These integral forms of the Helmholtz wave equation will be used throughout this document for the analysis of electromagnetic radiation, propagation and scattering.

3.1.2. Coherent Antenna Radiation and Reception

This section provides general expressions that describe the radiation and reception of antennas in terms of antenna parameters and antenna input/output voltages.

3.1.2.1. Antenna Radiation

The Helmholtz wave equation describing the radiated electric field $\mathbf{E}_i(\mathbf{r})$ due to a set of current density sources $\mathbf{J}_{ie}(\mathbf{r})$ and $\mathbf{J}_{im}(\mathbf{r})$ is shown in (3.1.27-3.1.28). The current sources may describe actual currents or equivalent sources.

$$\nabla \times \nabla \times \mathbf{E}_i(\mathbf{r}) - k^2 \mathbf{E}_i(\mathbf{r}) = \mathbf{Q}_i(\mathbf{r}) \tag{3.1.27}$$

$$\mathbf{Q}_i(\mathbf{r}) = -jk\eta \mathbf{J}_{ie}(\mathbf{r}) - \nabla \times \mathbf{J}_{im}(\mathbf{r}) \tag{3.1.28}$$

Alternatively, the radiated or incident field can be written using the integral form of the Helmholtz equation, as shown in (3.1.29).

$$\mathbf{E}_i(\mathbf{r}) = \int d\mathbf{r}' \, \overline{\overline{\mathbf{G}}} \cdot \mathbf{Q}_i(\mathbf{r}') = \int d\mathbf{r}' \left[(-jk\eta) \overline{\overline{\mathbf{G}}} \cdot \mathbf{J}_{ie}(\mathbf{r}') - \nabla \times \overline{\overline{\mathbf{G}}} \cdot \mathbf{J}_{im}(\mathbf{r}') \right] \tag{3.1.29}$$

We define the vector field pattern ($\mathbf{f}(\hat{\mathbf{r}})$) or simply the field pattern with equations (3.1.30-3.1.33), where (V_t) is the transmit voltage, ($\tilde{\mathbf{f}}(\hat{\mathbf{r}})$) is an auxiliary vector field with electric and magnetic components ($\tilde{\mathbf{f}}_{\boldsymbol{e}}(\hat{\mathbf{r}})$) and ($\tilde{\mathbf{f}}_{\boldsymbol{e}}(\hat{\mathbf{r}})$), respectively. The field pattern is a useful term that can be used to describe the radiation pattern maintaining the phase and polarization (vector components in space).

$$\mathbf{f}(\hat{\mathbf{r}}) = \frac{1}{V_t} \tilde{\mathbf{f}}(\hat{\mathbf{r}}) \tag{3.1.30}$$

$$\tilde{\mathbf{f}}(\hat{\mathbf{r}}) = \tilde{\mathbf{f}}_{\boldsymbol{e}}(\hat{\mathbf{r}}) + \tilde{\mathbf{f}}_{\boldsymbol{m}}(\hat{\mathbf{r}}) \tag{3.1.31}$$

$$\tilde{\mathbf{f}}_{\boldsymbol{e}}(\hat{\mathbf{r}}) = \left[\mathbf{I} - \hat{\mathbf{k}}\hat{\mathbf{k}} \right] \int \mathbf{J}_{\boldsymbol{e}}(\mathbf{r}') \, e^{-j\mathbf{k}\cdot(\mathbf{r}' - \mathbf{r}_o)} \, d\mathbf{r}' \tag{3.1.32}$$

$$\tilde{\mathbf{f}}_{\boldsymbol{m}}(\hat{\mathbf{r}}) = -\frac{1}{\eta} \hat{\mathbf{k}} \times \left[\mathbf{I} - \hat{\mathbf{k}}\hat{\mathbf{k}} \right] \int \mathbf{J}_{\boldsymbol{m}}(\mathbf{r}') e^{-j\mathbf{k}\cdot(\mathbf{r}' - \mathbf{r}_o)} \, d\mathbf{r}' \tag{3.1.33}$$

It can be shown that the squared-magnitude (squared complex-modulus) of the field-pattern is related to the antenna gain ($G(\hat{\mathbf{r}})$) and effective aperture ($A(\hat{\mathbf{r}})$) by the expression in (3.1.34),

where (λ) is the wavelength, (Z_a) is the antenna impedance and (η_0) is the free-space intrinsic impedance.

$$|\mathbf{f}(\hat{\mathbf{r}})|^2 = \frac{\lambda^2}{2\pi|Z_a|\eta_0} G(\hat{\mathbf{r}})\, \hat{\mathrm{f}}(\hat{\mathbf{r}}) = \frac{2}{|Z_a|\eta_0} A(\hat{\mathbf{r}})\, \hat{\mathrm{f}}(\hat{\mathbf{r}}) \tag{3.1.34}$$

Replacing equations (3.1.30-3.1.33) into the far-field form in equation (3.1.29) results in the expression for the radiated field at position ($\mathbf{r}$) due to an antenna with field pattern ($\mathbf{f}(\hat{\mathbf{r}})$) with transmitted voltage (V_t) (3.1.35). The radiated magnetic field is determined readily from (3.1.35) and it is shown in (3.1.36).

$$\mathbf{E}_i(\mathbf{r}, \omega) = -jk\eta\, \Phi(\mathbf{r}, \mathbf{r}_o)\, \mathbf{f}(\hat{\mathbf{k}}, \omega) V_t(\omega) \tag{3.1.35}$$

$$\mathbf{H}_i(\mathbf{r}, \omega) = -\frac{1}{\eta} \hat{\mathbf{k}} \times \mathbf{E}(\mathbf{r}, \omega) = jk\, \Phi(\mathbf{r}, \mathbf{r}_o)\, \hat{\mathbf{k}} \times \mathbf{f}(\hat{\mathbf{k}}, \omega) V_t(\omega) \tag{3.1.36}$$

The time domain forms of (3.1.35-3.1.36) can be found by taking the Fourier Transform and they are shown in (3.1.37-3.1.38), where ($*$) is the convolution operator.

$$\mathbf{E}_i(\mathbf{r}, t) = -\frac{\eta}{4\pi|\mathbf{r} - \mathbf{r}_o|c} \frac{\partial}{\partial t} \mathbf{f}(\hat{\mathbf{k}}, t) * \delta(t - r/c) * V_t(t) \tag{3.1.37}$$

$$\mathbf{H}_i(\mathbf{r}, t) = \frac{1}{4\pi|\mathbf{r} - \mathbf{r}_o|c} \frac{\partial}{\partial t} \hat{\mathbf{k}} \times \mathbf{f}(\hat{\mathbf{k}}, t) * \delta(t - r/c) * V_t(t) \tag{3.1.38}$$

3.1.2.2. Antenna Received Voltage

The voltage at the antenna is related to the field at the antenna by the expression in (3.1.39), where $\mathbf{h}(\hat{\mathbf{r}})$ is the effective height vector.

$$V_r = \mathbf{h}(\hat{\mathbf{k}}) \cdot \mathbf{E}_r \tag{3.1.39}$$

The effective height vector of the antenna is related to the field-pattern ($\mathbf{f}(\hat{\mathbf{r}})$), antenna voltage and current by equation (3.1.40).

$$\mathbf{f}(\hat{\mathbf{k}})V_r = -\mathrm{I}_r\, \mathbf{h}(\hat{\mathbf{k}}) \tag{3.1.40}$$

Combining the two previous equations, the frequency- (3.1.41) and time-domain (3.1.42) expressions for the received voltage in terms of the antenna impedance and field-pattern, where the symbol ($\dot{*}$) represents dot product and convolution.

$$V_r(\omega) = -Z_a(\omega)\, \mathbf{f}(\hat{\mathbf{k}}, \omega) \cdot \mathbf{E}_r(\omega) \tag{3.1.41}$$

$$V_r(t) = -Z_a(t) * \mathbf{f}(\hat{\mathbf{k}}, \boldsymbol{t}) \dot{*} \mathbf{E}_r(\mathbf{r}, t) \tag{3.1.42}$$

3.1.3. Scattered Field and the Scattering Dyad

3.1.3.1. Total and Scattered Field

In the previous section, we described the radiated field in free-space due to some source. In practical problems, the electric field radiates in the presence of objects (obstacles or targets). The electric field in the absence of obstacles is known as the incident field. In the presence of obstacles, the electric field is referred to as the total field. The scattered field is defined as the difference between the total and the incident field. Equation (3.1.43) shows an expression for the total field in terms of the incident and the scattered fields.

$$\mathbf{E}(\mathbf{r}) = \mathbf{E}_i(\mathbf{r}) + \mathbf{E}_s(\mathbf{r}) \tag{3.1.43}$$

It can be shown by the surface and volume equivalent principles that the scattered field due to the presence of objects is equivalent to the field radiated in free-space (k_0) due to an equivalent source ($\mathbf{Q}_s(\mathbf{r})$). The scattered field wave equation due to this equivalent source is given in (3.47).

$$\nabla \times \nabla \times \mathbf{E}_s(\mathbf{r}) - {k_0}^2 \mathbf{E}_s(\mathbf{r}) = \mathbf{Q}_s(\mathbf{r}) \tag{3.1.44}$$

The Helmholtz integral equation for the scattered field may then be written in terms of the free-space dyadic Green's function ($\overline{\overline{\mathbf{G}}}$) and the equivalent source ($\mathbf{Q}_s(\mathbf{r}')$), as shown in (3.1.45).

$$\mathbf{E}_s(\mathbf{r}) = \int d\mathbf{r}' \, \overline{\overline{\mathbf{G}}} \cdot \mathbf{Q}_s(\mathbf{r}') \tag{3.1.45}$$

Similarly, we may express the total field in terms of the equivalent source (3.1.46) and the incident field.

$$\mathbf{E}(\mathbf{r}) = \mathbf{E}_i(\mathbf{r}) + \int d\mathbf{r}' \, \overline{\overline{\mathbf{G}}} \cdot \mathbf{Q}_s(\mathbf{r}') \tag{3.1.46}$$

There are two ways for describing obstacles in terms of equivalent sources. Using the surface equivalent principle, homogeneous objects may be described in terms of surface fields (tangential component of the field at the object interface). Alternatively, inhomogeneous or homogeneous objects may be described in terms of the total field inside the object (internal field). These two cases are described in the following sections.

3.1.3.2. Surface Equivalent Source

Using the surface equivalent principle, which can be derived from Maxwell's equations, the field outside a given volume may be completely described by the tangential components to both electric and magnetic fields around the volume. We refer to these tangential fields as either surface fields or equivalent current densities. Using this principle, the equivalent source, defined only at the surface of the object, is given by (3.1.47). The equivalent current densities ($\mathbf{J}_{se}(\mathbf{r})$) and ($\mathbf{J}_{sm}(\mathbf{r})$) are given in (3.1.48-3.1.49) in terms of the total electric and magnetic fields.

$$\mathbf{Q}_s(\mathbf{r}) = -jk\eta\mathbf{J}_{se}(\mathbf{r}) - \nabla \times \mathbf{J}_{sm}(\mathbf{r}) \tag{3.1.47}$$

$$\mathbf{J}_{se}(\mathbf{r}) = +\hat{\mathbf{n}} \times \mathbf{H}(\mathbf{r}) \tag{3.1.48}$$

$$\mathbf{J}_{sm}(\mathbf{r}) = -\hat{\mathbf{n}} \times \mathbf{E}(\mathbf{r}) \tag{3.1.49}$$

The scattered field due to some object is given in terms of the surface equivalent source, as shown in (3.1.50). The far-field approximation of (3.1.50) is given in (3.1.51).

$$\mathbf{E}_s(\mathbf{r}) = \int d\mathbf{r}' \, \bar{\bar{\mathbf{G}}} \cdot \mathbf{Q}_s(\mathbf{r}') = \int d\mathbf{r}' \left[(-jk\eta)\bar{\bar{\mathbf{G}}} \cdot \left(\hat{\mathbf{n}} \times \mathbf{H}(\mathbf{r}')\right) + \nabla \times \bar{\bar{\mathbf{G}}} \cdot \left(\hat{\mathbf{n}} \times \mathbf{E}(\mathbf{r}')\right)\right] \tag{3.1.50}$$

$$\mathbf{E}_s(\mathbf{r}) = -jk\Phi(\mathbf{r}, \mathbf{r}_o) \int d\mathbf{r}' e^{-j\mathbf{k}\cdot(\mathbf{r}'-\mathbf{r}_o)} \left[\eta\left(\hat{v}_s\hat{v}_s + \hat{h}_s\hat{h}_s\right) \cdot \left(\hat{\mathbf{n}} \times \mathbf{H}(\mathbf{r}')\right) - \left(\hat{h}_s\hat{v}_s - \hat{v}_s\hat{h}_s\right) \cdot \left(\hat{\mathbf{n}} \times \mathbf{E}(\mathbf{r}')\right)\right] \tag{3.1.51}$$

Because the surface fields depend on the total field, they also depend on the scattered field. Equations (3.2.50-3.2.51) are useful to solve the scattered field numerically or using analytic approximations. If the total field at the surface (e.g. internal field) is known, this integral equation may be used to find the scattered field.

3.1.3.3. Volume Equivalent Source

Based on the volume-equivalence theorem, it can be shown that an equivalent electric current density can be defined in terms of the total field inside a volume with non-zero electric susceptibility. Similarly, an equivalent current density can be defined in terms of the total magnetic field inside a volume with non-zero magnetic susceptibility.

The total volume equivalent source ($\mathbf{Q}_s(\mathbf{r})$) due to both electric and magnetic current densities is given by (3.1.52). The current densities in (3.1.52) are defined by (3.1.53-3.1.54) in terms of the electric and the magnetic susceptibilities.

$$\mathbf{Q}_s(\mathbf{r}) = -jk\eta\mathbf{J}_{se}(\mathbf{r}) + \nabla \times \mathbf{J}_{sm}(\mathbf{r}) \tag{3.1.52}$$

$$\mathbf{J}_{se}(\mathbf{r}) = +j\omega\varepsilon_0\chi_e(\mathbf{r})\mathbf{E}(\mathbf{r}) = +j\omega\varepsilon_0[\varepsilon_r(\mathbf{r}) - 1]\mathbf{E}(\mathbf{r}) \tag{3.1.53}$$

$$\mathbf{J}_{sm}(\mathbf{r}) = +\chi_m(\mathbf{r})\nabla \times \mathbf{H}(\mathbf{r}) = +[\mu_r(\mathbf{r}) - 1]\nabla \times \mathbf{H}(\mathbf{r}) \tag{3.1.54}$$

The scattered field due to a volume equivalent source ($\mathbf{Q}_s(\mathbf{r}')$) can then be written using the integral Helmholtz equation (3.1.55). This equation is known as the volume integral equation.

$$\mathbf{E}_s(\mathbf{r}) = \int d\mathbf{r}'\, \overline{\overline{\mathbf{G}}} \cdot \mathbf{Q}_s(\mathbf{r}') = \int d\mathbf{r}' \left[k^2\overline{\overline{\mathbf{G}}} \cdot [\varepsilon_r(\mathbf{r}') - 1]\mathbf{E}(\mathbf{r}') - \nabla \times \overline{\overline{\mathbf{G}}} \cdot [\mu_r(\mathbf{r}') - 1]\nabla \times \mathbf{H}(\mathbf{r}')\right] \tag{3.1.55}$$

In this document, all considered objects are non-magnetic. The volume integral equation simplifies to that given in (3.1.56) and its far-field expression to that given in (3.1.57).

$$\mathbf{E}_s(\mathbf{r}) = k^2 \int d\mathbf{r}' \left[\overline{\overline{\mathbf{G}}} \cdot [\varepsilon_r(\mathbf{r}') - 1]\mathbf{E}(\mathbf{r}')\right] \tag{3.1.56}$$

$$\mathbf{E}_s(\mathbf{r}) = \Phi(\mathbf{r}, \mathbf{r}_o)\, k^2 \left(\mathbf{I} - \hat{k}\hat{k}\right) \int d\mathbf{r}' \left[e^{-j\mathbf{k}\cdot(\mathbf{r}'-\mathbf{r}_o)} \cdot [\varepsilon_r(\mathbf{r}') - 1]\mathbf{E}(\mathbf{r}') \right] \tag{3.1.57}$$

3.1.3.4. The Scattering Dyad

Given some equivalent source ($\mathbf{Q}_s(\mathbf{r}')$) representing an obstacle, the scattered field ($\mathbf{E}_s(\mathbf{r})$) can be determined using the Helmholtz integral equation (3.1.58), where $\overline{\overline{\mathbf{G}}}(\mathbf{r}, \mathbf{r}')$ is the dyadic Green's function.

$$\mathbf{E}_s(\mathbf{r}) = \int d\mathbf{r}'\, \overline{\overline{\mathbf{G}}}(\mathbf{r}, \mathbf{r}') \cdot \mathbf{Q}_s(\mathbf{r}') \tag{3.1.58}$$

Using the far-field approximation of the DGF (3.1.59), with source at an arbitrary location, the scattered field takes the form in (3.1.60). In (3.1.60), we used the propagation function $\Phi_r(\mathbf{r}, \mathbf{r}_o)$ defined by (3.1.61).

$$\overline{\overline{\mathbf{G}}}(\mathbf{r}, \mathbf{r}') \approx \left(\mathbf{I} - \hat{k}_s\hat{k}_s\right) \Phi(\mathbf{r}, \mathbf{r}_o)\, e^{-j\mathbf{k}_s\cdot(\mathbf{r}'-\mathbf{r}_o)} \tag{3.1.59}$$

$$\mathbf{E}_s(\mathbf{r}) = \Phi_r(\mathbf{r}, \mathbf{r}_o) \left(\mathbf{I} - \hat{k}_s\hat{k}_s\right) \cdot \int d\mathbf{r}' e^{-j\mathbf{k}_s\cdot(\mathbf{r}'-\mathbf{r}_o)}\, \mathbf{Q}_s(\mathbf{r}') \tag{3.1.60}$$

$$\Phi_r(\mathbf{r}, \mathbf{r}_o) = \frac{e^{jk|\mathbf{r}-\mathbf{r}_o|}}{4\pi|\mathbf{r} - \mathbf{r}_o|} \tag{3.1.61}$$

The scattering wave-vector $\mathbf{k}_s$ and its unit vector used in (3.1.60) are defined in (3.1.62-3.1.63).

$$\mathbf{k}_s = k\frac{\mathbf{r} - \mathbf{r}_o}{|\mathbf{r} - \mathbf{r}_o|} \tag{3.1.62}$$

$$\hat{k}_s = \frac{\mathbf{r} - \mathbf{r_o}}{|\mathbf{r} - \mathbf{r_o}|} \tag{3.1.63}$$

We define the 'scattering dyad' as the linear operator that transforms some incident field $\mathbf{E_i}(\mathbf{r_o}, \mathbf{k_i})$ to the term in the left-hand-side of (3.1.64). In (3.1.64), the incident field is evaluated at the center of the obstacle (scattering center) $\mathbf{r_o}$.

$$\left(\mathbf{I} - \hat{k}_s\hat{k}_s\right) \cdot \int d\mathbf{r}' e^{-j\mathbf{k_s}\cdot(\mathbf{r}'-\mathbf{r}_o)}\, \mathbf{Q_s}(\mathbf{r}') \approx \bar{\bar{\mathbf{F}}}(\mathbf{k_s}, \mathbf{k_i}) \cdot \mathbf{E_i}(\mathbf{r_o}, \mathbf{k_i}) \tag{3.1.64}$$

Using the definition of the 'scattering dyad,' the scattered field takes the form shown in (3.1.65).

$$\mathbf{E_s}(\mathbf{r}) = \Phi_r(\mathbf{r}, \mathbf{r_o})\, \bar{\bar{\mathbf{F}}}(\mathbf{k_s}, \mathbf{k_i}) \cdot \mathbf{E_i}(\mathbf{r_o}, \mathbf{k_i}) \tag{3.1.65}$$

The radar-cross-section (σ) is defined by equation (3.1.66). The relationship between the radar-cross-section and the scattering dyad is given in (3.1.67). Thus, the scattering dyad can be considered as the coherent-dyadic form of the radar-cross-section.

$$\sigma = \lim_{|\mathbf{r}-\mathbf{r_o}|\to\infty} 4\pi|\mathbf{r} - \mathbf{r_o}|^2 \frac{\left|\hat{f}_s \cdot \mathbf{E_s}(\mathbf{r})\right|^2}{\left|\hat{f}_i \cdot \mathbf{E_i}(\mathbf{r_o})\right|^2} \tag{3.1.66}$$

$$\sigma = \frac{1}{4\pi}\left|\hat{f}_s \cdot \bar{\bar{\mathbf{F}}} \cdot \hat{f}_i\right|^2 \tag{3.1.67}$$

A similar term that is used in scattering theory is the 'scattering amplitude' ($\bar{\bar{\mathbf{S}}}(\mathbf{k_s}, \mathbf{k_i})$ **)**. The scattering amplitude is defined by (3.1.68) and its relationship to the radar-cross-section is show in (3.1.69). The scattering amplitude is usually used assuming a plane-wave incident field. Because of that, the 4π denominator in the propagation function is absorbed by the scattering amplitude. Since the form of the 'scattering dyad' maintains the form of the propagation function,

it simplifies the use of incident and reflected propagation function, including the case of spherical incident propagation. For this reason, we will use the 'scattering dyad' in this document.

$$\mathbf{E}_s(\mathbf{r}) = \frac{e^{jk_s|\mathbf{r}-\mathbf{r}_o|}}{|\mathbf{r}-\mathbf{r}_o|}\,\bar{\bar{\mathbf{S}}}(\mathbf{k}_s,\mathbf{k}_i)\cdot\,\mathbf{E}_i(\mathbf{r}_o,\mathbf{k}_i) \tag{3.1.68}$$

$$\sigma = \lim_{r\to\infty} 4\pi r^2 \frac{\left|\hat{f}_s\cdot\mathbf{E}_s(\mathbf{r})\right|^2}{\left|\hat{f}_i\cdot\mathbf{E}_{io}(\mathbf{r})\right|^2} = \,4\pi\left|\hat{f}_s\cdot\bar{\bar{\mathbf{S}}}\cdot\hat{f}_i\right|^2 \tag{3.1.69}$$

The relationship between the 'scattering dyad' **($\bar{\bar{\mathbf{F}}}$)** defined here and the classical scattering amplitude **($\bar{\bar{\mathbf{S}}}$)** is given in (3.1.70).

$$\bar{\bar{\mathbf{F}}} = 4\pi\,\bar{\bar{\mathbf{S}}} \tag{3.1.70}$$

3.1.3.5. Rotation Operator and Rotated Scattering Dyad

If the scattering dyad of a target is known at a given reference frame, the scattering dyad of the same target with a different orientation can be readily found using linear transformations.

We first consider the 'base' reference frame for which the scattering dyad is known. Vectors in this reference frame will be denoted with a '*b*' superscript. In this reference frame, the scattered field $\mathbf{E}_s{}^b(\mathbf{r}_r{}^b)$ can be written in terms of the incident field $\mathbf{E}_i{}^b(\mathbf{r}_o{}^b)$ and the known scattering dyad $\bar{\bar{\mathbf{F}}}^b(\mathbf{k}_s{}^b,\mathbf{k}_i{}^b)$**,** as given in (3.1.71).

$$\mathbf{E}_s{}^b(\mathbf{r}_r{}^b) = \,\Phi_r(\mathbf{r}_r{}^b,\mathbf{r}_o{}^b)\,\bar{\bar{\mathbf{F}}}^b(\mathbf{k}_s{}^b,\mathbf{k}_i{}^b)\cdot\,\mathbf{E}_i{}^b(\mathbf{r}_o) \tag{3.1.71}$$

Since we used the far-field approximation in defining the scattering dyad, the scattered field at or near the scattering center cannot be obtained using equation (3.1.71). However, for simplicity we may define a 'fictitious scattered field' located at the scattering center $\mathbf{E_s}^{\boldsymbol{b}}(\mathbf{r_o}^{\boldsymbol{b}})$, given by (3.1.72).

$$\mathbf{E_s}^{\boldsymbol{b}}(\mathbf{r_o}^{\boldsymbol{b}}) = \bar{\bar{\mathbf{F}}}^{\boldsymbol{b}}(\mathbf{k_s}^{b}, \mathbf{k_i}^{b}) \cdot \mathbf{E_i}^{\boldsymbol{b}}(\mathbf{r_o}^{\boldsymbol{b}}) \tag{3.1.72}$$

We consider a reference frame, which is a rotated version of the previous reference frame. The vectors in this reference frame are written without superscripts. The rotation center is the scattering center, so that $\mathbf{r_o}^{\boldsymbol{b}} = \mathbf{r_o}$. In the rotated reference frame the 'fictitious' scattered field and the incident field at the scattering center behave as given by (3.1.73), where $\bar{\bar{\mathbf{F}}}(\mathbf{k}_s, \mathbf{k}_i)$ is the rotated scattering dyad.

$$\mathbf{E_s}(\mathbf{r}_o) = \bar{\bar{\mathbf{F}}}(\mathbf{k}_s, \mathbf{k}_i) \cdot \mathbf{E_i}(\mathbf{r_o}) \tag{3.1.73}$$

We define $\bar{\bar{\mathbf{T}}}(\alpha, \theta, \phi)$ as the rotation matrix, described by equation (3.1.74). This linear operator applies three rotations with angles α, θ and ϕ and achieve any orientation. The first rotation with angle α is a rotation about the 'z' axis. The second rotation with angle θ is the elevation rotation, which rotates the vector about its 'y' axis. The last rotation with angle ϕ is the azimuth rotation and it is applied about the 'z' axis.

$$\bar{\bar{\mathbf{T}}} = \bar{\bar{\mathbf{T}}}(\alpha, \theta, \phi) = \begin{bmatrix} \cos\phi & -\sin\phi & 0 \\ \sin\phi & \cos\phi & 0 \\ 0 & 0 & 1 \end{bmatrix} \begin{bmatrix} \cos\theta & 0 & \sin\theta \\ 0 & 1 & 0 \\ -\sin\theta & 0 & \cos\theta \end{bmatrix} \begin{bmatrix} \cos\alpha & -\sin\alpha & 0 \\ \sin\alpha & \cos\alpha & 0 \\ 0 & 0 & 1 \end{bmatrix} \tag{3.1.74}$$

Using the rotation matrix, we can relate the vector fields and vectors from the base reference frame to the rotated reference frame. These relations are shown in (3.1.75-3.1.78).

$$\mathbf{E_s}(\mathbf{r}_o) = \overline{\overline{\mathbf{T}}} \cdot \mathbf{E_s}^{\boldsymbol{b}}(\mathbf{r}_o) \tag{3.1.75}$$

$$\mathbf{E_i}(\mathbf{r}_o) = \overline{\overline{\mathbf{T}}} \cdot \mathbf{E_i}^{\boldsymbol{b}}(\mathbf{r}_o) \tag{3.1.76}$$

$$\mathbf{k}_i = \overline{\overline{\mathbf{T}}} \cdot \mathbf{k}_i{}^{b} \tag{3.1.77}$$

$$\mathbf{k}_s = \overline{\overline{\mathbf{T}}} \cdot \mathbf{k}_s{}^{b} \tag{3.1.78}$$

Combining (3.1.75-3.1.78), the scattered field in the far-field can be written in terms of the scattering dyad of the base reference frame, as shown in (3.1.79).

$$\mathbf{E_s}(\mathbf{r}_r) = \Phi_r(\mathbf{r}_r, \mathbf{r}_o)\left[\overline{\overline{\mathbf{T}}} \cdot \overline{\overline{\mathbf{F}}}^{\boldsymbol{b}}\left(\overline{\overline{\mathbf{T}}}^{\mathbf{-1}} \cdot \mathbf{k}_s, \overline{\overline{\mathbf{T}}}^{\mathbf{-1}} \cdot \mathbf{k}_i\right) \cdot \overline{\overline{\mathbf{T}}}^{\mathbf{-1}}\right] \cdot \mathbf{E_i}(\mathbf{r}) \tag{3.1.79}$$

Similarly, the equivalent scattering dyad in the rotated reference frame can be found in terms of the scattering dyad of the base reference frame. To simplify notation, we define the rotation function $Rot\left(\overline{\overline{\mathbf{F}}}^{\boldsymbol{b}}(\mathbf{k}_s, \mathbf{k}_i), \mathbf{o}\right)$ as the rotation of the base scattering dyad $\overline{\overline{\mathbf{F}}}^{\boldsymbol{b}}(\mathbf{k}_s, \mathbf{k}_i)$ in the orientation given by the vector **'o'** containing the three rotation angles (3.1.80-3.1.81).

$$\overline{\overline{\mathbf{F}}}(\mathbf{k}_s, \mathbf{k}_i) = \overline{\overline{\mathbf{T}}} \cdot \overline{\overline{\mathbf{F}}}^{\boldsymbol{b}}\left(\overline{\overline{\mathbf{T}}}^{\mathbf{-1}} \cdot \mathbf{k}_s, \overline{\overline{\mathbf{T}}}^{\mathbf{-1}} \cdot \mathbf{k}_i\right) \cdot \overline{\overline{\mathbf{T}}}^{\mathbf{-1}} = Rot\left(\overline{\overline{\mathbf{F}}}^{\boldsymbol{b}}(\mathbf{k}_s, \mathbf{k}_i), \mathbf{o}\right) \tag{3.1.80}$$

$$\mathbf{o} = [\alpha, \theta, \phi]^{\boldsymbol{T}} \tag{3.1.81}$$

3.1.4. The Coherent Radar Equation

The coherent radar equation describes the relationship between the transmit and receive antenna voltages of a radar system. In contrast to the classical (incoherent) radar equation, the coherent radar equation maintains the phase information of the signal. The coherent radar equation is derived from first principles (Maxwell's Equations) and it is a useful concept for coherent scattering analysis. It is also used in the Constructive-Geometry-Method (CGM), which is described in section 3.3.

This equation takes into account the antenna radiation pattern, accounting for its system response and variations of polarization with radiation direction. It also accounts for the spherical spreading of the incident field and the reflected/scattered field. It uses the 'scattering dyad' to treat the reflection from the target as a linear transformation from the incoming incident field, evaluated at the scattering center, to the scattered field that is captured by the receive antenna.

In section 3.1.2, it was shown that the phasor of the incident vector field due to transmitting antenna has the form shown in (3.1.82). In this equation, V_t is the voltage at the antenna feed, $\mathbf{f_t}(\hat{\mathbf{k}}_i)$ is the field pattern of the antenna, $\Phi_t(\mathbf{r}, \mathbf{r}_o)$ is the propagation function, k is the wave number of the medium and η is the intrinsic impedance of the medium. The propagation function $\Phi_t(\mathbf{r_o}, \mathbf{r}_t)$ from the source position (transmit antenna position) $\mathbf{r}_t$ to the observation point (scattering center $\mathbf{r}_o$) is given in (3.1.83). The incident wave vector used in (3.1.82) is defined in (3.1.84).

$$\mathbf{E}_i(\mathbf{r}) = -jk\eta\, \Phi_t(\mathbf{r_o}, \mathbf{r}_t)\, \mathbf{f_t}(\hat{\mathrm{k}}_i) V_t \tag{3.1.82}$$

$$\Phi_t(\mathbf{r_o}, \mathbf{r}_t) = \frac{e^{jk|\mathbf{r_o}-\mathbf{r}_t|}}{4\pi|\mathbf{r_o}-\mathbf{r}_t|} \tag{3.1.83}$$

$$\mathbf{k_i} = k\frac{\mathbf{r_o}-\mathbf{r_t}}{|\mathbf{r_o}-\mathbf{r_t}|} \tag{3.1.84}$$

In section 3.1.2, it was shown that the voltage at the antenna feed due to the captured field at the antenna aperture may be written in terms of the antenna impedance and the field pattern, as shown in (3.1.85).

$$V_r(\omega) = -Z_a(\omega)\,\mathbf{f_r}(\hat{\mathbf{k}}, \omega) \cdot \mathbf{E}_r(\omega) \tag{3.1.85}$$

In the previous section, the scattering dyad was defined to act as the linear operator between the incident field evaluated at the scattering center and the scattered field. The scattered field at the receiver antenna location ($\mathbf{r_r}$) in the far-field region from the target is given by equation (3.1.86). The scattering wave vector, used in (3.1.86), is defined in (3.1.87).

$$\mathbf{E_s}(\mathbf{r_r}) = \Phi_r(\mathbf{r_r}, \mathbf{r_o})\,\bar{\bar{\mathbf{F}}}(\mathbf{k_s}, \mathbf{k_i}) \cdot \mathbf{E_i}(\mathbf{r_o}, \mathbf{k_i}) \tag{3.1.86}$$

$$\mathbf{k_s} = k\frac{\mathbf{r_r}-\mathbf{r_o}}{|\mathbf{r_r}-\mathbf{r_o}|} \tag{3.1.87}$$

Combining (3.1.82), (3.1.85) and (3.1.86), the receive voltage takes the form shown in equation (3.1.88), which is the coherent radar equation.

$$V_r(\omega) = jk\eta Z_a\,\Phi_r(\mathbf{r_r}, \mathbf{r_o})\,\Phi_t(\mathbf{r_o}, \mathbf{r}_t)\;\; \mathbf{f_r}(\hat{\mathrm{k}}_s, \omega) \cdot\; \bar{\bar{\mathbf{F}}}(\mathbf{k_s}, \mathbf{k_i}) \cdot\; \mathbf{f_t}(\hat{\mathrm{k}}_i, \omega)\, V_t(\omega) \tag{3.1.88}$$

If we evaluate the power of the receive signal in (3.1.88), we obtain the classical (incoherent) radar equation, shown in (3.1.89).

$$P_r(\omega) = P_t(\omega)\left[\frac{G_r(\mathbf{k_s})G_t(\mathbf{k_i})\lambda^2\sigma_{pq}(\mathbf{k_s},\mathbf{k_i})}{(4\pi)^3|\mathbf{r_o}-\mathbf{r_t}|^2|\mathbf{r_r}-\mathbf{r_o}|^2}\right] \tag{3.1.89}$$

The squared-amplitude of the factors in (3.1.88) are shown in (3.1.90-3.1.95).

$$|jk\eta Z_a|^2 = \eta^2|Z_a|^2\frac{4\pi^2}{\lambda^2} \tag{3.1.90}$$

$$|\Phi_t(r_{ot})\,\Phi_r(r_{ro})|^2 = \frac{1}{(4\pi)^2|\mathbf{r_r}-\mathbf{r_o}|^2|\mathbf{r_o}-\mathbf{r_t}|^2} \tag{3.1.91}$$

$$\left|\mathbf{f_r}(\hat{\mathrm{k}}_s)\cdot\bar{\bar{\mathbf{F}}}(\mathbf{k_s},\mathbf{k_i})\cdot\mathbf{f_r}(\hat{\mathrm{k}}_i)\right|^2 = \frac{\lambda^4 G_r G_t}{4\pi^2\eta^2|Z_a|^2}\left|\hat{p}\cdot\bar{\bar{\mathbf{F}}}(\mathbf{k_s},\mathbf{k_i})\cdot\hat{q}\right|^2 \tag{3.1.92}$$

$$\sigma_{pq}(\mathbf{k_s},\mathbf{k_i}) = \frac{1}{4\pi}\left|\hat{p}\cdot\bar{\bar{\mathbf{F}}}(\mathbf{k_s},\mathbf{k_i})\cdot\hat{q}\right|^2 \tag{3.1.93}$$

$$\hat{p} = \hat{f_r}(\hat{\mathrm{k}}_s) \tag{3.1.94}$$

$$\hat{q} = \hat{f_t}(\hat{\mathrm{k}}_i) \tag{3.1.95}$$

3.1.5. Radar-Response and Scattering-Response

We define the “radar response” as the ratio of the transmit to the receive signals at the antenna ports, as shown in (3.1.96). This parameter is used in chapter 5 for model-based radar analysis. It is also the main output of the radar simulator, described in chapter 4.

$$H_t(f) = V_r(f)/V_t(f) \tag{3.1.96}$$

The radar response may be found using the coherent radar equation, in the form shown in (3.1.97).

$$H_t(f) = \left[jk\eta Z_a \, \Phi_r(\mathbf{r_r}, \mathbf{r_o}) \, \Phi_t(\mathbf{r_o}, \mathbf{r}_t)\right]\left[\, \mathbf{f_r} \cdot \, \bar{\bar{\mathbf{F}}}_{\boldsymbol{o}}(\mathbf{k_s}, \mathbf{k_i}) \cdot \mathbf{f_t}\right] \tag{3.1.97}$$

Another parameter that is referred to throughout this document is the "scattering response," which we define as $F_{o,qp}(f)$ in (3.1.98). The scattering response is the scalar function that results from pre- and post- multiplying the scattering dyad by the polarization unit vectors of the transmit and receive antennas, respectively.

$$F_{o,qp}(f) = F_{o,qp}(\mathbf{k_s}, \mathbf{k_i}) = \left[\, \hat{q} \cdot \, \bar{\bar{\mathbf{F}}}_{\boldsymbol{o}}(\mathbf{k_s}, \mathbf{k_i}) \cdot \hat{p}\right] = \left[jk\eta Z_a \, \Phi_r(\mathbf{r_r}, \mathbf{r_o}) \, \Phi_t(\mathbf{r_o}, \mathbf{r}_t)|\mathbf{f_r}|_v|\mathbf{f_t}|_v\right]^{-1} H_t(f) \tag{3.1.98}$$

The frequency- and time- domain radar waveforms are given by (3.1.99) and (3.1.100), respectively.

$$\sigma_{qp}(f) = \frac{1}{4\pi} \left|F_{o,qp}(f)\right|^2 \tag{3.1.99}$$

$$\sigma_{qp}(t) = \frac{1}{4\pi B} \left|F_{o,qp}(t)\right|^2 \tag{3.1.100}$$

3.2. Scattering Dyad of Simple Targets

3.2.1. Scattering Dyad of Simple Targets

A simple target is defined as a target whose scattering dyad is intrinsically defined from first principles and analytic approximations. In contrast, complex targets have scattering dyads that are defined in terms of a collection of scattering dyads of simple or other complex targets. The main property of a simple target is that it has a single scattering point, which is the scattering center. In contrast, a complex target has multiple scattering points and one overall scattering center.

The scattering center of target is assumed to be in the far-field region of the source, so that the incident wave at the scattering center behaves as a plane-wave with wave-vector $\mathbf{k}_i$, defined in (3.2.1). Similarly, the scattered field at the source is considered to be in the far-field region with respect to the scattering center. Thus, the scattered field near the source behaves as a plane-wave with wave-vector $\mathbf{k}_s$, defined in (3.2.2).

$$\mathbf{k}_i = k\frac{\mathbf{r}_o - \mathbf{r}_t}{|\mathbf{r}_o - \mathbf{r}_t|} \tag{3.2.1}$$

$$\mathbf{k}_s = k\frac{\mathbf{r}_r - \mathbf{r}_o}{|\mathbf{r}_r - \mathbf{r}_o|} \tag{3.2.2}$$

As shown in previous sections, the scattered field has the form shown in (3.2.3) when evaluated in the far-field region. The equivalent source ($\mathbf{Q}_s$) inside the integral, depends on the total field at the source, which depends on the incident field.

$$\mathbf{E}_{\boldsymbol{s}}(\mathbf{r}) = \Phi_r(\mathbf{r}, \mathbf{r}_{\boldsymbol{o}}) \ \left(\mathbf{I} - \hat{k}_s\hat{k}_s\right) \cdot \int d\mathbf{r}' e^{-j\mathbf{k}_{\boldsymbol{s}}\cdot(\mathbf{r}'-\mathbf{r}_o)} \ \mathbf{Q}_{\boldsymbol{s}}(\mathbf{r}', \mathbf{E}_{\boldsymbol{i}}(\mathbf{r}_{\boldsymbol{o}}, \mathbf{k}_{\boldsymbol{i}})) \tag{3.2.3}$$

The scattering dyad is defined as the linear transformation between the incident and the scattered field, as shown in (3.2.4).

$$\mathbf{E}_{\boldsymbol{s}}(\mathbf{r}) = \Phi_r(\mathbf{r}, \mathbf{r}_{\boldsymbol{o}}) \ \ \bar{\bar{\mathbf{F}}}(\mathbf{k}_{\boldsymbol{s}}, \mathbf{k}_{\boldsymbol{i}}) \cdot \mathbf{E}_{\boldsymbol{i}}(\mathbf{r}_{\boldsymbol{o}}, \mathbf{k}_{\boldsymbol{i}}) \tag{3.2.4}$$

The scattering dyad may be solved with the following steps:

1. Choose an approximated geometry for which the total field can be solved at its surface (or inside its volume). Find the total field at its surface (or inside its volume).
2. Determine the surface or volume equivalent source $\mathbf{Q}_{\boldsymbol{s}}$ using the total field found in (1).
3. Evaluate the integral in (3.2.3) using the equivalent source found in (2).
4. Factor out the scattering dyad from the expression found in (3).

The only finite shape for which step (1) can be solved exactly is the sphere. All other finite shapes require the use of analytic approximation.

Once the scattering dyad of a simple target is known, the received signal can be determined using the coherent radar equation for a simple target, given by (3.2.5).

$$V_r(\omega) = jk\eta Z_a \ \Phi_r(\mathbf{r}_{\boldsymbol{r}}, \mathbf{r}_{\boldsymbol{o}}) \ \Phi_t(\mathbf{r}_{\boldsymbol{o}}, \mathbf{r}_t) \ \ \mathbf{f}_{\boldsymbol{r}}\left(\hat{\mathbf{k}}_{\boldsymbol{s}}, \omega\right) \cdot \ \bar{\bar{\mathbf{F}}}(\mathbf{k}_{\boldsymbol{s}}, \mathbf{k}_{\boldsymbol{i}}) \cdot \ \mathbf{f}_{\boldsymbol{t}}(\hat{\mathbf{k}}_{\boldsymbol{i}}, \omega) V_t(\omega) \tag{3.2.5}$$

3.2.2. Scattering from a Facet of a PEC or Dielectric Surface

As it was discussed in section 3.13, it suffices to determine the scattering dyad in a single reference frame. Using a scattering dyad at a base reference frame, scattering dyads at other reference frames can be readily obtained. We determine the scattering dyad following the steps laid out in (3.2.1).

3.2.2.1. Total Field of Approximated Geometry

We choose the infinite flat surface as the approximated geometry for the flat facet.

We assume that the medium above the surface (medium 0) is free-space. The medium below the surface will be referred to as medium one, and it may be a dielectric medium or a perfect electric conductor (PEC).

The total field at the surface of the infinite flat surface is the sum of the incident and the reflected fields (3.2.6).

$$\mathbf{E}(\mathbf{r}) = \mathbf{E}_{\boldsymbol{i}}(\mathbf{r}) + \mathbf{E}_{\boldsymbol{r}}(\mathbf{r}) \tag{3.2.6}$$

The incident and reflected fields can be decomposed in terms of their $\hat{v}$ and $\hat{h}$ components as shown in (3.2.7-3.2.8).

$$\mathbf{E}_{\boldsymbol{i}}(\mathbf{r}) = \left(\hat{v}_i E_{iv} + \hat{h}_i E_{ih}\right) e^{j\mathbf{k_i}\cdot\mathbf{r}} \tag{3.2.7}$$

$$\mathbf{E}_{\boldsymbol{r}}(\mathbf{r}) = \left(\hat{v}_r E_{rv} + \hat{h}_r E_{rh}\right) e^{j\mathbf{k_r}\cdot\mathbf{r}} \tag{3.2.8}$$

For a flat surface, the wave vector of the reflected field can be readily found and it is given by (3.2.9), where k_{iz} is the z-component of the incident wave vector.

$$\mathbf{k_r} = \mathbf{k_i} - 2k_{iz}\hat{z} \tag{3.2.9}$$

Using the relations in (3.2.10-3.2.11), we can determine the horizontal and vertical unit vectors of the reflected field with respect to those of the incident field, where the term k_{inz} is defined by (3.2.12).

$$\hat{h}_r = \frac{\hat{z} \times \hat{k}_r}{\left|\hat{z} \times \hat{k}_r\right|} = \frac{\hat{z} \times \hat{k}_i - \hat{z} \times 2k_{inz}\hat{z}}{\left|\hat{z} \times \hat{k}_i - \hat{z} \times 2k_{inz}\hat{z}\right|} = \hat{h}_i \tag{3.2.10}$$

$$\hat{v}_r = \hat{h}_r \times \hat{k}_r = \hat{h}_i \times \hat{k}_i - 2k_{inz}\hat{h}_i \times \hat{z} = \hat{v}_i - 2k_{inz}\hat{h}_i \times \hat{z} \tag{3.2.11}$$

$$k_{inz} = k_{iz}/k \tag{3.2.12}$$

Using boundary conditions it can be shown that the vector components of the incident and reflected fields are related linearly, as shown in (3.2.13-3.2.14). These factors of proportionality are known as the Fresnel reflection coefficients, and they are defined by equation (3.2.15) and (3.2.16). In (3.2.15-3.2.16), k, k_1, k_{iz} and k_{1iz} are the wave number in medium 0, the wave number in medium 1, the z-component of the incident wave-vector $\mathbf{k}_i$ in medium 0 and the z-component of $\mathbf{k}_i$ in medium 1.

$$E_{rh} = R_h E_{ih} \tag{3.2.13}$$

$$E_{rv} = R_v E_{iv} \tag{3.2.14}$$

$$R_v = \frac{{k_1}^2 k_{iz} - k^2 k_{1iz}}{{k_1}^2 k_{iz} + k^2 k_{1iz}} \tag{3.2.15}$$

$$R_h = \frac{k_{iz} - k_{1iz}}{k_{iz} + k_{1iz}} \tag{3.2.16}$$

Combining (3.2.6-3.2.16) results in the total electric and magnetic fields at the surface, as given by (3.2.17-3.2.18). In these equations, $\mathbf{k}_{i\rho}$ and $\boldsymbol{\rho}'$ are the horizontal wave-vector and horizontal position vector, respectively.

$$\mathbf{E}_r(\boldsymbol{\rho}') = \left[\left(\hat{v}_i - 2k_{inz}\hat{h}_i \times \hat{z}\right)R_v E_{iv} + \hat{h}_i R_h E_{ih}\right] e^{j\mathbf{k}_{i\rho}\cdot\boldsymbol{\rho}'} \tag{3.2.17}$$

$$\mathbf{H}_r(\boldsymbol{\rho}') = \frac{1}{\eta}\left[\left(\hat{v}_i - 2k_{inz}\hat{h}_i \times \hat{z}\right)R_h E_{ih} - \hat{h}_i R_v E_{iv}\right] e^{j\mathbf{k}_{i\rho}\cdot\boldsymbol{\rho}'} \tag{3.2.18}$$

3.2.2.2. Equivalent Source

The surface equivalent source (3.2.19) is given in terms of the equivalent current densities, described in (3.2.20-3.2.21). We consider the normal unit vector $\hat{\mathrm{n}}$ to be equal to $\hat{z}$.

$$\mathbf{Q}_s(\mathbf{r}) = -jk\eta\mathbf{J}_{se}(\mathbf{r}) - \nabla \times \mathbf{J}_{sm}(\mathbf{r}) \tag{3.2.19}$$

$$\mathbf{J}_{se}(\mathbf{r}) = +\hat{\mathrm{n}} \times \mathbf{H}(\mathbf{r}) \tag{3.2.20}$$

$$\mathbf{J}_{sm}(\mathbf{r}) = -\hat{\mathrm{n}} \times \mathbf{E}(\mathbf{r}) \tag{3.2.21}$$

The equivalent current densities are then found by applying a cross product on (3.2.22-3.2.23).

$$\mathbf{J_{sm}}(\mathbf{r}') = -\hat{z} \times \mathbf{E}(\mathbf{r}') = -\left(\hat{h}_i k_{inz}(1 - R_v)E_{iv} + \hat{z} \times \hat{h}_i(1 + R_h)E_{ih}\right)e^{j\mathbf{k_i}\cdot\mathbf{r}'} \quad (3.2.22)$$

$$\mathbf{J_{se}}(\mathbf{r}') = +\hat{z} \times \mathbf{H}(\mathbf{r}') = \eta^{-1}\left(\hat{h}_i k_{inz}(1 - R_h)E_{ih} - \hat{z} \times \hat{h}_i(1 + R_v)E_{iv}\right)e^{j\mathbf{k_i}\cdot\mathbf{r}'} \quad (3.2.23)$$

The equivalent source is found using the relation in (3.2.24).

$$\mathbf{Q_s}(\mathbf{r}') = \quad (3.2.24)$$

$$-jk\Big[\left(\hat{h}_i k_{inz}(1 - R_h)E_{ih} - \hat{z} \times \hat{h}_i(1 + R_v)E_{iv}\right) + \hat{k} \times \left(\hat{h}_i k_{inz}(1 - R_v)E_{iv} + \hat{z} \times \hat{h}_i(1 + R_h)E_{ih}\right)\Big]e^{j\mathbf{k_i}\cdot\mathbf{r}'}$$

3.2.2.3. Solution of Integral Equation

The scattered field evaluated at a point ($\mathbf{r}$) in the far-field region with respect to the scattering center ($\mathbf{r_o}$) due to an equivalent source $\mathbf{Q_s}(\mathbf{r}')$ is given by (3.2.25), where $\Phi_r(\mathbf{r}, \mathbf{r_o})$ is the propagation function.

$$\mathbf{E_s}(\mathbf{r}) = \Phi_r(\mathbf{r}, \mathbf{r_o})\left(\hat{v}_s\hat{v}_s + \hat{h}_s\hat{h}_s\right) \cdot \int_{\boldsymbol{A}} d\mathbf{r}'\, e^{-j\mathbf{k_s}\cdot(\mathbf{r}' - \mathbf{r_o})}\, \mathbf{Q_s}(\mathbf{r}') \quad (3.2.25)$$

Replacing the source into (3.2.25), the scattered field takes the form in (3.2.26), where the $\overline{\overline{\mathbf{R}}}$ is the reflection dyadic defined in (3.2.27).

$$\mathbf{E_s}(\mathbf{r}) = -jk_s\Phi_r(\mathbf{r}, \mathbf{r_o})\,\overline{\overline{\mathbf{R}}} \cdot \mathbf{E_i}(\mathbf{r_o})\left[\int_{\boldsymbol{A}} d\mathbf{r}'\, e^{-j\mathbf{k_d}\cdot(\mathbf{r}')}\right] \quad (3.2.26)$$

$$\overline{\overline{\mathbf{R}}} = \left(\hat{v}_s\hat{v}_s + \hat{h}_s\hat{h}_s\right) \cdot \left[\hat{h}_i\hat{h}_i k_{inz}(1 - R_h) - \left(\hat{z} \times \hat{h}_i\right)\hat{v}_i(1 + R_v)\right] \quad (3.2.27)$$

$$+\ \left(\hat{h}_s\hat{v}_s+\hat{v}_s\hat{h}_s\right)\cdot\left[\hat{h}_i\hat{v}_i k_{inz}(1-R_v)+\left(\hat{z}\times\hat{h}_i\right)\hat{h}_i(1+R_h)\right]$$

Rearranging terms in (3.2.27), ($\bar{\bar{\mathbf{R}}}$) can be written showing explicitly the coefficients of the dyadic components as shown in (3.2.28).

$$\begin{aligned}\bar{\bar{\mathbf{R}}} = &+\hat{v}_s\hat{v}_i\left[\hat{h}_s\cdot\hat{h}_i k_{inz}(1-R_v)-\hat{v}_s\cdot\left(\hat{z}\times\hat{h}_i\right)(1+R_v)\right]\\ &+\hat{h}_s\hat{h}_i\left[\hat{h}_s\cdot\hat{h}_i k_{inz}(1-R_h)+\hat{v}_s\cdot\left(\hat{z}\times\hat{h}_i\right)(1+R_h)\right]\\ &+\hat{v}_s\hat{h}_i\left[\hat{v}_s\cdot\hat{h}_i k_{inz}(1-R_h)+\hat{h}_s\cdot\left(\hat{z}\times\hat{h}_i\right)(1+R_h)\right]\\ &+\hat{h}_s\hat{v}_i\left[\hat{v}_s\cdot\hat{h}_i k_{inz}(1-R_v)-\hat{h}_s\cdot\left(\hat{z}\times\hat{h}_i\right)(1+R_v)\right]\end{aligned} \tag{3.2.28}$$

The integral term in (3.2.26) is the shape function (S), defined in (3.2.29). The shape function of a $L_x \times L_y$ rectangular facet is given in (3.2.31). If the facet has circular shape with a radius of 'a', the shape function is given by (3.2.30). In equation (3.2.30-3.2.31), $\mathbf{k}_d$ is the difference wave vector ($\mathbf{k}_d = \mathbf{k}_s - \mathbf{k}_i$)**.** In (3.2.30-3.2.31), the $\boldsymbol{\rho}$**,** $\boldsymbol{x}$ and $\boldsymbol{y}$ subscripts refer to the radial, x-axis and y-axis components of the vector. In (3.2.30), we used the jinc function defined as $\mathrm{jinc(x)} = 2\mathrm{J}_1(\mathrm{x})/\mathrm{x}$, where $\mathrm{J}_1(\mathrm{x})$ is the Bessel function of the first kind.

$$S = \int_{\boldsymbol{A}} d\mathbf{r}'\, e^{-j\mathbf{k}_d\cdot\mathbf{r}'} \tag{3.2.29}$$

$$S = A\ \mathrm{jinc}\left(k_{d\rho}a\right) = (\pi a^2)\ \mathrm{jinc}\left(k_{d\rho}a\right) \tag{3.2.30}$$

$$S = A\ \mathrm{sinc}(k_{dx}\,0.5L_x)\ \mathrm{sinc}\left(k_{dy}\,0.5L_y\right) = L_xL_y\ \mathrm{sinc}(k_{dx}\,0.5L_x)\ \mathrm{sinc}\left(k_{dy}\,0.5L_y\right) \tag{3.2.31}$$

Thus, the scattered field due to a facet results in the expression in (3.2.32).

$$\mathbf{E}_s(\mathbf{r}) = -jk\,\Phi_r(\mathbf{r},\mathbf{r}_o)\,S\;\bar{\bar{\mathbf{R}}}\cdot\mathbf{E}_i(\mathbf{r}_o) \tag{3.2.32}$$

By inspection of (3.2.32), the scattering dyad of a facet is given by (3.2.33).

$$\bar{\bar{\mathbf{F}}}(\mathbf{k}_s,\mathbf{k}_i) = -jk\,S\;\bar{\bar{\mathbf{R}}} \tag{3.2.33}$$

3.2.3. Scattering from a Thin Dielectric Sheet

In this section, we use the procedure laid out in section 3.2.1 to solve for the scattering dyad of a thin dielectric sheet.

3.2.3.1. Total Field of Approximated Geometry

The approximated geometry for the thin dielectric sheet is a three-layer structure with two semi-infinite layers (free-space) and one finite layer in the middle (dielectric).

For simplicity, we choose the normal of the layer interfaces to be parallel to the z-axis. Thus, the layer interfaces are infinite in the x- and y- axis (i.e. horizontally infinite).

The total field inside each interface can be decomposed into an upward-going field and a downward-going field, as shown in (3.2.34). In (3.2.34), the downward- and upward- going field coefficients are $\tilde{\mathbf{a}}_m$ and $\tilde{\mathbf{b}}_m$, respectively. The 'z' dependent phase factor can be combined with the aforementioned coefficients to get the alternative expression for the total field in (3.2.35).

$$\mathbf{E}_m(\mathbf{r}) = \tilde{\mathbf{a}}_m e^{j\mathbf{k}_{m-}\cdot\mathbf{r}} + \tilde{\mathbf{b}}_m e^{j\mathbf{k}_{m+}\cdot\mathbf{r}} = e^{j\mathbf{k}_\rho\cdot\boldsymbol{\rho}}\left[\tilde{\mathbf{a}}_m e^{-j\mathrm{k}_{mz}\cdot z} + \tilde{\mathbf{b}}_m e^{j\mathrm{k}_{mz}\cdot z}\right] \tag{3.2.34}$$

$$\mathbf{E}_{\boldsymbol{m}}(\mathbf{r}) = e^{j\mathbf{k}_{\rho}\cdot\boldsymbol{\rho}}[\mathbf{a}_{\boldsymbol{m}}(z) + \mathbf{b}_{\boldsymbol{m}}(z)] \tag{3.2.35}$$

The wave-vectors for the upward and downward going waves, at any layer, can be decomposed in terms of the perpendicular wave-vector ($\mathbf{k}_{\boldsymbol{\rho}}$) and its z-component ($\pm \mathrm{k}_{mz}\hat{z}$), as shown in (3.2.36-3.2.37).

$$\mathbf{k}_{\boldsymbol{m}+} = \mathbf{k}_{\boldsymbol{\rho}} + \mathrm{k}_{mz}\hat{z} \tag{3.2.36}$$

$$\mathbf{k}_{\boldsymbol{m}-} = \mathbf{k}_{\boldsymbol{\rho}} - \mathrm{k}_{mz}\hat{z} \tag{3.2.37}$$

By the phase matching principle, the perpendicular wave-vector is constant across all layers (3.2.38). The absolute value of the z-component can be determined using the dispersion relation in (3.2.39).

$$\mathbf{k}_{\boldsymbol{\rho}} = \mathbf{k}_{\boldsymbol{m\rho}+} = \mathbf{k}_{\boldsymbol{m\rho}-} = \mathbf{k}_{\boldsymbol{n\rho}+} = \mathbf{k}_{\boldsymbol{n\rho}-} \tag{3.2.38}$$

$$\mathrm{k}_{mz} = \sqrt{\left|\mathbf{k}_{\boldsymbol{m}\pm}\right|^2 - \left|\mathbf{k}_{\boldsymbol{\rho}}\right|^2} \tag{3.2.39}$$

Combining equations (3.2.36-3.2.38), the upward going wave-vector can be written in terms of the downward-going wave as shown in (3.2.40). This is similar to the relation given between the incident and reflected fields in the previous section.

$$\mathbf{k}_{\boldsymbol{m}+} = \mathbf{2k}_{\boldsymbol{\rho}} - \mathbf{k}_{\boldsymbol{m}-} \tag{3.2.40}$$

Using relationship (3.2.40), the upward going vertical and horizontal unit vectors can be written in terms of the downward-going vertical and horizontal unit vectors, as shown in (3.2.41-3.2.42).

$$\hat{v}_{m+} = \hat{v}_{m-} - 2\frac{\mathrm{k}_{mz}}{\mathrm{k}_m}\left(\hat{h}_{\boldsymbol{m}-} \times \hat{z}\right) \tag{3.2.41}$$

$$\hat{h}_{m+} = \hat{h}_{m-} \tag{3.2.42}$$

One method to solve for the fields of a plane-wave in a multi-layer structure is the signal-flow method. In this technique, the field coefficients are considered 2-component vectors defined by their vertical and horizontal components, as described by equations (3.2.43-3.2.44).

$$\mathbf{a}_{\boldsymbol{m}}(z) = a_{vm}(z)\hat{v}_{m-} + a_{hm}(z)\hat{h}_{m-} = \begin{bmatrix} a_{vm}(z) \\ a_{hm}(z) \end{bmatrix} \tag{3.2.43}$$

$$\mathbf{b}_{\boldsymbol{m}}(z) = b_{vm}(z)\hat{v}_{m-} + b_{hm}(z)\hat{h}_{m-} = \begin{bmatrix} b_{vm}(z) \\ b_{hm}(z) \end{bmatrix} \tag{3.2.44}$$

We are interested in the field coefficients inside the layer '1' (medium 1) of the 3-layer structure, in terms of the downward-going coefficient at layer '0' (medium 0) evaluated at the scattering center ($\mathbf{r}_o$). Thus, we sought to find the linear operators (matrices) that transform the field coefficient $\mathbf{a_0}(z_o)$ into the field coefficients $\mathbf{a_1}(z)$ and $\mathbf{b_1}(z)$ (3.2.45-3.2.46), where z is inside layer 2 (i.e. $|z - z_o| \leq t/2$).

$$\mathbf{a_1}(z) = \mathbf{\Pi}(z)\ \mathbf{a_0}(z_o) \tag{3.2.45}$$

$$\mathbf{b_1}(z) = \mathbf{\Gamma}(z)\ \mathbf{a_0}(z_o) \tag{3.2.46}$$

The signal flow diagram in figure 3.2.1 depicts the 3-layer problem. The blocks containing the propagation operator $\mathbf{\Phi_m}$, where m is '0' or '1', describe the propagation through one of these

layers. A block with the $\mathbf{R}_{mn}$ and $\mathbf{T}_{mn}$ matrices represents the interface which connects layers m and n, where $\mathbf{R}_{mn}$ is a reflection matrix and $\mathbf{T}_{mn}$ is the transmission matrix.

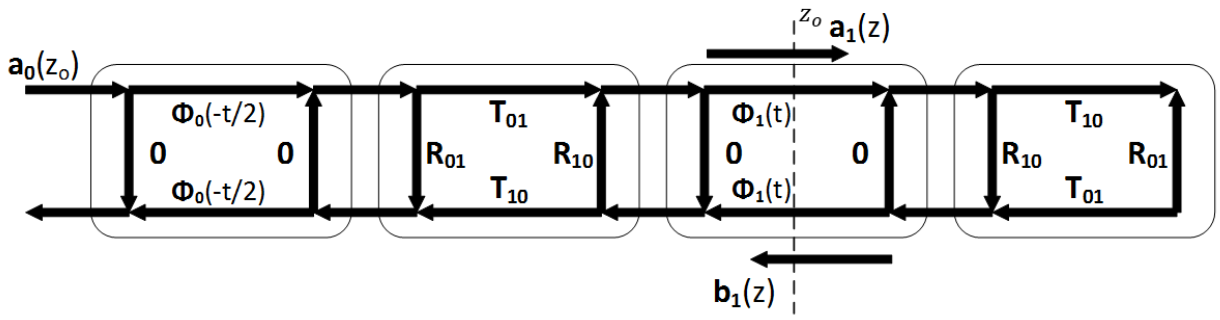

Figure 3.2.1 – Signal Flow for the two-interface structure

By inspection of the signal flow diagram, the linear operators $\mathbf{\Pi}(z)$ and $\mathbf{\Gamma}(z)$ are given by equations (3.2.47-3.2.48).

$$\mathbf{\Pi}(z) = \mathbf{\Phi_1}(t/2 - (z - z_o))[\mathbf{I} - \mathbf{R_{10}}\mathbf{\Phi_1}(t)\mathbf{R_{10}}\mathbf{\Phi_1}(t)]^{-1}\mathbf{T_{01}}\mathbf{\Phi_0}(-t/2) \tag{3.2.47}$$

$$\mathbf{\Gamma}(z) = [\mathbf{I} - \mathbf{\Phi_1}(t)\mathbf{R_{10}}\mathbf{\Phi_1}(t)\mathbf{R_{10}}]^{-1}\mathbf{\Phi_1}(-\frac{t}{2} + (z - z_o))\mathbf{R_{10}}\mathbf{\Phi_1}(t)\mathbf{T_{01}}\mathbf{\Phi_0}(-t/2) \tag{3.2.48}$$

The reflection and transmission matrices from medium ‘0’ to medium ‘1’ are given explicitly in (3.2.49-3.2.50) in terms of the Fresnel reflection and transmission coefficients from medium ‘0’ to medium ‘1’. The Fresnel reflection and transmission coefficients are defined in (3.2.51-3.2.54).

$$\mathbf{R_{01}} = \begin{bmatrix} R_{v\_01} & 0 \\ 0 & R_{h\_01} \end{bmatrix} = \begin{bmatrix} R_v & 0 \\ 0 & R_h \end{bmatrix} \tag{3.2.49}$$

$$\mathbf{T_{01}} = \begin{bmatrix} T_{v\_01} & 0 \\ 0 & T_{h\_01} \end{bmatrix} = \begin{bmatrix} T_v & 0 \\ 0 & T_h \end{bmatrix} \tag{3.2.50}$$

$$R_{v\_01} = \frac{k_{0z} - k_{1z}/\varepsilon_{r1}}{k_{0z} + k_{1z}/\varepsilon_{r1}} \tag{3.2.51}$$

$$R_{h\_01} = \frac{k_{0z} - k_{1z}}{k_{0z} + k_{1z}} \tag{3.2.52}$$

$$T_{v\_01} = (R_{v\_01} + 1)\sqrt{1/\varepsilon_{r1}} \tag{3.2.53}$$

$$T_{h\_01} = (R_{h\_01} + 1) \tag{3.2.54}$$

The propagation operator (matrix) through medium '*m*' is given explicitly in (3.2.55). This operator accounts for the amplitude decay and phase change of the plane wave at some position inside a layer with medium '*m*'.

$$\mathbf{\Phi_m}(z) = \begin{bmatrix} \Phi_m(z) & 0 \\ 0 & \Phi_m(z) \end{bmatrix} = \begin{bmatrix} e^{jk_{mz}z} & 0 \\ 0 & e^{jk_{mz}z} \end{bmatrix} \tag{3.2.55}$$

Since the interfaces are planar, there is no depolarization terms in the matrices $\mathbf{\Pi}(z)$ and $\mathbf{\Gamma}(z)$**.** The co-polarization terms of these two matrices are given explicitly by equations (3.2.56-3.2.59). In these equations, the equality $\mathrm{R}_{10} = -\mathrm{R}_{01}$ was used.

$$\Pi_{vv}(z) = \frac{\mathrm{T}_v\, \Phi_1(t/2 - (z - z_o))\Phi_0(-t/2)}{1 - \Phi_1^2(t)R_v^2} \tag{3.2.56}$$

$$\Pi_{hh}(z) = \frac{\mathrm{T}_h\ \Phi_1(t/2 - (z - z_o))\Phi_0(-t/2)}{1 - \Phi_1^2(t)R_h^2} \tag{3.2.57}$$

$$\Gamma_{vv}(z) = -\frac{\mathrm{R}_v\mathrm{T}_v\ \Phi_1(-\frac{t}{2} + (z - z_o))\Phi_1(t)\Phi_0(-t/2)}{1 - \Phi_1^2(t)R_v^2} \tag{3.2.58}$$

$$\Gamma_{hh}(z) = -\frac{\mathrm{R}_h\mathrm{T}_h\Phi_1(-\frac{t}{2} + (z - z_o))\Phi_1(t)\Phi_0(-t/2)}{1 - \Phi_1^2(t)R_h^2} \tag{3.2.59}$$

Given the co-polarization matrix terms, we define the dyadic operators in (3.2.60-3.2.61). We used the equality $\mathbf{k_i} = \mathbf{k}_{0-}$. The vertical and horizontal unit vectors at layer '1' can be solved in terms of the incident unit vectors and they are given in (3.2.62-3.2.63).

$$\bar{\bar{\mathbf{\Pi}}}(z) = \Pi_{\boldsymbol{vv}}(z)\hat{v}_{1-}\hat{v}_i + \Pi_{hh}(z)\hat{h}_{1-}\hat{h}_i \tag{3.2.60}$$

$$\bar{\bar{\mathbf{\Gamma}}}(z) = \ \Gamma_{vv}(z)\hat{v}_{1+}\hat{v}_i\ + \Gamma_{hh}(z)\hat{h}_{1+}\hat{h}_i \tag{3.2.61}$$

$$\hat{v}_{1\pm} = \hat{v}_i - (-\mathrm{k}_{iz}/k_0 \mp \mathrm{k}_{i1z}/k_1)\big(\hat{h}_{\boldsymbol{i}} \times \hat{z}\big) \tag{3.2.62}$$

$$\hat{h}_{1-} = \hat{h}_{1+} = \hat{h}_i \tag{3.2.63}$$

$$\mathrm{k}_{i1z} = sign(\mathrm{k}_{iz})\sqrt{{\mathrm{k}_1}^2 - {\mathrm{k}_{i\rho}}^2} \tag{3.2.64}$$

Using the dyadic operators defined in (3.2.60-3.2.61), the total field inside layer '1' is given by (3.3.2.65), where $\mathbf{E_i}(\mathbf{r_o})$ (3.2.66) is the incident field evaluated at the scattering center.

$$\mathbf{E_1}(\mathbf{r}) = e^{-j\mathbf{k}_\rho\cdot\boldsymbol{\rho}}\big[\bar{\bar{\mathbf{\Pi}}}(z) + \bar{\bar{\mathbf{\Gamma}}}\ (z)\big] \cdot \mathbf{E}_{\boldsymbol{i}}(\mathbf{r}_o) \tag{3.2.65}$$

$$\mathbf{E}_i(\mathbf{r}_o) = \mathbf{a_0}(z_o) + \mathbf{b_0}(z_o) \tag{3.2.66}$$

3.2.3.2. Equivalent Source

The volume equivalent source was described in section 3.1.3 and it is given by (3.2.67), where $\varepsilon_{r1}(\mathbf{r})$ is the dielectric distribution and $\mathbf{E_1}(\mathbf{r})$ is the total field inside the volume. For this problem, the dielectric is constant inside the volume, so the equivalent source has the form in (3.2.68).

$$\mathbf{Q}_s(\mathbf{r}) = [\varepsilon_{r1}(\mathbf{r}) - 1]\mathbf{E_1}(\mathbf{r}) \tag{3.2.67}$$

$$\mathbf{Q}_s(\mathbf{r}) = [\varepsilon_{r1} - 1]\mathbf{E_1}(\mathbf{r}) \tag{3.2.68}$$

3.2.3.3. Solution of Integral Equation

The scattered field due to $\mathbf{Q}_s(\mathbf{r})$ evaluated in the far-field region with respect to the scattering center ($\mathbf{r}_o$) is given by (3.2.69).

$$\mathbf{E}_s(\mathbf{r}) = \Phi(\mathbf{r}, \mathbf{r}_o)\, k^2[\varepsilon_{r1} - 1]\ \left(\bar{\bar{\mathbf{I}}} - \hat{k}_s\hat{k}_s\right) \cdot \int d\mathbf{r}' \left[e^{-j\mathbf{k}\cdot(\mathbf{r}'-\mathbf{r_o})}\ \mathbf{E_1}(\mathbf{r}')\right] \tag{3.2.69}$$

We approximate the field inside the thin sheet to behave as it would in a 3-layer media over its cross section, with a small distinction. The field inside a thin sheet is approximated to propagate perpendicular to the face, regardless of the incident field direction. The wave-vector inside the thin sheet takes the form in (3.2.70).

$$\mathbf{k}_1 = sign(\mathbf{k}_i \cdot \hat{z})|k_1|\hat{z} \tag{3.2.70}$$

The scattered field is solved using equation (3.2.69) and evaluating the integral over the horizontal cross section of the target. Thus, the scattered field due to a thin sheet is given by the expression in (3.2.71), where $\bar{\bar{\mathbf{K}}}$ is a dyadic operator defined in (3.2.72). The term S is the shape function, which was defined in section 3.2.2.

$$\mathbf{E_s}(\mathbf{r}) = -jk\ \Phi(\mathbf{r}, \mathbf{r}_o)\ \ S \cdot \bar{\bar{\mathbf{K}}} \cdot \mathbf{E_i}(\mathbf{r_o}) \tag{3.2.71}$$

$$\bar{\bar{\mathbf{K}}}(\mathbf{k_s}, \mathbf{k_i}; k_1) = \tag{3.2.72}$$

$$jk\ [\varepsilon_{r1} - 1]\ \left(\bar{\bar{\mathbf{I}}} - \hat{k}_s\hat{k}_s\right) \cdot \left\{\bar{\bar{\mathbf{\Pi}}}(z_o)\ \mathrm{sinc}[(k_{sz} - k_{i1z})t/2] + \bar{\bar{\mathbf{\Gamma}}}(z_o)\ \mathrm{sinc}[-(k_{sz} + k_{i1z})t/2]\right\}$$

By inspection of (3.2.71), the scattering dyad of a thin dielectric sheet is given by (3.2.73).

$$\bar{\bar{\mathbf{F}}}(\mathbf{k_s}, \mathbf{k_i}) = -jk\ t\ S \cdot \bar{\bar{\mathbf{K}}}(\mathbf{k_s}, \mathbf{k_i}; k_1) \tag{3.2.73}$$

Using the approximation of the wave-vector inside the sheet (3.2.70), the Fresnel reflection coefficients and the propagation functions simplify to the expressions in (3.2.74-3.2.78). The wave-vectors are also generalized to take into account incident waves from all directions (3.2.79).

$$R_{v\_01} = \frac{k_0 - k_1/\varepsilon_{r1}}{k_0 + k_1/\varepsilon_{r1}} \tag{3.2.74}$$

$$R_{h\_01} = \frac{k_0 - k_1}{k_0 + k_1} \tag{3.2.75}$$

$$T_{v\_01} = (R_{v\_01} + 1)\sqrt{1/\varepsilon_{r1}} \tag{3.2.76}$$

$$T_{h\_01} = (R_{h\_01} + 1) \tag{3.2.77}$$

$$\boldsymbol{\Phi_m}(z) = \begin{bmatrix} e^{-j\,k_{imz}\,z} & 0 \\ 0 & e^{-j\,k_{imz}\,z} \end{bmatrix} \tag{3.2.78}$$

$$\mathrm{k}_{imz} = sign(\mathrm{k}_{iz})\sqrt{{\mathrm{k}_m}^2 - {\mathrm{k}_{i\rho}}^2} = sign(\mathrm{k}_{iz})\mathrm{k}_m \tag{3.2.79}$$

3.2.3.4. Model Validation

We validate the solution of the scattering dyad in (3.2.73) by comparing its related RCS to the RCS determined using the Method of Moments (MoM). The method of moments is a full-wave numerical method. Full-wave methods, such as the MoM, are commonly used to validate electromagnetic models, since they do not rely in analytic approximations.

We consider a thin sheet with a length 80mm, a width 5mm and a thickness of 0.2mm. The permittivity constant of the sheet is 10.46-j6.7. The sheet is placed at the origin with its length aligned to the x-axis, its width with the y-axis and its thickness with the z-axis.

The RCS is computed at a range of incident/scattered angles at the frequency of 16 GHz for HH polarizations (y-y). The incident and scattered wave-vectors used are given in (3.2.80-3.2.81). The incident and scattered azimuth angles (ϕ_i, ϕ_s) are set to zero and the elevation angles (θ_i, θ_s) are function of the variable parameter (θ). The incident and scattered elevation angles have a fixed separation of $2 \cdot 0.4128$ between each other. The RCS is computed for the range of angles (θ) from 0 to 90 degrees.

$$\mathbf{k_i} = k_o \cos\phi_i \sin\theta_i(\theta)\ \hat{x} + k_o \sin\phi_i \sin\theta_i(\theta)\ \hat{y} + k_o \cos\theta_i(\theta)\ \hat{z} \tag{3.2.80}$$

$$\mathbf{k_s} = k_o \cos\phi_s \sin\theta_s(\theta)\ \hat{x} + k_o \sin\phi_s \sin\theta_s(\theta)\ \hat{y} + k_o \cos\theta_s(\theta)\ \hat{z} \tag{3.2.81}$$

$$\theta_i(\theta) = \pi - 0.4128 + \theta \text{ rad} \tag{3.2.82}$$

$$\theta_s(\theta) = 0.4128 + \theta \text{ rad} \tag{3.2.83}$$

$$\phi_i = \phi_s = 0 \tag{3.2.84}$$

Figure 3.2.2 shows different views of the three-dimensional model of the thin dielectric sheet considered.

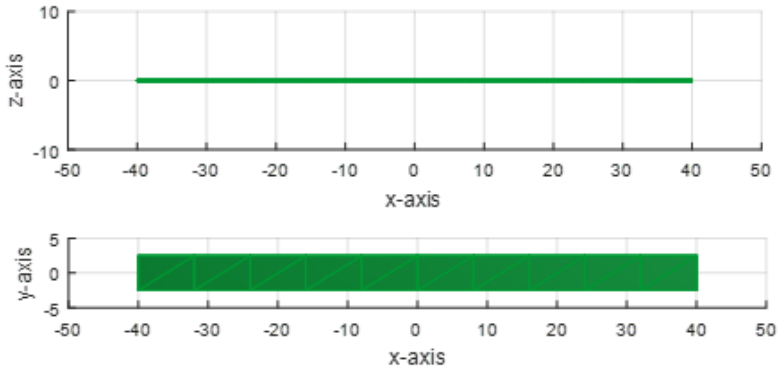

Figure 3.2.2 – Visualization of the Geometric Model of the Dielectric Thin Sheet. Front view (top inset) and top view (bottom inset).

Figure 3.2.3 shows the RCS as a function of the angle (θ) calculated using the MoM, the model presented here and the model given in [1]. Both analytic models agree at incidence near the

face of the sheet. The model presented here is more accurate at incidence near the ends of the dielectric sheet.

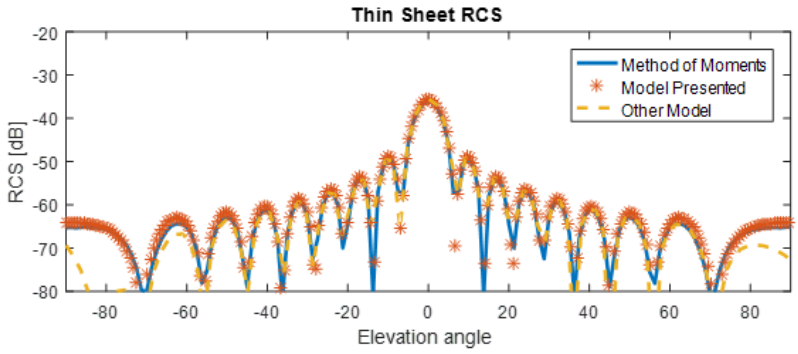

Figure 3.2.3 – RCS of a thin dielectric sheet

The model can also be used at a set of frequencies to determine the RCS as a function of delay (delay-power-profile), by using the Inverse Fourier Transform. In this case, we use the same dimensions than the previous example. The frequency range used is 14-18 GHz. The dielectric constant of this thin sheet is 13.97-j5.41 and the sheet is oriented with its normal parallel to the z-axis. Figure 3.2.4 shows a comparison of the RCS computed with the model in (3.2.73) against a solution found using the MOM.

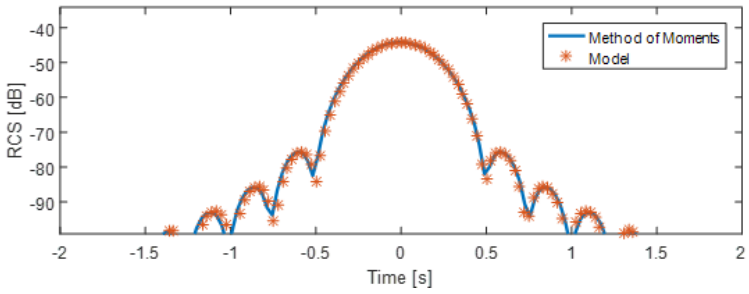

Figure 3.2.4 – Time-domain RCS of a thin dielectric sheet

3.2.4. Scattering from a Dielectric Circular Cylinder

In this section, we show the solution of the scattering field and scattering dyad due to a finite dielectric circular cylinder. We follow the steps laid out in section 3.2.1 to solve for the scattering dyad of a simple target.

3.2.4.1. Total Field of Approximated Geometry

We choose an infinite cylinder as the approximated geometry. In this section, we show the solution to the scattered field from a dielectric cylinder with infinite length. Likewise, we show the solution to the total field inside the dielectric cylinder with infinite length.

As in previous sections, we approximate the incident field to behave as a plane wave near the scattering center of the simple target, as the target is considered to be in the far-field region with respect to the source of the incident wave. This plane-wave incident field can be written in terms of its vertical and horizontal vector components, as shown in (3.2.85).

$$\mathbf{E}_{\boldsymbol{i}}(\mathbf{r}) = \left(E_{iv}\hat{v}_i + E_{ih}\hat{h}_i\right)\boldsymbol{e}^{j\mathbf{k_i}\cdot\mathbf{r}} \tag{3.2.85}$$

The incident field can also be written using vector cylindrical wave expansion (VCWE) as shown in (3.2.86). VCWE is a useful decomposition of vector fields when dealing with cylindrical structures. In (3.2.86), $\mathbf{M}_{\boldsymbol{jn}}$ and $\mathbf{N}_{\boldsymbol{jn}}$ are orthogonal cylindrical vector fields, described in (3.2.87-3.2.88). The VCWE coefficients for the incident field ($u_n\ v_n$) are given in (3.2.89-3.2.90).

$$\mathbf{E}_{\boldsymbol{i}}(\mathbf{r}) = \sum_{\boldsymbol{n}=-\infty}^{\infty} u_n\mathbf{M}_{jn} + v_n\mathbf{N}_{jn} \tag{3.2.86}$$

$$\mathbf{M}_{jn} = \left[-\hat{\rho}\frac{jn}{\rho k}J_n(k_{i\rho}\rho) - \hat{\phi}\frac{k_{i\rho}}{k}J_n{}'(k_{i\rho}\rho)\right]e^{-jn\phi - jk_{iz}z} \tag{3.2.87}$$

$$\mathbf{N}_{jn} = \left[-\hat{\rho}\frac{jk_{i\rho}k_{iz}}{k^2}J_n{}'(k_{i\rho}\rho) - \hat{\phi}\frac{nk_{iz}}{\rho k^2}J_n(k_{i\rho}\rho) + \hat{z}\frac{k_{i\rho}{}^2}{k^2}J_n(k_{i\rho}\rho)\right]e^{-jn\phi - jk_{iz}z} \tag{3.2.88}$$

$$u_n = -jE_{ih}\frac{k}{k_{i\rho}}(-j)^n e^{jn\phi_i} = E_{ih}\tilde{u}_n \tag{3.2.89}$$

$$v_n = -\ E_{iv}\frac{k}{k_{i\rho}}(-j)^n e^{jn\phi_i} = E_{iv}\tilde{v}_n \tag{3.2.90}$$

Similarly, the scattered and the internal electric fields are given by (3.2.91) and (3.2.93) respectively. Their respective magnetic fields are given in (3.2.92, 3.2.94).

$$\mathbf{E}_{\boldsymbol{s}}(\mathbf{r}) = \sum_{\boldsymbol{n}=-\infty}^{\infty} a_n\mathbf{M}_{hn} + b_n\mathbf{N}_{hn} \tag{3.2.91}$$

$$\mathbf{H}_{\boldsymbol{s}}(\mathbf{r}) = \sum_{\boldsymbol{n}=-\infty}^{\infty} (j/\eta)a_n\mathbf{N}_{hn} + (j/\eta)b_n\mathbf{M}_{hn} \tag{3.2.92}$$

$$\mathbf{E}_{\mathbf{1}}(\mathbf{r}) = \sum_{\boldsymbol{n}=-\infty}^{\infty} c_n\mathbf{M}_{jn} + d_n\mathbf{N}_{jn} \tag{3.2.93}$$

$$\mathbf{H}_{\mathbf{1}}(\mathbf{r}) = \sum_{\boldsymbol{n}=-\infty}^{\infty} (j/\eta_1)c_n\mathbf{N}_{jn} + (j/\eta_1)d_n\mathbf{M}_{jn} \tag{3.2.94}$$

In order to find the scattered field and the internal field due to a specified incident field impinging into an infinite cylinder, we apply boundary conditions and solve for the field coefficients. The

tangential component of the total field must be continuous across the interface of the infinite cylinder. The boundary condition is described by equations (3.2.95-3.2.98).

$$\left(\mathbf{E}_{\boldsymbol{i}}(\mathbf{r}) + \mathbf{E}_{\boldsymbol{s}}(\mathbf{r})\right) \cdot \hat{z} = \mathbf{E}_{\boldsymbol{in}}(\mathbf{r}) \cdot \hat{z} \tag{3.2.95}$$

$$\left(\mathbf{E}_{\boldsymbol{i}}(\mathbf{r}) + \mathbf{E}_{\boldsymbol{s}}(\mathbf{r})\right) \cdot \hat{\phi} = \mathbf{E}_{\boldsymbol{in}}(\mathbf{r}) \cdot \hat{\phi} \tag{3.2.96}$$

$$\left(\mathbf{H}_{\boldsymbol{i}}(\mathbf{r}) + \mathbf{H}_{\boldsymbol{s}}(\mathbf{r})\right) \cdot \hat{z} = \mathbf{H}_{\boldsymbol{in}}(\mathbf{r}) \cdot \hat{z} \tag{3.2.97}$$

$$\left(\mathbf{H}_{\boldsymbol{i}}(\mathbf{r}) + \mathbf{H}_{\boldsymbol{s}}(\mathbf{r})\right) \cdot \hat{\phi} = \mathbf{H}_{\boldsymbol{in}}(\mathbf{r}) \cdot \hat{\phi} \tag{3.2.98}$$

Applying the conditions above and performing algebraic simplifications, the VCWE coefficients for the scattered (a_n, b_n) and internal (c_n, d_n) fields are given by (3.2.99-3.2.102).

$$a_n = u_n \frac{A_{n\_n1} + A_{n\_an2}}{A_{n\_d1} + A_{n\_d2}} + v_n \frac{A_{n\_n3} + A_{n\_n4} + A_{n\_an5}}{A_{n\_d1} + A_{n\_d2}} = E_{ih}\tilde{a}_{nh} + E_{iv}\tilde{a}_{nv} \tag{3.2.99}$$

$$b_n = u_n \frac{A_{n\_n3} + A_{n\_n4} + A_{n\_bn5}}{A_{n\_d1} + A_{n\_d2}} + v_n \frac{A_{n\_n1} + A_{n\_bn2}}{A_{n\_d1} + A_{n\_d2}} = E_{ih}\tilde{b}_{nh} + E_{iv}\tilde{b}_{nv} \tag{3.2.100}$$

$$c_n = u_n \frac{B_{n\_cn4} + B_{n\_cn5}}{B_{n\_d1} + B_{n\_d2}} + v_n \frac{B_{n\_cn1} + B_{n\_cn2} + B_{n\_cn3}}{B_{n\_d1} + B_{n\_d2}} = E_{ih}\tilde{c}_{nh} + E_{iv}\tilde{c}_{nv} \tag{3.2.101}$$

$$d_n = u_n \frac{B_{n\_dn1} + B_{n\_dn2} + B_{n\_dn3}}{B_{n\_d1} + B_{n\_d2}} + v_n \frac{B_{n\_dn4} + B_{n\_dn5}}{B_{n\_d1} + B_{n\_d2}} = E_{ih}\tilde{d}_{nh} + E_{iv}\tilde{d}_{nv} \tag{3.2.102}$$

The expression for the VCWE coefficients in (3.2.99-3.2.102) are given in terms of the parameters defined in (3.103-3.123).

$$A_{n\_n1} = -HJJ_1{}^2 k_{iz} n^2 (k_\rho{}^2 - k_{1\rho}{}^2)(k_{iz} k_\rho{}^2 - k_{sz} k_{1\rho}{}^2) \quad (3.2.103)$$

$$A_{n\_an2} = -A_{n_{d2}} (JJ_1{}' k_\rho - J_1 J' k_{1\rho}) / (HJ_1{}' k_\rho - H' J_1 k_{1\rho}) \quad (3.2.104)$$

$$A_{n\_bn2} = -A_{n_{d2}} (J' J_1 k_{in\rho} - JJ_1{}' k_\rho \varepsilon_r) / (H' J_1 k_{1\rho} - HJ_1{}' k_\rho \varepsilon_r) \quad (3.2.105)$$

$$A_{n\_n3} = HJ_1{}^2 J' k k_\rho k_{1\rho}{}^2 n a (k_{iz} k_\rho{}^2 - k_{sz} k_{1\rho}{}^2) \quad (3.2.106)$$

$$A_{n\_n4} = -H' JJ_1{}^2 k k_{iz} k_\rho k_{1\rho}{}^2 n a (k_\rho{}^2 - k_{1\rho}{}^2) \quad (3.2.107)$$

$$A_{n\_an5} = -HJJ_1 J_1{}' k k_\rho{}^2 k_{1\rho}{}^3 n \varepsilon_r a (k_{iz} - k_{sz}) \quad (3.2.108)$$

$$A_{n\_bn5} = A_{n\_an5} / \varepsilon_r \quad (3.2.109)$$

$$A_{n\_d1} = H^2 J_1{}^2 n^2 (k_{iz} k_\rho{}^2 - k_{sz} k_{1\rho}{}^2)^2 \quad (3.2.110)$$

$$A_{n\_d2} = \left(k k_\rho \, k_{1\rho} \, a\right)^2 (HJ_1{}' k_\rho - H' J_1 k_{1\rho})(H' J_1 k_{1\rho} - HJ_1{}' k_\rho \varepsilon_r) \quad (3.2.111)$$

$$B_{n\_cn1} = H^2 J_1 J' k k_\rho{}^3 n \sqrt{\varepsilon_r} \, a (k_{iz} k_\rho{}^2 - k_{sz} k_{1\rho}{}^2) \quad (3.2.112)$$

$$B_{n\_n2} = -n \sqrt{\varepsilon_r} a H H' J J_1 k k_{iz} k_\rho{}^3 (k_\rho{}^2 - k_{1\rho}{}^2) \quad (3.2.113)$$

$$B_{n\_cn3} = -n \sqrt{\varepsilon_r} \varepsilon_r a H^2 J J_1{}' k k_\rho{}^4 k_{1\rho} (k_{iz} - k_{sz}) \quad (3.2.114)$$

$$B_{n\_n4} = H^2 J J_1 k_\rho{}^2 n^2 \sqrt{\varepsilon_r} (k_{iz} k_\rho{}^2 - k_{sz} k_{1\rho}{}^2)(k_{iz} - k_{sz}) \quad (3.2.115)$$

$$B_{n\_cn5} = \frac{2j}{\pi} \sqrt{\varepsilon_r} a k^2 k_\rho{}^3 k_{1\rho} (\, k_{1\rho} H' J_1 - k_\rho \, HJ_1{}' \varepsilon_r \,) \quad (3.2.116)$$

$$B_{n\_dn5} = \frac{2j}{\pi}\varepsilon_r \;\; ak^2{k_\rho}^3 k_{1\rho}(k_{1\rho}H'J_1 - k_\rho HJ_1') \tag{3.2.117}$$

$$B_{n\_dn1} = {\varepsilon_r}^{1/2} B_{n\_cn1} \tag{3.2.118}$$

$$B_{n\_dn2} = {\varepsilon_r}^{1/2} B_{n\_dn2} \tag{3.2.119}$$

$$B_{n\_dn3} = {\varepsilon_r}^{-1/2} B_{n\_cn3} \tag{3.2.120}$$

$$B_{n\_dn4} = {\varepsilon_r}^{1/2} B_{n\_cn3} \tag{3.2.121}$$

$$B_{n\_d1} = H^2{J_1}^2 n^2({k_{iz}{k_\rho}^2 - k_{sz}{k_{1\rho}}^2})\text{^}2 \tag{3.2.122}$$

$$B_{n\_d2} = \left(kk_\rho k_{1\rho}a\right)^2 (HJ_1'k_\rho - H'J_1k_{1\rho})(H'J_1k_{1\rho} - HJ_1'k_\rho\varepsilon_r\ ) \tag{3.2.123}$$

The terms J, J_1 and H used above are defined in (3.2.124-3.2.126), where $J_n(x)$ is the Bessel function of the first kind with order '*n'* and $H_n^{(2)}(x)$ is the Hankel function of the second with order '*n*'.

$$J = J_n\left(k_\rho a\right) \tag{3.2.124}$$

$$J_1 = J_n\left(k_{1\rho} a\right) \tag{3.2.125}$$

$$H = H_n^{(2)}\left(k_\rho a\right) \tag{3.2.126}$$

In the solution of the VCWE coefficients given in (3.2.99-3.2.102), we made use of the Wronskian, shown in (3.2.127).

$$H_n^{(2)}(z)\,J_n'(z) - H_n'^{(2)}(z)\,J_n(z) = \frac{2j}{\pi z} \tag{3.2.127}$$

We also used the fact that the z-component of the wave-vectors is constant due to the phase matching principle (3.2.128). The radial component of the wave-vector $k_{1\rho}$ inside the cylinder was determined using the dispersion relation given in (3.2.129).

$$k_{iz} = k_{1z} = \sqrt{\varepsilon_r}k\,cos\theta_{in} \tag{3.2.128}$$

$$k_{1\rho} = \sqrt{\varepsilon_r k^2 - {k_{iz}}^2} \tag{3.2.129}$$

By setting the z-components of the wave vectors to zero, the VCWE coefficients simplify to the expressions given in (3.2.130-3.2.133). This solution of the coefficients can be used when the problem is approximated as a 2-dimensional one.

$$a_n = u_n\left[-\frac{k_\rho J_n(k_\rho a)\quad J_n'(k_{1\rho}a)\quad -k_{1\rho}J_n'(k_\rho a)\quad J_n(k_{1\rho}a)}{k_\rho H_n^{(2)}(k_\rho a)\,J_n'(k_{1\rho}a) - k_{1\rho}H_n'^{(2)}(k_\rho a)\,J_n(k_{1\rho}a)}\right] \tag{3.2.130}$$

$$b_n = v_n\left[-\frac{k_{1\rho} J_n(k_{1\rho}a)\quad J_n'(k_\rho a) - k_\rho\,\varepsilon_r\,J_n'(k_{1\rho}a)\;J_n(k_{1\rho}a)}{k_{1\rho} J_n(k_{1\rho}a)\,H_n'^{(2)}(k_\rho a) - k_\rho\,\varepsilon_r\;J_n'(k_{1\rho}a)H_n^{(2)}(k_\rho a)}\right] \tag{3.2.131}$$

$$c_n = u_n\left[-\frac{2jk_\rho\sqrt{\varepsilon_r}}{\pi a k_{1\rho}\left(k_\rho H_n^{(2)}(k_\rho a)\,J_n'(k_{1\rho}a) - k_{1\rho}H_n'^{(2)}(k_\rho a)\,J_n(k_{1\rho}a)\right)}\right] \tag{3.2.132}$$

$$d_n = u_n\left[-\frac{2jk_\rho\varepsilon_r}{\pi a k_{1\rho}\left(\varepsilon_r k_\rho H_n^{(2)}(k_\rho a)\,J_n'(k_{1\rho}a) - k_{1\rho}H_n'^{(2)}(k_\rho a)\,J_n(k_{1\rho}a)\right)}\right] \tag{3.2.133}$$

3.2.4.2. Equivalent Source

As described in section 3.1.3, the surface equivalent source is given by (3.2.134), where $\mathbf{E}(\mathbf{r}')$ and $\mathbf{H}(\mathbf{r}')$ are the total electric and magnetic fields evaluated at the surface of the target $(\mathbf{r}')$.

$$\mathbf{Q_s}(\mathbf{r}') = -jk\eta\big(\hat{\mathbf{n}} \times \mathbf{H}(\mathbf{r}')\big) + \nabla \times \big(\hat{\mathbf{n}} \times \mathbf{E}(\mathbf{r}')\big) \tag{3.2.134}$$

$$\mathbf{Q_s}(\mathbf{r}') = -jk\eta\big(\hat{\boldsymbol{\rho}} \times \mathbf{H_1}(\mathbf{r}')\big) + \nabla \times \big(\hat{\boldsymbol{\rho}} \times \mathbf{E_1}(\mathbf{r}')\big) \tag{3.2.135}$$

Taking the cross product of the radial unit vector to the internal fields at the surface results in the expressions in (3.2.136-3.2.137).

$$-jk\eta\hat{\boldsymbol{\rho}} \times \mathbf{H_1}(\mathbf{r}') = \sum_{n=-\infty}^{\infty} \Bigg\{ c_n k_{in} \left[-\hat{z}\frac{nk_{iz}}{{k^2}_{in}a} J_n\big(k_{in\rho}a\big) - \hat{\phi}\frac{{k^2}_{in\rho}}{{k^2}_{in}} J_n\big(k_{in\rho}a\big) \right] + d_n k_{in} \left[-\hat{z}\frac{k_{in\rho}}{k_{in}} {J'}_n\big(k_{in\rho}a\big) \right] e^{-jn\phi' - jk_{iz}z'} \Bigg\} \tag{3.2.136}$$

$$-jk\hat{\boldsymbol{\rho}} \times \mathbf{E_1}(\mathbf{r}') = \sum_{n=-\infty}^{\infty} \Bigg\{ -jk\, c_n \left[-\hat{z}\frac{k_{in\rho}}{k_{in}} {J'}_n\big(k_{in\rho}a\big) \right] - jk\, d_n \left[-\hat{z}\frac{nk_{iz}}{{k^2}_{in}a} J_n\big(k_{in\rho}a\big) - \hat{\phi}\frac{{k^2}_{in\rho}}{{k^2}_{in}} J_n\big(k_{in\rho}a\big) \right] e^{-jn\phi' - jk_{iz}z'} \Bigg\} \tag{3.2.137}$$

3.2.4.3. Solution of Integral Equation

The scattered field evaluated in the far-field region with respect to the scattering center $(\mathbf{r_o})$ due to some surface equivalent source $\mathbf{Q_s}(\mathbf{r}')$ has the form given in (3.2.138).

$$\mathbf{E_s}(\mathbf{r}) = \Phi_r(\mathbf{r}, \mathbf{r_o})\left(\hat{v}_s\hat{v}_s + \hat{h}_s\hat{h}_s\right) \cdot \int_{\boldsymbol{A}} d\mathbf{r}'\, e^{-j\mathbf{k_s}\cdot(\mathbf{r}'-\mathbf{r_o})}\, \mathbf{Q_s}(\mathbf{r}') \tag{3.2.138}$$

Replacing the general expression of the surface equivalent source from (3.2.135) into (3.2.138), we obtain (3.2.139). In (3.2.139), the integral is evaluated over the finite cylinder with length L_z.

$$\mathbf{E_s}(\mathbf{r}) = -jk\Phi_r(\mathbf{r}, \mathbf{r_o})\left(\hat{v}_s\hat{v}_s + \hat{h}_s\hat{h}_s\right) \tag{3.2.139}$$
$$\cdot \int_{-L_z/2}^{+L_z/2} dz' \int_{0}^{2\pi} d\phi' a\, e^{-j\mathbf{k}\cdot(\mathbf{r}'-\mathbf{r_o})}\left[\eta \cdot \left(\hat{\boldsymbol{\rho}} \times \mathbf{H_1}(\mathbf{r}')\right) - \hat{k}_s \times \left(\hat{\boldsymbol{\rho}} \times \mathbf{E_1}(\mathbf{r}')\right)\right]$$

By replacing the surface fields from (3.2.136-3.2.137) into (3.2.139) and evaluating the integral, the scattered field takes the form in (3.2.140). The coefficients C_n^{ch}, C_n^{dh}, C_n^{cv} and C_n^{dv} used in equation (3.2.140) are given in (3.2.141-3.2.142). The term S_v in (3.2.140) is the volumetric shape function, defined in (3.2.145). The dyadic operator $\overline{\overline{\mathbf{X}}}$ is defined in (3.2.146).

$$\mathbf{E_s}(\mathbf{r}) = -jk\Phi_r(\mathbf{r}, \mathbf{r_o})\, S_v\, \overline{\overline{\mathbf{X}}} \cdot \mathbf{E_i}(\mathbf{r_o}) \tag{3.2.140}$$

$$C_n^{ch} = -\frac{k_{in\rho}}{kk_{s\rho}}\left[k_{in\rho}J_n(k_{in\rho}a)J'_n(k_{s\rho}a) - k_{s\rho}J'_n(k_{in\rho}a)J_n(k_{s\rho}a)\right] \tag{3.2.141}$$

$$C_n^{dh} = -n\frac{1}{ak_{in}k{k_{s\rho}}^2}\left({k_{sz}k^2}_{in\rho} - {k_{iz}k^2}_{s\rho}\right)J_n(k_{in\rho}a)J_n(k_{s\rho}a) \tag{3.2.142}$$

$$C_n^{cv} = -jn\frac{1}{k^2{k_{s\rho}}^2}\left({k_{sz}k^2}_{in\rho} - {k_{iz}k^2}_{s\rho}\right)J_n(k_{in\rho}a)J_n(k_{s\rho}a) \tag{3.2.143}$$

$$C_n^{dv} = -j\,\frac{k_{in\rho}}{ak_{s\rho}}\left[{\varepsilon_r}^{-1/2}k_{in\rho}\,J_n(k_{in\rho}a)J'_n(k_{s\rho}a) - {\varepsilon_r}^{1/2}k_{s\rho}J'_n(k_{in\rho}a)J_n(k_{s\rho}a)\right] \tag{3.2.144}$$

$$S_v = 2\pi a L_z \operatorname{sinc}\left(\frac{k_{dz} L_z}{2}\right) \tag{3.2.145}$$

$$\begin{aligned}\bar{\bar{\mathbf{X}}} = \sum_{\boldsymbol{n}=-\infty}^{\infty} e^{-jn\phi_s} j^n \{ & \hat{h}_s \hat{h}_i \left[\tilde{c}_{nh} C_n^{ch} + \tilde{d}_{nh} C_n^{dh}\right] + \hat{h}_s \hat{v}_i \left[\tilde{c}_{nv} C_n^{ch} + \tilde{d}_{nv} C_n^{dh}\right] \\ & + \hat{v}_s \hat{h}_i \left[\tilde{c}_{nh} C_n^{cv} + \tilde{d}_{nh} C_n^{dv}\right] + \hat{v}_s \hat{v}_i \left[\tilde{c}_{nv} C_n^{cv} + \tilde{d}_{nv} C_n^{dv}\right]\}\end{aligned} \tag{3.2.146}$$

By inspection of equation (3.2.140), the scattering dyad for a finite cylinder is given by (3.2.147).

$$\bar{\bar{\mathbf{F}}}(\mathbf{k}_s, \mathbf{k}_i) = -jk\, S_v\, \bar{\bar{\mathbf{X}}} \tag{3.2.147}$$

Similar to the thin sheet problem, we approximate the internal field to be perpendicular to the interface (3.2.148), for cylinders with moderately small radius ($k\, a < 0.25$).

$$\mathbf{k}_{in} \approx sign(k_i) k_1 \hat{\rho} \tag{3.2.148}$$

3.2.4.4. Model Validation

In order to validate the scattering model given in (3.2.147), its related RCS solution is compared 1) against the RCS solution solved using the Method of Moments and 2) against another analytic approximation reported in [2].

The RCS is computed at a range of incident/scattered angles. The incident and scattered wave-vectors used are given in (3.2.149-3.2.150) and at the frequency of 8 GHz. The polarization pair considered in this example is HH (yy). The incident and scattered azimuth angles (ϕ_i, ϕ_s) are set to zero and the elevation angles (θ_i, θ_s) depend on the variable parameter (θ) and are given in (3.2.151-3.2.153). The incident and scattered elevation angles have a fixed separation of $2 \cdot$

0.4128 between each other. The RCS is computed for the range of angles (θ) from 0 to 90 degrees.

$$\mathbf{k_i} = k_o \cos\phi_i \sin\theta_i(\theta)\ \hat{x} + k_o \sin\phi_i \sin\theta_i(\theta)\ \hat{y} + k_o \cos\theta_i(\theta)\ \hat{z} \tag{3.2.149}$$

$$\mathbf{k_s} = k_o \cos\phi_s \sin\theta_s(\theta)\ \hat{x} + k_o \sin\phi_s \sin\theta_s(\theta)\ \hat{y} + k_o \cos\theta_s(\theta)\ \hat{z} \tag{3.2.150}$$

$$\theta_i(\theta) = \pi - 0.4128 + \theta \text{ rad} \tag{3.2.151}$$

$$\theta_s(\theta) = 0.4128 + \theta \text{ rad} \tag{3.2.152}$$

$$\phi_i = \phi_s = 0 \tag{3.2.153}$$

Figure 3.2.5 shows different views of a three-dimensional model of the cylinder considered.

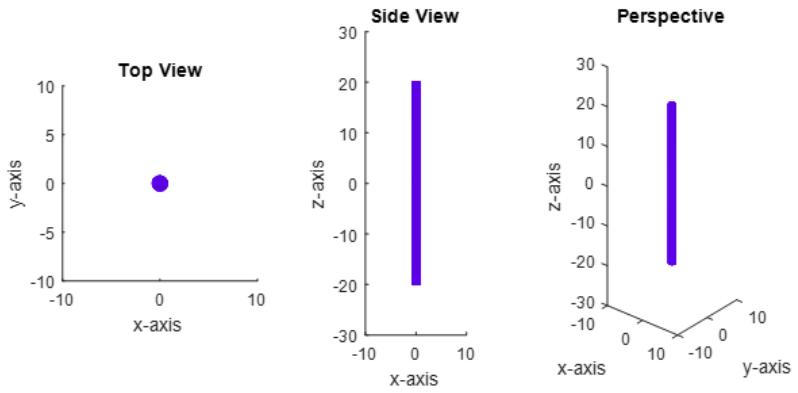

Figure 3.2.5 – Visualization of the geometric model of a dielectric cylinder. Top, side and perspective views of cylinder

Figure 3.2.6 shows the comparison of the RCS solutions found using the model described in this document (Model 2), the model reported in [2] (Model 1) and the Method of Moments (Full wave numerical simulation). The results show that the model presented in [2] is accurate at radial incidence, but inaccurate near axial incidence. In contrast, the model presented in this document agrees well with the MoM (exact) solution for both radial and axial incidence.

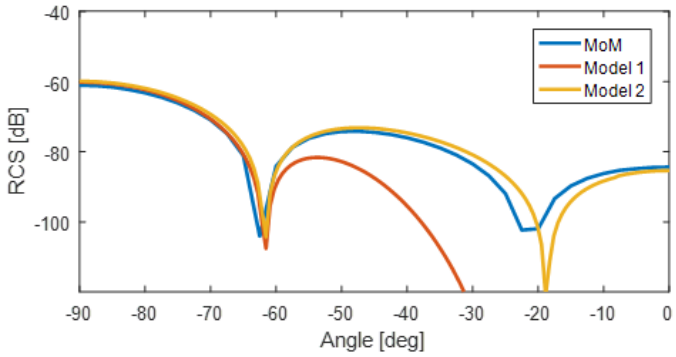

Figure 3.2.6 – Comparison of calculated RCS for a dielectric cylinder using the MoM, Model in [2] (Model 1) and the Model presented here (Model 2).

3.3. Constructive-Geometry-Method (CGM)

This section presents a new scattering analysis method, which is referred to as the Constructive-Geometric-Method or CGM.

3.3.1. The Coherent Radar Equation for Complex Targets: CGM

We define a complex target as a target with a geometric shape that can be described as the union of a set of targets for which the scattering dyad is known. The set of targets that make up a complex target are referred to as sub-targets. These sub-targets may be simple targets or complex targets.

In its current form, the Constructive-Geometry-Method (CGM), presented in this section, only includes single scattering terms. Therefore, the scattering analysis of complex targets with geometric structures containing acute concave surfaces and pairs of surfaces facing each other will not render accurate solutions.

Two types of complex targets are considered: 1) complex targets made up of joint sub-targets, 2) complex targets made up of disjointed sub-targets.

For the second type of complex targets, the distribution of sub-targets must be sparse. In this case, the effective propagation constant through the medium is computed using the distorted Born approximation, described in appendix E.

In the first-order CGM (current version), the scattered field of a complex target is equal to the superposition of the scattered fields due to the sub-targets. The received voltage of a complex target is the superposition of the received voltage due to each sub-target. Thus, the coherent radar equation for a complex target has the form given in (3.3.1). In this equation, $\bar{\bar{\mathbf{F}}}_{\boldsymbol{n}}(\mathbf{k}_{\boldsymbol{s}}(\mathbf{r}_{\boldsymbol{n}}), \mathbf{k}_{\boldsymbol{i}}(\mathbf{r}_{\boldsymbol{n}}))$ is the scattering dyad and $\mathbf{r}_{\boldsymbol{n}}$ is the scattering center of each sub-target. The scattered $\mathbf{k}_{\boldsymbol{s}}(\mathbf{r}_{\boldsymbol{n}})$ and incident $\mathbf{k}_{\boldsymbol{i}}(\mathbf{r}_{\boldsymbol{n}})$ wave-vectors for each sub-target is given by (3.3.2) and (3.3.3), respectively.

$$V_r(\omega) = jk\eta Z_a V_t(\omega) \sum_{n=1}^{N} \Phi_r(\mathbf{r}_r, \mathbf{r}_n)\, \Phi_t(\mathbf{r}_n, \mathbf{r}_t)\, \left[\, \mathbf{f}_r\big(\hat{\mathbf{k}}_s(\mathbf{r}_n)\big) \cdot\, \bar{\bar{\mathbf{F}}}_n(\mathbf{k}_s(\mathbf{r}_n), \mathbf{k}_i(\mathbf{r}_n)) \cdot\, \mathbf{f}_t(\hat{\mathbf{k}}_i(\mathbf{r}_n))\right] \tag{3.3.1}$$

$$\mathbf{k}_s(\mathbf{r}_n) = k\frac{\mathbf{r}_r - \mathbf{r}_n}{|\mathbf{r}_r - \mathbf{r}_n|} \tag{3.3.2}$$

$$\mathbf{k}_i(\mathbf{r}_n) = k\frac{\mathbf{r}_r - \mathbf{r}_n}{|\mathbf{r}_r - \mathbf{r}_n|} \tag{3.3.3}$$

The key feature of CGM is that the scattering dyads of the sub-targets are first computed at their based orientation and the rotation function is used to find the scattering dyad at the sub-targets actual orientation. The rotation of the scattering dyad was presented in section 3.1.3. For a orientation vector given by (3.3.4), the rotation function applied to a scattering dyad is given by (3.3.5), where the rotation matrix $\bar{\bar{\mathbf{T}}}_{\boldsymbol{n}}$ is given in (3.3.6).

$$\mathbf{o}_{\boldsymbol{n}} = [\alpha_n \quad \theta_n \quad \phi_n]^T \tag{3.3.4}$$

$$\bar{\bar{\mathbf{F}}}_{\boldsymbol{n}}(\mathbf{k}_s, \mathbf{k}_i) = Rot\big(\bar{\bar{\mathbf{F}}}_{\boldsymbol{n}}^{\boldsymbol{b}}(\mathbf{k}_s, \mathbf{k}_i), \mathbf{o}_{\boldsymbol{n}}\big) = \bar{\bar{\mathbf{T}}}_{\boldsymbol{n}} \cdot \bar{\bar{\mathbf{F}}}_{\boldsymbol{n}}^{\boldsymbol{b}} \left(\bar{\bar{\mathbf{T}}}_{\boldsymbol{n}}^{\,-1} \cdot\, \mathbf{k}_s, \bar{\bar{\mathbf{T}}}_{\boldsymbol{n}}^{\,-1} \cdot\, \mathbf{k}_i\right) \cdot\, \bar{\bar{\mathbf{T}}}_{\boldsymbol{n}}^{\,-1} \tag{3.3.5}$$

$$\bar{\bar{\mathbf{T}}}_{\boldsymbol{n}} = \bar{\bar{\mathbf{T}}}(\alpha_n, \theta_n, \phi_n) = \tag{3.3.6}$$

$$\begin{bmatrix} \cos\phi_n & -\sin\phi_n & 0 \\ \sin\phi_n & \cos\phi_n & 0 \\ 0 & 0 & 1 \end{bmatrix} \begin{bmatrix} \cos\theta_n & 0 & \sin\theta_n \\ 0 & 1 & 0 \\ -\sin\theta_n & 0 & \cos\theta_n \end{bmatrix} \begin{bmatrix} \cos\alpha_n & -\sin\alpha_n & 0 \\ \sin\alpha_n & \cos\alpha_n & 0 \\ 0 & 0 & 1 \end{bmatrix}$$

Taking into account these rotations, a more general form of the coherent radar equation for a complex target is shown in (3.3.7). In equation (3.3.7), $\bar{\bar{\mathbf{F}}}_{\boldsymbol{n}}^{\boldsymbol{b}}(\mathbf{k}_s, \mathbf{k}_i)$ is the scattering dyad at the base orientation, $\mathbf{r}_{\boldsymbol{n}}$ is the scattering center and $\mathbf{o}_{\boldsymbol{n}}$ is the orientation of each sub-target.

$$V_r(\omega) = jk\eta Z_a V_t(\omega) \sum_{n=1}^{N} \Phi_r(\mathbf{r}_{\boldsymbol{r}}, \mathbf{r}_{\boldsymbol{n}})\, \Phi_t(\mathbf{r}_{\boldsymbol{n}}, \mathbf{r}_t)\, \left[\mathbf{f}_{\boldsymbol{r}}\left(\hat{\mathbf{k}}_{\boldsymbol{s}}(\mathbf{r}_{\boldsymbol{n}})\right) \cdot\ Rot\left(\bar{\bar{\mathbf{F}}}_{\boldsymbol{n}}^{\boldsymbol{b}}(\mathbf{k}_s, \mathbf{k}_i), \mathbf{o}_{\boldsymbol{n}}\right) \cdot\ \mathbf{f}_{\boldsymbol{t}}(\hat{\mathbf{k}}_{\boldsymbol{i}}(\mathbf{r}_{\boldsymbol{n}})) \right] \tag{3.3.7}$$

The use of the coherent sum in (3.3.7) to determine the received signal or scattering dyad from a complex target will be referred to as the Constructive-Geometry-Method (CGM). This method relies on the knowledge of the scattering centers, orientations and base scattering dyads of each sub-target that make up the complex target. The use of the CGM to determine the scattering dyad of a complex target is discussed in the next section.

3.3.2. The Scattering Dyad of a Complex Target: The CGM

The Constructive-Geometry-Method (CGM), introduced in the previous section, can also be used to determine the scattering dyad of a complex target. The scattering dyad is determined based on the base scattering dyads, scattering centers and orientations of the sub-targets. The use of this technique to determine the scattering dyad is only valid if the antenna field patterns are approximately constant over the volume that spans the complex target (3.3.8-3.3.9).

$$\mathbf{f}_r\left(\hat{\mathbf{k}}_s(\mathbf{r}_n)\right) \approx \mathbf{f}_r\left(\hat{\mathbf{k}}_s(\mathbf{r}_o), \omega\right) \tag{3.3.8}$$

$$\mathbf{f}_t(\hat{\mathbf{k}}_i(\mathbf{r}_n)) \approx \mathbf{f}_t(\hat{\mathbf{k}}_i(\mathbf{r}_o), \omega) \tag{3.3.9}$$

The coherent radar equation of a complex target with scattering dyad $\bar{\bar{\mathbf{F}}}_o(\mathbf{k}_s, \mathbf{k}_i)$ and scattering center $\mathbf{r}_o$ is given by (3.3.10). The related scattering and incident wave vectors, which depend on the scattering center and antenna positions, are given in (3.3.11-3.3.12).

$$V_r(\omega) = jk\eta Z_a V_t(\omega)\, \Phi_r(\mathbf{r}_r, \mathbf{r}_o)\, \Phi_t(\mathbf{r}_o, \mathbf{r}_t)\ \ \mathbf{f}_r\left(\hat{\mathbf{k}}_s, \omega\right) \cdot\ \bar{\bar{\mathbf{F}}}_o(\mathbf{k}_s, \mathbf{k}_i) \cdot\ \mathbf{f}_t(\hat{\mathbf{k}}_i, \omega) \tag{3.3.10}$$

$$\mathbf{k}_s = k\frac{\mathbf{r}_r - \mathbf{r}_o}{|\mathbf{r}_r - \mathbf{r}_o|} \tag{3.3.11}$$

$$\mathbf{k}_i = k\frac{\mathbf{r}_o - \mathbf{r}_t}{|\mathbf{r}_o - \mathbf{r}_t|} \tag{3.3.12}$$

$$\bar{\bar{\mathbf{F}}}_o(\mathbf{k}_s, \mathbf{k}_i) = \bar{\bar{\mathbf{F}}}(\mathbf{k}_s(\mathbf{r}_o), \mathbf{k}_i(\mathbf{r}_o)) \tag{3.3.13}$$

Combining equation (3.3.7) and (3.3.10), the scattering dyad of a complex target ($\bar{\bar{\mathbf{F}}}_o(\mathbf{k}_s, \mathbf{k}_i)$) is given by (3.3.14). In (3.3.14), $\bar{\bar{\mathbf{F}}}_n^b(\mathbf{k}_s, \mathbf{k}_i)$ is the base scattering dyad, $\mathbf{o}_n$ is the orientation and $\mathbf{r}_n$ is the scattering center of each sub-target.

$$\bar{\bar{\mathbf{F}}}_o(\mathbf{k}_s, \mathbf{k}_i) = \left[\Phi_r(\mathbf{r}_r, \mathbf{r}_o)\, \Phi_t(\mathbf{r}_o, \mathbf{r}_t)\right]^{-1} \sum_{n=1}^{N} \Phi_r(\mathbf{r}_r, \mathbf{r}_n)\, \Phi_t(\mathbf{r}_n, \mathbf{r}_t)\ \ Rot\left(\bar{\bar{\mathbf{F}}}_n^b(\mathbf{k}_s, \mathbf{k}_i), \mathbf{o}_n\right) \tag{3.3.14}$$

3.3.3. Scattering from a Curved Thin Sheet

A curved thin sheet can be modeled as the aggregate of multiple (flat) thin sheets. This section first presents the parametric equations that describe the geometry of the curved sheet. This geometrical description and the scattering dyad of a flat thin sheet are used in the CGM method to find the scattering dyad of the curved thin sheet.

Geometrical Description

We consider a curved thin sheet, which is slightly curved in its longer dimension. We define the 'length path' as the distance covered from one side of the longer dimension to the other. The sheet is considered to have constant width 'w' and thickness 't' along the length path.

We approximate curved thin sheet as an array of small flat thin sheets arranged along the length path. Dividing the length path in '*N*' segments, we define the length path as (3.3.15).

$$s_n = L\left(\frac{n - 1/2}{N}\right) \tag{3.3.15}$$

We define the shape of the curved sheet in terms of its initial (θ_1) and final (θ_N) elevation angles as well as in terms of the radius of curvature (R) at the apex (s_o). The apex is the point in the length path with maximum curvature (i.e. minimum radius of curvature). The parametric equation for the elevation angle as a function of length path is given as the logistic function in (3.3.16).

$$\theta_n = \theta_1 + \frac{\theta_N - \theta_1}{1 + e^{-\alpha(s_n - s_o)}} \tag{3.3.16}$$

$$\alpha = \frac{4}{R(\theta_N - \theta_1)} \tag{3.3.17}$$

The other two angles will remain as zero for this example for all segments.

$$\alpha_n = 0\,;\, \phi_n = 0 \tag{3.3.18}$$

In order to keep a low number of segments in long thin sheets with localized points of curvature, the length of the segments are made variable with elevation angle. Specifically, the parametric equation (3.3.19) defines the length of the segments so that the length of segments decreases with curvature along the length path (i.e. the length of the segments is less near the apex than near the ends of the sheet).

$$L_n = L\frac{\theta_1 + \frac{\theta_N - \theta_1}{1 + 10e^{-\alpha|s_n - s_o|}}}{\left|\theta_1 + \frac{\theta_N - \theta_1}{1 + 10e^{-\alpha|s_n - s_o|}}\right|} \tag{3.3.19}$$

Given the length of the segments and the orientation vector, defined by the orientation angles, the position vectors of the segments can be defined. The position vectors of the segments ($\mathbf{r}_n$) are given by the parametric equations in (3.3.21-3.3.22). In equation (3.3.22), $\overline{\overline{\mathbf{T}}}(\mathbf{o}_n)$ is the rotation matrix applied in the direction defined by the angles in $\mathbf{o}_n$.

$$\mathbf{o}_n = [\alpha_n, \theta_n, \phi_n]^T \tag{3.3.20}$$

$$\mathbf{r}_0 = 0\hat{x} + 0\hat{y} + 0\hat{z} \tag{3.3.21}$$

$$\mathbf{r}_n = \mathbf{r}_{n-1} + \overline{\overline{\mathbf{T}}}(\mathbf{o}_{n-1}) \cdot \left[\frac{L_{n-1}}{2}\hat{z}\right] + \overline{\overline{\mathbf{T}}}(\mathbf{o}_n) \cdot \left[\frac{L_n}{2}\hat{z}\right] \tag{3.3.22}$$

Coherent Radar Equation and Scattering Dyad

The curved thin sheet was modeled above as an array of flat thin sheets. If the curved sheet faces the antennas with a convex surface, the curved sheet can be treated as a complex target. The sub-targets of this complex target are the flat thin sheets.

Using the geometrical description of the dimensions, position and orientation of the small thin sheets, the coherent radar equation for the curved thin sheet is fully determined by (3.3.23).

$$V_r(\omega) = jk\eta Z_a V_t(\omega) \sum_{n=1}^{N} \Phi_r(\mathbf{r}_r, \mathbf{r}_n)\, \Phi_t(\mathbf{r}_n, \mathbf{r}_t)\, \left[\, \mathbf{f}_r\left(\hat{\mathbf{k}}_s(\mathbf{r}_n)\right) \cdot\ Rot\left(\bar{\bar{\mathbf{F}}}_n^b(\mathbf{k}_s, \mathbf{k}_i), \mathbf{o}_n\right) \cdot\ \mathbf{f}_t(\hat{\mathbf{k}}_i(\mathbf{r}_n))\right] \tag{3.3.23}$$

The scattering dyad of a flat thin sheet at a base orientation was determined in section 3.2.3. It is given again in (3.3.24). In (3.3.24), the shape function of each segment is a function of the segment length and the width, as shown in (3.3.26).

$$\bar{\bar{\mathbf{F}}}_n^b(\mathbf{k}_s, \mathbf{k}_i) = -jk\ \ S(L_n) \cdot \bar{\bar{\mathbf{K}}}(\mathbf{k}_s, \mathbf{k}_i; k_1) \tag{3.3.24}$$

$$\bar{\bar{\mathbf{K}}}(\mathbf{k}_s, \mathbf{k}_i; k_1) = jk\ t\ [\varepsilon_{r1} - 1]\ \left(\bar{\bar{\mathbf{I}}} - \hat{k}_s \hat{k}_s\right) \cdot \left\{\bar{\bar{\mathbf{\Pi}}}(z_o)\ \mathrm{sinc}[(k_{sz} + k_{1z})t/2] + \bar{\bar{\mathbf{\Gamma}}}(z_o)\ \mathrm{sinc}[-(k_{sz} - k_{1z})t/2]\right\} \tag{3.3.25}$$

$$S(L_n) = L_n\, w\ \mathrm{sinc}(k_{dx} L_n/2)\ \mathrm{sinc}(k_{dy}\, w/2) \tag{3.3.26}$$

$$\mathbf{k}_s(\mathbf{r}_n) = k\frac{\mathbf{r}_r - \mathbf{r}_n}{|\mathbf{r}_r - \mathbf{r}_n|} \tag{3.3.27}$$

$$\mathbf{k}_i(\mathbf{r}_n) = k\frac{\mathbf{r}_r - \mathbf{r}_n}{|\mathbf{r}_r - \mathbf{r}_n|} \tag{3.3.28}$$

The scattering dyad of the curved thin sheet is found using CGM (3.3.29).

$$\bar{\bar{\mathbf{F}}}_{\boldsymbol{o}}(\mathbf{k}_s, \mathbf{k}_i) = [\Phi_r(\mathbf{r}_r, \mathbf{r}_o)\, \Phi_t(\mathbf{r}_o, \mathbf{r}_t)]^{-1} \sum_{n=1}^{N} \Phi_r(\mathbf{r}_r, \mathbf{r}_n)\, \Phi_t(\mathbf{r}_n, \mathbf{r}_t)\; Rot\left(\bar{\bar{\mathbf{F}}}_{\boldsymbol{n}}^{\boldsymbol{b}}(\mathbf{k}_s, \mathbf{k}_i), \mathbf{o}_n\right) \tag{3.3.29}$$

Validation

To validate the solution in (3.3.29) for the scattering dyad of a thin curved sheet, we calculate RCS at three different set of curvature parameters. The thin sheet considered has a width of 5mm, thickness of 0.2mm, and length of 80mm. The dielectric constant of the thin sheet is $\boldsymbol{\varepsilon_r} = 13.97 - j5.4148$. The three parameters that define the curved sheet (radius of curvature at apex, initial and final elevation angles. The set of curvature parameters for the three thin sheets considered are listed in table 3.1.1. The elevation angle is the only angle of rotation considered in this example. The other two angles are set to zero. The apex is set at the middle of the length of the thin sheet.

Table 3.3.1 – Curvature parameters for three cases of curved thin sheets

Case	**Radius of Curvature** $\boldsymbol{R = \frac{1}{\kappa}}$	**Initial Elevation Angle** $\boldsymbol{\theta_1}$	**Final Elevation Angle** $\boldsymbol{\theta_N}$
1	3 cm	90 - 15 deg	90 + 15 deg
2	2 cm	90 - 22.5 deg	90 + 22.5 deg
3	1 cm	90 - 30 deg	90 + 30 deg

Figure 3.3.1 shows the front view of a three-dimensional model of the curved thin sheet of case 2.

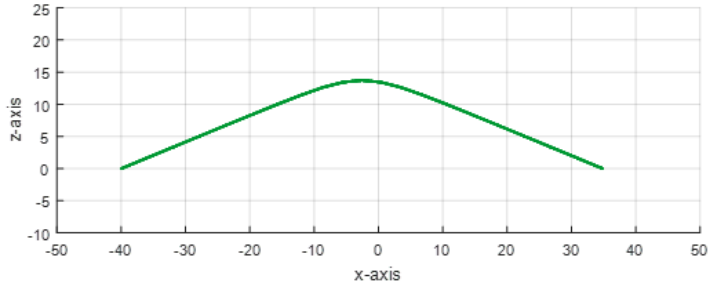

Figure 3.3.1 – Visualization of Geometric Model of Curved Thin Sheet (Front View).

a)

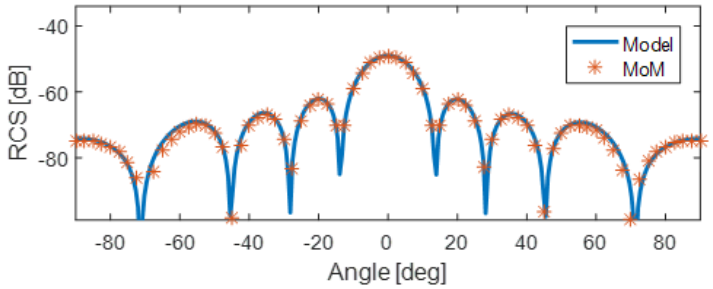

b)

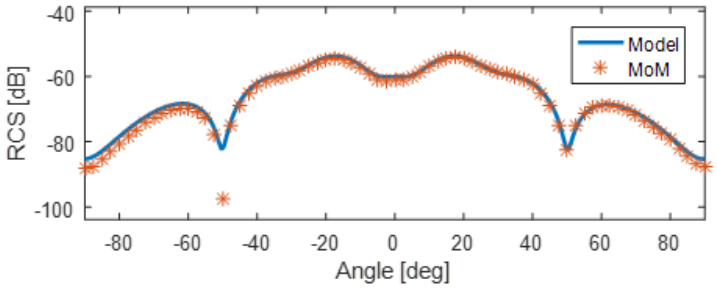

c)

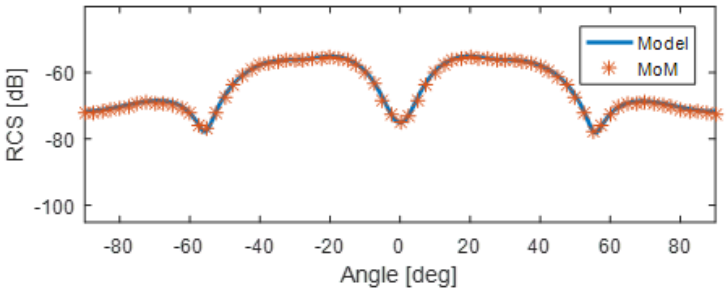

Figure 3.3.2 – Comparison of RCS computed using CGM (model) and MOM

The RCS is computed for the incident and scattered wave-vectors given by (3.3.30-3.3.31) at the frequency of 8 GHz. The polarization pair of the simulation is HH (y-axis = h).

$$\mathbf{k_i} = k_o \cos\phi_i \sin\theta_i(\theta)\ \hat{x} + k_o \sin\phi_i \sin\theta_i(\theta)\ \hat{y} + k_o \cos\theta_i(\theta)\ \hat{z} \tag{3.3.30}$$

$$\mathbf{k_s} = k_o \cos\phi_s \sin\theta_s(\theta)\ \hat{x} + k_o \sin\phi_s \sin\theta_s(\theta)\ \hat{y} + k_o \cos\theta_s(\theta)\ \hat{z} \tag{3.3.31}$$

$$\theta_i(\theta) = \pi - 0.4128 + \theta \text{ rad} \tag{3.3.32}$$

$$\theta_s(\theta) = 0.4128 + \theta \text{ rad} \tag{3.3.33}$$

$$\phi_i = \phi_s = 0 \tag{3.3.34}$$

Figure 3.3.2 shows a comparison of the RCS computed using the MoM and the CGM approaches. The solution of the analytic model (CGM) is accurate for all elevation angles.

3.3.4. Scattering from a Curved Cylinder

Similar to the previous problem, a curved cylinder may be modeled as an array of small cylinders along its length path. In this section, we present the geometrical description of the curved cylinder and its scattering dyad.

Geometrical Description

The curved cylinder is fully described by the cylinder radius, the cylinder length, the initial and end elevation angles, the azimuth angle and the radius of curvature.

We use the same parametric equations used in section 3.3.3 to describe the length path, the orientation ($\mathbf{o_n}$), the length of segments (L_{nz}) and the position vector of segments ($\mathbf{r_n}$) of the curved cylinder.

The Scattering Dyad

The scattering dyad of the curved cylinder can be determined using the CGM method (3.3.35).

$$\bar{\bar{\mathbf{F}}}_{\boldsymbol{o}}(\mathbf{k}_s, \mathbf{k}_i) = [\Phi_r(\mathbf{r}_r, \mathbf{r}_o)\, \Phi_t(\mathbf{r}_o, \mathbf{r}_t)]^{-1} \sum_{n=1}^{N} \Phi_r(\mathbf{r}_r, \mathbf{r}_n)\, \Phi_t(\mathbf{r}_n, \mathbf{r}_t)\; Rot\big(\bar{\bar{\mathbf{F}}}_{\boldsymbol{n}}^{\boldsymbol{b}}(\mathbf{k}_s, \mathbf{k}_i), \mathbf{o}_n\big) \tag{3.3.35}$$

The base scattering dyad in (3.3.35) is the scattering dyad of a finite cylinder, which was solved in section 3.2.4 and it is given again in (3.3.36). The shape function $S_v(L_{nz})$ is given as a function of the (cylinder) segment length (3.3.37). The dyadic operator $\bar{\bar{\mathbf{X}}}$ in (3.3.35) is given in (3.3.38) and its terms are fully described in section 3.2.4.

$$\bar{\bar{\mathbf{F}}}_{\boldsymbol{n}}^{\boldsymbol{b}}(\mathbf{k}_s, \mathbf{k}_i) = -jk\, S_v\, \bar{\bar{\mathbf{X}}} \tag{3.3.36}$$

$$S_v(L_{nz}) = 2\pi a L_z\, \mathrm{sinc}\left(\frac{k_{dz} L_{nz}}{2}\right) \tag{3.3.37}$$

$$\bar{\bar{\mathbf{X}}} = \sum_{\boldsymbol{n}=-\infty}^{\infty} e^{-jn\phi_s} j^n \{\hat{h}_s \hat{h}_i \left[\tilde{c}_{nh} C_n^{ch} + \tilde{d}_{nh} C_n^{dh}\right] + \hat{h}_s \hat{v}_i \left[\tilde{c}_{nv} C_n^{ch} + \tilde{d}_{nv} C_n^{dh}\right] + \hat{v}_s \hat{h}_i \left[\tilde{c}_{nh} C_n^{cv} + \tilde{d}_{nh} C_n^{dv}\right] \tag{3.3.38}$$

$$+ + \hat{v}_s \hat{v}_i \left[\tilde{c}_{nv} C_n^{cv} + \tilde{d}_{nv} C_n^{dv}\right]\}$$

Validation

To validate the solution given in (3.3.35), we determine the RCS of a curved cylinder with radius 2.0mm and length 80mm and compare it to the RCS computed using a numerical full-wave method (Method of Moments).

The radius of curvature of the cylinder is 8cm. The initial and final elevation angles are 5 and 60 degrees, respectively. Figure 3.3.3 shows a three-dimensional model of the curved cylinder.

The RCS is computed at a range of incident/scattered angles. The incident and scattered wave-vectors used are given in (3.3.39-3.3.40) and at the frequency of 8 GHz. The polarization chosen for this example is HH (yy). The incident and scattered azimuth angles (ϕ_i, ϕ_s) are set to zero and the elevation angles (θ_i, θ_s) are function of the variable parameter (θ). The incident and scattered elevation angles have a fixed separation of $2 \cdot 0.4128$ between each other. The RCS is computed for the range of angles (θ) from -90 to 0 degrees.

$$\mathbf{k_i} = k_o \cos\phi_i \sin\theta_i(\theta)\ \hat{x} + k_o \sin\phi_i \sin\theta_i(\theta)\ \hat{y} + k_o \cos\theta_i(\theta)\ \hat{z} \tag{3.3.39}$$

$$\mathbf{k_s} = k_o \cos\phi_s \sin\theta_s(\theta)\ \hat{x} + k_o \sin\phi_s \sin\theta_s(\theta)\ \hat{y} + k_o \cos\theta_s(\theta)\ \hat{z} \tag{3.3.40}$$

$$\theta_i(\theta) = \pi - 0.4128 + \theta \text{ rad} \tag{3.3.41}$$

$$\theta_s(\theta) = 0.4128 + \theta \text{ rad} \tag{3.3.42}$$

$$\phi_i = \phi_s = 0 \tag{3.3.43}$$

A comparison of the RCS computed using the MoM and the CGM are shown in figure 3.3.4. The CGM method is accurate over the all angles.

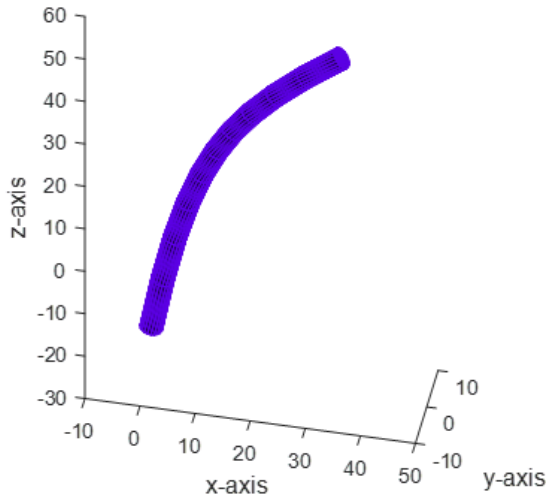

Figure 3.3.3 – Visualization of the Geometric Model of the curved cylinder

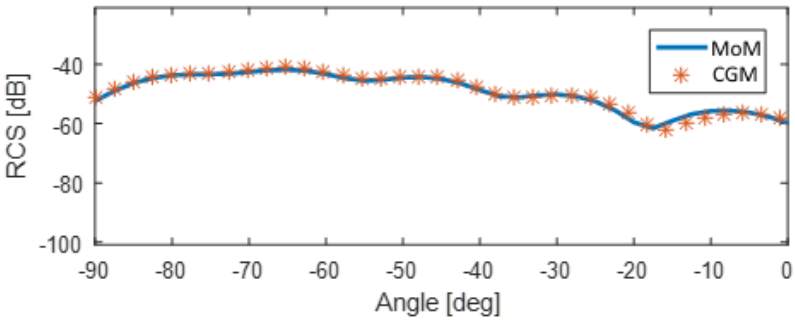

Figure 3.3.4 – Comparison of the RCS computed using CGM (Model) and MoM.

3.3.5. Scattering from a Dielectric Rough Surface

Incoherent scattering of rough surfaces at a single frequency is a mature area of research. The modeling of the delay-power-profile or waveform was reported in [3,4] for the inversion of

altimetry-waveforms and in [5] GPS-reflected-waveform from the Ocean. These waveform models are determined for narrow-band signals, where the wide-sense stationary uncorrelated scattering (WSSUS) approximation applies. In the WSSUS approximation, the random system is assumed to be uncorrelated in the frequency domain (i.e. coherency effects are negligible). In wideband systems, the coherency effects cannot be neglected to determine the time-domain waveform (delay-power-profile).

In this section, we use of the CGM approach to determine the received signal due to a rough surface. The delay power profile may be found by taking the squared amplitude of the time-domain received signal.

A dielectric rough surface can be modeled as a complex target composed of a two-dimensional array of facets. The geometric model of the rough surface is given by (3.3.44-3.3.49).

$$\mathbf{r}_{mn} = \left(m\Delta x - \frac{L_x + \Delta x}{2}\right)\hat{x} + \left(n\Delta y - \frac{L_y + \Delta y}{2}\right)\hat{y} + h(x,y)\hat{z} \tag{3.3.44}$$

$$\hat{n}(x,y) = \frac{\hat{z} - \boldsymbol{\nabla_h} h(x,y)}{|\hat{z} - \boldsymbol{\nabla_h} h(x,y)|} \tag{3.3.45}$$

$$\phi(x,y) = \begin{cases} \arctan\left(\dfrac{\hat{n}\cdot\hat{y}}{\hat{n}\cdot\hat{x}}\right) & for\ \ \hat{n}\cdot\hat{x} > 0 \\ \arctan\left(\dfrac{\hat{n}\cdot\hat{y}}{\hat{n}\cdot\hat{x}}\right) + \pi & for\ \ \hat{n}\cdot\hat{x} < 0 \\ 0 & for\ \ \hat{n}\cdot\hat{x} = 0 \end{cases} \tag{3.3.46}$$

$$\theta(x,y) = \arccos(\hat{n}\cdot\hat{z}) \tag{3.3.47}$$

$$L_{xn} = \Delta x\sqrt{1 + \left(\frac{h(x_{n+1},y) - h(x_{n-1},y)}{2\Delta x}\right)^2} \tag{3.3.48}$$

$$L_{yn} = \Delta y \sqrt{1 + \left(\frac{h(x, y_{n+1}, y) - h(x, y_{n-1})}{2\Delta y} \right)^2} \tag{3.3.49}$$

The coherent radar equation for the rough surface is given by (3.3.50), where the scattering dyad in base orientation is show in (3.3.51). The reflection dyadic function, which was solved for in (3.2.2) is show again in (3.3.52). The shape function considered for the facets is expressed in (3.3.53).

$$V_r(\omega) = jk\eta Z_a V_t(\omega) \sum_{n,m} \Phi_r(\mathbf{r_r}, \mathbf{r_{mn}})\, \Phi_t(\mathbf{r_n}, \mathbf{r}_t) \left[\mathbf{f_r}\left(\hat{\mathbf{k}}_s(\mathbf{r_n})\right) \cdot Rot\left(\bar{\bar{\mathbf{F}}}^{\boldsymbol{b}}_{\boldsymbol{mn}}(\mathbf{k}_s, \mathbf{k}_i), \mathbf{o_n}\right) \cdot \mathbf{f_t}(\hat{\mathbf{k}}_i(\mathbf{r_n})) \right] \tag{3.3.50}$$

$$\bar{\bar{\mathbf{F}}}^{\boldsymbol{b}}_{\boldsymbol{n}}(\mathbf{k}_s, \mathbf{k}_i) = -jk\, S\left(L_{xn}, L_{yn}\right) \bar{\bar{\mathbf{R}}} \tag{3.3.51}$$

$$\begin{aligned} \bar{\bar{\mathbf{R}}} = {} & +\left(\hat{v}_s\hat{v}_s + \hat{h}_s\hat{h}_s\right) \cdot \left[\hat{h}_i\hat{h}_i k_{inz}(1 - R_h) - \left(\hat{z} \times \hat{h}_i\right)\hat{v}_i(1 + R_v)\right] \\ & +\left(\hat{h}_s\hat{v}_s - \hat{v}_s\hat{h}_s\right) \cdot \left[\hat{h}_i\hat{v}_i k_{inz}(1 - R_v) + \left(\hat{z} \times \hat{h}_i\right)\hat{h}_i(1 + R_h)\right] \end{aligned} \tag{3.3.52}$$

$$S(L_{xn}, L_{yn}) = A\, \mathrm{sinc}(k_{dx}\, L_{xn}/2)\, \mathrm{sinc}(k_{dy}\, L_{yn}/2) \tag{3.3.53}$$

3.4. References

[1] D. M. LeVine, R. Meneghini, R. H. Lang, S. S. Seker, “Scattering from arbitrarily oriented dielectric disk in the physical optics regime,” Journal of the Optical Society of America, vol. 73, Issue 10, pp. 1255-1262, 1983.

[2] James White, “Scattering of a plane wave from a circular dielectric cylinder at oblique incidence,” Canadian Journal of Physics, vol. 33 no. 5, pp. 189-195, 1955.

[3] M. H. Newkirk and G. S. Brown, "A waveform model for surface and volume scattering from ice and snow," in IEEE Transactions on Geoscience and Remote Sensing, vol. 34, no. 2, pp. 444-456, Mar 1996.

[4] G. S. Brown, “A useful approximation for the flat surface impulse response,” *IEEE Trans. Antennas Propagat.*, vol. 37, pp. 764-767, 1989.

[5] V. U. Zavorotny, A. G. Voronovich, “Scattering of GPS signals from the ocean with wind remote sensing applications,” IEEE Transactions on Geoscience and Remote Sensing, vol. 38, no. 2, pp. 951-964, March 2000.

4. Coherent UWB Radar Simulator for Wheat-Plant-Related Targets

This chapter provides a detailed description of a novel coherent UWB radar simulator. The simulator was developed to compute an approximation of the coherent radar response from 2 GHz to 18 GHz due to wheat canopies and related targets. The radar-cross-section as a function of time and frequency are calculated from the coherent radar response, as described in section 4.1.

The radar simulator is based on the coherent scattering concepts presented in chapter 3 and it is used to compute the radar response and the scattering response of complex targets. As a first step, the radar simulator generates a geometric description of the complex target. The second step of the simulator is the computation of the forward scattering, which results in the radar response and scattering response of the target.

This chapter is divided in five sections.

Section 4.1 presents an overview of the simulator. This section provides a brief description of the main steps of the radar simulator algorithm. It also describes the configuration of the antennas with respect to the target within the simulator.

Section 4.2 describes the geometric modeling performed by the simulator of the wheat canopy and related targets.

Section 4.3 shows the forward scattering equations for all the considered targets considered in this study related to wheat canopies.

In section 4.4, simulation results are shown for various configurations of the different targets considered. The radar simulation results are validated by comparing them against results computed with a full-wave simulator package from a commercial vendor.

Section 4.5 presents an experimental validation of the numerical simulator. Multiple measurements are performed using different configurations of wheat-related targets, and the results are compared against the radar simulations.

4.1. Overview of the Coherent UWB Radar Simulator

A radar simulator was developed to compute the approximated coherent radar response due to a wheat canopy for a given set of antenna and wheat canopy parameters, over the 2-18 GHz frequency range. The coherent radar response is used to calculate the frequency and time dependent radar-cross-section due to the wheat canopy at a given configuration. The simulator may also be used to compute the radar response and radar-cross-section due to a single plant or plant constituent.

The simulator algorithm is divided in two main steps: geometric modeling and forward scattering modeling. In the first step, the simulator constructs a description of the geometry of the complex target (e.g. wheat canopy), based on a set of defined geometric parameters. In the second step, the geometrical description of the complex target is used with its related coherent radar equation to solve for the radar response of the complex target.

This section (4.1) provides an overview of the radar simulator. Section 4.1.1 defines the coherent radar response, scattering response and radar-cross-section. Section 4.1.2 shows the

configuration of the antennas with respect to the target and it lists the antenna parameters required by the simulator. Section 4.1.3 and section 4.1.4 provide an overview of the two main steps of the simulator and list the target parameters required for the simulator.

4.1.1. Coherent Radar Response, Scattering Response and Radar-Cross-Section

The coherent radar response $H_t(f)$ is the ratio of the received $V_r(f)$ to the transmitted $V_t(f)$ signals of a radar due to a target, as shown in (4.1.1). These signals are the frequency-domain voltages at the receive and transmit antenna ports, respectively.

$$H_t(f) = V_r(f)/V_t(f) \tag{4.1.1}$$

For a given target with scattering center $\mathbf{r}_o$ and scattering dyad $\bar{\bar{\mathbf{F}}}_o(\mathbf{k}_s, \mathbf{k}_i)$, the coherent radar response can be calculated using the coherent radar equation (4.1.2). The terms k, η, Z_a, $\Phi_r(\mathrm{r}_r, \mathrm{r}_o)$, $\Phi_t(\mathrm{r}_o, \mathrm{r}_t)$ are the wave number, intrinsic impedance of free space, the reflected propagation function and the transmitted propagation function, respectively. The vectors $\mathbf{r}_r$ and $\mathbf{r}_t$ are the position vectors of the receive and transmit antennas, respectively.

$$H_t(f) = [jk\eta Z_a\, \Phi_r(\mathbf{r}_r, \mathbf{r}_o)\, \Phi_t(\mathbf{r}_o, \mathbf{r}_t)]\left[\mathbf{f}_r \cdot \bar{\bar{\mathbf{F}}}_o(\mathbf{k}_s, \mathbf{k}_i) \cdot \mathbf{f}_t\right] \tag{4.1.2}$$

The incident $\mathbf{k}_i$ and scattering $\mathbf{k}_s$ wave vectors, used in (4.1.2), are defined in (4.1.3) and (4.1.4), respectively. The propagation functions for the transmitted and reflected signals are defined in (4.1.5) and (4.1.6), respectively.

$$\mathbf{k}_i = k\frac{\mathbf{r_o} - \mathbf{r_t}}{|\mathbf{r_o} - \mathbf{r_t}|} \tag{4.1.3}$$

$$\mathbf{k}_s = k\frac{\mathbf{r_r} - \mathbf{r_o}}{|\mathbf{r_r} - \mathbf{r_o}|} \tag{4.1.4}$$

$$\Phi_t(\mathbf{r_t}, \mathbf{r}_o) = \frac{e^{j\mathbf{k_i}\cdot(\mathbf{r_o}-\mathbf{r_t})}}{4\pi|\mathbf{r_o} - \mathbf{r_t}|} \tag{4.1.5}$$

$$\Phi_r(\mathbf{r_o}, \mathbf{r}_r) = \frac{e^{j\mathbf{k_i}\cdot(\mathbf{r_r}-\mathbf{r_o})}}{4\pi|\mathbf{r_r} - \mathbf{r_o}|} \tag{4.1.6}$$

The scattering response due to a target with scattering dyad $\bar{\bar{\mathbf{F}}}_o(\mathrm{k}_s, \mathrm{k}_i)$, evaluated at the scattering center $\mathbf{r_o}$ can be computed from the radar response H_t, as shown in (4.1.7). In (4.1.7), the operation $|*|_v$ is the vector magnitude, not to be confused with the operator for the complex-value amplitude $|*|$. It should be noted that the scattering dyad and the scattering response are defined with respect to a scattering center, which need not be equal to the geometric center of the target.

$$F_{o,qp}(f) = F_{o,qp}(\mathbf{k_s}, \mathbf{k_i}) = \left[\,\hat{q}\cdot\,\bar{\bar{\mathbf{F}}}_o(\mathbf{k_s}, \mathbf{k_i})\cdot\hat{p}\right] = \,[jk\eta Z_a\,\Phi_r(\mathbf{r_r}, \mathbf{r_o})\,\Phi_t(\mathbf{r_o}, \mathbf{r}_t)|\mathbf{f_r}|_v|\mathbf{f_t}|_v]^{-1}\,H_t(f) \tag{4.1.7}$$

The radar-cross-section (RCS) can be solved from the scattering response in the time and frequency domains (4.1.8-4.1.9), where $F_{o,qp}(t)$ is the inverse Fourier transform of $F_{o,qp}(f)$.

$$\sigma_{qp}(f) = \frac{1}{4\pi}\left|F_{o,qp}(f)\right|^2 \tag{4.1.8}$$

$$\sigma_{qp}(t) = \frac{1}{4\pi B}\left|F_{o,qp}(t)\right|^2 \tag{4.1.9}$$

4.1.2. Antenna Parameters and Configuration

The simulator considers a transmit antenna, which radiates electromagnetic waves, and a receive antenna, which captures the scattered electromagnetic waves from the target. The simulator may define two different antennas or a single antenna for transmission and reception of electromagnetic signals. In the framework considered in this work, the simulator uses two antennas with similar or identical position to those used by the actual radar system.

Antenna Parameters

The antenna parameters required by the simulator are the transmit antenna position $\mathbf{r}_t$, the receive antenna position $\mathbf{r}_r$, the transmit antenna field pattern $\mathbf{f}_t$, and the receive antenna field pattern $\mathbf{f}_r$.

The radar simulations considered in this document attempt to replicate the parameters of the antennas used in the actual radar. The antennas are placed at some height above the target, which is located on or above the ground, and they are separated by some distance from each other.

For simulations involving targets confined to narrow antenna beamwidths, the simulator uses a normalized antenna field pattern. This choice of field pattern allows the simulation results to be compared against full-wave simulations using commercial software. On the other hand, wheat canopy simulations, which involves a target illuminated at a wide range of antenna angles, use specified antenna field patterns. The specified antenna field pattern used in these canopy

simulations may be the measured field pattern of the actual radar antenna or some other approximation. The measured field pattern of the radar antennas is described in chapter 5.

The electric field incident to a point with position $\mathbf{r}_o$, due to an antenna with field pattern $\mathbf{f_t}(\mathbf{k_i})$, is given by (4.1.10). Equation (4.1.10) is described in chapter 3.

$$\mathbf{E}_i(\mathbf{r}) = -jk\eta\ \Phi_t(\mathbf{r}, \mathbf{r}_o)\ \mathbf{f_t}(\mathbf{k_i}) V_t(f) \tag{4.1.10}$$

The received signal (voltage) due to a field $\mathbf{E}_r$, captured by the receive antenna with field pattern $\mathbf{f_r}(\mathbf{k_s})$, is given by (4.1.11). Equation (4.1.11) is also described in chapter 3.

$$V_r(f) = -Z_a\ \mathbf{f_r}(\mathbf{k_s}) \cdot \mathbf{E}_r \tag{4.1.11}$$

Figure 4.1 shows two antennas separated by 2 ft, and positioned at a height of 2 m from the z-axis origin. Specifically, the position of the transmit and receive antennas are (-0.3048 m, 0, 2m) and (+0.3048 m, 0, 2 m), respectively. Both antennas are polarized parallel to the y-axis (H-H).

Figure 4.1 also shows the coherent amplitude of the y-component of the field radiated by the transmit antenna. This coherent amplitude was computed using equation (4.1.10). The radiated field was evaluated below 0.6 m, which is in the far-field region of the transmit antennas. This figure shows that the phase of the electric field spreads spherically away from the transmit antenna. The magnitude of the amplitude of the field decays with increasing distance from the antenna.

The radiated field in the example depicted by figure 4.1.1 assumes that the antenna is omnidirectional. In other words, the amplitude of the field pattern was assumed constant with

respect to angle. As mentioned earlier, the antenna field pattern used by the simulator need not be constant.

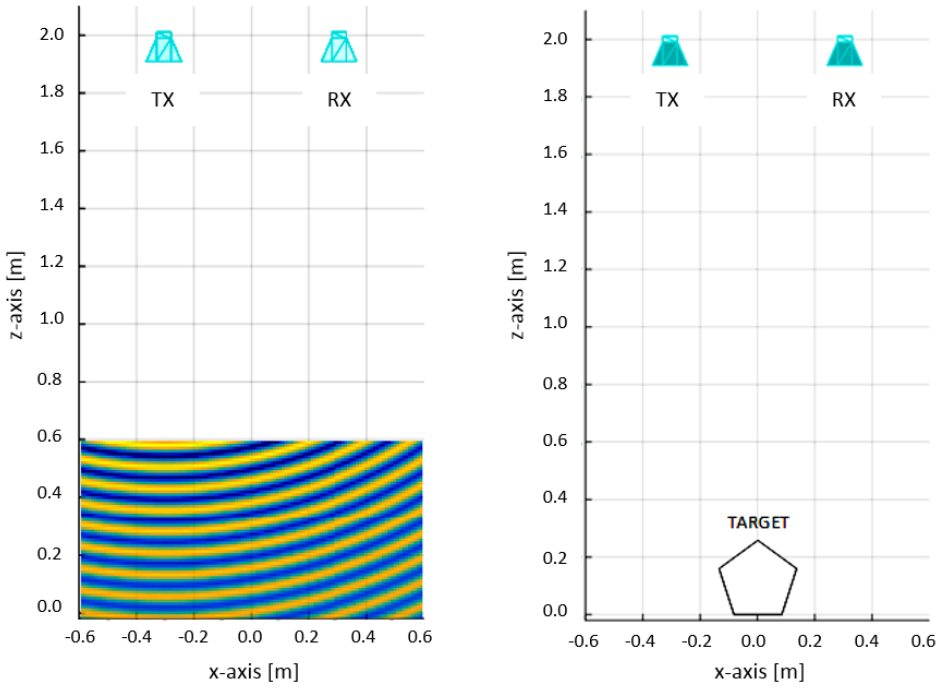

Figure 4.1.1 – Antenna Configuration: Amplitude of the y component of the E-Field Radiated by the Transmit Antenna (left inset); Antennas positions with respect a target located at the origin (right inset)

As mentioned earlier, the antennas are oriented with their main beam pointing downward. Unless specified otherwise, the defined scattering center of the complex targets considered by the simulator will be the origin. An example of this type of configuration is shown in figure 4.1

(right). A simple pentagon is shown in figure 4.1 as a placeholder for any complex-target considered by the simulator.

It should be noted that the pentagon in figure 4.1 (right) has its base at the origin of the coordinate system, but its geometric center is not at the origin. As it was mentioned in section 4.1.1, the scattering center is not necessarily equal to the geometric center. Unless noted otherwise, the origin is considered by the simulation as the scattering center of complex targets.

4.1.3. First Step of the Simulator: Geometric Model

The geometric modeling of wheat canopies used by the simulator is described in detail in section 4.2. This geometric model considers two types of targets: complex and primitive targets. Primitive targets are defined as those for which its scattering dyad and radar response can be computed based on its attributes alone. Complex targets are the geometric union of multiple targets, which may be primitive or complex. The scattering response and radar response of complex targets are found using the coherent radar equation of complex targets, described in chapter 3. This equation depends on the radar responses of the targets that make up the aforementioned union.

For this simulator, the geometric model of a complex target is the set of parametric equations that describe all its attributes and the attributes of all targets that geometrically make up the complex target. The only attribute considered for a complex target is its position. In contrast, the attributes of primitive targets are their position, orientation, material properties and dimensions.

The first step of the simulator consists of generating the geometric model of the complex target based on ‘description’ parameters given by the user. These ‘description’ parameters are the input parameters to the parametric equations that describe the geometrical models of the targets. The parametric equations of the attributes of all considered targets are given in section 4.2.

4.1.4. Second Step of the Simulator: Forward Scattering

The forward scattering step of the simulator computes the radar response and scattering dyad of the complex target considered (i.e. wheat canopy). The inputs to this step are the antenna parameters, discussed in section 4.1.1, and the geometric model of the complex target, fully described in section 4.2. The forward scattering step of the simulator is based on the coherent radar equation of complex targets, described in chapter 3. The equations for the radar response and scattering dyad of all considered targets are given in section 4.3.

In order to define the coherent radar equation of complex targets, we first consider a complex target as a target that can be expressed as the geometric union of other targets. We refer to these other targets as the sub-targets of the complex targets. The coherent radar equation of is complex targets approximates its radar response as the coherent superposition of the coherent radar responses due to its sub-targets.

Wheat canopies are sparse inhomogeneous media. The simulator uses the distorted Born approximation to account for propagation effects of the incident and scattered signals through the canopy. To apply this correction, the simulator includes a propagation correction function

$\Phi_e(\mathbf{r}_r, \mathbf{r}_t, \mathbf{r}_n)$ in the computation of the radar response, which is described in appendix E. Equation (4.1.12) shows an example of a coherent radar equation for a complex target made up of '*n*' sub-targets and propagation correction function $\Phi_e(\mathbf{r}_r, \mathbf{r}_t, \mathbf{r}_n)$. In (4.1.13), $\mathbf{r}_n$ and $\mathbf{o}_n$ are the scattering center and orientation of each sub-target. The rotation function $Rot(*)$ is defined in chapter 3.

$$H_t(f) = jk\eta Z_a \sum_{n=1}^{N} \Phi_e(\mathbf{r}_r, \mathbf{r}_t, \mathbf{r}_n)\Phi_r(\mathbf{r}_r, \mathbf{r}_n)\,\Phi_t(\mathbf{r}_n, \mathbf{r}_t)\,\left[\,\mathbf{f}_r\left(\hat{\mathbf{k}}_s(\mathbf{r}_n)\right)\cdot\, Rot\left(\bar{\bar{\mathbf{F}}}_n^b(\mathbf{k}_s, \mathbf{k}_i), \mathbf{o}_n\right)\cdot\, \mathbf{f}_t(\hat{\mathbf{k}}_i(\mathbf{r}_n))\right] \tag{4.1.12}$$

4.2. Geometric Modeling of Wheat Canopies

Broadly, geometric modeling is the mathematical description of a geometric shape. This section describes the geometric modeling of wheat canopies and its constituents. Since these shapes (canopies and its constituents) are geometric solids, the geometric model is a description of three-dimensional objects.

The goal of the geometric modeling defined in this section is to provide a mathematical description of the geometry of the object being modeled, based on a set of 'description' parameters of the object. We refer to any object to be measured by a radar as a 'target'. We consider two types of targets: complex targets and primitive targets (or simply primitives). A primitive target is any target for which its scattering dyad can be defined solely in terms of its dimensions, material properties and position. A complex target is any target with a geometry that can be approximated as the union of other targets. The targets that make up a complex targets are the sub-targets of the complex targets. Sub-targets may be primitives or complex

targets. Primitive solids can be fully described geometrically by its dimensions, material properties, position and orientation. A complex target is then defined by its position and by the geometrical description of all its sub-targets. This type of geometric description was chosen because it is the only information required by the forward scattering step of the simulator. In this document, we refer to the parameters required to describe geometrically a target as ‘attributes’.

As mentioned above, a complex target may have sub-targets that are complex targets themselves. Moreover, some of the sub-targets that geometrically make up a complex target have related attributes. For this reason, we organize the main complex target, a wheat canopy, using a tree data structure. Every node in the tree correspond to a target related to the canopy. This tree structure is described in section 4.2.1. The tree structure aids in identifying all the targets using an indexing system. The same indexing convention is used for the all the attributes. With the indexing system, the attributes of target that are siblings in the tree structure can be expressed using parametric equations. Therefore, the entire geometrical description of the canopy is defined using parametric equations, based on a set of ‘description’ parameters given by the simulator user.

4.2.1. Tree Structure and Indexing Convention

4.2.1.1. Tree Structure

The relationship between a complex target and all the related sub-targets forms a tree data structure, where each node corresponds to a target. For the case of a canopy being the main target, the canopy is the root of the tree. Figure 4.2.1 depicts the tree structure with a wheat canopy as the root node.

The depth or order of a node in a tree structure is defined as the number of edges (i.e. direct links) between the node and the root. The canopy, which is the root of the considered tree structure, has order zero. The plants, directly linked to the canopy, have order one. The plants' constituents (heads, stems and leaves) are nodes of order two. The solid primitives, which have order three, sit at the bottom of the tree structure.

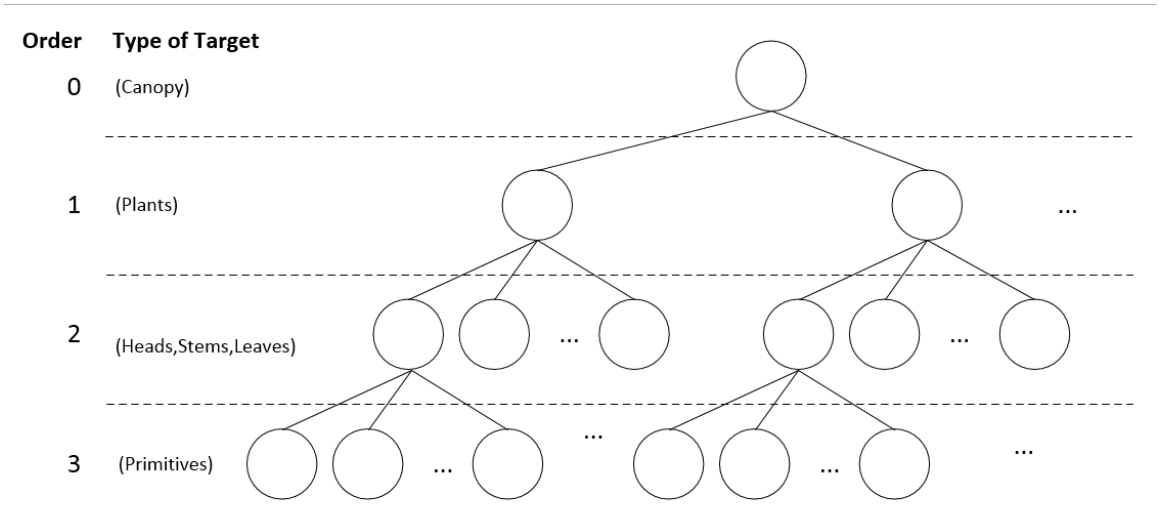

Figure 4.2.1 – Tree Structure Diagram for a Wheat Canopy

In a tree structure, the node that connects to one or more nodes of lower order is a parent node. The nodes of lower hierarchy connected to a parent node are its children nodes. The nodes that share a parent node are siblings.

All the nodes in the tree structure are targets. All targets are data objects that share similar attributes. Specifically, all targets have a position, described by a position vector. Additionally, all primitive targets have a solid shape, dimensions and material properties. Target attributes are defined in section 4.2.2.

Each target in the tree structure represents a type of target (e.g. plant, leave or cylinder). Sibling nodes with the same target type are distinguished from each other by an index. Additionally, the index of each parent is transmitted to its children. This indexing scheme is used for the identification of each individual target. The indexing system is explained in section 4.2.1.2.

4.2.1.2. Node Indexing and Target Sets

Indexing is used to identify each individual target within the tree structure. Each set of siblings is indexed sequentially from one to the maximum number of siblings of the same target type. Additionally, the index of each parent is passed down through each generation.

We define the set T as the set of all targets, as shown in (4.2.1). The targets in set T have the form $t_{X,\mathbf{m}}$. The subscript X refers to the type of target. The term X, which belongs to F_T, is also the sub-set of targets of type X. The family of sub-sets F_T contains the sub-sets of all the target types considered (4.2.2). The list of indices $\mathbf{m}$ belongs to the set M, defined by (4.2.3). In (4.2.3), $d(t_{X,\mathbf{m}})$ is the depth function, which outputs the depth or order of the target.

$$T = \{\, t_{X,\mathbf{m}} \mid (X \in F_T) \wedge (\mathbf{m} \in M) \,\} \tag{4.2.1}$$

$$F_T = \{C, P, S, L, H, Q, U, V\} \tag{4.2.2}$$

$$M = \begin{cases} \emptyset & for\ d(t_{X,\mathbf{m}}) = 0 \\ \mathbb{N}^2 & for\ d(t_{X,\mathbf{m}}) = 1 \\ \mathbb{N}^2 \times \mathbb{N} & for\ d(t_{X,\mathbf{m}}) = 2 \\ \mathbb{N}^2 \times \mathbb{N} \times \mathbb{N} & for\ d(t_{X,\mathbf{m}}) = 3 \end{cases} \tag{4.2.3}$$

The depth function $d(t_{X,\mathbf{m}})$ (4.2.4), mentioned above, outputs the depth or order of the node in the tree (4.2.5).

$$d: T \rightarrow \mathbb{N} \tag{4.2.4}$$

$$d(t_{X,\mathbf{m}}) = depth\ of\ node\ (i.e. target)\ in\ the\ tree\ structure \tag{4.2.5}$$

The members (targets) of the set T follow the order relationship given in (4.2.6).

$$(t_{X,\mathbf{m}} < t_{Y,\mathbf{n}})\ if\ (d(t_{X,\mathbf{m}}) < d(t_{Y,\mathbf{n}})), \qquad X, Y \in F_T, \qquad \mathbf{m}, \mathbf{n} \in M \tag{4.2.6}$$

The members of F_T are disjoint sub-sets of T. The set T is the union of all its sub-sets (4.2.7). The sub-set of all targets with type canopy is C. Likewise, the sub-sets of all targets with type plant, stem, leaf and head are P, S, L and H, respectively. The sub-sets Q, U and V are the ones containing the primitives. The sub-set Q contains all the leaf sheets, the sub-set U contains all the stem- cylinders and the sub-set V contains all the head- cylinders. Head and stem have different kind of primitives because they follow different shape rules and they have different types of material properties.

$$T = C \cup P \cup S \cup L \cup H \cup Q \cup U \cup V \tag{4.2.7}$$

Zero-Order Targets

The sub-set C contains all targets of type “canopy.” There is only one member (t_C) in this sub-set and it has order zero in the tree structure.

$$C = \{t_C\} \tag{4.2.8}$$

First-Order Targets

The targets of order one are the all the siblings of targets with type “plant.” The sub-set P is the set of all targets with the form $t_{P,(\mathbf{i}_P)}$, given that for all indices $\mathbf{i}_P$ there exist a target t_C that has lower order than $t_{P,(\mathbf{i}_P)}$ (4.2.9). Since $t_{P,(\mathbf{i}_P)}$ is order one, this means that there must exist a target with order zero (i.e. a root node). The index set for the targets of type “plant” is given by (4.2.10).

$$P = \left\{ t_{P,(\mathbf{i}_P)} \in T \mid \left(\forall \mathbf{i}_P \in I_P \, , \exists t_C < t_{P,(\mathbf{i}_P)} \right) \right\} \tag{4.2.9}$$

$$I_P = \left\{ \mathbf{i}_P \in \mathbb{N}^2 \mid \left[\mathbf{i}_P = \left(i_{px}, i_{py} \right) \right] \wedge \left(1 \leq i_{px} \leq N_{px} \right) \wedge \left(1 \leq i_{py} \leq N_{py} \right) \right\} \tag{4.2.10}$$

Second Order Targets

The targets of type “leaf,” “stem,” or “head” are second order. The sub-sets L, L and L contain all targets of type “leaf,” “stem,” and “head,” respectively. For each one of these sets, the list of indices has two members. The first index corresponds to the parent’s index and the second one to the target index with respect to their siblings. There must be a parent (plant) related to each target in the sub-sets in (4.2.11-4.2.13).

$$L = \left\{ t_{L,(\mathbf{i}_P,i_L)} \in T \mid \left(\forall i_L \in I_L \, , \exists t_{P,(\mathbf{i}_P)} < t_{L,(\mathbf{i}_P,i_L)} \right) \wedge \left(\mathbf{i}_P \in I_P \right) \right\} \tag{4.2.11}$$

$$S = \left\{ t_{S,(\mathbf{i}_P,i_S)} \in T \mid \left(\forall i_S \in I_S \, , \exists t_{P,(\mathbf{i}_P)} < t_{S,(\mathbf{i}_P,i_S)} \right) \wedge \left(\mathbf{i}_P \in I_P \right) \right\} \tag{4.2.12}$$

$$H = \left\{ t_{H,(\mathbf{i}_P,i_H)} \in T \mid \left(\forall i_H \in I_H \, , \exists t_{P,(\mathbf{i}_P)} < t_{H,(\mathbf{i}_P,i_H)} \right) \wedge \left(\mathbf{i}_P \in I_P \right) \right\} \tag{4.2.13}$$

The index sets for the leaf, stem and head sub-sets are given by (4.2.14-4.2.16).

$$I_L = \{i_L \ \in \mathbb{N} \mid (1 \leq i_L \leq N_L)\} \tag{4.2.14}$$

$$I_S = \{i_S \ \in \mathbb{N} \mid (1 \leq i_S \leq N_S)\} \tag{4.2.15}$$

$$I_H = \{i_H \in \mathbb{N} \mid (1 \leq i_H \leq N_H)\} \tag{4.2.16}$$

Third Order Targets

The third order targets are the target primitives, with type “leaf-sheet” (Q), “stem-cylinder” (U) and “head-cylinder” (V). The sub-sets containing all targets of each type of primitive are given in (4.2.17-4.2.19). For each primitive target in each set, there must be a related parent (plant constituent).

$$Q = \left\{t_{Q,(\mathbf{i}_P,i_L,i_Q)} \ \in T \mid \left(\forall i_Q \in I_Q, \exists t_{L,(\mathbf{i}_P,i_L)} < t_{Q,(\mathbf{i}_P,i_L,i_Q)}\right) \ \wedge (\mathbf{i}_P \in I_P) \wedge (\mathbf{i}_L \in I_L)\right\} \tag{4.2.17}$$

$$U = \left\{t_{U,(\mathbf{i}_P,i_S,i_U)} \ \in T \mid \left(\forall i_U \in I_U, \exists t_{S,(\mathbf{i}_P,i_S)} < t_{U,(\mathbf{i}_P,i_S,i_U)}\right) \ \wedge (\mathbf{i}_P \in I_P) \wedge (\mathbf{i}_S \in I_S)\right\} \tag{4.2.18}$$

$$V = \left\{t_{V,(\mathbf{i}_P,i_H,i_V)} \ \in T \mid \left(\forall i_V \in I_V, \exists t_{H,(\mathbf{i}_P,i_H)} < t_{V,(\mathbf{i}_P,i_H,i_V)}\right) \ \wedge (\mathbf{i}_P \in I_P) \wedge (\mathbf{i}_H \in I_H)\right\} \tag{4.2.19}$$

The sub-set indices for the Q, U and V sub-sets are given by (4.2.20-4.2.21).

$$I_Q = \left\{i_Q \ \in \mathbb{N} \mid \left(1 \leq i_Q \leq N_Q\right)\right\} \tag{4.2.20}$$

$$I_U = \{i_U \ \in \mathbb{N} \mid (1 \leq i_U \leq N_U)\} \tag{4.2.21}$$

$$I_U = \{ i_U \ \in \mathbb{N} \mid (1 \leq i_U \ \leq N_U) \} \tag{4.2.22}$$

Figure 4.2.2 shows a diagram of zero and first order targets in the tree structure. The diagram uses the indexing convention specified in this section. Figure 4.2.3 shows the diagram for the connection between first and second order targets. Figure 4.2.4 shows the diagram for the connection between second and third order targets.

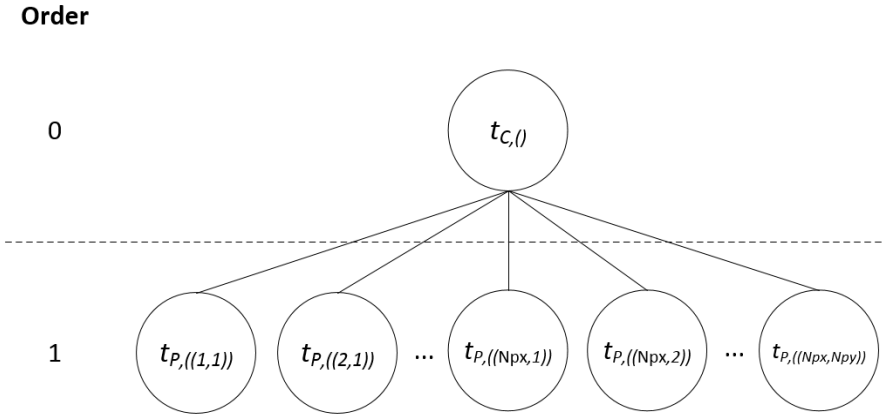

Figure 4.2.2 – Tree Structure: Canopy (zero-order node) to Plants (first-order nodes)

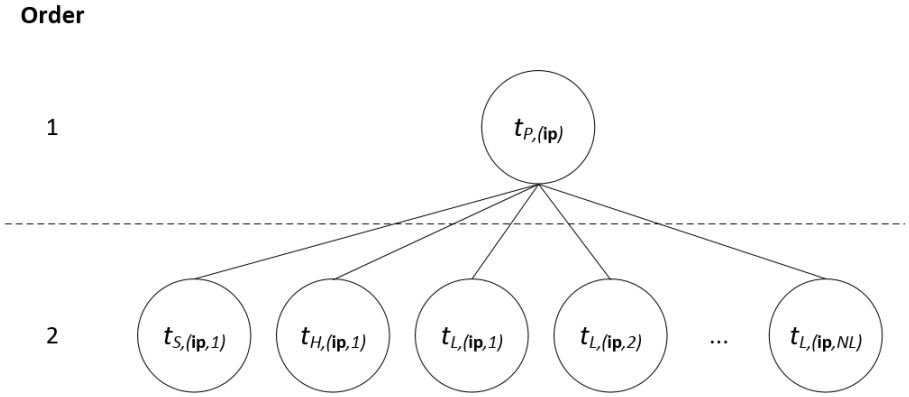

Figure 4.2.3 – Tree Structure: One Plant (first-order node) to Plant Constituents (head, stem and leaves) (second-order nodes)

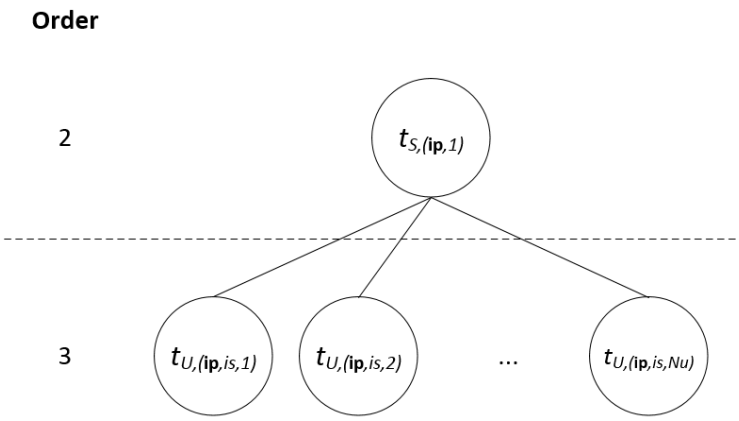

Figure 4.2.4 – Tree Structure: One Stem (second-order node) to its Primitive Solids (Stem Cylinders) (third-order nodes)

4.2.2. Target Attributes: Sets, functions and indexing

Each target that belongs to the tree data structure has related attributes. Specifically, all targets have a position, represented by a vector. Additionally, all primitives also have an orientation, dimensions and material properties. The number of dimensions of a solid depends on the type of geometric shape that it represents. The only material property considered for the targets is its complex relative permittivity.

Theoretically, each target is related to each one of its attributes through a mapping function. Computationally, the target is implemented as an object with attributes, and each attribute is accessed by means of a dot operator.

4.2.2.1. Position Vector

The position vector of the target is the vector that goes from the origin to the target's scattering center. It represents the target's position or location in the three dimensional Euclidian space.

The set A_r, which is a sub-set of $\mathbb{R}^3$, of contains the position vector for each target in the set T. The set A_r can be organized in an identical tree-structure as that of the target objects. The members of the set A_r follow the same indexing convention as the targets. The position vectors of the form $\mathbf{r}_{X,\mathbf{m}}$ are related to the targets of the form $t_{X,\mathbf{m}}$ and can be accessed through the function f_r, defined in (4.2.23-4.2.24).

$$f_r: T \to A_r \ , \ A_r \subset \mathbb{R}^3 \tag{4.2.23}$$

$$f_r(t_{X,\mathbf{m}}) = \mathbf{r}_{X,\mathbf{m}}, \qquad \mathbf{r}_{X,\mathbf{m}} \in A_r \tag{4.2.24}$$

4.2.2.2. Orientation

The primitive targets have three angles that describe their orientation with respect to the base orientation of the primitive solid that they represent.

The set A_o is the attribute set for the orientation of the targets and follows the same indexing convention as the targets. The function that relates a target to its dimension parameters is f_o. The function f_o is only defined for the primitive targets and has a null output for targets that are not primitive.

$$f_o: T \to A_o \ , \ A_o \subset \mathbb{R}^3 \tag{4.2.25}$$

$$f_o(t_{X,\mathbf{m}}) = \mathbf{o}_{X,\mathbf{m}}, \qquad \mathbf{o}_{X,\mathbf{m}} \in A_o \tag{4.2.26}$$

4.2.2.3. Dimensions

The number of dimension parameters of a primitive depend on the type of solid it represents. Specifically, the leaf-sheets have three dimension parameters (length, width and thickness) and both cylinder types of solids (head-cylinder and stem-cylinder) have two parameters (radius and length).

The set A_d is the attribute set for the dimension parameters of the targets and follows the same indexing convention as the targets. The function that relates a target to its dimension parameters is f_d. As indicated by (4.2.28), the function f_d outputs the length $L_{X,\mathbf{m}}$, width $w_{X,\mathbf{m}}$ and thickness $a_{X,\mathbf{m}}$ for a leaf-sheet. In contrast, it outputs the radius and cylinder length for a head- or stem-cylinder. The function outputs null if the target is not a primitive.

$$f_d: T \to A_d \ , \ A_d \subset \mathbb{R}^n \tag{4.2.27}$$

$$f_d(t_{X,\mathbf{m}}) = \mathbf{d}_{X,\mathbf{m}} = \begin{cases} (d_{x,X,\mathbf{m}}, d_{y,X,\mathbf{m}}, d_{z,X,\mathbf{m}}) = (a_{X,\mathbf{m}}, w_{X,\mathbf{m}}, L_{X,\mathbf{m}}) & if\ X = Q \\ (d_{\rho,X,\mathbf{m}}, d_{z,X,\mathbf{m}}) = (\rho_{X,\mathbf{m}}, L_{z,X,\mathbf{m}}) & if\ (X = U)\ or\ (X = V) \\ null \qquad otherwise \end{cases} \tag{4.2.28}$$

4.2.2.4. Relative Permittivity

All materials are considered non-magnetic. Thus, the targets' material properties may be represented by the complex-valued relative permittivity, which accounts for the conductance and the relative permittivity. Vegetation materials are not homogeneous media. Effective

permittivity models, described in appendix D, are used in the simulator to approximate the vegetation materials as homogeneous media.

The set A_ε is the attribute set for the relative permittivity of the targets and follows the same indexing convention as the targets. The function that relates a target to its relative permittivity is f_ε. The function has a null output if the target is not a primitive.

$$f_\varepsilon: T \to A_\varepsilon \ , \ A_\varepsilon \subset \mathbb{C} \tag{4.2.29}$$

$$f_\varepsilon(t_{X,\mathbf{m}}) = \begin{cases} \varepsilon_{X,\mathbf{m}} & if\ (X{=}U)\ or\ (X{=}V)\ \mathbf{or}\ (X{=}V) \\ null & otherwise \end{cases} \tag{4.2.30}$$

4.2.3. Parametric Models

Since sibling targets at each order of the tree structure are identified with an index, the attributes of each type of target can be described using parametric equations. This section shows the parametric equations used to model all the different targets' attributes.

4.2.3.1. Canopy

Position

For simplicity, we assign the position of the canopy to be at the origin (4.2.31).

$$\mathbf{r}_{C,()} = (0,0,0) \tag{4.2.31}$$

4.2.3.2. Plant(s)

Position

The arrangement of the plants in the canopy depends on the number of rows in the canopy N_{CR}, the distance between rows d_{CR}, the length of each row L_{CR} and the number of plants in the canopy N_{CP}.

Given these parameters, the plant density in the canopy m_{CP} is given by (4.2.32), which is the number of plants per unit area.

$$m_{CP} = \frac{N_{CP}}{d_{CR} \cdot L_{CR} \cdot N_{CR}} \tag{4.2.32}$$

The number of plants N_P can be found based on the plant density m_{CP} using (4.2.32).

The number of plants per row N_{CPR} and the average distance between plants in a row d_{CPR} are given by (4.2.33) and (4.2.34), respectively.

$$N_{CPR} = \lfloor m_{CP} \cdot d_{CR} \cdot L_{CR} \rfloor \tag{4.2.33}$$

$$d_{CPR} = L_{CR}/N_{CPR} \tag{4.2.34}$$

The expressions in (4.2.35) and (4.2.36) describe the position vectors for the plants in a canopy when the direction of the rows aligns with the y-axis and the x-axis, respectively. In expressions (4.2.35) and (4.2.36), the position vector $\mathbf{r}_{n,P,\left((i_{px},i_{py})\right)}$ is a random vector and it is added to the uniformly spaced position vector component to account for the randomness of the position.

$$\mathbf{r}_{P,\left((i_{px},i_{py})\right)} = \left(d_{CR}\left[i_{px} - \frac{N_{px}+1}{2}\right], d_{CPR}\left[i_{px} - \frac{N_{px}+1}{2}\right], 0\right) + \mathbf{r}_{n,P,\left((i_{px},i_{py})\right)} \quad (4.2.35)$$

$$\mathbf{r}_{P,\left((i_{px},i_{py})\right)} = \left(d_{CPR}\left[i_{px} - \frac{N_{px}+1}{2}\right], d_{CR}\left[i_{px} - \frac{N_{px}+1}{2}\right], 0\right) + \mathbf{r}_{n,P,\left((i_{px},i_{py})\right)} \quad (4.2.36)$$

4.2.3.3. Stem(s)

Position

We defined the position of the stem as the position of the bottom of the stem (4.2.37). We assume that all plants have only one stem. Therefore, the stem targets are given the same position as their related plants.

$$\mathbf{r}_{S,(\mathbf{i}_p,i_S=1)} = \mathbf{r}_{P,(\mathbf{i}_p)} \quad (4.2.37)$$

4.2.3.4. Head(s)

Position

The position of the head is defined as the position of the end of the head that is attached to the stem (4.2.38). Therefore, the position of the head ($\mathbf{r}_{H,(\mathbf{i}_p,i_h)}$) is equal to the position of the top of the stem ($\mathbf{r}_{S,(\mathbf{i}_p,i_S,T)}$). The position of the top of the stem is described in section 4.2.3.6.

$$\mathbf{r}_{H,(\mathbf{i}_p,i_h=1)} = \mathbf{r}_{S,(\mathbf{i}_p,i_S,T)} \quad (4.2.38)$$

4.2.3.5. Leaf/Leaves

Position

The position of a leaf is defined as the position of the part of the leaf that is attached to the stem. Therefore, the leaves of a plant have positions along the length of the stem.

The stem is assumed straight. The position of the leaves are given with respect to the position of the stem in (4.2.39). The vectors d_{L,i_L} indicates the distance of each leaf from the base of the plant. The unit vector $\hat{\mathrm{v}}_S$ indicates the direction of inclination of the stem (4.2.40), where θ_S and φ_S are the inclination and azimuth angles of rotation of the stem. The parameters θ_S and φ_S are 'description' parameters, which are listed in section 4.2.4.

$$\mathbf{r}_{L,(\mathbf{i}_p,i_L)} = \mathbf{r}_{S,(\mathbf{i}_p,i_L)} + d_{\boldsymbol{L},i_L}\,\hat{\mathrm{v}}_{\boldsymbol{S}} \tag{4.2.39}$$

$$\mathbf{v}_{\boldsymbol{S}} = \begin{bmatrix} \sin(\theta_S)\cos(\varphi_S) \\ \sin(\theta_S)\sin(\varphi_S) \\ \cos(\theta_S) \end{bmatrix} \tag{4.2.40}$$

If the leaves are defined to be uniformly spaced along the stem, equation (4.2.41) describes the distance d_{L,i_L}. In (4.2.41), $r_{n,L,iL}$ is a random variable, which is uniformly distributed between -0.5 and 0.5. In (4.2.41), L_S is the length of the stem and N_L is the number of leafs.

$$d_{\boldsymbol{L},i_L} = \frac{L_S}{N_L}\{r_{n,L,iL} + (i_L - 0.5)\} \tag{4.2.41}$$

4.2.3.6. Stem-Cylinders

The stem-cylinders are primitive solids. The geometric union of these solids makes up the geometrical model of the stem. The attributes of the stem-cylinders are their relative permittivity, orientation, dimensions and position. This section provides the parametric equations that describe these attributes.

In this simulator, we assume that the stem is straight (i.e. not curved). Stems in nature are usually not curved, so we use that assumption. However, the equations in this section are sufficiently general that apply to both straight and curved stems.

Considering a straight line divided in even sections, the distance from one end of the line to the center of each section is given by (4.2.42). This variable, which we refer to as the path length, is used in the parametric equations that describe the length, orientation and position of the stem-cylinders. The point in the path length where the curvature is maximum (i.e. radius of curvature is minimum) will be refer to as the curve apex and it is denoted by the symbol s_o.

$$s_{i_U} = \frac{L_S}{N_U}(i_U - 1/2) \tag{4.2.42}$$

Relative Permittivity

The simulator could have different values for the relative permittivity of the cylinders along the stem. However, in this implementation of the simulator, this parameter is assumed a constant along the stem. The relative permittivity $\varepsilon_{Q,(\mathbf{i}_p,i_L,i_U)}$ is calculated using the effective permittivity model for a vegetation material, described in appendix D..

Orientation

The orientation of each stem-cylinder solid is described by the vector $\mathbf{o}_{U,(\mathbf{i}_p,i_S,i_U)}$, which contains the three angles of rotation. These angles of rotation were described in chapter 3.

$$\mathbf{o}_{U,(\mathbf{i}_p,i_S,i_U)} = \left(\alpha_{U,(\mathbf{i}_p,i_S,i_U)}, \theta_{U,(\mathbf{i}_p,i_S,i_U)}, \phi_{U,(\mathbf{i}_p,i_S,i_U)}\right) \tag{4.2.43}$$

For a cylinder the first angle of rotation $\alpha_{U,(\mathbf{i}_p,i_S,i_U)}$ does not modify the circular cylinder, so it is fixed to a value of zero.

$$\alpha_{U,(\mathbf{i}_p,i_S,i_U)} = 0 \tag{4.2.44}$$

In the base orientation of the cylinder (no rotation), the main axis of the cylinder (i.e. the axis that runs through the center of the circular cross section) is aligned to the z-axis.

The second angle of rotation $\theta_{U,(\mathbf{i}_p,i_S,i_U)}$ is the angle of inclination between its main axis and the z-axis. To simplify notation, we make the equality in (4.2.45).

$$\theta_{U,(\mathbf{i}_p,i_S,i_U)} = \theta_{i_U} \tag{4.2.45}$$

As mentioned earlier, the parametric equations of the stem-cylinder in this section describe the stem as a curved cylinder. This curve refers to the main axis of the curved cylinder. The parameters given to describe the curved cylinder are the initial inclination angle θ_1, the final inclination angle θ_{N_U} and the minimum radius of curvature R_U along the curve. The curvature is the derivative of the inclination angle with respect to the path length. The radius of curvature is the inverse of the curvature.

We chose to describe the transition between the initial to the final inclination angles using a logistic function. The parametric equation that describes the inclination angle is given by (4.2.46). In (4.2.46), the curvature factor β_U is defined in (4.2.47) in terms of the radius of curvature R_U.

$$\theta_{i_U} = \theta_1 + \frac{\theta_{N_U} - \theta_1}{1 + e^{-\beta_U(s_{i_U} - s_o)}} \tag{4.2.46}$$

$$\beta_U = \frac{4}{R_U(\theta_{N_U} - \theta_1)} \tag{4.2.47}$$

The azimuth angle of each stem-cylinder is equal to the azimuth angle of the cylinder (4.2.48). In Monte Carlo simulations, this parameter is defined as a random variable with a uniform distribution.

$$\phi_{U,(\mathbf{i}_p, i_S, i_U)} = \phi_S \tag{4.2.48}$$

Dimensions

The dimensions of the stem-cylinders are described by $\mathbf{d}_{U,(\mathbf{i}_p, i_S, i_U)}$, which contains the radius $\rho_{U,(\mathbf{i}_p, i_S, i_U)}$ and length $L_{U,(\mathbf{i}_p, i_S, i_U)}$ of the primitive cylinders (4.2.49).

$$\mathbf{d}_{U,(\mathbf{i}_p, i_S, i_U)} = (\rho_{U,(\mathbf{i}_p, i_S, i_U)}, L_{U,(\mathbf{i}_p, i_S, i_U)}) \tag{4.2.49}$$

The radius of the stem-cylinders is a parameter given by the user and it is assumed constant along the stem (4.2.50).

$$\rho_{U,(\mathbf{i}_p,i_S,i_U)} = \rho_S \tag{4.2.50}$$

We define the length of the stem-cylinder so that it is proportional to the radius of curvature along the path of the stem. Doing so, shorter cylinders are used at regions of the stem where the curvature is greater and longer cylinders where the curvature is smaller. In this manner, the number of cylinders required to form a stem with a small minimum radius of curvature is less than it would be required if the stem-cylinders were divided evenly.

If the stem is straight (i.e. the curvature is zero for any point along the path), the stem is divided evenly. In this case, the length of the stem-cylinders is given by (4.2.52), where L_S is the stem length and N_U is the number of primitives.

$$L_{U,(\mathbf{i}_p,i_S,i_U)} = L_{i_U} \tag{4.2.51}$$

$$L_{i_U} = L_S/N_U \tag{4.2.52}$$

If the stem is curved, the length of the stem-cylinders are defined with the parametric equation in (4.2.53).

$$L_{i_U} = L_S \frac{\theta_1 + \dfrac{\theta_{N_U} - \theta_1}{1 + 10e^{-\beta_U \left| s_{i_U} - s_o \right|}}}{\sum_{i_U}^{N_U} \left| \theta_1 + \dfrac{\theta_{N_U} - \theta_1}{1 + 10e^{-\beta_U \left| s_{i_U} - s_o \right|}} \right|} \tag{4.2.53}$$

Position

The position of each stem-cylinder $t_{U,(\mathbf{i}_p,i_L,i_U)}$ can be described as the sum of a reference position plus a vector that is the product of a length increment and a unit vector in the direction of the curve. The reference position vector of the first stem-cylinder is the position vector of the stem. The reference position vector for each of the other stem-cylinders is the position vector of the previous stem-cylinder. Therefore, the position vector of the first stem cylinder is given by (4.2.54) and the position vector of each of the other stem-cylinders is given by (4.2.55).

$$\mathbf{r}_{U,(\mathbf{i}_p,i_S,1)} = \mathbf{r}_{S,(\mathbf{i}_p,i_S)} + \left[\frac{1}{2}L_{U,(\mathbf{i}_p,i_S,1)}\right]\overline{\overline{\mathbf{T}}}(\mathbf{o}_{U,(\mathbf{i}_p,i_S,1)}) \cdot \hat{z} \tag{4.2.54}$$

$$\mathbf{r}_{U,(\mathbf{i}_p,i_S,i_U)} = \mathbf{r}_{U,(\mathbf{i}_p,i_S,i_U-1)} + \left[\frac{1}{2}L_{U,(\mathbf{i}_p,i_S,i_U-1)}\right]\overline{\overline{\mathbf{T}}}(\mathbf{o}_{U,(\mathbf{i}_p,i_S,i_U-1)}) \cdot \hat{z} + \left[\frac{1}{2}L_{U,(\mathbf{i}_p,i_S,i_U)}\right]\overline{\overline{\mathbf{T}}}(\mathbf{o}_{U,(\mathbf{i}_p,i_S,i_U)}) \cdot \hat{z} \tag{4.2.55}$$

The position of the top of the stem $\mathbf{r}_{S,(\mathbf{i}_p,i_S,T)}$ is given by (4.2.56). This position vector is equal to the position of the head.

$$\mathbf{r}_{S,(\mathbf{i}_p,i_S,T)} = \mathbf{r}_{U,(\mathbf{i}_p,i_S,N_U)} + \left[\frac{1}{2}L_{U,(\mathbf{i}_p,i_S,N_U)}\right]\overline{\overline{\mathbf{T}}}(\mathbf{o}_{U,(\mathbf{i}_p,i_S,N_U)}) \cdot \hat{z} \tag{4.2.56}$$

4.2.3.7. Leaf-Sheets

The leaf-sheets are primitive solids. The geometric union of these solids makes up the geometrical model of a leaf. The attributes of the leaf-sheets are their relative permittivity, orientation, dimensions and position. This section provides the parametric equations that describe these attributes.

The geometric model of the leaf-sheets considers the leaf to be curved. Additionally, this geometric model considers the dihedral angle at the cross section of a leaf. The geometric model of the leaf is the union of two curved thin sheets joint at the midrib. The position, orientation and length of the leaf-sheets are described using parametric equations similar to those used to describe the stem-cylinders of a curved stem.

In case the dihedral angle of the leaf is equal or approximately equal to π, the index of the leaf-sheets is a scalar $i_Q = (i_{Qz})$. Otherwise, it is an ordered pair $\mathbf{i}_Q = (i_{Qy}, i_{Qz})$.

Considering a straight line divided in even sections, the distance from one end of the line to the center of each section is given by (4.2.57). This variable, which we refer to as the path length, is used in the parametric equations that describe the length, orientation and position of the leaf-sheets. The point in the path length where the curvature is maximum (i.e. radius of curvature is minimum) will be refer to as the curve apex and it is denoted by the symbol s_o.

$$s_{i_{Qz}} = \frac{L_L}{N_Q}\left(i_{Qz} - 1/2\right) \tag{4.2.57}$$

Relative Permittivity

The relative permittivity of the leaf-sheets $\varepsilon_{Q,(\mathbf{i}_p, i_L, i_Q)}$ is calculated using the effective permittivity model for a vegetation material, described in appendix D. In this simulator, the relative permittivity is considered constant along the leaf.

Orientation

The orientation of each leaf-sheet is described by the vector $\mathbf{o}_{Q,(\mathbf{i}_p,i_L,i_Q)}$, which contains the three angles of rotation. These angles of rotation were described in chapter 3. We define the thin sheets to have their base orientation (no rotation), where the main axis (length-related) is aligned to the z-axis, the second axis (width-related) is aligned to the y-axis and the third axis (thickness-related) to be aligned with the x-axis.

$$\mathbf{o}_{Q,(\mathbf{i}_P,i_L,\mathbf{i}_Q)} = \left(\alpha_{Q,(\mathbf{i}_P,i_L,\mathbf{i}_Q)}, \theta_{Q,(\mathbf{i}_P,i_L,\mathbf{i}_Q)}, \phi_{Q,(\mathbf{i}_P,i_L,\mathbf{i}_Q)}\right) \tag{4.2.58}$$

The first angle of rotation $\alpha_{Q,(\mathbf{i}_p,i_L,\mathbf{i}_Q)}$ corresponds to the first rotation performed along the main axis of the thin sheet. If the dihedral angle of the leaf is different than π radians, the first angle of rotation of a leaf-sheet is given by (4.2.59-4.2.60). The angle α_d is defined in terms of the dihedral angle of the leaf γ and an offset angle α_o (4.2.61).

$$\alpha_{Q,(\mathbf{i}_P,i_L,(1,i_{Qz}))} = \alpha_o + \alpha_d \tag{4.2.59}$$

$$\alpha_{Q,(\mathbf{i}_P,i_L,(2,i_{Qz}))} = \alpha_o - \alpha_d \tag{4.2.60}$$

$$\alpha_d = \frac{\pi - \gamma}{2} \tag{4.2.61}$$

If the dihedral angle of the leaf is equal to π radians or it could be approximated as such, the first rotation angle is only given by the offset parameter α_o, determined by the user of the simulator.

$$\alpha_{Q,(\mathbf{i}_P,i_L,i_Q)} = \alpha_o \tag{4.2.62}$$

The second angle of rotation (the inclination angle) of each leaf-sheet is $\theta_{Q,(\mathbf{i}_p,i_S,i_Q)}$. The derivative of this angle with respect to the path length is the local curvature along the leaf. For simplicity of notation, we use the equality in (4.2.63) for the definition of the inclination angle. We choose to define the inclination angle using a logistic function (4.2.64), which depends on the initial angle, final angle and the radius of curvature at the apex of the curve. The apex of the curve is the point in the curve where the curvature reaches the maximum point (i.e. the radius of curvature is minimum). The factor β_Q in (4.2.64) is defined by (4.2.65), where R_Q is the radius of curvature at the apex.

$$\theta_{Q,(\mathbf{i}_P,i_L,\mathbf{i_Q})} = \theta_{\mathbf{i}_Q} \tag{4.2.63}$$

$$\theta_{\mathbf{i}_Q} = \theta_1 + \frac{\theta_{N_Q} - \theta_1}{1 + e^{-\beta_Q(s_{i_Q} - s_o)}} \tag{4.2.64}$$

$$\beta_Q = \frac{4}{R_Q\left(\theta_{N_Q} - \theta_1\right)} \tag{4.2.65}$$

The third angle of rotation is the angle of rotation around the z-axis after the other two rotations have been performed. This rotation angle defines the rotation of the leaf-sheet in the azimuth direction. This parameter is a constant determined by the user.

$$\phi_{Q,(\mathbf{i}_P,i_L,\mathbf{i}_Q)} = \phi_L \tag{4.2.66}$$

Dimensions

The dimensions of the leaf-sheet are described by $\mathbf{d}_{Q,(\mathbf{i}_P,i_L,\mathbf{i}_Q)}$, which contains the length $L_{Q,(\mathbf{i}_P,i_L,\mathbf{i}_Q)}$, the width $w_{Q,(\mathbf{i}_P,i_L,\mathbf{i}_Q)}$ and the thickness $a_{Q,(\mathbf{i}_P,i_L,\mathbf{i}_Q)}$.

$$\mathbf{d}_{Q,(\mathbf{i}_P,i_L,\mathbf{i}_Q)} = (a_{Q,(\mathbf{i}_P,i_L,\mathbf{i}_Q)}, w_{Q,(\mathbf{i}_P,i_L,\mathbf{i}_Q)}, L_{Q,(\mathbf{i}_P,i_L,\mathbf{i}_Q)}) \tag{4.2.67}$$

If the dihedral angle is different than π and the leaf is described by two curved thin sheets, the width of the leaf-sheets is half of the defined leaf width (4.2.68).

$$w_{Q,(\mathbf{i}_P,i_L,\mathbf{i}_Q)} = w_L/2 \tag{4.2.68}$$

If the dihedral angle is π, so that the leaf can be described with a single curved thin sheet, the width of each leaf-sheet is equal to the width of the leaf.

$$w_{Q,(\mathbf{i}_P,i_L,\mathbf{i}_Q)} = w_L \tag{4.2.69}$$

The width of the leaf is a parameter defined by the user.

The thickness of the leaf-sheet is equal to the thickness of the leaf, defined by the user.

$$a_{Q,(\mathbf{i}_P,i_L,\mathbf{i}_Q)} = a_L \tag{4.2.70}$$

The length of the leaf-sheets is proportional to the curvature along the curve of the leaf so that only a small number of sheets are required to represent it while representing the small radius of curvature at the apex.

If the leaf is straight (i.e. the curvature is zero for any point along the path), the leaf is divided evenly. In this case, the length of the leaf-sheets is given by (4.2.72), where L_L is the leaf length and N_Q is the number of primitives.

$$L_{Q,(\mathbf{i}_P,i_L,(1,i_{Qz}))} = L_{Q,(\mathbf{i}_P,i_L,(2,i_{Qz}))} = L_{Q,i_{Qz}} \tag{4.2.71}$$

$$L_{Q,i_{Qz}} = L_L/N_Q \tag{4.2.72}$$

If the leaf is curved, the length of the leaf-sheets are defined with the parametric equation in (4.2.73).

$$L_{Q,i_{Qz}} = L_L \frac{\theta_1 + \frac{\theta_{N_Q} - \theta_1}{1 + 10e^{-\beta_Q|s_Q - s_o|}}}{\sum_{i_Q}^{N_Q} \left| \theta_1 + \frac{\theta_{N_Q} - \theta_1}{1 + 10e^{-\beta_Q|s_{i_Q} - s_o|}} \right|} \tag{4.2.73}$$

Position

The position of each leaf-sheet $t_{Q,(\mathbf{i}_p,i_L,\mathbf{i}_Q)}$ can be described as the sum of a reference position plus a vector that is the product of a length increment and a unit vector in the direction of the curve.

If the dihedral angle of the leaf is π, the leaf can be described with a single curved sheet. The index of the leaf-sheets $\mathbf{i}_Q = i_{QX}$ becomes a scalar. In this case, the reference position vector is the leaf position vector. The position vector of the leaf-sheets for this case is given by (4.2.74-4.2.75).

$$\mathbf{r}_{Q,(\mathbf{i}_P,i_L,1)} = \mathbf{r}_{L,(\mathbf{i}_P,1)} + \left[\frac{1}{2}L_{Q,1}\right] \overline{\overline{\mathbf{T}}}(\mathbf{o}_{Q,(\mathbf{i}_P,i_L,1)}) \cdot \hat{z} \tag{4.2.74}$$

$$\mathbf{r}_{Q,(\mathbf{i}_P,i_L,i_{Qz})} = \mathbf{r}_{Q,(\mathbf{i}_P,i_L,i_{Qz}-1)} + \left[\frac{1}{2}L_{Q,(i_{Qz}-1)}\right] \overline{\overline{\mathbf{T}}}(\mathbf{o}_{Q,(\mathbf{i}_P,i_L,i_{Qz}-1)}) \cdot \hat{z} + \left[\frac{1}{2}L_{Q,i_{Qz}}\right] \overline{\overline{\mathbf{T}}}(\mathbf{o}_{Q,(\mathbf{i}_P,i_L,i_{Qz})}) \cdot \hat{z} \tag{4.2.75}$$

If the dihedral angle is different than π, the leaf is described by two curved sheets attached at the middle of the width of the leaf (the midrib). The vector positions of the leaf-sheets are the sum of a reference position vector and the vector that accounts to the incremental position change. The parametric equations for the position vectors of the leaf-sheets are given by (4.2.76-4.2.79).

$$\mathbf{r}_{Q,(\mathbf{i}_P,i_L,(1,1))} = \mathbf{r}_{L,(\mathbf{i}_P,i_L)} - \left[\frac{1}{4}w_L\cos(\alpha_d) + \frac{1}{2}a_L\sin(\alpha_d)\right] \overline{\overline{\mathbf{T}}}(\mathbf{o}_{Q,(\mathbf{i}_P,i_L,(1,1))}) \cdot \hat{y} + \left[\frac{1}{2}L_{Q,1}\right] \overline{\overline{\mathbf{T}}}(\mathbf{o}_{Q,(\mathbf{i}_P,i_L,(1,1))}) \cdot \hat{z} \tag{4.2.76}$$

$$\mathbf{r}_{Q,(\mathbf{i}_P,i_L,(1,i_{Qz}))} = \mathbf{r}_{Q,(\mathbf{i}_P,i_L,(1,1))} - \left[\frac{1}{4}w_L\cos(\alpha_d) + \frac{1}{2}a_L\sin(\alpha_d)\right] \overline{\overline{\mathbf{T}}}(\mathbf{o}_{Q,(\mathbf{i}_P,i_L,(1,i_{Qz}))}) \cdot \hat{y} + \left[\frac{1}{2}L_{Q,(i_{Qz}-1)}\right] \overline{\overline{\mathbf{T}}}(\mathbf{o}_{Q,(\mathbf{i}_P,i_L,(1,i_{Qz}-1))}) \cdot \hat{z} + \left[\frac{1}{2}L_{Q,i_{Qz}}\right] \overline{\overline{\mathbf{T}}}(\mathbf{o}_{Q,(\mathbf{i}_P,i_L,(1,i_{Qz}))}) \cdot \hat{z} \tag{4.2.77}$$

$$\mathbf{r}_{Q,(\mathbf{i}_P,i_L,(1,2))} = \mathbf{r}_{L,(\mathbf{i}_P,i_L)} - \left[\frac{1}{4}w_L\cos(\alpha_d) + \frac{1}{2}a_L\sin(\alpha_d)\right] \overline{\overline{\mathbf{T}}}(\mathbf{o}_{Q,(\mathbf{i}_P,i_L,(1,2))}) \cdot \hat{y} \tag{4.2.78}$$

$$+\left[\frac{1}{2}L_{Q,1}\right]\overline{\overline{\mathbf{T}}}(\mathbf{o}_{Q,(\mathbf{i}_P,i_L,(1,2))})\cdot\hat{z}$$

$$\mathbf{r}_{Q,(\mathbf{i}_P,i_L,(2,i_{Qz}))}=\mathbf{r}_{Q,(\mathbf{i}_P,i_L,(1,2))}-\left[\frac{1}{4}w_L\cos(\alpha_d)+\frac{1}{2}a_L\sin(\alpha_d)\right]\overline{\overline{\mathbf{T}}}(\mathbf{o}_{Q,(\mathbf{i}_P,i_L,(2,i_{Qz}))})\cdot\hat{y} \quad (4.2.79)$$

$$+\left[\frac{1}{2}L_{Q,(i_{Qz}-1)}\right]\overline{\overline{\mathbf{T}}}(\mathbf{o}_{Q,(\mathbf{i}_P,i_L,(2,i_{Qz}-1))})\cdot\hat{z}+\left[\frac{1}{2}L_{Q,i_{QX}}\right]\overline{\overline{\mathbf{T}}}(\mathbf{o}_{Q,(\mathbf{i}_P,i_L,(2,i_{Qz}))})\cdot\hat{z}$$

4.2.3.8. Head-Cylinders

The head-cylinders are primitive solids. The geometric union of these solids makes up the geometrical model of the head. The attributes of the head-cylinders are their relative permittivity, orientation, dimensions and position. This section provides the parametric equations that describe these attributes.

$$s_{i_V}=\frac{L_H}{N_V}(i_V-1/2) \quad (4.2.80)$$

Relative Permittivity

The simulator could have different values for the relative permittivity of the cylinders along the stem. However, in this implementation of the simulator, this parameter is assumed a constant along the stem. The relative permittivity $\varepsilon_{V,(\mathbf{i}_P,i_H,i_V)}$ is calculated using the effective permittivity model for a vegetation material, described in appendix D.

Orientation

The orientation of each head-cylinder solid is described by the vector $\mathbf{o}_{V,(\mathbf{i}_P,i_H,i_V)}$, which contains the three angles of rotation. These angles of rotation were described in chapter 3.

$$\mathbf{o}_{V,(\mathbf{i}_P,i_H,i_V)} = \left(\alpha_{V,(\mathbf{i}_P,i_H,i_V)}, \theta_{V,(\mathbf{i}_P,i_H,i_V)}, \phi_{V,(\mathbf{i}_P,i_H,i_V)}\right) \tag{4.2.81}$$

For a cylinder the first angle of rotation $\alpha_{V,(\mathbf{i}_P,i_H,i_V)}$ does not modify the circular cylinder, so it is fixed to a value of zero.

$$\alpha_{V,(\mathbf{i}_P,i_H,i_V)} = 0 \tag{4.2.82}$$

$$\theta_{V,(\mathbf{i}_P,i_H,i_V)} = \theta_H \tag{4.2.83}$$

$$\phi_{V,(\mathbf{i}_P,i_H,i_V)} = \phi_H \tag{4.2.84}$$

Dimensions

The dimensions of the stem-cylinders are described by $\mathbf{d}_{V,(\mathbf{i}_P,i_H,i_V)}$, which contains the radius $\rho_{V,(\mathbf{i}_P,i_H,i_V)}$ and length $L_{V,(\mathbf{i}_P,i_H,i_V)}$ of the primitive cylinders.

$$\mathbf{d}_{V,(\mathbf{i}_P,i_H,i_V)} = (\rho_{V,(\mathbf{i}_P,i_H,i_V)}, L_{V,(\mathbf{i}_P,i_H,i_V)}) \tag{4.2.85}$$

The length of the head is divided evenly for all N_V head-cylinders. The length of the head-cylinders is given by (4.2.86), where L_H is the total length of the head.

$$L_{V,(\mathbf{i}_P,i_H,i_V)} = L_H/N_V \tag{4.2.86}$$

The radius of the head is not a constant along the length of the head. To account for the variation of the radius of the head along its length, the radius of the head-cylinders is defined using the parametric equations in (4.2.87-4.2.88). These equations are logistic-type equations. They depend on the initial radius ρ_{Ho} (radius at the base of the head), radius at the middle of its length ρ_{Hm}, and radius at the top end ρ_{Hf}. The parameters β_V controls the rate of the transition from the radius at the base to the radius at the middle and to the radius at the top. This parameter is defined by the user.

$$\rho_{V,(\mathbf{i}_P,i_H,i_V)} = \rho_{Hf} + \frac{\rho_T - \rho_{Hf}}{1 + e^{\beta_V(s-3L_H/4)}} \tag{4.2.87}$$

$$\rho_T = \rho_{Hm} + \frac{\rho_{Ho} - \rho_{Hm}}{1 + e^{\beta_V(s-L_H/4)}} \tag{4.2.88}$$

The parametric equation in (4.2.87) may be modified as shown in (4.2.89) to add a type of roughness to the model. In (4.2.89), ρ_r is a fraction ($0 < \rho_r < 1$).

$$\rho_{V,(\mathbf{i}_P,i_H,i_V)} = \rho_{Hf} + \frac{\rho_T - \rho_{Hf}}{1 + e^{\beta(s-3L_H/4)}} + \rho_r\rho_{Hm}(-1)^{(i_V-1)} \tag{4.2.89}$$

Position

The position of each head-cylinder $\mathbf{r}_{V,(\mathbf{i}_P,i_H,,i_V)}$ can be described as the sum of a reference position plus the vector, which directs towards the top end of the head. The parametric equations that describe the position of the head-cylinders are shown in (4.2.90-4.2.91).

$$\mathbf{r}_{V,(\mathbf{i}_P,i_H,1)} = \mathbf{r}_{H,(\mathbf{i}_P,i_H)} + \left[\frac{1}{2}L_{V,(\mathbf{i}_P,i_H,1)}\right]\overline{\overline{\mathbf{T}}}(\mathbf{o}_{V,(\mathbf{i}_P,i_H,1)}) \cdot \hat{z} \quad (4.2.90)$$

$$\mathbf{r}_{V,(\mathbf{i}_P,i_H,i_V)} = \mathbf{r}_{V,(\mathbf{i}_P,i_H,i_V-1)} + \left[L_{V,(\mathbf{i}_P,i_H,i_V)}\right]\overline{\overline{\mathbf{T}}}(\mathbf{o}_{V,(\mathbf{i}_P,i_H,i_V)}) \cdot \hat{z} \quad (4.2.91)$$

4.2.4. Description Parameters

The ‘description’ parameters are a list of general parameters that describe the wheat-related targets. These parameters are given by the user of the simulator.

The ‘description’ parameters related to a straight stem are: Length, L_S, radius ρ_S, azimuth φ_S, elevation angle θ_S and (gravimetric) moisture content m_S.

The ‘description’ parameters related to the head are: Length, L_H, radius (initial) $\rho_{i,H}$, radius (middle), $\rho_{m,H}$, radius (final) $\rho_{m,H}$, azimuth φ_H, elevation angle θ_H, radius factor β_H volume fraction v_H, and (gravimetric) moisture content m_H.

The ‘description’ parameters related to the leaf are: Length L_L, width w_L, thickness a_L, first-rotation angle $\alpha_{L,}$, initial elevation angle $\theta_{i,L}$, final elevation angle $\theta_{f,L}$, radius of curvature R_L, apex Location $s_{o,L}$, dihedral angle $\gamma_{,L}$ and (gravimetric) moisture cont., m_L.

The only ‘description’ parameter of a plant is the number of leaves N_L.

These parameters may be deterministic or random, depending on the type of simulation performed.

4.3. Forward Scattering Modeling

Once the geometric modeling for the complex target is defined (i.e. wheat canopy), the radar response of each target is computed using their related attributes. In the forward scattering step (second step) of the simulator, the radar response $H_t(f)$ of the canopy or related targets are calculated. The radar response of the canopy depends on the radar response of the related sub-targets. The input to the forward scattering equations to calculate the radar response are the attributes obtained from the geometric modeling.

As defined in section 4.1.1, the radar response $H_{t,X,\mathbf{m}}(f)$ due to a target $t_{X,\mathbf{m}}$ is given by (4.3.1).

$$H_t(f) = H_{t,X,\mathbf{m}}(f) = V_r(f)/V_t(f) \tag{4.3.1}$$

The scattering response $F_{qp,X,\mathrm{m}}(f)$ is found from the radar response $H_{t,X,\mathrm{m}}$ using (4.3.2).

$$F_{qp,X,\mathbf{m}}(f) = \left[\,\hat{q}\cdot\,\bar{\bar{\mathbf{F}}}_{X,\mathbf{m}}(\mathbf{k_s},\mathbf{k_i})\cdot\hat{p}\right] = \left[jk\eta Z_a\;\Phi_e\Phi_r(\mathbf{r_r},\mathbf{r}_{X,\mathbf{m}})\;\Phi_t(\mathbf{r}_{X,\mathbf{m}},\mathbf{r}_t)|\mathbf{f_r}|_v|\mathbf{f_t}|_v\right]^{-1}\left[H_{t,X,\mathbf{m}}\right] \tag{4.3.2}$$

The scattering $\mathbf{k_s}(\mathbf{r}_r,\mathbf{r}_{X,\mathbf{m}})$ and incident $\mathbf{k_i}(\mathbf{r}_{X,\mathbf{m}},\mathbf{r_t})$ wave-vector are given by (4.3.3) and (4.3.4), respectively.

$$\mathbf{k_s}(\mathbf{r}_r,\mathbf{r}_{X,\mathbf{m}}) = k\frac{\mathbf{r}_r-\mathbf{r}_{X,\mathbf{m}}}{|\mathbf{r}_r-\mathbf{r}_{X,\mathbf{m}}|} \tag{4.3.3}$$

$$\mathbf{k_i}(\mathbf{r}_{X,\mathbf{m}},\mathbf{r_t}) = k\frac{\mathbf{r}_{X,\mathbf{m}}-\mathbf{r_t}}{|\mathbf{r}_{X,\mathbf{m}}-\mathbf{r_t}|} \tag{4.3.4}$$

The receive $\Phi_r(\mathbf{r_r},\mathbf{r}_{X,\mathbf{m}})$ and transmit $\Phi_t(\mathbf{r}_{X,\mathbf{m}},\mathbf{r}_t)$ propagation function are given by (4.3.5) and (4.3.6), respectively.

$$\Phi_r(\mathbf{r}_r, \mathbf{r}_{X,\mathbf{m}}) = \frac{e^{jk|\mathbf{r}_r - \mathbf{r}_{X,\mathbf{m}}|}}{4\pi|\mathbf{r}_r - \mathbf{r}_{X,\mathbf{m}}|} \tag{4.3.5}$$

$$\Phi_t(\mathbf{r}_{X,\mathbf{m}}, \mathbf{r}_t) = \frac{e^{jk|\mathbf{r}_{X,\mathbf{m}} - \mathbf{r}_t|}}{4\pi|\mathbf{r}_{X,\mathbf{m}} - \mathbf{r}_t|} \tag{4.3.6}$$

The difference wave vector $\mathbf{k}_d$ is given by (4.3.7), which is used in the definition of the scattering dyad of the primitive targets.

$$\mathbf{k}_d = \mathbf{k}_s - \mathbf{k}_i = k_{dx}\hat{x} + k_{dy}\hat{y} + k_{dz}\hat{z} \tag{4.3.7}$$

4.3.1. Forward Scattering: Stem-Cylinder (Primitive)

From chapter 3, the scattering dyad of a primitive stem-cylinder $t_{U,(\mathbf{i}_P, i_S, i_U)}$ with length $L_{U,(\mathbf{i}_P, i_S, i_U)}$ and radius $\rho_{U,(\mathbf{i}_P, i_S, i_U)}$ in base orientation is given by (4.3.8). In (4.3.8) S_v is the shape function and it is given by (4.3.9), in terms of the cylinder dimensions. The dyadic operator $\overline{\overline{\mathbf{X}}}$ is defined in chapter 3.

$$\overline{\overline{\mathbf{F}}}^{(b)}_{U,(\mathbf{i}_P, i_S, i_U)}(\mathbf{k}_s, \mathbf{k}_i) = -jk\, S_v(\rho_{i_U}, L_{i_U})\, \overline{\overline{\mathbf{X}}} \tag{4.3.8}$$

$$S_v(\rho_{i_U}, L_{i_U}) = 2\pi\rho_{i_U}L_{i_U}\,\mathrm{sinc}\left(\frac{k_{dz}L_{i_U}}{2}\right) \tag{4.3.9}$$

In the equations (4.3.8-4.3.9), we use the relations in (4.3.10-4.3.11) to simplify notation.

$$\rho_{i_U} = \rho_{U,(\mathbf{i}_P, i_S, i_U)} \tag{4.3.10}$$

$$L_{i_U} = L_{U,(\mathbf{i}_P, i_S, i_U)} \tag{4.3.11}$$

Using the *Rot* function, the scattering dyad is converted the target orientation described by $\mathbf{o}_{U,(\mathbf{i}_P, i_S, \mathbf{i}_U)}$.

$$\bar{\bar{\mathbf{F}}}_{U,(\mathbf{i}_P, i_S, \mathbf{i}_U)}(\mathbf{k}_s, \mathbf{k}_i) = Rot\left(\bar{\bar{\mathbf{F}}}^{(b)}_{U,(\mathbf{i}_P, i_S, \mathbf{i}_U)}(\mathbf{k}_s, \mathbf{k}_i), \mathbf{o}_{U,(\mathbf{i}_P, i_S, \mathbf{i}_U)}\right) \tag{4.3.12}$$

The radar response is found using the CGM in (4.3.13).

$$H_{t,U,(\mathbf{i}_P, i_S, \mathbf{i}_U)} = jk\eta Z_a \, \Phi_e \, \Phi_r\left(\mathbf{r}_r, \mathbf{r}_{U,(\mathbf{i}_P, i_S, \mathbf{i}_U)}\right) \Phi_t\left(\mathbf{r}_{U,(\mathbf{i}_P, i_S, \mathbf{i}_U)}, \mathbf{r}_t\right) \cdot \left[\, \mathbf{f}_r \cdot \bar{\bar{\mathbf{F}}}_{U,(\mathbf{i}_P, i_S, \mathbf{i}_U)}(\mathbf{k}_s, \mathbf{k}_i) \cdot \mathbf{f}_t \right] \tag{4.3.13}$$

4.3.2. Forward Scattering: Head-Cylinder (Primitive)

Similar to the section 4.3.1, the scattering dyad of head-cylinder $t_{V,(\mathbf{i}_P, i_H, i_V)}$ with radius $\rho_{V,(\mathbf{i}_P, i_H, i_V)}$ and length $L_{V,(\mathbf{i}_P, i_H, i_V)}$ at its base orientation is given by (4.3.14). The shape function $S_V(\rho_{i_V}, L_{i_V})$ is given by (4.3.15).

$$\bar{\bar{\mathbf{F}}}^{(b)}_{V,(\mathbf{i}_P, i_H, i_V)}(\mathbf{k}_s, \mathbf{k}_i) = -jk \, S_V(\rho_{i_V}, L_{i_V}) \, \bar{\bar{\mathbf{X}}} \tag{4.3.14}$$

$$S_V(\rho_{i_V}, L_{i_V}) = 2\pi\rho_{i_V} L_{i_V} \operatorname{sinc}\left(\frac{k_{dz} L_{i_V}}{2}\right) \tag{4.3.15}$$

The relations in (4.3.16-4.3.17), were used in (4.3.14-4.3.15).

$$\rho_{i_V} = \rho_{V,(\mathbf{i}_P, i_H, i_V)} \tag{4.3.16}$$

$$L_{i_V} = L_{V,(\mathbf{i}_P, i_H, i_V)} \tag{4.3.17}$$

The scattering dyad of the head-cylinder at its orientation described by $\mathbf{o}_{\boldsymbol{V},(\mathbf{i}_P, i_H, \mathbf{i}_V)}$ is given by (4.3.18).

$$\bar{\bar{\mathbf{F}}}_{\boldsymbol{V},(\mathbf{i}_P, i_H, \mathbf{i}_V)}(\mathbf{k}_s, \mathbf{k}_i) = Rot\left(\bar{\bar{\mathbf{F}}}^{(\boldsymbol{b})}_{\boldsymbol{V},(\mathbf{i}_P, i_H, \mathbf{i}_V)}(\mathbf{k}_s, \mathbf{k}_i), \mathbf{o}_{\boldsymbol{V},(\mathbf{i}_P, i_H, \mathbf{i}_V)}\right) \tag{4.3.18}$$

The radar response of the head-cylinder is given by (4.3.19), using the CRE.

$$H_{t,V,(\mathbf{i}_P, i_H, \mathbf{i}_V)} = jk\eta Z_a \, \Phi_e \, \Phi_r\left(\mathbf{r}_r, \mathbf{r}_{U,(\mathbf{i}_P, i_H, \mathbf{i}_V)}\right) \Phi_t\left(\mathbf{r}_{V,(\mathbf{i}_P, i_H, \mathbf{i}_V)}, \mathbf{r}_t\right) \cdot \left[\, \mathbf{f}_r \cdot \bar{\bar{\mathbf{F}}}_{V,(\mathbf{i}_P, i_H, \mathbf{i}_V)}(\mathbf{k}_s, \mathbf{k}_i) \cdot \mathbf{f}_t\right] \tag{4.3.19}$$

4.3.3. Forward Scattering: Leaf-Sheet (Primitive)

From chapter 3, the scattering dyad of a primitive leaf-sheet $t_{Q,(\mathbf{i}_P, i_L, i_Q)}$ with length $L_{Q,(\mathbf{i}_P, i_L, i_Q)}$ width $w_{Q,(\mathbf{i}_P, i_L, i_Q)}$ and thickness $a_{Q,(\mathbf{i}_P, i_L, i_Q)}$ at its base orientation is given by (4.3.20). The shape function S is given by (4.3.21), in terms of the thin sheet dimensions. The dyadic operator $\bar{\bar{\mathbf{K}}}(\mathbf{k}_s, \mathbf{k}_i; k_1)$ is defined in chapter 3.

$$\bar{\bar{\mathbf{F}}}^{(\boldsymbol{b})}_{Q,(\mathbf{i}_P, i_L, \mathbf{i}_Q)}(\mathbf{k}_s, \mathbf{k}_i) = -jk \;\; S(L_{i_Q}) \cdot \bar{\bar{\mathbf{K}}}(\mathbf{k}_s, \mathbf{k}_i; k_1) \tag{4.3.20}$$

$$S(L_{i_Q}) = L_{i_Q} \, w_{i_Q} \, \mathrm{sinc}\left(k_{\boldsymbol{dz}} L_{i_Q}/2\right) \, \mathrm{sinc}(k_{\boldsymbol{dy}} \, w_{i_Q}/2) \tag{4.3.21}$$

The relations in (4.3.22-4.3.24), were used in (4.3.20-4.3.21) to simplify notation.

$$a_{i_Q} = a_{Q,(\mathbf{i}_P,i_L,i_Q)} \tag{4.3.22}$$

$$w_{i_Q} = w_{Q,(\mathbf{i}_P,i_L,i_Q)} \tag{4.3.23}$$

$$L_{i_Q} = L_{Q,(\mathbf{i}_P,i_L,i_Q)} \tag{4.3.24}$$

The scattering dyad of the leaf-sheet at its orientation $\mathbf{o}_{Q,(\mathbf{i}_P,i_L,\mathbf{i_Q})}$ is found using the rotation operation (4.3.25).

$$\bar{\bar{\mathbf{F}}}_{Q,(\mathbf{i}_P,i_L,\mathbf{i_Q})}(\mathbf{k_s},\mathbf{k_i}) = Rot\left(\bar{\bar{\mathbf{F}}}^{(\boldsymbol{b})}_{Q,(\mathbf{i}_P,i_L,\mathbf{i_Q})}(\mathbf{k}_s,\mathbf{k}_i),\mathbf{o}_{Q,(\mathbf{i}_P,i_L,\mathbf{i_Q})}\right) \tag{4.3.25}$$

The radar response of the leaf-sheet is given by (4.3.26), using the CRE.

$$H_{t,Q,(\mathbf{i}_P,i_L,\mathbf{i_Q})} = jk\eta Z_a\,\Phi_e\,\Phi_r\left(\mathbf{r_r},\mathbf{r}_{Q,(\mathbf{i}_P,i_L,\mathbf{i_Q})}\right)\,\Phi_t\left(\mathbf{r}_{Q,(\mathbf{i}_P,i_L,\mathbf{i_Q})},\mathbf{r}_t\right)\cdot\left[\,\mathbf{f_r}\cdot\,\bar{\bar{\mathbf{F}}}_{Q,(\mathbf{i}_P,i_L,\mathbf{i_Q})}(\mathbf{k_s},\mathbf{k_i})\cdot\,\mathbf{f_t}\right] \tag{4.3.26}$$

4.3.4. Forward Scattering: Stem

By the CGM method, the radar response $H_{t,S,(\mathbf{i}_P,i_S)}$ of the stem (complex target) is given the superposition of the radar response of its related stem-cylinders, as shown in (4.3.27). The scattering response $F_{qp,S,(\mathbf{i}_P,i_S)}(f)$ of each stem with scattering center $\mathbf{r}_{S,(\mathbf{i}_P,i_S)}$ is given by (4.3.28).

$$H_{t,S,(\mathbf{i}_P,i_S)} = \sum_{i_U=1}^{N_U} H_{t,U,(\mathbf{i}_P,i_S,i_U)} \tag{4.3.27}$$

$$F_{qp,S,(\mathbf{i}_P,i_S)}(f) = \left[\, \hat{q} \cdot \bar{\bar{\mathbf{F}}}_{S,(\mathbf{i}_P,i_S)}(\mathbf{k}_s, \mathbf{k}_i) \cdot \hat{p}\right] \tag{4.3.28}$$

$$= \left[jk\eta Z_a \, \Phi_e \Phi_r\left(\mathbf{r}_r, \mathbf{r}_{S,(\mathbf{i}_P,i_S)}\right) \Phi_t\left(\mathbf{r}_{S,(\mathbf{i}_P,i_S)}, \mathbf{r}_t\right) |\mathbf{f}_r|_v |\mathbf{f}_t|_v\right]^{-1} \left[H_{t,S,(\mathbf{i}_P,i_S)}\right]$$

4.3.5. Forward Scattering: Head

The radar response $H_{t,V,(\mathbf{i}_P,i_H,i_V)}$ of the head (complex target) is given the superposition of the radar response of its related head-cylinders, as shown in (4.3.29). The scattering response $F_{qp,H,(\mathbf{i}_P,i_H)}(f)$ of each stem with scattering center $\mathbf{r}_{\boldsymbol{H},(\mathbf{i}_P,i_H)}$ is given by (4.3.30).

$$H_{t,H,(\mathbf{i}_P,i_H)} = \sum_{i_V=1}^{N_U} H_{t,V,(\mathbf{i}_P,i_H,i_V)} \tag{4.3.29}$$

$$F_{qp,H,(\mathbf{i}_P,i_H)}(f) = \left[\, \hat{q} \cdot \bar{\bar{\mathbf{F}}}_{\boldsymbol{H},(\mathbf{i}_P,i_H)}(\mathbf{k}_s, \mathbf{k}_i) \cdot \hat{p}\right] \tag{4.3.30}$$

$$= \left[jk\eta Z_a \, \Phi_e \Phi_r\left(\mathbf{r}_r, \mathbf{r}_{S,(\mathbf{i}_P,i_H)}\right) \Phi_t\left(\mathbf{r}_{\boldsymbol{H},(\mathbf{i}_P,i_H)}, \mathbf{r}_t\right) |\mathbf{f}_r|_v |\mathbf{f}_t|_v\right]^{-1} \left[H_{t,H,(\mathbf{i}_P,i_H)}\right]$$

4.3.6. Forward Scattering: Leaves

The radar response $H_{t,L,(\mathbf{i}_P,i_L)}$ of the leaf (complex target) is given the superposition of the radar response of its related leaf-sheets, as shown in (4.3.31). The scattering response $F_{qp,\boldsymbol{L},(\mathbf{i}_P,i_L)}(f)$ of each stem with scattering center $\mathbf{r}_{\boldsymbol{L},(\mathbf{i}_P,i_L)}$ is given by (4.3.32).

$$H_{t,L,(\mathbf{i_P},i_L)} = \sum_{i_{Qy}=1}^{2} \sum_{i_{Qz}=1}^{N_{Qz}} H_{t,Q,\left(\mathbf{i_P},i_L,(i_{Qy},i_{Qz})\right)} \tag{4.3.31}$$

$$F_{qp,\boldsymbol{L},(\mathbf{i_P},i_L)}(f) = \left[\, \hat{q} \cdot \bar{\bar{\mathbf{F}}}_{\boldsymbol{L},(\mathbf{i_P},i_L)}(\mathbf{k_s},\mathbf{k_i}) \cdot \hat{p}\right] \tag{4.3.32}$$

$$= \left[jk\eta Z_a\, \Phi_e \Phi_r\left(\mathbf{r_r}, \mathbf{r}_{\boldsymbol{L},(\mathbf{i_P},i_L)}\right) \Phi_t\left(\mathbf{r}_{\boldsymbol{L},(\mathbf{i_P},i_L)}, \mathbf{r}_t\right) |\mathbf{f_r}|_v |\mathbf{f_t}|_v\right]^{-1} \left[H_{t,\boldsymbol{L},(\mathbf{i_P},i_L)}\right]$$

4.3.7. Forward Scattering: Wheat Plant

The radar response $H_{t,P,(\mathbf{i_P})}$ of the plant (complex target) is given the superposition of the radar response of all its sub-targets, as shown in (4.3.33). The scattering response $F_{qp,P,(\mathbf{i_P})}(f)$ of each stem with scattering center $\mathbf{r}_{P,(\mathbf{i_P})}$ is given by (4.3.34).

$$H_{t,P,(\mathbf{i_P})} = \sum_{i_H=1}^{N_H} H_{t,H,(\mathbf{i_P},i_H)} + \sum_{i_S=1}^{N_S} H_{t,S,(\mathbf{i_P},i_S)} + \sum_{i_L=1}^{N_L} H_{t,L,(\mathbf{i_P},i_L)} \tag{4.3.33}$$

$$= H_{t,H,(\mathbf{i_P},1)} + H_{t,S,(\mathbf{i_P},1)} + \sum_{i_L=1}^{N_L} H_{t,L,(\mathbf{i_P},i_L)}$$

$$F_{qp,P,(\mathbf{i_P})}(f) = \left[\, \hat{q} \cdot \bar{\bar{\mathbf{F}}}_{P,(\mathbf{i_P})}(\mathbf{k_s},\mathbf{k_i}) \cdot \hat{p}\right] \tag{4.3.34}$$

$$= \left[jk\eta Z_a\, \Phi_e \Phi_r\left(\mathbf{r_r}, \mathbf{r}_{P,(\mathbf{i_P})}\right) \Phi_t\left(\mathbf{r}_{P,(\mathbf{i_P})}, \mathbf{r}_t\right) |\mathbf{f_r}|_v |\mathbf{f_t}|_v\right]^{-1} \left[H_{t,P,(\mathbf{i_P})}\right]$$

4.3.8. Forward Scattering: Wheat Canopy

The radar response $H_{t,C}$ of the wheat canopy (complex target) is given the superposition of the radar response of all its plants (sub-targets), as shown in (4.3.35). The scattering response $F_{qp,C}(f)$ of each stem with scattering center $\mathbf{r}_C$ is given by (4.3.36).

$$H_{t,C} = \sum_{i_{PY}}^{N_{PY}} \sum_{i_{PX}}^{N_{PX}} H_{t,P,((i_{PX},i_{PY}))} \tag{4.3.35}$$

$$F_{qp,C}(f) = \left[\hat{q} \cdot \bar{\bar{\mathbf{F}}}_C(\mathbf{k_s}, \mathbf{k_i}) \cdot \hat{p} \right] \tag{4.3.36}$$

$$= \left[jk\eta Z_a \, \Phi_e \Phi_r(\mathbf{r_r}, \mathbf{r}_C) \, \Phi_t(\mathbf{r}_C, \mathbf{r}_t) |\mathbf{f_r}|_v |\mathbf{f_t}|_v \right]^{-1} \left[H_{t,C} \right]$$

4.4. Comparison of Radar Simulator vs Full-Wave Commercial Simulator

In order to validate the radar simulator, simulations performed with the radar simulator described in this chapter were compared against simulations computed using a commercial full-wave simulator. The software package chosen for this validation is the Integral-Equation solver of the Ansys High-Frequency Structure Simulator (HFSS). This solver employs the method-of-moments technique to solve the RCS of targets. The RCS of wheat leaves, heads and stems as well as wheat plants were computed with the full-wave tool to validate the simulator developed in this investigation.

For a given set of target parameters, the radar simulator generated the geometric model for each simulated target, as described in section 4.2. The geometric model was translated to STL format to be imported by the HFSS modeler and for visualization purposes. The antennas are specified to be located at the positions given by (4.4.1) and (4.4.2) for the transmit and receive antennas, respectively. In (4.4.1-4.4.2), θ_v is a variable elevation angle. We define the line that crosses the origin and the delay center of the antennas as the main axis of the antennas. The variable angle θ_v is the elevation angle of the main axis of the antennas and it is varied for RCS simulations as a function of angle.

The simulations are computed in the frequency domain. The inverse Fourier transform is used to compute the scattering response in the time domain and the RCS as a function of time. For all the simulations in this section, both antennas are polarized parallel to the y-axis (i.e. H-H). Moreover, for all RCS simulations as a function of frequency and time/range, the antenna elevation angle θ_v is set to zero.

$$\mathbf{r_t} = r_t \begin{bmatrix} \sin(\theta_t)\cos(\varphi_t) \\ \sin(\theta_t)\sin(\varphi_t) \\ \cos(\theta_t) \end{bmatrix} = 2.1418\, m \begin{bmatrix} \sin(-0.1423 + \theta_v) \\ 0 \\ \cos(-0.1423 + \theta_v) \end{bmatrix} \tag{4.4.1}$$

$$\mathbf{r_r} = r_r \begin{bmatrix} \sin(\theta_r)\cos(\varphi_r) \\ \sin(\theta_r)\sin(\varphi_r) \\ \cos(\theta_r) \end{bmatrix} = 2.1418\, m \begin{bmatrix} \sin(+0.1423 + \theta_v) \\ 0 \\ \cos(+0.1423 + \theta_v) \end{bmatrix} \tag{4.4.2}$$

4.4.1. Leaf (Case 1): Straight and Flat

We define a straight leaf as a leaf that is not curved in its main axis. A flat leaf is defined as a leaf that is not folded about its main axis. In this section, we consider a straight and flat leaf. Specifically, we consider a leaf $t_{L,(1,1)}$ with the parameters given by table 4.4.1. The leaf parameters in this table are used to compute the geometric model of the leaf and its leaf-sheets, as described in section 4.2. A depiction of the resulting geometric model of the leaf is shown in figure 4.4.1. In figure 4.4.1, the leaf is composed of 20 leaf-sheets. However, for a straight/flat leaf the simulation results are independent on the number of segments.

Simulations were performed for the RCS as a function of angle, frequency and time/range.

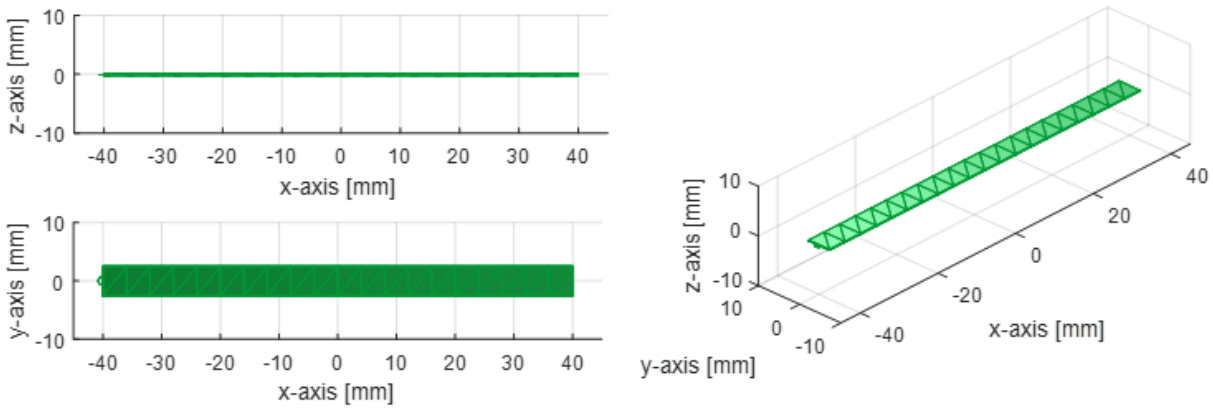

Figure 4.4.1 – Leaf (Case 1): Visualization of Geometric Model. (Top-Left: Side view; Bottom-Left: Top view; Right: Perspective view)

Table 4.4.1 – Leaf (Case 1): List of Leaf Parameters

Parameter	**Leaf 1, $t_{L,(1,1)}$**
Position, $\mathbf{r}_{L,(1,i_L)}$	$(-L_v/2,0,a_v/2)$
Length, $\boldsymbol{L}_{L,(1,i_L)}$	80 mm
Width, $\boldsymbol{w}_{L,(1,i_L)}$	5 mm
Thickness, $\boldsymbol{a}_{L,(1,i_L)}$	0.2 mm
First-rot. $\boldsymbol{\alpha}_{L,(1,i_L)}$	0 deg
Azimuth, $\boldsymbol{\varphi}_{L,(1,i_L)}$	0 deg
Initial Elev, $\boldsymbol{\theta}_{i,L,(1,i_L)}$	90 deg
Final Elev, $\boldsymbol{\theta}_{f,L,(1,i_L)}$	90 deg
Rad. of Curv., $\boldsymbol{R}_{L,(1,i_L)}$	Inf. (straight leaf)
Moist. Cont., $\boldsymbol{m}_{L,(1,i_L)}$	0.5

4.4.1.1. Leaf (Case 1): RCS vs Elevation Angle

The RCS of the leaf was computed for different values (-90 to 90 degrees) of the antenna elevation angle θ_v. Figure 4.4.2 shows the RCS of the flat/straight leave as a function of elevation angle at 2, 8 and 12 GHz. The RCS computed with the radar simulator agrees well with the full-wave simulations.

The simulations show that the RCS is larger when the leaf's largest facet is perpendicular to the antenna's main axis.

4.4.1.2. Leaf (Case 1): RCS vs Frequency

The RCS of the flat/straight leaf was computed over the 2 GHz to 18 GHz frequency range. The antenna elevation angle was set to zero. Figure 4.4.3 shows the result of the simulation. The radar simulation agrees well with the full-wave simulation.

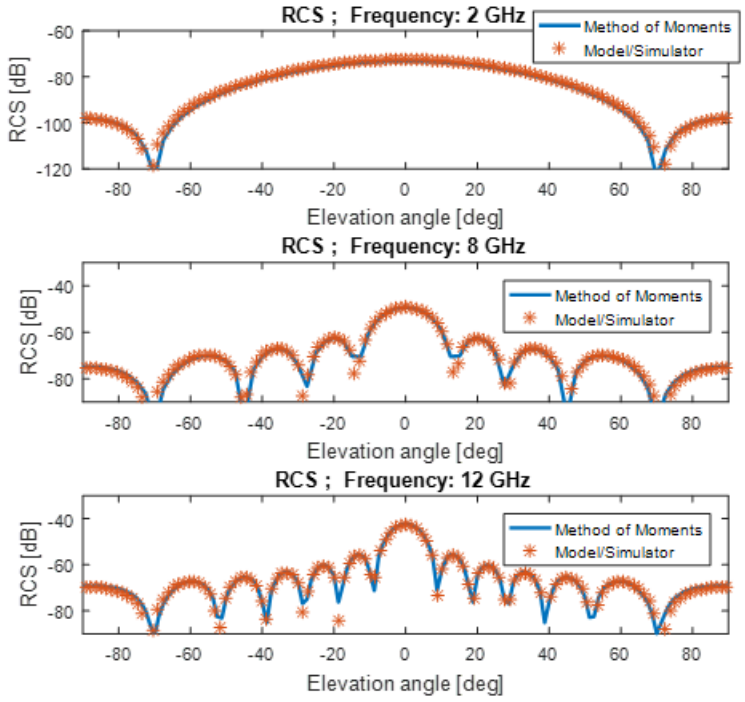

Figure 4.4.2 – Leaf (Case 1): RCS vs Elevation Angle. (top: freq. = 2 GHz; center: freq. = 8 GHz; bottom: freq. = 12 GHz)

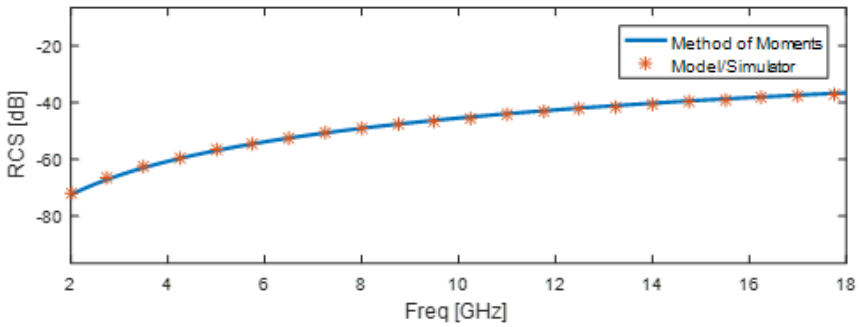

Figure 4.4.3 – Leaf (Case 1): RCS vs Frequency

4.4.1.3. Leaf (Case 1): RCS vs Time/Range

Figure 4.4.4 shows the RCS as a function of range for the straight/flat leaf. The radar simulation agrees well with the full-wave simulation result.

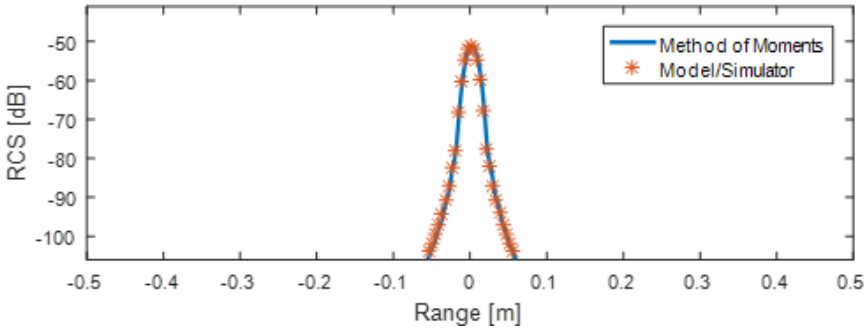

Figure 4.4.4 – Leaf (Case 1): RCS vs Range

4.4.2. Leaf (Case 2): Straight and Folded

In this section, we consider a leaf that is straight along its main axis but folded about its main axis. We define the angle between the two folds as the dihedral angle of the leaf $\gamma_{,L,(1,i_L)}$. The geometric model of folded leaves is composed of pairs of leaf-sheets, instead of a single array of leaf-sheets. The parameters of this leaf are given in table 4.4.2.

First, we simulated the RCS of the leaf when the leaf's main axis is aligned to the x-axis (i.e. leaf's azimuth angle is zero. The results of the simulation of the RCS as a function of antenna elevation angle, frequency and time is almost identical as the results from the previous section. The different of the simulations for the folded and flat cases was less than 0.1 dB.

Secondly, we simulated the RCS of the leaf when the leaf's main axis is aligned to the y-axis (i.e. the leaf's azimuth angle is 90 degrees). The RCS as a function of frequency and time at an antenna elevation of zero are also almost identical to those from section 4.4.1. In contrast, the RCS as a function of antenna elevation angle vary as much as 0.1 dB between a leaf with a dihedral angle of 140 degrees and a leaf with a dihedral angle of 180 degrees. In this section, we show the results the simulation of the RCS as a function of elevation angle for three different leaf dihedral angles $\gamma_{,L,(1,i_L)}$. It should be noted that varying the antenna elevation is equivalent to varying the leaf's first-rotation angle $\alpha_{,L,(1,i_L)}$.

From the results of this section, we conclude that for practical leaf configurations, the leaf's dihedral angle has little effect in the RCS. Therefore, the dihedral angle is not specified in other leaf simulation in this chapter, unless noted otherwise.

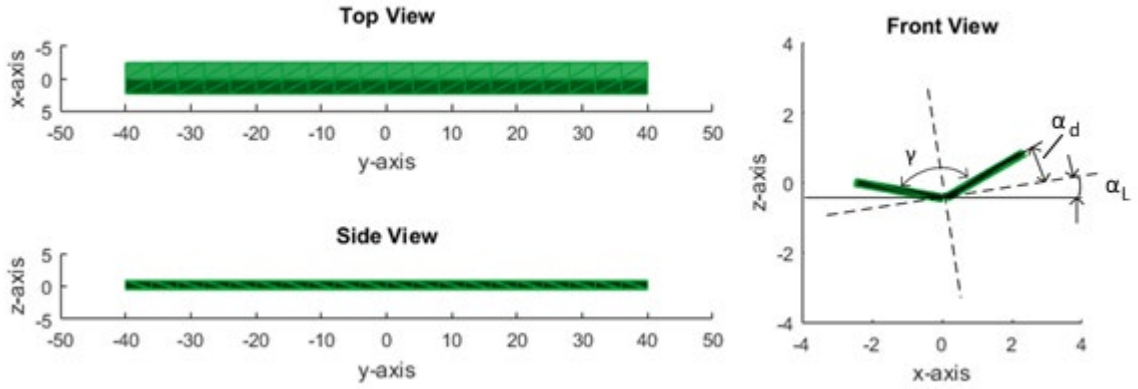

Figure 4.4.5 – Leaf (Case 2): Visualization of Geometric Model (Top-left: Top view; Bottom-left: Side view; Right: Front view)

Table 4.4.2 – Leaf (Case 2): List of Leaf Parameters

Parameter	**Leaf 1, $t_{L,(1,1)}$**
Position, $\mathrm{r}_{L,(1,i_L)}$	$(-L_v/2, 0, a_v/2)$
Length, $L_{S,(1,i_L)}$	80 mm
Width, $w_{L,(1,i_L)}$	5 mm
Thickness, $a_{L,(1,i_L)}$	0.2 mm
First-rot. $\alpha_{L,(1,i_L)}$	0 deg
Azimuth, $\varphi_{L,(1,i_L)}$	90 deg
Initial Elev, $\theta_{i,L,(1,i_L)}$	90 deg
Final Elev, $\theta_{f,L,(1,i_L)}$	90 deg
Rad. of Curv., $R_{,L,(1,i_L)}$	Inf. (straight leaf)
Dihedral Ang., $\gamma_{,L,(1,i_L)}$	180 deg, 180-20 deg, 180-40 deg
Moist. Cont., $m_{\,L,(1,i_L)}$	0.5

4.4.2.1. Leaf (Case 2): RCS vs Elevation Angle

The RCS of the folded and straight leaf, described by the parameters in table 4.4.2, was simulated as a function of the antenna's elevation angle. Simulations were performed for three different dihedral angles. Figure 4.4.6 show the simulation results. The full-wave simulations agree well with the radar simulations.

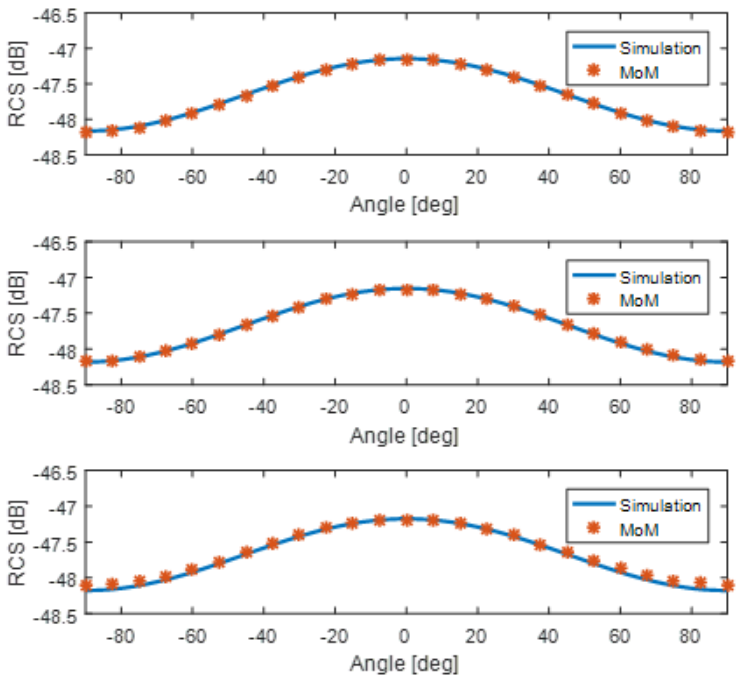

Figure 4.4.6 – Leaf (Case 2): RCS vs First-Rotation Offset Angle. (top: $\gamma_{,L,(1,i_L)} = 180$ deg; center: $\gamma_{,L,(1,i_L)} = 160$ deg deg; bottom: $\gamma_{,L,(1,i_L)} = 140$ deg deg)

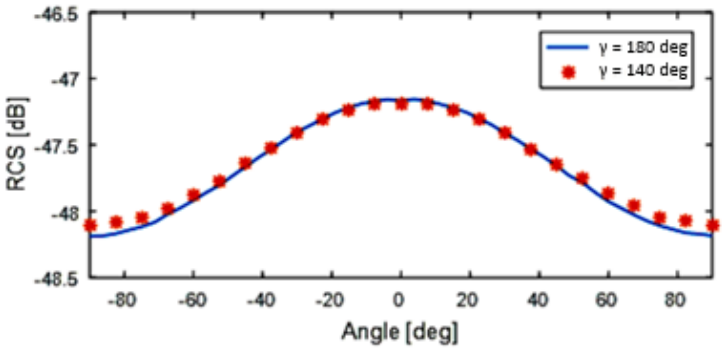

Figure 4.4.7 – Leaf (Case 2): RCS vs First-Rotation Offset Angle. (Blue: $\gamma_{,L,(1,i_L)} = 180$ deg; Red: $\gamma_{,L,(1,i_L)} = 140$ deg)

Figure 4.4.7 show a comparison between the simulations of the RCS for dihedral angles 180 and 140 degrees. The maximum difference between both simulations occurs when the antenna's elevation angle is 90 degrees. This is equivalent to a leaf's first-rotation angle of 90 degrees. At this firs-rotation angle, the difference in the RCS reaches 0.1 dB.

Most leaves in nature have a first-rotation angle close to zero (i.e. they face upwards, not sideways). Therefore, the difference in the RCS of a folded leaf with dihedral angles larger than 140 degrees ($\gamma_{,L,(1,i_L)} > 140 \text{ deg}$) and a flat leaf ($\gamma_{,L,(1,i_L)} = 0 \text{ deg}$) is negligible. For this reason, the simulations of leaves in this chapter will not specify the dihedral angle, unless noted otherwise. Moreover, the leaves will be geometrically modeled using a single array of leaf-sheets, unless noted otherwise.

The simulation results show that for a curved leaf the RCS is larger when the axis of the antenna's main axis is perpendicular to the regions of the curved leaf with the smallest curvature.

4.4.3. Leaf (Case 3): Curved Leaf (Different Radius of Curvatures)

In this section, we consider a leaf that is curved at their main axis. The leaf parameters are listed in table 4.4.3. The geometric model of this curved leaf is depicted in figure 4.4.8.

The geometric model of a curved leaf is described in section 4.2. For a curved leaf, the minimum radius of curvature $R_{,L,(1,i_L)}$ has a finite value. The location of the minimum radius of curvature in the path length of the leaf is given by $s_{o,,L,(1,i_L)}$.

The RCS of the curved leaf was simulated as a function of the antenna elevation angle for three different radius of curvature. The simulation results show that the radar simulator accurately predicts the RCS as a function of angle for a curved leaf.

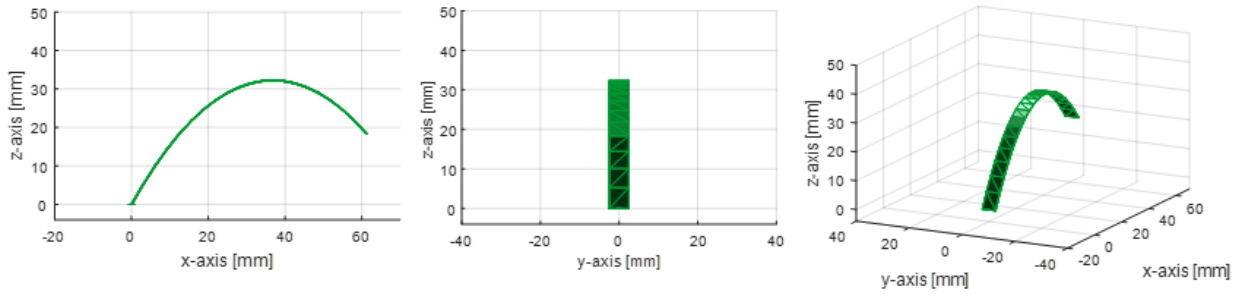

Figure 4.4.8 – Leaf (Case 3): Visualization of Geometric Model (left: front view; center: side view; right: perspective view)

Table 4.4.3 – Leaf (Case 3): List of Leaf Parameters

Parameter	**Leaf 1, $t_{L,(1,1)}$**
Position, $r_{L,(1,i_L)}$	$(-L_v/2, 0, a_v/2)$
Length, $L_{S,(1,i_L)}$	80 mm
Width, $w_{L,(1,i_L)}$	5 mm
Thickness, $a_{L,(1,i_L)}$	0.2 mm
First-rot. $\alpha_{L,(1,i_L)}$	0 deg
Azimuth, $\varphi_{L,(1,i_L)}$	0 deg
Initial Elev, $\theta_{i,L,(1,i_L)}$	90-70 deg
Final Elev, $\theta_{f,L,(1,i_L)}$	90+70 deg
Rad. of Curv., $R_{,L,(1,i_L)}$	20 mm, 30 mm, 40 mm
Apex Loc., $s_{o,,L,(1,i_L)}$	0.6 $L_{S,(1,i_L)}$
Moist. Cont., $m_{L,(1,i_L)}$	0.5

4.4.3.1. Leaf (Case 3): RCS vs Elevation Angle

The RCS of the curved leaf, described by the parameters in table 4.4.3, was simulated as a function of the antenna elevation angle. The simulations were performed for different values of $R_{,L,(1,i_L)}$. Figures 4.4.9, 4.4.10 and 4.4.11 show the simulation results for minimum radius of curvature equal to 20mm, 30mm and 40mm, respectively. The results of the full-wave simulations agree well with those of the radar simulation.

In section, 4.4.1, it was seen that RCS of a straight leaf is larger when the leaf's largest facet is perpendicular to the antenna's main axis. For a curved leaf, the RCS is larger when the axis of

the antenna's main axis is perpendicular to the regions of the curved leaf with the smallest curvature (largest radius of curvature). The regions of the leaf with largest radius of curvature occur before and after the apex of the leaf. In the figures below, these two regions correspond to the two humps present in each plot.

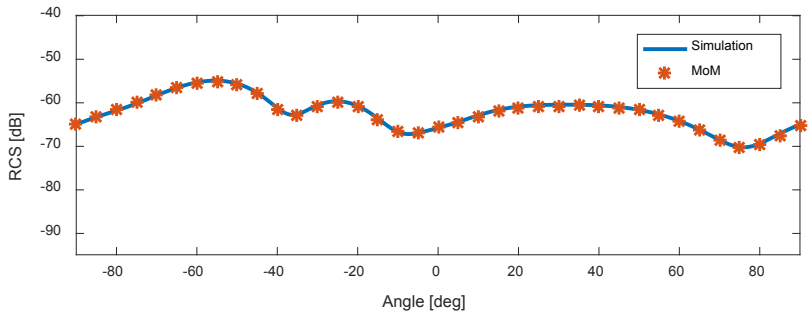

Figure 4.4.9 – Leaf (Case 3): RCS vs Elevation Angle. ($R_{,L,(1,i_L)}$ = 20 mm)

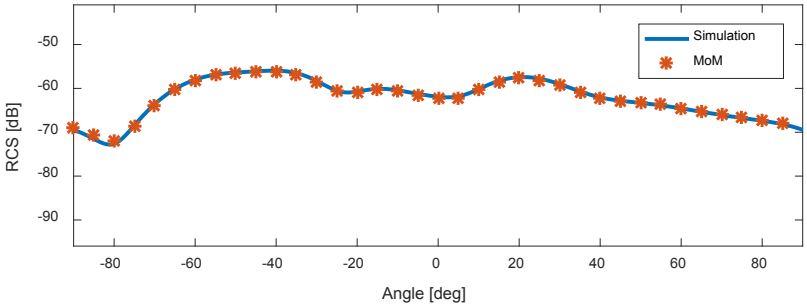

Figure 4.4.10 – Leaf (Case 3): RCS vs Elevation Angle. ($R_{,L,(1,i_L)}$ = 30 mm)

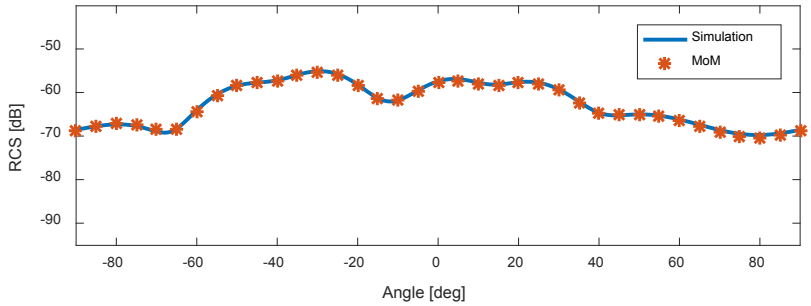

Figure 4.4.11 – Leaf (Case 3): RCS vs Elevation Angle. ($R_{,L,(1,i_L)}$ = 40 mm)

4.4.4. Leaf (Case 4): Curved Leaf (Different Azimuth Angles)

In this section, we consider another curved leaf, with different parameters than those of the previous section. The parameters of the curved leaf considered in this section are listed in table 4.4.4.

In this section, two leaf azimuth angles $\varphi_{L,(1,i_L)}$ are considered for the curved leaf: 0 and 90 degrees. Figure 4.4.12 and 4.4.13 show a depiction of the geometric model for the leaf in both configurations.

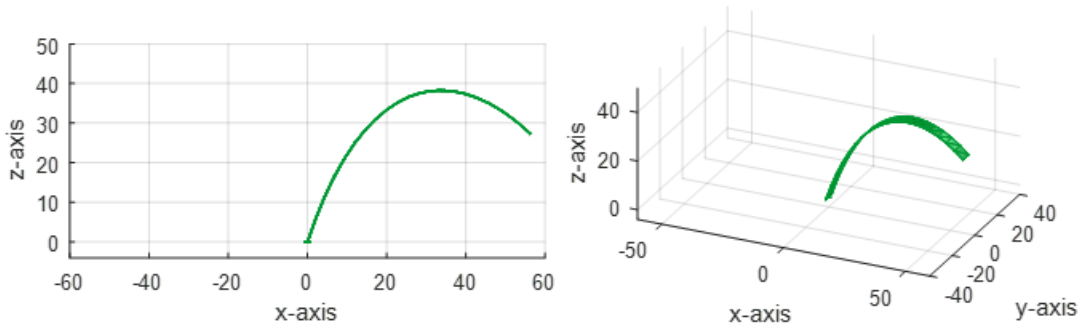

Figure 4.4.12 – Leaf (Case 4): Visualization of Geometric Model. ($\varphi_{L,(1,i_L)}$ = 0 deg)

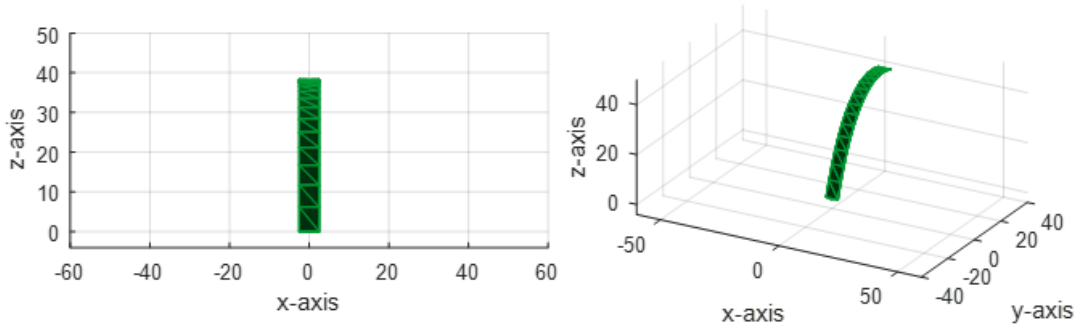

Figure 4.4.13 – Leaf (Case 4): Visualization of Geometric Model. ($\varphi_{L,(1,i_L)}$= 90 deg)

Table 4.4.4 – Leaf (Case 4): List of Leaf Parameters

Parameter	**Leaf 1, $t_{L,(1,1)}$**
Position, $\mathrm{r}_{L,(1,i_L)}$	$(0,0,0)$
Length, $L_{L,(1,i_L)}$	80 mm
Width, $w_{L,(1,i_L)}$	5 mm
Thickness, $a_{L,(1,i_L)}$	0.2 mm
First-rot. $\alpha_{L,(1,i_L)}$	0 deg
Azimuth, $\varphi_{L,(1,i_L)}$	0 deg; 90 deg
Initial Elev, $\theta_{i,L,(1,i_L)}$	90-85 deg
Final Elev, $\theta_{f,L,(1,i_L)}$	90+70 deg
Rad. of Curv., $R_{L,(1,i_L)}$	30 mm
Apex Loc., $s_{o,,L,(1,i_L)}$	0.6
Moist. Cont., $m_{L,(1,i_L)}$	0.5

4.4.4.1. Leaf (Case 4): RCS vs Inclination Angle

The RCS of the curved leaf was computed as a function of antenna's elevation angle. Simulations were performed for two different leaf's azimuth angles $\varphi_{L,(1,i_L)}$, 0 and 90 degrees. Figures 4.4.14 and 4.4.15 show the simulation results. The results of the radar simulator agree well with the full-wave simulations.

As noted in the previous section, the RCS is largest when the main axis of the antenna is perpendicular to the region of the leaf with the lowest curvature. In the first configuration ($\varphi_{L,(1,i_L)} = 0$ deg) the two leaf regions with the lowest curvature occur before and after the apex of the leaf. These two regions correspond to two humps in the RCS plot of figure 4.4.14.

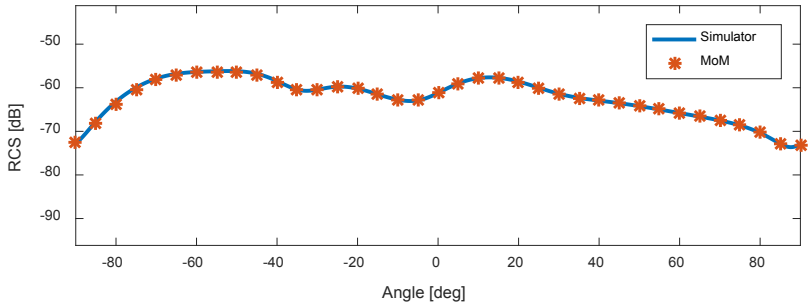

Figure 4.4.14 – Leaf (Case 4): RCS vs Elevation Angle: ($\varphi_{L,(1,i_L)}$ = 0 deg)

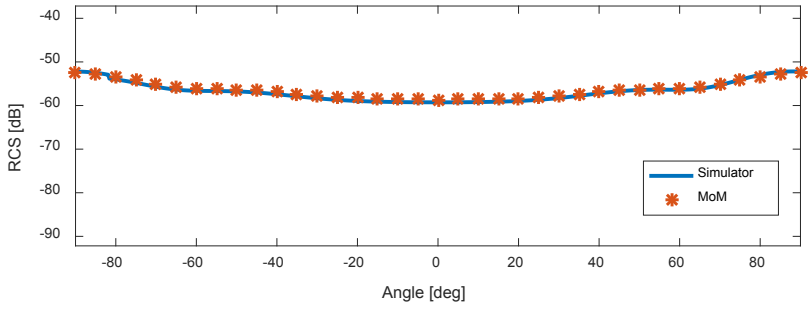

Figure 4.4.15 – Leaf (Case 4): RCS vs Elevation Angle: ($\varphi_{L,(1,i_L)}$ = 90 deg)

4.4.4.2. Leaf (Case 4): RCS vs Frequency

The RCS of the curved leaf was computed as a function of frequency (2-18 GHz) for the two different leaf configurations. For these simulations, the antenna elevation angle is set to zero. Figure 4.4.16 and 4.4.17 show the simulation results. The results of the radar simulator agree well with the full-wave simulations.

Besides three small resonant regions in the first plot, the RCS as a function of frequency has almost the same values for both configurations. This means that the RCS of the curved leave is approximately independent of azimuth angle.

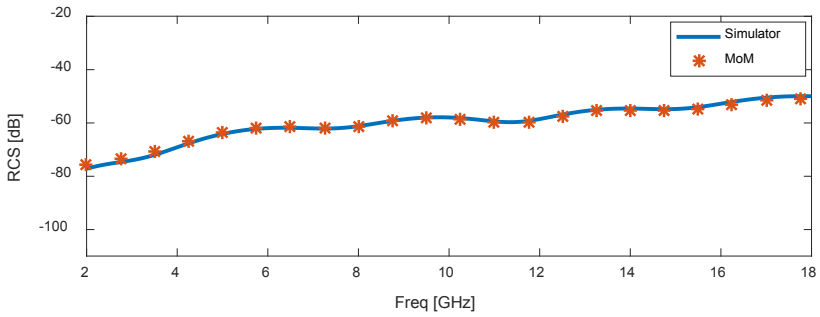

Figure 4.4.16 – Leaf (Case 4): RCS vs Frequency: ($\varphi_{L,(1,i_L)}$ = 0 deg)

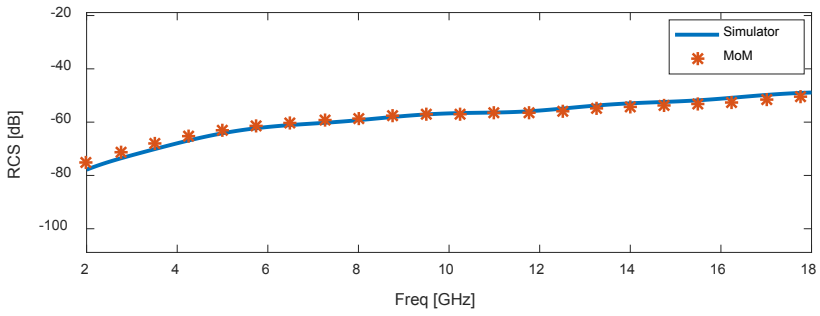

Figure 4.4.17 – Leaf (Case 4): RCS vs Frequency: ($\varphi_{L,(1,i_L)}$ = 90 deg)

4.4.4.3. Leaf (Case 4): RCS vs Time/Range

Taking the inverse Fourier transform of the scattering responses found in the previous section results in the RCS as a function of time.

Figures 4.4.18-4.4.19 show the simulation results. The results of the radar simulator agree well with the full-wave simulations. The RCS as a function of time is almost identical for both configurations. This means that the RCS of the curved leave is approximately independent of azimuth angle. The two peaks in the RCS plots correspond to the top (leaf's apex) and the bottom of the leaf.

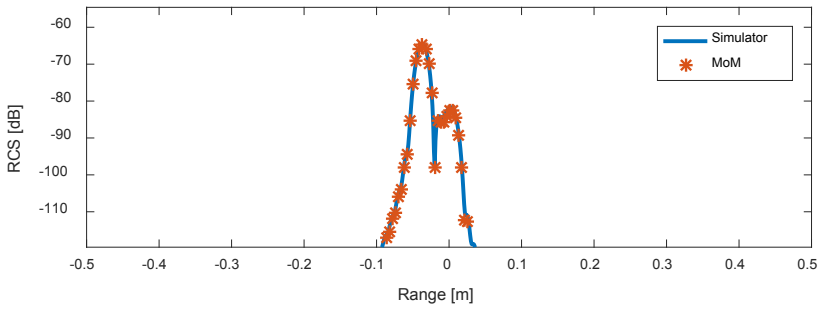

Figure 4.4.18 – Leaf (Case 4): RCS vs Range: (φ_Q = 0 deg)

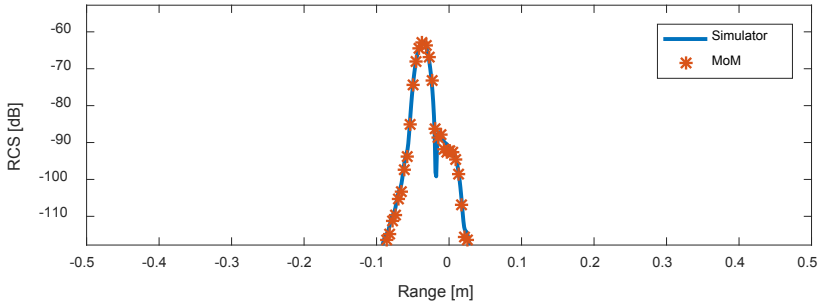

Figure 4.4.19 – Leaf (Case 4): RCS vs Range: (φ_Q = 90 deg)

4.4.5. Stem (Case 1): Straight Stem

In this section, we consider a straight wheat stem. The stem parameters are listed in table 4.4.5. Two stem lengths are considered, as listed in table 4.4.5. Figure 4.4.20 and 4.4.21 show depictions of the geometric model of the stems for both lengths.

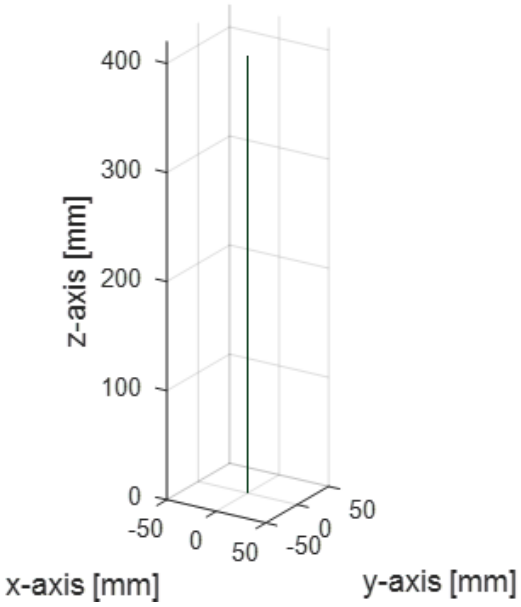

Figure 4.4.20 – Stem (Case 1): Visualization of Geometric Model. $L_{S,(1,i_S)} = 400\ \mathrm{mm}$.

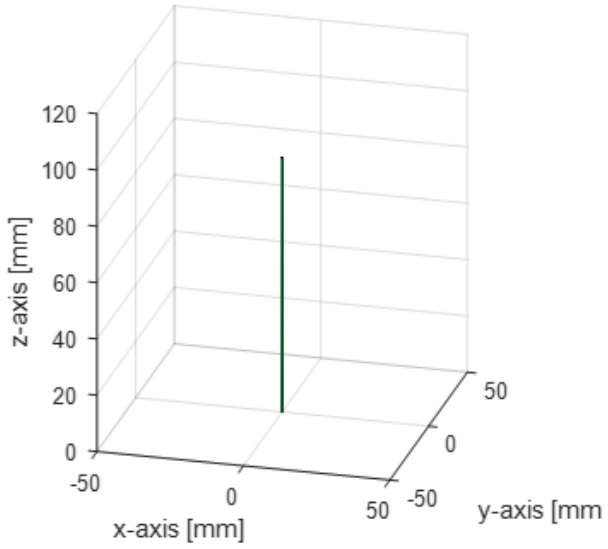

Figure 4.4.21 – Stem (Case 1): Visualization of Geometric Model. $L_{S,(1,i_S)} = 90$ mm.

Table 4.4.5 – Stem (Case 1): List of Stem Parameters

Parameter	**Stem 1, $t_{S,(1,1)}$**
Position, $\mathrm{r}_{S,(1,i_S)}$	Origin
Length, $L_{S,(1,i_S)}$	400 mm, 90mm
Radius, $\rho_{S,(1,i_S)}$	0.75 mm
Azimuth, $\varphi_{S,(1,i_S)}$	0 deg
Elev., $\theta_{S,(1,i_S)}$	0 deg
Moist. Cont., $m_{S,(1,i_S)}$	0.5

4.4.5.1. Stem (Case 1): RCS vs Elevation Angle

The RCS of the stem was simulated as a function of antenna elevation angle. Figure 4.4.22 and 4.4.23 show the result of the simulations. In general, the full wave simulation agrees well with the results of the radar simulator. As expected, the RCS is largest when the main axis of the stem is perpendicular to the main axis of the antenna.

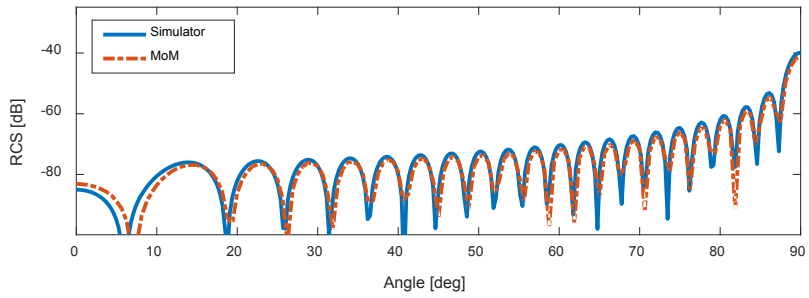

Figure 4.4.22 – Stem (Case 1): RCS vs Elevation Angle. $L_{S,(1,i_S)} = 400$ mm.

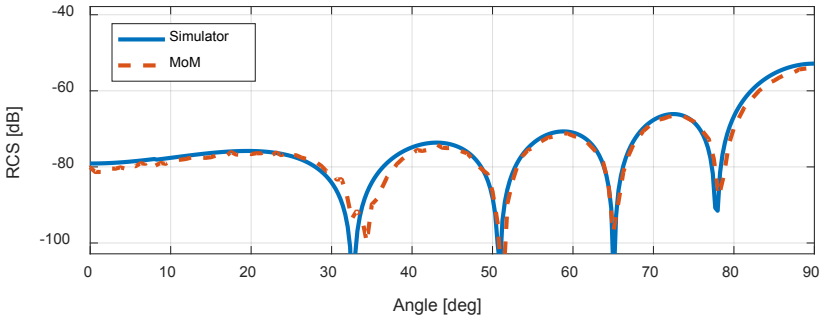

Figure 4.4.23 – Stem (Case 1): RCS vs Elevation Angle. $L_{S,(1,i_S)} = 90$ mm.

4.4.5.2. Stem (Case 1): RCS vs Frequency

The RCS of the stem was simulated over the 2-18 GHz frequency range for the stem length $L_{S,(1,i_S)} = 90$ mm. Figure 4.4.24 shows the result of the simulation. The radar simulation agrees well with the full-wave simulator. The antenna elevation angle was set to zero in this simulation.

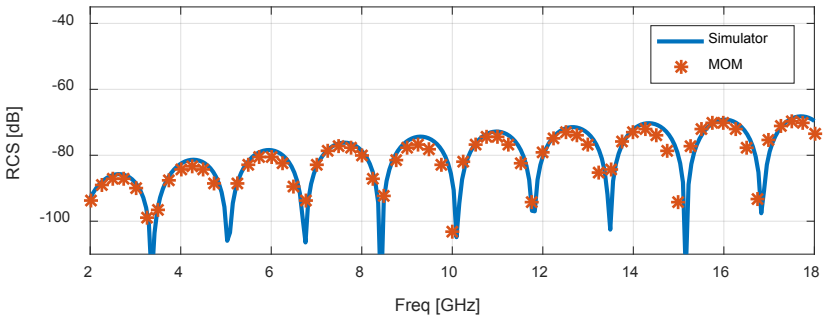

Figure 4.4.24 – Stem (Case 1): RCS vs Frequency. $L_{S,(1,i_S)} = 90$ mm.

4.4.5.3. Stem (Case 1): RCS vs Range

The antenna elevation angle was set to zero and the RCS was computed as a function of range for the length stem $L_{S,(1,i_S)} = 90$ mm. In this configuration, the main reflections are related to the ends of the stem. Figure 4.4.25 shows the result of the simulation. The radar simulation agrees well with the full-wave simulation. The RCS simulated with the full-wave simulator shows larger RCS between the two ends, which is related to multiple reflections. Since only single scattering is considered in the radar simulator, these multiple reflections are not accounted for.

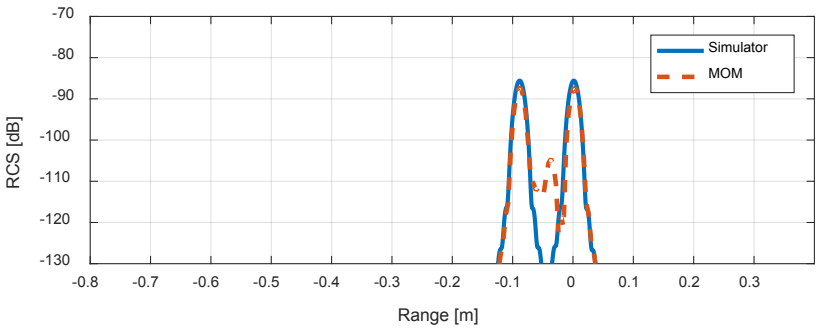

Figure 4.4.25 – Stem (Case 1): RCS vs Elevation Angle. $L_{S,(1,i_S)} = 90$ mm.

4.4.6. Head (Case 1): Smooth Surface

In this section, we consider a head with a smooth surface. The head geometric model, described in section 4.2, is composed of a stack of head-cylinders (primitives), which are stacked on top of each other. In the geometric model, the parameters ρ_r is used to add a deterministic variation between adjacent head-cylinders. When this roughness parameter is zero, radius of the head-cylinders varies smoothly between adjacent head-cylinders. In this case, we consider surface of the head to be smooth. The head parameters are listed in table 4.4.6. Figure 4.4.26 shows a depiction of the geometric model of the head.

The RCS of the head is simulated as a function of frequency and range for different head elevation angles $\theta_{H,(1,i_H)}$. In general, the radar simulations show good agreement against the full-wave simulations. The largest discrepancies between the two simulations occurs at high frequencies (>12 GHz) for small head elevation angles (10 deg).

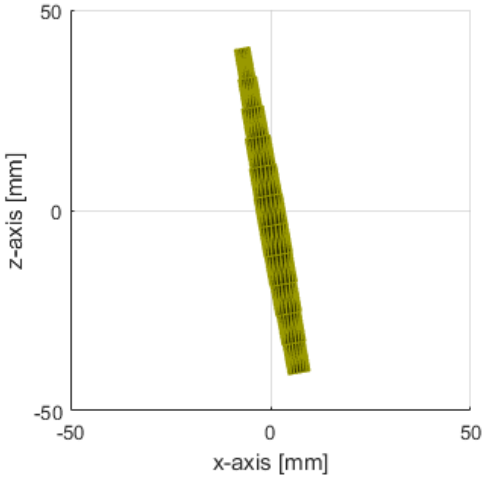

Figure 4.4.26 – Head (Case 1): Visualization of Geometrical Model

Table 4.4.6 – Head (Case 1): List of Head Parameters

Parameter	**Head 1, $t_{H,(1,1)}$**
Position, $\mathrm{r}_{H,(1,i_H)}$	Centered at origin
Length, $L_{H,(1,i_H)}$	82 mm
Radius init., $\rho_{i,H,(1,i_H)}$	1.13 mm
Radius mid., $\rho_{m,H,(1,i_H)}$	4.05 mm
Radius mid., $\rho_{m,H,(1,i_H)}$	2.25 mm
Azimuth, $\varphi_{H,(1,i_H)}$	0 deg
Elev., $\theta_{H,(1,i_H)}$	90, 70, 10 deg
Rad. fac., β_H	80
Moist. Cont., $m_{H,(1,i_H)}$	0.15
Vol. frac., $v_{H,(1,i_H)}$	0.6

4.4.6.1. Head (Case 1): RCS vs Frequency

The RCS as a function of frequency was simulated for the smooth head. Figures 4.4.27-4.4.29 show the simulation results. The full-wave simulations is in good agreement with the results of the radar simulator. The RCS computed with the radar simulator is slightly larger at frequencies above 12 GHz at the head elevation angle of 10 deg.

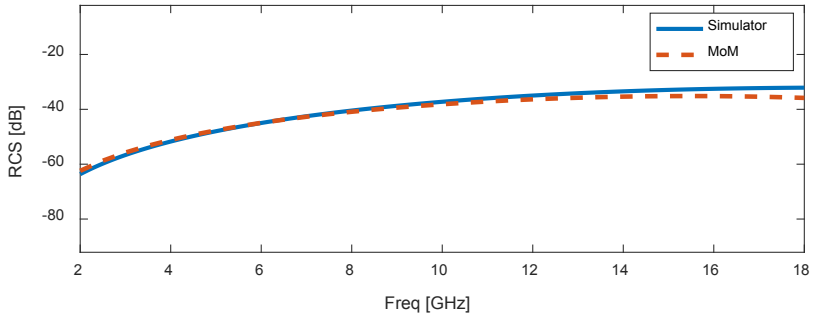

Figure 4.4.27 – Head (Case 1): RCS vs Frequency. $\theta_{H,(1,i_H)} = 90$ deg

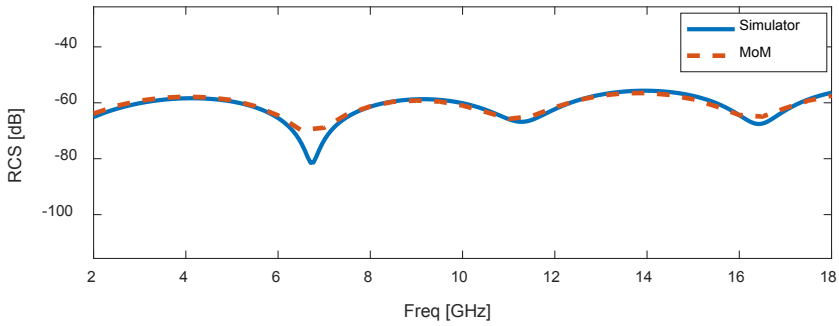

Figure 4.4.28 – Head (Case 1): RCS vs Frequency. $\theta_{H,(1,i_H)} = 70$ deg

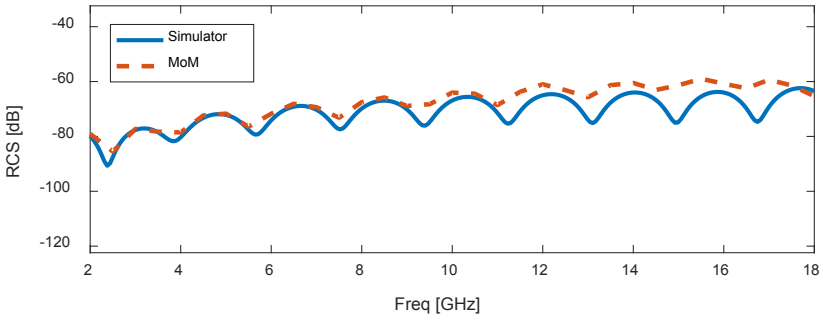

Figure 4.4.29 – Head (Case 1): RCS vs Frequency. $\theta_{H,(1,i_H)} = 10$ deg

4.4.6.2. Head (Case 1): RCS vs Time

Taking the inverse Fourier transform of the scattering response, the RCS as a function of time is found. Figure 4.4.30, 4.4.31 and 4.4.32 show the results of the simulations for head elevations angles 90, 70 and 10 deg. The results of the radar simulator are in good agreement with the results from the full-wave simulator. The largest discrepancy is seen when the head is inclined by only 10 deg.

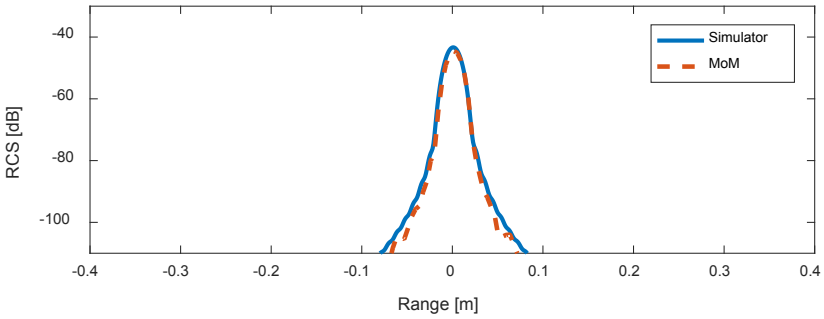

Figure 4.4.30 – Head (Case 1): RCS vs Range. $\theta_{H,(1,i_H)} = 90$ deg

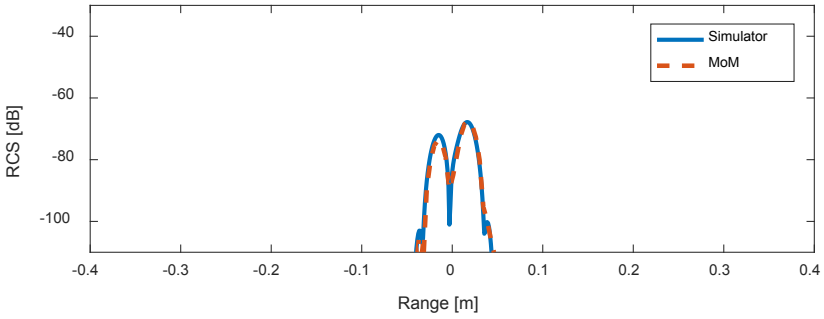

Figure 4.4.31 – Head (Case 1): RCS vs Range. $\theta_{H,(1,i_H)} = 70$ deg

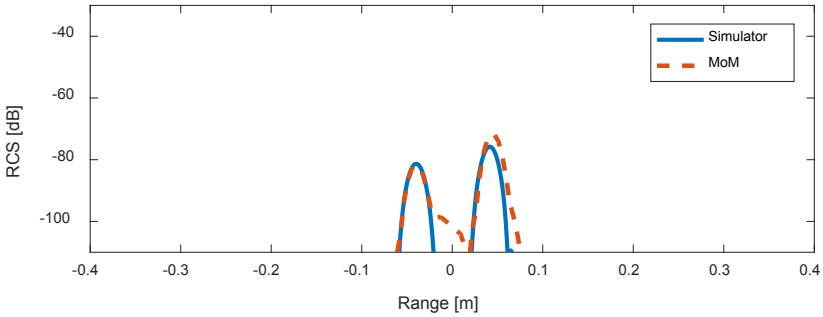

Figure 4.4.32 – Head (Case 1): RCS vs Range. $\theta_{H,(1,i_H)} = 10$ deg

4.4.7. Head (Case 2): Rough Surface

In this section, a head is considered with a pseudo-rough surface. The roughness of the surface is deterministic and it is given by the roughness value ρ_r, which varies the radius of adjacent head-cylinders. A value of 0.1 was chosen for the roughness parameter. The parameters of the considered head are the same as those listed in table 4.4.6, from the previous section. Figure 4.4.33 shows a depiction of the geometric model of the considered head.

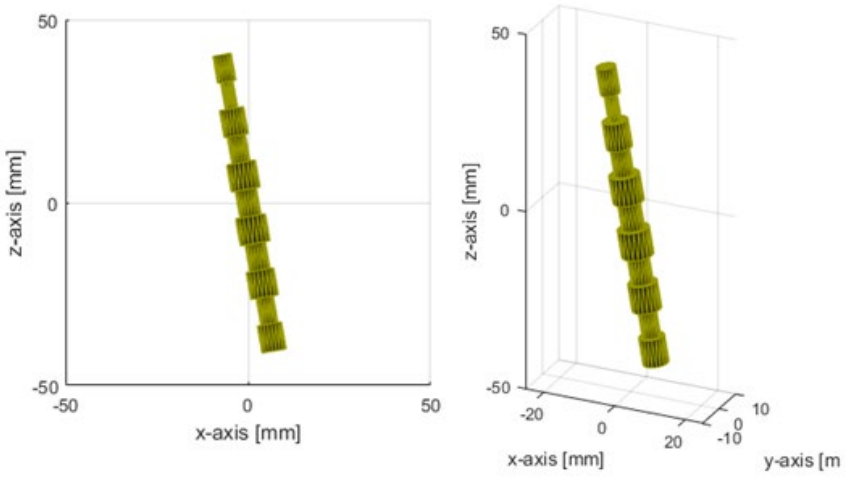

Figure 4.4.33 – Head (Case 2): Visualization of Geometric Model

4.4.7.1. Head (Case 2): RCS vs Frequency

The RCS as a function of frequency was computed for the head at different head elevation angles. The antenna elevation angle is set to zero. Figures 4.4.34, 4.4.35 and 4.4.36 show the simulation results when the head elevation angle is 90, 70 and 10 degrees, respectively. The results from the radar simulator agree well with the results from the full-wave simulator. The

largest discrepancies occur at frequencies larger than 12 GHz when the head elevation angle is 10 deg.

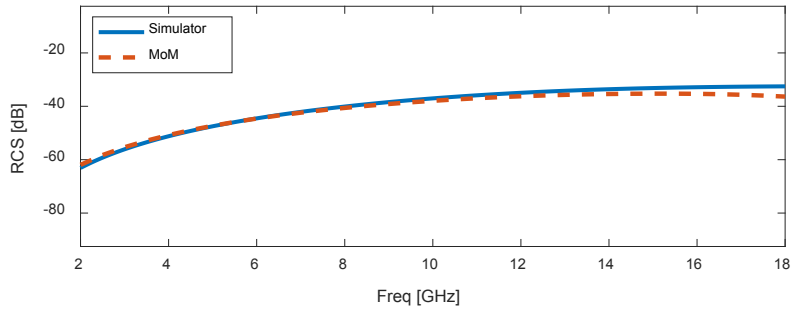

Figure 4.4.34 – Head (Case 1): RCS vs Frequency. $\theta_{H,(1,i_H)} = 90$ deg

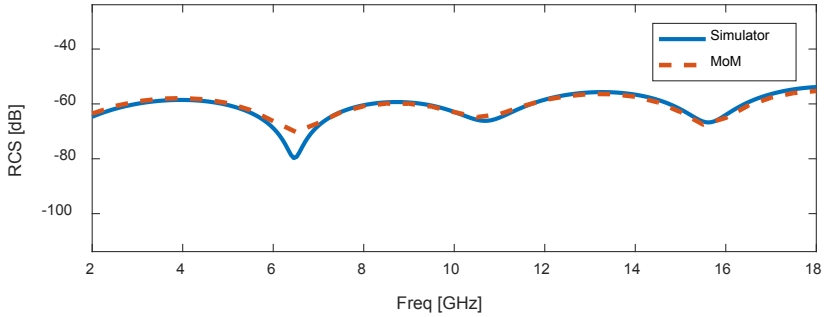

Figure 4.4.35 – Head (Case 1): RCS vs Frequency. $\theta_{H,(1,i_H)} = 70$ deg

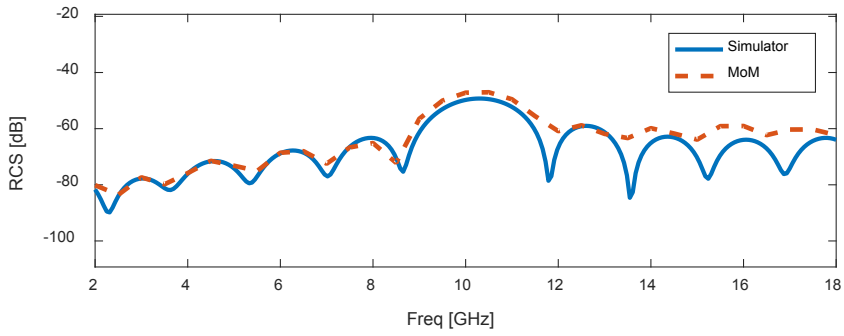

Figure 4.4.36 – Head (Case 1): RCS vs Frequency. $\theta_{H,(1,i_H)} = 10$ deg

4.4.7.2. Head (Case 2): RCS vs Time/Range

The RCS as a function of range was computed for the head at different head elevation angles. The antenna elevation angle is set to zero. Figures 4.4.37, 4.4.38 and 4.4.39 show the simulation results when the head elevation angle is 90, 70 and 10 degrees, respectively. The results from the radar simulator agree well with the results from the full-wave simulator for head elevation angles of 70 deg. and 90 deg. In figure 4.4.39, there are noticeable difference between the two solutions. These differences may be caused by multiple scattering contributions, which the radar simulator (model) does not consider.

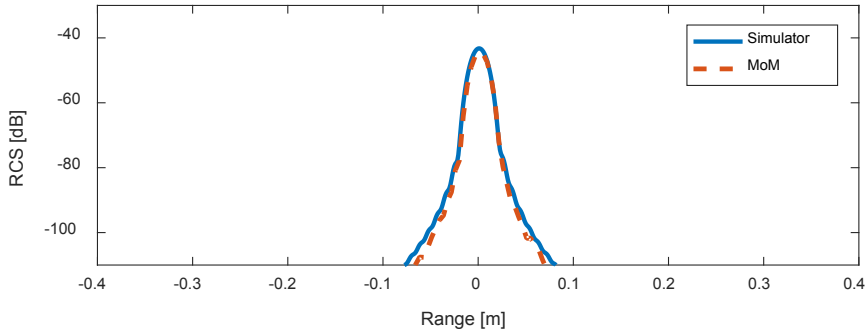

Figure 4.4.37 – Head (Case 1): RCS vs Range. $\theta_{H,(1,i_H)} = 90$ deg

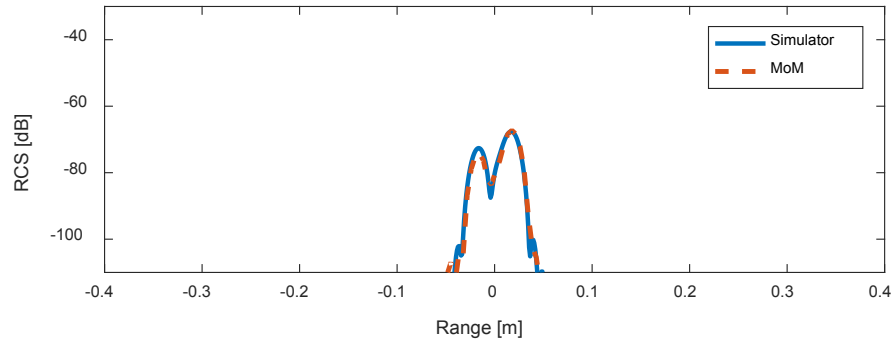

Figure 4.4.38 – Head (Case 1): RCS vs Range. $\theta_{H,(1,i_H)} = 70$ deg

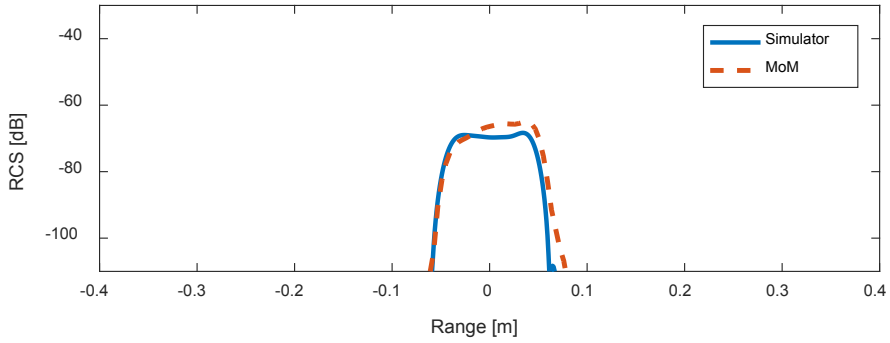

Figure 4.4.39 – Head (Case 1): RCS vs Range. $\theta_{H,(1,i_H)} = 10$ deg

4.4.8. Plant (Case 1): Short plant, 4 curved leaves, no stem, no head

In this section, we consider a short plant with four curved leaves, no stem and no head. The plant parameters are listed in tables 4.4.7, 4.4.8 and 4.4.9. The geometric model of the plant is depicted in figure 4.4.40. The stem is modeled geometrically and it is shown in figure 4.4.40, but it is not considered in the scattering simulation.

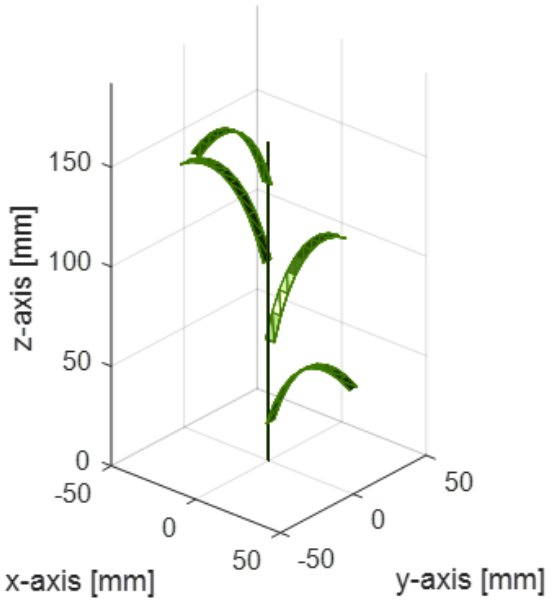

Figure 4.4.40 - Plant (Case 1): Visualization of the Geometric Model

Table 4.4.7 - Plant (Case 1): List of Stem Parameters

Parameter	**Stem 1, $t_{S,(1,1)}$**
Position, $r_{S,(1,i_S)}$	Origin
Length, $L_{S,(1,i_S)}$	160 mm
Radius, $\rho_{S,(1,i_S)}$	0.75 mm
Azimuth, $\varphi_{S,(1,i_S)}$	0 deg
Elev., $\theta_{S,(1,i_S)}$	0 deg
Moist. Cont., $m_{S,(1,i_L)}$	0.5

Table 4.4.8 - Plant (Case 1): List of Leaves Parameters

Parameter	**Leaf 1, $t_{L,(1,1)}$**	**Leaf 2,$t_{L,(1,2)}$**	**Leaf 3, $t_{L,(1,3)}$**	**Leaf 4, $t_{L,(1,4)}$**
Position, $r_{L,(1,i_L)}$	Evenly spaced			
Length, $L_{L,(1,i_L)}$	80 mm	80 mm	80 mm	80 mm
Width, $w_{L,(1,i_L)}$	5 mm	5 mm	5 mm	5 mm
Thickness, $a_{L,(1,i_L)}$	0.2 mm	0.2 mm	0.2 mm	0.2 mm
First-rot. $\alpha_{L,(1,i_L)}$	0 deg	0 deg	0 deg	0 deg
Azimuth, $\varphi_{L,(1,i_L)}$	0 deg	90 deg	180 deg	270 deg
Initial Elev, $\theta_{i,L,(1,i_L)}$	90-85 deg	90-85 deg	90-85 deg	90-85 deg
Final Elev, $\theta_{f,L,(1,i_L)}$	90+70 deg	90+70 deg	90+70 deg	90+70 deg
Rad. of Curv., $R_{L,(1,i_L)}$	30 mm	30 mm	30 mm	30 mm
Apex Loc., $s_{o,,L,(1,i_L)}$	0.6	0.6	0.6	0.6
Moist. Cont., $m_{L,(1,i_L)}$	0.5	0.5	0.5	0.5

Table 4.4.9 – Plant (Case 1): List of Plant Parameters

Parameter	Plant 1, $\mathbf{t_{P,(1)}}$
Position, $r_{P,(1)}$	Origin

4.4.8.1. Plant (Case 1): RCS vs Elevation Angle

The RCS of the plant was simulated as a function of antenna elevation angle. Figure 4.4.41 shows a comparison of the RCS simulated with the radar simulator and the full-wave simulator. The radar simulation agrees well with the full-wave simulation.

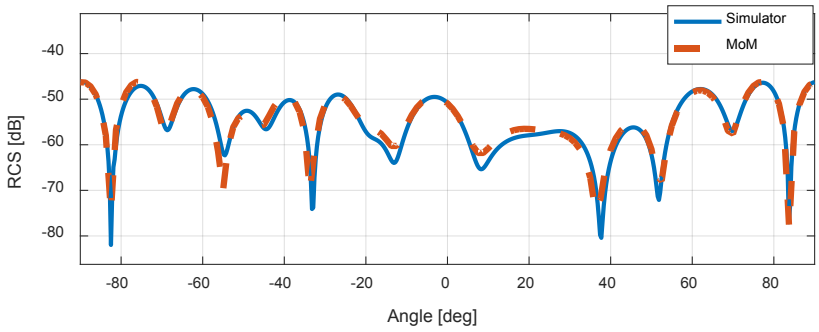

Figure 4.4.41 – Plant (Case 1): RCS vs Elevation Angle

4.4.8.2. Plant (Case 1): RCS vs Frequency

The RCS of the plant was simulated as a function of frequency. Figure 4.4.42 shows a comparison of the RCS simulated with the radar simulator and a full-wave simulator. The radar simulation agrees well with the full-wave simulation.

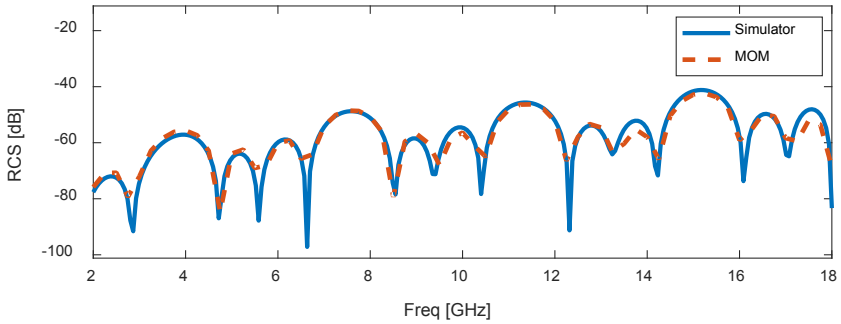

Figure 4.4.42 – Plant (Case 1): RCS vs Frequency

One feature to notice on the plot of figure 4.4.42 is that the RCS has periodic peaks spaced at frequency intervals given by (4.4.3). In (4.4.3), the term d_z is the z-component of the average distance between leaves. In this case, the average distance between leaves is 40mm, so that the Δf is 3.75 GHz.

$$\Delta f = \frac{c}{2d_z} = \frac{c}{2\frac{1}{N_L - 1}\sum_{i_L=2}^{N_L}\left(\mathbf{r}_{L,(1,i_L)} - \mathbf{r}_{L,(1,i_L-1)}\right)\cdot \hat{z}} \tag{4.4.3}$$

4.4.8.3. Plant (Case 1): RCS vs Time/Range

Figure 4.4.43 shows the modified RCS of the plant as a function of time. The radar simulation agrees well with the full-wave simulation.

The four peaks correspond to the apex of the four leaves in the plant. The peaks show that the plants are evenly space by 40 mm, as expected. The small return from the bottom of the leaves is only noticeable for the bottom-most leaf.

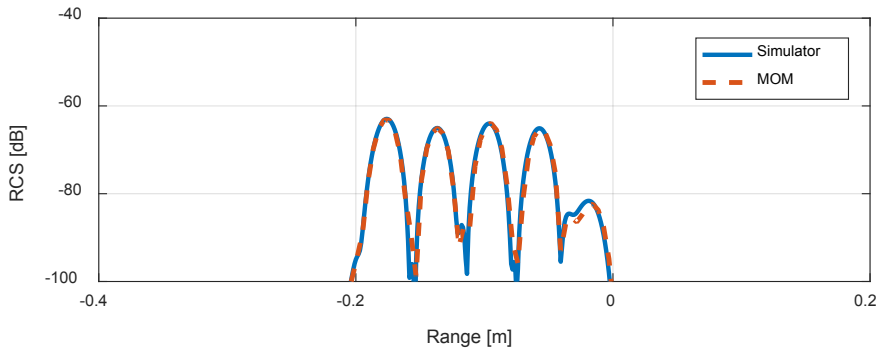

Figure 4.4.43 –Plant (Case 1): RCS vs Range

4.4.9. Plant (Case 2): Plant, 4 curved leaves, no stem, no head

In this section, we consider a tall plant with four leaves, with no stem and no head. The plant parameters are listed in tables 4.4.10-4.4.12. The geometric model of the plant is depicted in figure 4.4.44. The stem of the plant is modeled geometrically and it is shown in figure 4.4.44, but it is not considered in the scattering simulation of this section. The parameters considered for this plant are typical morphological parameters of an adult wheat plant.

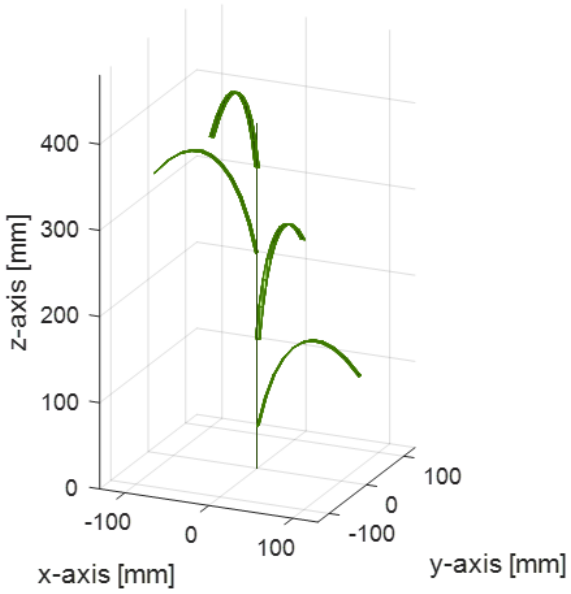

Figure 4.4.44 - Plant (Case 2): Visualization of Geometric Model

Table 4.4.10 - Plant (Case 2): List of Stem Parameters

Parameter	**Stem 1, $t_{S,(1,1)}$**
Position, $r_{S,(1,i_S)}$	Origin
Length, $L_{S,(1,i_S)}$	400 mm
Radius, $\rho_{S,(1,i_S)}$	0.75 mm
Azimuth, $\varphi_{S,(1,i_S)}$	0 deg
Elev., $\theta_{S,(1,i_S)}$	0 deg
Moist. Cont., $m_{S,(1,i_L)}$	0.5

Table 4.4.11 - Plant (Case 2): List of Leaves Parameters

Parameter	**Leaf 1, $t_{L,(1,1)}$**	**Leaf 2,$t_{L,(1,2)}$**	**Leaf 3, $t_{L,(1,3)}$**	**Leaf 4, $t_{L,(1,4)}$**
Position, $r_{L,(1,i_L)}$	Evenly spaced			
Length, $L_{L,(1,i_L)}$	200 mm	200 mm	200 mm	200 mm
Width, $w_{L,(1,i_L)}$	5 mm	5 mm	5 mm	5 mm
Thickness, $a_{L,(1,i_L)}$	0.2 mm	0.2 mm	0.2 mm	0.2 mm
First-rot. $\alpha_{L,(1,i_L)}$	0 deg	0 deg	0 deg	0 deg
Azimuth, $\varphi_{L,(1,i_L)}$	0 deg	90 deg	180 deg	270 deg
Initial Elev, $\theta_{i,L,(1,i_L)}$	90-85 deg	90-85 deg	90-85 deg	90-85 deg
Final Elev, $\theta_{f,L,(1,i_L)}$	90+70 deg	90+70 deg	90+70 deg	90+70 deg
Rad. of Curv., $R_{L,(1,i_L)}$	60 mm	60 mm	60 mm	60 mm
Apex Loc., $s_{o,,L,(1,i_L)}$	0.6	0.6	0.6	0.6
Moist. Cont., $m_{L,(1,i_L)}$	0.5	0.5	0.5	0.5

Table 4.4.12 – Plant (Case 2): List of Plant Parameters

Parameter	**Plant 1, $\mathbf{t_{P,(1)}}$**
Position, $r_{P,(1)}$	Origin

4.4.9.1. Plant (Case 2): RCS vs Elevation Angle

The RCS of the plant was simulated as a function of elevation angle.

Figure 4.4.45 shows a comparison of the RCS simulated with the radar simulator and a full-wave simulator. The radar simulation agrees well with the full-wave simulation.

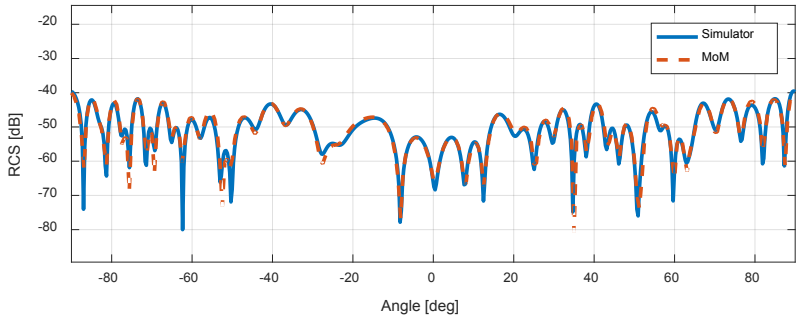

Figure 4.4.45 - Plant (Case 2) – RCS vs Elevation Angle

4.4.9.2. Plant (Case 2): RCS vs Frequency

The RCS of the plant was simulated as a function of frequency. Figure 4.4.46 shows a comparison of the RCS simulated with the radar simulator and a full-wave simulator. The radar simulation agrees well with the full-wave simulation.

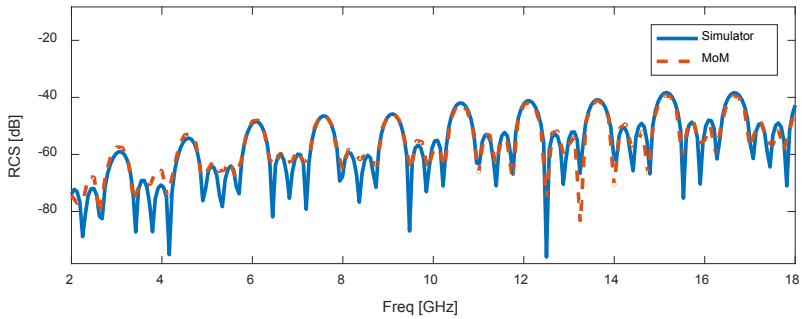

Figure 4.4.46 – Plant (Case 2): RCS vs Frequency

As mentioned in the previous section, the peaks in the RCS are spaced in frequency intervals given by (4.4.3). In this case, the average distance between leaves is 100mm, so that Δf is 1.5 GHz.

4.4.9.3. Plant (Case 2): RCS vs Time/Range

Figure 4.4.47 shows the RCS as a function of time for the plant. The radar simulation agrees well with the full-wave simulation. The four peaks correspond to the apex of the four leaves in the plant. The peaks are spaced by 100mm in range, which is the leaf spacing in the vertical dimension.

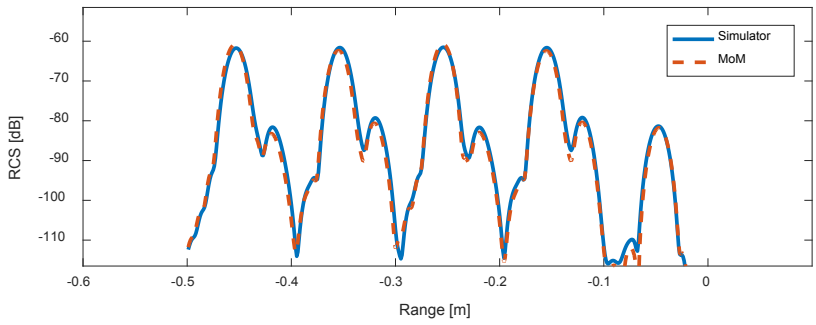

Figure 4.4.47 – Plant (Case 2): RCS vs Range

4.4.10. Plant (Case 3): Plant, 4 curved leaves, stem, no head

In this section, we consider a plant with four leaves, a straight stem and no head. The plant parameters are listed in tables 4.4.13-4.4.15. The geometric model of the plant is depicted in figure 4.4.4.48. The parameters considered for this plant are typical morphological parameters of an adult wheat plant.

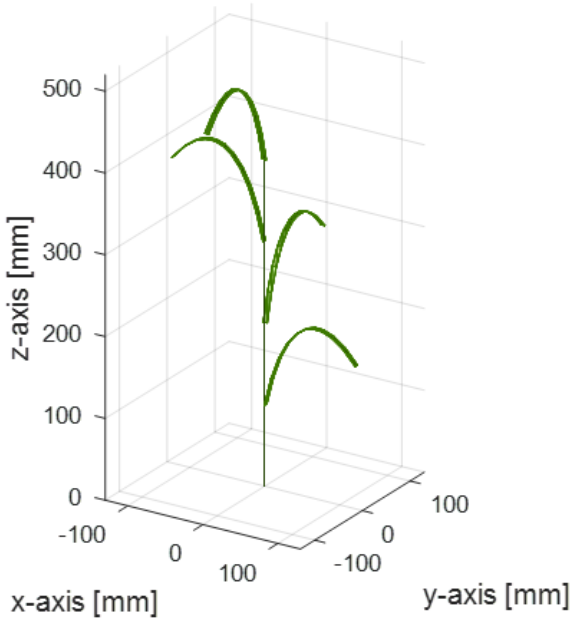

Figure 4.4.48 - Plant (Case 3): Geometric Model

Table 4.4.13 - Plant (Case 3): List of Stem Parameters

Parameter	**Stem 1, $t_{S,(1,1)}$**
Position, $r_{S,(1,i_S)}$	Origin
Length, $L_{S,(1,i_S)}$	400 mm
Radius, $\rho_{S,(1,i_S)}$	0.75 mm
Azimuth, $\varphi_{S,(1,i_S)}$	0 deg
Elev., $\theta_{S,(1,i_S)}$	0 deg
Moist. Cont., $m_{S,(1,i_L)}$	0.5

Table 4.4.14 - Plant (Case 3): List of Leaves Parameters

Parameter	**Leaf 1, $t_{L,(1,1)}$**	**Leaf 2,$t_{L,(1,2)}$**	**Leaf 3, $t_{L,(1,3)}$**	**Leaf 4, $t_{L,(1,4)}$**
Position, $r_{L,(1,i_L)}$	Evenly spaced			
Length, $L_{L,(1,i_L)}$	80 mm	80 mm	80 mm	80 mm
Width, $w_{L,(1,i_L)}$	5 mm	5 mm	5 mm	5 mm
Thickness, $a_{L,(1,i_L)}$	0.2 mm	0.2 mm	0.2 mm	0.2 mm
First-rot. $\alpha_{L,(1,i_L)}$	0 deg	0 deg	0 deg	0 deg
Azimuth, $\varphi_{L,(1,i_L)}$	0 deg	90 deg	180 deg	270 deg
Initial Elev, $\theta_{i,L,(1,i_L)}$	90-85 deg	90-85 deg	90-85 deg	90-85 deg
Final Elev, $\theta_{f,L,(1,i_L)}$	90+70 deg	90+70 deg	90+70 deg	90+70 deg
Rad. of Curv., $R_{L,(1,i_L)}$	30 mm	30 mm	30 mm	30 mm
Apex Loc., $s_{o,,L,(1,i_L)}$	0.6	0.6	0.6	0.6
Moist. Cont., $m_{L,(1,i_L)}$	0.5	0.5	0.5	0.5

Table 4.4.15 – Plant (Case 3): List of Plant Parameters

Parameter	**Plant 1, $\mathbf{t_{P,(1)}}$**
Position, $r_{P,(1)}$	Origin

4.4.10.1. Plant (Case 3): RCS vs Elevation Angle

The RCS of the plant was simulated as a function of elevation angle. Figure 4.4.49 shows a comparison of the RCS simulated with the radar simulator and a full-wave simulator. The radar simulation agrees well with the full-wave simulation. In this simulation, the RCS peaks at +90 and -90 degrees. At these angles, the RCS of the stem reaches its maximum. This feature was not present in case 2, which did not include a stem in the simulation.

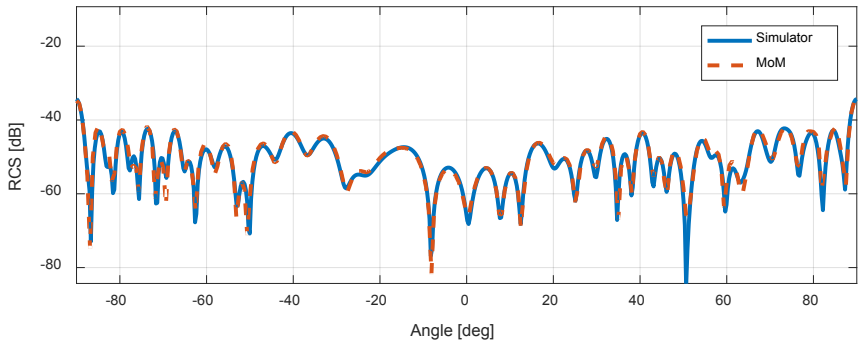

Figure 4.4.49 - Plant (Case 3) – RCS vs Elevation Angle

4.4.10.2. Plant (Case 3): RCS vs Frequency

The RCS of the plant was simulated as a function of frequency. Figure 4.4.50 shows a comparison of the RCS simulated with the radar simulator and a full-wave simulator. The radar simulation agrees well with the full-wave simulation. This simulation result is identical to the

simulation from case 2. The stem's RCS is much smaller than the RCS of the leaves, in this configuration.

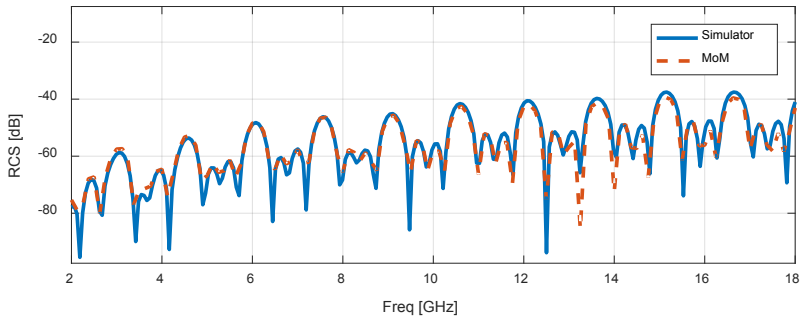

Figure 4.4.50 – Plant (Case 3): RCS vs Frequency

4.4.10.3. Plant (Case 3): RCS vs Time/Range

Figure 4.4.51 shows the RCS as a function of range of the plant. The radar simulation agrees well with the full-wave simulation. The largest four peaks correspond to the apex of the four leaves in the plant. The last peak correspond to the bottom end of the stem. The top end of the stem is not detectable, since it is much smaller than the leaf's returns. The second-to-last peak corresponds to the bottom end of the last leaf.

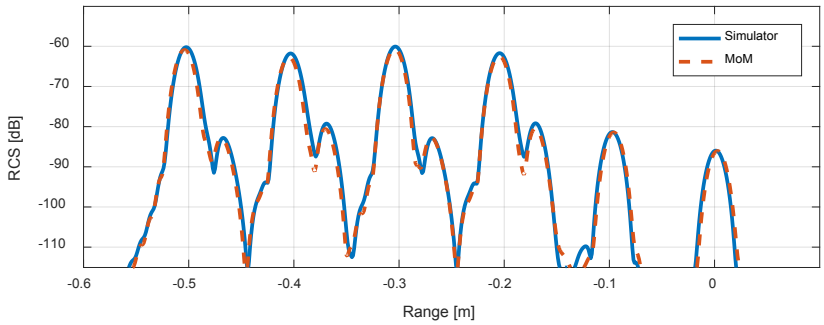

Figure 4.4.51 – Plant (Case 3): RCS vs Range

4.4.11. Plant (Case 4): Plant, 4 curved leaves, head, stem

In this section, we consider a plant with four leaves, a straight stem and a head. The plant parameters are listed in tables 4.4.16-4.4.19. The geometric model of the plant is depicted in figure 4.4.4.52. The parameters considered for this plant are typical morphological parameters of an adult wheat plant.

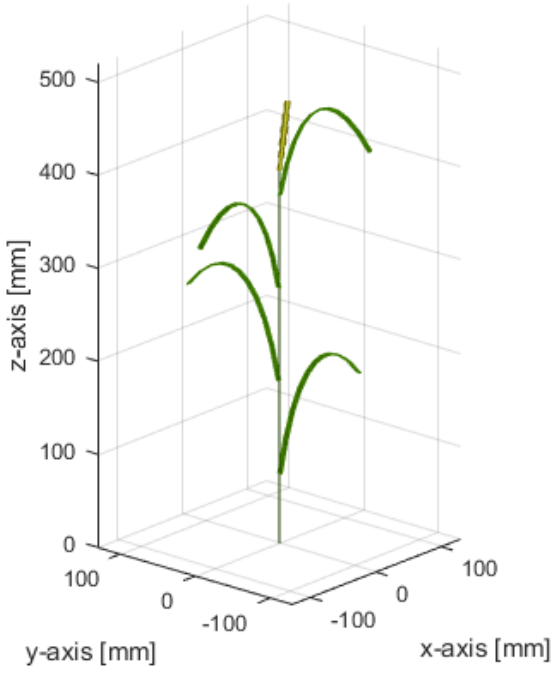

Figure 4.4.52 – Plant (Case 4): Visualization of Geometric Model

Table 4.4.16 - Plant (Case 3): List of Stem Parameters

Parameter	**Stem 1, $t_{S,(1,1)}$**
Position, $r_{S,(1,i_S)}$	Origin
Length, $L_{S,(1,i_S)}$	400 mm
Radius, $\rho_{S,(1,i_S)}$	0.75 mm
Azimuth, $\varphi_{S,(1,i_S)}$	0 deg
Elev., $\theta_{S,(1,i_S)}$	0 deg
Moist. Cont., $\boldsymbol{m}_{S,(1,i_L)}$	0.5

Table 4.4.17 - Plant (Case 3): List of Leaves Parameters

Parameter	**Leaf 1, $t_{L,(1,1)}$**	**Leaf 2,$t_{L,(1,2)}$**	**Leaf 3, $t_{L,(1,3)}$**	**Leaf 4, $t_{L,(1,4)}$**
Position, $\mathbf{r}_{L,(1,i_L)}$	Evenly spaced			
Length, $\boldsymbol{L}_{L,(1,i_L)}$	80 mm	80 mm	80 mm	80 mm
Width, $\boldsymbol{w}_{L,(1,i_L)}$	5 mm	5 mm	5 mm	5 mm
Thickness, $\boldsymbol{a}_{L,(1,i_L)}$	0.2 mm	0.2 mm	0.2 mm	0.2 mm
First-rot. $\alpha_{L,(1,i_L)}$	0 deg	0 deg	0 deg	0 deg
Azimuth, $\varphi_{L,(1,i_L)}$	0 deg	90 deg	180 deg	270 deg
Initial Elev, $\theta_{i,L,(1,i_L)}$	90-85 deg	90-85 deg	90-85 deg	90-85 deg
Final Elev, $\theta_{f,L,(1,i_L)}$	90+70 deg	90+70 deg	90+70 deg	90+70 deg
Rad. of Curv., $R_{L,(1,i_L)}$	30 mm	30 mm	30 mm	30 mm
Apex Loc., $s_{o,,L,(1,i_L)}$	0.6	0.6	0.6	0.6
Moist. Cont., $m_{L,(1,i_L)}$	0.5	0.5	0.5	0.5

Table 4.4.18 – Plant (Case 3): List of Plant Parameters

Parameter	**Plant 1, $\mathbf{t_{P,(1)}}$**
Position, $r_{P,(1)}$	Origin

Table 4.4.19 – Head (Case 1): List of Head Parameters

Parameter	**Head 1, $\boldsymbol{t_{H,(1,1)}}$**
Position, $\mathrm{r}_{H,(1,i_H)}$	Centered at origin
Length, $L_{H,(1,i_H)}$	72 mm
Radius init., $\rho_{i,H,(1,i_H)}$	1.13 mm
Radius mid., $\rho_{m,H,(1,i_H)}$	4.05 mm
Radius mid., $\rho_{m,H,(1,i_H)}$	2.25 mm
Azimuth, $\varphi_{H,(1,i_H)}$	0 deg
Elev., $\theta_{H,(1,i_H)}$	10 deg
Rad. fac., β_H	80
Moist. Cont., $m_{H,(1,i_H)}$	0.15
Vol. frac., $v_{H,(1,i_H)}$	0.6

4.4.11.1. Plant (Case 4): RCS vs Frequency

Figure 4.4.53 shows a comparison of the RCS as a function of time simulated with the radar simulator and the full-wave simulator. The radar simulation agrees well with the full wave simulation.

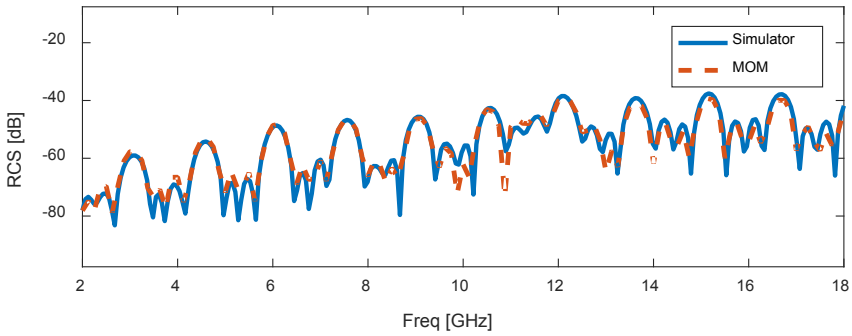

Figure 4.4.53 – Plant (Case 4): RCS vs Frequency.

4.4.11.2. Plant (Case 4): RCS vs Range

Figure 4.4.54 shows the RCS as a function of range of the plant. For the most part, the radar simulation agrees well with the full-wave simulation.

Compared to case 3, this plot has an extra hump near the return that corresponds to the apex of the top leaf. This hump corresponds to the head, which was not present in the simulation of case 3.

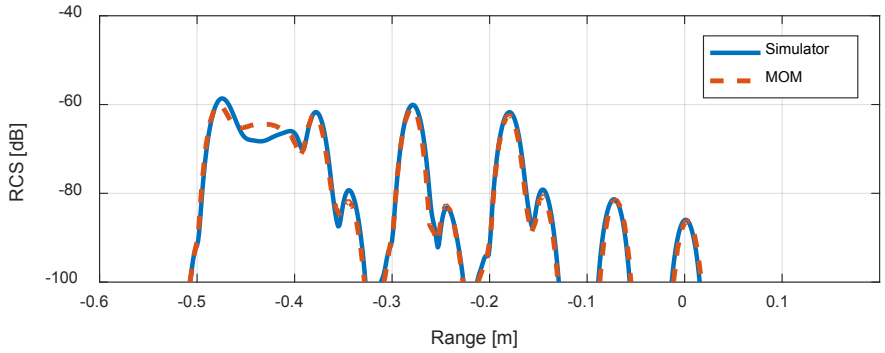

Figure 4.4.54 – Plant (Case 4): RCS vs Range.

4.5. Comparison of Radar Simulator vs Measurement Results

In the previous section, RCS simulations due to plants and plant's constituents were compared against full-wave simulations to validate the simulator. These simulations were performed for a specified geometric model of the wheat plants and constituents. These simulations showed that the radar simulator is able of computing the RCS at that specified geometric model.

The geometric models used so far are only approximations of the actual shapes of the plants and plant constituents. In this section, we compare radar simulations of the RCS due to plants and plant constituents against measurements. In this manner, the geometric models are validated as well as the forward scattering simulation.

For these measurements and simulations, the transmit and receive antennas are located as given by (4.5.1) and (4.5.2), respectively. The separation used between the antennas is 2 ft. The antenna's polarization is parallel to the y-axis (i.e. H-H).

$$\mathbf{r_t} = r_t \begin{bmatrix} \sin(\theta_t)\cos(\varphi_t) \\ \sin(\theta_t)\sin(\varphi_t) \\ \cos(\theta_t) \end{bmatrix} = 2.14\,m \begin{bmatrix} \sin(-0.1423) \\ 0 \\ \cos(-0.1423) \end{bmatrix} \tag{4.5.1}$$

$$\mathbf{r_r} = r_r \begin{bmatrix} \sin(\theta_r)\cos(\varphi_r) \\ \sin(\theta_r)\sin(\varphi_r) \\ \cos(\theta_r) \end{bmatrix} = 2.14\,m \begin{bmatrix} \sin(+0.1423) \\ 0 \\ \cos(+0.1423) \end{bmatrix} \tag{4.5.2}$$

The RCS measurements were collected using a Vector Network Analyzer (VNA) (Agilent Technologies N5222A) between January 24th and February 7th of 2018. The samples measured (targets) were placed on a Styrofoam table to minimize the effect of the test fixture. The

antennas are separated by 2 ft. from each other. The distance from each antenna to the target is 2.14m. The VNA was configured to transmit a frequency sweep spanning 1.9 GHz to 18.1 GHz, with a time-average power of 30 dBm. The VNA was setup to sweep 2001 points and perform 50 coherent averages. The Figure 4.5.1 shows a photograph of the measurement setup.

Ideally, the radar response $H_{t,X,\mathbf{m}}(f)$ due to a target $t_{X,\mathbf{m}}$ placed on the setup table can be found by subtracting the table's radar response $H_{t,table}(f)$ from the total radar response $H_{t,total}(f)$ measured by the VNA, as shown by (4.5.3).

$$H_{t,X,\mathbf{m}}(f) = H_{t,total}(f) - H_{t,table}(f) \tag{4.5.3}$$

In practice, the table is always slightly disturbed after placing the target on top of it. So that the measured table's response before placing the target on it is just an estimate of the table's radar response $\widehat{H}_{t,table}(f)$. Subtracting $\widehat{H}_{t,table}(f)$ from $H_{t,total}(f)$ results in the target's radar response plus a small error related to the table's radar response, as shown in (4.5.3).

$$H_{t,X,\mathbf{m}}(f) + \Delta H_{t,table}(f) = H_{t,total}(f) - \widehat{H}_{t,table}(f) \tag{4.5.3}$$

As described in section 4.1, the scattering response $F_{qp,X,\mathbf{m}}(f)$ due to $t_{X,\mathbf{m}}$ is found from its radar response $H_{t,X,\mathbf{m}}$ as shown by (4.5.4). Equation (4.5.4) is a linear operation, so that applying it to the measured radar response ($H_{t,X,\mathbf{m}}(f) + \Delta H_{t,table}(f)$) results in the measured scattering response ($F_{qp,X,\mathbf{m}}(f) + \Delta F_{qp,table}(f)$), which contains the target's scattering response and a remnant of the table's scattering response.

$$F_{qp,X,\mathbf{m}}(f) = \left[\, \hat{q} \cdot \bar{\bar{\mathbf{F}}}_{X,\mathbf{m}}(\mathbf{k}_s, \mathbf{k}_i) \cdot \hat{p}\right] = \left[jk\eta Z_a \, \Phi_e \Phi_r(\mathbf{r}_r, \mathbf{r}_{X,\mathbf{m}}) \, \Phi_t(\mathbf{r}_{X,\mathbf{m}}, \mathbf{r}_t) |\mathbf{f}_r|_v |\mathbf{f}_t|_v\right]^{-1} \left[H_{t,X,\mathbf{m}}\right] \tag{4.5.4}$$

$$F_{qp,X,\mathbf{m}}(f) + \Delta F_{qp,table}(f) = \left[jk\eta Z_a \, \Phi_e \Phi_r(\mathbf{r}_r, \mathbf{r}_{X,\mathbf{m}}) \, \Phi_t(\mathbf{r}_{X,\mathbf{m}}, \mathbf{r}_t) |\mathbf{f}_r|_v |\mathbf{f}_t|_v\right]^{-1} \left[H_{t,X,\mathbf{m}}(f) + \Delta H_{t,table}(f)\right] \tag{4.5.5}$$

In this section, the scattering response measurements contain both the target's scattering response $F_{qp,X,\mathbf{m}}(f)$ and the remnant scattering response $\Delta F_{qp,table}(f)$. The measured RCS as a function of frequency $\sigma_{qp}(f)$ and time $\sigma_{qp}(t)$ are given by (4.5.6) and (4.5.7), respectively.

$$\sigma_{qp,X,\mathbf{m}}(f) = \frac{1}{4\pi} \left|F_{qp,X,\mathbf{m}}(f) + \Delta F_{qp,table}(f)\right|^2 \tag{4.5.6}$$

$$\sigma_{qp,X,\mathbf{m}}(t) = \frac{1}{4\pi T} \left|F_{qp,X,\mathbf{m}}(t) + \Delta F_{qp,table}(t)\right|^2 \tag{4.5.7}$$

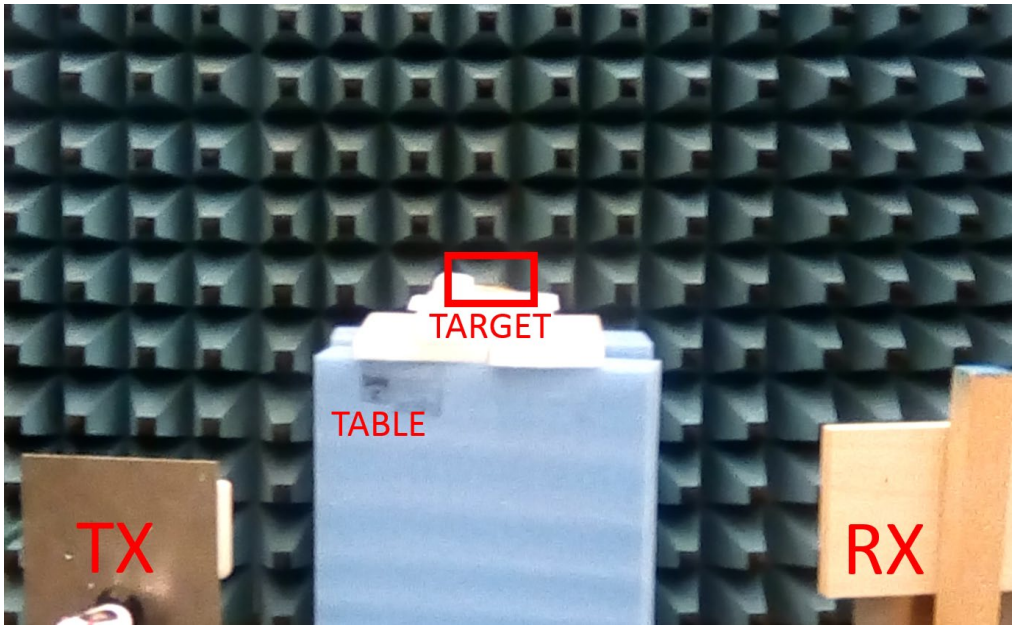

Figure 4.5.1 – Photograph of the RCS measurement Setup

4.5.1. Leaf (Case 1): Straight Leaf

In this case, we measured a single straight leaf. The parameters of the leaf are listed in table 4.5.1. Figure 4.5.2 shows a photograph of leaf under test. Two small pieces of porous Styrofoam were used to fix the leaf in place. These fixture pieces were shaved to reduce its RCS. Figure 4.5.3 shows a depiction of the geometric model of the straight leaf.

The leaf's RCS was measured at different elevation angles. For a straight leaf, the initial and final elevation angles are the same. These angles are defined in table 4.5.1 as (90 deg - $\boldsymbol{\theta_{c,L,(1,i_L)}}$), where $\boldsymbol{\theta_{c,L,(1,i_L)}}$ is a variable elevation angle.

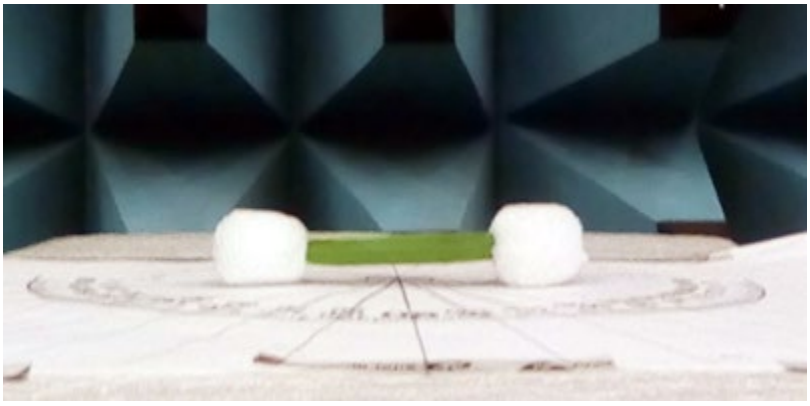

Figure 4.5.2 – Leaf (Case 1): Photograph of the measurement set-up

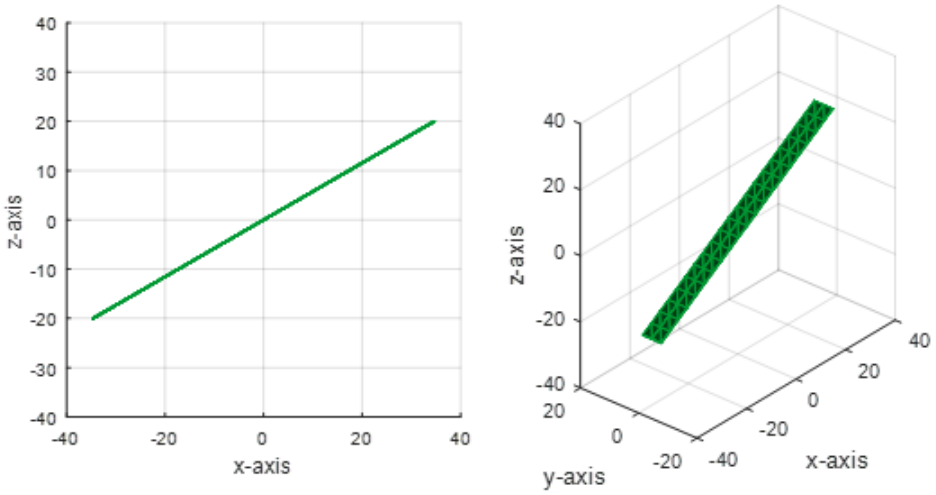

Figure 4.5.3 – Leaf (Case 1): Visualization of Geometric Model

Table 4.5.1 – Leaf (Case 1): List of Leaf Parameters

Parameter	**Leaf 1, $\boldsymbol{t_{L,(1,1)}}$**
Position, $\mathrm{r}_{L,(1,i_L)}$	Centered at the origin
Length, $L_{L,(1,i_L)}$	80 mm
Width, $w_{L,(1,i_L)}$	6.3 mm
Thickness, $a_{L,(1,i_L)}$	0.2 mm
First-rot. $\alpha_{L,(1,i_L)}$	0 deg
Azimuth, $\varphi_{L,(1,i_L)}$	0 deg
Initial Elev, $\theta_{i,L,(1,i_L)}$	90 deg - $\boldsymbol{\theta_{c,L,(1,i_L)}}$
Final Elev, $\theta_{f,L,(1,i_L)}$	90 deg - $\boldsymbol{\theta_{c,L,(1,i_L)}}$
Common Elev., $\theta_{c,L,(1,i_L)}$	0, 5, 10 deg
Rad. of Curv., $R_{L,(1,i_L)}$	Inf. (straight leaf)
Moisture Cont., $m_{L,(1,i_L)}$	0.75

4.5.1.1. Leaf (Case 1): RCS vs Frequency

Figures 4.5.4, 4.5.5 and 4.5.6 show the measured RCS as a function of frequency at angles $\boldsymbol{\theta_{c,L,(1,i_L)}}$ equal to 0, 5 and 10 degrees. The measurements are in good agreement with the simulation results. As it is shown in the section 4.5.1.2, the discrepancies between the measurements and the simulations can be attributed to the component of the scattering response due to the remnant of the table's scattering response.

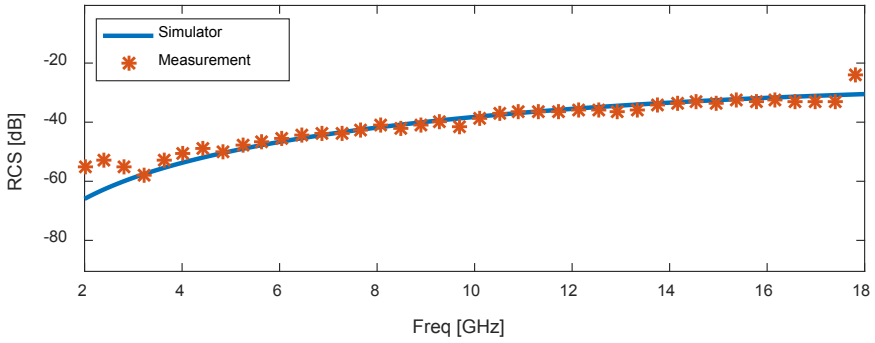

Figure 4.5.4 – Leaf (Case 1): RCS vs Frequency. $\boldsymbol{\theta_{c,L,(1,i_L)}}$ = *0 deg*

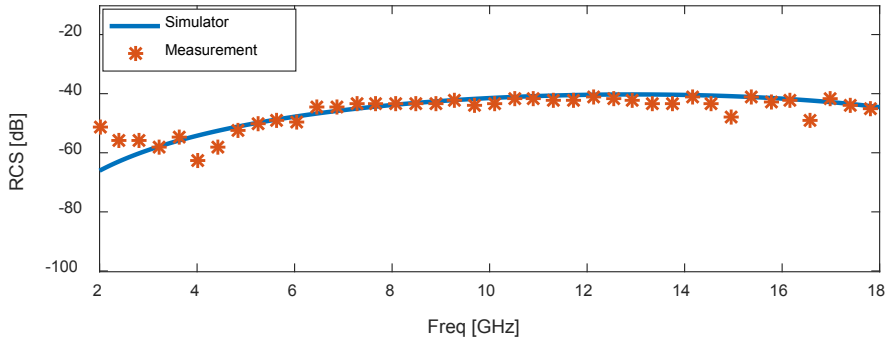

Figure 4.5.5 – Leaf (Case 1): RCS vs Frequency. $\boldsymbol{\theta_{c,L,(1,i_L)}}$ = *5 deg*

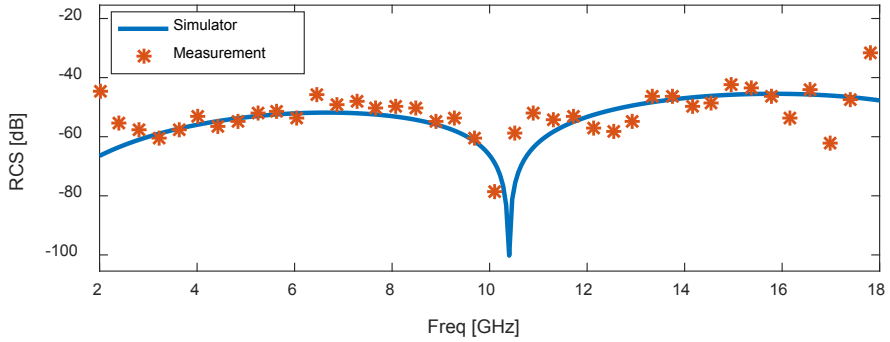

Figure 4.5.6 – Leaf (Case 1): RCS vs Frequency. $\boldsymbol{\theta_{c,L,(1,i_L)}}$ = *10 deg*

4.5.1.2. Leaf (Case 1): RCS vs Time/Range

Figures 4.5.7-4.5.9 show the measured RCS as a function of range due to the straight leaf at elevation angles $\boldsymbol{\theta_{c,L,(1,i_L)}}$ equal to 0, 5 and 10 degrees. The measurements show good agreement with the simulations. Figure 4.5.7 show the breakdown of the RCS components, which include the leaf's component and the remnant of the table. In this figure (4.5.7), the measured leaf's RCS includes a trailing edge, which is not included in the simulated RCS. This trailing edge shows that there is a small mismatch between the simulated model and the actual measured leaf. This small mismatch could be related to a variation of the dielectric along the leaf or a variation of the cross sectional dimensions (width or thickness) along the leaf.

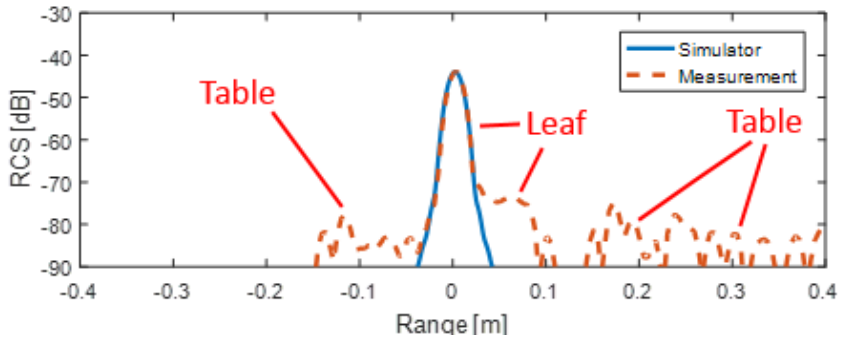

Figure 4.5.7 – Leaf (Case 1): RCS vs Range. $\boldsymbol{\theta_{c,L,(1,i_L)}}$ = *0 deg*

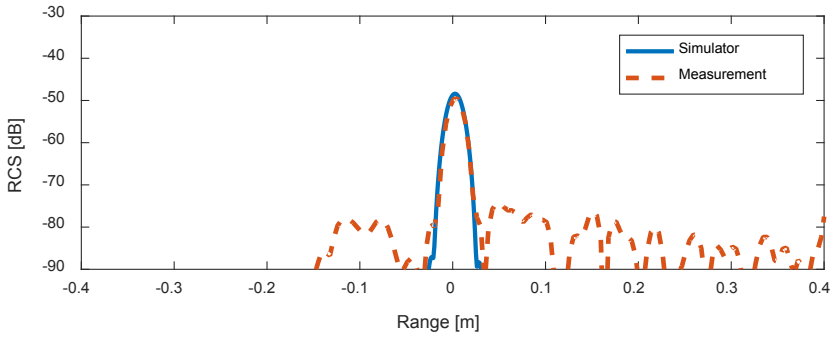

Figure 4.5.8 – Leaf (Case 1): RCS vs Range. $\boldsymbol{\theta_{c,L,(1,i_L)}}$ = *5 deg*

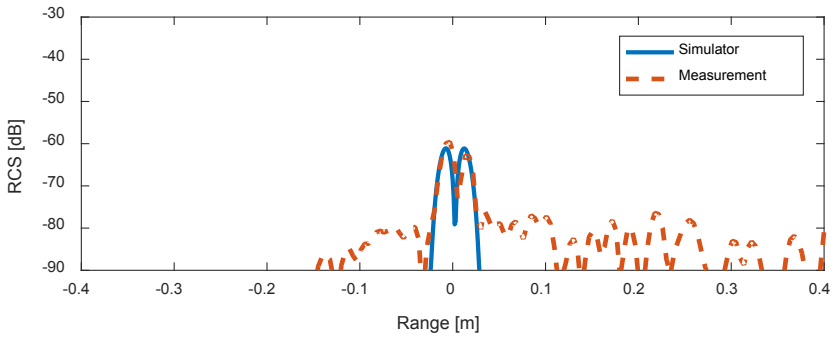

Figure 4.5.9 – Leaf (Case 1): RCS vs Range. $\boldsymbol{\theta_{c,L,(1,i_L)}}$ = *10 deg*

4.5.2. Leaf (Case 2): Curved Leaf (Different Curvatures)

In this case, we measured a single curved leaf. The parameters of the leaf are listed in table 4.5.2. Figure 4.5.10 shows a photograph of the measured leaf. An L-shaped Styrofoam piece is used to support the curved leaf. This piece is shown in figure 4.5.10. The RCS of the Styrofoam piece was measured to be smaller than the table's remnant RCS component. In other words, the fixture does not interfere with the measurement of the leaf's RCS. Figure 4.5.11 shows a depiction of the geometric model of the leaf.

In this configuration, the apex of the curved leaf, which is the region of the leaf with the lowest radius of curvature, is placed facing the main axis of the antennas. The RCS of the leaf is measured at different minimum radii of curvature (different radii of curvature at the apex). The minimum radii of curvature used are listed in table 4.5.2.

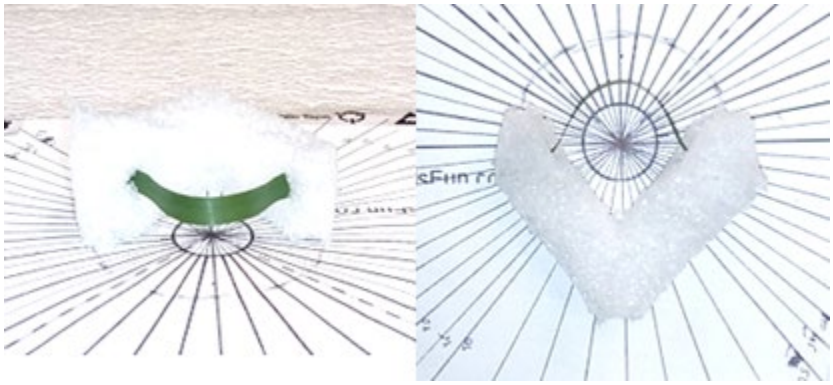

Figure 4.5.10 – Leaf (Case 2): Photograph of Measurement Set-up. (Left: Front view; Right: Top View)

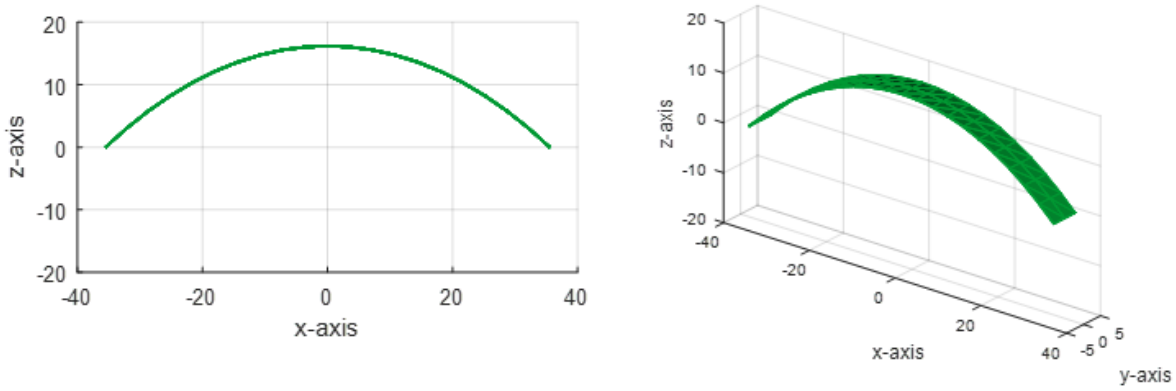

Figure 4.5.11 – Leaf (Case 2): Visualization of Geometric Model (For this figure $R_{L,(1,i_L)}$ = 45mm)

Table 4.5.2 – Leaf (Case 2): List of Leaf Parameters

Parameter	**Leaf 1, $t_{L,(1,1)}$**
Position, $\mathrm{r}_{L,(1,i_L)}$	Centered at the origin
Length, $L_{L,(1,i_L)}$	80 mm
Width, $w_{L,(1,i_L)}$	6.3 mm
Thickness, $a_{L,(1,i_L)}$	0.2 mm
First-rot. $\alpha_{L,(1,i_L)}$	0 deg
Azimuth, $\varphi_{L,(1,i_L)}$	0 deg
Initial Elev, $\theta_{i,L,(1,i_L)}$	90-70 deg - $\boldsymbol{\theta_{c,L,(1,i_L)}}$
Final Elev, $\theta_{f,L,(1,i_L)}$	90+70 deg - $\boldsymbol{\theta_{c,L,(1,i_L)}}$
Common Elev., $\theta_{c,L,(1,i_L)}$	0 deg
Rad. of Curv., $R_{L,(1,i_L)}$	25mm, 40mm, 45mm, 56mm, 60, 120mm
Moisture Cont., $m_{L,(1,i_L)}$	0.75

4.5.2.1. Leaf (Case 2): RCS vs Frequency

Figure 4.5.12-4.5.17 show the measured RCS as a function of frequency for the curved leaf. These measurements were taken for different minimum radii of curvature. The radius of curvature used in each case is shown in the caption of each related figure. These figures show that the simulation agrees well with measurements. As in case 1, there is some discrepancy between the measurement and the simulation, which is again mostly caused by the presence of the remnant component of the table's scattering response.

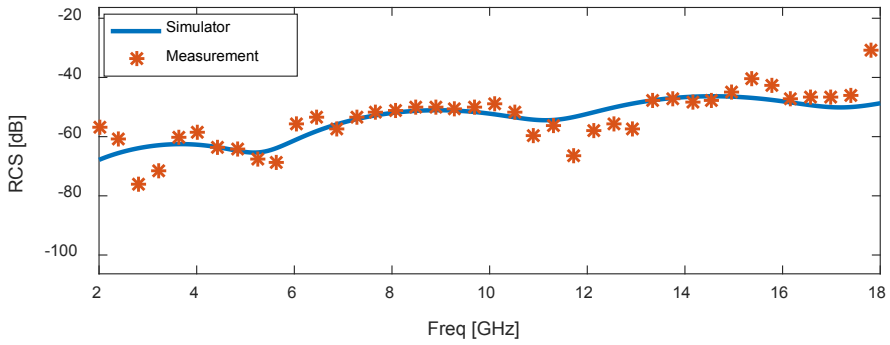

Figure 4.5.12 – Leaf (Case 2): RCS vs Frequency. $R_{L,(1,i_L)}$ = *25 mm*

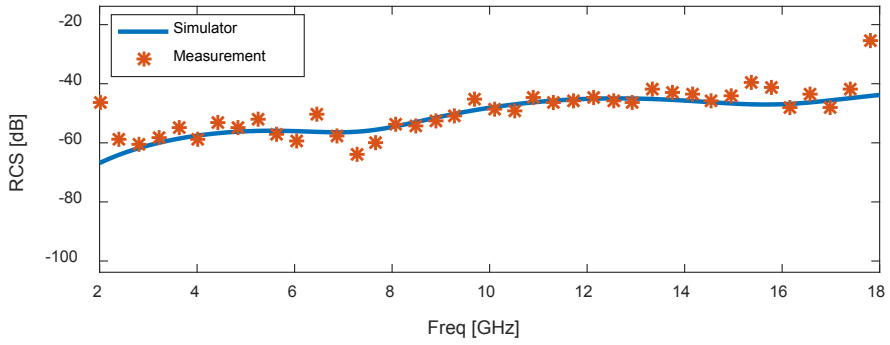

Figure 4.5.13 – Leaf (Case 2): RCS vs Frequency. $R_{L,(1,i_L)}$ = *40 mm*

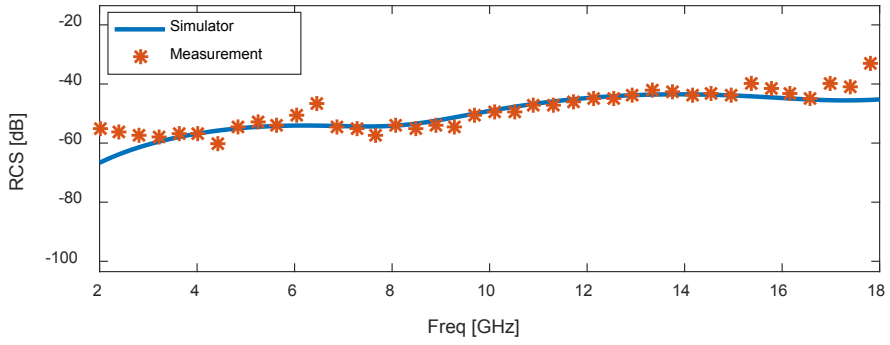

Figure 4.5.14 – Leaf (Case 2): RCS vs Frequency. $R_{L,(1,i_L)}$ = *45 mm*

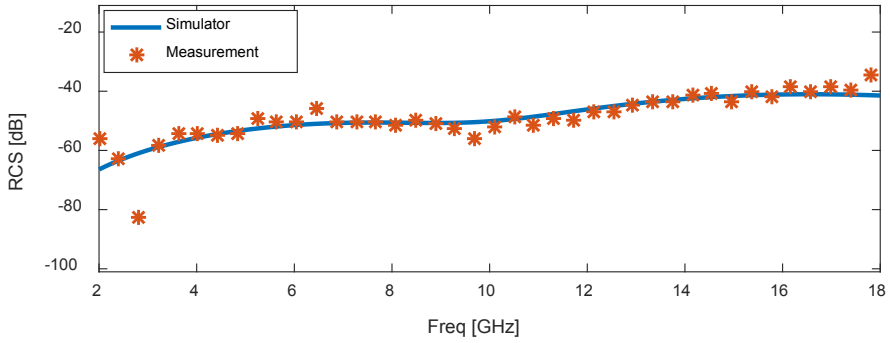

Figure 4.5.15 – Leaf (Case 2): RCS vs Frequency. $R_{L,(1,i_L)}$ = *56 mm*

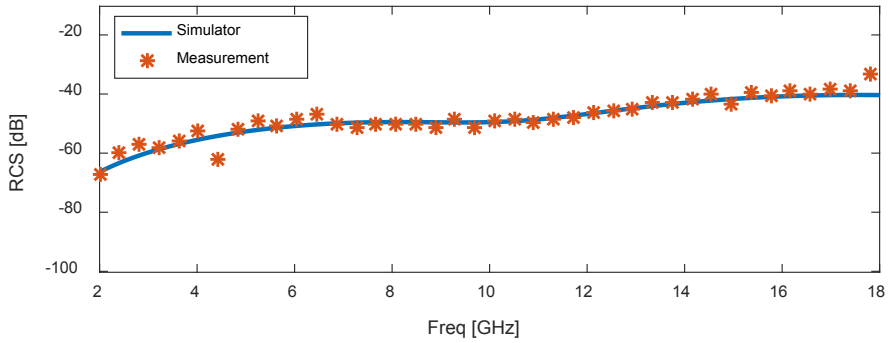

Figure 4.5.16 – Leaf (Case 2): RCS vs Frequency. $R_{L,(1,i_L)}$ = *60 mm*

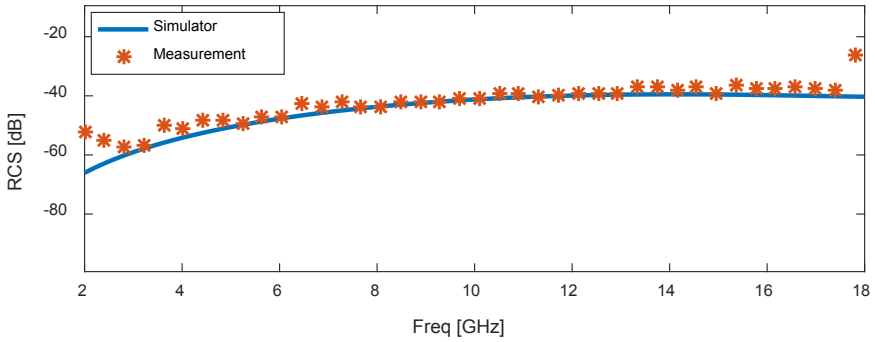

Figure 4.5.17 – Leaf (Case 2): RCS vs Frequency. $R_{L,(1,i_L)}$ = *120 mm*

4.5.2.2. Leaf (Case 3): RCS vs Time/Range

Figures 4.5.18-4.5.23 show the RCS measurements as a function of range for the curve leaf at different curvature configurations. These radius of curvature used in each case is indicated at the caption of the related figure. The figures show that the measured RCS agrees well with the simulated RCS. The remnant of the table's scattering response is present in all the plots.

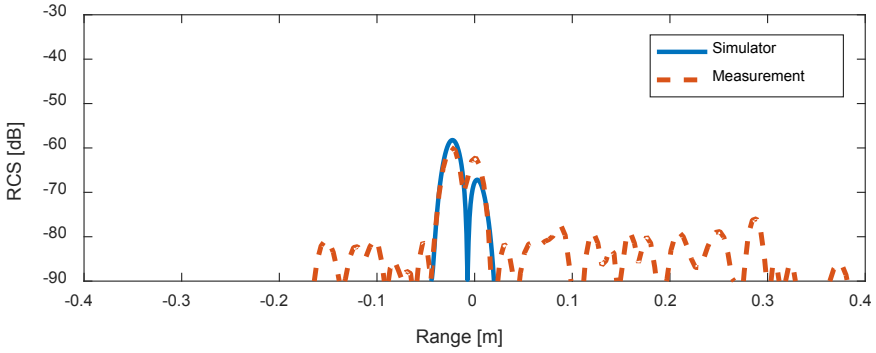

Figure 4.5.18 – Leaf (Case 2): RCS vs Range. $R_{L,(1,i_L)}$ = *20 cm*

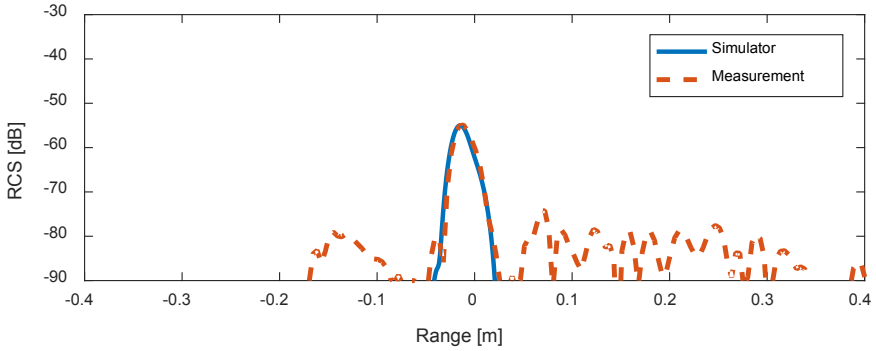

Figure 4.5.19 – Leaf (Case 2): RCS vs Range. $R_{L,(1,i_L)}$ = *40 cm*

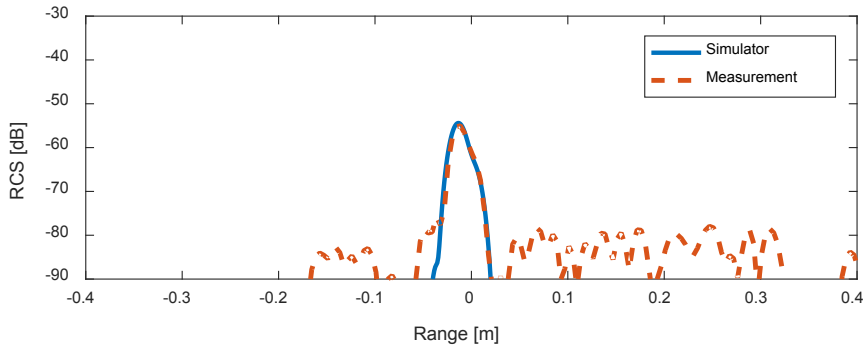

Figure 4.5.20 – Leaf (Case 2): RCS vs Range. $R_{L,(1,i_L)}$ = *45 cm*

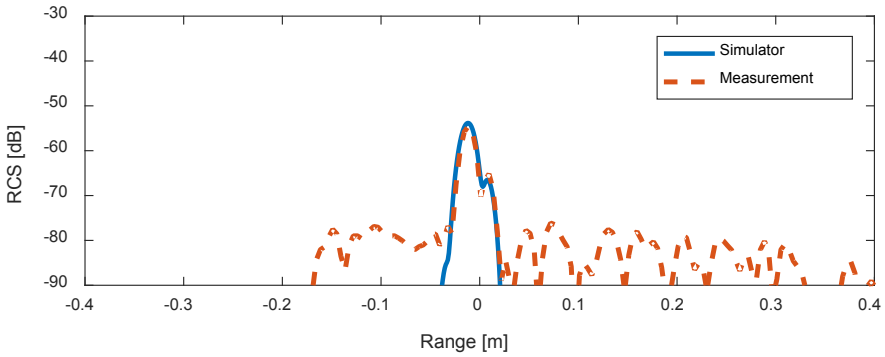

Figure 4.5.21 – Leaf (Case 2): RCS vs Range. $R_{L,(1,i_L)}$ = *56 cm*

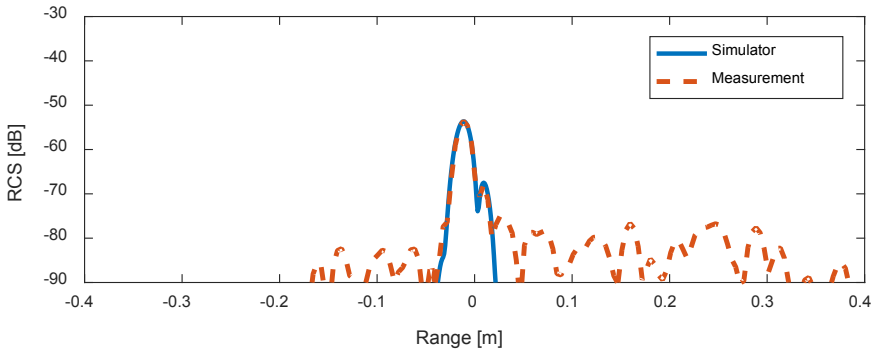

Figure 4.5.22 – Leaf (Case 2): RCS vs Range. $R_{L,(1,i_L)}$ = *60 cm*

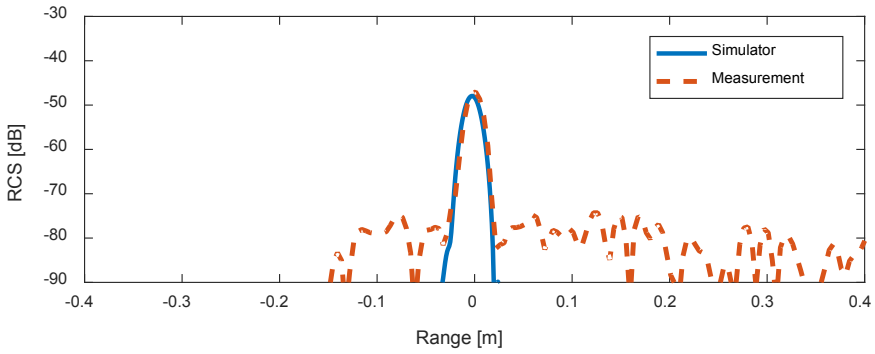

Figure 4.5.23 – Leaf (Case 2): RCS vs Range. $R_{L,(1,i_L)}$ = *120 cm*

4.5.3. Leaf (Case 3): Curved Leaf (Different Inclination Angles)

In this case, a single curved leaf was measured with a fixed minimum radius of curvature at different leaf elevation angles. The leaf's parameters are listed in table 4.5.3. Figure 4.5.24 shows a depiction of the leaf's geometric model.

The measured leaf was placed on the table using the same fixture as the one used for the previous case.

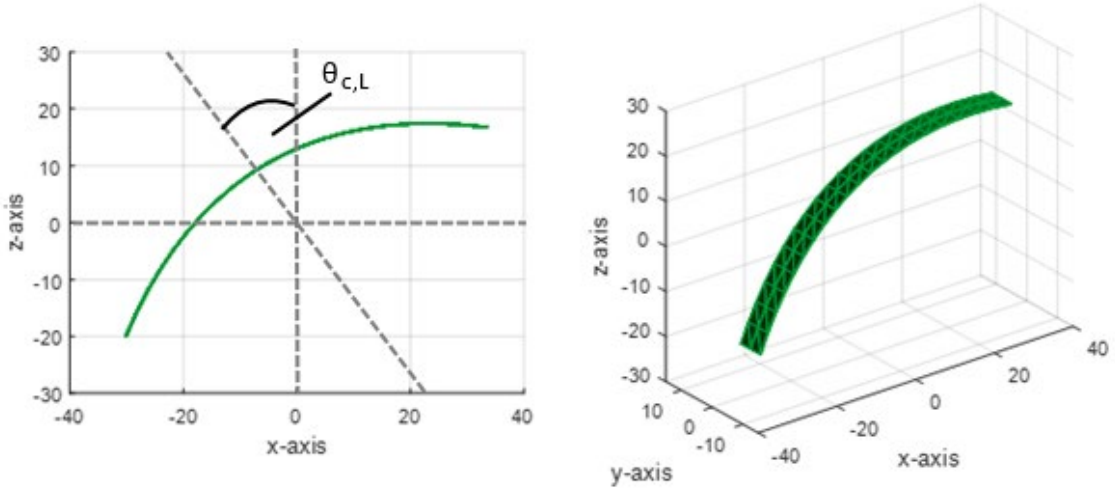

Figure 4.5.24 – Leaf (Case 3): Visualization of Geometric Model

Table 4.5.3 – Leaf (Case 3): List of Leaf Parameters

Parameter	**Leaf 1, $\boldsymbol{t_{L,(1,1)}}$**
Position, $\mathrm{r}_{L,(1,i_L)}$	Centered at the origin
Length, $L_{L,(1,i_L)}$	80 mm
Width, $w_{L,(1,i_L)}$	6.3 mm
Thickness, $a_{L,(1,i_L)}$	0.2 mm
First-rot. $\alpha_{L,(1,i_L)}$	0 deg
Azimuth, $\varphi_{L,(1,i_L)}$	0 deg
Initial Elev, $\theta_{i,L,(1,i_L)}$	90-70 deg - $\boldsymbol{\theta_{c,L,(1,i_L)}}$
Final Elev, $\theta_{f,L,(1,i_L)}$	90+70 deg - $\boldsymbol{\theta_{c,L,(1,i_L)}}$
Common Elev., $\theta_{c,L,(1,i_L)}$	0, 10, 20, 30 deg
Rad. of Curv., $R_{L,(1,i_L)}$	55mm
Moisture Cont., $m_{L,(1,i_L)}$	0.75

4.5.3.1. Leaf (Case 3): RCS vs Frequency

Figures 4.5.25-4.5.28 show the measured RCS as a function of frequency of the curved leaf. The measurements were taken at different elevation angles. These elevation angles are given in table 4.5.3 as a function of the variable $\boldsymbol{\theta_{c,L,(1,i_L)}}$. The variable angle $\boldsymbol{\theta_{c,L,(1,i_L)}}$ value used for each measurement is indicated at the caption of each related measurement. The figures show good agreement between the simulation and the measurement. As with the previous cases, the source of discrepancy in these measurements is the presence of a remnant of the table's scattering response in each plot.

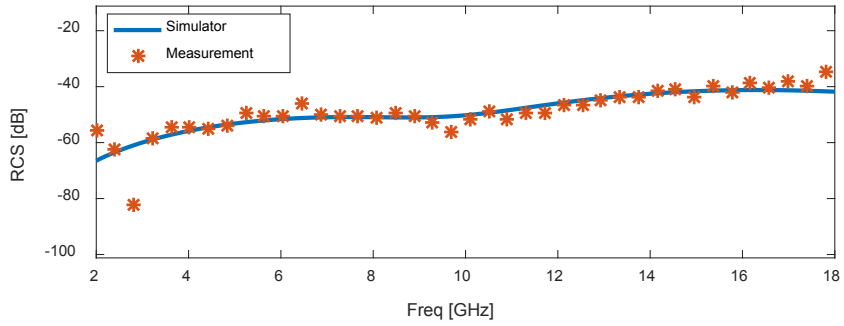

Figure 4.5.25 – Leaf (Case 3): RCS vs Frequency. $\boldsymbol{\theta_{c,L,(1,i_L)}}$ = *0 deg*

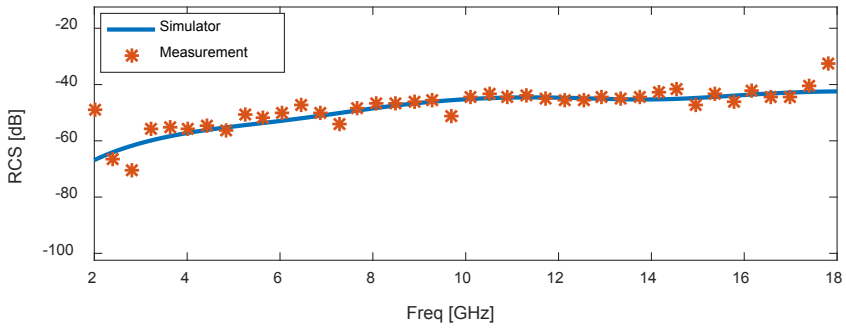

Figure 4.5.26 – Leaf (Case 3): RCS vs Frequency. $\boldsymbol{\theta_{c,L,(1,i_L)}}$ = *10 deg*

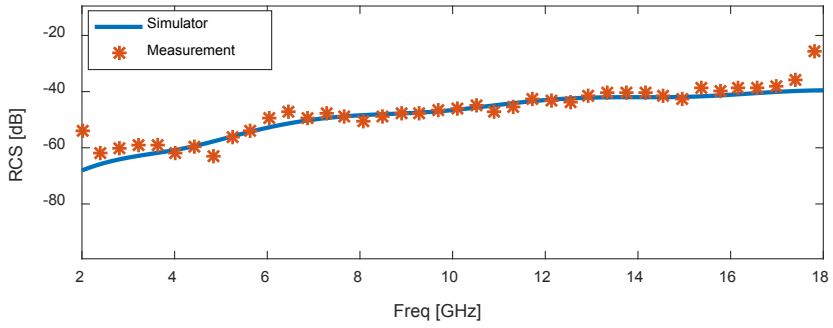

Figure 4.5.27 – Leaf (Case 3): RCS vs Frequency. $\boldsymbol{\theta_{c,L,(1,i_L)}}$ = *20 deg*

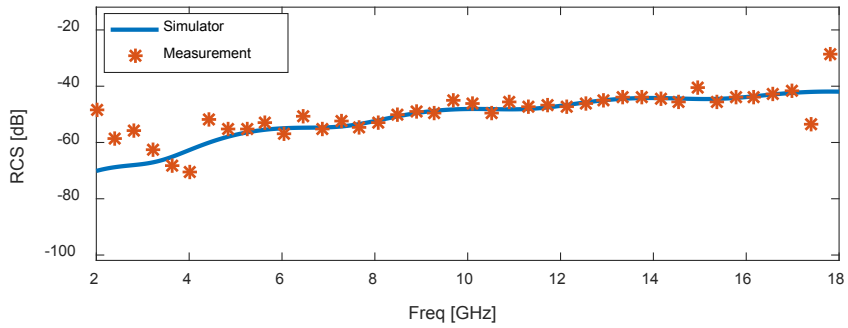

Figure 4.5.28 – Leaf (Case 3): RCS vs Frequency. $\boldsymbol{\theta_{c,L,(1,i_L)}}$ = *30 deg*

4.5.3.2. Leaf (Case 3): RCS vs Range

Figures 4.5.29-4.5.32 show RCS measurements as a function of range for the curved leaf. The elevation angle variable $\boldsymbol{\theta_{c,L,(1,i_L)}}$ related to each measurement is indicated in the figure caption. The figures show good agreement between the measured RCS and the simulations. As with the previous cases, the main discrepancy between the measurement and the simulation is the remnant of the table's scattering response.

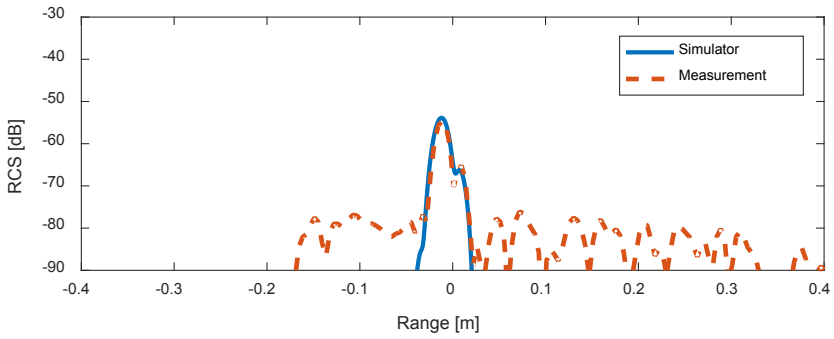

Figure 4.5.29 – Leaf (Case 3): RCS vs Range. $\boldsymbol{\theta_{c,L,(1,i_L)}}$ = *0 deg*

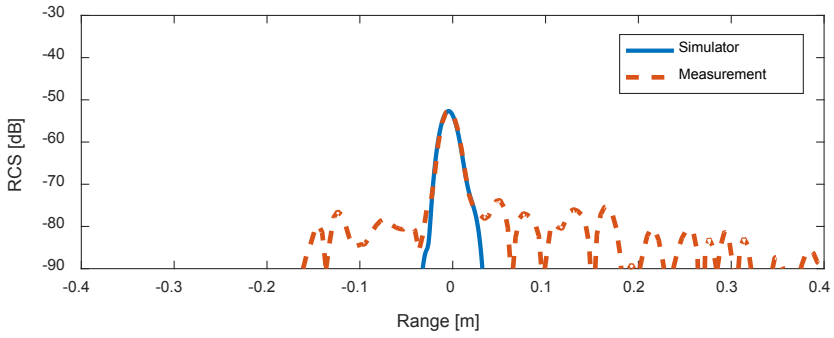

Figure 4.5.30 – Leaf (Case 3): RCS vs Range. $\boldsymbol{\theta_{c,L,(1,i_L)}}$ = *10 deg*

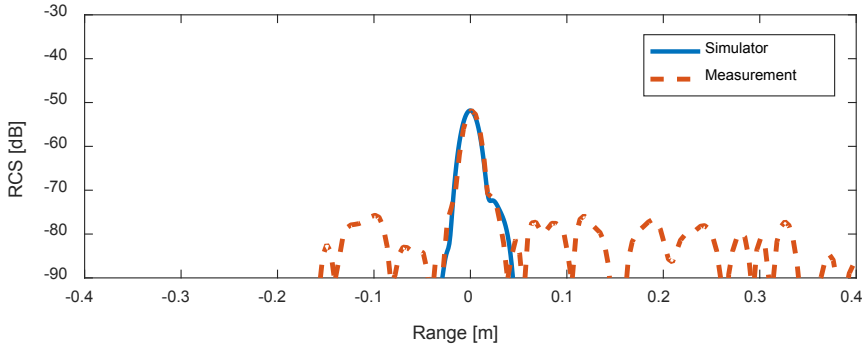

Figure 4.5.31 – Leaf (Case 3): RCS vs Range. $\boldsymbol{\theta_{c,L,(1,i_L)}}$ = *20 deg*

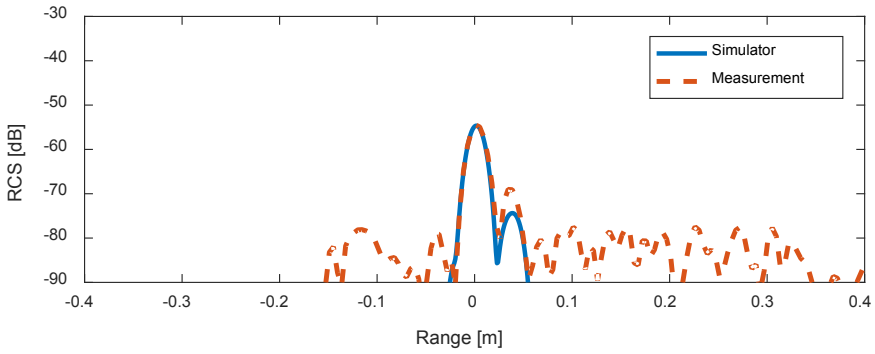

Figure 4.5.32 – Leaf (Case 3): RCS vs Range. $\boldsymbol{\theta_{c,L,(1,i_L)}}$ = *30 deg*

4.5.4. Stem (Case 1): Straight Stem (Stem axis perpendicular to antenna field vector)

In this case, the RCS of a straight was measured. The stem was placed perpendicular to the polarization of the antennas. The RCS of the stem was measured at different stem elevation angles $\theta_{S,(1,i_S)}$. The stem parameters are listed in table 4.5.4. Figure 4.5.33 shows a depiction of the geometric model of the leaf. In figure 4.5.33, the geometric model has an elevation angle of 10 degrees.

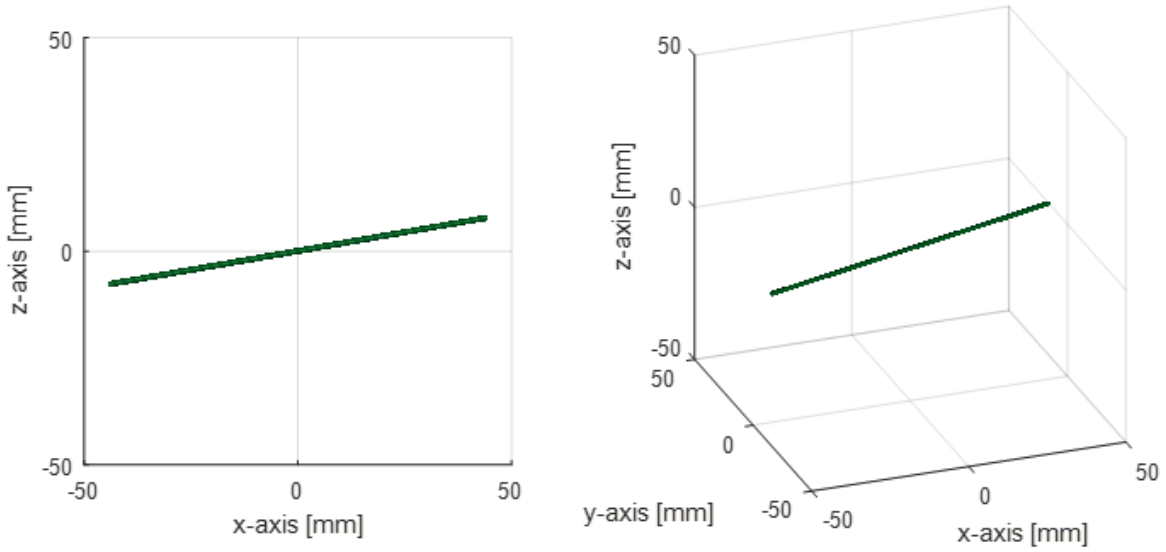

Figure 4.5.33 – Stem (Case 1): Visualization of Geometric Model ($\theta_{S,(1,i_S)} = 10\ \mathrm{deg}$)

Table 4.5.4 – Stem (Case 1): List of Stem Parameters

Parameter	**Stem 1, $t_{S,(1,1)}$**
Position, $r_{S,(1,i_S)}$	Centered at origin
Length, $L_{S,(1,i_S)}$	90 mm
Radius, $\rho_{S,(1,i_S)}$	0.75 mm
Azimuth, $\varphi_{S,(1,i_S)}$	0 deg
Elev., $\theta_{S,(1,i_S)}$	87.5, 85, 80 deg
Moist. Cont., $m_{S,(1,i_S)}$	0.7

4.5.4.1. Stem (Case 1): RCS vs Frequency

Figures 4.5.34-4.5.35 show the measured RCS as a function of frequency of the straight leaf. The measurements were taken at different elevation angles as indicated by the figure captions. The measured RCS agrees well with the simulation. The main source of interference is the remnant of the table's scattering response. Only measurements for elevation angles (90-2.5) and (90-5) degrees are shown. At smaller elevation angles, the RCS of the stem becomes too small compared to the table.

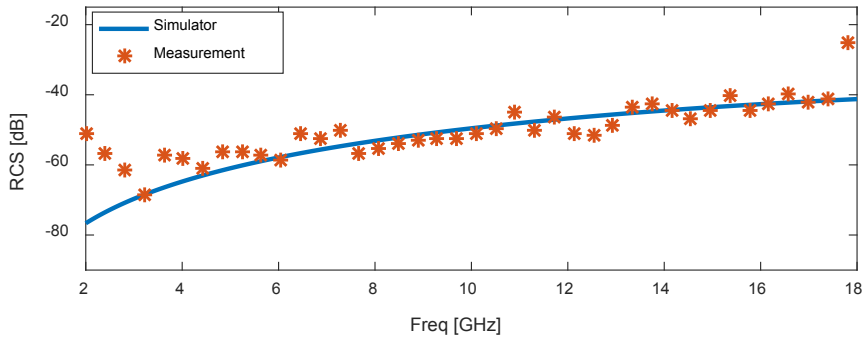

Figure 4.5.34 – Stem (Case 1): RCS vs Frequency. $\theta_{S,(1,i_S)}$*=(90-2.5) deg*

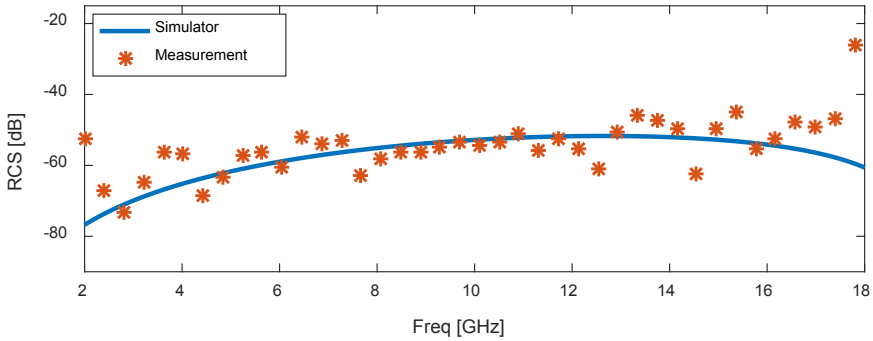

Figure 4.5.35 – Stem (Case 1): RCS vs Frequency. $\theta_{S,(1,i_S)}$*=(90-5) deg*

4.5.4.2. Stem (Case 1): RCS vs Time/Range

Figure 4.5.36-4.5.38 show the stem's RCS measured as a function of range at different stem elevation angles. The measurements are in good agreement with the simulation. The remnant of the table's scattering response is these RCS measurements. The RCS is only shown at angles (90-2.5), (90-5) and (90-10) degrees. The stem's RCS becomes smaller than the remnant table's RCS at smaller elevation angles.

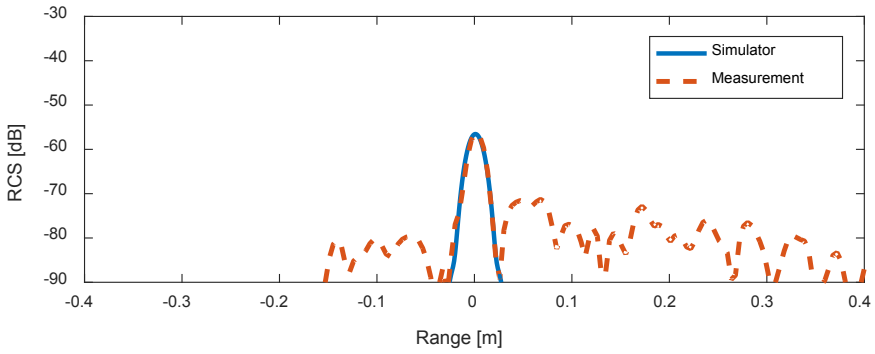

Figure 4.5.36 – Stem (Case 1): RCS vs Range. $\theta_{S,(1,i_S)}$=*(90-2.5) deg*

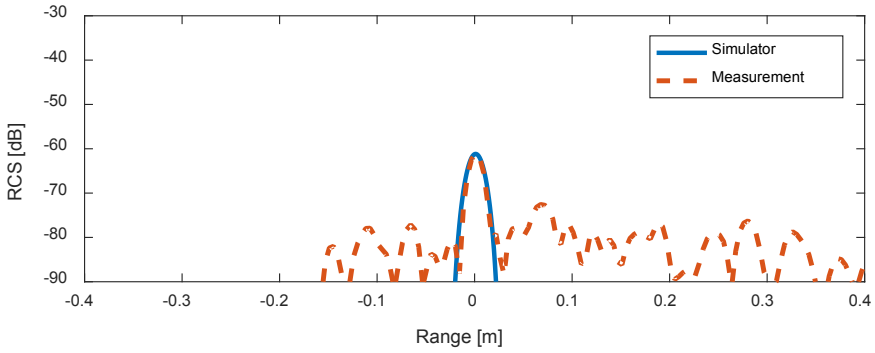

Figure 4.5.37 – Stem (Case 1): RCS vs Range. $\theta_{S,(1,i_S)}$=*(90-5) deg*

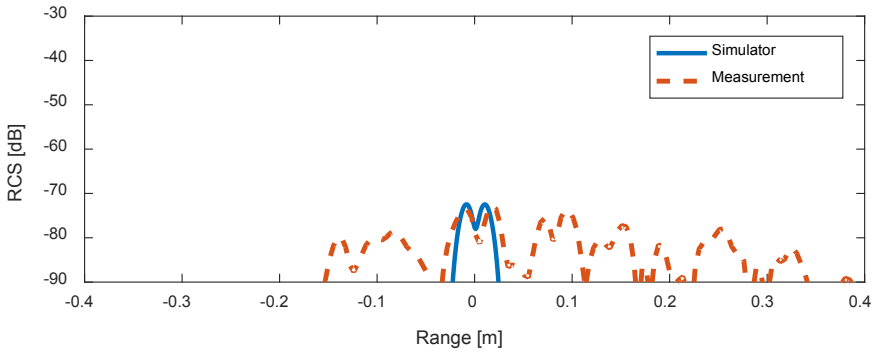

Figure 4.5.38 – Stem (Case 1): RCS vs Range. $\theta_{S,(1,i_S)}$=*(90-10) deg*

4.5.5. Stem (Case 2): Straight (Stem's axis is parallel to antennas' polarization)

In this case, the RCS of a straight stem is measured, in which the stem's main axis is aligned parallel to the antennas' polarization. The antenna parameters are listed in table 4.5.5. Figure 4.5.39 shows a photograph of the measurement setup. Figure 4.5.40 shows a depiction of the geometric model. In this case, the stem was measured a single configuration.

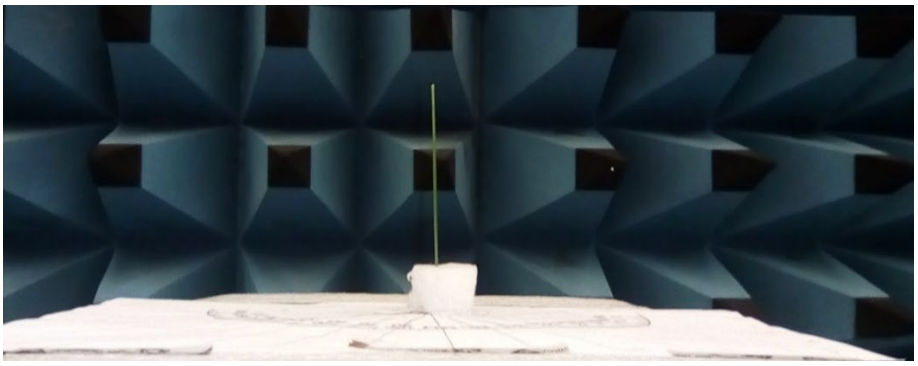

Figure 4.5.39 – Stem (Case 2): Photograph of the Measurement set-up

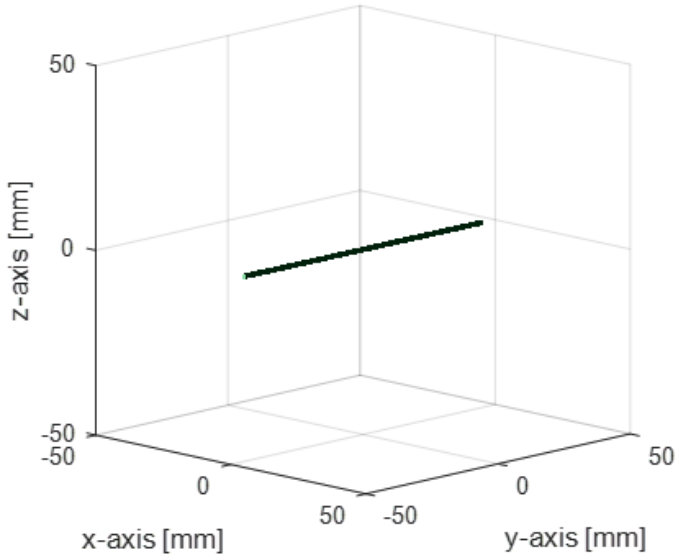

Figure 4.5.40 – Stem (Case 2): Visualization of Geometric Model

Table 4.5.5 – Stem (Case 2): List of Stem Parameters

Parameter	**Stem 1, $t_{S,(1,1)}$**
Position, $\mathrm{r}_{S,(1,i_S)}$	Centered at origin
Length, $L_{S,(1,i_S)}$	90 mm
Radius, $\rho_{S,(1,i_S)}$	0.75 mm
Azimuth, $\varphi_{S,(1,i_S)}$	90 deg
Elev., $\theta_{S,(1,i_S)}$	90 deg
Moist. Cont., $m_{S,(1,i_S)}$	0.7

4.5.5.1. Stem (Case 2): RCS vs Frequency

Figure 4.5.51 shows the measured stem's RCS as a function of frequency. The figure shows that the simulation is in good agreement with the measurement. In this case, the RCS of the stem is much larger than the table's remnant component, so that interference related to the table has little effect in the stem's RCS curve.

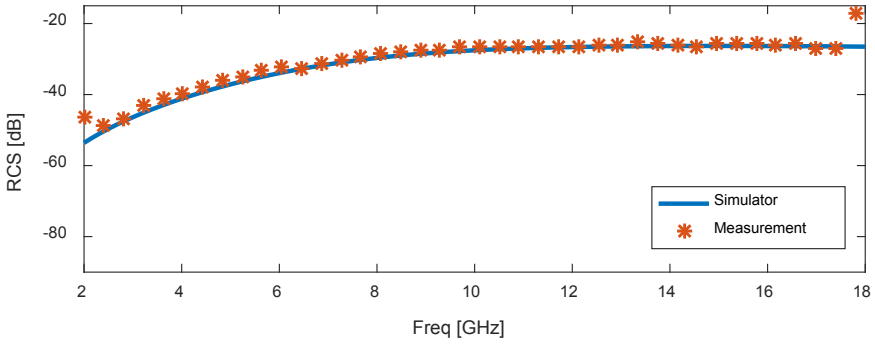

Figure 4.5.41 – Stem (Case 2): RCS vs Frequency. $\theta_{S,(1,i_S)}$*=90 deg;* $\varphi_{S,(1,i_S)}$*=90 deg*

4.5.5.2. Stem (Case 2): RCS vs Time/Range

Figure 4.5.42 shows the measured stem's RCS as a function of range. The figure shows that the simulation is in good agreement with the measurement. The remnant of the scattering response of the table is present but it is much smaller than the peak of the RCS due to the stem in this configuration.

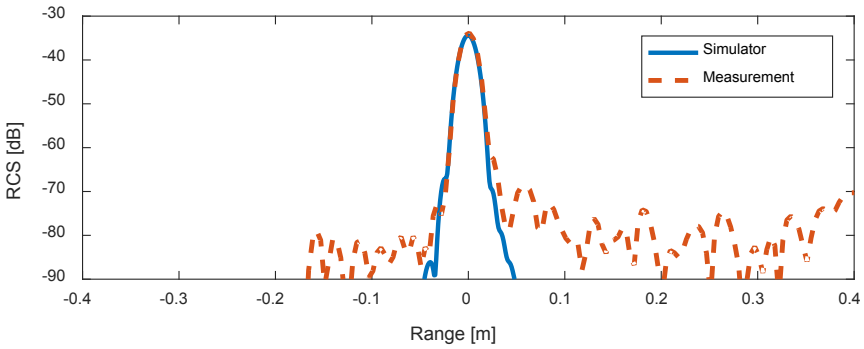

Figure 4.5.42 – Stem (Case 2): RCS vs Range. $\theta_{S,(1,i_S)}$=*90 deg;* $\varphi_{S,(1,i_S)}$=*90 deg*

4.5.6. Head (Case 1): Tilted Head

In this case, a dry wheat head was measured at different elevation angles. The head was aligned perpendicular to the polarization of the antennas. The head parameters are listed in table 4.5.6. Figure 4.5.43 shows a photograph of the measured head. Figure 4.5.44 shows a depiction of the geometric model generated by the simulator. The head was measured at different head elevation angles.

Figure 4.5.43 – Head (Case 1): Photograph of the measured plant head

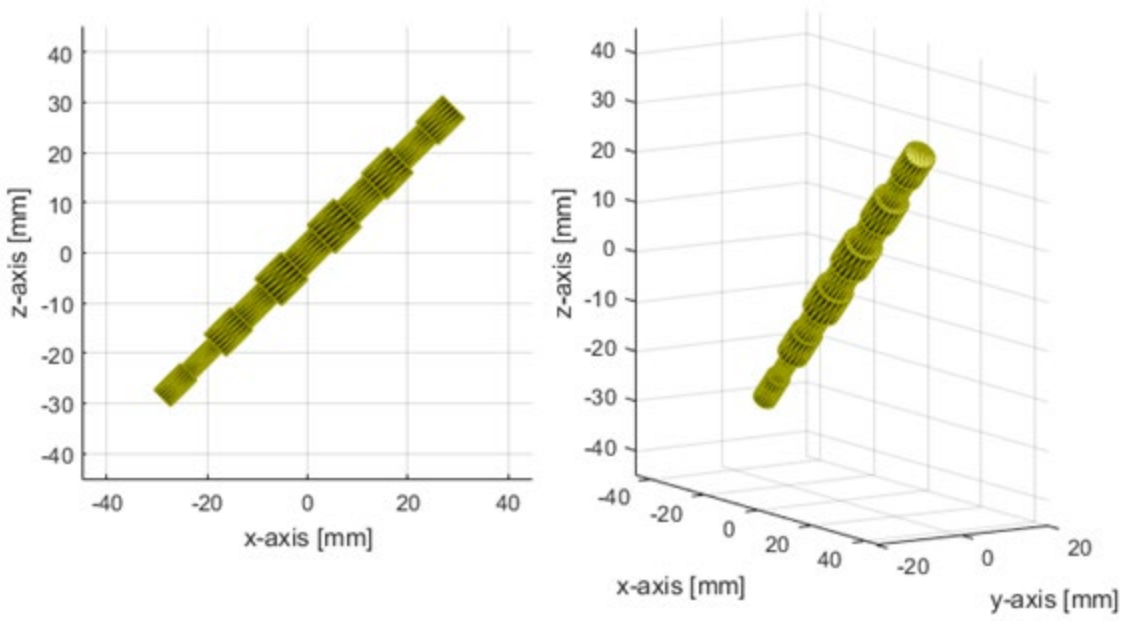

Figure 4.5.44 - Head (Case 1): Visualization of Geometric Model ($\boldsymbol{\theta}_{\boldsymbol{H},(\mathbf{1},\boldsymbol{i}_{\boldsymbol{H}})}$=45 deg)

Table 4.5.6 – Head (Case 1): List of Head Parameters

Parameter	**Head 1, $t_{H,(1,1)}$**
Position, $\mathrm{r}_{H,(1,i_H)}$	Centered at origin
Length, $L_{H,(1,i_H)}$	82 mm
Radius init., $\rho_{i,H,(1,i_H)}$	1.13 mm
Radius mid., $\rho_{m,H,(1,i_H)}$	4.05 mm
Radius mid., $\rho_{m,H,(1,i_H)}$	2.25 mm
Azimuth, $\varphi_{H,(1,i_H)}$	0 deg
Elev., $\theta_{H,(1,i_H)}$	85, 82.5, 80, 70, (65+180), (60+180), 55, 50, 45, 40, 35, 30, 25, 20, 15, 10 deg
Rad. fac., β_H	80
Moist. Cont., $m_{H,(1,i_H)}$	0.15
Vol. frac., $v_{H,(1,i_H)}$	0.6

4.5.6.1. Head (Case 1): RCS vs Frequency

Figure 4.5.45-4.5.47 show the head's RCS measurements as a function of frequency. The RCS measurements were performed at different elevation angles, as indicated in table 4.5.6. The elevation angles related to each measurement are indicated at the caption of each related figure. The figures show that the simulated RCS agrees well with the measurements. Only results of measurements for head elevation angles (90-5), (90-7.5) and (90.10) degrees are shown. The RCS of the head at smaller elevation angles becomes small compared to the remnant of the tables scattering response.

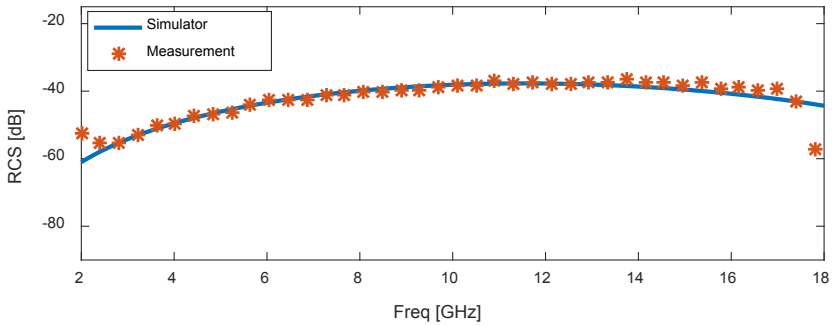

Figure 4.5.45 – Head (Case 1): RCS vs Frequency. $\theta_{H,(1,i_H)}$= *(90-5) deg*

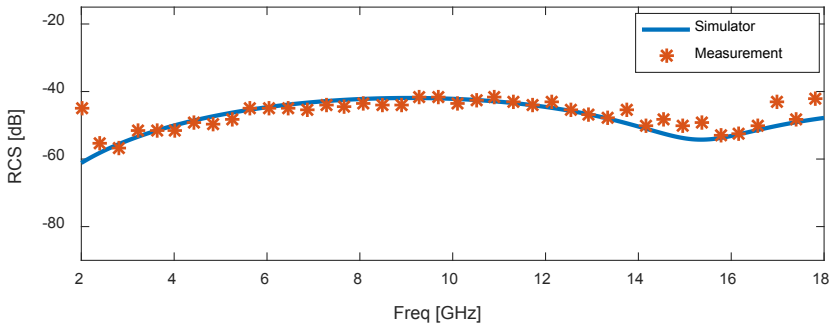

Figure 4.5.46 – Head (Case 1): RCS vs Frequency. $\theta_{H,(1,i_H)}$= *(90-7.5) deg*

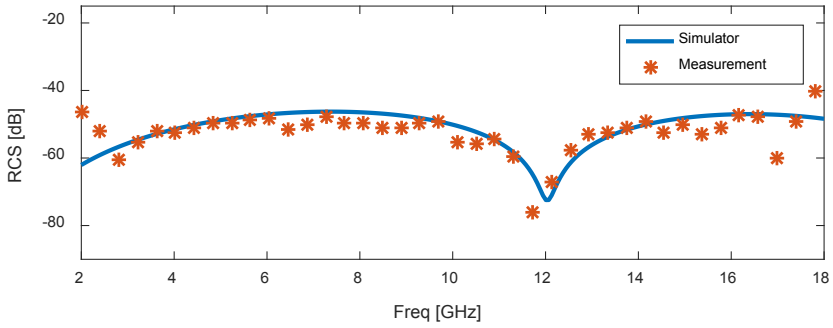

Figure 4.5.47 – Head (Case 1): RCS vs Frequency. $\theta_{H,(1,i_H)}$= *(90-10) deg*

4.5.6.2. Head (Case 1): RCS vs Time/Range

Figures 4.5.48-4.5.63 show the measured RCS as a function of range due to a head at different elevation angles. The elevation angles related to each measurement are indicated at the caption of each figure. The RCS simulations are in good agreement with the measurements. The component related to the remnant of the table's scattering response is present in all these plots. At elevation angles of 55 degrees and below there exist a larger discrepancy between the simulation and the measurement. This indicates that the geometric model could be improved further. So far, we found that this geometric model is the one that best approximates the measured RCS.

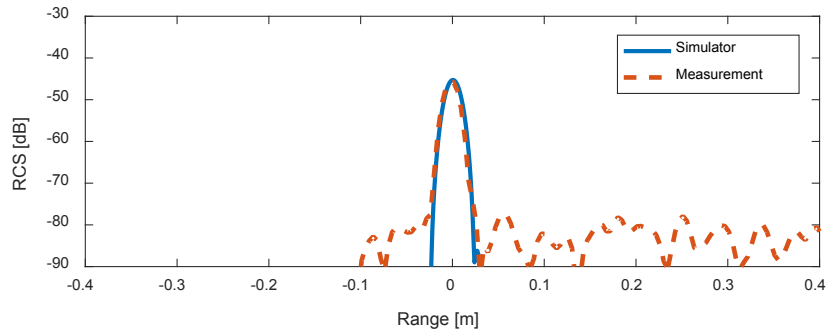

Figure 4.5.48 – Head (Case 1): RCS vs Range. $\theta_{H,(1,i_H)}$= *85 deg*

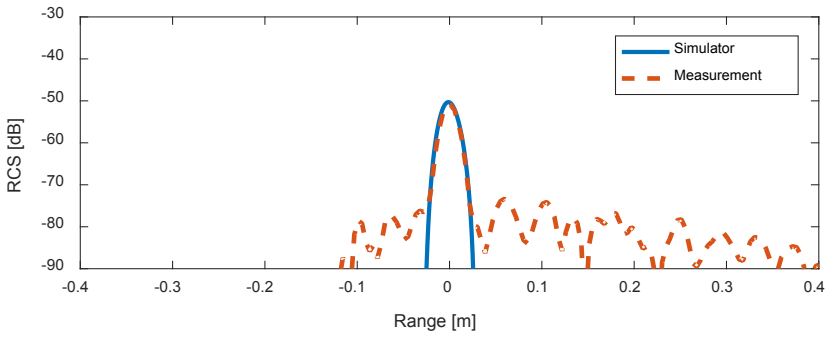

Figure 4.5.49 – Head (Case 1): RCS vs Range. $\theta_{H,(1,i_H)}$= *82.5 deg*

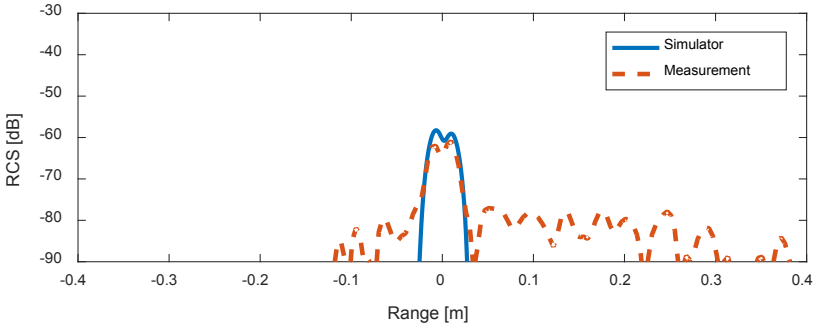

Figure 4.5.50 – Head (Case 1): RCS vs Range. $\theta_{H,(1,i_H)}$= *80 deg*

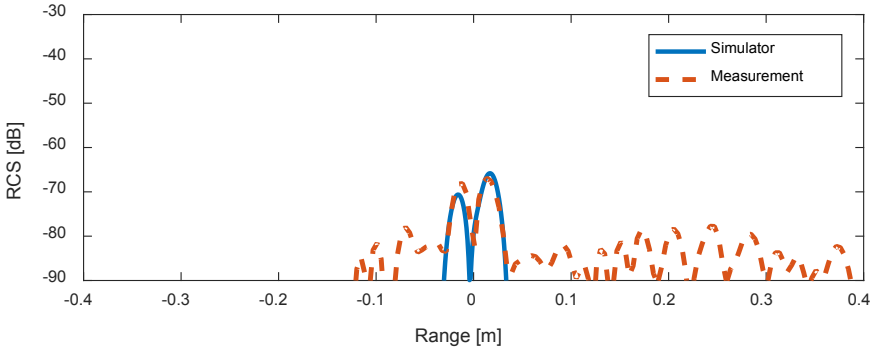

Figure 4.5.51 – Head (Case 1): RCS vs Range. $\theta_{H,(1,i_H)}$= *70 deg*

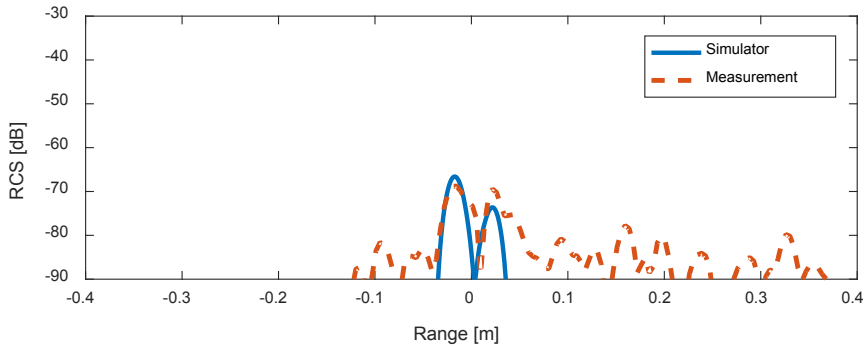

Figure 4.5.52 – Head (Case 1): RCS vs Range. $\theta_{H,(1,i_H)}$= *(65+180) deg*

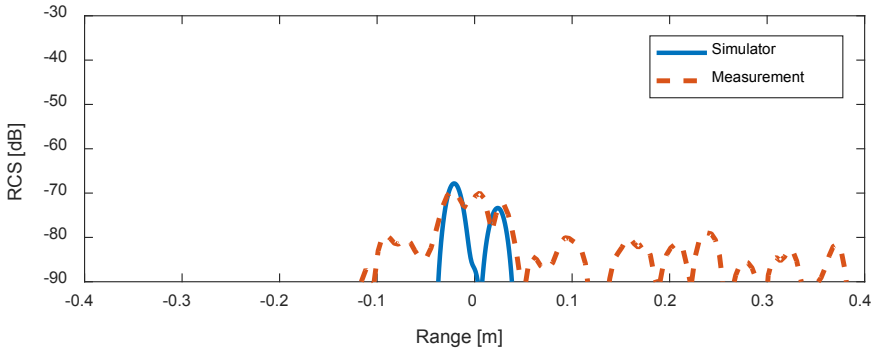

Figure 4.5.53 – Head (Case 1): RCS vs Range. $\theta_{H,(1,i_H)}$= *(60+180) deg*

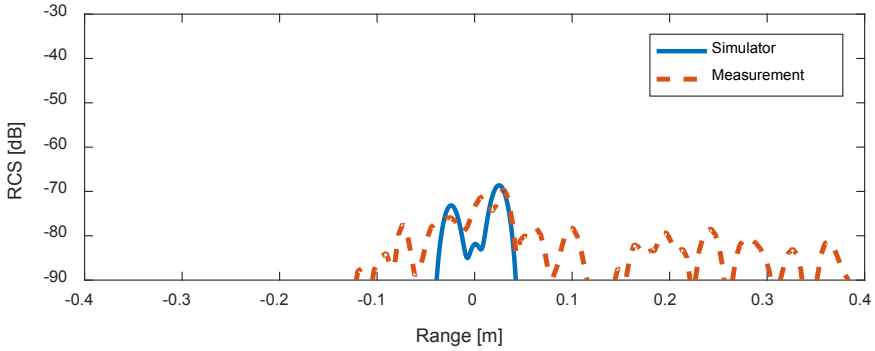

Figure 4.5.54 – Head (Case 1): RCS vs Range. $\theta_{H,(1,i_H)}$= *55 deg*

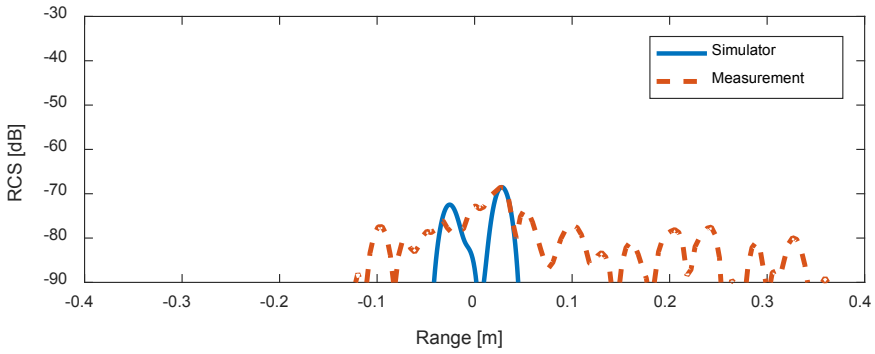

Figure 4.5.55 – Head (Case 1): RCS vs Range. $\theta_{H,(1,i_H)}$= *50 deg*

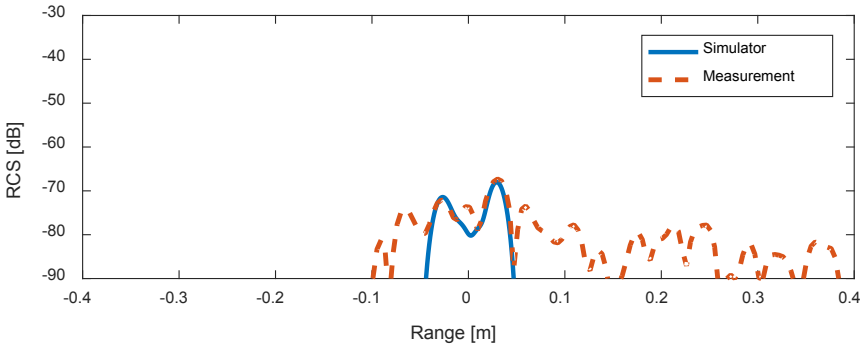

Figure 4.5.56 – Head (Case 1): RCS vs Range. $\theta_{H,(1,i_H)}$= *45 deg*

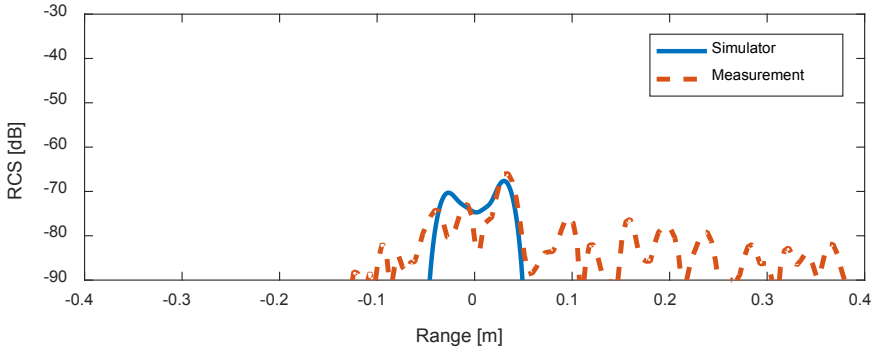

Figure 4.5.57 – Head (Case 1): RCS vs Range. $\theta_{H,(1,i_H)}$= *40 deg*

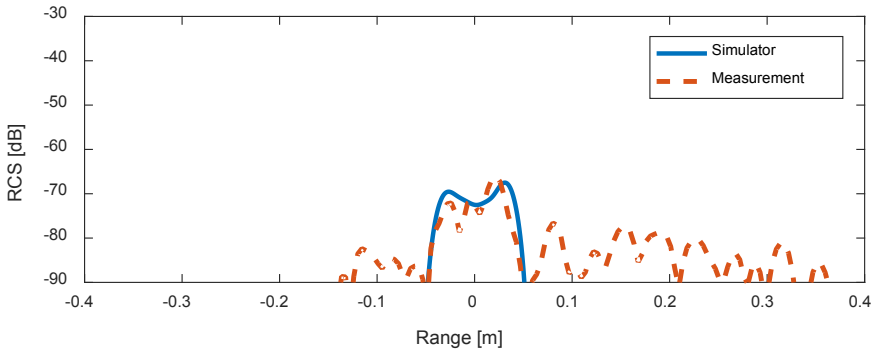

Figure 4.5.58 – Head (Case 1): RCS vs Range. $\theta_{H,(1,i_H)}$= *35 deg*

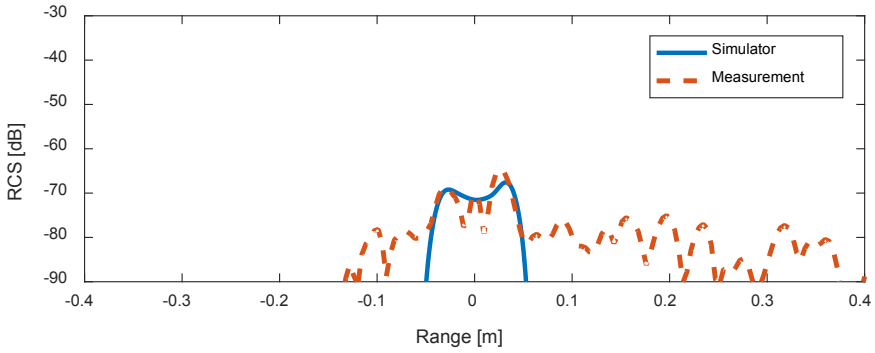

Figure 4.5.59 – Head (Case 1): RCS vs Range. $\theta_{H,(1,i_H)}$= *30 deg*

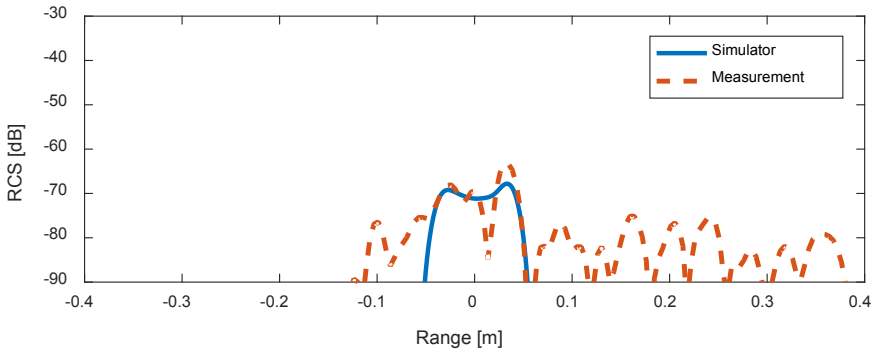

Figure 4.5.60 – Head (Case 1): RCS vs Range. $\theta_{H,(1,i_H)}$= *25 deg.*

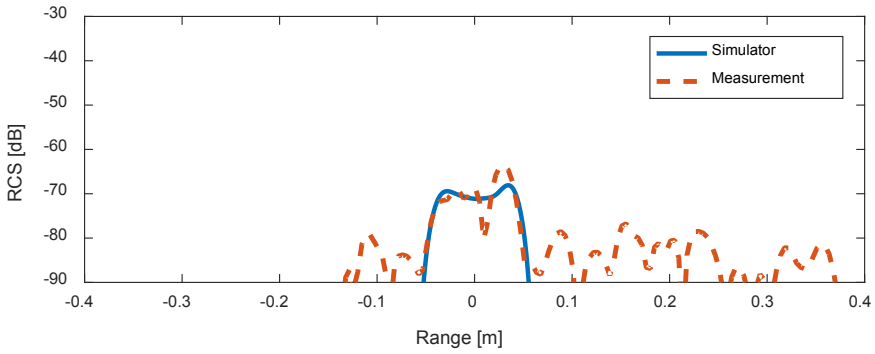

Figure 4.5.61 – Head (Case 1): RCS vs Range. $\theta_{H,(1,i_H)}$= *20 deg*

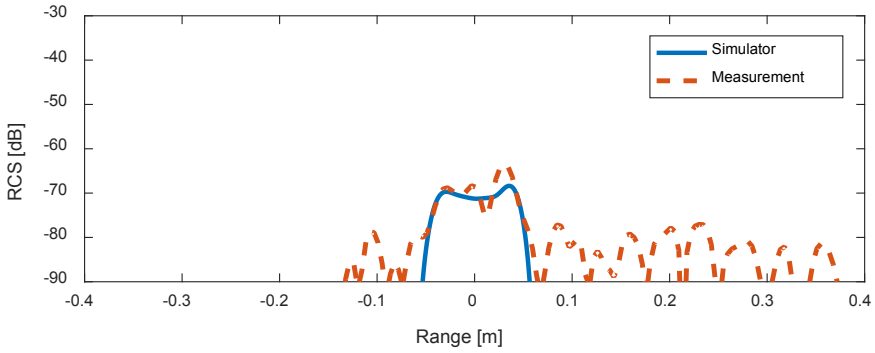

Figure 4.5.62 – Head (Case 1): RCS vs Range. $\theta_{H,(1,i_H)}$= *15 deg*

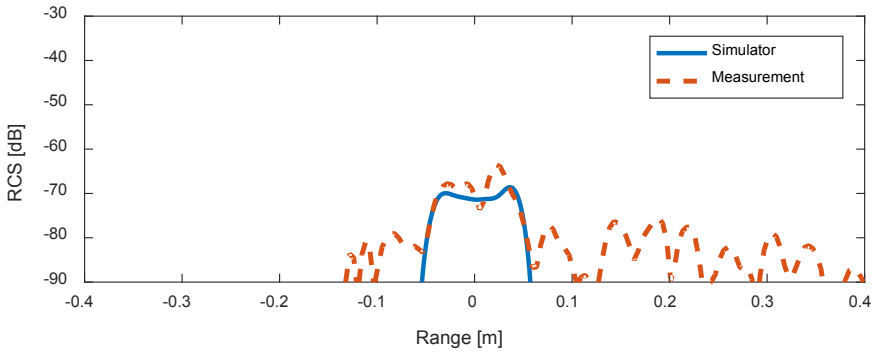

Figure 4.5.63 – Head (Case 1): RCS vs Range. $\theta_{H,(1,i_H)}$= *10 deg*

4.5.7. Plant (Case 1): Plant, Stem, Head

The RCS of two different plants was measured. The first plant is used for cases 1 through 4 and the second plant is used for case 5. In this case, the first plant was measured with the leaves cut-off. In other words, this case considers the first plant with no head and no stem. The plant parameters are listed in table 4.5.7-4.5.9. A depiction of the plant's geometric model generated by the simulator is shown in figure 4.5.64.

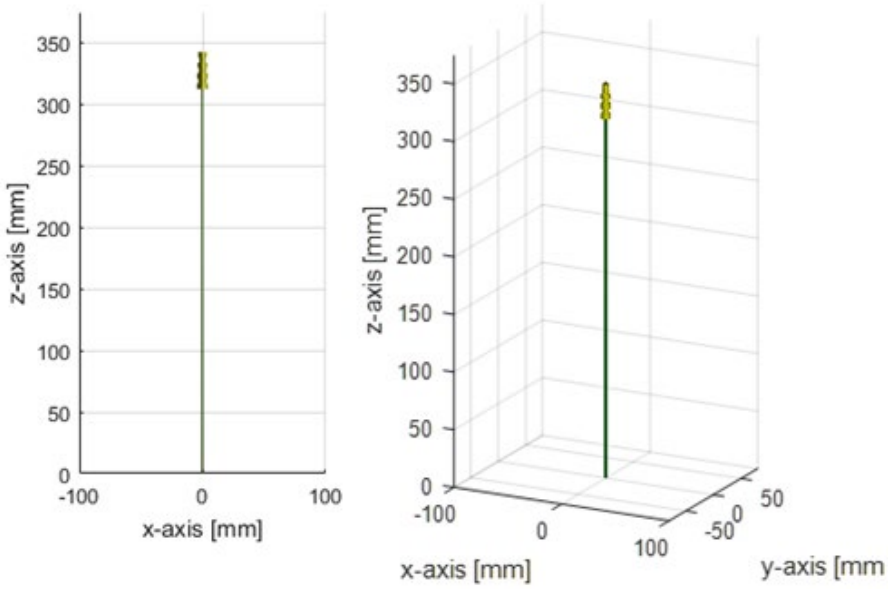

Figure 4.5.64 – Plant (Case 1): Visualization of geometric model. (Left: front view; right: perspective view)

Table 4.5.7 - Plant (Case 1): List of Stem Parameters

Parameter	**Stem 1, $t_{S,(1,1)}$**
Position, $r_{S,(1,i_S)}$	Origin
Length, $L_{S,(1,i_S)}$	312 mm
Radius, $\rho_{S,(1,i_S)}$	0.75 mm
Azimuth, $\varphi_{S,(1,i_S)}$	0 deg
Elev., $\theta_{S,(1,i_S)}$	0 deg
Moist. Cont., $m_{S,(1,i_S)}$	0.7

Table 4.5.8 – Plant (Case 1): List of Plant Parameters

Parameter	**Plant 1, $t_{P,(1)}$**
Position, $r_{P,(1)}$	Origin

Table 4.5.9 – Plant (Case 1): List of Head Parameters

Parameter	**Head 1, $t_{H,(1,1)}$**
Position, $\mathrm{r}_{H,(1,i_H)}$	Centered at origin
Length, $L_{H,(1,i_H)}$	30 mm
Radius init., $\rho_{i,H,(1,i_H)}$	1.1 mm
Radius mid., $\rho_{m,H,(1,i_H)}$	4.95 mm
Radius mid., $\rho_{m,H,(1,i_H)}$	3.85 mm
Azimuth, $\varphi_{H,(1,i_H)}$	0 deg
Elev., $\theta_{H,(1,i_H)}$	0 deg
Rad. fac., β_H	80
Moist. Cont., $m_{H,(1,i_H)}$	0.3
Vol. frac., $v_{H,(1,i_H)}$	0.6

4.5.7.1. Plant (Case 1): RCS vs Range

Figure 4.5.65 shows the plant's measured RCS as a function of range. The figure shows the components related to the plant's head and the bottom of the stem. The head's first and second peaks are related to the top and bottom ends of the head. The RCS due to the bottom of the head appears larger in the measurement than its simulated return. This discrepancy could indicate that the effective permittivity of the head is not constant, as it is assumed by the simulator.

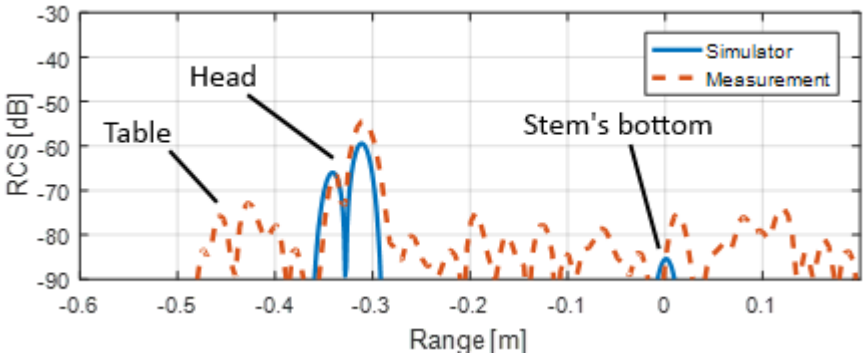

Figure 4.5.65 – Plant (Case 1): RCS vs Range

4.5.8. Plant (Case 2): Tall Plant, Head, Stem, 1 curved leaf

In this case, a plant is considered with one curved leaf, a head and a stem. Figure 4.5.66 (left) shows a photograph of the measured plant. Figure 4.5.66 (center and right) shows a depiction of the geometric model, generated by the simulator. The plant parameters are listed in tables 4.5.10-4.5.13.

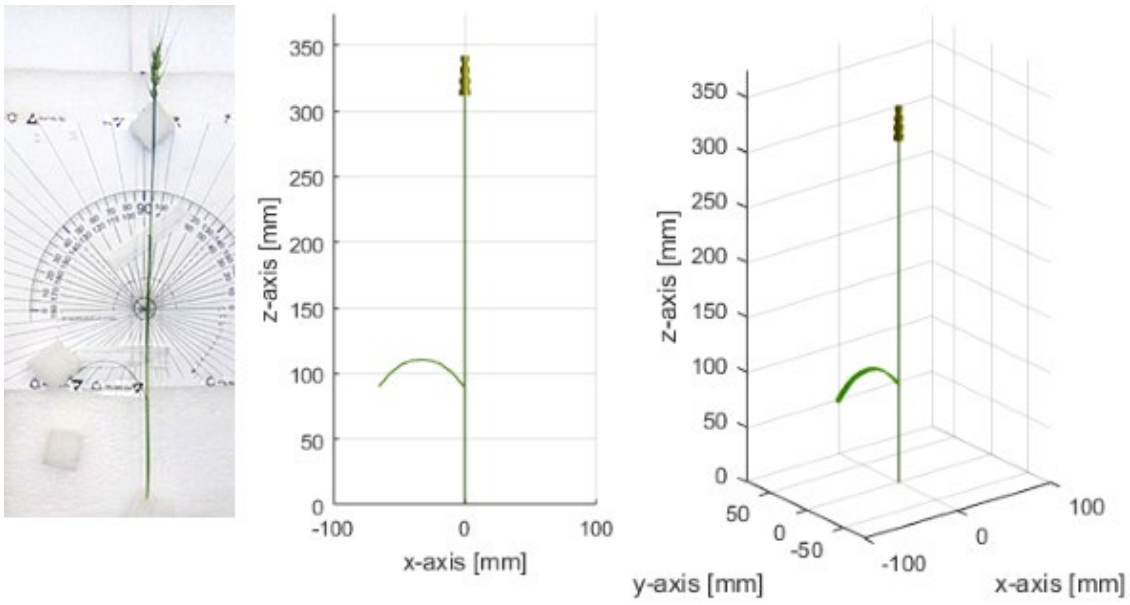

Figure 4.5.66 – Plant (Case 2): Photograph (Left); Visualization of Geometric Model (Center and Right)

Table 4.5.10 - Plant (Case 2): List of Stem Parameters

Parameter	**Stem 1, $t_{S,(1,1)}$**
Position, $r_{S,(1,i_S)}$	Origin
Length, $L_{S,(1,i_S)}$	312 mm
Radius, $\rho_{S,(1,i_S)}$	0.75 mm
Azimuth, $\varphi_{S,(1,i_S)}$	0 deg
Elev., $\theta_{S,(1,i_S)}$	0 deg
Moist. Cont., $m_{S,(1,i_S)}$	0.7

Table 4.5.11 – Plant (Case 2): List of Plant Parameters

Parameter	**Plant 1, $t_{P,(1)}$**
Position, $r_{P,(1)}$	Origin

Table 4.5.12 – Leaf (Case 2): List of Leaf Parameters

Parameter	**Leaf 1, $t_{L,(1,1)}$**
Position, $r_{L,(1,i_L)}$	(-0.75mm,0,90mm)
Length, $L_{L,(1,i_L)}$	80 mm
Width, $w_{L,(1,i_L)}$	4.5 mm
Thickness, $a_{L,(1,i_L)}$	0.2 mm
First-rot. $\alpha_{L,(1,i_L)}$	0 deg
Azimuth, $\varphi_{L,(1,i_L)}$	180 deg
Initial Elev, $\theta_{i,L,(1,i_L)}$	90-70 deg
Final Elev, $\theta_{f,L,(1,i_L)}$	90+70 deg
Common Elev., $\theta_{c,L,(1,i_L)}$	0 deg
Rad. of Curv., $R_{L,(1,i_L)}$	30mm
Moisture Cont., $m_{L,(1,i_L)}$	0.75

Table 4.5.13 – Plant (Case 2): List of Head Parameters

Parameter	**Head 1, $t_{H,(1,1)}$**
Position, $\mathrm{r}_{H,(1,i_H)}$	Centered at origin
Length, $L_{H,(1,i_H)}$	30 mm
Radius init., $\rho_{i,H,(1,i_H)}$	1.1 mm
Radius mid., $\rho_{m,H,(1,i_H)}$	4.95 mm
Radius mid., $\rho_{m,H,(1,i_H)}$	3.85 mm
Azimuth, $\varphi_{H,(1,i_H)}$	0 deg
Elev., $\theta_{H,(1,i_H)}$	0 deg
Rad. fac., β_H	80
Moist. Cont., $m_{H,(1,i_H)}$	0.3
Vol. frac., $v_{H,(1,i_H)}$	0.6

4.5.8.1. Plant (Case 2): RCS vs Range

The plant's measured RCS as a function of range is shown in figure 4.5.67. This plot is identical to the previous case with the addition of the curved leaf at about -0.1 m range. The RCS component related to the curve leaf is well approximated by the simulation. The head's RCS component is not noticeable changed by the presence of the leaf.

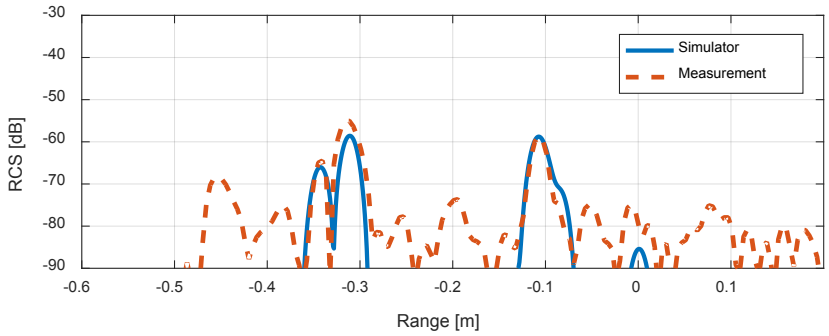

Figure 4.5.67 – Plant (Case 2): RCS v Range

4.5.9. Plant (Case 3): Plant, Head, Stem, 2 curved leaves

In this case, a plant is considered with two curved leaves, one head and one stem. The parameters of the plant are listed in table 4.5.14-4.5.17. Figure 4.5.68 (left) shows a photograph of the measured plant. Figure 4.5.68 (center and right) shows a depiction of the plant's geometric model, generated by the simulator.

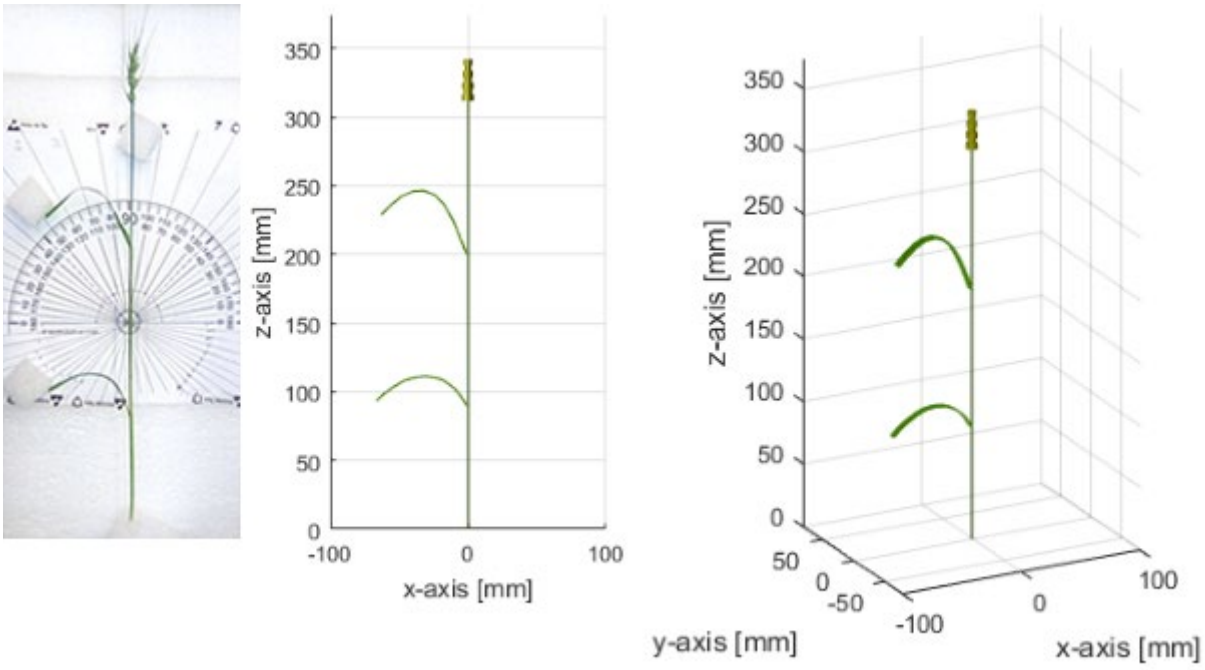

Figure 4.5.68 – Plant (Case 3): Visualization of Geometric Model

Table 4.5.14 - Plant (Case 3): List of Stem Parameters

Parameter	**Stem 1, $t_{S,(1,1)}$**
Position, $r_{S,(1,i_S)}$	Origin
Length, $L_{S,(1,i_S)}$	312 mm
Radius, $\rho_{S,(1,i_S)}$	0.75 mm
Azimuth, $\varphi_{S,(1,i_S)}$	0 deg
Elev., $\theta_{S,(1,i_S)}$	0 deg
Moist. Cont., $m_{S,(1,i_S)}$	0.7

Table 4.5.15 – Plant (Case 3): List of Plant Parameters

Parameter	**Plant 1, $t_{P,(1)}$**
Position, $r_{P,(1)}$	Origin

Table 4.5.16 – Leaf (Case 3): List of Leaf Parameters

Parameter	**Leaf 1, $t_{L,(1,1)}$**	**Leaf 2, $t_{L,(1,2)}$**
Position, $r_{L,(1,i_L)}$	(-0.75mm,0,90mm)	(-0.75mm,0,200mm)
Length, $L_{L,(1,i_L)}$	80 mm	95 mm
Width, $w_{L,(1,i_L)}$	4.5 mm	6.3 mm
Thickness, $a_{L,(1,i_L)}$	0.2 mm	0.2 mm
First-rot. $\alpha_{L,(1,i_L)}$	0 deg	0 deg
Azimuth, $\varphi_{L,(1,i_L)}$	180 deg	180 deg
Initial Elev, $\theta_{i,L,(1,i_L)}$	90-80 deg	90-70 deg
Final Elev, $\theta_{f,L,(1,i_L)}$	90+50 deg	90+50 deg
Common Elev., $\theta_{c,L,(1,i_L)}$	0 deg	0 deg
Rad. of Curv., $R_{L,(1,i_L)}$	30mm	20mm
Apex Loc., $s_{o,L,(1,i_L)}$	0.4	0.6
Moisture Cont., $m_{L,(1,i_L)}$	0.75	0.75

Table 4.5.17 – Plant (Case 3): List of Head Parameters

Parameter	**Head 1, $t_{H,(1,1)}$**
Position, $\mathrm{r}_{H,(1,i_H)}$	Centered at origin
Length, $L_{H,(1,i_H)}$	30 mm
Radius init., $\rho_{i,H,(1,i_H)}$	1.1 mm
Radius mid., $\rho_{m,H,(1,i_H)}$	4.95 mm
Radius mid., $\rho_{m,H,(1,i_H)}$	3.85 mm
Azimuth, $\varphi_{H,(1,i_H)}$	0 deg
Elev., $\theta_{H,(1,i_H)}$	0 deg
Rad. fac., β_H	80
Moist. Cont., $m_{H,(1,i_H)}$	0.3
Vol. frac., $v_{H,(1,i_H)}$	0.6

4.5.9.1. Plant (Case 3): RCS vs Range

Figure 4.5.69 shows the plant's measured RCS as a function of range. The simulation approximates well the RCS components of both leaves. As with the previous cases, the second peak of the RCS of the head is larger in the measurement than that of the simulation.

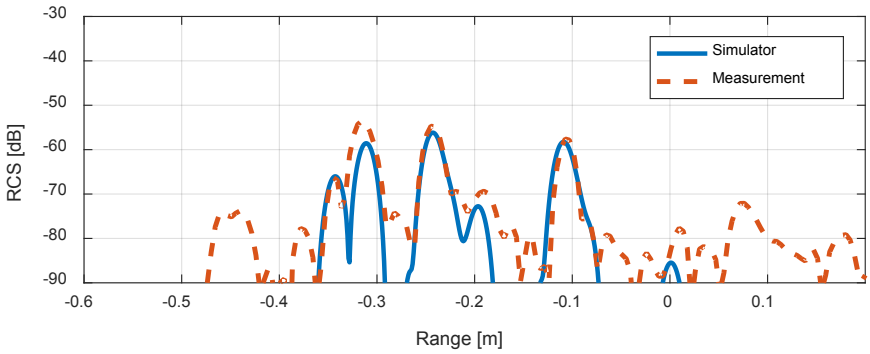

Figure 4.5.69 – Plant (Case 3): RCS vs Range.

4.5.10. Plant (Case 4): Plant, Head, Stem, 2 Straight Leaves

In this case, a plant is considered with two straight leaves. The plant parameters are listed in tables 4.5.18-4.5.21. RCS measurements of the plant are taken at different leaf elevation angles. Figure 4.5.70 (right) shows a photograph of the plant with straight leaves measured at a particular configuration. In this configuration, the elevation angles of the top and bottom leaves are 83 and 82 degrees, respectively. Figure 4.5.70 (center and right) shows a depiction of the geometric model of the plant, generated by the simulator.

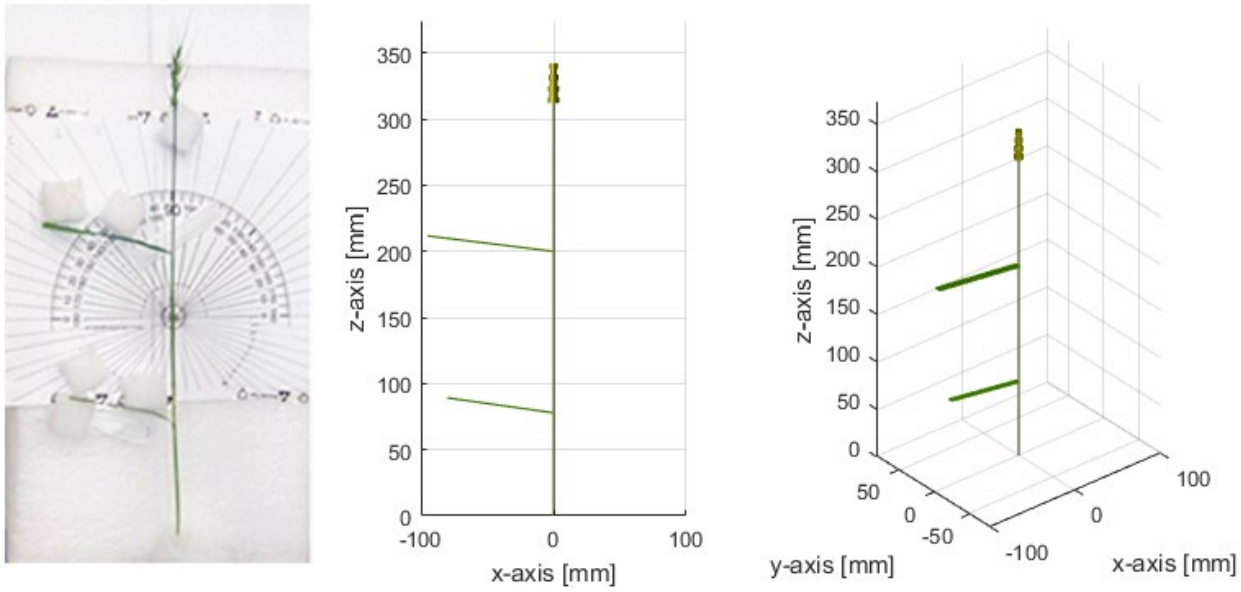

Figure 4.5.70 – Plant (Case 4): Photograph (Left) and Geometric Model (Center and Right) (Example 82, 83 deg)

Table 4.5.18 - Plant (Case 4): List of Stem Parameters

Parameter	**Stem 1, $t_{S,(1,1)}$**
Position, $r_{S,(1,i_S)}$	Origin
Length, $L_{S,(1,i_S)}$	312 mm
Radius, $\rho_{S,(1,i_S)}$	0.75 mm
Azimuth, $\varphi_{S,(1,i_S)}$	0 deg
Elev., $\theta_{S,(1,i_S)}$	0 deg
Moist. Cont., $m_{S,(1,i_S)}$	0.7

Table 4.5.19 – Plant (Case 4): List of Plant Parameters

Parameter	**Plant 1, $t_{P,(1)}$**
Position, $r_{P,(1)}$	Origin

Table 4.5.20 – Leaf (Case 4): List of Leaf Parameters

Parameter	**Leaf 1, $t_{L,(1,1)}$**	**Leaf 2, $t_{L,(1,2)}$**
Position, $\mathrm{r}_{L,(1,i_L)}$	(-0.75mm,0,90mm)	(-0.75mm,0,200mm)
Length, $L_{L,(1,i_L)}$	80 mm	95 mm
Width, $w_{L,(1,i_L)}$	4.5 mm	6.3 mm
Thickness, $a_{L,(1,i_L)}$	0.2 mm	0.2 mm
First-rot. $\alpha_{L,(1,i_L)}$	0 deg	0 deg
Azimuth, $\varphi_{L,(1,i_L)}$	180 deg	180 deg
Initial Elev, $\theta_{i,L,(1,i_L)}$	88 deg	87 deg
Final Elev, $\theta_{f,L,(1,i_L)}$	$\boldsymbol{\theta_{c,L,(1,1)}}$	$\boldsymbol{\theta_{c,L,(1,2)}}$
Common Elev., $\theta_{c,L,(1,i_L)}$	$\boldsymbol{\theta_{c,L,(1,1)}}$	$\boldsymbol{\theta_{c,L,(1,2)}}$
Rad. of Curv., $R_{L,(1,i_L)}$	30mm	20mm
Moisture Cont., $m_{L,(1,i_L)}$	0.75	0.75

Table 4.5.21 – Plant (Case 4): List of Head Parameters

Parameter	**Head 1, $t_{H,(1,1)}$**
Position, $\mathrm{r}_{H,(1,i_H)}$	Centered at origin
Length, $L_{H,(1,i_H)}$	30 mm
Radius init., $\rho_{i,H,(1,i_H)}$	1.1 mm
Radius mid., $\rho_{m,H,(1,i_H)}$	4.95 mm
Radius mid., $\rho_{m,H,(1,i_H)}$	3.85 mm
Azimuth, $\varphi_{H,(1,i_H)}$	0 deg
Elev., $\theta_{H,(1,i_H)}$	0 deg
Rad. fac., β_H	80
Moist. Cont., $m_{H,(1,i_H)}$	0.3
Vol. frac., $v_{H,(1,i_H)}$	0.6

4.5.10.1. Plant (Case 4): RCS vs Range

Figures 4.5.71-4.5.73 show the plant's measured RCS as a function of range. The measurements were taken at different leaf elevation angles, indicated in the caption of each related figure. As indicated by table 4.5.20, $\boldsymbol{\theta_{c,L,(1,1)}}$ is the elevation angle of the bottom leaf and $\boldsymbol{\theta_{c,L,(1,2)}}$ is the elevation angle of the top leaf. In figure 4.5.71 and 4.5.73, the simulated RCS component related to the leaves agrees well with their related measurement. In 4.5.72, there is a small discrepancy between the RCS component of the simulated leaves and their measurement. This discrepancy may be caused by the interference of the table's RCS, which is significant with respect to the leaves' RCS, in that configuration.

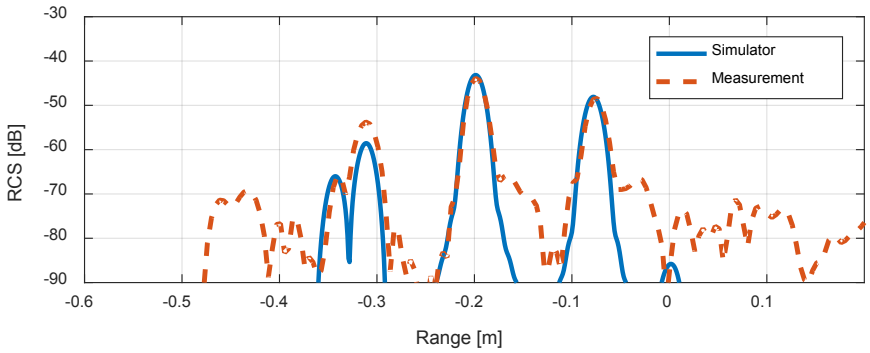

Figure 4.5.71 – Plant (Case 4): RCS vs Range. ($\boldsymbol{\theta_{c,L,(1,1)}} = 87$ deg, $\boldsymbol{\theta_{c,L,(1,2)}} = 88$ deg)

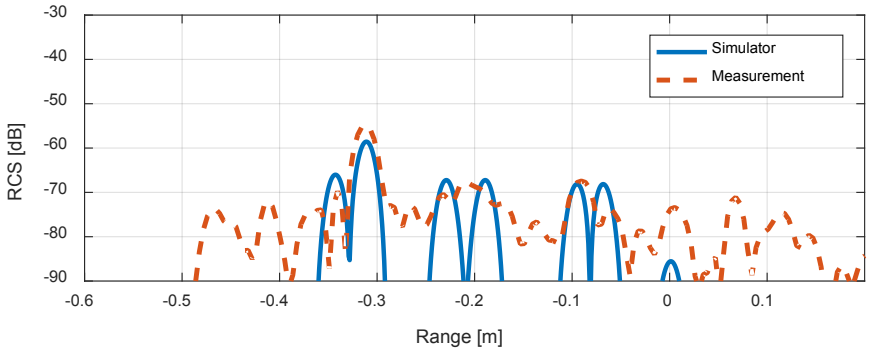

Figure 4.5.72 – Plant (Case 4): RCS vs Range. ($\boldsymbol{\theta_{c,L,(1,1)}} = 65$ deg, $\boldsymbol{\theta_{c,L,(1,2)}} = 70$ deg)

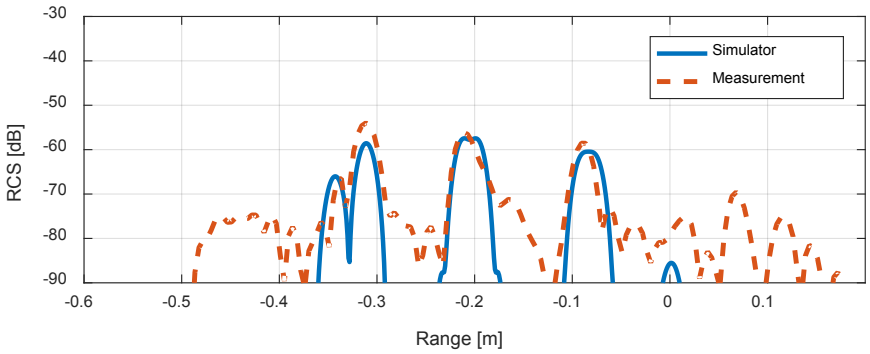

Figure 4.5.73 – Plant (Case 4): RCS vs Range. ($\boldsymbol{\theta_{c,L,(1,1)}} = 82$ deg, $\boldsymbol{\theta_{c,L,(1,2)}} = 83$ deg)

4.5.11. Plant (Case 5): Plant, head, stem, 3 curved leaves

In this case, a plant is considered with three curved leaves, a head and a stem. The properties of the plant are listed in tables 4.5.22-4.5.25. Figure 4.5.74 (left) shows a photograph of the measured plant. Figure 4.5.74 (center and right) shows a depiction of the plant's geometric model, generated by the simulator.

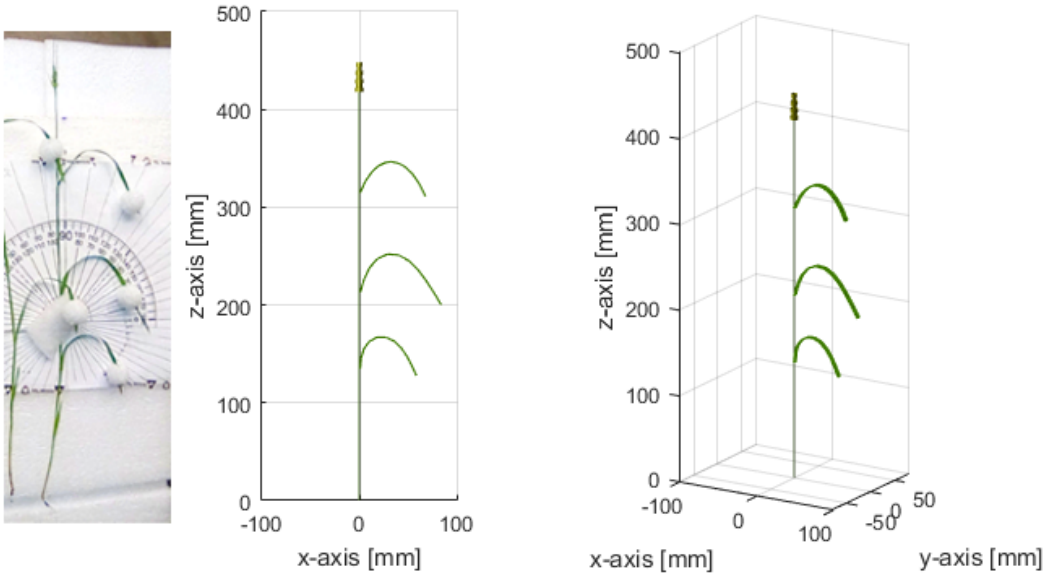

Figure 4.5.74 – Plant (Case 5): Photograph (Left) and Visualization of the Geometric Model (Center and Right)

Table 4.5.22 - Plant (Case 5): List of Stem Parameters

Parameter	**Stem 1, $t_{S,(1,1)}$**
Position, $r_{S,(1,i_S)}$	Origin
Length, $L_{S,(1,i_S)}$	418 mm
Radius, $\rho_{S,(1,i_S)}$	0.75 mm
Azimuth, $\varphi_{S,(1,i_S)}$	0 deg
Elev., $\theta_{S,(1,i_S)}$	0 deg
Moist. Cont., $m_{S,(1,i_S)}$	0.7

Table 4.5.23 – Plant (Case 5): List of Plant Parameters

Parameter	**Plant 1, $t_{P,(1)}$**
Position, $r_{P,(1)}$	Origin

Table 4.5.24 – Plant (Case 5): List of Leaf Parameters

Parameter	**Leaf 1, $t_{L,(1,1)}$**	**Leaf 2, $t_{L,(1,2)}$**	**Leaf 3, $t_{L,(1,3)}$**
Position, $r_{L,(1,i_L)}$	(-0.75mm,0,135mm)	(-0.75mm,0,213mm)	(-0.75mm,0,315mm)
Length, $L_{L,(1,i_L)}$	100 mm	130 mm	100 mm
Width, $w_{L,(1,i_L)}$	4.5 mm	5.0 mm	6.0 mm
Thickness, $a_{L,(1,i_L)}$	0.2 mm	0.2 mm	0.2 mm
First-rot. $\alpha_{L,(1,i_L)}$	0 deg	0 deg	0 deg
Azimuth, $\varphi_{L,(1,i_L)}$	0 deg	0 deg	0 deg
Initial Elev, $\theta_{i,L,(1,i_L)}$	90-100 deg	90-80 deg	90-85 deg
Final Elev, $\theta_{f,L,(1,i_L)}$	90+70 deg	90+60 deg	90+80 deg
Common Elev., $\theta_{c,L,(1,i_L)}$	0	0	0
Rad. of Curv., $R_{L,(1,i_L)}$	20mm	25mm	30mm
Apex Loc., $s_{o,L,(1,i_L)}$	0.4	0.4	0.48
Moisture Cont., $m_{L,(1,i_L)}$	0.75	0.75	0.75

Table 4.5.25 – Plant (Case 5): List of Head Parameters

Parameter	**Head 1, $t_{H,(1,1)}$**
Position, $\mathrm{r}_{H,(1,i_H)}$	Centered at origin
Length, $L_{H,(1,i_H)}$	20 mm
Radius init., $\rho_{i,H,(1,i_H)}$	0.7 mm
Radius mid., $\rho_{m,H,(1,i_H)}$	3.15 mm
Radius mid., $\rho_{m,H,(1,i_H)}$	1.75 mm
Azimuth, $\varphi_{H,(1,i_H)}$	0 deg
Elev., $\theta_{H,(1,i_H)}$	0 deg
Rad. fac., β_H	80
Moist. Cont., $m_{H,(1,i_H)}$	0.3
Vol. frac., $v_{H,(1,i_H)}$	0.6

4.5.11.1. Plant (Case 5): RCS vs Range

Figure 4.5.75 shows the plant's measured RCS as a function of range. From left to right, the first peak corresponds to the head and the next three peaks correspond to the three leaves. The RCS component related to the head is similar in amplitude to the table's RCS, so that its measurement is corrupted. The RCS components related to the leaves agree well with their related componets.

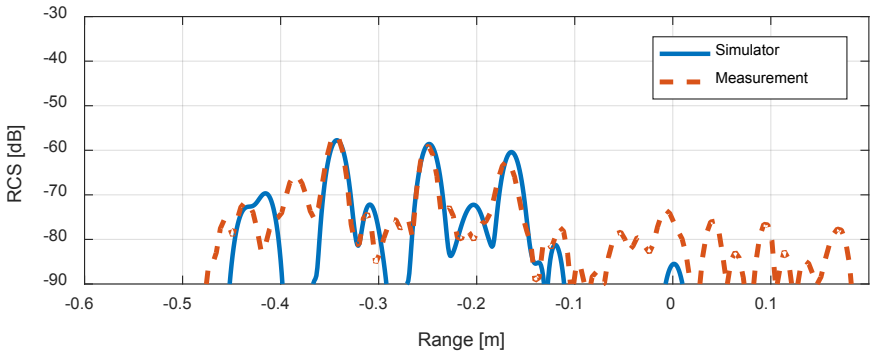

Figure 4.5.75 – Plant (Case 5): RCS vs Range

4.6. References

[1] F. Ulabi, R. K. Moore, A. K. Fung, “Microwave Remote Sensing, Active and Passive”, Volume III, Norwood, MA: Artech House, 1986.

[2] P. Debye, “Polar Molecules,” New York: Dover, 1929.

[3] A. Chukhlantsev, “Microwave Radiometry of Vegetation Canopies,” The Netherlands: Springer, 2006.

[4] M. A. El-Rayes, “The Measurement and Modeling of the Dielectric Behavior of Vegetation Materials in the Microwave Region (0.5-20.4 GHz),” Doctoral Dissertation, University of Kansas, 1986.

[5] D. Polder, J. Van Santeen, “The effective permeability of mixture of solids,” Physica, vol. 12, no. 5, pp. 257-271, 1946.

[6] G. P. De Loor, “Dielectric properties of heterogeneous mixtures with a polar constituent,” Applied Scientific Research, Section B, vol. 11, no. 3, pp 310-320, 1964.

[7] G. P. De Loor, “Dielectric Properties of Heterogeneous Mixtures containing water,” Journal of Microwave Power, vol. 3, no. 2, pp. 67-73, 1968.

[8] M. A. El-Rayes and F. T. Ulaby, "Microwave Dielectric Spectrum of Vegetation-Part I: Experimental Observations," in *IEEE Transactions on Geoscience and Remote Sensing*, vol. GE-25, no. 5, pp. 541-549, Sept. 1987.

[9] F. T. Ulaby and M. A. El-Rayes, "Microwave Dielectric Spectrum of Vegetation - Part II: Dual-Dispersion Model," in *IEEE Transactions on Geoscience and Remote Sensing*, vol. GE-25, no. 5, pp. 550-557, 1987.

[10] C. Matzler, "Microwave (1-100 GHz) dielectric model of leaves," in *IEEE Transactions on Geoscience and Remote Sensing*, vol. 32, no. 4, pp. 947-949, Jul 1994.

[11] R. H. Lang, J. S. Sidhu, “Electromagnetic backscattering from a layer of vegetation: a discrete approach,” IEEE Transactions on Geoscience and Remote Sensing, vol. GE-21, no. 1, Jan. 1983.

[12] L. Tsang, J. A. Kong, *Scattering of Electromagnetic Waves: Advanced Topics*, New York: Wiley Inter-science, 2000.

5. PLL-Based 2-18 GHz UWB FMCW Radar Sensor

The radar system described in this chapter is the result of several years of ultra-wideband (UWB) radar development performed by the author of this document. The Center for Remote Sensing of Ice Sheets has routinely performed airborne measurements of snow-cover thickness using FMCW ultra-wideband radars, referred to as the Snow Radar and the Ku-Band Altimeter. The main challenge in the development of these radars has been the design of their chirp generators. The chirp generator is the sub-system that produces the ultra-wideband linear-frequency-modulated waveform (i.e. chirp). The chirp is required to sweep fast for these applications. If the instantaneous frequency at the output of the chirp is not sufficiently linear, the system response of the radar is degraded. Specifically, the range-domain sidelobes increase in amplitude. If the range side-lobes of the ground response become too large, the radar becomes unable to detect the smaller snow-cover contributions. Compensation systems or methods are used to generate very-linear UWB chirps. Chirp generators with wider bandwidths require faster frequency-compensation systems. In 2011, the author of this document developed the first chirp generator and radar for airborne snow-cover measurements that had sufficient linearity to operate with 6 GHz of bandwidth [1-3]. This high-performing radar was based on a new dual-compensation system [4]. In 2013, the linearity of the chirp generator was further improved using a FPGA-based Direct-Digital-Synthesizer and phase pre-distortion [5]. With the advent of new microwave components available, the author of this document developed the first 2-18 GHz chirp generator with sufficient linearity to measure snow-cover from an airborne platform at 450 m [6].

The chirp generators described in [5, 6] are bulky because of the several stages of frequency multipliers. Using high-slew rate voltage-feedback Operational Amplifier [7], a smaller PLL-based 2-18 GHz chirp generator was developed in 2016. This chapter describes the architecture and performance of the radar systems along with different design considerations for best performance.

The sensitivity of the radar system is determined by several factors that will be discussed in this chapter. Two important issues that arise with the use of FMCW radars are the “coherent” and “incoherent” phase noise of self-interference signals. These are often the main contributors to the system’s output noise. Both of these types of noise spread over most if not all of the radar’s output bandwidth, adversely affecting performance. Thus, understanding the source of self-interference and their phase noise is beneficial in the design of FMCW radars. More importantly, having a formulation that predicts the amplitude and shape of these undesirable signals would aid radar engineers in reducing the total amount of coherent and incoherent noise of the system and thus obtain maximum sensitivity. In this chapter, we identify the most important sources of self-interference and noise in an FMCW radar. Most importantly, we derive the expressions for the self-interference signals and their associated phase noise at the output. We also present formulae relating quantization and thermal noise at the output of the radar.

From the noise and interference analysis, we learned that the phase noise of self-interference signals could be greater than the thermal noise level. Therefore, the design of the FMCW radar for this study focused on minimizing coherent and incoherent phase noise at the chirp generator, decreasing the amplitude of self-interference signals, as well as maintaining a low thermal noise level.

At the core of the radar is the chirp generator, which produces an UWB chirp that spans from 2 GHz to 18 GHz. The chirp generator is based on a DDS-driven phase-locked loop (PLL). For the design of this sub-system, special attention was put in minimizing the level of coherent and incoherent phase noise. Specifically, the loop bandwidth was made significantly large so that phase noise is attenuated over a wider bandwidth, reducing its peak value.

The two largest self-interference signals identified are those related to LO leakage and antenna feedthrough. The radar was designed to keep the amplitude of these signals low. The antennas were separated to a maximum distance, limited by the footprint, so that the feed-through was kept low. The LO-Leakage is a self-interference signal that is independent of the RF receiver gain and noise figure. Therefore, if the LO Leakage is the main contributor of noise, increasing the RF receiver gain would improve the signal-to-noise ratio. Moreover, improving the RF receiver return loss decreases the total noise due to LO Leakage. We used these concepts to keep this signal and its associated phase noise below thermal noise.

This chapter is divided in two parts. The first part presents an analysis of FMCW radars and introduces useful expressions to approximate the signal output due to a target, self-interference signals or different kinds of noise. The second part describes a prototype of the proposed radar for high-throughput phenotyping of wheat canopies.

Part 1: FMCW Radar Analysis

Section 5.1 presents an overview of a typical FMCW radar system and describes its system model. This section also derives the output signal of an FMCW radar due to a given target response.

Section 5.2 presents a broad analysis of noise and self-interference signals in FMCW radars. It derives the output due to each type of self-interference and noise identified. These expressions are used in the design of the radar to improve the performance of the radar.

Part 2: Radar Description

Section 5.3 presents a list of the radar requirements and the rationale behind them. This section also summarizes the radar parameters.

Section 5.4 describes the antenna and platform chosen for the radar. It also shows measurements of the antenna pair performance.

Section 5.5 presents the architecture of the chirp generator. The main component of the chirp generator, the DDS-driven PLL, is described in significant detail. Approximated models for the phase noise of the PLL and the chirp generator are presented. These phase noise expressions may be used to calculate the noise level at the output of the radar due to phase noise of self-interference signals.

Section 5.6 presents the architecture of the transmitter, the receiver and the LO sub-system. This section also provides a brief description of the data-acquisition-system.

Section 5.7 presents measurements of the output of the radar due to the main self-interference signals. Measurements are compared to numerical simulations and to approximated models.

Section 5.8 describes the procedure to calibrate the system response. Specifically, this section shows how to update the system response of the antennas using calibration targets.

PART I – FMCW RADAR ANALYSIS

5.1. FMCW RADAR ANALYSIS: System Model and De-Chirping

5.1.1. FMCW Radar Overview and System Model

5.1.1.1. Radar Definition

Radio Detection and Ranging (RADAR) is the acronym that refers to the technology that uses electromagnetic waves to sense properties from targets at a distance. A radar system or simply radar is the sensor that uses this technology. A radar system is the aggregate of all the electronic components that generate, radiate, capture and process the radar signals involved in the sensing operation.

5.1.1.2. FMCW Radar

A Linear-Frequency-Modulate-Continuous-Wave (LFMCW) radar system is a type of radar that performs chirp-demodulation (de-chirping) with analog processing to measure a target's coherent frequency response. The wide bandwidths allowed by analog microwave circuits permit wideband frequency-response measurements and narrow-impulse response measurements (e.g. fine range-resolution measurements). This document only considers linear-frequency-modulation (LFM) and the terms Frequency-Modulation-Continuous-Wave (FMCW) and LFMCW are used interchangeably.

5.1.1.3. Sub-Systems of a FMCW Radar

Figure 5.1.1 shows a high-level block diagram of a typical FMCW radar system. The radar is composed by a chirp generator (CG), the FMCW radar transceiver or RF front-end, the data acquisition system and the radar antennas. The chirp signal, produced by the CG and conditioned by the transmitter (TX) part of the transceiver, is radiated by the transmitter antenna. This radiated electromagnetic wave is reflected or scattered by the target and captured by the receiver antenna. This received signal is linearly conditioned by the RF section of the receiver (RX-RF), which is a sub-system of the transceiver. This conditioned signal is frequency demodulated in a process called de-chirping, using an RF mixer. The de-chirped signal at the intermediate-frequency (IF) port of the mixer is conditioned by the IF stage of the receiver (RX-IF) before it is fed into the data-acquisition-system (DAQ). The signal at the output of the RX-IF, the IF signal, is digitized and stored by the DAQ. The radar antenna and the target are described by a single block diagram as the parameters of the antenna, such as gain, are determined by the target's position with respect to the antenna.

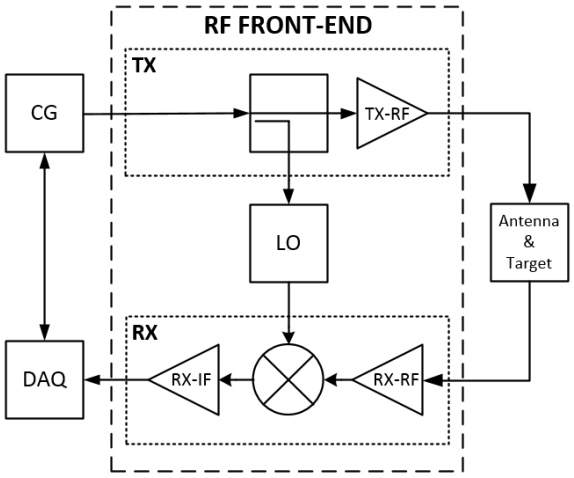

Figure 5.1.1 – High-Level FMCW Radar Architecture

5.1.1.4. FMCW Radar System Model

In order to analyze the system performance, the FMCW radar can be described in terms of sub-systems, which are described by specific models. Each of the radar sections described above can be described by a system model that relates the input and output signals. If amplifiers are operated in the linear region, the receiver RF and IF stages can be modeled as linear 2-port networks. Thus, they can be described using the scattering-parameters (S-parameters). Similarly, the TX and LO stages can be modeled with S-parameters, when their components operate in the linear region. All sub-systems are designed to have a large return loss at their ports. Thus, the reflections from most sub-systems are very small and have little effect in the performance of the radar. Internal reflections of each subsystem are integrated into their system response. Thus, FMCW radar systems can be modeled using only the transmission (S_{21}) component of the S-parameters. We describe these systems using their frequency-domain response ($H(\omega)$) or their time-domain impulse response ($h(t)$). Figure 5.1.2 shows a block diagram of the FMCW radar in terms of the system response of each sub-system.

Time-domain multiplication (i.e. mixing) is an important process that is used in systems where frequency modulation or demodulation takes place. For the analysis of FMCW radars systems, we use the multiplication symbol ($\otimes$) to represent time-domain signal multiplication. Time-domain multiplication is also used in section 5.2.4, to model multiplicative noise. The de-chirping process of FMCW radar, which involves time-domain multiplication, is an important operation that defines some of the benefits and limitations of this type of radar. This process is described in section 5.1.2.

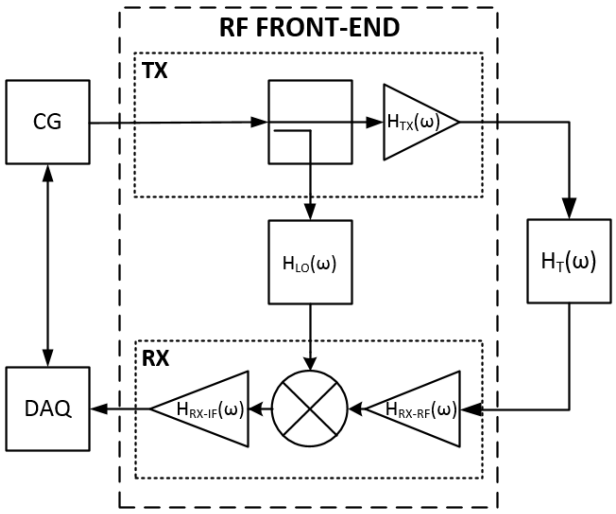

Figure 5.1.2 – System-Level FMCW Radar Block Diagram

5.1.1.5. Mixer System Model

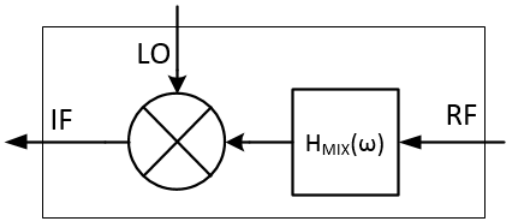

Figure 5.1.3 – Mixer System Model

The time-domain signal at the output of the RX-RF goes through a mixer, which performs the de-chirping operation. Figure 5.1.3 shows a system model for the mixer. This model describes the mixer as a system conformed of a linear operation and a time-domain multiplication operation. The linear operation is described by the system response $H_{MIX}(\omega)$, which accounts

for the conversion gain of the mixer. Mixer's conversion gain is usually less than one and its inverse is referred to as the conversion loss.

The second part of the mixer model accounts for the time-domain multiplication. This operation will be performed in a way that only the down-conversion components are kept and the up-converted terms are rejected. This is true in most mixers used for de-chirping since the up-conversion signals fall far outside of the IF maximum frequency. Moreover, the odd and even distortion products are also ignored. This applies for most mixers since the most mixer distortion products fall far outside the IF band. The distortion products that do fall inside the IF band are significantly rejected by a good mixer (>45 dB).

5.1.2. Linear Frequency Demodulation: De-Chirping

5.1.2.1. De-Chirping Definition

De-chirping is a frequency-domain pulse compression method, where a sum of delayed chirps are demodulated by a reference chirp. The reference chirp has the same chirp rate and usually the same frequency range than the delayed chirps.

For wideband chirps, this operation is performed by mixing the delayed chirps to a reference chirp. The high order components that were not removed by the mixer should be filter out at the IF stage. In narrow-band systems, IQ demodulation may be used instead.

We can model this operation by a multiplication followed by a filtering operation. Alternatively, de-chirping could be modeled as the time-domain multiplication of the complex conjugate of the delayed signals with a reference chirp in analytic and normalized form. This simpler operation

does not require the filtering stage. Here, we use this operation model for numerical simulation and for analytic modeling.

5.1.2.2. De-Chirping Operation

The de-chirping operation is the time-domain multiplication of the complex-conjugate of the signal to be de-chirped and the reference signal $v_{CGa}(t)$. The reference signal is the normalized (i.e. $|v_{CGa}(t)|^2 = 1$) and analytic form of the chirp generator output. The signal that is de-chirped in an FMCW radar is the signal at the RF port of the mixer ($v_{imx}(t)$) convolved with the mixer impulse response ($h_{MX}(t)$). This signal at the output of the de-chirping operation ($v_{di}(t)$) can be expressed by equation (5.1.1).

$$v_{di}(t) = v_{CGa}(t) \cdot [h_{MX}(t) * v_{imx}(t)]^* \tag{5.1.1}$$

In an ideal FMCW radar, the signal at the input of the RF port of the mixer $v_{imx}(t)$ is given by the convolution operation shown in (5.1.2), where $v_{CG}(t)$ is the output of the chirp generator and $h_{pi}(t)$ is the impulse response of the ideal signal path. The ideal signal path is the path between the chirp generator and the RF input of the mixer described by the block diagram in figure 5.1.2. From figure 5.1.2, the ideal signal path $h_{pi}(t)$ can be expanded as shown in (5.1.3). This signal path accounts for the system response of the transmitter ($h_{TX}(t)$), the receiver ($h_{RX}(t)$), and the radar response $h_T(t)$. The radar response is defined in chapter 3 as the system that accounts for the antenna target interactions and it is define using the coherent radar equation (5.1.4).

$$v_{imx}(t) = h_{pi}(t) * v_{CG}(t) \tag{5.1.2}$$

$$h_{pi}(t) = h_{RX-RF}(t) * h_T(t) * h_{TX}(t) \tag{5.1.3}$$

$$H_T(\omega) = [\Phi_{to}\Phi_{or}]\left[jkZ\eta\ \mathbf{f_r} \cdot \bar{\bar{\mathbf{F}}} \cdot \mathbf{f_t}\right] \tag{5.1.4}$$

5.1.2.3. De-Chirped Signal to Output Signal

The signal at the output of the receiver or input of the data-acquisition system that is related to the ideal signal path can be written as the convolution of the de-chirped signal $v_{di}(t)$ and the impulse response of the RX-IF ($h_{RX-IF}(t)$) (5.1.5).

$$v_{oi}(t) = h_{RX-IF}(t) * v_{di}(t) \tag{5.1.5}$$

Combining, the equation for the de-chirped operation (5.1.1) and (5.1.5), the ideal output signal results in (5.1.6). In terms of the ideal signal path, the ideal output signal results in (5.1.7). Expanding the ideal signal path, the ideal output signal yields (5.1.8). Equation (5.1.8) is the expression we use to simulate numerically the ideal output.

$$v_{oi}(t) = h_{RX-IF}(t) * \{v_{CGa}(t) \cdot [h_{MX}(t) *\ v_{imx}(t)]^*\} \tag{5.1.6}$$

$$v_{oi}(t) = h_{RX-IF}(t) * \left\{v_{CGa}(t) \cdot \left[h_{MX}(t) * h_{pi}(t) *\ v_{CG}(t)\right]^*\right\} \tag{5.1.7}$$

$$v_{oi}(t) = h_{RX-IF}(t) * \{v_{CGa}(t) \cdot [h_{MX}(t) * h_{RX-RF}(t) * h_T(t) * h_{TX}(t) *\ v_{CG}(t)]^*\} \tag{5.1.8}$$

5.1.2.4. PSD of De-Chirped Signal and Ideal Output

This section derives the spectrum and power spectral density (PSD) of the de-chirped signal and the ideal output of an FMCW radar.

The signal at the output of the chirp generator can be represented by the voltage signal $v_{CG}(t)$, expressed by (5.1.9). The reference signal is then given by (5.1.10). In (5.1.9-5.1.10), T is the chirp length, u is the chirp rate and v_{CGo} is the chirp amplitude. The chirp rate is defined as the ratio of the chirp bandwidth (B) to the chirp length (T), as shown in (5.1.11).

$$v_{CG}(t) = v_{CGo}\,\mathrm{rect}\left(\frac{t}{T}\right)\cdot e^{j2\pi\left(\frac{1}{2}ut^2\right)} \tag{5.1.9}$$

$$v_{CGa}(t) = \mathrm{rect}\left(\frac{t}{T}\right)\cdot e^{j2\pi\left(\frac{1}{2}ut^2\right)} \tag{5.1.10}$$

$$u = \frac{B}{T} \tag{5.1.11}$$

The time-averaged power of the chirp signal can be approximated by (5.1.12), where R_o is the output port characteristic impedance. The PSD of $v_{CG}(t)$ can be approximated by (5.1.13).

$$P_{CG} \approx \frac{|v_{CGo}|^2}{R_o} \tag{5.1.12}$$

$$S_{v_{CG}v_{CG}}(f) = S_{v_{CG}v_{CG}0}\,\mathrm{rect}\left(\frac{f}{B}\right) \tag{5.1.13}$$

$$S_{v_{CG}v_{CG}0} \approx \frac{P_{CG}}{B} = \frac{|v_{CGo}|^2}{R_o B} \tag{5.1.14}$$

As it was defined earlier, the de-chirped signal ($v_{di}(t)$) is given by (5.1.15). To short-hard notation, we use the term $h_{mxpi}(t)$ to represent the convolution of the impulse responses of the mixer ($h_{MX}(t)$) and the ideal signal path ($h_{pi}(t)$).

$$v_{di}(t) = v_{CGa}(t) \cdot \left[h_{mxpi}(t) * v_{CG}(t)\right]^* \tag{5.1.15}$$

$$h_{mxpi}(t) = h_{MX}(t) * h_{pi}(t) \tag{5.1.16}$$

Expanding the convolution sum of (5.1.15) in integral form yields (5.1.17). Replacing (5.1.9-5.1.10) into (5.1.17) results in (5.1.18). The integral in equation (5.1.18) is equivalent to the inverse Fourier transform of the impulse response ${h_{mxpi}}^*(\tau)$. Equation (5.1.18), is the time-domain de-chirped signal.

$$v_d(t) = \int d\tau \left\{v_{CGa}(t) \cdot \left[{h_{mxpi}}^*(\tau) \cdot {v_{CG}}^*(t-\tau)\right]\right\} \tag{5.1.17}$$

$$v_d(t) = v_{CGo}\ \mathrm{rect}\left(\frac{t}{T}\right) \int d\tau\ {h_{mxpi}}^*(\tau)\ e^{j2\pi u\tau t} \tag{5.1.18}$$

Taking the Fourier transform of (5.1.18), results in the spectrum of the de-chirped signal. The spectrum can be written in terms of the frequency or the roundtrip delay, as shown in (5.1.19) and (5.1.20), respectively. The relationship between the roundtrip delay and the frequency is given by (5.1.21). The spectrum of the de-chirped signal in (5.1.19) is proportional to the sinc pulse convolved by the system impulse response ${h_{mxpi}}^*(\tau)$. The 3 dB pulse width of the spectrum in (5.1.19) is $1/B$.

$$V_d(f) = v_{CGo}\ T\left[\ {h_{mxpi}}^*(\tau) * \mathrm{sinc}(B\tau)\ \right] \tag{5.1.19}$$

$$V_d(f) = v_{CGo}\, T \left[h_{mxpi}{}^{*}\left(\frac{f}{u}\right) * \operatorname{sinc}(Tf) \right] \tag{5.1.20}$$

$$\tau = \frac{f}{u} \tag{5.1.21}$$

The deterministic PSD of the de-chirped signal can be solved from (5.1.19) and it yields the expression in (5.1.22). This result shows that the PSD of the de-chirped signal has a pulse compression gain of BT.

$$S_{v_{di}v_{di}}(f) = \frac{1}{TR_o}|V_d(f)|^2 = BT \left| h_{mxpi}{}^{*}\left(\frac{f}{u}\right) * \operatorname{sinc}\left(B\frac{f}{u}\right)\right|^2 S_{v_{CG}v_{CG}0} \tag{5.1.22}$$

The ideal output signal is related to the de-chirped signal as shown in (5.1.23). Thus, the PSD of the ideal output signal can be results in (5.1.24) or (5.1.25).

$$v_{oi}(t) = h_{RX-IF}(t) * v_{di}(t) \tag{5.1.23}$$

$$S_{v_{oi}v_{oi}}(f) = |H_{RX-IF}(f)|^2\, S_{v_{di}v_{di}}(f) \tag{5.1.24}$$

$$S_{v_{oi}v_{oi}}(f) = BT\, |H_{RX-IF}(f)|^2 \left| h_{mxpi}{}^{*}\left(\frac{f}{u}\right) * \operatorname{sinc}\left(B\frac{f}{u}\right)\right|^2 S_{v_{CG}v_{CG}0} \tag{5.1.25}$$

The PSD of the ideal output signal in terms of the ideal signal path is given by (5.1.26). Expanding the ideal signal path, the PSD can be written as (5.1.27).

$$S_{v_{oi}v_{oi}}(f) = BT\, |H_{RX-IF}(f)|^2 \left|\left[h_{MX}\left(\frac{f}{u}\right) * h_{pi}\left(\frac{f}{u}\right)\right]^{*} * \operatorname{sinc}\left(B\frac{f}{u}\right)\right|^2 S_{v_{CG}v_{CG}0} \tag{5.1.26}$$

$$S_{v_{oi}v_{oi}}(f) = BT\,|H_{RX-IF}(f)|^2 \left|\left[h_{MX}\left(\frac{f}{u}\right) * h_{RX-RF}\left(\frac{f}{u}\right) * h_T\left(\frac{f}{u}\right) * h_{TX}\left(\frac{f}{u}\right)\right]^* * \operatorname{sinc}\left(B\frac{f}{u}\right)\right|^2 S_{v_{CG}v_{CG}0} \quad (5.1.27)$$

5.1.2.5. De-Chirping Benefits and Limitations

The de-chirping operation or linear frequency-demodulation is a powerful pulse compression method that can be achieved with microwave analog hardware. Since microwave circuitry allows much wider bandwidths than digital circuits, de-chirping can be performed on wideband and ultra-wideband FMCW radars while requiring modest sampling rates in their digitizers. This means that FMCW radars may provide fine range resolution measurements without requiring high sampling rates.

This section dealt with an ideal chirp generator output. In practice, the chirp generator has coherent and random phase noise. These types of noise may result in a degradation of the pulse width and it may degrade the signal-to-noise ratio of the FMCW radar output. This topic is discussed in section 5.2.

5.1.2.6. Comparison of De-Chirping Simulation and Analytic Solution

In order to test the performance of an FMCW radar, the output signal may be computed numerically or using the analytical solutions. The analytical solutions of the PSD of the output signal, as described in section 5.1.2.4, provide a faster and less computationally intensive method to evaluate the output signal. Analytic solutions also provide some insight into the shape and amplitude of the output signal. The drawbacks of the analytic solutions is that they use some approximations and their result represent the statistical average only. Numerical

simulations are more computationally intensive. However, they provide a more accurate result because they do not make analytical approximations. Numerical simulations also may be used to test single realizations of cases where random signals (e.g. noise) are involved. Analytical and numerical results of the FMCW output involving noise is discussed in section 5.2.

Numerical Simulation

From section 5.1.2.3, the output signal can be solved using (5.1.28) for a given chirp output signal, FMCW radar sub-system response and a given antenna-target system response. The operation described by (5.1.28) can be solved numerically. The spectrum and deterministic PSD of the output signal can be found using the Fast Fourier Transform algorithm, as shown by (5.1.29) and (5.1.30), respectively.

$$v_{oi}(t) = h_{RX-IF}(t) * \{v_{CGa}(t) \cdot [h_{MX}(t) * h_{RX-RF}(t) * h_T(t) * h_{TX}(t) * v_{CG}(t)]^*\} \quad (5.1.28)$$

$$V_{oi}(f) = V_{oi}(f = m\Delta f) = FFT\{v_{oi}(t = n\Delta t)\} \cdot \Delta f \quad (5.1.29)$$

$$S_{v_{oi}v_{oi}}(f) = \frac{1}{R_o T}|V_{oi}(f = m\Delta f)|^2 \quad (5.1.30)$$

Analytic Solution

The analytic solution of the ideal output signal was derived in section 5.1.2.4 and it is given by (5.1.31). This expression depends on the chirp signal, the impulse responses of the radar sub-systems and the time-domain radar response.

$$S_{v_{oi}v_{oi}}(f) = BT\ |H_{RX-IF}(f)|^2 \left|\left[h_{MX}\left(\frac{f}{u}\right) * h_{RX-RF}\left(\frac{f}{u}\right) * h_T\left(\frac{f}{u}\right) * h_{TX}\left(\frac{f}{u}\right)\right]^* * \operatorname{sinc}(B\tau)\right|^2 S_{v_{CG}v_{CG}0} \tag{5.1.31}$$

Simulation: Simple Target Example

We consider a signal at the output of the chirp generator expressed by (5.1.32). The center frequency of the chirp (f_o), chirp bandwidth (B) and chirp length (T) are 3.5 GHz, 1 GHz and 100 μs, respectively. The amplitude out of the chirp generator (v_{CGo}) was chosen to be $\sqrt{R_o B}$ so that the $S_{v_{CG}v_{CG}0}$ has unity over the chirp band. The reference signal is given by (5.1.34).

$$v_{CG}(t) = v_{CGo}\ \operatorname{rect}\left(\frac{t}{T}\right) \cdot e^{j2\pi\left(f_o t + \frac{1}{2}ut^2\right)} = \sqrt{R_o B}\ \operatorname{rect}\left(\frac{t}{T}\right) \cdot e^{j2\pi\left(f_o t + \frac{1}{2}ut^2\right)} \tag{5.1.32}$$

$$S_{v_{CG}v_{CG}}(f) = S_{v_{CG}v_{CG}0}\ \operatorname{rect}\left(\frac{f}{B}\right) = \operatorname{rect}\left(\frac{f}{B}\right) \tag{5.1.33}$$

$$v_{CGa}(t) = \operatorname{rect}\left(\frac{t}{T}\right) \cdot e^{j2\pi\left(f_o t + \frac{1}{2}ut^2\right)} \tag{5.1.34}$$

In this example, the main goal is to see how the original chirp is affected by the de-chirping process. So, the impulse responses of the radar sub-systems are simplified to be the delta function, as shown in (5.1.35).

$$h_{MX}(t) = h_{RX-RF}(t) = h_{TX}(t) = h_{RX-IF}(t) = \delta(t) \tag{5.1.35}$$

The system response of the radar response ($H_T(f)$) is given by the coherent radar equation. The antenna gain and scattering dyad are assumed to be such that $H_T(f)$ is given by (5.1.36). This system response results in an impulse response $h_t(t)$ equal to a delta pulse delayed τ_o, as given by (5.1.37). The delay of the pulse is the round-trip delay of the radiated signal from the transmitter antenna to the target and back to the receiver antenna. The target is assumed to be at 1.5 m away from the antennas, so that the roundtrip delay is 10 μs.

$$H_T(f) = jk\eta Z \Phi_r \Phi_t \mathbf{f} \cdot \bar{\bar{\mathbf{F}}} \cdot \mathbf{f} = e^{j2\pi\omega\tau_o} \tag{5.1.36}$$

$$h_t(t) = \delta(t - \tau_o) \tag{5.1.37}$$

Figure 5.1.4 shows the simulated PSD of the output of the chirp generator. The amplitude of this PSD over the chirp band is approximately 0 dB, as expected. This PSD can be approximated by a boxcar function centered at the chirp center frequency of 3.5 GHz and with a width equal to the chirp bandwidth of 1 GHz.

Figure 5.1.5 and figure 5.1.6 show the PSD of the ideal output signal of the receiver. The de-chirped signal is a sinc pulse centered at 100 MHz and with a peak amplitude of 50 dBm/Hz. Figure 5.1.6 shows that both the numerical simulation and the analytic solution agree with each other. This means that the analytic solution predicts accurately the shape, size and center frequency of the output signal's PSD. This simulation also shows how a chirp with a PSD of 0 dBm/Hz over its band results in an output signal with a peak amplitude of 50 dBm/Hz, where the pulse compression gain is (BT) is 50 dB.

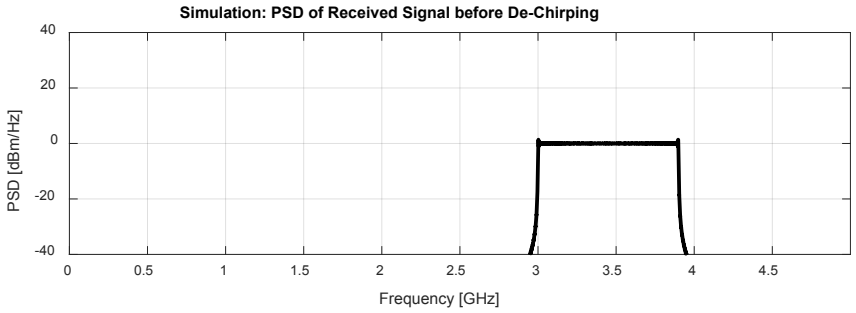

Figure 5.1.4 – PSD of Chirp Generator Output

This simulation also demonstrates how the wide bandwidth of the original chirp can be compressed by the de-chirping process. Since de-chirping can be performed with analog hardware, chirps with wide bandwidths may be used by FMCW radars with modest ADC sampling rates.

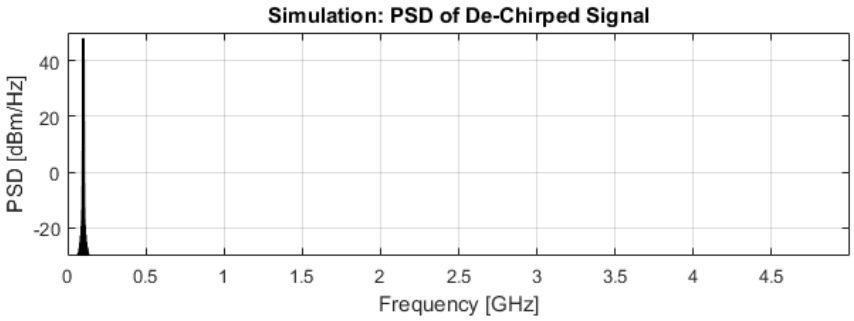

Figure 5.1.5 – PSD of Ideal Output Signal

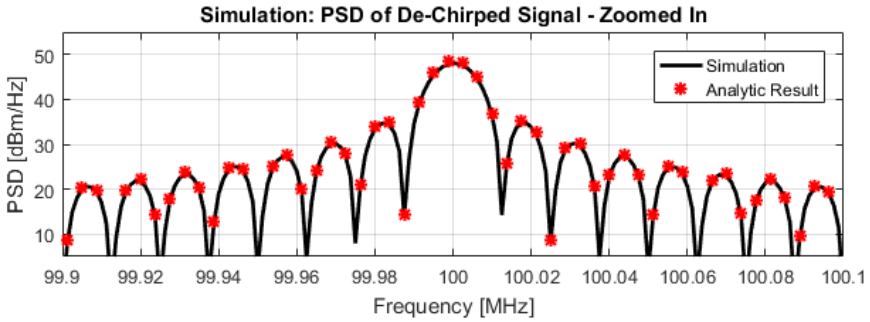

Figure 5.1.6 - PSD of Ideal Output Signal

5.2. FMCW RADAR ANALYSIS: Self-Interference and Noise

Section 5.1.2 described the de-chirping process and provided expressions to solve for the ideal output signal of an FMCW radar, analytically or numerically. This output was referred to as the ideal output because it is the result of an ideal input chirp in the absence of noise or interference. In practice, the chirp signal is corrupted by multiplicative noise, and the output signal includes content related to interference signals and noise. This section discusses the most important sources of noise and interference in FMCW radars. This section also provides expressions to compute the PSD of the signal content related to noise and interference.

The most important types of noise in an FMCW radar are quantization noise, additive thermal noise and phase noise of the chirp generator. The most significant self-interference signals are the ones related to the antenna feed-through and the mixer LO leakage.

Figure 5.2.1 shows a block diagram of an FMCW radar including noise sources and self-interference paths. In the block diagram, the bottom left and bottom right show where quantization noise $v_q(t)$ and thermal noise ($v_n(t)$) are added to the system, respectively. Quantization and thermal noise are described in section 5.2.2 and 5.2.3, respectively. Phase noise at the output of the chirp generator is modeled as multiplicative noise applied to the ideal chirp output, as shown at the top left of the diagram. The system block represented by the system response $H_F(\omega)$ represents the antenna feedthrough and it is part of one of the self-interference paths. The system response $H_{LL}(\omega)$ accounts for the LO leakage system response between the LO signal and the input of the mixer. This system response is part of the second self-interference path. Both interference paths are discussed in section 5.2.1.

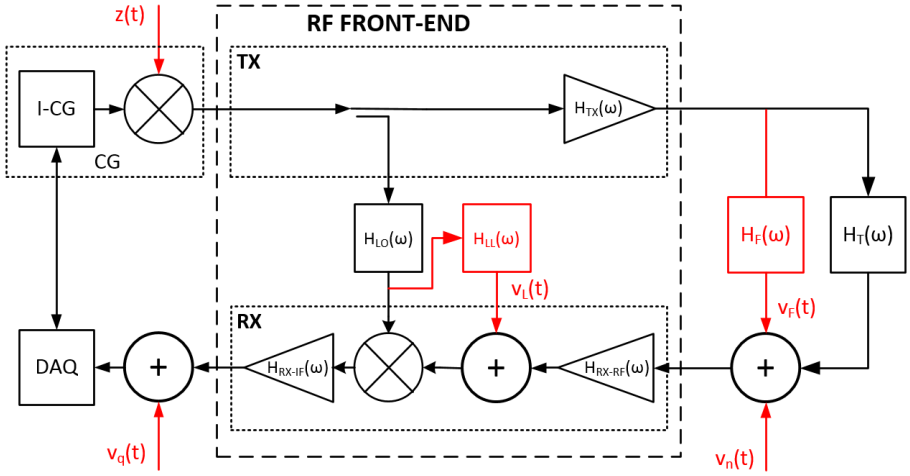

Figure 5.2.1 – System-Level of FMCW radar with Noise and Interference

Taking into account noise sources and self-interference signals, the output signal of the FMCW radar is given by (5.2.1). In (5.2.1), $v_o(t)$ is the total output signal, $v_{oi}(t)$ is the ideal output signal, $v_{os1}(t)$ is the self-interference signal related to antenna feed-through, $v_{os2}(t)$ is the self-interference signal related to the LO leakage, $v_{otn}(t)$ is the output signal related to thermal noise and $v_{oqn}(t)$ is the output signal related to quantization noise (5.2.1).

$$v_o(t) = v_{oi}(t) + v_{os1}(t) + v_{os2}(t) + v_{otn}(t) + v_{oqn}(t) \tag{5.2.1}$$

5.2.1. Self-Interference Paths

The self-interference signals in an FMCW radar are the signals at the receiver output that stem from the chirp generator and are different from the ideal signal path. The two most significant self-interference paths in an FMCW are the paths related to the antenna feedthrough and the mixer LO leakage. The phase noise of these self-interference signals contribute significantly to the overall noise of the FMCW radar system. Thus, a proper understanding of the self-interference paths is useful for the analysis and design of FMCW radars.

Figure 5.2.2 shows the ideal signal path and the two self-interference signal paths considered in this section. The ideal signal path is depicted in green. The self-interference signal paths related to the antenna-feedthrough and the LO leakage are shown with blue and purple arrow, respectively.

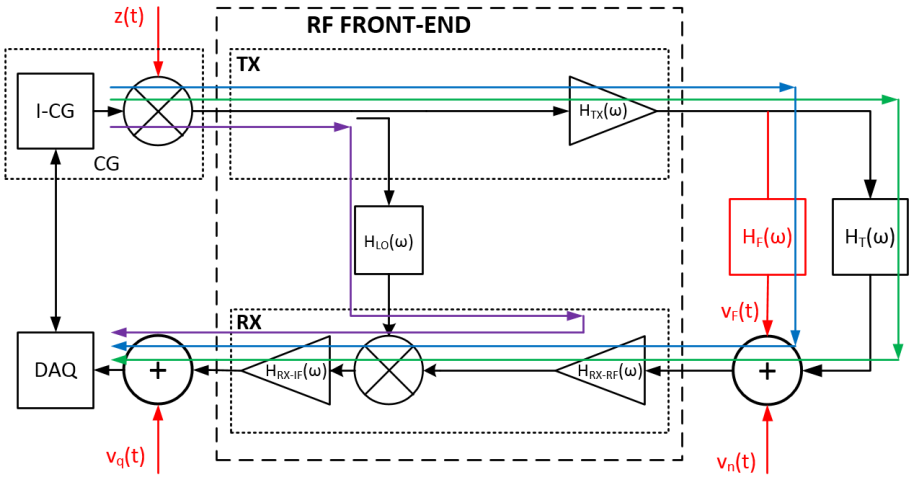

Figure 5.2.2 – FMCW Radar Block Diagram: Signal Paths. Ideal (Green); Antenna Feedthrough (Blue); LO leakage (Purple)

As described by equation (5.2.1), the components of the total output signal $v_o(t)$ related to the self-interference paths are the self-interference signals $v_{os1}(t)$ and $v_{os2}(t)$. Specifically, the

terms $v_{os1}(t)$ and $v_{os2}(t)$ account for the self-interference paths related to the antenna feedthrough and the LO leakage.

From section 5.1.2, the output of the ideal signal in terms of the ideal signal path is given by (5.2.2). The ideal signal path ($h_{pi}(t)$) is the path between the chirp generator output and the input of the RF port of the mixer, which goes through the radar response.

$$v_{oi}(t) = h_{RX-IF}(t) * \left\{ v_{CGa}(t) \cdot \left[h_{MX}(t) * \ h_{pi}(t) * v_{CG}(t) \right]^* \right\} \tag{5.2.2}$$

Both self-interference paths start at the chirp generator and reach the RF port of the mixer. Thus, we can define the output signals related to both self-interference paths ($v_{os1}(t)$ and $v_{os2}(t)$) in terms of their signal paths between the chirp generator and the mixer input. These output signals are given in (5.2.3) and (5.2.4) for the self-interference paths related to the antenna feedthrough and LO leakage, respectively.

$$v_{os1}(t) = h_{RX-IF}(t) * \left\{ v_{CGa}(t) \cdot \left[h_{MX}(t) * \ h_{p1}(t) * v_{CG}(t) \right]^* \right\} \tag{5.2.3}$$

$$v_{os2}(t) = h_{RX-IF}(t) * \left\{ v_{CGa}(t) \cdot \left[h_{MX}(t) * \ h_{p2}(t) * v_{CG}(t) \right]^* \right\} \tag{5.2.4}$$

5.2.1.1. Antenna Feedthrough Signal Path

The antenna feedthrough is the part of the radiated signal by the transmit antenna that is directly captured by the receiver antenna, without interacting with the desired target. The antenna feedthrough system is represented in figure 5.2.2 by $H_F(\omega)$. This system accounts for the antenna gain, propagation losses and any interactions between the two. From the block diagram of figure 5.2.2, the impulse response of this self-interference path is given by (5.2.5).

$$h_{p1}(t) = h_{RX-RF}(t) * h_F(t) * h_{TX}(t) \quad (5.2.5)$$

5.2.1.2. LO Leakage Signal Path

The LO leakage is the part of the LO signal (i.e. signal at the LO port of the mixer) that leaks to the RF port of the mixer and is reflected by the output of the RX-RF. In figure 5.2.3, the LO leakage is represented by a system $H_{LL}(\omega)$. This system response accounts for the LO-RF leakage in the mixer and the reflection at the output of the RX-RF. This self-interference path from the chirp generator output to the RF input of the mixer is represented by the impulse response $h_{p2}(t)$.

$$h_{p2}(t) = h_{LL}(t) * h_{LO}(t) \quad (5.2.6)$$

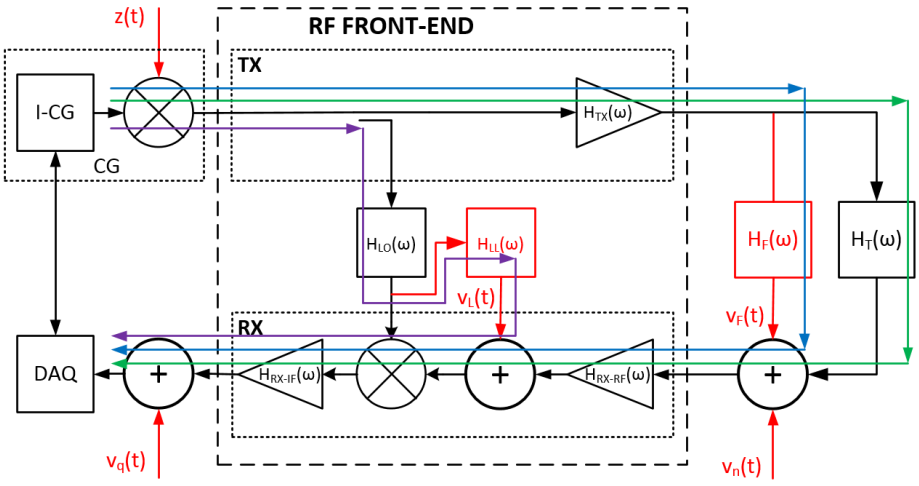

Figure 5.2.3 – FMCW Radar Block Diagram: Signal Paths. Ideal Path (Green); Antenna-Feedthrough Path (Blue); LO Leakage Path (Purple)

5.2.2. ADC Quantization Noise

The ADC of the DAQ has a maximum voltage range and a finite number of bits used to encode the digitized signal. The voltage range is the difference of the maximum to the minimum voltages of the ADC input. The ADC voltage resolution (δv_q) is the ratio of the voltage range (v_{q_range}) to the number of possible values (2^b). The quantization noise is additive white Gaussian noise, which is added to the ideal digitized signal. It can be shown that the root-mean-square (RMS) voltage of the quantization noise (v_{qn_rms}) is equivalent to the voltage resolution, as given by (5.2.7).

$v_{qn\_rms} = \delta v_q = v_{q\_range}/2^b$	(5.2.7)

Given the RMS voltage of the quantization noise, the time-average power is given by the expression (5.2.8). In (5.2.8), R_o is the ADC port input impedance.

$P_{qn} = \frac{1}{R_o} {v_{qn\_rms}}^2 = \frac{\left(v_{q\_range}/2^b \right)^2}{R_o}$	(5.2.8)

Since the quantization noise is band-limited white noise, its power spectral density is given by (5.2.9), in which B_n is the noise bandwidth. The noise bandwidth of the ADC is the sampling rate.

$$S_{v_{qn}v_{qn}} = \frac{P_{qn}}{B_n} = \frac{\left(v_{q\_range}/2^b \right)^2}{R_o B_n} \tag{5.2.9}$$

The maximum voltage also determines the maximum power of a sinusoid that can be digitized by the ADC without distortion. This maximum power is given by (5.2.10).

$$P_{q\_max} = \frac{v^2{}_{q\_max}}{2 \cdot R_o} \tag{5.2.10}$$

5.2.3. Additive Thermal Noise

5.2.3.1. Antenna Thermal Noise

The thermal noise or Johnson-Nyquist noise is the noise that is generated by thermal agitation of charge carriers inside an electronic device. The thermal noise produced by a resistor at microwave frequency is additive Gaussian noise. At the microwave region of the electromagnetic spectrum, this noise behaves as white noise.

The power spectral density of the thermal noise produced across the resistor with temperature T_R is given by (5.2.11), where k_b is the Boltzmann's constant. If the noise power across this resistor is measured at some microwave frequency range with noise bandwidth B_n, the time-averaged power of the noise across the resistor is given by (5.2.12). If the resistance of this resistor is R_o, the RMS noise voltage across the resistor with given by (5.2.13). To derive (5.2.13), we used the relation in (5.2.14).

$$S_{rn}(f) = 4\, k_b T_R \tag{5.2.11}$$

$$P_{rn} = 4\, k_b T_R B_n \tag{5.2.12}$$

$$v_{rn\_rms} = 2\sqrt{k_b T_R B R_o} \tag{5.2.13}$$

$$P_{rn} = \frac{1}{R_o} v_{rn\_rms}{}^2 \tag{5.2.14}$$

If the electrodes across the resistor are connected to another device with input resistance R_o, then, by voltage division, half of the noise voltage is transferred to the device. In this case, the power spectral density, average power and RMS voltage of the thermal noise transferred to the device are given by (5.2.15), (5.2.16) and (5.2.17), respectively.

$$S_{tn}(f) = k_b T_R \tag{5.2.15}$$

$$P_{tn} = k_b T_R B \tag{5.2.16}$$

$$v_{tn\_rms} = \sqrt{k_b T_R B R_o} \tag{5.2.17}$$

The antenna thermal noise is the noise captured by an antenna from the environment that would be transferred to a system with matched input impedance connected to the antenna. The antenna temperature is the equivalent resistor temperature T_R that would transfer the power spectral density in (5.2.15). Similarly, the antenna thermal noise has RMS voltage and average power given by (5.2.17, 5.2.15), where R_o is the antenna resistance and B is the antenna bandwidth.

5.2.3.2. Receiver Processing of Thermal Noise

The receiver subsystem is the device that is connected to the receiver antenna, assuming that the transmission line connected to the antenna is considered part of the receiver. The receiver processes the input signal of interest and the input noise. During this step, the receiver also adds its internally generated thermal noise. For a given input noise, the noise addition can be

casted as a linear operation on the transfer function that the receiver applies to the input noise. Thus, the receiver can be characterized as having two different transfer functions, one for the signal of interest and one for the noise. In other words, the receiver is characterized by a transfer function ($H_{RX}(f)$) that is applied to the signal of interest, as shown in (5.2.18), and a modified transfer function ($\left[|F_{RX}(f)|^{1/2} H_{RX}(f)\right]$) that is applied to the input noise, as shown in (5.2.19). The term $|F_{RX}|^{1/2}$ is a factor that modifies the receiver's original transfer function. The term $F_{RX}(f)$ is called the receiver's noise figure.

$$V_{s_{out}}(f) = H_{RX}(f)\, V_{s\_in}(f) \tag{5.2.18}$$

$$V_{n_{out}}(f) = \left[|F_{RX}(f)|^{1/2}\, H_{RX}(f)\right] V_{n\_in}(f) \tag{5.2.19}$$

The noise figure of a device is defined for a given input noise temperature. The noise figure of a device with equivalent temperature T_e at an input temperature T_{in} is given by (5.2.20). Typically, RF devices are characterized with a noise figure at the input noise temperature of 290 degrees, which is the IEEE standard for room temperature.

$$F = 1 + \frac{T_e}{T_{in}} \tag{5.2.20}$$

The noise figure of a receiver made out of cascaded RF devices is given by (5.2.21), where $F_i(f)$ and $H_i(f)$ are the noise figure and transfer function of 'i^{th}' device, respectively. The overall transfer function of the receiver that is applied to the input signal of interest is given by (5.2.22).

$$F_{RX}(f) = F_1(f) + \frac{F_2(f) - 1}{|H_1(f)|^2} + \frac{F_3(f) - 1}{|H_1(f)|^2 |H_2(f)|^2} + \frac{F_4(f) - 1}{|H_1(f)|^2 |H_2(f)|^2 |H_3(f)|^2} + \cdots \tag{5.2.21}$$

$$H_{RX}(f) = H_1(f)H_2(f)H_3(f)H_4(f) \ldots \quad (5.2.22)$$

The average PSD, time-average power and the RMS voltage of the thermal noise at the output of the receiver are given by (5.2.23), (5.2.24) and (5.2.25), respectively.

$$S_{tn\_out}(f) = k_b T_0 \, F_{RX} |H_{RX}|^2 \quad (5.2.23)$$

$$P_{tn\_out} = k_b T_0 B \, F_{RX} |H_{RX}|^2 \quad (5.2.24)$$

$$v_{tn\_rms\_out} = \sqrt{k_b T_0 B R_o F_{RX}} \, |H_{RX}| \quad (5.2.25)$$

In an FMCW radar, the RF part of the RX (i.e. the RX-RF) is composed of cascaded RF components. So that equations (5.2.23), (5.2.24) and (5.2.25) may be used for the RF part of the receiver. The next section discusses the effect of de-chirping on thermal noise.

5.2.3.3. Effect of De-Chirping on Thermal Noise

The previous section provides expressions for the noise PSD, RMS voltage and time-average power at the output of a receiver made up of linear systems. Therefore, we can use such expressions to compute these noise levels at the output of the RX-RF. However, it does not provide an expression for the effect of the de-chirping operation at the mixer, which is a non-linear process. This section describes the effect de-chirping on thermal noise.

The output signal of an FMCW due to additive noise at the antenna is given by (5.2.26). In (5.2.26), $h_{RX-IF}(t)$, $h_{MX}(t)$ and $h_{RX-RF}(t)$ are the impulse responses of the RX-IF, mixer and RX-RF, respectively. $v_{CGa}(t)$ is the chirp generator signal in analytic and normalized form. $v_n(t)$ is the additive noise random signal.

$$v_{on}(t) = h_{RX-IF}(t) * \{v_{CGa}(t) \cdot [h_{MX}(t) * h_{RX-RF}(t) * \ v_n(t)]^*\} \tag{5.2.26}$$

To simplify notation, we define the signal $v_r(t)$ as given by (5.2.27). The output of the mixer or de-chirped signal $v_d(t)$ is given by (5.2.28).

$$v_r(t) = h_{MX}(t) * h_{RX-RF}(t) * \ v_n(t) \tag{5.2.27}$$

$$v_d(t) = v_{CGa}(t) \cdot v_r(t)^* \tag{5.2.28}$$

The output of the RX-RF can be expressed as a product of a baseband or envelope function $z(t)$, which is band-limited, and a complex sinusoid with frequency equal to the RX-RF center frequency. This expression is given in (5.2.29).

$$v_r(t) = \ z(t)e^{j2\pi f_o t} \tag{5.2.29}$$

The LO signal, which is the normalized and analytic form of the output of the CG, is given by (5.2.30) and (5.2.31). The term $x(t)$ is the complex envelope of the chirp that was factored out for convenience.

$$v_{CGa}(t) = \text{rect}\left(\frac{t}{T}\right) \cdot e^{j2\pi\left(f_o t + \frac{1}{2}ut^2\right)} = x(t) \cdot e^{j2\pi f_o t} \tag{5.2.30}$$

$$x(t) = \text{rect}\left(\frac{t}{T}\right) \cdot e^{j\pi u t^2} \tag{5.2.31}$$

Replacing (5.2.29) and (5.2.30) into (5.2.28), results in the expression in (5.2.32) for the de-chirped signal.

$$v_d(t) = x(t) \cdot z^*(t) \tag{5.2.32}$$

If the input of the receiver is a random signal, that is Gaussian and white over the RX-RF band, the envelope of the RX-RF output will be band-limited white at baseband and Gaussian. Since, the envelope of the noise ($z(t)$) is uncorrelated to the baseband chirp ($x(t)$), the average-autocorrelation of the de-chirped signal $\langle R_{v_d v_d}(\tau)\rangle$ is given by the product of the average-autocorrelation of the baseband noise and the autocorrelation of the baseband chirp, as given in (5.2.33). In (5.2.33), the symbol "⟨ ⟩" represents ensemble average.

$$\langle R_{v_d v_d}(\tau)\rangle = \langle R_z(\tau)\rangle \cdot R_{xx}(\tau) \tag{5.2.33}$$

In (5.2.33), the autocorrelation functions are written in terms of only one time variable (τ). This is because the noise is assumed to be WSS and the autocorrelation of the baseband chirp only depends on one time variable as shown below. In (5.2.34), we expand the autocorrelation function of the baseband chirp $x(t)$. For values of τ much smaller than T, the autocorrelation can be given by (5.2.35), or (5.2.36). Since $R_x(\tau)$ only depends on τ, the (deterministic) PSD of $x(t)$ is given by the Fourier transform of $R_x(\tau)$. The PSD of $x(t)$ is shown in (5.2.37).

$$R_{xx}(t, t+\tau) = \frac{1}{TR_o}\int dt\ x(t)x^*(t-\tau) \tag{5.2.34}$$

$$R_{xx}(\tau) = \frac{1}{TR_o}\int_{-T/2}^{T/2} dt\ e^{j2\pi u(-\frac{1}{2}\tau^2 + t\cdot\tau)} = \frac{1}{TR_o}\ e^{-j\pi u\tau^2}[\,T\,\mathrm{sinc}(B\tau)] \tag{5.2.35}$$

$$R_{xx}(\tau) \approx \frac{1}{R_o}\mathrm{sinc}(B\tau) \tag{5.2.36}$$

$$S_{xx}(f) \approx \frac{1}{R_o B} rect\left(\frac{f}{B}\right) \tag{5.2.37}$$

Assuming a flat frequency response of the RX-RF over its band, the average-autocorrelation function and average-PSD of the baseband noise $z(t)$ are given by (5.2.38-5.2.39). The RMS voltage of $z(t)$ is given by (5.2.40). In (5.2.40), $G_{RX-RF/MX}$ and $F_{RX-RF/MX}$ are the combined gain and noise figure of the RF-RX and mixer, respectively. In (5.2.40), B_n is the noise bandwidth, which is equal to the chirp bandwidth at the output of the RX-RF.

$$\langle R_{zz}(\tau) \rangle = \left(\frac{{v_{z\_rms}}^2}{R_o}\right) \operatorname{sinc}(B\tau) \tag{5.2.38}$$

$$\langle S_{zz}(f) \rangle = k_b T_o G_{RX-RF/MX} F_{RX-RF/MX} \ \operatorname{rect}\left(\frac{f}{B}\right) \tag{5.2.39}$$

$$v_{z\_rms} = \sqrt{k_b T_o G_{RX-RF/MX} F_{RX-RF/MX} B_n R_o} \tag{5.2.40}$$

The average PSD of $\langle R_{v_d v_d}(\tau) \rangle$ can be found by taking its Fourier Transform and it is given by (5.2.41).

$$\langle S_{v_d v_d}(\tau) \rangle = \langle S_{zz}(-f) \rangle * S_{xx}(f) \tag{5.2.41}$$

Replacing (5.2.37) and (5.2.39) into (5.2.41) yields (5.2.42). Assuming that the frequency response of all sub-systems are flat, the PSD of the additive noise component of the output is approximated to (5.2.43). This expression can further approximated to (5.2.44) for frequencies much smaller than the chirp bandwidth.

$$\langle S_{v_d v_d}(\tau)\rangle = k_b T_o G_{RX-RF/MX} F_{RX-RF/MX}\, tri(f/B) \quad (5.2.42)$$

$$\langle S_{v_{no} v_{no}}(f)\rangle \approx k_b T_o F_{RX}\, G_{RX}\, tri(f/B) \quad (5.2.43)$$

$$\langle S_{v_{no} v_{no}}(f)\rangle \approx k_b T_o F_{RX}\, G_{RX} \qquad for \quad (f \ll B) \quad (5.2.44)$$

The RMS voltage at the output due to thermal noise is given by (5.2.45). If the bandwidth of the RX-IF is larger or equal to the chirp bandwidth the noise bandwidth is equal to the chirp bandwidth. Otherwise, the noise bandwidth is equal to the RX-IF bandwidth.

$$v_{no\_rms} = \sqrt{k_b T_o G_{RX} F_{RX} B_n R_o} \quad 5.2.45)$$

Similarly, the time-average output power due to thermal noise is given by (5.2.46).

$$P_{no} = k_b T_o G_{RX} F_{RX} B_n \quad (5.2.46)$$

This analysis shows the following three points about the effect of de-chirping operation on thermal noise.

- De-chirping shifts the frequency of the noise content from $(fo - \frac{B}{2}, fo + \frac{B}{2})$ to $(-B, +B)$.
- De-chirping modifies the shape of the noise average-PSD, from a rectangular function to a triangular function.
- The peak of the average-PSD of noise is not changed by de-chirping.

5.2.3.4. FMCW Radar Simulation: Thermal Noise Only

In order to test the analytic expressions for the average-PSD of the noise found above, we compare solutions of these analytic expressions against numerical simulations.

In this simulation, the input to an FMCW receiver is thermal noise. This noise is assumed white and Gaussian. The antenna equivalent temperature is 290 K, so that the PSD of noise at the input of the receiver is -174 dBm/Hz.

For this simulation, we use a total receiver gain and a noise figure of 50 dB and 10 dB, respectively. Two approximations were given above for the PSD at the output due to thermal noise. These first and second approximations are shown again in (5.2.47) and (5.2.48), respectively. For this simulation the value of $S_{v_{no}v_{no}0}$ is -114 dBm/Hz.

$$S_{v_{no}v_{no}}(f) = S_{v_{no}v_{no}0}\, tri\left(\frac{f}{B}\right) \tag{5.2.47}$$

$$S_{v_{no}v_{no}}(f) \approx S_{v_{no}v_{no}0} \qquad for \quad (f \ll B) \tag{5.2.48}$$

$$S_{v_{no}v_{no}0} = k_b T_o F_{RX}\, G_{RX} = -114 \text{ dBm/Hz} \tag{5.2.49}$$

Figure 5.2.4 and figure 5.2.5 show plots of the simulated PSD of the output of an FMCW radar due to thermal noise compared against the two analytical approximations, given above. In figure 5.2.4, the RX-IF bandwidth used in the simulation was larger than the chirp bandwidth. In figure 5.2.5, the cutoff frequency of the RX-IF is 50 MHz. In Fig. 2.2.4, the first approximation agrees well with the simulation over the entire band. The second approximation is only accurate for low output frequencies, as expected. In the second figure (Fig. 2.2.5), the cut-off frequency of the IF is much smaller than the chirp bandwidth, so that both approximations agree well with the numerical simulation.

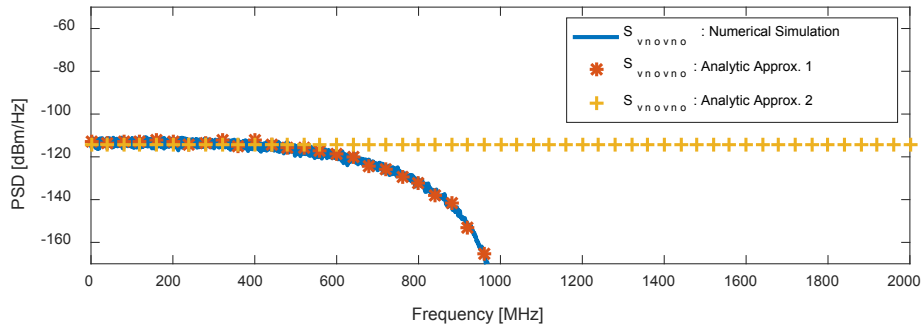

Figure 5.2.4 – FMCW Radar Simulation: Additive Thermal Noise – IF Bandwidth larger than chirp bandwidth

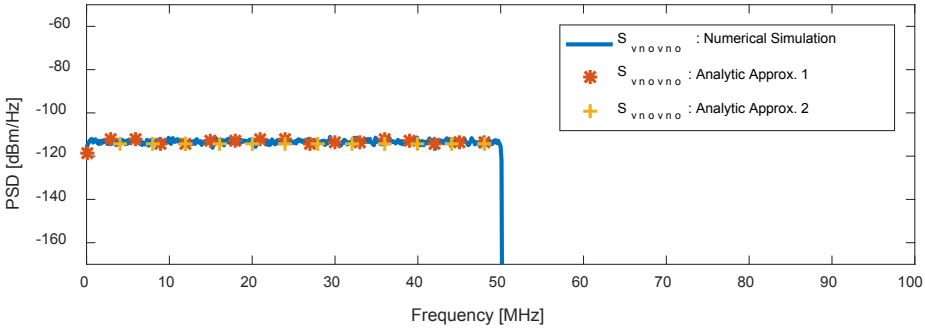

Figure 5.2.5 – FMCW Radar Simulation: Additive Thermal Noise – 50 MHz IF Bandwidth

5.2.4. Phase Noise

Up to this point, it was assumed that the chirp generator outputs an ideal chirp, as given by (5.2.50). In reality, the output of the chirp contains undesired amplitude and phase modulation due to random and coherent sources. This undesired modulation can be modeled as a multiplication to the ideal chirp, as shown by (5.2.51) and (5.2.52). For this reason, this type of noise, coherent or not, is referred to as multiplicative noise.

$$v_{CGi}(t) = \text{rect}(t/T)\, e^{j2\pi\left(f_o t + \frac{1}{2}ut^2\right)} \tag{5.2.50}$$

$$v_{CG}(t) = z(t)\, v_{CGi}(t) \tag{5.2.51}$$

$$z(t) = [1 + A(t)]\, e^{j\varphi(t)} \tag{5.2.52}$$

Random amplitude-multiplicative noise ($A(t)$) is small and usually not an issue. Coherent amplitude-multiplicative noise can be compensated at the IF in post-processing. Thus, amplitude-multiplicative noise is not considered a problem in FMCW radars.

In this section, the power spectral density (PSD) of the de-chirped signal is solved when phase noise is present. Simulations results are provided to verify the analytic solutions and to illustrate the effect of phase noise of the chirp to the output noise performance of the radar.

5.2.4.1. PSD of output signal due to chirp with phase noise

Coherent and incoherent phase noise may be present at the chirp signal. This type of noise is present at the output signal related to the desired target and at the output signals related to self-interference paths. Phase noise degrades the performance of the impulse response. It may also degrade the signal to noise ratio if the self-interference signals are significantly large. In this section, the PSD of the output signal is derived when phase noise is present at the chirp.

From section 5.1.2, the output signal of an FMCW radar due to its signal $v_{CG}(t)$ is given by (5.2.53). In (5.2.53), $h_{RX-IF}(t)$, $h_{MX}(t)$ and $h_{pk}(t)$ are the impulse response of the RX-IF, RF part of mixer and the signal path between the chirp generator and RF port of the mixer, respectively. This signal path may be the target related path or any other self-interference path. The term $v_{CGa}(t)$ is the reference signal, which is the normalized and analytic form of the chirp signal.

$$v_{ok}(t) = h_{RX-IF}(t) * \left\{ v_{CGa}(t) \cdot \left[h_{MX}(t) * h_{pk}(t) * \ v_{CG}(t) \right]^{*} \right\} \tag{5.2.53}$$

The chirp signal with phase noise $v_{CG}(t)$ can be expanded in terms of the ideal chirp signal $v_{CGi}(t)$ and the multiplicative noise term $z(t)$, as shown in (5.2.24). Similarly, it can be expanded in terms of the multiplicative noise, normalized ideal chirp signal $v_{CGni}(t)$ and the chirp amplitude v_{CGo}. The reference chirp with phase noise is given by (5.2.55). The multiplicative noise is given in (5.2.56), where $\varphi(t)$ is the instantaneous phase noise. The instantaneous phase noise is a random variable with autocorrelation function $R_{\varphi\varphi}(\tau)$ and power spectral density $S_{\varphi\varphi}(f)$. In this section, we assume that the phase noise is wide-sense stationary.

$$v_{CG}(t) = \ z(t)\ v_{CGi}(t) = v_{CGo}\ z(t)\ v_{CGni}(t) \tag{5.2.54}$$

$$v_{CGa}(t) = v_{CGo}\, z(t)\, v_{CGni}(t) \tag{5.2.55}$$

$$z(t) = e^{j\varphi(t)} \tag{5.2.56}$$

Replacing the chirp in (5.2.54) to equation (5.2.53), the output signal may be written as (5.2.57). In (5.2.57), we use the impulse response $h_{mxpk}(t)$, defined in (5.2.58), to simplify notation.

$$v_{ok}(t) = v_{CGo}\, h_{RX-IF}(t) * \left\{ z(t)\, v_{CGni}(t) \cdot \left[h_{mxpk}(t) * z(t)\, v_{CGni}(t) \right]^* \right\} \tag{5.2.57}$$

$$h_{mxpk}(t) = h_{mx}(t) * h_{pk}(t) \tag{5.2.58}$$

Expanding the convolution operation of (5.2.57) in integral form yields (5.2.59).

$$v_{ok}(t) = v_{CGo}\, h_{RX-IF}(t) * \int d\tau \left\{ h_{mxpk}(\tau)\, v_{CGni}(t) v_{CGni}{}^*(t-\tau) \cdot z_c(t) \right\} \tag{5.2.59}$$

The term $z_c(t)$ in (5.2.59) is defined in (5.2.60). Using the small angle approximation, $z_c(t)$ can be expressed as shown in (5.2.61).

$$z_c(t) = z(t)z^*(t-\tau) = e^{j[\varphi(t)-\varphi(t-\tau)]} = \cos[\varphi(t)-\varphi(t-\tau)] + j\sin[\varphi(t)-\varphi(t-\tau)] \tag{5.2.60}$$

$$z_c(t) \approx 1 + j[\varphi(t)-\varphi(t-\tau)] \tag{5.2.61}$$

The (expected) autocorrelation function of the random variable z_c is defined by (5.2.62) or (5.2.63). Solving for (5.2.63) yields the expression in (5.2.64). By the Wiener-Khintchine theorem (WKT), the PSD of z_c is found by taking the Fourier transform of $R_{z_c z_c}(\tau)$ and it is shown in (5.2.65).

$$R_{z_c z_c}(\tau') = E\{z_c(t) z_c{}^*(t-\tau')\} \tag{5.2.62}$$

$$\begin{aligned} R_{z_c z_c}(\tau') = E\{1 + j[\varphi(t) - \varphi(t-\tau') + \varphi(t-\tau-\tau') - \varphi(t-\tau)] \\ + [\varphi(t)\varphi(t-\tau') - \varphi(t)\varphi(t-\tau-\tau') - \varphi(t-\tau)\varphi(t-\tau') \\ + \varphi(t-\tau)\varphi(t-\tau-\tau')]\} \end{aligned} \tag{5.2.63}$$

$$R_{z_c z_c}(\tau') = 1 + 2R_{\varphi\varphi}(\tau') - \left[R_{\varphi\varphi}(\tau-\tau') + R_{\varphi\varphi}(\tau+\tau')\right] \tag{5.2.64}$$

$$S_{z_c z_c}(f) = \delta(f) + 2S_{\varphi\varphi}(f)[1 - \cos(2\pi\tau f)] \tag{5.2.65}$$

Since the multiplicative noise is independent of the chirp, the autocorrelation function of the output signal may be written as given by (5.2.66). In (5.2.66), $R_{v_{oik} v_{oik}}(\tau')$ is the autocorrelation function of the output signal v_{oik}, which is due to an ideal chirp ($v_{CGi}(t)$) and signal path $h_{pk}(t)$. The PSD of the output signal becomes (5.2.67), by the WKT.

$$R_{v_{ok} v_{ok}}(\tau') \approx R_{v_{oik} v_{oik}}(\tau')\, R_{z_c z_c}(\tau') \tag{5.2.66}$$

$$S_{v_{ok} v_{ok}}(f) \approx S_{v_{oik} v_{oik}}(f) * S_{z_c z_c}(f) \tag{5.2.67}$$

From section 5.1.2, the PSD of the output signal v_{oik} is given by (5.2.68).

$$S_{v_{oik} v_{oik}}(f) = |H_{RX-IF}(f)|^2 BT \; S_{v_{CG} v_{CG}0} \left| h_{mx}\left(\frac{f}{u}\right) * h_{pk}\left(\frac{f}{u}\right) * \operatorname{sinc}(Tf) \right|^2 \tag{5.2.68}$$

The PSD of the output signal v_{ok} yields (5.2.69).

$$S_{v_{ok}v_{ok}}(f) = |H_{RX-IF}(f)|^2\ BT\ \ S_{v_{CG}v_{CG}0}\ \left|h_{mx}\left(\frac{f}{u}\right) * h_{pk}(\frac{f}{u}) * \mathrm{sinc}(Tf)\right|^2 \\ * \left\{\delta(f) + 2S_{\varphi\varphi}(f)[1 - \cos(2\pi\tau f)]\right\} \tag{5.2.69}$$

The PSD $S_{v_{ok}v_{ok}}(f)$ may be decomposed as the sum of the PSD of the output due to an ideal chirp v_{oik} and a PSD term related to the phase noise $S_{v_{onk}v_{onk}}(f)$.

$$S_{v_{ok}v_{ok}}(f) = S_{v_{oik}v_{oik}}(f) + S_{v_{onk}v_{onk}}(f) \tag{5.2.70}$$

$$S_{v_{onk}v_{onk}}(f) = |H_{RX-IF}(f)|^2\ BT\ \ S_{v_{CG}v_{CG}0}\ \left|h_{mx}\left(\frac{f}{u}\right) * h_{pk}(\frac{f}{u}) * \mathrm{sinc}(Tf)\right|^2 \\ * 2S_{\varphi\varphi}(f)[1 - \cos(2\pi\tau f)] \tag{5.2.71}$$

5.2.4.2. Types of Phase Noise

The overall phase noise in an oscillator and a chirp generator is the result of different kinds or noise sources that create different kinds of phase noise. The different kind of phase noise are categorized by the order of decay of the PSD as a function of frequency. For instance, zeroth-order, first-order and second-order phase noise decay as a function of f^0, f^1 and f^2, respectively. Zeroth order, first-order and second order noise are also known as “white phase,” “Flicker,” and “white frequency” noise. Moreover, the oscillator may be connected to a compensation system, which reduces the phase noise below a cut-off frequency. For instance, a phase-locked-loop suppresses the phase noise from the oscillator and other sources below its cutoff frequency, determined by the loop bandwidth. This type of compensation is modeled as a high-pass filter applied to the instantaneous phase noise.

We can express the total instantaneous phase noise $\varphi(t)$ as the sum of all these orders convolved by the impulse response of the compensation filter $h_{pn}(f)$, as shown in (5.2.72). Similarly, the PSD of the total phase noise is given by (5.2.73). Zeroth order phase noise is band-limited white Gaussian noise in phase, second order phase noise is band-limited white Gaussian noise in frequency and so on. We define the term $S_{\varphi\varphi u}(f)$ as the unfiltered phase noise. The expanded form of the unfiltered phase noise is given by (5.2.75), where φ_{rmsk} is the RMS phase noise of order 'k' and B_n is the noise bandwidth.

$$\varphi(t) = h_{pn}(f) * \{\varphi_0(t) + \varphi_1(t) + \varphi_2(t) + \cdots\} \tag{5.2.72}$$

$$S_{\varphi\varphi}(f) = \left|H_{pn}(f)\right|^2 \{S_{\varphi_0\varphi_0}(f) + S_{\varphi_1\varphi_1}(f) + S_{\varphi_2\varphi_2}(f) + \cdots\} \tag{5.2.73}$$

$$S_{\varphi\varphi}(f) = \left|H_{pn}(f)\right|^2 S_{\varphi\varphi u}(f) \tag{5.2.74}$$

$$S_{\varphi\varphi u}(f) = \frac{1}{(j2\pi f)^0}\frac{{\varphi_{rms0}}^2}{B_n}\,\mathrm{rect}\left(\frac{f}{B_{no}}\right) + \frac{1}{(j2\pi f)^1}\frac{{\varphi_{rms1}}^2}{B_n}\,\mathrm{rect}\left(\frac{f}{B_{n1}}\right) + \frac{1}{(j2\pi f)^2}\frac{{\varphi_{rms2}}^2}{B_n}\,\mathrm{rect}\left(\frac{f}{B_{n2}}\right) + \cdots \tag{5.2.75}$$

Furthermore, we may also decompose the PSD of the unfiltered phase noise as the sum of its coherent $S_{\varphi\varphi ucoh}(f)$ and incoherent $S_{\varphi\varphi uincoh}(f)$ components.

$$S_{\varphi\varphi}(f) = \left|H_{pn}(f)\right|^2 \left[S_{\varphi\varphi ucoh}(f) + S_{\varphi\varphi uincoh}(f)\right] \tag{5.2.76}$$

5.2.4.3. FMCW Radar Simulation: Phase Noise Effect on FMCW Output Signal

From section 5.1.2, the output signal of an FMCW radar can be found numerically by solving (5.2.77). This results is valid for any signal path $h_{pk}(t)$, which may be the signal path related to the target or a self-interference path. The PSD of the output signal can be found numerically using the Fourier transform as described in section 5.1.2.6.

$$v_{ok}(t) = h_{RX-IF}(t) * \left\{ v_{CGa}(t) \cdot \left[h_{mx}(t) * h_{pk}(t) * v_{CG}(t) \right]^* \right\} \tag{5.2.77}$$

For these simulations, the output of the chirp generator with phase noise is given by (5.2.78), where $z(t)$ is the multiplicative noise term.

$$v_{CG}(t) = z(t)\, v_{CGi}(t) \tag{5.2.78}$$

$$z(t) = e^{j\varphi(t)} \tag{5.2.79}$$

The main goal of these simulations is to evaluate the effects of phase noise in the chirp for a point target. Thus, the impulse response of the radar sub-systems are assigned to be an impulse delta function.

$$h_{mx}(t) = h_{RX-IF}(t) = h_{RX}(t) = h_{TX}(t) = \delta(t) \tag{5.2.80}$$

The chirp used in the simulations has an amplitude v_{CGo} of one, chirp length of 10 μs and chirp bandwidth of 1 GHz.

The impulse response of the signal path $h_{pk}(t)$ is assigned to be delta function with a delay of τ.

$$h_{pk}(t) = \delta(t - \tau) \tag{5.2.81}$$

The PSD of the noise term in the output signal, for an FMCW with phase noise at the chirp, simplifies to the expression in (5.2.82). The expression in (5.2.82) can be further simplified to (5.2.83).

$$S_{v_{onk}v_{onk}}(f) = T\ |\mathrm{sinc}[T(f-u\tau)]|^2 * 2S_{\varphi\varphi}(f)[1-\cos(2\pi\tau f)] \quad (5.2.82)$$

$$S_{v_{onk}v_{onk}}(f) \approx 2S_{\varphi\varphi}(f)\left[1-\cos[2\pi\tau(f-u\tau)]\right] \quad (5.2.83)$$

The PSD of the ideal term of the output signal is given by (5.2.84). As mentioned in the previous section, the PSD of the total output signal is given by (5.2.85).

$$S_{v_{oik}v_{oik}}(f) = T\ |\mathrm{sinc}[T(f-u\tau)]|^2 \quad (5.2.84)$$

$$S_{v_{ok}v_{ok}}(f) = S_{v_{oik}v_{oik}}(f) + S_{v_{onk}v_{onk}}(f) \quad (5.2.85)$$

FMCW Simulation with Phase Noise at Chirp: Zero-order phase noise

The first simulation uses zero-order phase noise only at the chirp. The PSD of zero-order phase noise is given by (5.2.86). The RMS of the zero-order phase noise and the noise bandwidth used are 48.5 mrad and 50 GHz, respectively. The maximum value of the PSD of the ideal term and noise terms are computed as shown by (5.2.86) and (5.2.87), respectively. In this simulation, we assume a 50 ohm impedance. The SNR is 77 dBm as given by (5.2.88). In Figure 5.2.6, we plot the PSD of the simulated total output vs the analytically computed noise term. The plot shows that both the simulated and analytically computed noise terms agree with each other.

$$S_{\varphi_0\varphi_0}(f) = \frac{{\varphi_{rms0}}^2}{B_n}\ \mathrm{rect}(f/B_n) \tag{5.2.86}$$

$$max\{S_{v_{oik}v_{oik}}(f)\} = \frac{1}{R_0}T = -37\ \mathrm{dBm} \tag{5.2.87}$$

$$max\{S_{v_{onk}v_{onk}}(f)\} = \frac{1}{R_0}4\ \frac{{\varphi_{rms0}}^2}{B_n} = -114\ \mathrm{dBm} \tag{5.2.88}$$

$$SNR_{\varphi_0} = \frac{T\ B_n}{4{\varphi_{rms}}^2} = 77\ \mathrm{dBM} \tag{5.2.89}$$

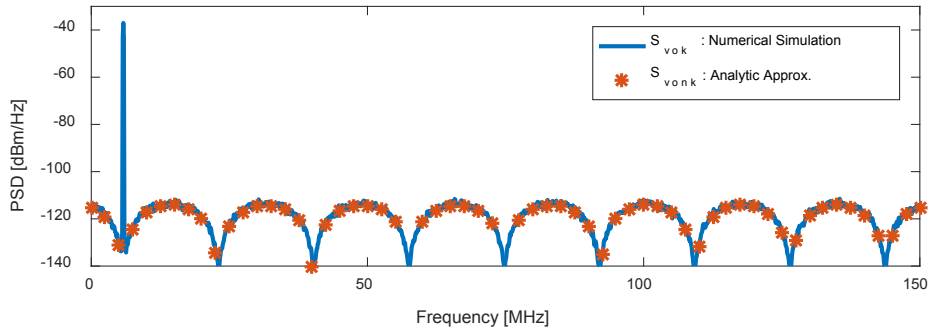

Figure 5.2.6 – PSD of FMCW Output Signal due to a Chirp with zero-Order Phase Noise

The second simulation uses second-order phase noise only. The PSD of second-order phase noise is given by (5.2.90). The RMS value of the second-order phase noise φ_{rms2} and the noise bandwidth used in the simulation are 20 Mrad/s and 50 GHz, respectively The PSD of the maximum values of the ideal and noise terms are given by (5.2.91) and (5.2.92), respectively. The SNR of this simulation yields 57 dBm as shown by (5.2.93).

$$S_{\varphi_0\varphi_0}(f) = \frac{1}{(j2\pi f)^2}\,\frac{{\varphi_{rms2}}^2}{B_n}\,\mathrm{rect}\left(\frac{f}{B_n}\right) \tag{5.2.90}$$

$$max\{S_{v_{oik}v_{oik}}(f)\} = \frac{1}{R_0}T = -36\ \mathrm{dBm} \tag{5.2.91}$$

$$max\{S_{v_{onk}v_{onk}}(f)\} = \frac{1}{R_0}\,\frac{(\tau_o\ \varphi_{rms2})^2}{B_n} = -93\ \mathrm{dBm} \tag{5.2.92}$$

$$SNR_{\varphi_2} = \frac{T\ B_n}{(\tau_o\ \varphi_{rms2})^2} = 57\ \mathrm{dB} \tag{5.2.93}$$

In Figure 5.2.7, we plot the PSD of the simulated total output against the analytically computed noise term. The plot shows that both the simulated and analytically computed noise terms agree well with each other.

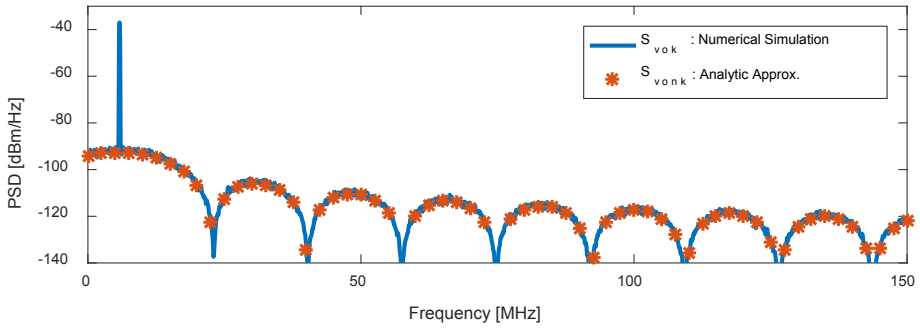

Figure 5.2.7 – PSD of FMCW Output Signal due to a Chirp with Second-Order Phase Noise

PART 2 – UWB FMCW RADAR DESCRIPTION

5.3. RADAR DESCRIPTION: System Overview

A 2-18 GHz UWB FMCW radar was developed to measure RCS measurements of wheat canopy plots. This section presents the objectives of the radar, lists the system requirements and provides a summary of the radar architecture and main parameters.

5.3.1. Target and Radar Objectives

5.3.1.1. Target: Wheat Canopy Plot

The targets of interest are wheat canopy plots. The wheat plots considered for radar measurements are approximately 1.4 [m] wide and 4 [m] long. The vertical dimension or canopy height is dependent on growth stage. Mature wheat plants reach a typical height of 0.6 [m]. The wheat plots considered are arranged in six rows separated by 9 inches. The plant density is approximately 400 [pt/m^2].

5.3.1.2. Radar System Objectives

The following points outline the objectives of the radar.

- The radar should provide a vertical distribution of the RCS of a wheat canopy plot.
- The RCS should significantly vary with plant architecture parameters (e.g. leaf area).

- The vertical resolution should result in at least 15 points (range bins) for a 60 [cm] tall plant.
- The radar should be sensitive to the projected leaf area as a function of height. The radar should be able to detect the RCS of the canopy over the broad range of leaf parameters listed in section 4.4.

5.3.2. Radar System Requirements

5.3.2.1. Frequency Range, Bandwidth and Coherency

In chapter 4, scattering analysis was performed using a Monte Carlo simulator. This analysis revealed that over the 2-18 GHz frequency range, the RCS of the canopy varied by more than 15 dB over the range of leaf areas considered. For this reason, we chose the 2-18 GHz frequency range.

The vertical resolution is given by equation (5.3.1), where c, K, n and B are the speed of light, pulse-broadening factor (e.g. 1.4 for Hanning Window), effective index of refraction and chirp bandwidth, respectively. Typical wheat canopies have low vegetation density within its volume, so that the effective index of refraction can be approximated to one. For the 16 GHz of bandwidth considered, and a pulse-broadening factor of 1.4, the vertical resolution becomes 1.3 cm. This vertical resolution results in 46 vertical points for a 60 cm tall canopy.

$$\delta R = K\frac{c}{2Bn} = 1.3\ [\text{cm}] \tag{5.3.1}$$

The radar should collect a coherent signal that can be related to the amplitude and phase of the target's frequency response over the 2-18 GHz frequency range. This way both time and frequency responses of the target become available for analysis.

In summary, the radar should be an UWB coherent radar operating in the 2-18 GHz frequency range.

5.3.2.2. Minimum Distance to Target and Maximum Unambiguous Range

The scattering analysis of chapter 4 assumed that the target was in the far-field region of the antennas. The far-field region of the antennas is given by (5.3.2). In (5.3.2), D is the maximum dimension of the antenna, which is 10 cm, and lambda is the wavelength. The minimum wavelength of the radar waveform is 1.67 cm. Thus, the minimum distance from the antennas to the target is 1.2 m. The mobile platform developed for this radar mounts the antennas at 1.8 m above the ground. This means that the plants as tall as 60 cm will be in the far-field region of the antennas.

$$R_{FF} = \frac{2D^2}{\lambda} \tag{5.3.2}$$

The radar will operate in near-nadir mode looking at the canopy from above. Thus, it is expected that the ground will reflect a large signal back to the radar. This ground return should be measured at a range that is unambiguous so that it does not contaminate the canopy returns, by aliasing or other means. Thus, the maximum unambiguous range of the radar should be the largest distance from the antennas to the furthest region on the ground seen by the antennas.

The antenna height is 1.8 m, the antenna beamwidth is 56.6 and the antenna cable length is 8 ft for both the transmit and receive antennas. The distance from one of the antenna to a point on

the ground at the edge of the beam is 7.3 m. Given that in practice the antennas are separated from each other by a small distance, we multiply this distance by a buffer factor of 1.2 to get the maximum unambiguous range of 8.8 m. This distance is approximately equivalent to a roundtrip delay of 59 ns.

5.3.2.3. Minimum and Maximum RCS

From the scattering analysis of chapter 4, the minimum RCS for semi-curved leaves is about -38 dB. This analysis used standard values for all other leaf parameters. The plant density and canopy dimensions used are the same parameters expected by the measured target.

The Maximum RCS is given by the ground reflection, which is maximum when moisture content reaches capacity and roughness is significantly low (i.e. $k\, h_{rms}<1$). In this case, the RCS due to a ground return for a footprint area of 1.78 m^2 is about 0 dB.

5.3.2.4. Summary of Radar Requirements

Table 5.3.1 shows a list of the pre-selected radar parameters described earlier. Table 5.3.2 shows a list of the radar requirements.

Table 5.3.1 – List of Radar System Requirements

Radar Parameter	**Value [Unit]**
Frequency Range (Bandwidth)	2-18 [GHz] (16 GHz)
Minimum Distance from Ant. to Target	1.2 [m]
Maximum Unambiguous Range	8.8 m
Minimum RCS	-38 dB
Maximum RCS	0 dB

5.3.3. Overview of Radar Architecture and Main Parameters

5.3.3.1. FMCW Radar Topology

From the last section, the radar was specified to record a coherent signal over its entire frequency range, so that the coherent target response can be derived.

Coherent chirp pulsed radars digitize the full bandwidth of the waveform. Digitizing a signal spanning the 2-18 GHz frequency range directly would require 36 GSPS sampling rate. If the signal were down-converted using IQ demodulation, the required sampling rate would be 16 GSPS.

Alternatively, Frequency-Modulated-Continuous-Wave radars apply the pulse compression in analog hardware, so that the sampling rate is only dictated by the maximum unambiguous range. For the chirp length of 240 µs, bandwidth of 16 GHz and a maximum unambiguous range of 8.8 m, the maximum frequency 3.9 MHz. Thus, the minimum required sampling rate would be

7.8 MHz in this case. We choose the FMCW topology for this radar due to its low sampling rate requirements.

Another topology of radar that performs the pulse-compression in the frequency domain and requires a low to modest sampling rate is the step-frequency-continuous-wave (SFCW) radar topology. This type of topology could have also been used.

5.3.3.2. Overview of Radar Architecture

As a part of this investigation, the 2-18 GHz FMCW radar was designed, built and tested. This section only provides a brief overview of the radar architecture. Further details will be given in sections 5.4-5.8. Figure 5.3.2 shows the block diagram of the radar architecture.

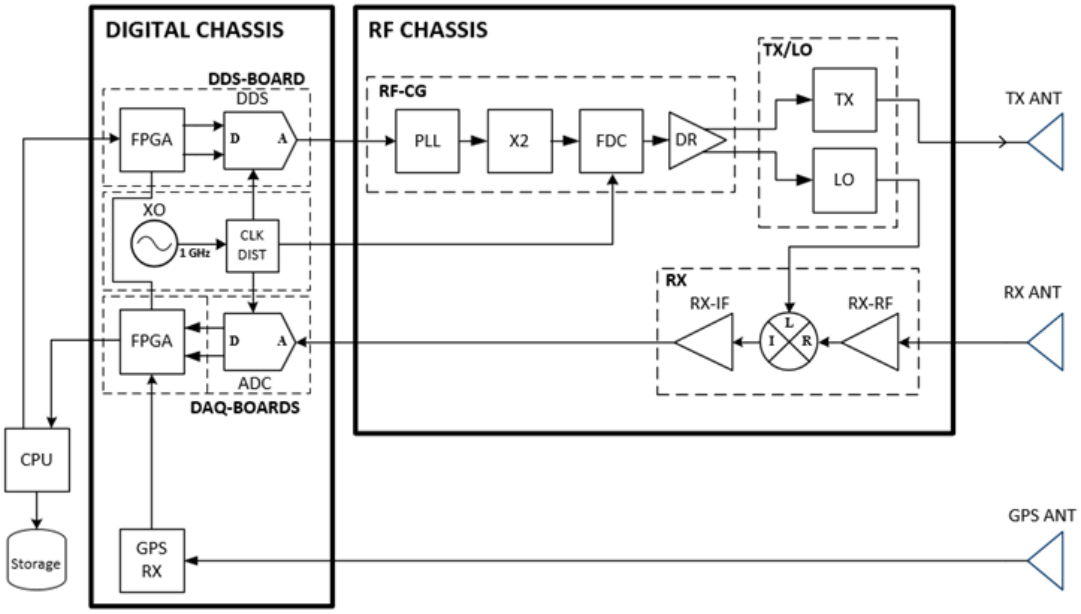

Figure 5.3.1 – Block Diagram of 2-18 GHz FMCW Radar System Architecture

The Chirp Generator (CG)

The digital section of the chirp generator is composed of a DDS board and a clock distribution board. The DDS board generates the baseband chirp that spans from 196.43 to 339.29 MHz. A phase-locked-loop (PLL) multiplies the frequency of the baseband chirp by a factor of 56 to obtain generate a 11-19 GHz chirp. A sub-sequent frequency doubler (X2) and frequency down-conversion (FDC) sub-systems convert this signal to output the 2-18 GHz radar chirp. The CG is described in section 5.5.

TX/LO

The radar's TX and LO sub-systems condition the signal so that the output power becomes -12.4 dBm and the power level at the output power becomes 10.3 dBm. The TX and LO are described in section 5.6.

RX: RX-RF, MX, RX-IF

The receiver is divided in three sub-systems, the RF and IF sections of the RX and the mixer. The frequency-average gain of the RX-RF, RX-IF and mixer are 16.7 dB, 37.1 dB and -6.5 dB, respectively. Therefore, the total receiver gain is 47.3 dB. The receiver has a total noise figure of 13 dB. The receiver is described in section 5.6.

Besides considering the noise figure, the receiver was designed to lower the LO leakage at the mixer. Section 5.7 describes the noise performance of the radar. The total incoherent noise level at the radar output is -95.6 dBm/Hz. This noise level is equivalent to a radar-cross-section

of -43.2 dB. Given a 4 dB minimum SNR, the minimum RCS detected by the radar would be -38 dB.

The total coherent noise has a level of -96 dBmm/Hz. This type of noise is removed in post-processing, so it is ignored here.

The maximum signal at the output of the receiver depends on the P1dB of the RX-IF. The P1dB of the IF amplifier is 12 dBm, so that the P1dB of the RX-IF is -3 dBm. A CW tone signal with 240 μs length and -3 dBm average power has PSD peak of -39 dBm/Hz. This signal at the output of the radar with this PSD level is equivalent to a point target with a RCS of 13.4 dB. Thus, the maximum RCS that the radar is capable of measuring is 13.4 dB.

DAQ

The DAQ digitizes and stores the received signal. The sampling rate of the digitizer is 62.5 MHz. The DAQ is described in section 5.6. At this sampling rate and considering the chirp parameters, the maximum unambiguous range is 70.3 m.

5.3.3.3. Radar System Parameters

Table 5.3.2 shows a list of the radar performance parameters. Table 5.3.3 shows a list of the main radar system parameters. The minimum and maximum RCS values are given for a target scattering center 1.8 m from the antennas center.

Table 5.3.2 – List of Radar Performance Parameters

Radar Parameter	**Value [Unit]**
Frequency Range (Bandwidth)	2-18 [GHz] (16 GHz)
Distance from Ant. to Target	1.2 [m]
Maximum Unambiguous Range	70.3 m
Minimum RCS (Noise Equivalent RCS)	-38 dB (-43 dB)
Maximum RCS	13.4 dB

Table 5.3.3 – General Radar System Parameters

Parameter	**Value**
Chirp Frequency (Bandwidth)	2-18 GHz (16 GHz)
Chirp Length	240 μs
TX Time-Averaged Power	-12.4 dBm
TX PSD	-114 dBm/Hz
RX Gain	47.3 dB
RX Noise Figure	13 dB
DAQ ADC Sampling Rate	62.5 MHz

5.4. RADAR DESCRIPTION: Platform and Antenna

5.4.1. Platform Description

A mobile platform was developed to collect radar measurements of wheat canopies. This mobile platform or cart has three wheels (one front and two back wheels). Drawings of the front and side views of the cart are depicted in figures 5.4.1 and 5.4.2, respectively.

The platform supports the two antennas and the electronics. The antennas are mounted at 1.8 m from the ground and separated by 0.61 m from each other. The electronics are mounted on one of the sides of the structure as shown on the drawings. The gap between the two legs of the structure has a width of 1.54 m, as shown in the drawing, which results in an average clearance of 7 cm between each leg and the canopy. A photograph of the structure is shown in figure 5.4.3.

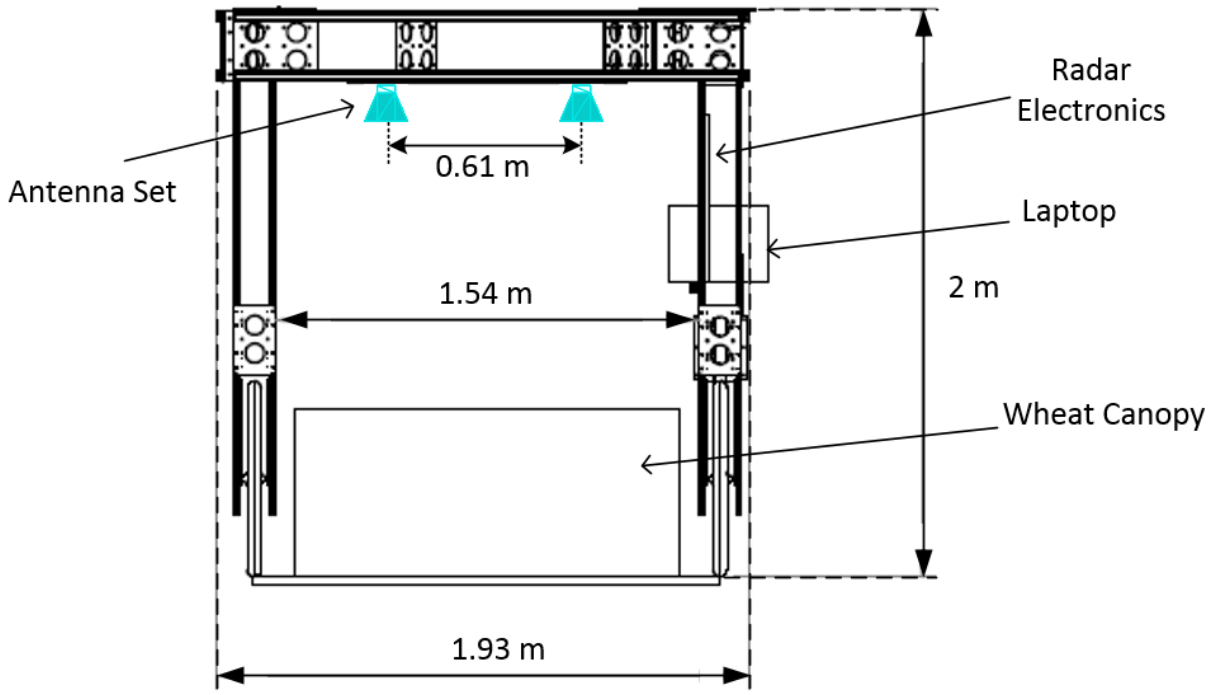

Figure 5.4.1 – Drawing of Front View of the radar platform or cart

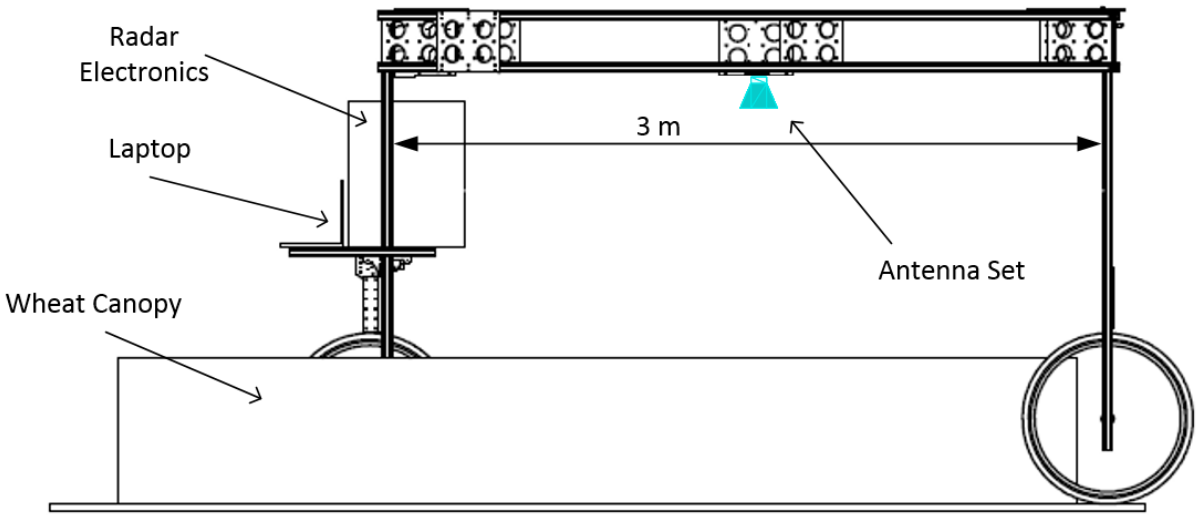

Figure 5.4.2 – Drawing of Side View of Cart

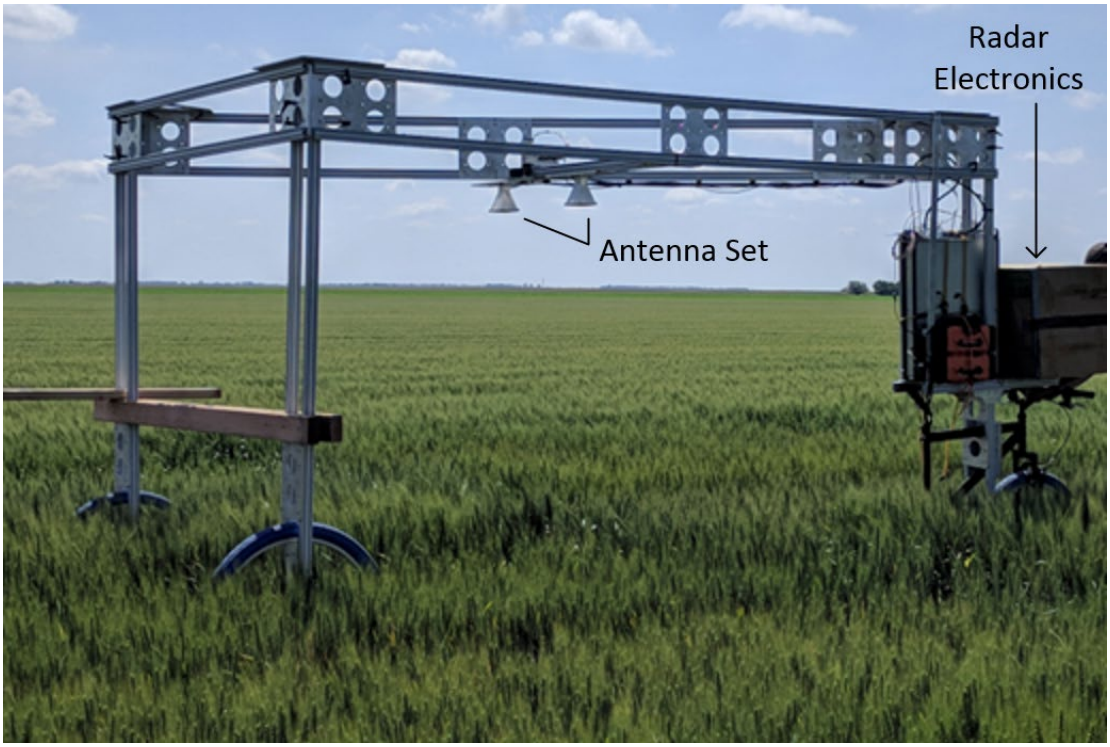

Figure 5.4.3 – Photograph of the cart with antennas and radar equipment

5.4.2. Radar Antenna Description

This section indicates the types of antennas selected for the radar, shows measurements of their impulse and frequency response, describes the average beamwidth and footprint, and shows measurements of the antenna feed-through. Table 5.4.1 shows a list summarizing the antenna pair parameters.

Table 5.4.1 – List of Antenna Pair Parameters

Parameter	**Value**
Operating Frequency (Bandwidth)	2-18 GHz (16 GHz)
(Minimum) Return Loss	7.4 dB
Average Gain (Elevation Angle 9.6 degrees)	10.3 dB
Average Beamwidth	56.6 degrees
Average Footprint	1.79 m^2
Average Feedthrough	61 dB
Antenna Pair Separation	60.96 cm
Antenna Height from Ground	1.8 m

5.4.2.1. Antenna Return Loss and Part Number

The selected transmit and receive antennas are identical pyramidal horns, with part number QWH-SL-2-18-S-SG-R and manufactured by Steatite Q-Par. The operating frequency range of these antennas is 2-18 GHz. According to the datasheet, the VSWR of the antenna port is less than 2.5:1. This is equivalent to a minimum return loss of 7.4 dB over the operating frequency range.

5.4.2.2. Antenna Frequency and Impulse Responses

The coherent frequency response of the antenna was measured over its operating frequency range. The antenna response was measured before (stand-alone) and after installing the antennas on the platform. A ray impinging a point on the ground between both antennas would

have incident elevation angle of 9.6 degrees and an azimuth angle of 0 degrees. The measurements were collected at this orientation.

Figure 5.4.4 shows the frequency response of the antenna at the orientation indicated. The average gain of the antenna mounted on the structure is 10.3 dB. The frequency response is slightly modified by the supporting structure.

Figure 5.4.5 shows the impulse response of the structure- mounted antenna. The antenna has an (average) impulse delay of 0.76 ns. The impulse response was calculated by taking the inverse Fourier transform of the coherent frequency response of the antenna.

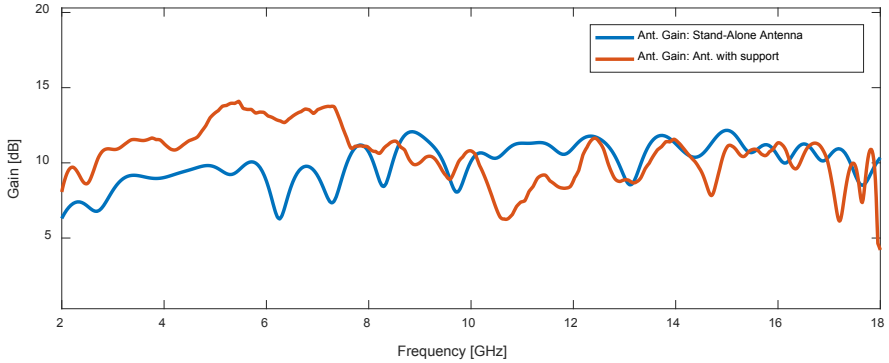

Figure 5.4.4 – Antenna Frequency Response (Gain) at zero degrees

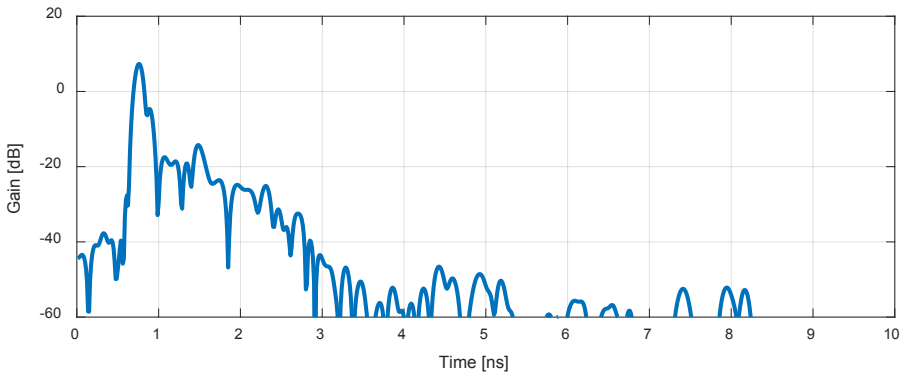

Figure 5.4.5 – Antenna Impulse Response at zero degrees

The frequency response of the stand-alone antenna over 2-18 GHz and -70 to 70 degrees is shown by figure 5.4.6.

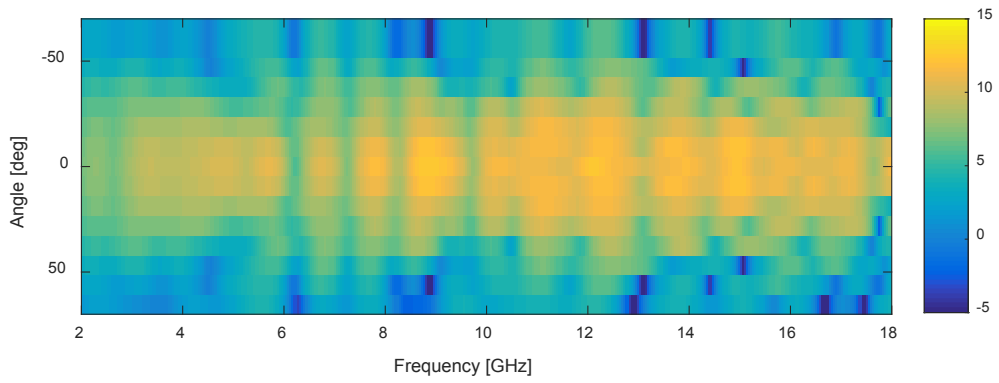

Figure 5.4.6 – Antenna Frequency Response (Gain [dB])

During the radar calibration process, the system frequency and impulse response is compensated for over the entire frequency range. This calibration process compensates the frequency response at a single antenna incident/reflection angle pair. Figure 5.4.7 show the normalized frequency response of the antenna, which has a zero dB amplitude at 0 degrees.

The effect of the frequency response variability over angle and frequency after normalization can be considered in the RCS analysis.

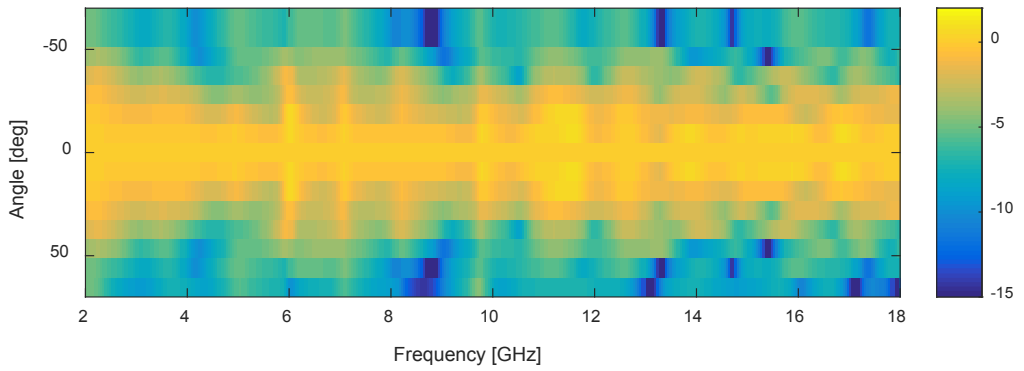

Figure 5.4.7 – Normalized Antenna Frequency Response (Gain [dB])

5.4.2.3. Average Beamwidth and Footprint

Using the Monte-Carlo simulator of chapter 4, which takes into account the antenna response, we computed the RCS of canopies with areas much larger than the antenna footprint. The antenna was set to have a boxcar beamwidth with unity gain over its beamwidth and zero gain elsewhere. It was found that an antenna with boxcar beamwidth of 56.6 degrees is equivalent to the measured normalized antenna gain of figure 5.4.8. Thus, we can say that the equivalent antenna beamwidth is 56.6 degrees. Figure 5.4.8 shows a comparison of the frequency-average normalized gain of the measured antenna and the equivalent antenna gain.

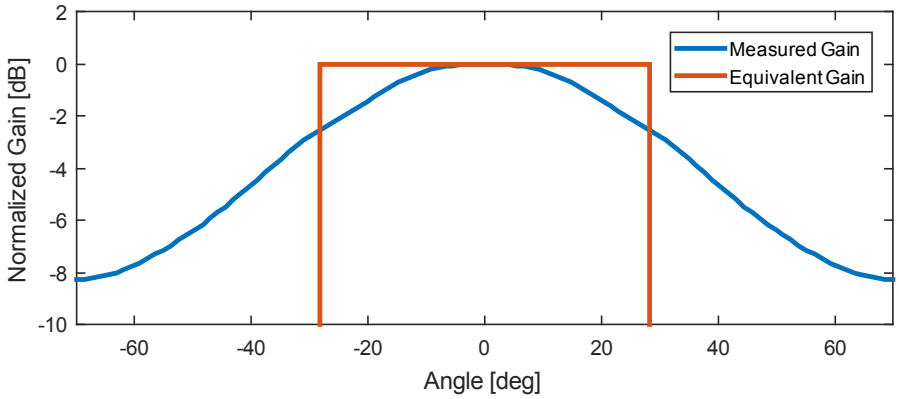

Figure 5.4.8 - Measured vs Equivalent Normalized Antenna Gains vs Angle

Considering that we use the same type of antenna for both transmission and reception, both antennas have the same effective beamwidth of 56.6 degrees. When the antennas are suspended at 1.8 [m] from the ground and separated by 2 feet from each other, their overlapping footprint (radar footprint) can be depicted by figure 5.4.9. This radar footprint has an area of 1.79 [m^2], a long dimension of 1.83 [m] and a width of 1.32 [m].

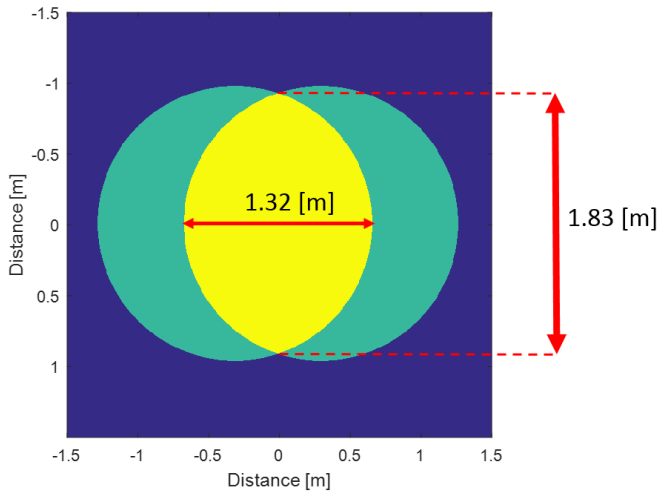

Figure 5.4.9 – Antenna Radar Footprint

Figure 5.4.10 shows how the antenna radar footprint superimposes on the wheat plot area. The image in the center of the figure shows that the radar footprint falls within the width of the wheat plot for an antenna height of 1.8 [m] and an antenna separation of 2 feet. In the field, the radar collects measurements moving from plot to plot in the direction parallel to the long axis of the plots. In the left and right images of figure 5.4.10, the radar footprint overlaps the two adjacent plots when the radar reaches their ends. Measurements collected within about 1 meter from each plot end should be disregarded.

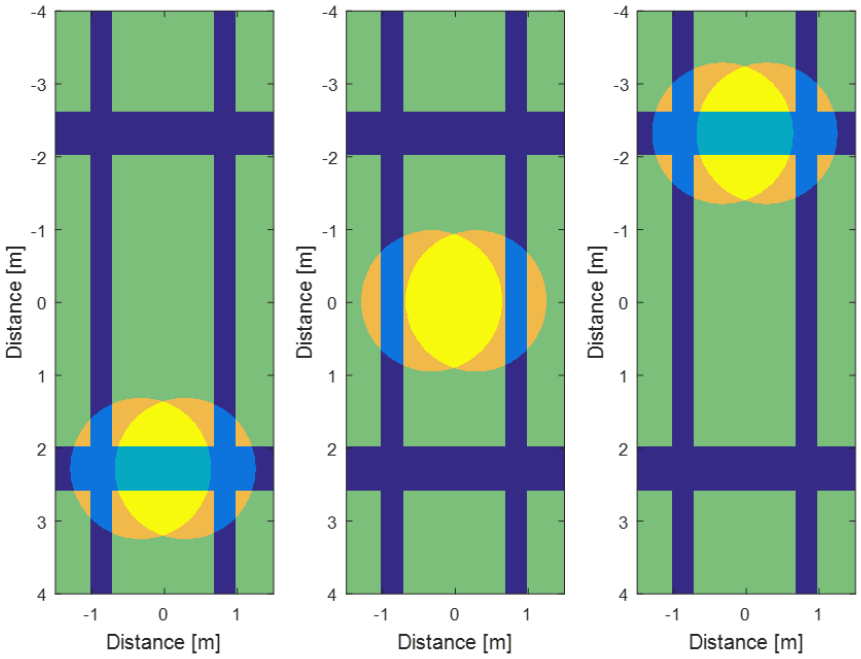

Figure 5.4.10 – Intersection of antenna radar footprint on wheat plot area

5.4.2.4. Antenna Feed-Through

The antenna feed-through is the part of the signal radiated by the transmitter antenna that leaks directly to the receiver antenna. The antenna feed-through is part of one of the self-interference paths of the radar and it is important in the noise/interference analysis.

The antenna feedthrough for the TX and RX antennas, separated by 2 ft, were measured with a VNA. The measured frequency and impulse responses of the antenna feed-through are shown in figures 5.4.11 and 5.4.12, respectively. The frequency response has an average insertion loss of 61 dB. The peak delay of the impulse response is 3.56 ns. This impulse delay is consistent with the 2 ft separation and the antenna impulse delay of 0.76 ns.

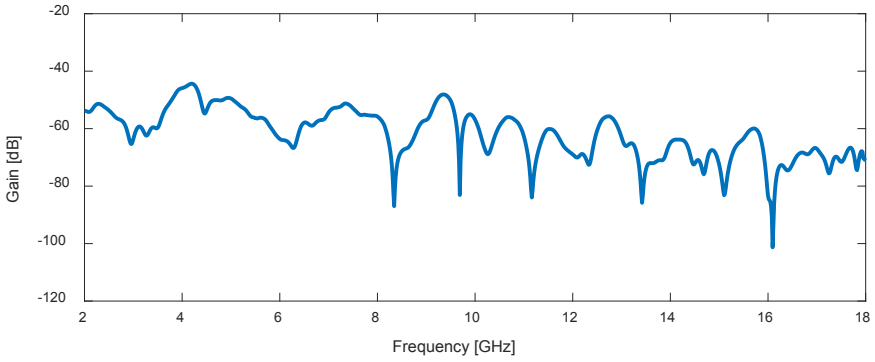

Figure 5.4.11 – Antenna Feed-Through Frequency Response (Measurement)

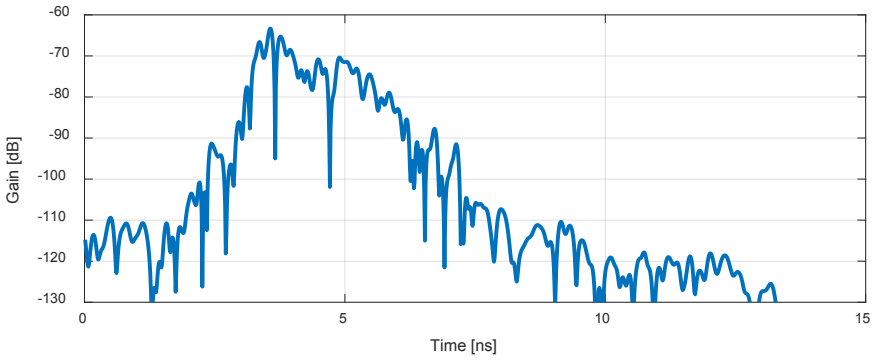

Figure 5.4.12 – Antenna Feed-Through Impulse Response (Measurement)

5.4.2.5. Antenna Cables

Antenna cables connect the antennas to the transmitter and receiver electronics. Both cables are identical. The part number of this type of cable is UFA210A-1-0960-300300, manufactured by Micro-Coax. The length of each cable is 2.44 m. Figure 5.4.13 and figure 5.4.14 show the cables' frequency and impulse response, respectively. The measured frequency response, depicted in figure 5.4.13, show that the cable has an average insertion loss of 1.65 dB. The measured impulse delay of the cable is 10.5 ns. This impulse delay corresponds to a relative effective permittivity of 1.67. In other words, the effective speed of a signal through the cable is 77% of the speed of light. The frequency responses of the transmit and receive antenna cables are accounted for by the transmitter and the receiver, respectively.

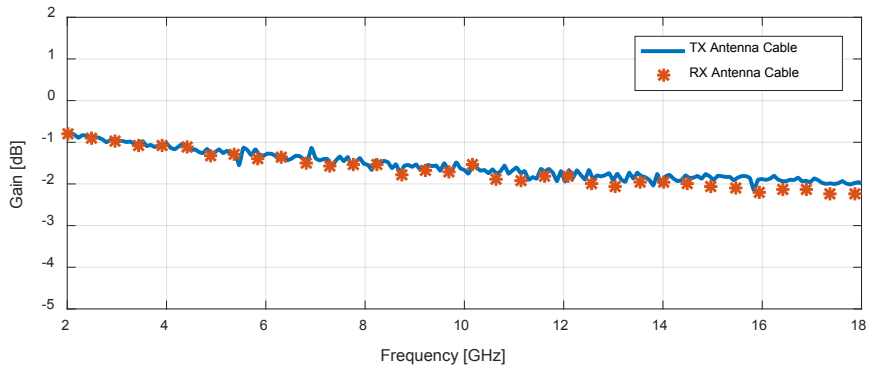

Figure 5.4.13 – Frequency Response of TX and RX Antenna Cables

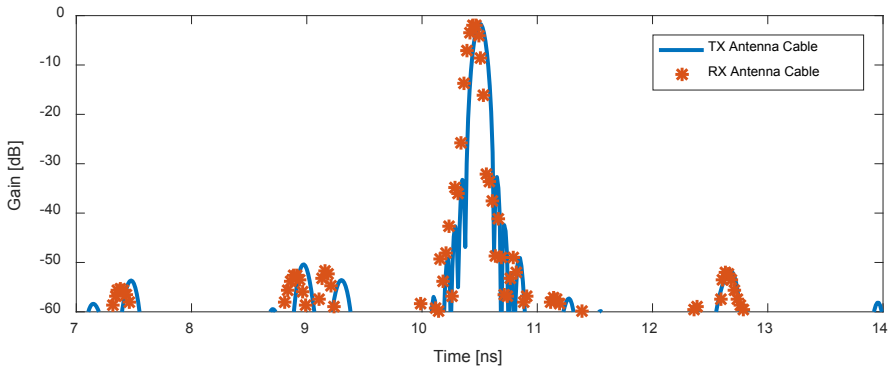

Figure 5.4.14 – Impulse Response of TX and RX Antenna Cables

5.5. RADAR DESCRIPTION: Chirp Generator

The chirp generator of the FMCW radar is the sub-system that outputs the radar linear-frequency-modulated waveform or chirp. The chirp generator outputs a signal spanning the 2-18 GHz frequency range, with a chirp length of 240 μs, and with an output average power of 16 dBm. Table 5.5.1 provides a list of the chirp generator parameters.

Table 5.5.1 – Radar Chirp Generator Parameters

Parameter	**Value [Unit]**
Frequency Range (Bandwidth - *B*)	2-18 GHz (16 GHz)
Chirp Length (*T*)	240 µs
Chirp Time-Averaged Output Power	16 dBm
Chirp PSD over band	-86 dBm/Hz
Max Incoherent Phase Noise PSD w.r.t. carrier	-45 dBc
Max Coherent Phase Noise PSD w.r.t. carrier	-42 dBc

This subsystem is composed of digital section (CG-Digital) and an analog-microwave section (CG-RF). Figure 5.5.1 shows a high-level block diagram of the chirp generator. The digital section uses a direct digital synthesizer (DDS) to generate the baseband chirp. This baseband chirp is used to drive a Phase Locked Loop (PLL), which effectively frequency-multiplies the baseband chirp by a factor of 56. The output of the PLL is frequency-multiplied by a factor of 2 using a microwave frequency multiplier. The output of the frequency multiplier is down-

converted in frequency by 10 GHz. The output driver (DR) conditions the chirp signal so that the CG output power is 16 dBm.

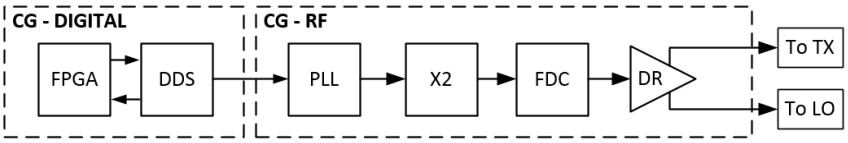

Figure 5.5.1 – High Level Block Diagram of the Radar Chirp Generator

5.5.1. Digital Section of the Chirp Generator

The main objective of the digital section of the chirp generator is to output the reference chirp, which drives the phase-locked-loop of the chirp generator, described in section 5.5.2. Table 5.5.2 lists the parameters of this reference chirp.

Table 5.5.2 – Reference Chirp Parameters

Parameter	**Value**
Chirp Length	240 μs
Chirp Center Frequency	267.86 MHz
Chirp Bandwidth	160.71 MHz
Pulse Repetition Frequency (PRF)	500 Hz

This digital system also generates the radar timing signals and receives the radar control signals from the user computer. The following is a list of the main tasks performed by this digital system:

- Receive radar control instructions and decode them.

- Generate baseband chirp (196.43 – 339.28 MHz) and timing signals (PRF, EPRI) according to instructions.
- Decode GPS NMEA stream from GPS receiver
- Relay radar control instructions to DAQ using a serial interface.
- Send UTC timing to DAQ using serial interface

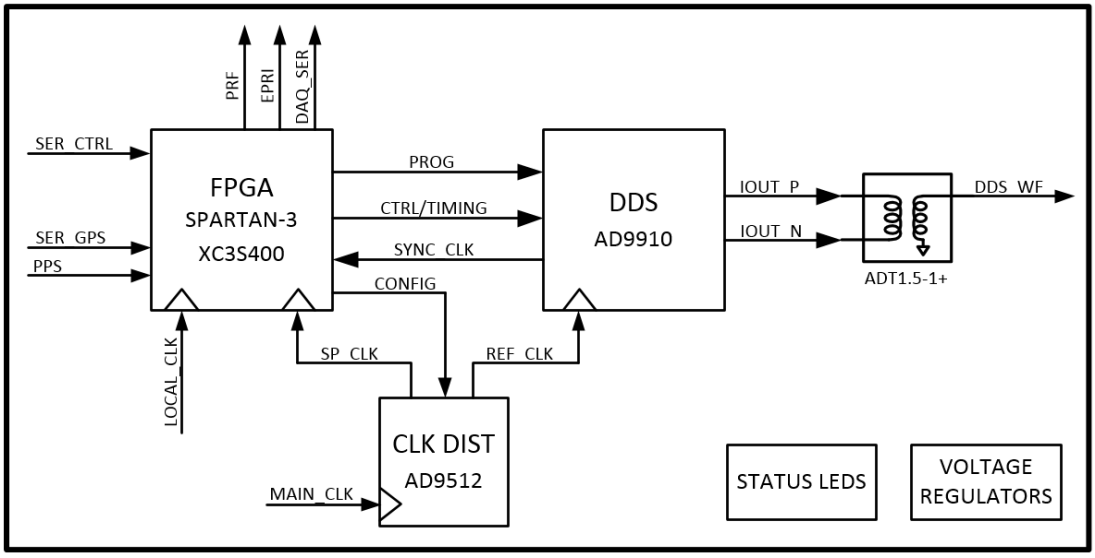

Figure 5.5.2 – DDS-Board Block Diagram

This digital system was implemented on a direct-digital-synthesizer (DDS) board designed as the Center for Remote Sensing of Ice Sheets [8]. A block diagram of this DDS board is shown in figure 5.5.2. The board uses a Xilinx Spartan 3 FPGA (PN XC3S400) to configure the DDS, generate timing signals, decode GPS NMEA stream and relay control signals to the DAQ. The DDS integrated circuit (IC) used is the 1 GSPS AD9910 by Analog Devices. The board also has a clock distribution IC (AD9512) that frequency divides and provides the clock signals to the DDS and FPGA. The FPGA also takes a clock signal produced by an on-board crystal oscillator.

The following sections provide a brief description of the DDS and the digital system implemented on the FPGA.

5.5.1.1. Direct Digital Synthesizer (DDS)

The AD9910 DDS is configured and controlled by the FPGA to output the reference chirp. This DDS has different options to modulate the amplitude, phase and frequency of the output of its numerically controlled oscillator (NCO). The parameters of the DDS, such as the NCO modulation and the selection of clock resources, can be configured through serial peripheral interface (SPI). Additionally, this DDS takes control signals to update the registers and optionally modify the output waveform in real time.

The registers of the DDS are configured by the FPGA through a serial port using standard serial-peripheral-interface (SPI). The register-data in the serial buffer is transferred to the internal DDS registers when the DDS IO_Update signal is triggered. Additional details on the NCO modulation, configuration, and other features are given in the AD9910 datasheet [9].

This section briefly describes the configuration of the NCO modulation and the DDS clock.

Modulation of Numerically Controlled Oscillator (AD9910)

At the core of the AD9910 DDS is the Numerically-Controlled-Oscillator (NCO). This oscillator includes signals that numerically control its frequency, its relative phase and its amplitude envelope. The digital signals to control the frequency, phase offset and envelope amplitude are

called the frequency tuning word (FTW), phase offset word (POW) and amplitude scale factor (ASF). The DDS offers internal modules to drive these digital signals.

Two of these modules are the digital-ramp-generator module and the random-access-memory (RAM) module. In order to produce a linear-frequency-modulated waveform (chirp), we use the digital-ramp-generator (DRG) module to drive the frequency modulation signal. The RAM module is used for amplitude modulation (AM) of the waveform. This AM feature is used to compensate for undesired AM caused by the frequency response of the conditioning system between the DDS and the PLL.

The DRG module is a 32-bit accumulator or counter. The destination bits define the type of modulation signal that is driven by the DRG. To generate a chirp with the DRG, we select the destination bits that correspond to the frequency modulation. It has manual and auto-clear options for the accumulator or counter. The auto-clear option is set so that the DRG goes back to the tuning word related to the start frequency every time it is triggered. The direction of the ramp is set to have a positive slope using the external DRG_CTL pin. The DRG limits (start and stop FTWs), the rate and the step size are configured through 32-bit registers. The start and stop FTWs are 32-bit words that can be calculated using equations (5.5.1-5.5.2). The rate of update is set to '1' so that the frequency modulation signal is updated at $f_{sys}/4$ (1GHz/4), to achieve the finest time step resolution allowed. At the chosen update rate, the frequency step word (FTW_{step}) defines the frequency slope and can be calculated using equations (5.5.3-5.5.4).

$$FTW_{start} = 2^{32}\frac{f_{start}}{f_{sys}} \tag{5.5.1}$$

$$FTW_{stop} = 2^{32}\frac{f_{stop}}{f_{sys}} \tag{5.5.2}$$

$$\Delta f_{step} = \frac{f_{stop} - f_{start}}{T}\frac{1}{f_{sys}/4} = \frac{f_{stop} - f_{start}}{N_{steps}} \tag{5.5.3}$$

$$FTW_{step} = 2^{32}\frac{\Delta f_{step}}{f_{sys}} \tag{5.5.4}$$

The RAM modules allow arbitrary waveforms to be used for modulation. We use this DDS feature to modulate the amplitude of the digital chirp. The amplitude waveform is loaded to the DDS in the same way that other registers are loaded. The registers for the RAM are a string of 32-bit words, where only the first 14 most significant bits (MSB) are used. The DDS allows eight different profiles, each of which may have a different RAM waveform. Only one type of chirp is considered in this radar, so only one profile is used (profile[0]). Similarly, to the DRG, destination bits are used to select the type of modulation signal associated to the RAM module. The RAM playback update rate is set by the parameter (RAM_{step}), which is calculated using equation (5.5.5). The DDS also allows selecting the direction in which the RAM waveform is play-backed.

$$RAM_{step} = \frac{\Delta t_{step}}{4\Delta t_{sys}} = \frac{\Delta t_{step}}{1/(f_{sys}/4)} \tag{5.5.5}$$

DDS Clock Configuration

The sampling clock of the DDS is derived from a reference clock signal that is fed to the IC. An internal PLL is used to frequency-multiply the reference clock frequency to the desired sampling

frequency. The reference frequency, provided by the clock distribution IC, is 62.5 MHz. The PLL multiplies this frequency by 16, so that the sampling or system frequency becomes 1 GHz. The PLL is set as a third order Type 2 PLL with a phase margin of 45 [deg] and 50 [kHz] loop bandwidth. The modulation signals are sampled at one fourth of the system frequency.

5.5.1.2. FPGA Modules

The digital system implemented in the FPGA performs a number of tasks. In broad terms, this system configures the DDS sample clock, generates the radar timing signals, configures the DDS registers, controls the DDS through real-time signals, relays radar control instructions or information to the DAQ and sends timing and GPS timing information to the DAQ. The interface of the FPGA to the control computer uses RS232 serial communication. This section briefly describes the different modules implemented at the FPGA.

Clock Distribution Configuration Module

This module defines and configures the registers of an on-board AD9512 clock distribution IC. This module defines the registers so that the input clock is divided by 2 on all three of the used outputs. Given the input clock frequency of 125 MHz, the output clock frequency is 62.5 MHz. The clock distribution IC feeds the FPGA and two DDSs with this clock signal. The FPGA interfaces the AD9512 using a standard serial peripheral interface.

Control Serial Receiver Module

The control computer transmits radar control instructions to the FPGA using a RS232 interface. This module has an RS232 receiver to accept asynchronously the radar control instructions. The radar control instructions are packets with a register address and the data related to that address.

Register Assignment Module

This module reads the control instructions received by the RS232 receiver and stores the register data into the appropriate FPGA register. These registers may be related to radar timing, GPS timing, DDS configuration or control, or DAQ control.

Timing Generator

This module generates the PRF and EPRI pulses. Both pulses have a pulse width of one clock cycle. They are based on the divided sample clock (62.5 MHz), given by the clock distribution IC. The number of clock cycles between each PRF are defined by a set of FPGA registers, specified by radar instructions sent by the control computer. Likewise, the number of PRF pulses per EPRI pulse is defined by a set of registers. Since only one type of waveform is used by this radar, the number of PRF pulses per EPRI pulse is equal to the number of presums. The number of presums are the number of coherent integrations performed by the DAQ FPGA.

DDS Controller Module

This module configures the DDS registers, generates the IO_Update trigger to load DDS registers and defines the DRG control signals.

The control computer sends the DDS configuration registers' addresses and data to the FPGA. This module uses SPI to transmit these registers to the DDS. The FPGA sends a trigger pulse (IO_Update) that is used by the DDS to load the register words from a buffer to the appropriate register destination. The FPGA starts transmitting the DDS registers to the DDS each PRF pulse. The DDS controller module waits for 10.7μs after the PRF pulse and sends the IO_Update trigger to the DDS.

The IO_Update pulse is generated by delaying the PRF pulse by the programmed number of clock cycles. To delay the PRF by 10.7μs, the PRF is delayed by 669 clock cycles (at 62.5 MHz). The IO_Update must be in the same clock domain as a DDS synchronized clock derived by the DDS sampling clock. Thus, the delayed PRF is converted to the DDS synchronized clock domain to generate the IO_Update trigger.

The DDS controller module also defines the digital ramp generator (DRG) control signals. The digital ramp control signal (DRCTL) and the digital ramp hold signal (DRHOLD) are set to one and zero, respectively. This configuration sets the digital ramp to always ramp 'up' and never stop.

GPS Timing Module

A GPS receiver sends a NMEA stream to the FPGA through a RS232 interface. This module implements the RS232 receiver that reads this stream. The module extracts the UTC time information from the data stream, converts the time to seconds and stores it in a 32-bit word. This module also receives the one Pulse-per-Second (PPS) trigger. A counter is defined to count the number of clock cycles between every PPS pulse. This count is also stored in a 32-bit word. We refer to this count as the UTC fraction. The 32-bit words corresponding to the UTC seconds and UTC fraction are combined into a 64-bit word. This 64-bit word is sent to the DAQ FPGA using a serial interface. In order to avoid glitches in the UTC time, the UTC time is updated from the GPS receiver NMEA stream only when a flag is set. This flag is provided in a register by the radar computer.

DAQ Interface

This module defines a serial (SPI) interface, which is used to send the UTC time, DAQ control and timing information to the DAQ. The DAQ control information sent are the number of presums (i.e. coherent integrations), the number of samples before the first considered sample and the length of samples. The first considered sample is the first sample after the PRF that is considered for presums and recording. Similarly, the length of samples that the DAQ considers is the number of samples after the first sample that the DAQ considers for presums and recording. The DAQ is briefly described in section 5.6.4.

5.5.1.3. External Clock Distribution

A clock distribution board generates all the reference clock signals of the radar. The source clock is a 1 GHz crystal oscillator with part number CCSO-914X, manufactured by Crystek. The 1 GHz signal from this oscillator is divided by a clock distribution IC (AD9512). The clock distribution IC is configured by a Xilinx Spartan 3 (XC3S200) FPGA through a serial interface.

The clock distribution IC provides reference clock signals for three radar sub-systems: the DDS, the DAQ and the Frequency-Down-Converter (FDC). The DDS board has a clock distribution board that takes 125 MHz. The Analog-to-Digital Converter (ADC) on the DAQ operates with a sampling rate 62.5 MHz. The phase-locked-oscillator (PLO) of the FDC uses a 100 MHz reference signal. Table 5.5.3 lists the reference clock signals provided by the clock distribution board and their respective division rates.

Table 5.5.3 – List of Reference Clock Signals

Destination Sub-System	**Reference Clock Frequency**	**Division Rate**
DDS (CG)	125 MHz	8
ADC (DAQ)	62.5 MHz	16
FDC (CG)	100 MHz	10

5.5.1.4. Reference Chirp Output

The output of the DDS is the reference signal or reference chirp of the chirp generator's PLL. The DDS is configured to output a chirp with the parameters listed in table 5.5.2, every 2 ms

(i.e. PRF is 500 Hz). To evaluate the instantaneous amplitude and frequency of the reference chirp, the DDS output was recorded using a 5 GSPS oscilloscope.

Figure 5.5.3 shows a screenshot of the DDS output. The DDS is configured so that the output power is within the required input power of the PLL. Moreover, it is also set to continue modulating the frequency up and down between the two limits of the chirp frequency. With both of these features, the PLL remains in the locked state for most of the time between PRF pulses. Both of these features can be seen in the screenshot. The amplitude of the waveform is within a certain range. There is a noticeable amplitude modulation, due to the frequency response of the DDS output interface, which shows how the waveform frequency modulation ramps up and down continuously.

As noted in the FPGA section, the DDS is re-configured so that the chirp restarts after every IO_Update trigger, which occurs 10.7 μs after the PRF. The figure shows a chirp pulse begins 10.72 μs after the EPRI pulse. The PRF pulse lags the EPRI pulse by 0.02 μs. Therefore, the chirp is delayed by 10.7 μs from the PRF, as expected.

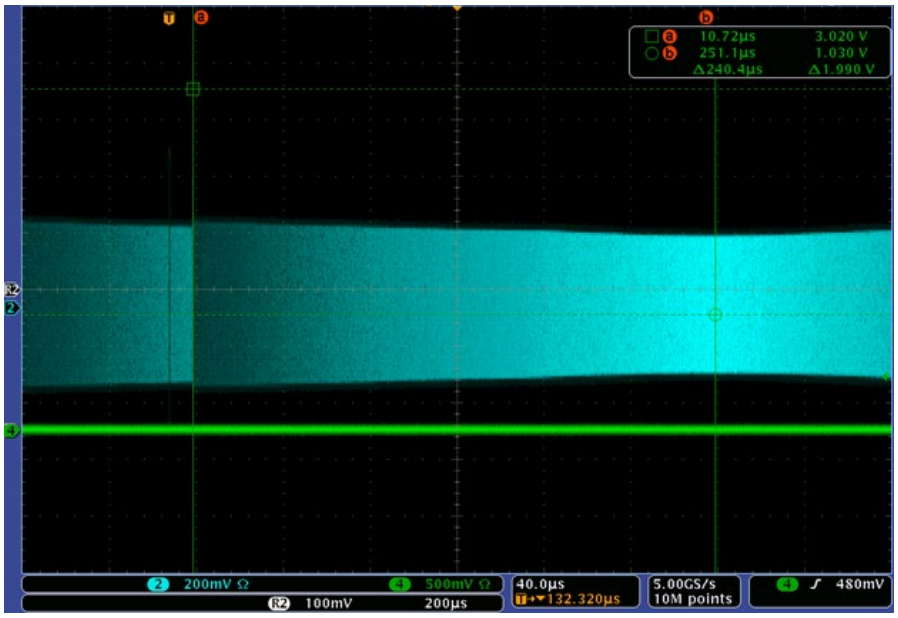

Figure 5.5.3 – Reference Chirp Oscilloscope Screen Capture

The output was recorded to a storage device. Figure 5.5.4 and figure 5.5.5 show the instantaneous power and frequency of the chirp. The amplitude variation over the chirp frequency range is about 2dB. The PLL has an input conditioning sub-system that is used to amplify this reference chirp to the required input power. If this amplitude variation of the reference chirp was large, amplitude modulation should be applied to the DDS output to minimize it. Since it is small (2dB) compared to the allowed variation of about 10dB, amplitude modulation is not required. Additionally, as long as the power of the reference chirp is within the required range, the PLL output is independent of the amplitude of the reference chirp.

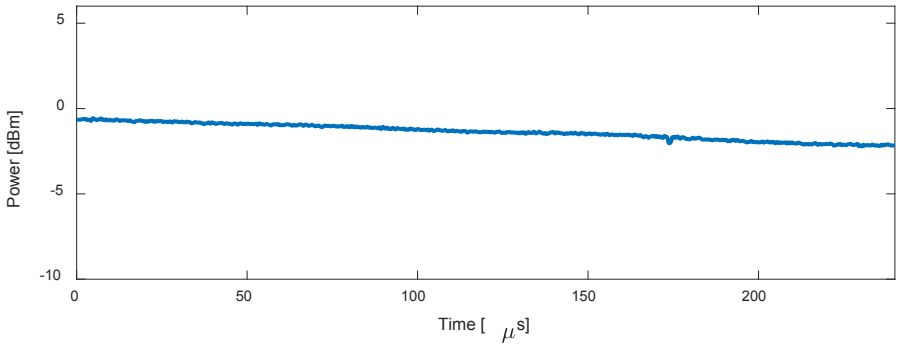

Figure 5.5.4 – Measured Reference Chirp Instantaneous Power

The measured instantaneous frequency shown in figure 5.5.5 shows that the chirp frequency is linearly modulated from 196.43 MHz to 339.29 MHz, as expected.

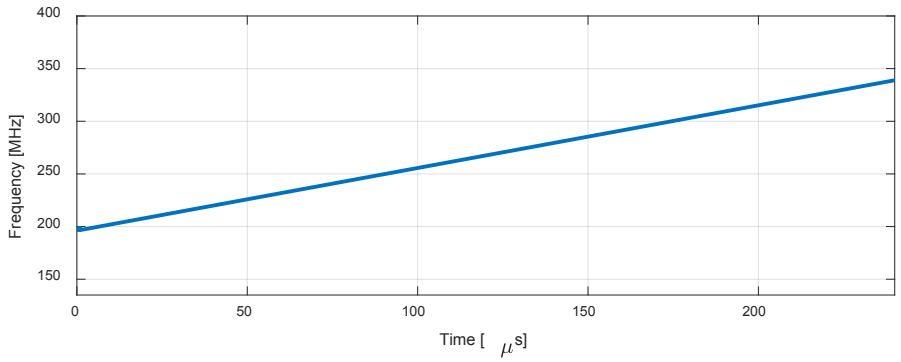

Figure 5.5.5 – Measured Reference Chirp Instantaneous Frequency

5.5.2. RF-CG: 11-19 GHz DDS-Driven Phase-Locked-Loop (PLL)

5.5.2.1. 11-19 GHz DDS-Driven PLL Summary

The 11-19 GHz Phase Locked Loop (PLL) is a frequency synthesizer, driven by a DDS, which outputs an 11-19 GHz chirp. The reference signal of the PLL is a 196.4-339.3 MHz chirp, which is generated by the DDS described in the previous section. A block diagram of the PLL architecture is shown in figure 5.5.6. The parameters of the chirp output of this chirp generator are listed in table 5.5.4.

This PLL was designed as a Type-2, 3rd Order PLL. It uses a 2nd order active loop filter. The PLL system loop bandwidth and phase margin were designed to be 4 MHz and 60 degrees, respectively. The PLL was designed to output the desired frequency range, attenuate phase noise and maintain low spur content.

The main sources of incoherent noise are the charge-pump and the VCO. The source of coherent phase noise is the VCO nonlinearity. A model that describes the measured phase noise at the output of the PLL chirp is given in section 5.5.2.8.

Table 5.5.4 – 11-19 GHz DDS-Driven PLL Output Parameters

Parameter	**Value**
Chirp Frequency Range (Bandwidth)	11-19 GHz (8 GHz)
Chirp Length	240 μs
Output Power	-9 dBm
Incoherent Phase Noise (Normalized)	-48 dBc/Hz
Coherent Phase Noise (Normalized)	-45 dBc/Hz

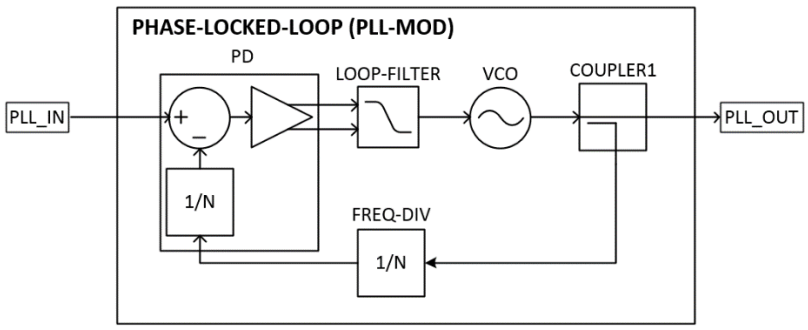

Figure 5.5.6 – 11-19 GHz PLL Architecture

5.5.2.2. PLL Design: Objectives

The main objective of the PLL control system is to drive a voltage-controlled-oscillator (VCO) to output a desired chirp, which is equal to the reference frequency multiplied by a factor N.

Additionally, the PLL is designed to suppress phase noise from the reference signal that is above the loop bandwidth. Similarly, it is also designed to suppress phase noise generated within the PLL that is below the loop bandwidth.

The loop filter is the compensator of the PLL, which sets the loop bandwidth and phase margin of the system. Additionally, the loop filter should attenuate harmonics generated by the phase detector. The loop bandwidth, which is the bandwidth of the closed loop system, is related to the ability of the loop filter to suppress harmonics. Increasing the loop bandwidth translates to larger spurious content at the output.

The phase noise from the DDS is negligible and the phase noise generated within the PLL is significant. Thus, the PLL is designed to have a large loop bandwidth so that phase noise is significantly suppressed while spurious content is kept at a modest level.

5.5.2.3. PLL Design: Component Selection

Figure 5.5.7 shows a block diagram of the designed PLL. The PLL components are listed in table 5.5.5. At the core of the PLL is the Voltage Controlled Oscillator (VCO). The VCO1 listed in table 5.5.5 was selected for its ability to output signals from 11 to 19 GHz.

The PLL multiplication rate from its reference to its output frequency is set to be 56. The multiplication rate is determined by the total frequency division rate at the feedback path. This division rate is achieved by a frequency divider DN1, which divides by 8, and a programmable divider inside (PD1), which is set to divide by 7. DN1 and PD1 are listed in table 5.5.5.

The phase detector PD1 was selected for its ability to operate over the reference frequency band. This device has a phase/frequency detector, a programmable divider and charge pumps. The differential output of the PD1 is proportional to the frequency difference between the reference and feedback signals, if the frequencies are different. If these two frequencies are

equal, the differential output of the PD1 is proportional to the phase difference. The part number and factor of proportionality of PD1 are listed in table 5.5.5.

The directional coupler CP1 has a coupling of 10 dB. It was selected for its operating frequency range.

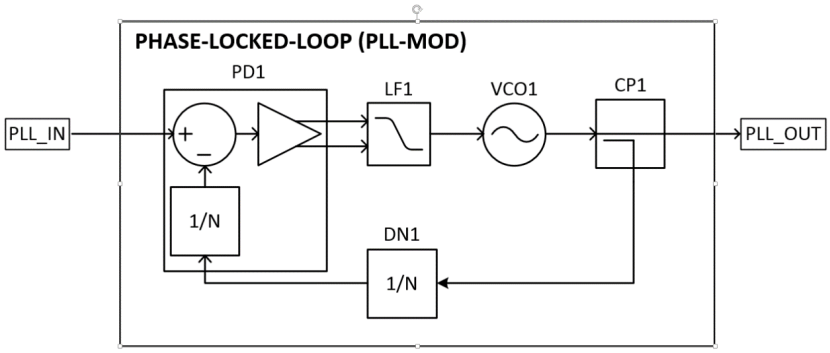

Figure 5.5.7 – 11-19 GHz PLL Block Diagram

Table 5.5.5 – List of Phase-Locked-Loop Module (PLL-MOD) Components

Description (Name)	**Part Number (Manufacturer)**	**Parameter(s)**
Voltage Controlled Oscillator (VCO1)	HMC733LC4B (Analog Devices)	Tuning Sens. (K_{vo}): 550 [MHz/V]
Phase Detector (PD1)	HMC440QS16GE (Analog Devices)	PD Gain (K_D): 1/π [V/rad] Progr. Freq. Div. (N): 2 – 32
Frequency Divider (DN1)	HMC494 (Mini-circuits)	Division Rate (N): 8
Loop Filter (LF1)	Custom Made	(Described in section 5.5.2.6)
Directional Coupler (CP1)	MC0618-10 (Fairview Microwave)	Coupling: 10 [dB]

5.5.2.4. PLL Design: System Model

System Overview

The PLL is a closed-loop control system with an output that tracks the reference phase or frequency. The systems in the forward path are the phase detector, the loop filter and the VCO. The transfer functions of the forward path are K_d, $Z(s)$, $2\pi K_v(s)/s$, respectively. The system in the feedback path are the frequency divider and its transfer function is $1/N$. The open loop transfer function is the product of the transfer functions of the forward and feedback paths. Figure 5.5.8 shows a block diagram of the PLL system model.

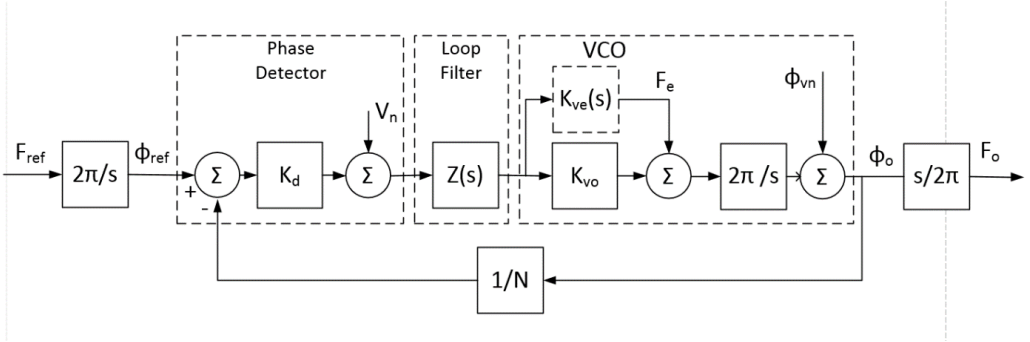

Figure 5.5.8 – Block Diagram of PLL System Model

Incoherent Noise

All the components, the phase detector, the charge pump, the loop filter, the VCO and the frequency divider, add random noise to the system. The most significant random noise sources in the PLL are the VCO and the charge pump. Noise sources in a PLL are described in detail in [10]. Figure 5.5.8 includes the random noise added to the output of the VCO and the phase-detector/charge-pump. If the waveform generated with the PLL, such as a chirp, is repeated

periodically, this type of noise is uncorrelated from one waveform to another. For this reason, we refer to this type of noise as incoherent noise.

Coherent Noise

Coherent noise is a deterministic signal that is undesired. In contrast to interference signals, which usually have PSDs with narrow band content, the deterministic PSD of coherent noise is usually spread in frequency, similar to those of random signals. Coherent noise is usually synchronized to another deterministic signal, such as the instantaneous frequency of a chirp.

The tuning sensitivity of a VCO (K_v) is the factor that relates the output frequency $F_o(s)$ to the input or tuning voltage $V_t(s)$ of the VCO, as shown by (5.5.6). The value of the tuning sensitivity depends on the neighborhood of the output frequency ($\approx F_{oi}(s)$). Thus, if we model the total tuning sensitivity $K_v(s)$ as the sum of the constant (K_{v0}) and a variable factor $K_{ve}(s)$ (5.5.7), the output frequency of the VCO becomes the sum an ideal frequency $F_{oi}(s)$ and an error term $F_e\ (s)$ that depends on the ideal output frequency ($F_{oi}(s)$) (5.5.8). This error term is undesired, noise-like, and it is synchronized to the output frequency. Thus, $F_e\ (s)$ is the coherent noise of the total output frequency of the VCO $F_o\ (s)$.

$$F_o(s) = V_t(s)\, K_v(s) \tag{5.5.6}$$

$$K_v(t) = K_{v0} + K_{ve}(t) \tag{5.5.7}$$

$$F_o(s) = F_{oi}(s) + F_e(s) \tag{5.5.8}$$

$$F_{oi}(s) = V_t(s)\, K_{v0} \tag{5.5.9}$$

$$F_e\,(s) = V_t(s)\, K_{ve}(s) \tag{5.5.10}$$

In a PLL, the coherent noise of the output frequency is modified by the transfer function $E(s)$, as shown in (5.5.11). The PLL is designed so that $E(s)$ suppresses noise below the cutoff frequency of the PLL.

$$F_o(s) = F_{oi}(s) + F_e(s)E(s) \tag{5.5.11}$$

Output Signal and Noise Models

From the block diagram in figure 5.5.8, the output frequency and phase of the PLL are given by (5.5.12) and (5.5.13), respectively. The term $F_{0i}(s)$ is the ideal output frequency which is given by (5.5.14). The terms $\Phi_{cn}(s)$ and $\Phi_{in}(s)$ are the coherent and incoherent noise terms of the phase output, given by (5.5.15) and (5.5.16), respectively.

$$F_0(s) = F_{0i}(s) + \frac{s}{2\pi}[\Phi_{cn}(s) + \Phi_{in}(s)]E(s) \tag{5.5.12}$$

$$\Phi_o(s) = \frac{2\pi}{s}F_{0i}(s) + [\Phi_{cn}(s) + \Phi_{in}(s)]E(s) \tag{5.5.13}$$

$$F_{0i}(s) = F_{ref}(s)H(s) \tag{5.5.14}$$

$$\Phi_{cn}(s) = \frac{2\pi}{s}\, F_e(s) \cdot E(s) \tag{5.5.15}$$

$$\Phi_n(s) = \frac{2\pi}{s} V_n(s) \cdot Z(s) K_v E(s) + \Phi_{vn}(s) E(s) \tag{5.5.16}$$

The closed-loop $H(s)$, open-loop $G(s)$ and disturbance $E(s)$ transfer functions are given by (5.5.17), (5.5.18) and (5.5.19). In this control system, coherent and incoherent noise sources within the PLL are considered disturbances. The closed-loop transfer function, which is the transfer function of the PLL, behaves as a low-pass filter with cut-off frequency equal to the loop-bandwidth. The closed-loop transfer function has a gain of N over its band, so that the output frequency is equal to the reference frequency multiplied by N. The disturbance transfer function has unity gain over its band and behaves as a high-pass filter. The disturbance transfer function suppresses the noise at the output below the PLL cutoff frequency.

$$H(s) = N \frac{G}{G+1} \tag{5.5.17}$$

$$G(s) = \frac{1}{sN} K_d K_{v0} Z(s) \tag{5.5.18}$$

$$E(s) = \frac{1}{G+1} \tag{5.5.19}$$

5.5.2.5. PLL Design: Phase Margin, Loop Bandwidth, Type and Order

Phase Margin

The phase margin is a stability parameter defined as the phase difference between 180 degrees and the phase of the open loop frequency response at the loop-bandwidth, as shown by (5.5.20) and (5.5.21). If the phase margin is less than 30 degrees, the PLL is prone to become unstable.

Typical values for the phase margin fall between 30 and 80 degrees, with 48 degrees being the optimal value with respect to settling and tracking times. However, larger values of phase margin are preferred to tolerate variations in the VCO tuning sensitivity. We choose the phase margin of 60 degrees, which provides a somewhat fast response while allowing some VCO gain variations.

$$\varphi_m = 180 - |\angle G(\omega_0)| \tag{5.5.20}$$

$$|G(\omega_0)| = 0\ dB \tag{5.5.21}$$

Loop Bandwidth

The loop bandwidth is one of the most important parameters of the PLL. In order to minimize phase noise from the VCO and other noise sources within the loop, the loop bandwidth should be as high as possible.

On the other hand, the loop bandwidth should be sufficiently low so that spurs related to the phase detector are attenuated to a tolerable level. A rule of thumb for the selection of the loop bandwidth is that it should be less than 1/10 of the minimum reference frequency.

We choose the loop bandwidth of 4.6 MHz, which is about 1/40 of the minimum reference frequency.

Type and Order

The type of a PLL is the number of poles at the origin of the open-loop transfer function, while the order is the total number of poles. Since this PLL is driven by a frequency ramp, the Laplace transform of the reference frequency is proportional to $1/s^2$. Thus, the PLL must have at least type 2 so that the output frequency has zero steady-state error, as shown by (5.5.22).

$$e(\infty) = \lim_{s\to 0}\left\{s\ 1/s^2 \frac{1}{1+G(s)}\right\} = \frac{1}{\lim_{s\to 0}\{s\ G(s)\}} = 0 \tag{5.5.22}$$

The order of the PLL is set to 3rd-order. A 3rd-order PLL uses a second order loop filter, which sufficiently attenuates the harmonics out of the phase detector in this PLL.

5.5.2.6. PLL Design: Loop Filter

The loop filter is the compensator of the PLL. It is designed to set the loop bandwidth, phase margin, type and order of the PLL. Additionally, the loop filter filters out the harmonics generated by the phase-detector/charge-pump.

In the previous section, the PLL was set to be third order and type-2. For this reason, the loop filter should be second order and have one pole at the origin. Additionally, the loop bandwidth and phase margin were set to 4.6 MHz and 60 degrees respectively. The two poles and one zero of the loop filter should be designed to achieve these specifications.

The desired output frequency of the VCO (11-19 GHz) requires a tuning voltage range of about 2-15 volts. The output voltage range of the phase detector is -1 to +1 volts. Therefore, voltage amplification is required to drive the VCO with the output signal form the phase detector.

Additionally, the output of the phase detector is a differential signal and the input of the VCO a single-ended signal. A differential active loop filter could be used to subtract the output of the phase detector and amplify that signal to the required level. This is the loop filter topology selected. Figure 5.5.9 shows the schematic of the differential active loop filter chosen, which is second order and has a pole at the origin.

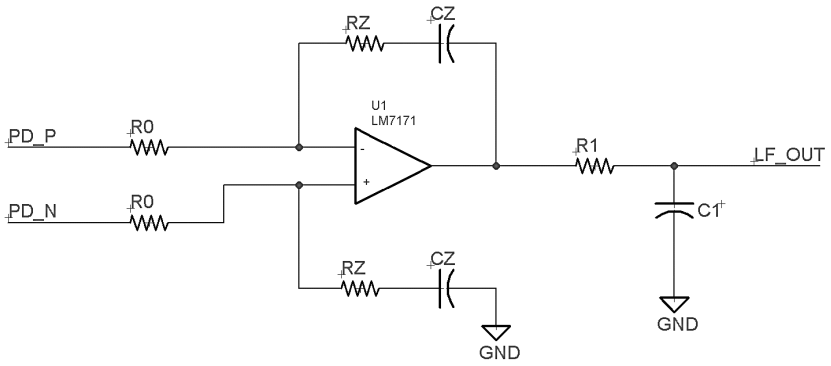

Figure 5.5.9 – Schematic of the Second-Order Active Loop Filter

The frequency response of the loop filter is given by (5.5.23). The time constants used in equation (5.5.23) are given by (5.5.24-5.5.26).

$$Z(\omega) = \frac{(1 + j\omega\tau_z)}{j\omega\ \tau_{p0}\left(1 + j\omega\ \tau_{p1}\right)} = \frac{1 + j\omega(R_z C_z)}{j\omega\ (R_0 C_z)\ [1 + j\omega\ (R_1 C_1)]} \tag{5.5.23}$$

$$\tau_z = R_z C_z \tag{5.5.24}$$

$$\tau_{p0} = R_0 C_z \tag{5.5.25}$$

$$\tau_{p1} = R_1 C_1 \tag{5.5.26}$$

It can be shown that the time constants of the loop filter for a given loop bandwidth ω_o, phase margin φ_m and PLL parameters (K_{v0}, K_d and N) are given by (5.5.27-5.5.59). Therefore, the poles are at 0 Hz and 17.2 MHz and the zero is at 1.2 MHz.

$$\tau_{p1} = \frac{\sec(\varphi_m)\text{-}\tan(\varphi_m)}{\omega_0} = 9.27\ ns \tag{5.5.27}$$

$$\tau_z = \frac{1}{{\omega_0}^2\ \tau_2} = 129.12\ ns \tag{5.5.28}$$

$$\tau_{p0} = \frac{K_{v0}K_d}{N{\omega_0}^2}\sqrt{\frac{1+(\omega_0\tau_z)^2}{1+\left(\omega_0\tau_{p1}\right)^2}} = 13.97\ ns \tag{5.5.29}$$

$$f_{p0} = 0\ \text{Hz} \tag{5.5.30}$$

$$f_{p1} = \frac{1}{2\pi\ \tau_{p1}} = 17.2\ \text{MHz} \tag{5.5.31}$$

$$f_z = \frac{1}{2\pi\ \tau_z} = 1.2\ \text{MHz} \tag{5.5.32}$$

We choose the capacitor values to be $C_z = 220\ \text{pF}$ and $C_1 = 22\ \text{pF}$. So that the required resistor values become $R_z = 586\ ohm$, $R_0 = 63\ ohm$ and $R_1 = 421\ ohm$. We choose the standard resistor values of $R_z = 510\ ohm$, $R_0 = 62\ ohm$ and $R_1 = 430\ ohm$.

The op-amp selected for the active loop filter is the LM7171. This op-amp was selected for its very high slew rate of 4100 V/μs, large 3 dB bandwidth of 220 MHz, and support of +/- 18 V supply voltage. The required voltage range for the tuning voltage of the VCO is about 2 to 15 V

so that it outputs 11-19 GHz. This op-amp has this output voltage range when supplied with +/-18 V. It was also selected for being a voltage-feedback amplifier, as opposed to a current-feedback amplifier. This type of amplifier allows the implementation of zeros by using a resistor in series with a capacitor in the feedback path.

5.5.2.7. PLL System Response Simulations

Loop Filter Frequency Response: *Z(f)*

The frequency response for the loop filter described in the previous section is plotted in figure 5.5.10. The loop filter was designed as a second order system with one pole at zero, one pole at 17.2 MHz and one zero at 1.2 MHz. The plot shows that the system response decays by -20 dB/decade from 0 to 1.2 MHz, 0 dB/decade from 1.2 MHz to 17.2 MHz and -20 dB/decade after 17.2 MHz, as expected by the pole/zero locations.

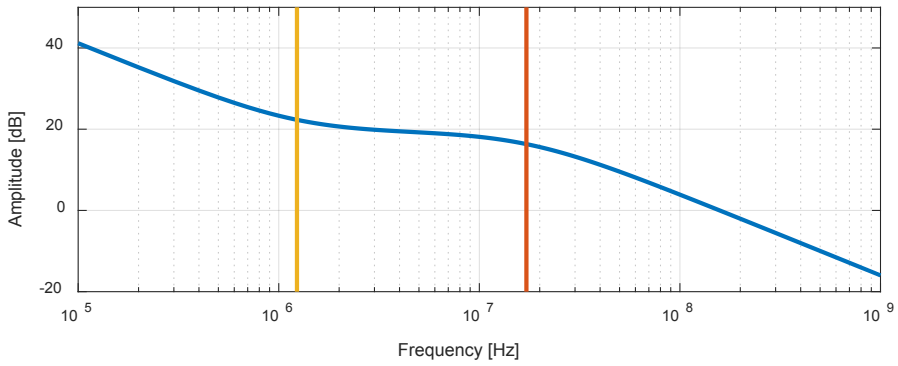

Figure 5.5.10 – Frequency Response of Loop Filter

Open Loop Frequency Response: *G(f)*

Replacing the frequency response of the loop filter in (5.5.23) and the PLL parameters in table 5.5.5 to equation (5.5.18), we can compute the frequency response of the open-loop system.

The amplitude of the frequency response for the open-loop system is plotted in figure 5.5.11. Its phase is plotted in figure 5.5.12. The amplitude plot shows that the 0 dB crossing occurs at the specified cutoff-frequency (i.e. loop bandwidth) (4.6 MHz). This simulation verifies that the simulated system has the specified loop bandwidth. The phase plot has an amplitude of -120 degrees at the cutoff frequency. This means that the phase margin of the system is 60 degrees, as specified in the design. This simulation of both amplitude and phase verifies the specified design parameters of the PLL.

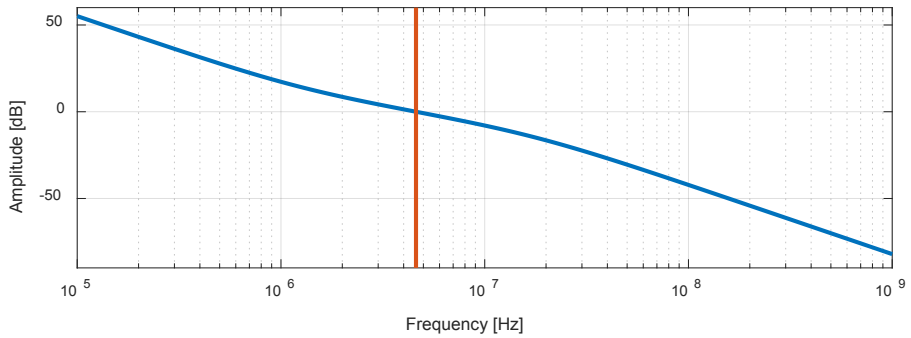

Figure 5.5.11 – Amplitude of Frequency Response of Open Loop System

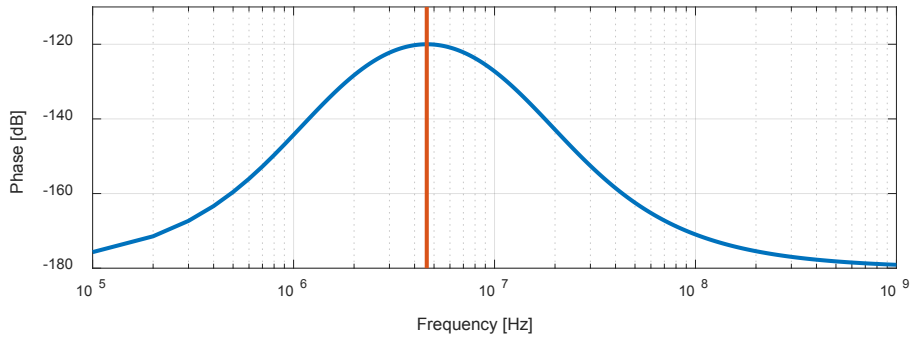

Figure 5.5.12 – Phase of Frequency Response of Open Loop System

Closed Loop Frequency Response: *H(f)*

Replacing the open-loop system response into equation (5.5.17), we can compute the closed-loop system response. Figure 5.5.13 shows a plot of the amplitude of the frequency response for the PLL closed-loop system. This plot shows that the closed-loop system acts as a low-pass filter with cutoff frequency of 4.6 MHz. The gain of the closed-loop system is equal to *N* (56). The simulation shows that both the gain and cutoff frequency agree with the specified parameters. Figure 5.5.14 shows the normalized closed-loop system.

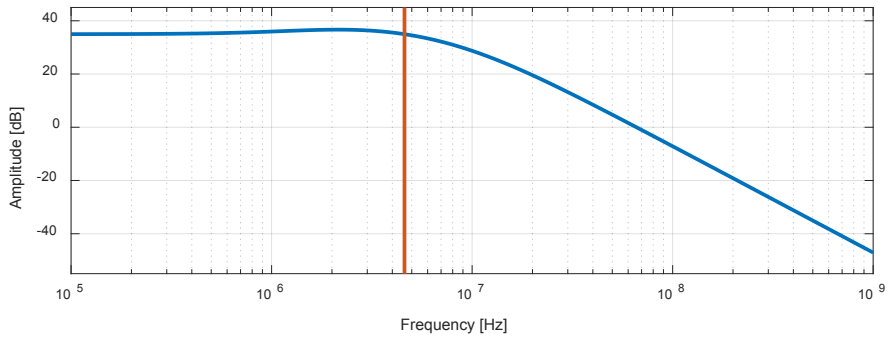

Figure 5.5.13 –Frequency Response of Closed-Loop System

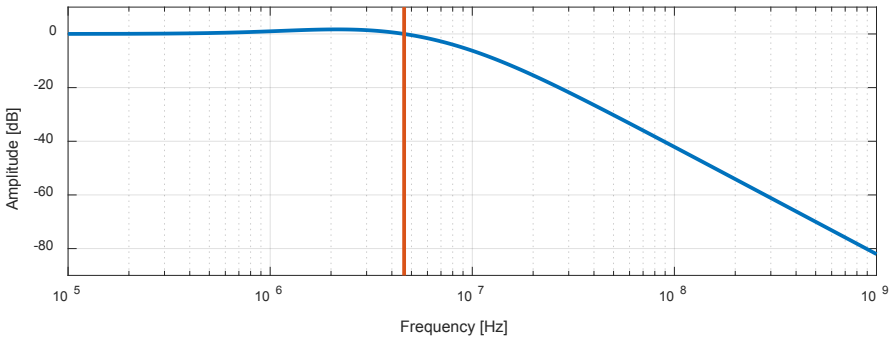

Figure 5.5.14 – Normalized Frequency Response of Closed-Loop System

Disturbance Frequency Response: *E(ω)*

Figure 5.5.15 shows the simulated disturbance frequency response. This system response acts as a high-pass filter, suppressing coherent and incoherent noise below the cutoff-frequency (loop bandwidth).

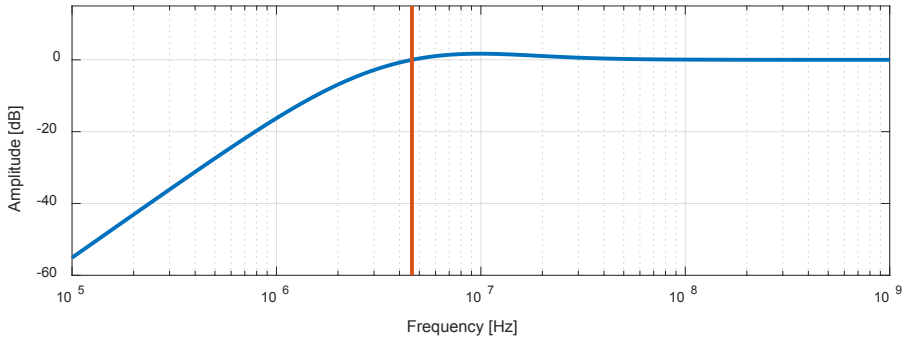

Figure 5.5.15 – Frequency Response for Disturbances (PLL Correction Term)

5.5.2.8. PLL Performance: Phase Noise and System Response

Incoherent Phase Noise

The PSD of the incoherent phase noise of the PLL is given by (5.5.33), where $S_{\varphi_{uin}\varphi_{uin}}(f)$ is the uncompensated/unfiltered incoherent phase noise and $E(f)$ is the disturbance system response applied by the PLL. From section 5.5.2.4, the PSD of the incoherent phase noise can be modeled as (5.5.34). The term $S_{v_n v_n}(f)$ is the PSD of the voltage noise due to the charge pump, which can be assumed white and Gaussian. The loop filter has a pole at the origin, a zero before the cutoff frequency and a pole after the cutoff frequency. Thus, the first summand in $S_{\varphi_{uin}\varphi_{uin}}(f)$ is phase noise that is greater than second but lower than fourth order.

$$S_{\varphi_{in}\varphi_{in}}(f) = |E(f)|^2 \, S_{\varphi_{uin}\varphi_{uin}}(f) \tag{5.5.33}$$

$$S_{\varphi_{uin}\varphi_{uin}}(f) = \frac{1}{(2\pi f)^2}\left|\frac{Z(f)K_{vo}}{2\pi}\right|^2 S_{v_n v_n}(f) + S_{\varphi_n\varphi_n}(f) \tag{5.5.34}$$

Finding a simple expression for the PSD of incoherent phase noise is useful for computing simulations and models of the output signal and noise of the radar. This type of analysis is performed in section 5.7. To find this simple expression, we measured the output of the PLL with an oscilloscope in single-tone mode, computed the phase noise PSD and fitted a PSD curve.

The output of the PLL was measured using an oscilloscope operating with a sampling rate of 50 GSPS. Single-tone measurements were taken with time length 240 μs at PLL output frequencies between 11 and 19 GHz, spaced by 1 GHz. The PSD of the phase noise was computed by using the small angle approximation and estimated using the Welch method. The normalized PSD of the phase noise was found by dividing the PSD of phase noise by the peak of the PSD of the carrier. Figure 5.5.16 shows the normalized PSD of the phase noise at 11, 15 and 19 GHz. Since the tuning sensitivity for single-tone measurements is constant, the phase noise only contains incoherent noise.

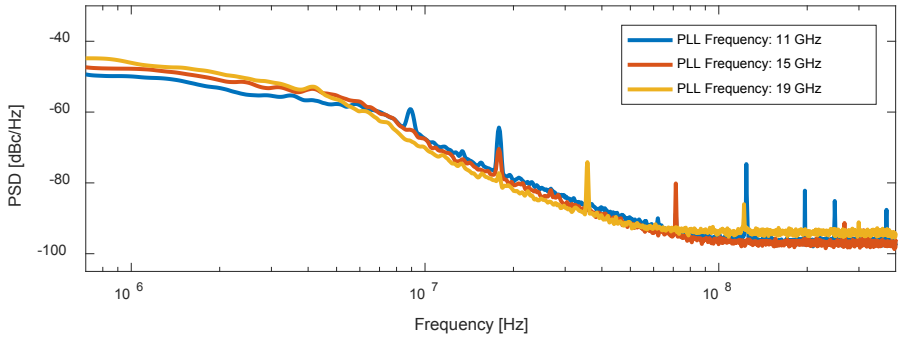

Figure 5.5.16 – Normalized PSD of Incoherent Phase Noise of PLL output at 11, 15 and 19 GHz

To find an approximated model of the incoherent phase noise, we assumed that the phase noise is composed of a zero order component (tail of phase noise) and a higher order component. Then, we found numerically the parameters that minimize the mean-squared-error between the model and the average of the measured phase noise. Since the PLL compensation *E(f)* term is insignificant for values much larger than the loop bandwidth, the curve fitting was performed only for frequencies between 15 MHz to 300 MHz. Using this procedure, an approximated model for the incoherent component of phase noise is given by (5.5.35). From (5.5.35), the uncompensated phase noise has a zero-order and a 3.5th order components.

$$S_{\varphi_{uin}\varphi_{uin}}(f) = \left[\frac{1}{(2\pi f)^0}\frac{{\varphi_{rms0}}^2}{B_n} + \frac{1}{(2\pi f)^{3.5}}\frac{{\varphi_{rms3.5}}^2}{B_n}\right] \tag{5.5.35}$$

The first summand in (5.5.36) is the zero-order component of the incoherent phase noise model. From section 5.2.4, the zero-order derivative of zero-order instantaneous phase noise is band-limited white Gaussian. Similarly, the 1.75th order derivative of 3.5th order phase noise is band-limited white Gaussian.

$$\varphi_0(t) = \frac{\partial^0 \varphi(t)}{\partial t^0} = \varphi(t) \tag{5.5.36}$$

$$\varphi_{1.75}(t) = \frac{\partial^{1.75} \varphi(t)}{\partial t^{1.75}} \tag{5.5.37}$$

The PSD of the zero-order derivative of the zero-order phase noise component is -135 dB/Hz. The PSD of the 1.75th order derivative of 3.5th-order phase noise component is 166.8 dB/Hz.

$$S_{\varphi_0\varphi_0}(f)_{dB} = \left[\frac{(\varphi_{rms0})^2}{B_n}\right]_{dB} = -135.0 \text{ dB/Hz} \tag{5.5.38}$$

$$S_{\varphi_{1.75}\varphi_{1.75}}(f)_{dB} = \left[\frac{(\varphi_{rms3.5})^2}{B_n}\right]_{dB} = +166.8 \text{ dB/Hz} \tag{5.5.39}$$

Figure 5.5.17 shows a comparison of the average of the measurements and the approximated unfiltered model described by (5.5.35).

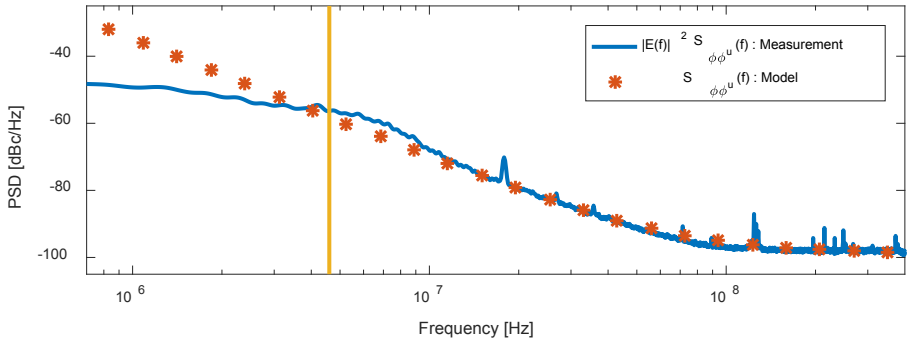

Figure 5.5.17 – Normalized PSD of Incoherent Phase Noise of PLL and PSD of Unfiltered Model

The compensation filter of the PLL or disturbance transfer function *E(f)* was described in section 5.5.2.4 and it was plotted in section 5.5.2.7. Figure 5.5.18 shows a comparison of the measured

PSD of the incoherent phase noise and the compensated model of incoherent phase noise. The compensated model agrees well with the measurement. The yellow line indicates the cutoff frequency of the PLL.

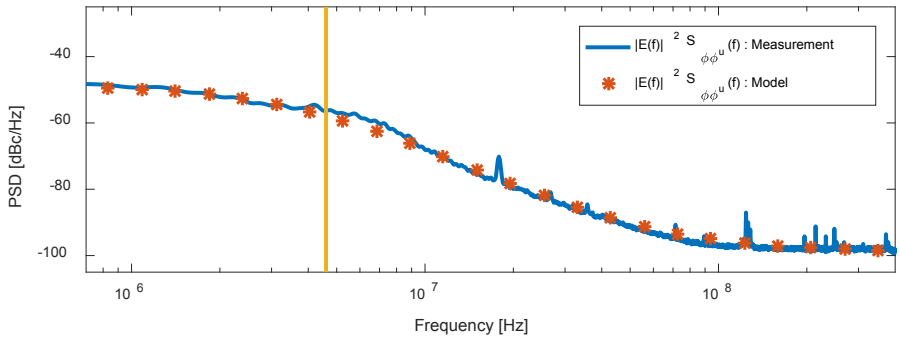

Figure 5.5.18 – Normalized PSD of Incoherent Phase Noise of PLL and PSD of Model

Coherent Phase Noise

From section 5.5.2.4, the PSD of the coherent phase noise of the PLL output is given by (5.5.40), where $S_{\varphi_{uin}\varphi_{uin}}(f)$ is the unfiltered coherent phase noise and $E(f)$ is the PLL compensation filter or disturbance transfer function. The PSD of the unfiltered coherent phase noise is given by (5.5.41).

$$S_{\varphi_{cn}\varphi_{cn}}(f) = |E(f)|^2 \, S_{\varphi_{uin}\varphi_{uin}}(f) \tag{5.5.40}$$

$$S_{\varphi_{ucn}\varphi_{ucn}}(f) = \frac{1}{(2\pi f)^2} |\, 2\pi \, F_e(f)|^2 \tag{5.5.41}$$

In order to find an approximated model for the PSD of the coherent phase noise, we followed a similar procedure performed for the incoherent component.

The coherent phase noise was measured by measuring the PLL output in chirp mode. The phase noise of the chirp was determined by the decorrelation method. This method involves mixing the chirp with itself digitally using a large delay and computing the envelope of the output. The phase noise is found by dividing this envelope by 4. The chirp used was the 11-19 GHz chirp at a chirp length of 240 μs.

The approximated model found for the PSD of coherent phase noise is given by (5.5.42). The coherent phase noise was found to have a zero-order and 3.5th-order components.

$$S_{\varphi_{ucn}\varphi_{ucn}}(f) = \left[\frac{1}{(2\pi f)^0}\frac{{\varphi_{rms0}}^2}{B_n} + \frac{1}{(2\pi f)^{3.5}}\frac{{\varphi_{rms3.5}}^2}{B_n}\right] \tag{5.5.42}$$

The PSD of the white phase noise component is 133.3 dB/Hz. The PSD of the 1.75-th derivative of the 3.5th-order component is 168.1 dB/Hz.

$$S_{\varphi_0\varphi_0}(f)_{dB} = \left[\frac{(\varphi_{rms0})^2}{B_n}\right]_{dB} = -133.3 \text{ dB/Hz} \tag{5.5.43}$$

$$S_{\varphi_{1.75}\varphi_{1.75}}(f)_{dB} = \left[\frac{(\varphi_{rms3.5})^2}{B_n}\right]_{dB} = +168.1 \text{ dB/Hz} \tag{5.5.44}$$

Figure 5.5.19 shows a comparison of the approximated model of the unfiltered coherent phase noise and the measured coherent phase noise.

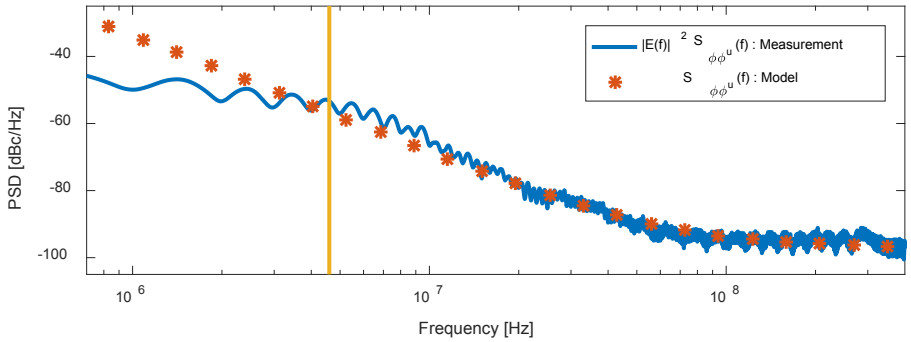

Figure 5.5.19 – Normalized PSD of Coherent Phase Noise of PLL and PSD of Unfiltered Model

The coherent phase noise model is then found by applying the PLL compensation filter to the unfiltered model. Figure 5.5.20 compares the PSD of the model and measurement of the normalized coherent phase noise.

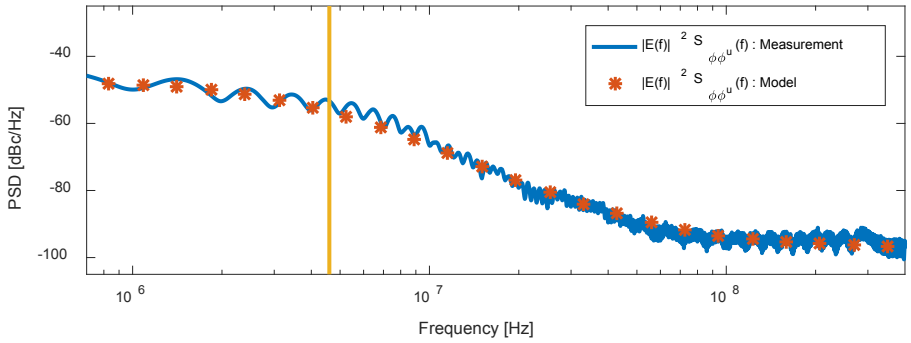

Figure 5.5.20 – Normalized PSD of Coherent Phase Noise of PLL and PSD of Model

5.5.2.9. PLL Performance: System Response

In this section, we evaluate the performance of the compensation applied by the PLL to the disturbances in the system (i.e. phase noise). The applied compensation filter or disturbance

transfer function can be determined by dividing the PSD of the compensated phase noise $S_{\varphi_n\varphi_n}(\omega)$ by the unfiltered phase noise $S_{\varphi_n\varphi_n u}(f)$, as shown in (5.5.45).

$$|E(f)|^2 = \frac{S_{\varphi_n\varphi_n}(f)}{S_{\varphi_n\varphi_n u}(f)} \tag{5.5.45}$$

We may compute the compensation filter using the incoherent or coherent noise. The designed or model compensation filter was plotted in section 5.5.2.7. Figure 5.5.21 and figure 5.5.22 show the measured compensation filter using the incoherent and coherent phase noises, respectively. Both measurements agree well with the designed model.

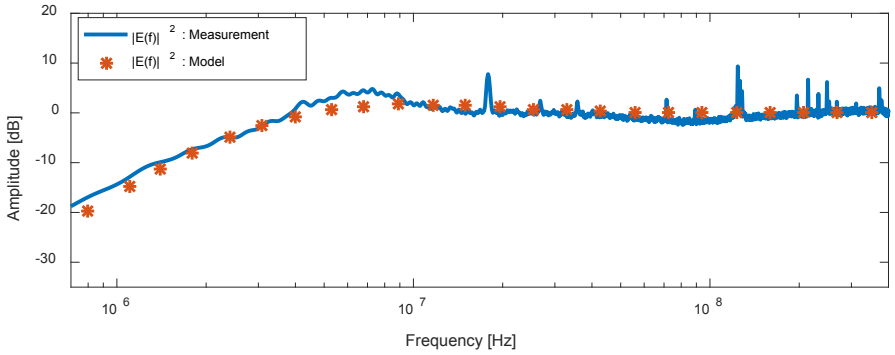

Figure 5.5.21 – Compensation filter determined using the measured incoherent phase noise

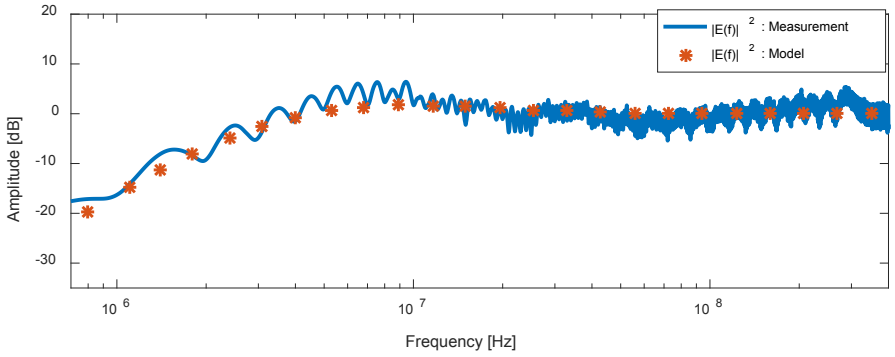

Figure 5.5.22 – Compensation filter determined using the measured coherent phase noise

5.5.2.10. PLL Performance: Output Power and Frequency

The PLL was designed to output an 11-19 GHz chirp, swept in 240 µs. The PLL itself outputs a signal with a time-average power of -9 dBm. Figure 5.5.23 shows a plot of the instantaneous power at the output of the PLL in chirp mode. This power level is amplified by a conditioning system described section 5.5.2.4. The

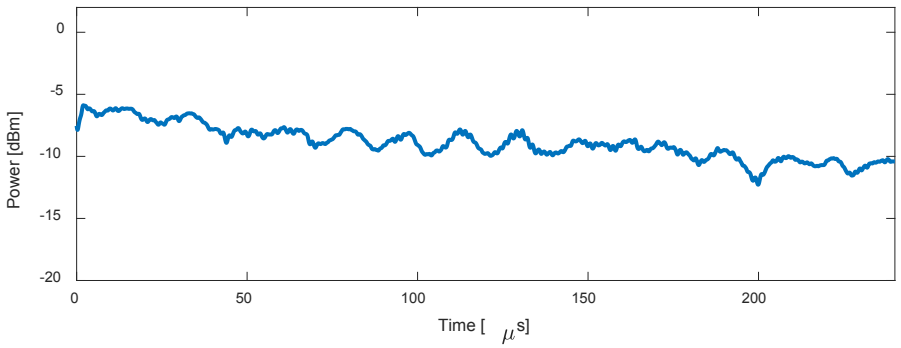

Figure 5.5.23 - Instantaneous Power of PLL Output

We may also compute the instantaneous frequency at the output of the PLL using the Hilbert transform. Figure 5.5.24 shows the instantaneous frequency for the 11-19 GHz chirp at the output of the PLL. This plot shows a frequency sweep of 11 to 19 GHz in a time length of 240 µs.

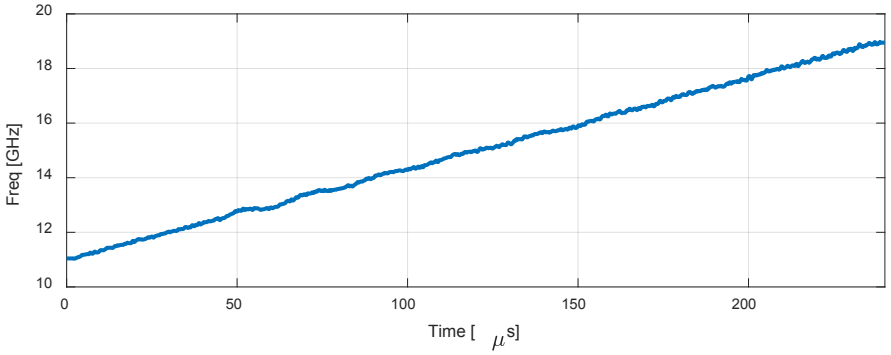

Figure 5.5.24 – Instantaneous Frequency of PLL Output

5.5.3. PLL Conditioning Systems

The input and output of the PLL interface with the DDS and the frequency multiplier (X2) sub-systems. Conditioning systems are used at these two interfaces so that power level requirements are met. The conditioning system also filter out undesired signals. Figure 5.5.25 shows a high-level block diagram of the PLL, including the conditioning systems.

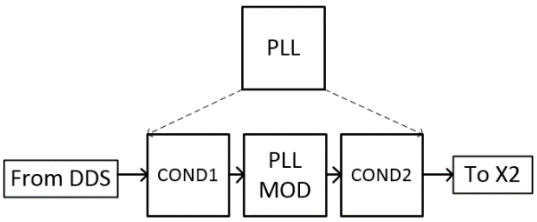

Figure 5.5.25 – High Level Block Diagram of PLL with Conditioning Systems

The time-average power at the output of the DDS is -1.37 dBm. The phase detector of the PLL requires a power level between -10 and +10 dBm. The conditioning system at the input of the PLL (COND1) effectively attenuates the DDS output signal by 6 dB, so that the power level of the reference signal of the PLL is -7.37 dBm. An amplifier is used in COND1 so that the phase detector is isolated from the DDS output signal when the RF front-end is turned off. COND1 also includes a 400 MHz low pass filter that serves as the reconstruction filter of the DDS output. Figure 5.5.26 shows a block diagram for COND1 and table 5.5.6 shows a list of its components.

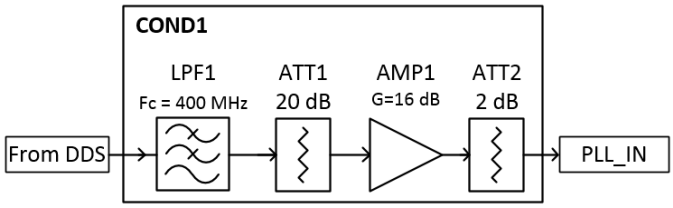

Figure 5.5.26 – Block Diagram of PLL Input Conditioning System (COND1)

Table 5.5.6 – List of COND1 Components

Description (Name)	**Part Number (Manufacturer)**	**Parameter(s)**
Low Pass Filter (LPF1)	Custom Made	3 dB Cutoff Frequency: 400 MHz
Attenuator (ATT1)	BW-S20W2+ (Mini-circuits)	IL: 20 dB
Amplifier (AMP1)	ZX60-V62+ (Mini-Circuits)	Gain: 16 dB
Attenuator (ATT2)	BW-S2W2+ (Mini-circuits)	IL: 2 dB

The time-average power of the chirp at the output of the PLL is -9 dBm. The required input power at the input of the frequency down-conversion sub-system is 7 dBm. The conditioning system at the output of the PLL (COND2) provides a 16 dB gain to meet power level requirements at the input of X2. Additionally, COND2 also filters harmonics created by the VCO and other out-of-band frequency content. Figure 5.5.27 shows a block diagram for COND2 and table 5.5.7 shows a list of its components.

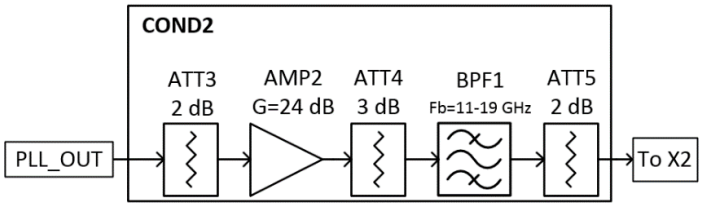

Figure 5.5.27 – Block Diagram of PLL Input Conditioning System (COND1)

Table 5.5.7 – List of COND2 Components

Description (Name)	**Part Number (Manufacturer)**	**Parameter(s)**
Attenuator (ATT3)	BW-S2W2+ (Mini-Circuits)	IL: 2 dB
Amplifier (AMP2)	ZX60-24+ (Mini-Circuits)	Gain: 24 dB
Attenuator (ATT4)	BW-S3W2+ (Mini-circuits)	IL: 3 dB
Band-Pass Filter (BPF1)	14 IZ7-15000/A9000-S/S (Lorch Microwave)	1dB Pass-Band: 11-19 GHz
Attenuator (ATT5)	BW-S2W2+ (Mini-circuits)	IL: 2 dB

5.5.4. RF-CG: Frequency Multiplier, Frequency Down-Conversion and Driver

Frequency Multiplier (X2)

A frequency multiplier (X2) sub-system is used to double the frequency at the output of the PLL from 11-19 GHz to 22-38 GHz. To accomplish this task, the X2 sub-system uses a frequency multiplier device (FM1) and a band pass filter, which rejects high frequency harmonics. The output power of the frequency multiplier (FM1) is 7 dBm and the output power of X2 is -6 dBm.

Figure 5.5.28 shows the X2 block diagram and its interaction with the FDC sub-system. Table 5.5.8 shows a list of the X2 components.

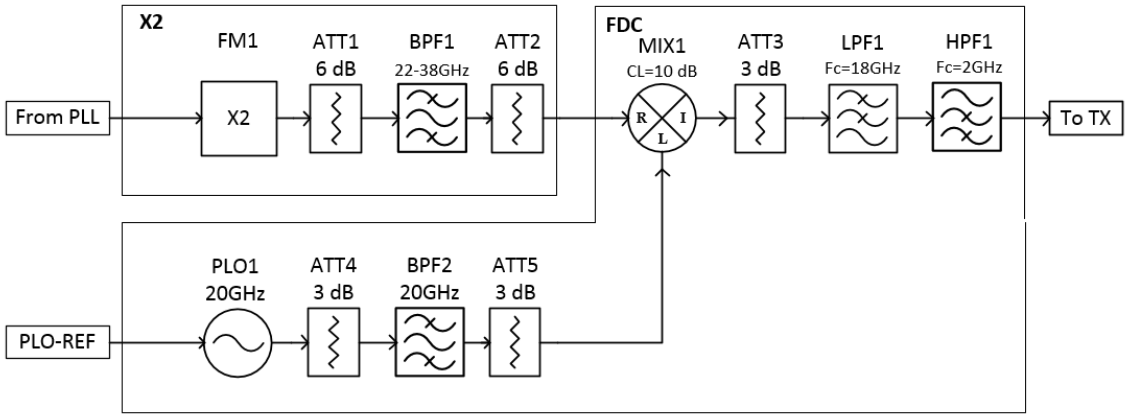

Figure 5.5.28 – Block Diagram of Frequency Doubler (X2) and Frequency Down-Conversion (FDC)

Table 5.5.8 – List of Frequency Doubler (X2) Components

Description (Name)	**Part Number (Manufacturer)**	**Parameter(s)**
Frequency Multiplier (FM1)	A2X1840-2 (Microwave Dynamics)	Multiplying Factor: 2 ; Output Power: +7 dBm Input Band: 9-20 GHz Output Band: 18-40 GHz
Attenuator (ATT1)	PE7090-3 (Pasternack)	IL: 3 dB
Band-Pass Filter (BPF1)	SWF-30316350-28-B2 (Sage Millimeter)	Pass-Band: 22-38 GHz IL: 2 dB
Attenuator (ATT2)	PE7395-2 (Pasternack)	IL: 2 dB

Frequency Down-Converter (FDC)

A frequency down-converter (FDC) of the chirp generator shifts the frequency at the output of X2 from 22-38 GHz to 2-18 GHz. The chirp at the output of X2 is fed to a mixer that is driven at the LO port by a 20 GHz single tone.

The LO signal of 20 GHz is generated with a phase-locked-oscillator (PLO1). High frequency harmonics at the output of the PLO are filtered out using a band-pass filter (BPF2). The output power of the PLO is 20 dBm. This signal is attenuated so that the signal at the LO port in the FDC is 13 dBm.

The output of the mixer used for down-conversion, the output at the IF port of the mixer, is filtered using a high-pass and a low-pass filter. The time-average power at the output of the FDC is -20 dBm.

The block diagram of the FDC is shown in figure 5.5.28. Table 5.5.9 shows the list of components of the FDC.

Table 5.5.9 – List of Frequency Down-Converter (FDC) Components

Description (Name)	**Part Number (Manufacturer)**	**Parameter(s)**
Mixer (MIX1)	TB0440LW1 (Narda-Miteq)	CL: 10 dB LO Power: 13 dBm RF Band: 4-40 GHz IF Band: 0.5 – 20 GHz
Attenuator (ATT1)	BW-S3W2+ (Mini-circuits)	IL: 3 dB
Low Pass Filter (LPF1)	L18G20G1 (Microwave Circuits)	Pass-Band: 2 - 18 GHz
High Pass Filter (HPF1)	H02G18G6 (Microwave Circuits)	Pass-band: DC-18 GHz
Phase-Locked-Oscillator (PLO1)	PLO-2000 (Microwave Dynamics)	Output Freq.: 20 GHz Output Power: 13 dBm
Attenuator (ATT4)	PE7090-3 (Pasternack)	IL: 3 dB
Band-Pass Filter (BPF2)	7 EZ7-20000/500-S/S (Lorch Microwave)	Center Frequency: 20 GHz Bandwidth: 500 MHz
Attenuator (ATT5)	PE7090-3 (Pasternack)	IL: 3 dB

CG Driver

A driver sub-system (DR) is used at the output of the chirp generator to amplify the signal, equalize it and split it to two ports.

The frequency equalizer used has slop of 15/16 dB/GHz. It is used to compensate the amplitude at the output of the FDC as a function of frequency. The power splitter is used so that the chirp generator outputs two identical 2-18 GHz chirps. One of these signals goes through the LO sub-system to drive LO port of the de-chirping mixer. The other chirp goes to the TX sub-system.

The overall gain of DR is 36.5 dB. The time-average power at both outputs of the chirp generator is 16 dBm. Figure 5.5.29 shows a block diagram of the driver. Table 5.5.10 shows a list of the driver components.

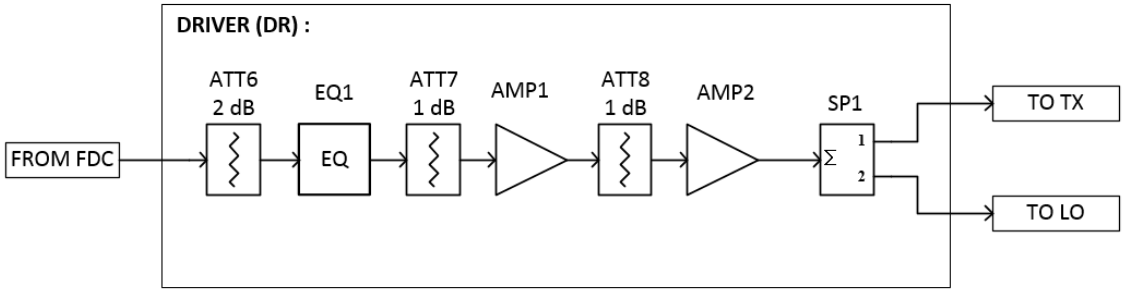

Figure 5.5.29 – Block Diagram of Chirp Generator Output Driver

Table 5.5.10 – List of Chirp Generator Output Driver (DR)

Description (Name)	**Part Number (Manufacturer)**	**Parameter(s)**
Attenuator (ATT6)	BW-S2W2+ (Mini-circuits)	IL: 2 dB
Equalizer (EQ1)	E02G18GE (Microwave Circuits)	IL (at 2 GHz): 15 dB IL (at 18 GHz): 1.5 dB
Attenuator (ATT7)	BW-S1W2+ (Mini-circuits)	IL: 1 dB
Amplifier (AMP1)	ZVA-183+ (Mini-Circuits)	Gain: 26 dB
Attenuator (ATT8)	BW-S1W2+ (Mini-circuits)	IL: 1 dB
Amplifier (AMP2)	ZVA-183+ (Mini-Circuits)	Gain: 26 dB
Power Splitter (SP1)	PE2028 (Pasternak)	IL: 1 dB (+3 dB)

5.5.5. Chirp Generator Output

Instantaneous Output Power

The time-averaged output power of the chirp generator is 16.3 dBm. Figure 5.5.30. shows measured the instantaneous output.

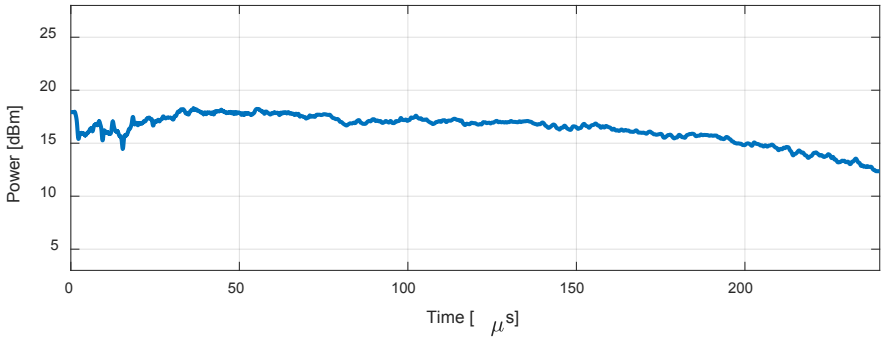

Figure 5.5.30 – Instantaneous Power of the output of CG

Instantaneous Frequency

The instantaneous frequency at the output of the chirp generator is a ramp that sweeps from 2 GHz to 18 GHz. Figure 5.5.31 shows a measurement of the instantaneous frequency.

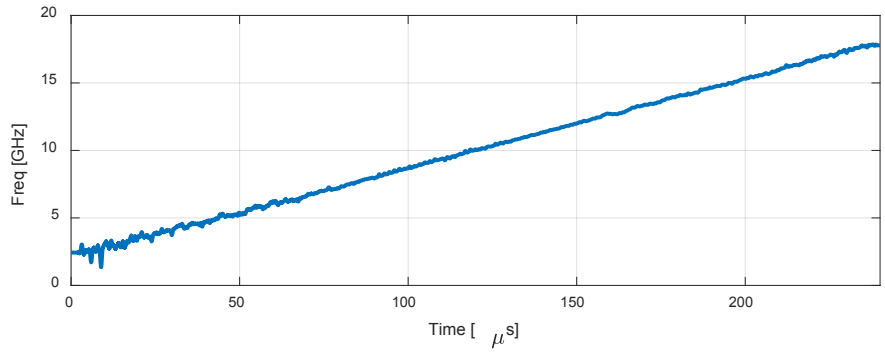

Figure 5.5.31 – Instantaneous Frequency of the output of CG

PSD of Chirp Generator Output

Over the chirp band, the frequency-averaged PSD at the output of the chirp generator is -85.7 dBm/Hz. Figure 5.5.32 shows a measurement of the PSD of the CG. The PSD was computed digitally from the time domain signal of the chirp, measured with an oscilloscope.

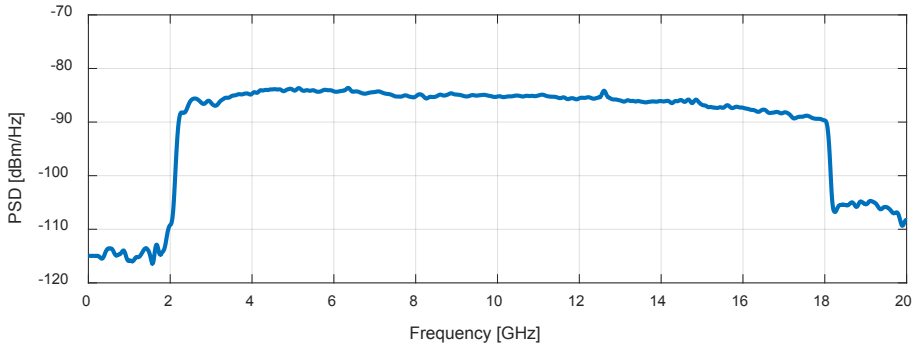

Figure 5.5.32 – PSD of Chirp Generator Output

PSD of Incoherent Phase Noise

We use the same approach described in section 5.5.2.8 to measure and model the incoherent phase noise at the output of the chirp generator.

The approximated model is given in (5.5.46), which is the sum of a zero-order and a 3.5th-order components.

$$S_{\varphi_{uin}\varphi_{uin}}(f) = \left[\frac{1}{(2\pi f)^0}\frac{{\varphi_{rms0}}^2}{B_n} + \frac{1}{(2\pi f)^{3.5}}\frac{{\varphi_{rms3.5}}^2}{B_n}\right] \tag{5.5.46}$$

$$S_{\varphi_0\varphi_0}(f)_{dB} = \left[\frac{(\varphi_{rms0})^2}{B_n}\right]_{dB} = -137 \text{ dB/Hz} \tag{5.5.47}$$

$$S_{\varphi_{1.75}\varphi_{1.75}}(f)_{dB} = \left[\frac{(\varphi_{rms3.5})^2}{B_n}\right]_{dB} = +173 \text{ dB/Hz} \tag{5.5.48}$$

Figure 5.5.33 shows a plot of the normalized PSD of the incoherent phase noise at the output of CG.

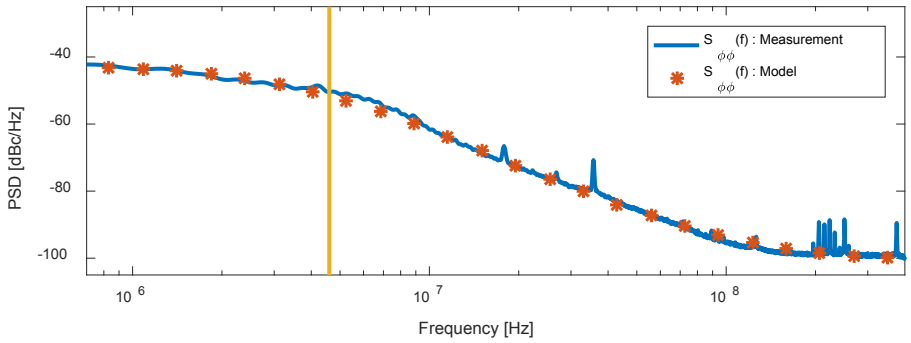

Figure 5.5.33 – Normalized PSD of Incoherent Phase Noise at CG Output

Coherent Phase Noise

We use the same approach described in section 5.5.2.8 to measure and model the coherent phase noise at the output of the chirp generator.

The approximated model is given in (5.5.49), which is the sum of a zero-order and a 3.5th-order components.

$$S_{\varphi_{uin}\varphi_{uin}}(f) = \left[\frac{1}{(2\pi f)^0}\frac{{\varphi_{rms0}}^2}{B_n} + \frac{1}{(2\pi f)^{3.5}}\frac{{\varphi_{rms3.5}}^2}{B_n}\right] \tag{5.5.49}$$

$$S_{\varphi_0\varphi_0}(f)_{dB} = \left[\frac{(\varphi_{rms0})^2}{B_n}\right]_{dB} = -132 \text{ dB/Hz} \tag{5.5.50}$$

$$S_{\varphi_{1.75}\varphi_{1.75}}(f)_{dB} = \left[\frac{(\varphi_{rms3.5})^2}{B_n}\right]_{dB} = +175 \text{ dB/Hz} \tag{5.5.51}$$

Figure 5.5.34 shows a plot of the normalized PSD of the coherent phase noise at the output of CG.

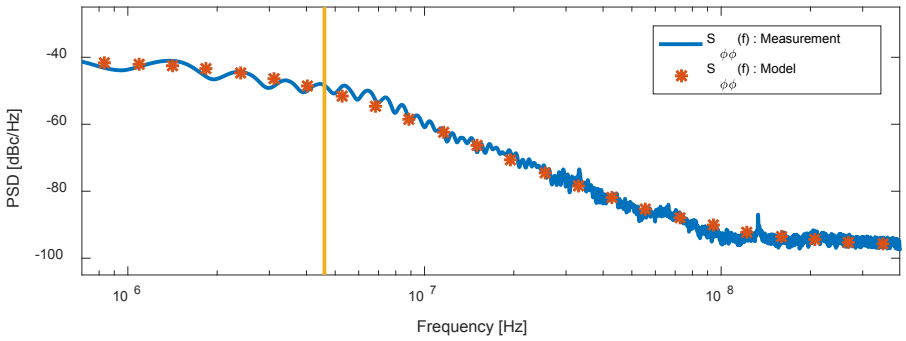

Figure 5.5.34 – Normalized PSD of Coherent Phase Noise at CG Output

5.6. RADAR DESCRIPTION: RX, TX and DAQ

5.6.1. Receiver (RX)

The FMCW radar receiver was designed with a total gain of 47.3 dB and noise figure of 13 dB. This receiver is composed of RF and IF sub-sections, as well as a mixer. The IF part of the receiver (RX-IF) includes all the components between the mixer and the receiver output. The average gain of each sub-system within the receiver, the total receiver average gain and noise figure are listed in table 5.6.1. Figure 5.6.1 shows the block diagram of the receiver. The RX-RF, RX-IF and mixer are described in the following sections.

Table 5.6.1 – Summary of Receiver Average Parameters

Sub-System	**Parameters**	**Average Value**
RX-RF	Gain	16.7 dB
Mixer	Conversion Loss	6.5 dB
RX-IF	Gain	37.1 dB
Overall RX	Gain	47.3 dB
	Noise Figure	13 dB

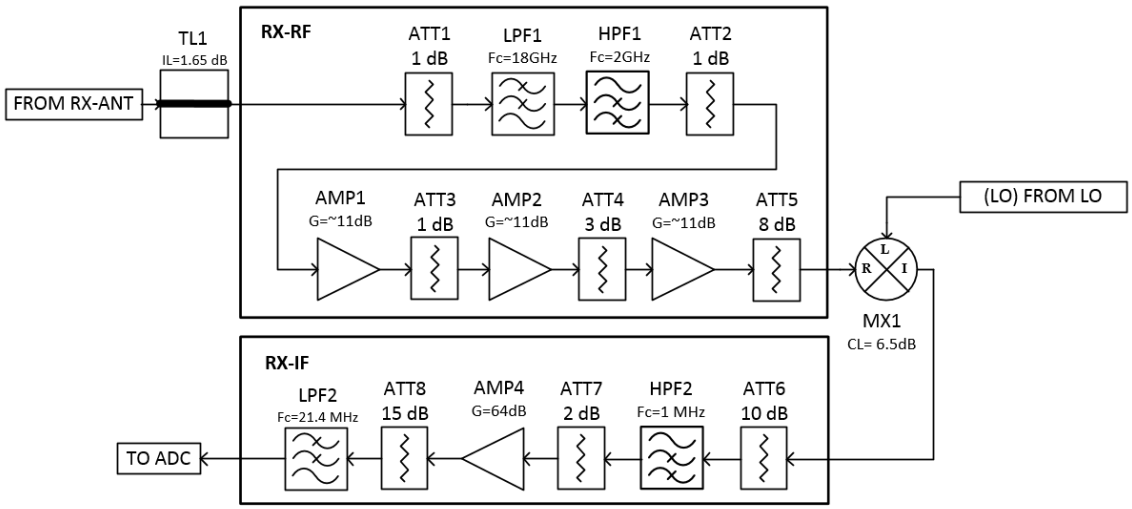

Figure 5.6.1 – Receiver (RX) Block Diagram

5.6.1.1. Receiver RF (RX-RF)

Figure 5.6.1 shows the arrangement of components of the RX-RF. All components of the RX-RF, their average gain and noise figure are listed in table 5.6.2. The RX antenna cable (TL1) connects the antenna to the rest of the RX-RF inside the chassis. The RX antenna cable was described in section 5.4.2 and we consider it as part of the RX-RF. Inside the chassis, the RX-RF has a high-pass (HPF1) and a low-pass (LPF1) filters to suppress signals outside the chirp band, which is 2-18 GHz. The RX-RF also has three low-noise-amplifiers (LNAs) (AMP1, AMP2, AMP3) to increase the amplitude of the signal. Attenuators are placed between the RX-RF components to reduce reflections between components. The last attenuator is placed to reduce the amplitude of the LO leakage signal, which contributes to the amplitude of the total noise. The total RX-RF gain is 16.7 dB.

Other than the LNAs, all components of the RX-RF have a frequency response with a flat amplitude over the 2-18 GHz frequency range. The measured gain of the LNA is shown in figure

5.6.2. The gain decreases from 2 GHz to 18 GHz by 6 dB. The average gain of the LNA is 11 dB.

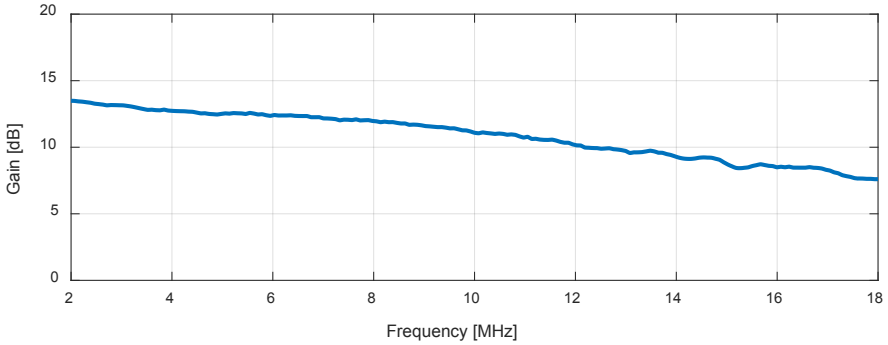

Figure 5.6.2 – LNA Measured Frequency Response

The frequency response of the RX-RF is shown in figure 5.6.3. The average gain of the RX-RF is 16.7 dB. The amplitude decreases from 2 GHz to 18 GHz by 18.

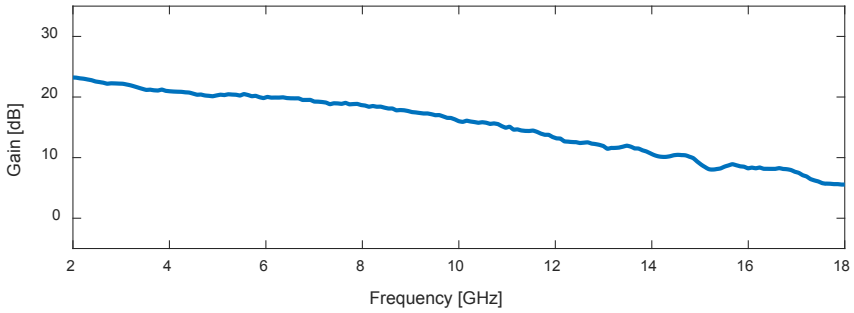

Figure 5.6.3 – RX-RF Measured Frequency Response

5.6.1.2. Mixer

The mixer selected for the receiver is listed in table 5.6.2. The mixer conversion loss as a function of input frequency at the RF port is show in figure 5.6.4. The average of the conversion loss is 6.5 dB over the 2.18 GHz. The selected mixer has a RF-LO isolation of 30 dB. The LO operating power range is 7 to 13 dBm.

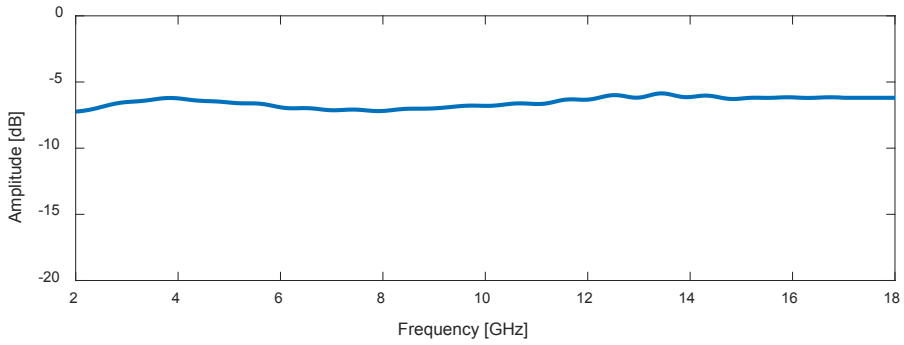

Figure 5.6.4 – Mixer Conversion Loss

5.6.1.3. Receiver IF (RX-IF)

Figure 5.6.1 shows the arrangement of the components in the RX-IF. Table 5.6.2 lists the components of the RX-IF, their gain and noise figure. The high-pass filter suppresses any signals below the minimum operating frequency of the IF amplifier. The IF low pass filter serves as the anti-aliasing filter and sets the maximum unambiguous range. The low pass filter also attenuates high frequency content that results from undesired intermodulation products by the mixer.

Figure 5.6.5 shows the frequency response of the RX-IF from DC to 5 MHz. The total pass-band of the RX-IF is 1-21.4 MHz. The RX-IF gain over the pass-band is 37 dB.

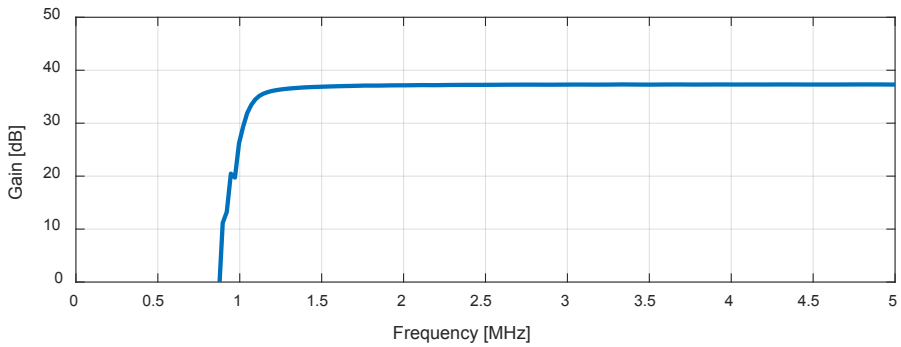

Figure 5.6.5 – RX-IF Frequency Response

5.6.1.4. Receiver Frequency and Impulse Responses

The frequency response of the entire receiver is show in figure 5.6.6. The average gain of the receiver is 47.3 dB. The impulse response of the receiver is shown in figure 5.6.7.

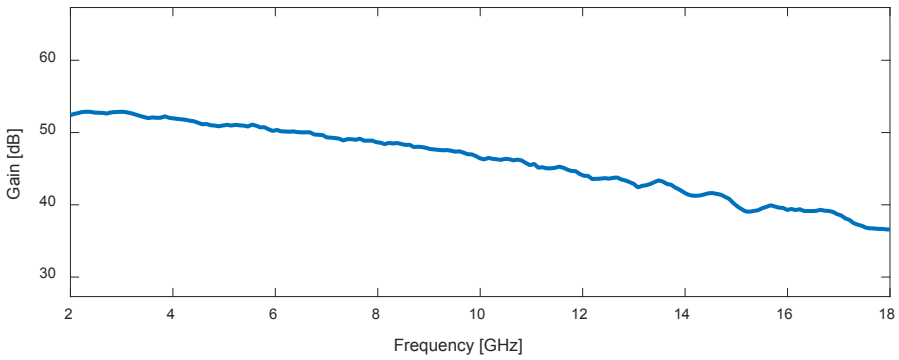

Figure 5.6.6 – RX Frequency Response

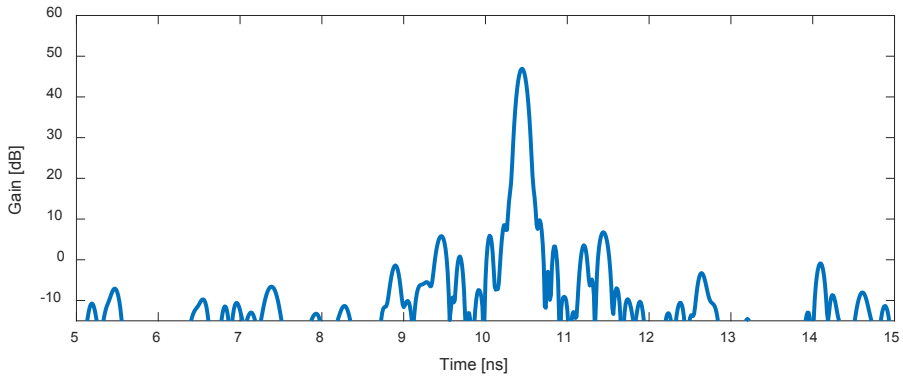

Figure 5.6.7 – RX Impulse Response

5.6.1.5. Receiver Components

Table 5.6.2 lists the components used in the RX. The table shows the part number, manufacturer, gain and noise figure of each individual component.

Table 5.6.2 – List of RX Components

Sub-System	Component	PN (Manufacturer)	Gain [dB]	Noise Figure [dB]
RX-RF	RX Antenna Cable (TL1)	UFA210A-1-0960-300300	-1.65	1.65
	Attenuator (ATT1)	BW-S2W2+ (Mini-circuits)	-1	1
	Low Pass Filter (LPF1)	L18G20G1	-0.3	0.3
	High Pass Filter (HPF1)	H02G18G6	-0.3	0.3
	Attenuator (ATT2)	BW-S1W2+ (Mini-circuits)	-1	1
	Low Noise Amplifier (AMP1)	HMC463LP4 (Analog-Devices)	11	3
	Attenuator (ATT3)	BW-S1W2+ (Mini-circuits)	-1	1
	Low Noise Amplifier (AMP2)	HMC463LP4 (Analog-Devices)	11	3
	Attenuator (ATT4)	BW-S3W2+ (Mini-circuits)	-3	3
	Low Noise Amplifier (AMP3)	HMC463LP4 (Analog-Devices)	11	3
	Attenuator (ATT5)	BW-S8W2+ (Mini-circuits)	-8	8
Mixer	Mixer (MX1)	DB0218LW2 (Narda-Miteq)	-6.5	6.5
RX-IF	Attenuator (ATT6)	BW-S10W2+ (Mini-circuits)	-10	10
	High Pass Filter (HPF)	Custom Made	-0.1	0.1
	Attenuator (ATT6)	BW-S1W2+ (Mini-circuits)	-2	2
	Amplifier (AMP4)	AU-1291 (Narda-Miteq)	64	1.3
	Attenuator (ATT7)	BW-S15W2+ (Mini-circuits)	-15	15
	Low Pass Filter (LPF2)	SLP-21.4+ (Mini-circuits)	-0.1	0.1

5.6.2. Transmitter (TX) and the LO Sub-Systems

We consider the LO sub-system as the cascade of components between the CG output and the LO port at the RX. The TX sub-system is the cascade of components between the CG and the TX antenna input port. The block diagrams of both LO and TX sub-systems are shown in figure 5.6.8. The list of components and their main parameters are listed in table 5.6.3.

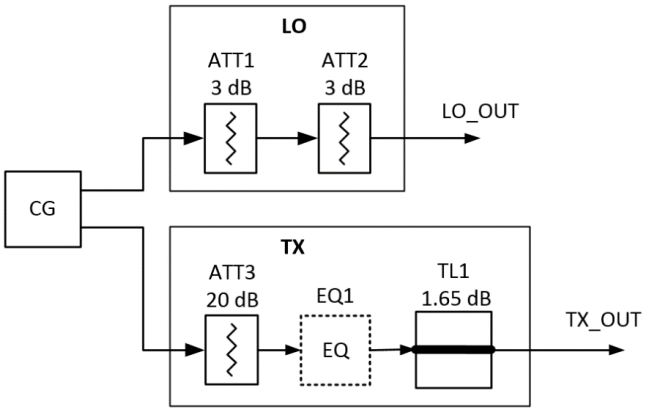

Figure 5.6.8 – TX and LO Paths

Table 5.6.3 – List of TX AND LO Components

Description (Name)	**Part Number (Manufacturer)**	**Parameter(s)**
Attenuator (ATT1)	BW-S3W2+ (Mini-circuits)	IL: 3 dB
Attenuator (ATT2)	BW-S3W2+ (Mini-circuits)	IL: 3 dB
Attenuator (ATT3)	BW-S20W2+ (Mini-circuits)	IL: 20 dB
Equalizer (EQ1)	E02G18GE (Microwave Circuits)	IL (at 2 GHz): 15 dB IL (at 18 GHz): 1.5 dB
TX Antenna Cable (TL1)	UFA210A-1-0960-300300 (Micro-Coax)	IL: 1.65 dB Length: 8 ft

Figure 5.6.9 shows a comparison of the instantaneous output power of the CG, LO and TX. The average output power of the CG, LO and TX are 16.3 dBm, 10 dBm and -12.4 dBm, respectively.

The LO sub-system has 6 dB insertion loss, so that the output instantaneous power is within the mixer LO power operation range (7 to 13 dBm). The TX sub-system includes an equalizer to compensate the RX system response.

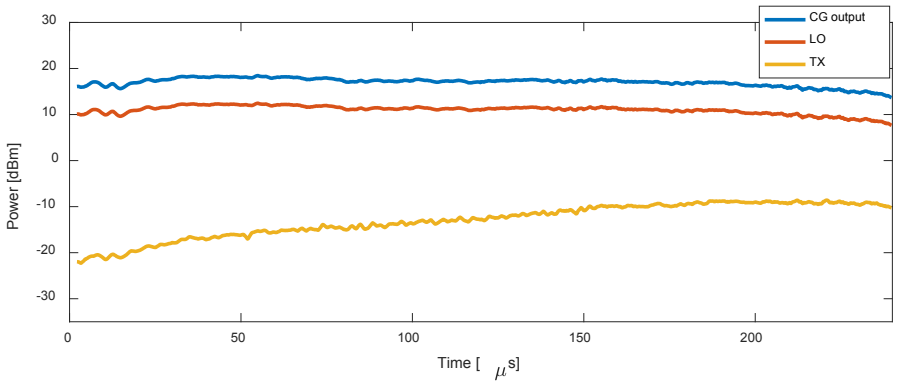

Figure 5.6.9 – Instantaneous Output Power of CG, TX and LO

5.6.3. Transmit Signal – Receiver Gain Product

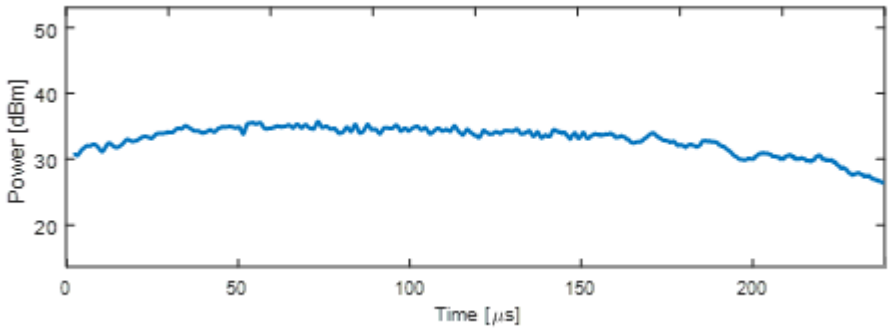

Figure 5.6.10 – Product of TX signal and RX gain

The TX includes an equalizer so that the product of the TX signal and RX gain has low amplitude variations over the entire frequency range. The instantaneous power of this product is shown in figure 5.6.10. The PSD of this product could be found by dividing the power level by the chirp bandwidth. The average of this product is 33.1 dBm. The ratio of the maximum and minimum power of this product is 9 dB. This amplitude variation is smaller than the RX amplitude variation of 18 dB.

5.6.4. Data Acquisition System

The data acquisition system (DAQ) is used to convert the receiver analog output to a digital signal, perform optional coherent integrations, package each radar return with a time tag and record the data into a storage device. The DAQ is also used to visualize the radar returns in real time.

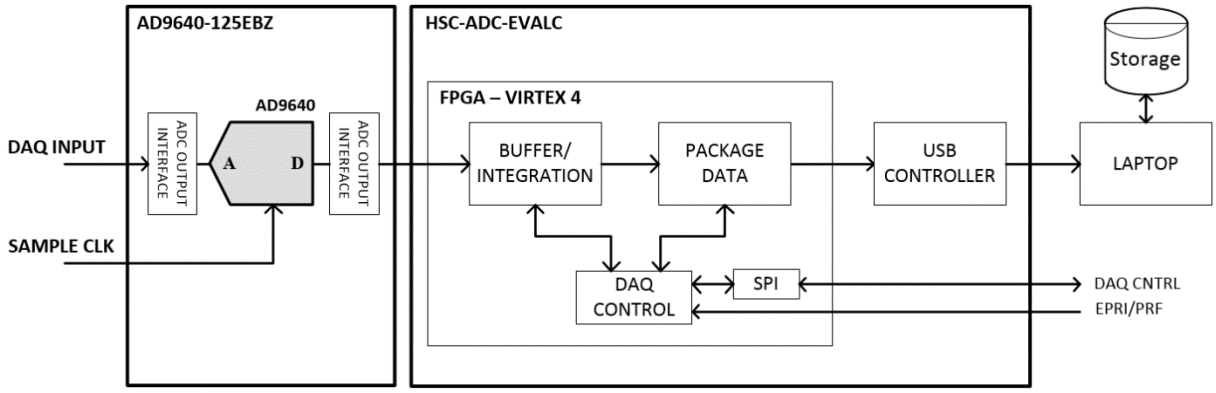

Figure 5.6.11 – Block Diagram of Data Acquisition System

Figure 5.6.11 shows a block diagram of the radar DAQ. The block on the left represents the ADC board. The ADC board used is an evaluation board for the ADC with part number AD9640 by Analog Devices. The board part number is AD9640-122EBZ. The AD9640 is a 2-channel 14-bit high-speed ADC. The board uses a double balun input interface configuration, so that the analog input is single ended and has a range of -1 to +1 Volt. The input interface also configures the input impedance to be 50 ohm. The output interface of the ADC to the FPGA provides series termination and buffering. The sample clock frequency is 62.5 MHz. This clock signal comes from a clock-distribution board, not shown on the block diagram.

The block on the center of the figure 5.6.11 represents the FPGA board. This DAQ uses the Virtex-4 FPGA, with part number XC4VFX20-10FFG672C. The board used is an evaluation board with part number HSC-ADC-EVALC. This board interfaces to the AD9640-122EBZ board through a data bus, using high-speed PCB-mounted connectors (part number 6469028-1, Tyco). The FPGA is configured through USB using an on-board USB controller. The USB-controller is also used to send the radar data from the FPGA to the laptop.

The DDS board described in section 5.5.1 sends control signals to the DAQ. These control signals sent are the digital waveform parameters and the UTC time. The parameters of the digital waveform are the start and the length of the waveform, given in number of samples, as well as the number of coherent integrations (presums). The DDS board also sends two timing signals: the PRF and EPRI pulses. The first module that receives the 14 digital signals from the ADC extends the word length to 24 bits and places them into 24 RAM blocks with a depth of 16k. The system has the option to perform coherent integrations by adding the input (24 bit word) to the accumulated value stored in the buffer (RAM blocks). The second block defines a header for each radar return, which includes the UTC time and other timing-related information. The header is divided into 14 bytes. The second block also extends the data word length from 24 to 32 bits. These 32-bit words are then divided into bytes. This second module appends the header to the data and sends this package to the USB controller. The USB controller on board is the CY7C68013A by Cypress. The computer receives the data through a USB interface. The received data, with packages representing radar returns, are stored serially in a binary file. The data files are limited to 512 MB.

Although signals are stored in 32-bit words, the effective number of bits is still 14, if we ignore spurs.

5.7. RADAR DESCRIPTION: Self-Interference and Noise

5.7.1. ADC Quantization Noise

From section 5.2.2, the quantization noise is given by (5.7.1). The ADC of the radar has 14 bits, a voltage range of 2 volts and a noise bandwidth of 62.5 MHz. Therefore, the quantization noise power is expected to be -65.25 dBm. The quantization noise PSD is given by (5.7.2), which results in -143.2 dBm/Hz.

$$P_{qn} = \frac{1}{R_o} {v_{qn\_rms}}^2 = \frac{\left(v_{q\_range}/2^b \right)^2}{R_o} \tag{5.7.1}$$

$$S_{v_{qn}v_{qn}} = \frac{P_{qn}}{B_n} \tag{5.7.2}$$

Figure 5.7.1 shows a measurement of the (averaged) instantaneous power of the ADC quantization noise over the 256μs. The average noise floor is measured to be at -64.4 dBm, which is 0.85 dB higher than the expected value.

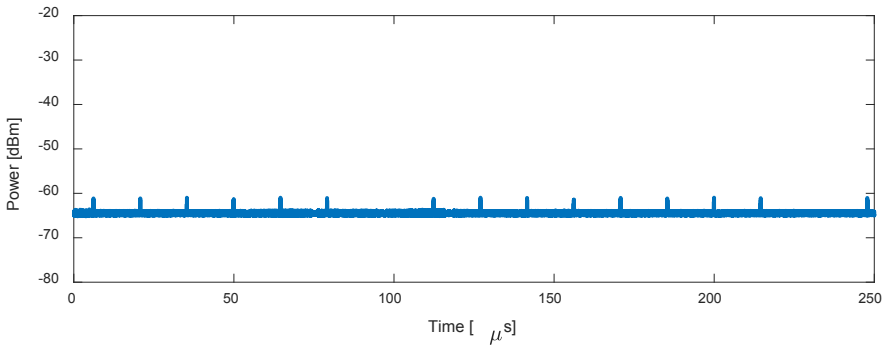

Figure 5.7.1 – Measured Instantaneous Power of ADC Quantization Noise

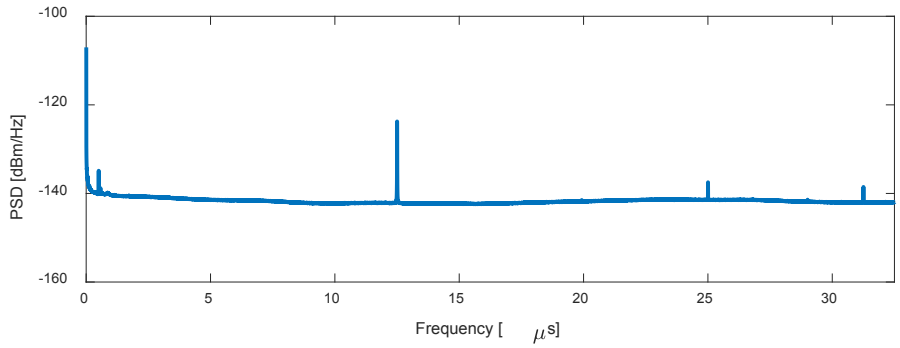

Figure 5.7.2 – Measured PSD of ADC Quantization Noise

Figure 5.7.2 shows the measured (averaged) PSD of the ADC quantization noise over the ADC frequency range. The PSD noise floor is at about -142.2 dBm/Hz, which is 1 dB higher than the expected value. The PSD has spurs that peak at -123.7 dBm/Hz.

5.7.2. Thermal Noise

From section 5.2.3, the PSD of the additive thermal noise at the output of an FMCW receiver can be approximated to (5.7.3), if the IF bandwidth is much lower than the chirp bandwidth. From section 5.6.1, the frequency averaged receiver gain and noise figure are 47.3 dB and 13 dB, respectively. The antenna temperature is approximated to be at 290 K. The PSD of the thermal noise at the output of the receiver is expected to be at -113.7 dBm/Hz.

$$S_{v_{no}v_{no}}(f) = kT_oG_{RX}F_{RX} \quad \text{for } f \ll B \tag{5.7.3}$$

From section 5.2.3, the time-averaged power of this kind of noise is approximated to be (5.7.4). In (5.7.4), B_n is the noise bandwidth, which is equal to the bandwidth of the IF section of the receiver. The frequency range of the IF section of the receiver is 1 to 21 MHz, so the noise

bandwidth is 20 MHz. The averaged power of the PSD of the thermal noise is expected to be at -40.7 dBm.

$$P_{td} = kT_o G_{RX} F_{RX} B_n \quad (5.7.4)$$

5.7.3. Interference Signals and Noise

The interference signal add both coherent and incoherent noise to the output. Thus, the total incoherent noise includes thermal and quantization noise, as well as the incoherent noise related to the phase noise of the interference signals. Likewise, the total coherent noise of the radar includes the phase noise contributions from all interference signals. The most significant self-interference signals of the radar are those related to the LO leakage and the antenna feed-through. In addition, the ground clutter is another interference signals that adds noise to the output of the radar.

5.7.3.1. Phase Noise at the Output of the Radar

From section 5.2.4, the PSD of the output signal and associated noise due to a self-interference path $h_{pk}(\mathrm{t})$ is given by (5.7.5) and (5.7.6), respectively. From (5.7.6), the normalized phase noise for a pulse at the output of the radar is (5.7.7). In (5.7.7), $\bar{S}_{\varphi\varphi}(f)$ and $\bar{S}_{\varphi_{IF}\varphi_{IF}}(f)$ are the normalized phase noise with respect to their carriers for the output of the chirp generator and the output of the radar, respectively. From (5.7.7), it can be seen that the normalized phase noise is modified by the de-chirping process by a factor of $2[1-\cos(2\pi\tau f)]$. Thus, the ripples of

normalized phase noise at the output signal peaks at four times the normalized phase noise of the chirp signal.

$$S_{v_{oik}v_{oik}}(f) = |H_{RX-IF}|^2 BT \; S_{v_{CG}v_{CG}0} \left|h_{mx}(\tau) * h_{pk}(\tau) * \mathrm{sinc}(Tf)\right|^2 \tag{5.7.5}$$

$$S_{v_{onk}v_{onk}}(f) = |H_{RX-IF}|^2 \; BT \; S_{v_{CG}v_{CG}0} \left|h_{mx}(\tau) * h_{pk}(\tau) * \mathrm{sinc}(Tf)\right|^2 * 2S_{\varphi\varphi}(f)[1 - \cos(2\pi\tau f)] \tag{5.7.6}$$

$$\bar{S}_{\varphi_{IF}\varphi_{IF}}(f) = 2\bar{S}_{\varphi\varphi}(f)[1 - \cos(2\pi\tau f)] \tag{5.7.7}$$

$$\bar{S}_{\varphi\varphi}(f) = S_{\varphi\varphi}(f)/max\{S_{vv}(f)\} \tag{5.7.8}$$

The coherent and incoherent phase noise at the output of the chirp generator was described in detail in section 5.5.5. The PSD of both of these types of phase noise can be expressed by equation (5.7.9). The values for the terms $S_{\varphi_0\varphi_0}(f)$ and $S_{\varphi_{1.75}\varphi_{1.75}}(f)$ for the coherent and incoherent noise are given in section 5.5.

$$S_{\varphi\varphi}(f) = \frac{1}{(2\pi f)^0} S_{\varphi_0\varphi_0}(f) + \frac{1}{(2\pi f)^{3.5}} S_{\varphi_{1.75}\varphi_{1.75}}(f) \tag{5.7.9}$$

Using a delay line, we measured a single pulse at the output of the radar and computed the PSD of the normalized phase noise. The only delay line used was the antenna cables already considered in the transmitter and receiver system response. The total delay is 27 ns. Additionally, an attenuator of 50 dB was used to avoid saturation. The band of the IF is 1 to 21 MHz. The phase noise was measured down to -59 dBc, which was limited by the IF cut-off frequency.

The PSD of the normalized phase noise at the output of the radar was computed using the analytical expression in (5.7.7), or model. It was also simulated numerically. Figure 5.7.3 shows a comparison of the measured, simulation and model for the incoherent component of this phase noise. In this plot, the expressions for the normalized phase noise at the output of the radar were divided by 4 so that the peaks of the ripples match the incoherent component of the phase noise of the chirp.

The same comparison as above was performed for the coherent component of the phase noise. This is shown in figure 5.7.4.

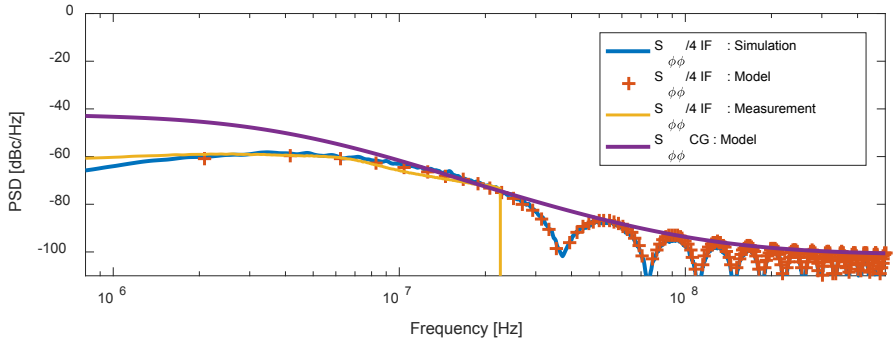

Figure 5.7.3 – Normalized PSD of Incoherent Phase Noise at the Radar Output

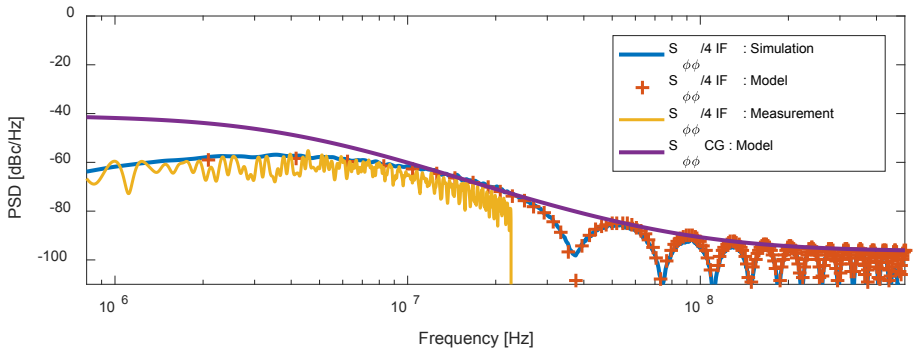

Figure 5.7.4 – Normalized PSD of Coherent Phase Noise at the Radar Output

In both of these plots, the measurement of the phase noise matches the expected phase noise. The simulation and model assumed that no additional phase noise was introduced by the transmitter or receiver. Thus, these plots show that the overall phase noise at the output of the radar is only determined by the phase noise at the chirp generator.

For a pulse at the output of the radar with a delay of 27 ns, the ratio of the peak of the phase noise to the carrier is -47 dBc and -45 dBc for the incoherent and coherent noise components, respectively.

The peak of the noise depends on the frequency of the ripples, which in turn depends on the signal path delay. For the signal path associated with the antenna feedthrough, the signal delay is 27 ns. The signal delay for the LO leakage signal path is 3.3 ns. Considering these delays and ignoring thermal noise, the signal to incoherent and coherent noise ratio for the antenna feed-through case is 47 dB and 45 dB, respectively. For the LO leakage signal, these ratios are -64 dB and -62.5 dB for the incoherent and coherent noise, respectively.

5.7.3.2. Self-Interference Signal and Noise: 50 dB attenuator

We measured the output of the radar due to a 50 dB attenuator attached between the transmit and receive antenna cables. The radar delay including the delay of these cables is 27 ns. This delay line test results in a pulse at the output with its associated coherent and incoherent phase noise. The signal path $h_{pk}(t)$ associated to this test is given by (5.7.10). In (5.7.10), $h_{TX}(t)$, $h_{RX-RF}(t)$ and $h_T(t)$ are the impulse response for the transmitter, RX-RF and the attenuator, respectively.

$$h_{pk}(t) = h_{TX}(t) * h_{RX-RF}(t) * h_T(t) \tag{5.7.10}$$

Using this signal path, the output signal and its associated phase noise can be computed analytically. We compute the output due to a chirp with both coherent phase noise and incoherent phase noise. For the measured results, the coherent component was extracted by coherently averaging the 1000 measurements. Similarly, for the incoherent case, the output was found by incoherently averaging 1000 measurements and subtracting the coherent component. Figures 5.7.5 and 5.7.6 show the outputs due to incoherent and coherent phase noise respectively. In the plots, the measurements agree with the expected outcomes. These results show the shape of the coherent and incoherent noise at the output of the radar noise due to phase noise is larger than thermal noise across the entire IF band. In this example, the thermal noise has little effect on the total incoherent noise.

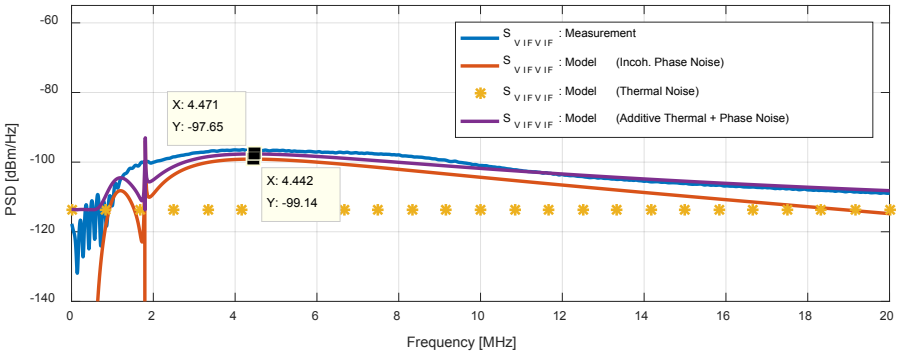

Figure 5.7.5 – Example of Incoherent Noise at Output with a 50 dB attenuator

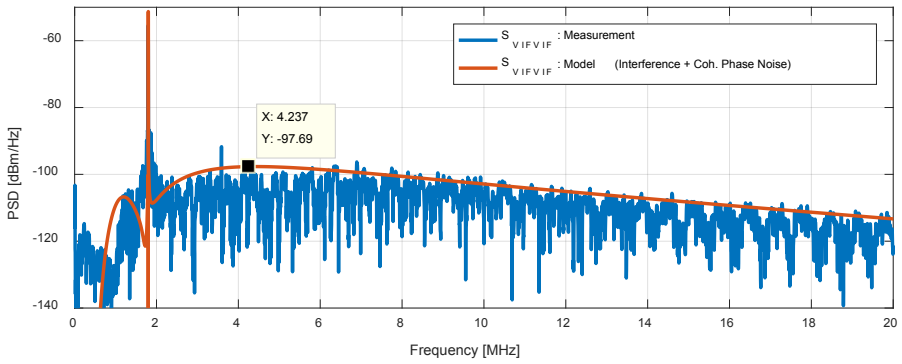

Figure 5.7.6 – Example of Coherent Noise at Output with a 50 dB attenuator

Alternatively, we could compute the peak noise levels approximately by using the average gains of the radar sub-systems, average PSD of the CG output power and the signal to phase noise level.

Replacing this signal path (5.7.10) into the PSD of the output signal $S_{v_{oik}v_{oik}}$ and using frequency-averaged values for the CG PSD and the responses of the radar sub-systems, we can approximate $S_{v_{oik}v_{oik}{}_{dB}}$ as shown in (5.7.11-5.7.12). The approximated amplitude of the pulse is -52.1 dBm/Hz. The peak of the incoherent and coherent phase noise are given by (5.7.13-5.7.14). These approximated results are close to the computed models above.

$$S_{v_{oik}v_{oik}{}_{dB}} = S_{v_{CG}v_{CG}{}_{dB}} + [BT]_{dB} + |H_{RX-IF}|^2{}_{dB} + |H_{MX}|^2{}_{dB} + |H_{RX-RF}|^2{}_{dB} + |H_T|^2{}_{dB} + |H_{TX}|^2{}_{dB} \quad (5.7.11)$$

$$S_{v_{oik}v_{oik}{}_{dB}} = -85.7\,\frac{\text{dBm}}{\text{Hz}} + 65.8\text{ dB} + 37\text{ dB} - 6.5\text{ dB} + 16.7\text{ dB} - 50\text{ dB} - 29.4\text{ dB} = -52.1\text{ dBm/Hz} \quad (5.7.12)$$

$$max\{S_{v_{onk}v_{onk}incoh}\}_{dB} = S_{v_{oik}v_{oik}{}_{dB}} - 47\ \text{dB} = -52.1\frac{\text{dBm}}{\text{Hz}} - 47\ \text{dB} = -99.1\ \text{dBm/Hz} \quad (5.7.13)$$

$$max\{S_{v_{onk}v_{onk}coh}\}_{dB} = S_{v_{oik}v_{oik}{}_{dB}} - 44\ \text{dB} = -52.1\frac{\text{dBm}}{\text{Hz}} - 45\ \text{dB} = -97.1\ \text{dBm/Hz} \quad (5.7.14)$$

5.7.3.3. Self-Interference Signal and Noise: 60 dB attenuator

This test is identical to the previous one with the exception that a 60 dB attenuator was used instead of a 50 dB attenuator. By using 60 dB for $|H_T|^2$ instead of 50 dB, the noise due to phase noise at the output reduces to a level where the thermal noise is not negligible.

Using the approximation in (5.7.11) for this case, the amplitude of the pulse $S_{v_{oik}v_{oik}{}_{dB}}$ results in -62.1 dBm/Hz, as shown in (5.7.15).

$$\begin{aligned} S_{v_{oik}v_{oik}{}_{dB}} &= -85.7\frac{\text{dBm}}{\text{Hz}} + 65.8\ \text{dB} + 37\ \text{dB} - 6.5\ \text{dB} + 16.7\ \text{dB} - 60\ \text{dB} - 29.4\ \text{dB} \\ &= -62.1\ \text{dBm/Hz} \end{aligned} \quad (5.7.15)$$

The approximated peaks of the phase noise for the incoherent and coherent cases would be -109.1 dBm/Hz and -106.1 dBm/Hz, respectively. The total incoherent noise is the sum of the incoherent phase noise and thermal noise, which results in -105.2 dBm/Hz.

$$max\{S_{v_{onk}v_{onk}incoh}\}_{dB} = S_{v_{oik}v_{oik}{}_{dB}} - 47\ \text{dB} = -62.1\frac{\text{dBm}}{\text{Hz}} - 47\ \text{dB} = -109.1\ \text{dBm/Hz} \quad (5.7.16)$$

$$max\{S_{v_{onk}v_{onk}coh}\}_{dB} = S_{v_{oik}v_{oik}{}_{dB}} - 44\ \text{dB} = -62.1\frac{\text{dBm}}{\text{Hz}} - 45\ \text{dB} = -107.1\ \text{dBm/Hz} \quad (5.7.17)$$

Figure 5.7.7 and 5.7.8 show the plots for output of the radar for the incoherent and coherent cases, respectively. The measurement agrees with the model results at the peak of the incoherent noise.

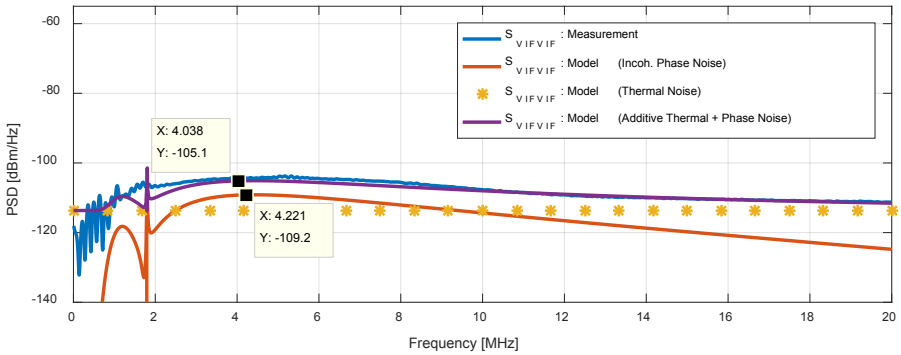

Figure 5.7.7 – Example of Incoherent Noise at Output with a 60 dB attenuator

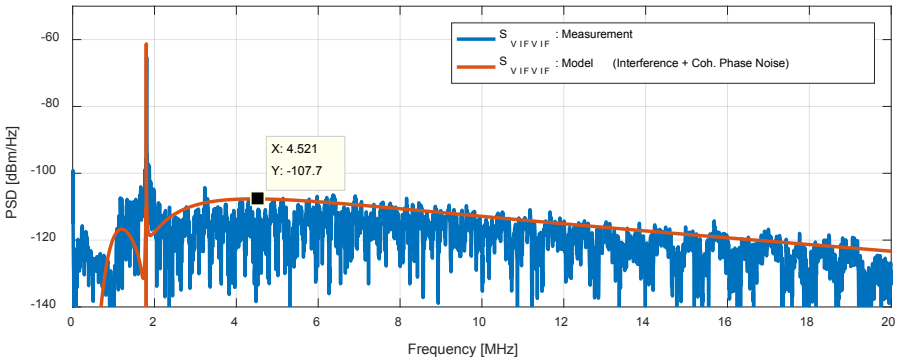

Figure 5.7.8 – Example of Coherent Noise at Output with a 60 dB attenuator

5.7.3.4. Self-Interference Signal and Noise: Antenna Feedthrough

From section 5.2, the signal path associated with the antenna feed-through is given by (5.7.18). The impulse and frequency response of the antenna feedthrough was discussed in section 5.4.

$$h_{p1}(t) = h_{RX-RF}(t) * h_F(t) * h_{TX}(t) \tag{5.7.18}$$

Using the frequency-averaged PSD of the CG and the average of the sub-system responses, the approximated amplitude (PSD) of this self-interference signal is -63.1 dBm/Hz. The approximated peak amplitudes for the incoherent and coherent phase noise are -110.1 dBm/Hz and -108.1 dBm/Hz. The total incoherent noise level is the incoherent sum of the thermal noise and the incoherent phase noise, which results in -105.8 dBm/Hz.

$$\begin{aligned} S_{v_{oik}v_{oik}{}_{dB}} &= -85.7\frac{\text{dBm}}{\text{Hz}} + 65.8\text{ dB} + 37\text{ dB} - 6.5\text{ dB} + 16.7\text{ dB} - 61\text{ dB} - 29.4\text{ dB} \\ &= -63.1\text{ dBm/Hz} \end{aligned} \tag{5.7.19}$$

$$max\{S_{v_{onk}v_{onk}incoh}\}_{dB} = S_{v_{oik}v_{oik}{}_{dB}} - 47\text{ dB} = -63.1\frac{\text{dBm}}{\text{Hz}} - 47\text{ dB} = -110.1\text{ dBm/Hz} \tag{5.7.20}$$

$$max\{S_{v_{onk}v_{onk}coh}\}_{dB} = S_{v_{oik}v_{oik}{}_{dB}} - 44\text{ dB} = -63.1\frac{\text{dBm}}{\text{Hz}} - 45\text{ dB} = -108.1\text{ dBm/Hz} \tag{5.7.21}$$

Figures 5.7.9 and 5.7.10 show the plots for the PSD of the output due to the antenna feed-through. The model results agree with the measurements.

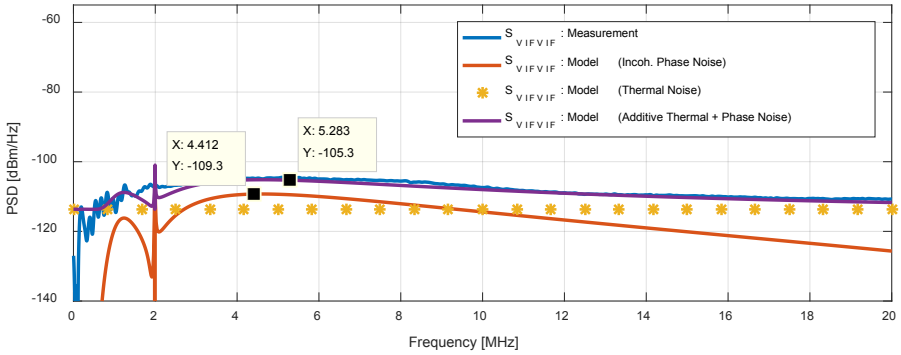

Figure 5.7.9 – Incoherent Noise at Output due to Antenna Feed-through

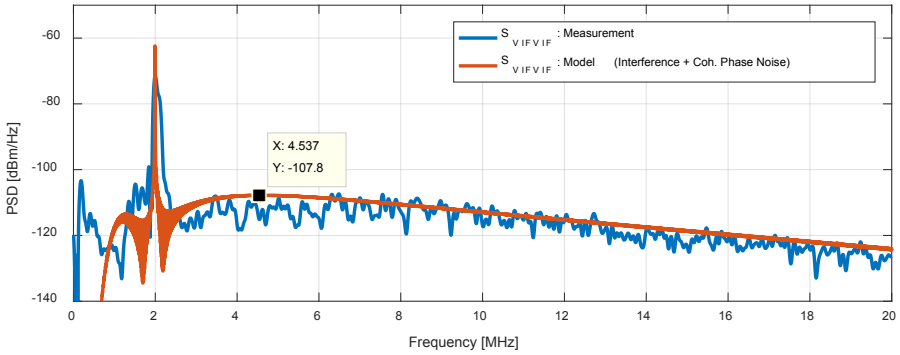

Figure 5.7.10 – Coherent Noise at Output due to Antenna Feed-through

5.7.3.5. Self-Interference Signal and Noise: LO Leakage

From 5.2, the signal path associated with the LO leakage self-interference is given by (5.7.22). In (5.7.22), $h_{LO}(t)$ is the impulse response for the LO sub-system. The term $h_{LL}(t)$ is the impulse response defined by (5.7.23). In (5.7.23), $h_{mx-LORF}(t)$ is the mixer LO-RF leakage and $h_{RX-ORL}(t)$ is the inverse of the return loss for the output of the RX-RF.

$$h_{p2}(t) = h_{LL}(t) * h_{LO}(t) \tag{5.7.22}$$

$$h_{LL}(t) = h_{mx-LORF}(t) * h_{RX-ORL}(t) \tag{5.7.23}$$

For this radar, the term $h_{RX-ORL}(t)$ can be further represented as shown in (5.7.24), where $h_{RX-OR-LNA}(t)$ is the impulse responses for the inverse of the return loss of the last LNA and $h_{ATT}(t)$ is the impulse response of the attenuator between the LNA and the mixer.

$$h_{RX-ORL}(t) = h_{ATT}(t) * h_{RX-OR-LNA}(t) * h_{ATT}(t) \tag{5.7.24}$$

Using frequency-averaged values, $|H_{RX-ORL}|^2$ is approximated to -26 dB. Similarly, $|H_{LL}|^2$ is approximated to be -61 dB on average. Thus, the signal path gain $\left|H_{p2}\right|^2$ can be approximated to be -67 dB on average.

$$|H_{RX-ORL}|^2{}_{dB} = 2|H_{ATT}|^2{}_{dB} + |H_{AX-OR-LNA}|^2{}_{dB} \tag{5.7.25}$$

$$|H_{RX-ORL}|^2{}_{dB} = 2 \cdot (-8\ \text{dB}) - 10\ \text{dB} = -26\ \text{dB} \tag{5.7.26}$$

$$|H_{LL}|^2{}_{dB} = |H_{mx-LORF}|^2{}_{dB} + |H_{RX-ORL}|^2{}_{dB} \tag{5.7.27}$$

$$|H_{LL}|^2{}_{dB} = -35\ \text{dB} - 26\ \text{dB} = -61\ \text{dB} \tag{5.7.28}$$

$$\left|H_{p2}\right|^2{}_{dB} = |H_{LL}|^2{}_{dB} + |H_{LO}|^2{}_{dB} \tag{5.7.29}$$

$$\left|H_{p2}\right|^2{}_{dB} = -61\ \text{dB} - 6\ \text{dB} = -67\ \text{dB} \tag{5.7.30}$$

Evaluating the signal amplitude due to the LO leakage self-interference path, the frequency-average PSD has a peak amplitude of -56.4 dBm/Hz, as shown in (5.7.31-5.7.32).

$$S_{v_{oik}v_{oik}{}_{dB}} = S_{v_{CG}v_{CG}{}_{dB}} + [BT]_{dB} + |H_{RX-IF}|^2{}_{dB} + |H_{MX}|^2{}_{dB} + \left|H_{p1}\right|^2{}_{dB} \tag{5.7.31}$$

$$S_{v_{oik}v_{oik}{}_{dB}} = -85.7\frac{\text{dBm}}{\text{Hz}} + 65.8\ \text{dB} + 37\ \text{dB} - 6.5\ \text{dB} - 67\ \text{dB} = -56.4\ \text{dBm/Hz} \tag{5.7.32}$$

The incoherent and coherent noise amplitudes due to this signal are approximated to be -120.4 dBm/Hz and -118.9 dBm/Hz, respectively. The approximation for the total incoherent noise level, which is the sum of the incoherent phase noise and thermal noise, is -110.6 dBm/Hz.

$$max\{S_{v_{onk}v_{onk}incoh}\}_{dB} = S_{v_{oik}v_{oik}{}_{dB}} - 47\ \text{dB} = -56.4\frac{\text{dBm}}{\text{Hz}} - 64\ \text{dB} = -120.4\ \text{dBm/Hz} \quad (5.7.33)$$

$$max\{S_{v_{onk}v_{onk}coh}\}_{dB} = S_{v_{oik}v_{oik}{}_{dB}} - 44\ \text{dB} = -56.4\frac{\text{dBm}}{\text{Hz}} - 62.5\ \text{dB} = -118.9\ \text{dBm/Hz} \quad (5.7.34)$$

Figures 5.7.11 and 5.7.12 show the incoherent and coherent noise due to the LO leakage self-interference signal. The measurement and the model agree with each other. The peak of the measured and simulated incoherent and coherent noises also agrees with the approximated value.

The self-interference signal due to LO leakage was designed in this radar to be very small. More specifically, the peak of coherent noise was designed to be similar in amplitude to thermal noise.

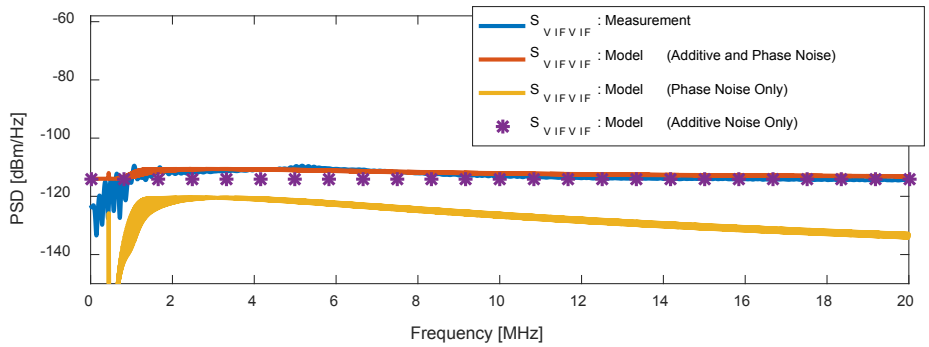

Figure 5.7.11 – PSD of Incoherent Noise due to LO Leakage

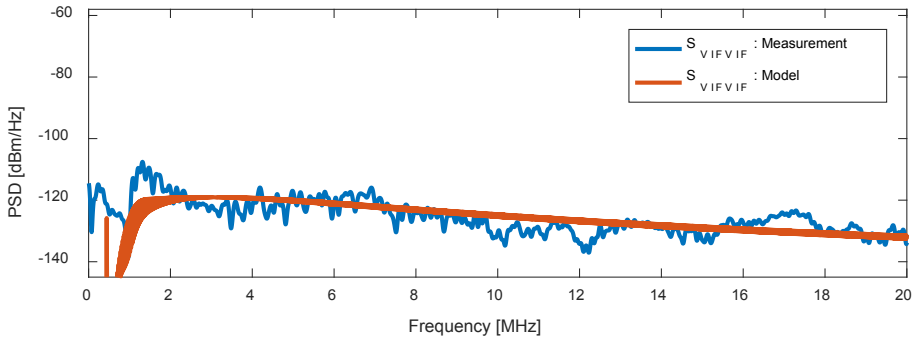

Figure 5.7.12 – PSD of Coherent Noise due to LO Leakage

Noise due to LO Leakage: Importance of Receiver Output Attenuator

The last LNA in the RX-RF has an average return loss of 10 dB. The average return loss of the the attenuators used (PN BW-SxW2+) is 26 dB or 1.1 VSWR. That means that the best return loss achievable by the receiver will be 26 dB. In order to achieve an output return loss of 26 dB for the RX-RF, the attenuator at the output must have at least an attenuation value of 8 dB. This is the attenuation chosen in the design.

This attenuator affects the amplitude of the self-interference signal, as indicated by (5.7.24). The amplitude of the LO leakage at the output and its noise is attenuated by twice the value of the attenuator. This attenuator is also part of the RX-RF, so it affect the RX gain and the thermal noise level. However, this attenuator only attenuates the thermal noise by one time its value. In other words, increasing this attenuator value decreases the noise due to the LO-Leakage by twice the amount it decreases the thermal noise level.

Figures 5.7.13 and 5.7.14 show the incoherent noise at the radar output due to LO leakage for attenuator values of 6 and 7 dB, respectively. These plots show that increasing the attenuator

value by 1 dB only decreases thermal noise by 1 dB, while it decreases incoherent phase noise by 2 dB. Similarly, in figures 5.7.15 and 5.7.16, it is shown that the coherent phase noise is also decreased by 2 dB when the attenuator is increased by 1 dB.

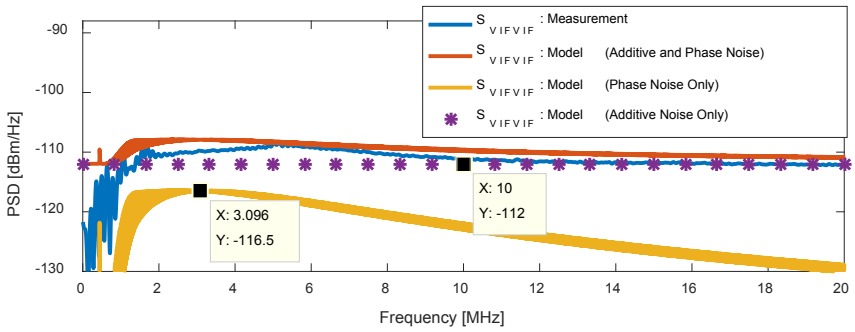

Figure 5.7.13 – PSD of Incoherent Noise due to LO Leakage: RX Output Attenuator is 6 dB

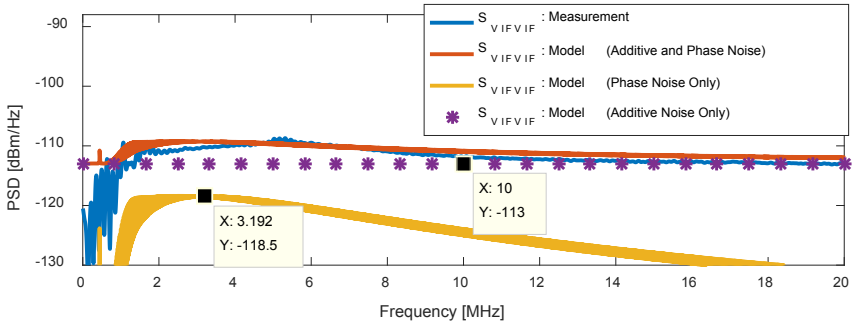

Figure 5.7.14 – PSD of Incoherent Noise due to LO Leakage: RX Output Attenuator is 7 dB

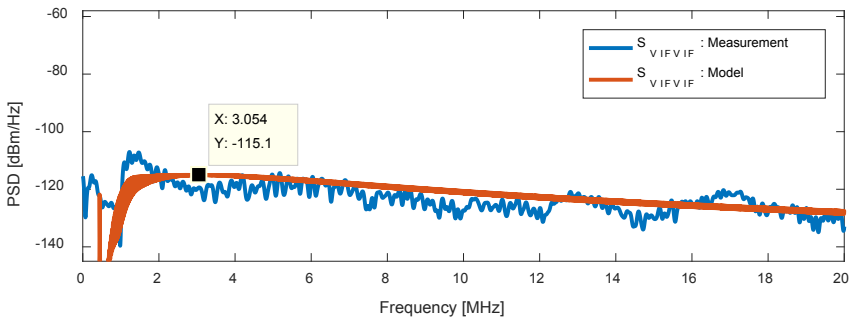

Figure 5.7.15 – PSD of Coherent Noise due to LO Leakage: RX Output Attenuator is 6 dB

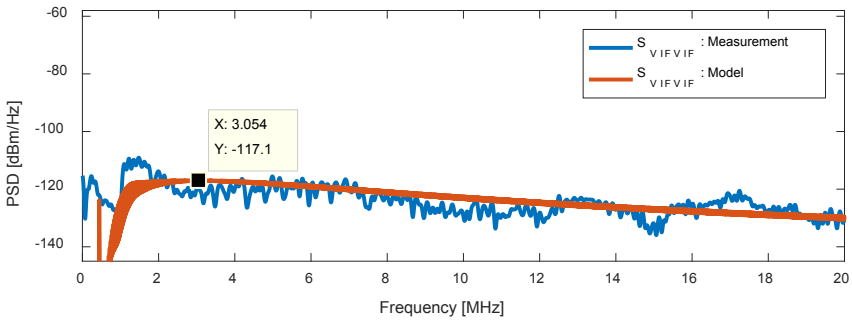

Figure 5.7.16 – PSD of Coherent Noise due to LO Leakage: RX Output Attenuator is 7 dB

5.7.3.6. Interference due to Ground: Ground Clutter

Another significant interference signal at the output of the radar is the ground clutter return. The RCS of the ground depends on the roughness and the moisture content. Using the structure, we took a measurement of the bare ground at mid-season. The RCS measured for the ground was -8.7 dB. The ground RCS of -8.7 dB is equivalent to an average antenna-target gain ($|H_T|^2{}_{dB}$) of -59 dB. This is a typical value of ground RCS, so we use this measurement to illustrate the effect of the ground clutter to the total noise level.

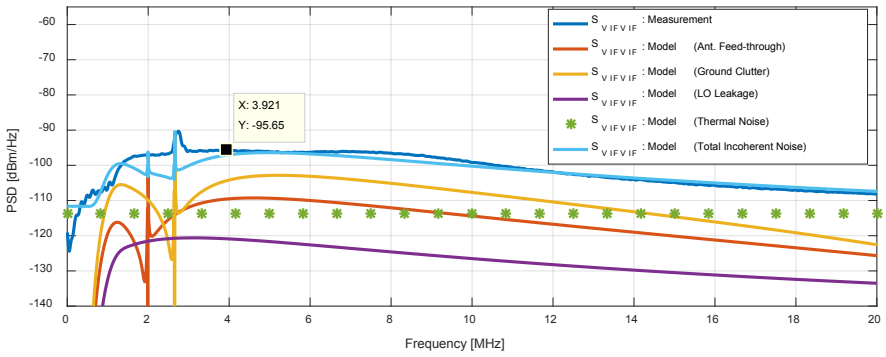

Figure 5.7.17 – Total Incoherent Noise

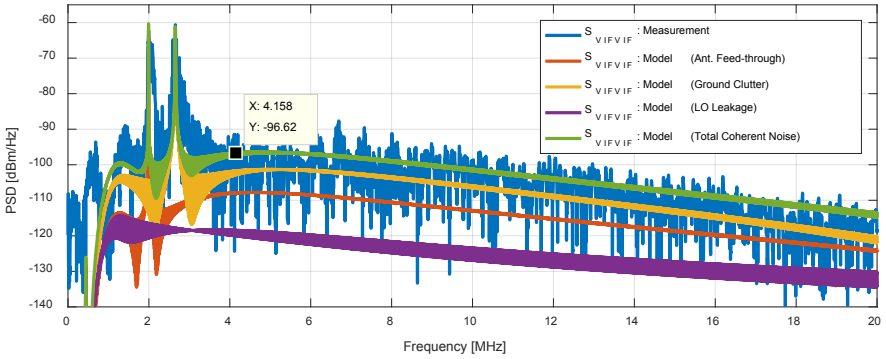

Figure 5.7.18 - Total Coherent Noise

Figures 5.7.17 and 5.7.18 show the total incoherent and coherent noise levels at the output of the radar, when ground clutter is present. The total coherent and incoherent noise levels agree with the models.

For this measurement, the total incoherent and coherent noise levels are -95.6 dB and -96.6 dB, respectively. After calibration, the incoherent and coherent noise levels result in an equivalent RCS of (-43.2) dB and (-44.2 dB), respectively.

In post-processing, the coherent noise is removed. The digital signal processing steps, performed in post-processing, are briefly described in chapter 6 (section 6.3.2).

Figure 5.7.19 shows an example of a range-domain RCS waveform due to a wheat canopy and ground. This signal includes contributions from both the wheat canopy and the ground. The contributions from the ground are filtered out in post-processing. The RCS-equivalent noise level of this waveform is -43 dB.

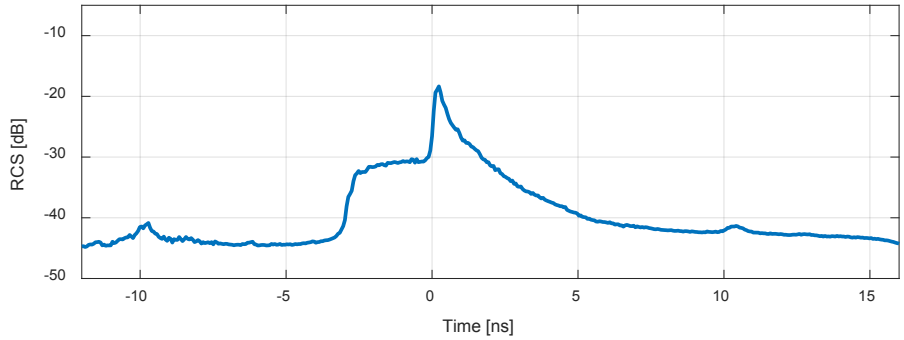

Figure 5.7.19 – Time-domain RCS after Coherent Noise Removal. (Average of a section of row 2)

5.8. RADAR DESCRIPTION: Calibration

5.8.1. Radar-Cross-Section from FMCW Radar Output

The calibration procedure is used to compute the radar-cross-section (RCS) waveforms for the time and frequency domain. This is accomplished by compensating the system response of all sub-systems.

From section 5.1.2, the spectrum of the output signal is given by (5.8.1).

$$V_{oi}(f) = v_{CGo}\, H_{RX-IF}(f)\, [\, {h_{mx}}^{*}(\mathrm{f/u}) * {h_{RX-RF}}^{*}(\mathrm{f/u}) * {h_T}^{*}(\mathrm{f/u}) * \, {h_{TX}}^{*}(\mathrm{f/u})\,] \tag{5.8.1}$$

Targets appear as narrow band signals at the IF of the FMCW radar, so that the $H_{RX-IF}(f)$ system response can be assumed constant. Using this approximation, the output signal in the time domain takes the form in (5.8.3).

$$H_{RX-IF}(f) \approx H_{RX-IF} \tag{5.8.2}$$

$$v_{oi}(t) = v_{CG}(t)\, H_{RX-IF}\, [\, H_{mx}(\mathrm{u\,t + f_o})\, H_{RX-RF}(\mathrm{u\,t + f_o})\, H_T(\mathrm{u\,t + f_o})\, H_{TX}(\mathrm{u\,t + f_o})\,] \tag{5.8.3}$$

Rearranging (5.8.3), the radar response $H_T(\mathrm{u\,t + f_o})$ is solved to be as shown in (5.8.4).

$$H_T(\mathrm{u\,t + f_o}) = \frac{v_{oi}(t)}{v_{CG}(t) H_{RX-IF}\, [\, H_{mx}(\mathrm{u\,t + f_o})\, H_{RX-RF}(\mathrm{u\,t + f_o})\, H_{TX}(\mathrm{u\,t + f_o})\,]} \tag{5.8.4}$$

$$H_T(f) = \, [\Phi_{to}\Phi_{or}] \left[jkZ\eta\, \mathbf{f_r} \cdot \bar{\bar{\mathbf{F}}} \cdot \mathbf{f_t}\right] \tag{5.8.5}$$

The radar response is given by the coherent radar equation (5.8.5). Solving for the scattering responses yields (5.8.6). The frequency and time domain radar-cross-section RCSs are given by (5.8.7-5.8.8).

$$F_{o,qp}(f) = F_{o,qp}(\mathbf{k}_s, \mathbf{k}_i) = \left[\hat{q} \cdot \bar{\bar{\mathbf{F}}}_o(\mathbf{k}_s, \mathbf{k}_i) \cdot \hat{p} \right] = \left[jk\eta Z_a \, \Phi_r(\mathbf{r}_r, \mathbf{r}_o) \, \Phi_t(\mathbf{r}_o, \mathbf{r}_t) |\mathbf{f}_r|_v |\mathbf{f}_t|_v \right]^{-1} H_t(f) \tag{5.8.6}$$

$$\sigma_{qp}(f) = \frac{1}{4\pi} \left| F_{o,qp}(f) \right|^2 \tag{5.8.7}$$

$$\sigma_{qp}(t) = \frac{1}{4\pi B} \left| F_{o,qp}(t) \right|^2 \tag{5.8.8}$$

5.8.2. Calibration of Antenna Response

This radar is designed to collect measurements routinely over crop canopies. Before data collection, the radar must be installed in the platform (cart). Each day slight changes made to the radar installation may modify the antenna system response. For instance, the antenna cables may be placed on a slightly different position behind the antennas.

For this reason, the system response of the antenna should be measured before each experiment. Moreover, the antennas must be measured in the same configuration in which they will be used for the experiment. To accomplish this task, we measure the radar return due to a target with known scattering amplitude for the polarization configuration of the radar $\mathrm{F}_{hh}(f)$. We use expression (5.8.4) to solve for $H_T(\mathrm{f})$. Finally, the updated antenna response can be solved using (5.8.10). This expression is valid for the transmit and receive antennas, since they are identical.

$$\mathrm{f}_{t,r}(f) = \sqrt{\frac{H_T(\mathrm{f})}{[\Phi_{to}\Phi_{or}]\,[jkZ\eta\ \mathrm{F}_{hh}(f)]}} \tag{5.8.10}$$

This procedure results in the system response of the antenna for the H/H antenna configuration and a particular angle, which depends on the height of the target. Since the antennas have a broad beamwidth (56.6 degrees), the exact location of the target with respect to the antennas is not very significant.

Figure 5.8.1 shows the measured frequency response of the antenna in different configurations. The blue curve represents the gain of the stand-alone antenna, without supports. The red and black represent the antenna gain installed with supports on a platform for installations performed in different days. The plot shows that the antenna gain changes significantly when supports are used. The plot also shows that there are slight changes in the gain after each different installation. This justifies the need to measure the antenna response before every experiment, as mentioned above.

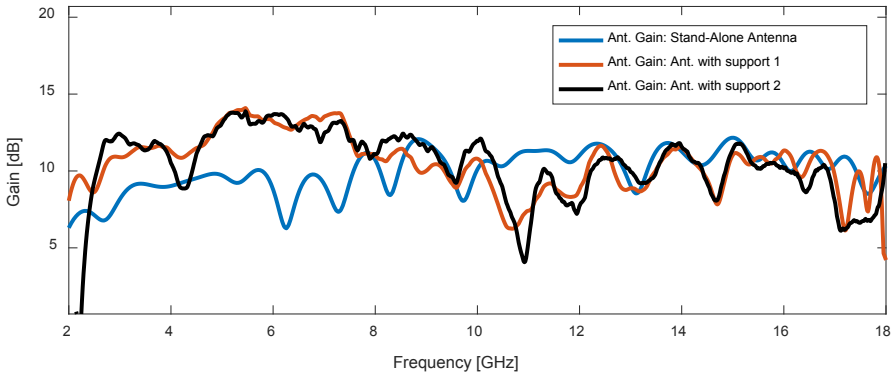

Figure 5.8.1 – Antenna frequency response at different configurations

5.8.3. Calibration Target Measurements

The calibration targets chosen were two aluminum cylinders denoted target 1 and 2, respectively. Figure 5.8.2 shows a picture of both cylinders. Target 1 has a length of 10.49 cm and a radius of 1.27 cm. Target 2 has a length of 7.95 cm and a radius of 0.47 cm.

The target's response in the time and frequency domains were simulated using the method of moments. These simulations were computed with Ansoft HFSS.

Figure 5.8.2 – Calibration Targets: Target 1 (Left); Target 2 (Right)

We measure the radar response to both targets. The radar response of the first target is used along with its simulated target response to calculate the antenna's frequency response. We compute the RCS for the second target using its radar return and its new antenna response. This RCS is compared against the numerical simulation to check the radar's ability to measure RCS with its new antenna response.

Figure 5.8.3 shows the frequency domain of the RCS of target 1 over the radar's bandwidth. The curved labeled measurement is the RCS derived from a radar measurement using the updated antenna gain. Figure 5.8.4 shows the modified time-domain RCS. As expected, both of them agree perfectly to the simulation.

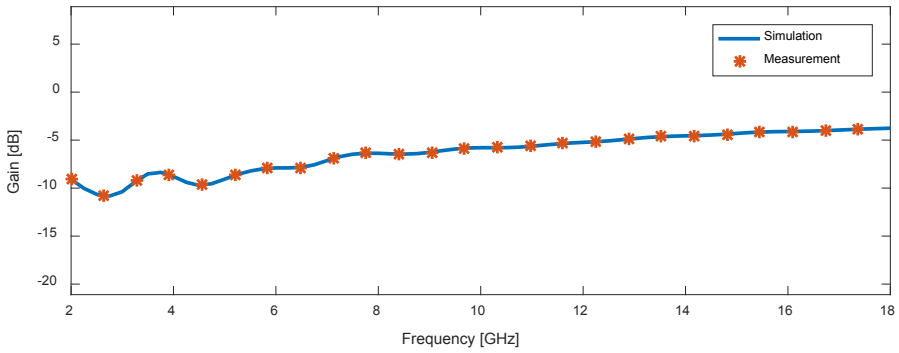

Figure 5.8.3 – Frequency-domain RCS for target 1

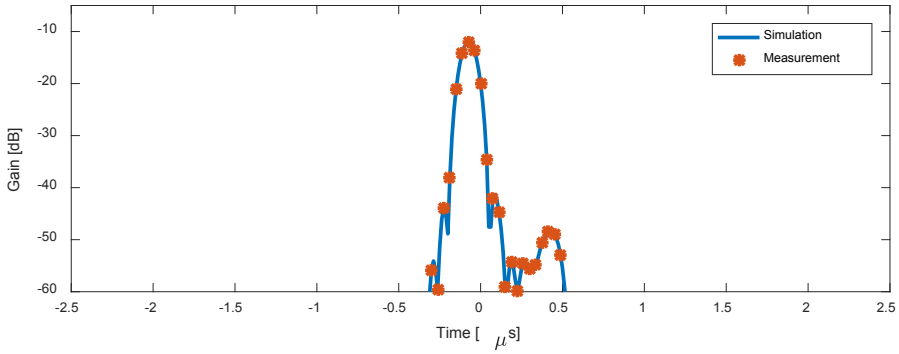

Figure 5.8.4 – Time-domain RCS for target 1

Figures 5.8.5 and 5.8.6 show the frequency-domain and modified-time-domain RCS of target 2.

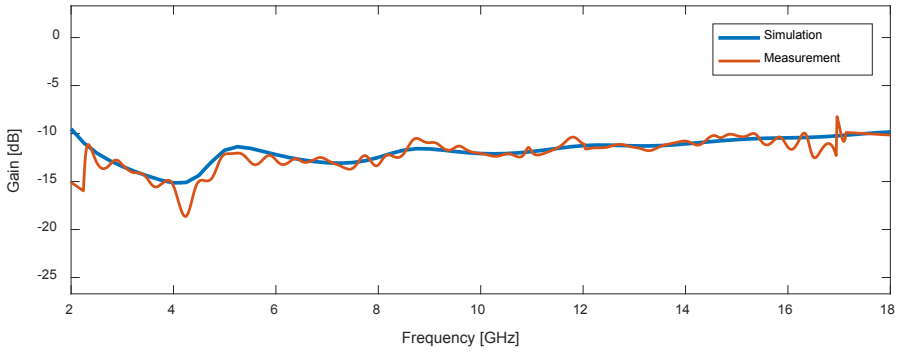

Figure 5.8.5 – Frequency-domain RCS for target 2

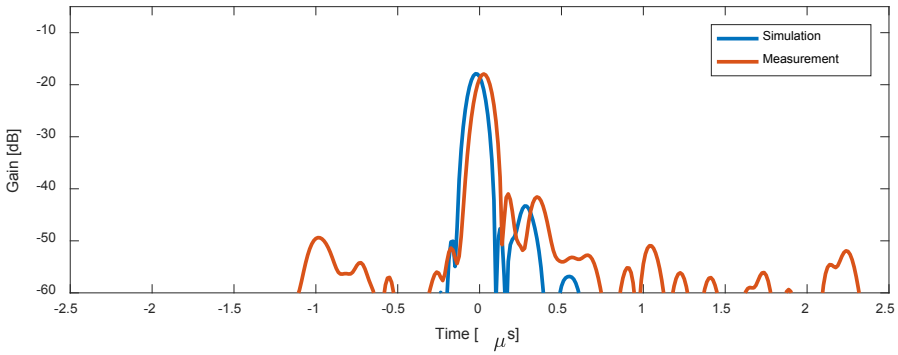

Figure 5.8.6 – Time-domain RCS for target 2

5.9. References

[1] F. Rodriguez-Morales, S. Gogineni, C. Leuschen, J. Paden, J. Li, C. Lewis, B. Panzer, D. Gomez-Garcia , A. Patel, K. Byers, R. Crowe, K. Player, R. Hale, E. Arnold, L. Smith, C. Gifford, D. Braaten, and C. Panton, "Advanced Multifrequency Radar Instrumentation for Polar Research," in IEEE Transactions on Geoscience and Remote Sensing, vol. 52, no. 5, pp. 2824-2842, May 2014.

[2] Panzer, B., D. Gomez-Garcia, A. Patel, C. Leuschen, J. Paden, T. Markus, and S. Gogineni, “Development of an ultra-wideband radar for measuring snow thickness on sea ice,” Journal of Glaciology Instruments and Methods, vol. 59, no. 214, pp. 244-254, April 2013.

[3] Daniel Gomez-Garcia , Fernando Rodriguez-Morales, Carlton Leuschen, Prasad Gogineni, "KU-Band radar altimeter for surface elevation measurements in polar regions using a wideband chirp generator with improved linearity," 2012 IEEE International Geoscience and Remote Sensing Symposium, Munich, 2012, pp. 4617-4620.

[4] Daniel Gomez-Garcia, “Linearization Method for a UWB VCO-based chirp generator using dual compensation,” M.S. Thesis Defense, Nov. 2011, Lawrence KS.

[5] D. Gomez-Garcia, C. Leuschen, F. Rodriguez-Morales, Jie-Bang Yan and P. Gogineni, "Linear chirp generator based on direct digital synthesis and frequency multiplication for airborne FMCW snow probing radar," 2014 IEEE MTT-S International Microwave Symposium (IMS2014), Tampa, FL, 2014, pp. 1-4.

[6] J. B. Yan, D. Gomez-Garcia, J. McDaniels, Y. Li, S. Gogineni, F. Rodriguez-Morales, J. Brozena, C. Leuschen, "Ultrawideband FMCW Radar for Airborne Measurements of Snow Over

Sea Ice and Land," in IEEE Transactions on Geoscience and Remote Sensing, vol. 55, no. 2, pp. 834-843, Feb. 2017.

[7] Texas Instruments, “LM7171 Very High Speed, High Output Current, Voltage Feedback Amplifier,” LM7171 datasheet, March 2013. [Revised Sep., 2014].

[8] John Ledford, “Eight Channel Waveform Generator for Beam-Forming Applications,” M.S. Thesis. Univ. of Kansas., Lawrence, KS, 2009.

[9] Analog Devices, “1 GSPS, 14-bit, 3.3 V, CMOS Direct Digital Synthesizer,” AD9910 datasheet, May 2007. [Revised Oct, 2016].

[10] S. A. Osmany, “Phase noise and jitter modeling for fractional N PLLs,” Adv. Radio Sci., 5, pp. 313-320, 2017.

6. Radar Simulations of Wheat Canopies and Retrieval of Architecture Parameters

This chapter applies the radar simulator, described in chapter 4, to calculate the radar response due to wheat canopy plots. Monte Carlo simulations are performed for different leaf parameters. These simulation results are used to formulate a simplified RCS model due to wheat canopies with no heads. They are also used to derive procedures to retrieve architecture parameters: wheat canopy height and projected leaf area density. The retrieval procedures are applied to radar measurements collected of wheat canopy plots. The results of the radar-based height retrievals are compared against manual measurements and the results of the radar-retrieved projected leave area densities are compared against image-derived retrievals.

This chapter is organized in three sections.

Section 6.1 applies the radar simulation of chapter 4 to wheat canopy plots. The first two sub-sections of section 6.1 describe the target and antenna configuration considered for the radar simulations. Sub-sections 6.1.3 and 6.1.4 discuss the distortion caused by wide-beam measurements on the RCS waveform. This type of distortion, which is accounted for by the simulator, results in limitations to the measurements of RCS profiles. The rest of the sub-sections in 6.1 show examples of Monte Carlo simulations due to wheat canopy plots with different configurations.

In the first part of section 6.2, the radar simulator is used to derive a simplified relationship between the RCS and the leaf parameters of a wheat canopy plot with no heads. In the second sub-section of 6.2, the relationships found in 6.2.1 are used to formulate a simplified RCS model

due to wheat canopies with no heads. Sub-sections 6.2.3 and 6.2.4 describe procedures for the retrieval of canopy height and projected leaf area density, respectively, from range-domain RCS waveforms. These procedures were derived using extensive radar simulations of RCS waveforms of wheat canopies.

In section 6.3, an experiment is described where radar measurements were collected on wheat canopy plots. The signal processing steps applied to the radar measurements are listed and briefly described. The retrieval procedures of section 6.2 were applied to the radar measurements. This section shows the results of the radar retrievals and the comparison of these retrievals against the values found with other methods.

6.1. Radar Simulations of Wheat Canopies

6.1.1. Target Configuration: Wheat Canopy Plot

The goal of the radar simulations is to serve as a tool to calculate the RCS due to wheat canopy plots, so that the RCS can be related to plant parameters. The type of canopy plots of interest are the wheat plots used for breeding by the Kansas State University (KSU). Specifically, we focus on the wheat plots used for breeding trials, located in the wheat fields of Tom Pauly in Conway Springs, KS. The arrangement and geographical location of the plots are given in 6.3.

The dimensions of the wheat plots of interest are 1.4x4 m. These plots are composed of six rows of plants. The rows of plants are separated from each other by 0.2286 m (9 inches). Figure 6.1.2 shows the top view of a wheat canopy model with these dimensions.

For the simulations, we align the horizontal long dimension and width of the wheat canopy to the y- and x- axes. The maximum length of the antenna footprint in the y-dimension is 1.8 m, as shown by the model in figure 6.1.2. Therefore, we restrict the y-dimension of the canopy plot to 2 m, with negligible effect on the simulation result. Figure 6.1.1 shows a comparison of radar simulations of wheat canopy plots with 2 and 4 meters of length (y-dimension). The difference of the two RCS waveforms below a relative range of 0 m is negligible. This truncation results in a reduction of the simulation time by a factor of two. Therefore, the simulations of the wheat plots are performed using a plot length of 2 m.

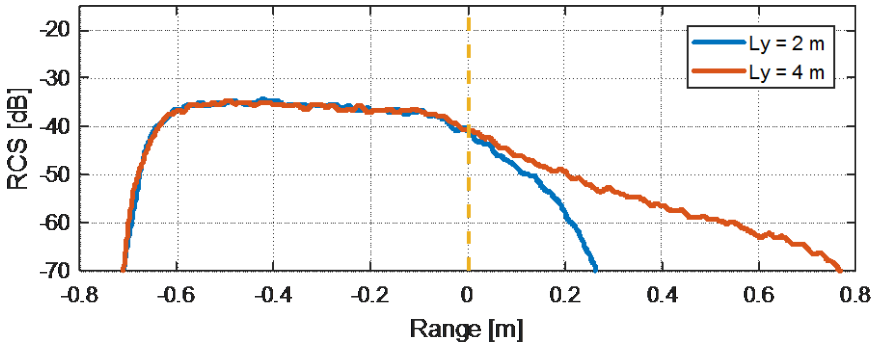

Figure 6.1.1 – Comparison of Radar Simulations due to Wheat Canopy Plots with 2 and 4 meters of length.

Figures 6.1.2 and 6.1.3 show a representation of geometric models for wheat plot with 4 and 2 meters of length. The former represents a wheat plot with the actual dimensions of the wheat canopy plot. The latter has the dimensions used for the radar simulations.

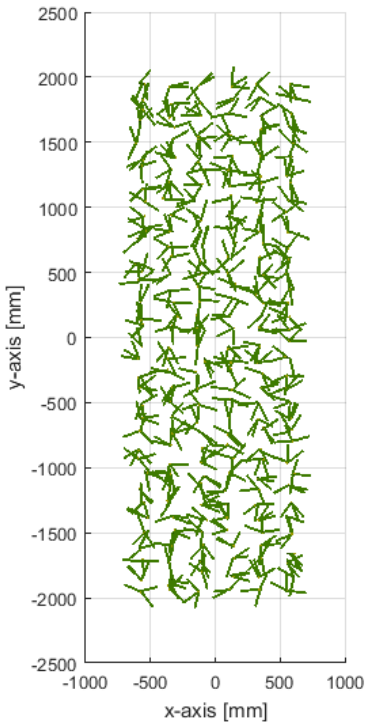

Figure 6.1.2 – Top View of Geometric Model of Canopy with a length of 4 m

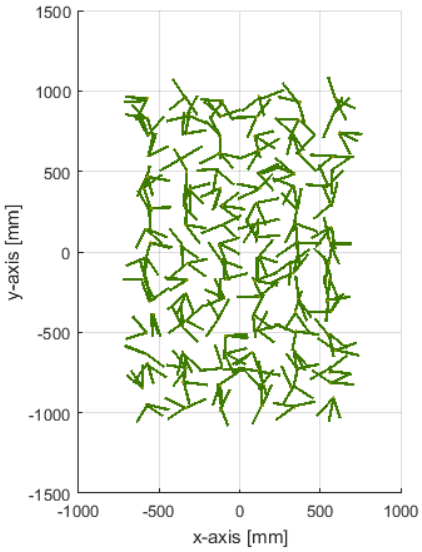

Figure 6.1.3 – Top View of Geometric Model of Canopy with a length of 2 m

6.1.2. Antenna Configuration

The position of the transmit and receive antennas used in the radar simulations are given by (6.1.1) and (6.1.2), respectively. The distance of the antennas from the origin is 1.8256 m. The antennas located at a height of 1.8 m from the ground. They are separated from each other by 0.6096 m (2 ft). This is the antenna configuration used by the radar in the field experiment, described in section 6.3.

$$\mathbf{r}_t = r_t \begin{bmatrix} \cos(\varphi_r)\sin(\theta_r) \\ \sin(\varphi_r)\sin(\theta_r) \\ \cos(\theta_r) \end{bmatrix} = 1.8256\ \text{m} \begin{bmatrix} \sin(-9.6\ \text{deg}) \\ 0 \\ \cos(-9.6\ \text{deg}) \end{bmatrix} = \begin{bmatrix} -0.3048\ \text{m} \\ 0 \\ +1.8\ \text{m} \end{bmatrix} \tag{6.1.1}$$

$$\mathbf{r}_r = r_r \begin{bmatrix} \cos(\varphi_r)\sin(\theta_r) \\ \sin(\varphi_r)\sin(\theta_r) \\ \cos(\theta_r) \end{bmatrix} = 1.8256\ \text{m} \begin{bmatrix} \sin(+9.6\ \text{deg}) \\ 0 \\ \cos(+9.6\ \text{deg}) \end{bmatrix} = \begin{bmatrix} +0.3048\ \text{m} \\ 0 \\ +1.8\ \text{m} \end{bmatrix} \tag{6.1.2}$$

The antenna field pattern used in the radar simulations is the same field pattern of the antennas of the radar described in chapter 5. The normalized antenna field pattern as a function of frequency and angle is shown in figure 6.1.4.

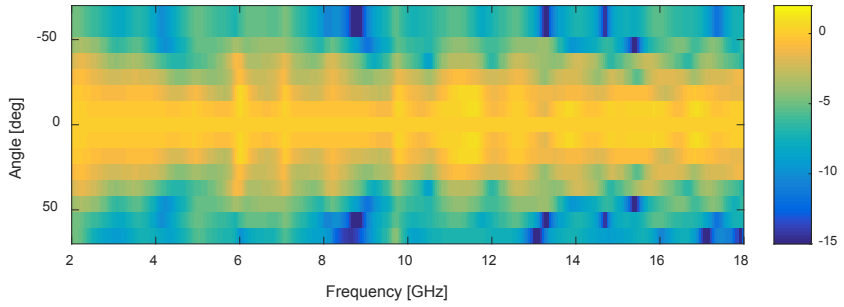

Figure 6.1.4 – Normalized Antenna Field Pattern (dB) vs Frequency and Angle

The simulations use the field pattern shown in 6.1.4. The half-power beamwidth of the antenna is not constant with frequency.

Only to be used for reference, not for simulations, the equivalent footprint is found using the simulator. The simulator is run using antennas with a field pattern that is constant in frequency and constant in angle below a given value. The result is compared against the simulation results found using the field pattern shown in figure 6.1.4. The equivalent beamwidth is that which results in the same RCS amplitude as the results found using the field pattern shown in figure 6.1.4. For these simulations, we used extended targets with very large areas. The value found for the equivalent beamwidth of the antenna is 56.6 degrees. For the two antennas located as indicated by equations (6.1.1) and (6.1.2), the equivalent footprint results in an area of 1.79 m^2. Figure 6.1.5 shows a depiction of effective antenna footprint.

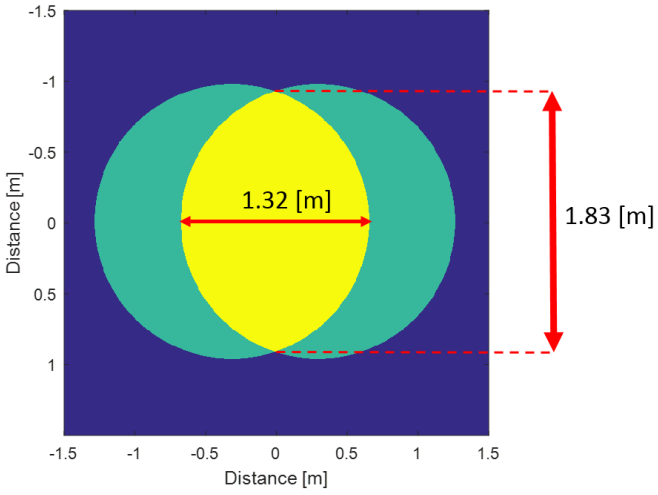

Figure 6.1.5 – Effective Antenna Footprint

6.1.3. Profile Approximation and Distortion

Profile Approximation

In near-nadir mode, the scattering response as a function of range can be approximated to the vertical profile of the target's scattering response, if the target spans a narrow beam of the antenna. This occurs in targets with small dimensions perpendicular to the antenna's main axis. Alternatively, this could also occur if the antennas are located very far away from the target.

In order to find the conditions at which this approximation becomes valid, we derive the relationship of the range of a sub-target, member of a complex target, to its vertical position.

We consider the scattering response $F_{qp}(f)$ of a target with respect to the scattering center $\mathbf{r_o}$. This is a complex target composed of N sub-targets $F_{qp,i}(f)$, where $i \in [1, N]$. The scattering response $F_{qp}(f)$ may be expressed as (6.1.3), assuming the sub-targets are sparse and the antenna field pattern is constant with angle.

$$F_{qp}(f) = \sum_{i}^{N} \frac{\Phi_r(\mathbf{r_{o,i}}, \mathbf{r_r})\Phi_t(\mathbf{r_t}, \mathbf{r_{o,i}})}{\Phi_r(\mathbf{r_o}, \mathbf{r_r})\Phi_t(\mathbf{r_t}, \mathbf{r_o})} F_{qp,i}(f) \tag{6.1.3}$$

The propagation function $\Phi(\mathbf{r_1}, \mathbf{r_2})$ from location $\mathbf{r_1}$ to location $\mathbf{r_2}$ is defined as given by (6.1.4). The time delay due to the propagation function is $|\mathbf{r_2} - \mathbf{r_1}|/c$. The relative-delay due to a sub-target's scattering center is given relative to the delay of the scattering center $\mathbf{r_o}$. In other words, the delay of a sub-target is the roundtrip delay ($\tau_{o,i}$) minus the round-trip delay to the scattering center τ_o. Therefore, the relative-delay (τ) due to each of these sub-targets is given by (6.1.5).

$$\Phi(\mathbf{r_1}, \mathbf{r_2}) = \frac{1}{4\pi|\mathbf{r_2} - \mathbf{r_1}|} e^{jk|\mathbf{r_2}-\mathbf{r_1}|} \tag{6.1.4}$$

$$\tau = \tau_{o,i} - \tau_o = \frac{1}{c}\left[\ \left|\mathbf{r}_{o,i} - \mathbf{r}_t\right| + \left|\mathbf{r}_r - \mathbf{r}_{o,i}\right| - \ |\mathbf{r}_o - \mathbf{r}_t| - |\mathbf{r}_r - \mathbf{r}_o|\ \right] \tag{6.1.5}$$

The relative-range is given by (6.1.6), in terms of the relative-delay. Replacing (6.1.5) into (6.1.6) results in (6.1.7), where R_o is the distance from the antenna center to the origin (6.1.8) and $R_{o,i}$ is the distance from the antenna center to each sub-target (6.1.9). The terms R_{To} and R_{Ro} used in (6.1.8) are the distance from origin to the transmit and receive antennas, respectively. Likewise, the terms R_T and R_R are the distances from the sub-target scattering center to the transmit and receive antennas, respectively. The distances $R_{o,i}$, R_T and R_R are depicted in the diagram of figure 6.1.6.

$$R = \tau\, c/2 \tag{6.1.6}$$

$$R = R_{o,i} - R_o \tag{6.1.7}$$

$$R_o = \frac{1}{2}[|\mathbf{r}_o - \mathbf{r}_t| + |\mathbf{r}_r - \mathbf{r}_o|] = \frac{1}{2}[R_{To} + R_{Ro}] \tag{6.1.8}$$

$$R_{o,i} = \frac{1}{2}\left[\left|\mathbf{r}_{o,i} - \mathbf{r}_t\right| + \left|\mathbf{r}_r - \mathbf{r}_{o,i}\right|\right] = \frac{1}{2}[R_T + R_R] \tag{6.1.9}$$

The position vector of the antenna center is $\mathbf{r}_c$. This position vector can be written as the average of the position vectors of the transmit and receive antennas, as given by (6.1.10).

$\mathbf{r}_c = \frac{1}{2}[\,\mathbf{r}_t + \mathbf{r}_r]$	(6.1.10)

Using the position vector of the antenna center, the distance from the antenna center to the scattering center of a sub-target is given by (6.1.11).

$R_{o,i} = \frac{1}{2}[R_T + R_R] = \left\|\mathbf{r}_c - \mathbf{r}_{o,i}\right\|$	(6.1.11)

In order to approximate the range $R_{o,i}$ to the vertical component of the vector $\left(\mathbf{r}_c - \mathbf{r}_{o,i}\right)$, we make the approximation shown in (6.1.12). Assuming the sub-target's z-component is small, this approximation is valid when the z-axis component of the antenna center ($\mathbf{r}_c \cdot \hat{z}$) is much smaller than the horizontal component of the sub-target's scattering center ($\left|\hat{z} \times \mathbf{r}_{o,i} \times \hat{z}\right|$).

$$R_{o,i} \approx \hat{z} \cdot \left(\mathbf{r}_c - \mathbf{r}_{o,i}\right) \quad for \quad \mathbf{r}_c \cdot \hat{z} \gg \left|\hat{z} \times \mathbf{r}_{o,i} \times \hat{z}\right| \tag{6.1.12}$$

If the antenna center has zero horizontal component, the distance R_o is given by the z-component of $\mathbf{r}_c$, as shown in (6.1.13).

$$R_o = \hat{z} \cdot \mathbf{r}_c \tag{6.1.13}$$

Replacing (6.1.12) and (6.1.13) into (6.1.7) results in (6.1.14).

$$R \approx -\hat{z} \cdot \mathbf{r}_{o,i} \tag{6.1.14}$$

In summary, the condition that is required to approximate the relative-range R of a sub-target to the vertical component of the sub-target $-\hat{z} \cdot \mathbf{r}_{o,i}$, the horizontal component of the sub-target

must be much smaller than the vertical component of the antenna center. This condition is given by the ratio shown in (6.1.15).

$$\frac{\mathbf{r_c} \cdot \hat{z}}{\left|\hat{z} \times \mathbf{r_{o,i}} \times \hat{z}\right|} \gg 1 \tag{6.1.15}$$

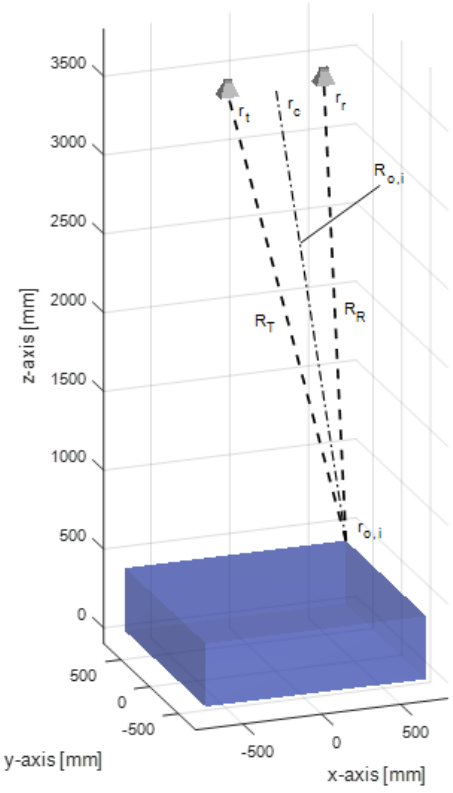

Figure 6.1.6 - Diagram showing the distances from the antennas to a sub-target's scattering center

Wide-Beam Distortion

As the antenna center approaches the targets or the horizontal component of the sub-target's position increases, the ratio in (6.1.15) decreases, making the approximation in (6.1.14) less effective. Reducing the ratio in (6.1.15) creates a distortion in the RCS profile (i.e. approximated RCS vs vertical component). The RCS profile of a point target develops a slow raising and a slow falling edge as it is distorted. These raising and falling edges reduces the dynamic range of close targets. In the case of a distributed target, such as a canopy, this distortion reduces the ability of a radar to detect a RCS profile with a high rate of change.

The radar simulator accounts for this type of distortion inherently. The simulator can be used to calculate RCS waveforms with and without this type of distortion. The simulator is also used to calculate the maximum rate of change of RCS in the vertical dimension, for a given target/antenna configuration. Results from this exercise are shown 6.1.4.

6.1.4. Effect of Wide-Beam Distortion on Radar Simulations of Wheat Canopies

In order to assess the effects of the wide-beam distortion, described in section 6.1.3, radar simulations were run, using a wheat canopy as the target and positioning the antennas at different altitudes. First, simulations were performed with the antennas located at a high altitude to obtain the RCS as a function of range that approximates the RCS profile with negligible limitations. Secondly, simulations were performed over the same target at an altitude of 1.8 m, which is the altitude of the radar antennas, as described in chapter 5.

The target used for the simulations is a wheat canopy. This canopy has the dimensions and the arrangement indicated in section 6.1.1. That is, it has 6 rows, spaced by 9 inches from each other. The rows are spaced from each other in the x-dimension. The length of the canopy in the y-dimension is 2 m. For these simulations, the canopy density is 40 plants/m^2. The plants of the canopy are composed of stems and three leaves each, with no heads.

The parameters of the stems and leaves of the plants are listed in tables 6.1.1 and 6.1.2, respectively. Some of the parameters are random. For instance, the stem elevation angle is a random variable, normally distributed with zero mean and 4 degrees of standard deviation, as listed in table 6.1.1. Each leaf and stem within a canopy realization is randomly generated. Sixty realizations of the canopy were performed.

Figures 6.1.7 and 6.1.8 show the front and perspective views, respectively, of a realization of the simulated canopy plot.

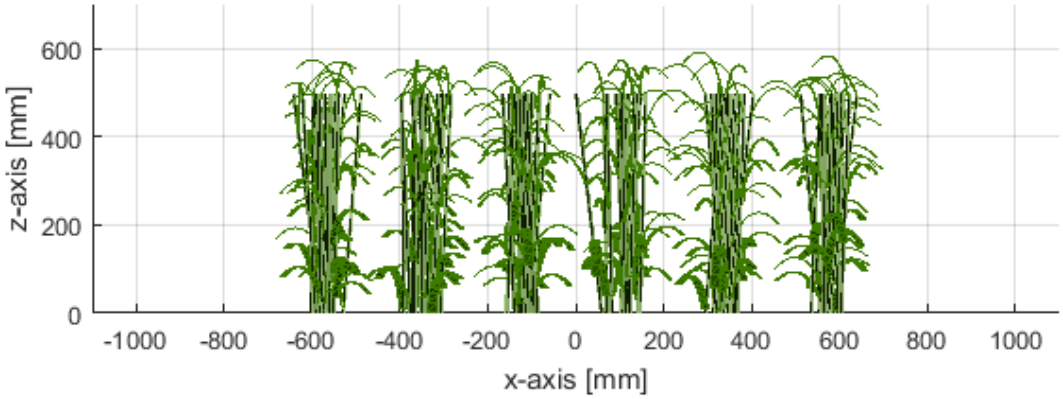

Figure 6.1.7 – Visualization of Geometric Model of Wheat Canopy: Front View

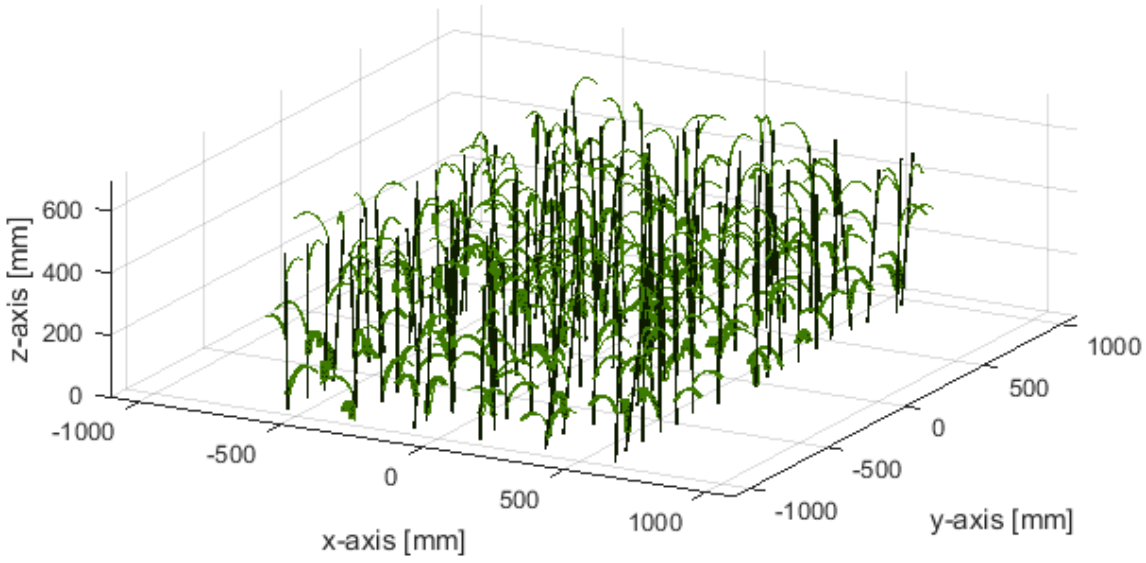

Figure 6.1.8 – Visualization of Geometric Model of Wheat Canopy: Perspective View

Table 6.1.1 – Canopy Simulation: List of Stem Parameters

Parameter	**Stem 1, $t_{S,(1,1)}$**
Position, $\mathrm{r}_{S,(1,i_S)}$	$\mathrm{r}_{p,(i_p)}$
Length, $L_{S,(1,i_S)}$	500 mm
Radius, $\rho_{S,(1,i_S)}$	0.75 mm
Azimuth, $\varphi_{S,(1,i_S)}$	0 deg
Elev., $\theta_{S,(1,i_S)}$	~N(0 deg, (4 deg)^2)
Moist. Cont., $m_{S,(1,i_S)}$	0.75

Table 6.1.2 – Canopy Simulation: List of Leaf Parameters

Parameter	**Leaf 1, $t_{L,(1,1)}$**	**Leaf 2, $t_{L,(1,2)}$**	**Leaf 3, $t_{L,(1,3)}$**
Position, $r_{L,(1,i_L)}$	Uniformly distributed along bottom third of stem	Uniformly distributed along center third of stem	Uniformly distributed along top third of stem
Length, $L_{L,(1,i_L)}$	~N(150 mm , (20mm)^2)	~N(150 mm , (20mm)^2)	~N(150 mm , (20mm)^2)
Width, $w_{L,(1,i_L)}$	20 mm	7.0 mm	2.5 mm
Thickness, $a_{L,(1,i_L)}$	0.2 mm	0.2 mm	0.2 mm
First-rot. $\alpha_{L,(1,i_L)}$	0 deg	0 deg	0 deg
Azimuth, $\varphi_{L,(1,i_L)}$	Uniformly distributed 0-360 deg	Uniformly distributed 0-360 deg	Uniformly distributed 0-360 deg
Initial Elev, $\theta_{i,L,(1,i_L)}$	~N(90-85 deg, (4 deg)^2)	~N(90-85 deg, (4 deg)^2)	~N(90-85 deg, (4 deg)^2)
Final Elev, $\theta_{f,L,(1,i_L)}$	~N(90+70 deg, (4 deg)^2)	~N(90+70 deg, (4 deg)^2)	~N(90+70 deg, (4 deg)^2)
Rad. of Curv., $R_{L,(1,i_L)}$	55mm	55mm	55mm
Apex Loc., $s_{o,L,(1,i_L)}$	0.6	0.6	0.6
Moisture Cont., $m_{L,(1,i_L)}$	0.75	0.75	0.75

We approximate the expected value of the range-domain RCS waveform due to the wheat canopy by taking the sample mean of 60 radar simulations. For each radar simulation, the geometric model of the wheat canopy was randomly generated. This approximation is also known as a type of Monte Carlo simulation. In this document, we refer to the result of the Monte Carlo simulation as the sample mean of the RCS waveform, using multiple realizations.

For the first Monte Carlo simulation, the antennas were placed at a high altitude of 100 m above the ground. At this altitude, the entire horizontal area of the target fits within the range bin used

of 1.4 cm. Therefore, the range-domain RCS approximates the RCS profile with no wide-beam distortion.

The blue waveform in figure 6.1.9 shows the result of the first Monte Carlo simulation. The red, yellow and purple waveforms show the contributions due to the bottom, middle and top leaves, respectively. The width of the leaves at different levels was set to different values. The amplitude of the RCS depends on the width of the leaf. Figure 6.1.9 shows a different RCS amplitude for each leaf level, indicating the dependence of the RCS to the leaf width at each level. More importantly, figure 6.1.9 shows that range-domain RCS approximates to the RCS profile. This RCS profile shows the RCS contributions due to the plant constituents at different vertical levels.

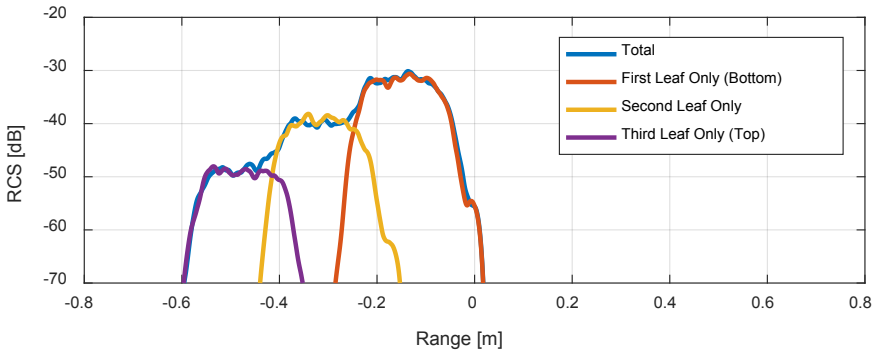

Figure 6.1.9 – Monte Carlo Simulation of Canopy: RCS vs Range. Long Range

For the second Monte Carlo simulation, the antennas were placed at 1.8 m above the ground. At this altitude, each range bin of 1.4 cm includes contributions from multiple vertical levels of the same dimension. This results in a distortion of the RCS profile, which is approximated by the range-domain RCS. This distortion degrades the ability to distinguish the RCS contributions from different vertical levels of the canopy. The antenna radiation pattern, which is larger near zero degrees and small at larger angles, reduces the effect of the wide-beam distortion.

Figure 6.1.10 shows the sample mean of the range-domain RCS waveform for the antennas placed at 1.8 m above the ground. This Monte Carlo simulation used 60 realizations of the canopies described by tables 6.1.1 and 6.1.2. This figure also shows the contributions due to each leaf level. The wide-beam distortion in this configuration results in a rising edge of 0.57 dB/cm and a falling edge of 2.86 dB/cm. The RCS contributions from target at adjacent vertical levels have to be above these rising and falling edge levels to be detected.

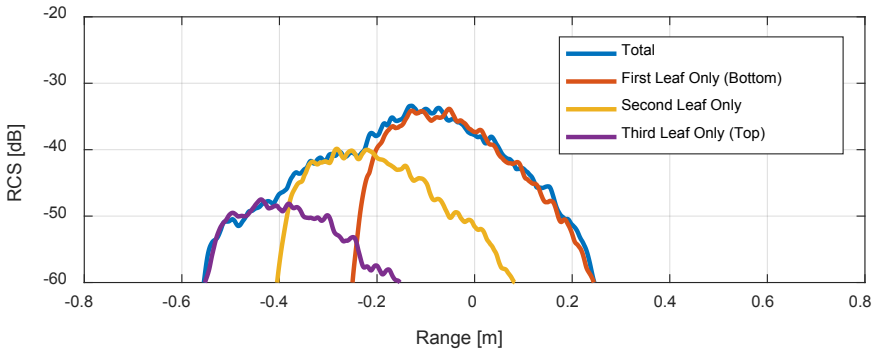

Figure 6.1.10 – Monte Carlo Simulation of Canopy: RCS vs Range. Short Range

6.1.5. Radar Simulation (Case 1): Straight Leaves

In this section, we show an example of a Monte Carlo radar simulation due to a canopy with straight leaves. The parameters of the stems and leaves of the plants are listed in tables 6.1.3 and 6.1.4, respectively. Figure 6.1.11 shows a depiction of the canopy geometric model.

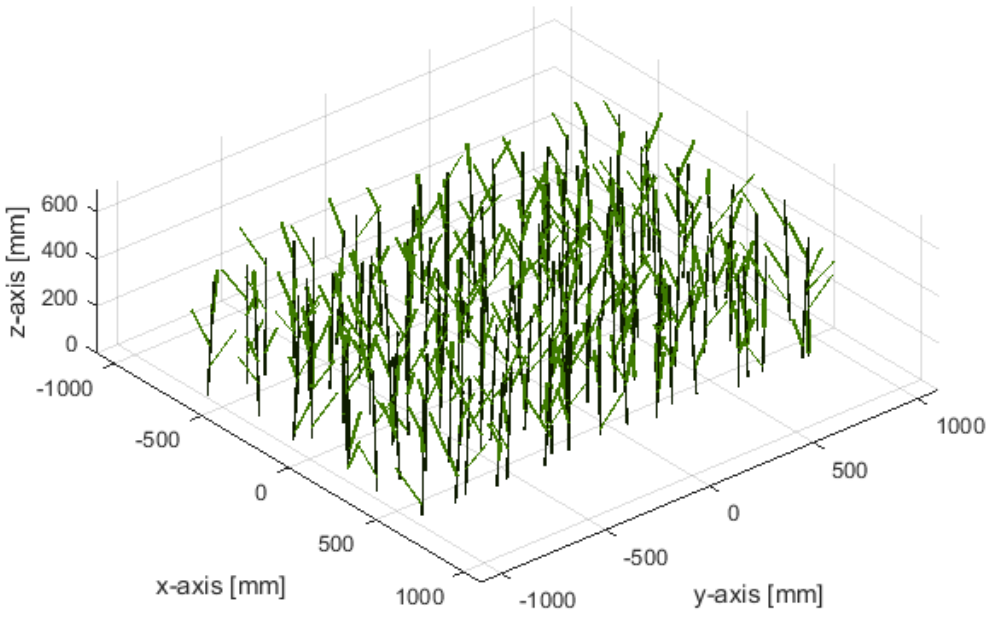

Figure 6.1.11 – Canopy (Straight Leaves): Visualization of Geometric Model

Table 6.1.3 – Canopy Simulation: List of Stem Parameters

Parameter	**Stem 1, $t_{S,(1,1)}$**
Position, $r_{S,(1,i_S)}$	$\mathbf{r}_{p,(i_p)}$
Length, $L_{S,(1,i_S)}$	500 mm
Radius, $\rho_{S,(1,i_S)}$	0.75 mm
Azimuth, $\varphi_{S,(1,i_S)}$	0 deg
Elev., $\theta_{S,(1,i_S)}$	~N(0 deg, (4 deg)^2)
Moist. Cont., $m_{S,(1,i_S)}$	0.75

Table 6.1.4 – Canopy Simulation: List of Leaf Parameters

Parameter	**Leaf 1, $t_{L,(1,1)}$**	**Leaf 2, $t_{L,(1,2)}$**	**Leaf 3, $t_{L,(1,3)}$**
Position, $r_{L,(1,i_L)}$	Uniformly distributed along bottom third of stem	Uniformly distributed along center third of stem	Uniformly distributed along top third of stem
Length, $L_{L,(1,i_L)}$	~N(150 mm , (20mm)^2)	~N(150 mm , (20mm)^2)	~N(150 mm , (20mm)^2)
Width, $w_{L,(1,i_L)}$	10 mm	10 mm	10 mm
Thickness, $a_{L,(1,i_L)}$	0.2 mm	0.2 mm	0.2 mm
First-rot. $\alpha_{L,(1,i_L)}$	0 deg	0 deg	0 deg
Azimuth, $\varphi_{L,(1,i_L)}$	Uniformly distributed 0-360 deg	Uniformly distributed 0-360 deg	Uniformly distributed 0-360 deg
Elev, $\theta_{i,L,(1,i_L)}$	~N(30,55,70 deg, (4 deg)^2)	~N(30,55,70 deg, (4 deg)^2)	~N(30,55,70 deg, (4 deg)^2)
Apex Loc., $s_{o,L,(1,i_L)}$	0.6	0.6	0.6
Moisture Cont., $m_{L,(1,i_L)}$	0.75	0.75	0.75

The radar simulations were performed using 60 realizations of the canopy, using the parameters listed in tables 6.1.3 and 6.1.4. Simulations were performed for canopies with leaves with mean elevation angles of 30, 50 and 70 degrees, as indicated by 6.1.4. Figure 6.1 shows the range-domain RCS for these three cases. The RCS waveform shows a different amplitude at each mean elevation angle of the leaves. The dependence between leaf elevation angle and RCS is discussed in section 6.2.

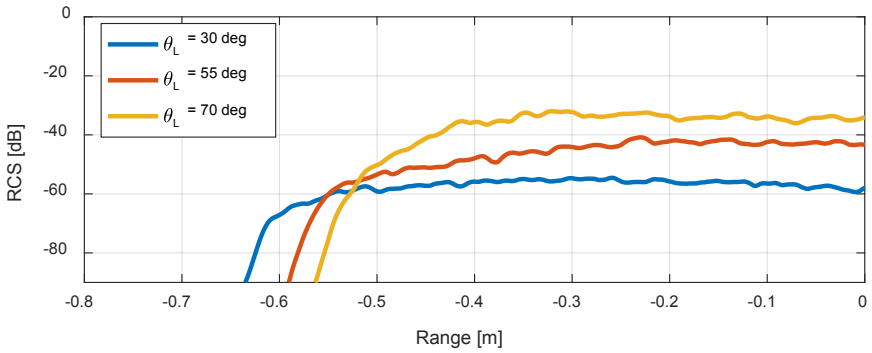

Figure 6.1.12 – Canopy Simulation (Case 1): RCS vs Range

6.1.6. Radar Simulation (Case 2): Curved Leaves (Large Final Inclination Angle)

In this second case, Monte Carlo simulations were performed for wheat canopies with curved leaves with a large final inclination angle. Large final inclination angles are inclination angles larger than 90 degrees. Simulations were performed at leaf curvatures. The stem and leaf parameters are listed in tables 6.1.5 and 6.1.6. Figures 6.1.13 and 6.1.14 show depictions of the geometric model of the wheat canopy.

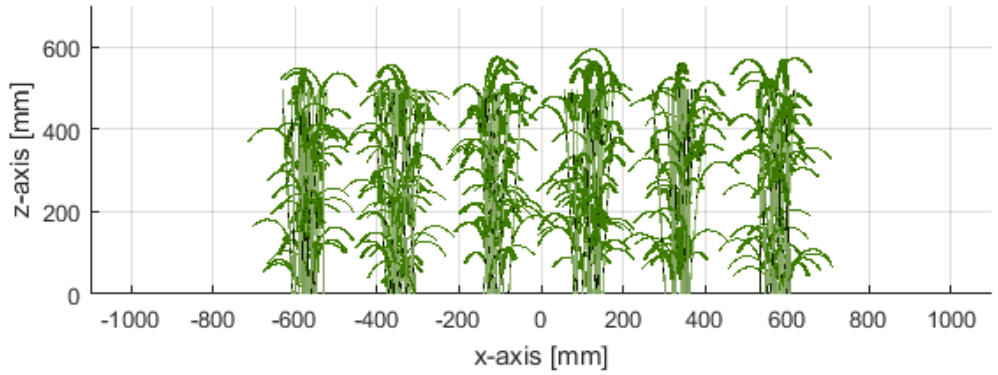

Figure 6.1.13 – Canopy (Case 2): Visualization of Geometric Model. Curved Leaves with Large Final Inclination Angle. Front View.

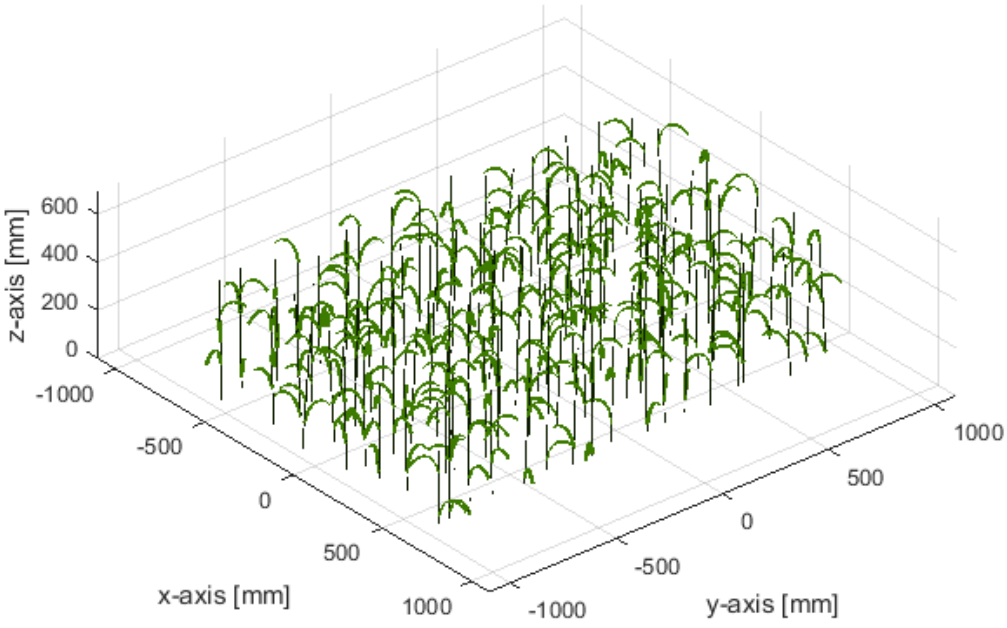

Figure 6.1.14 – Canopy (Case 2): Visualization of Geometric Model. Curved Leaves with Large Final Inclination Angle. Perspective View.

Table 6.1.5 – Canopy Simulation: List of Stem Parameters

Parameter	**Stem 1, $t_{S,(1,1)}$**
Position, $\mathrm{r}_{S,(1,i_S)}$	$\mathbf{r}_{p,(i_p)}$
Length, $L_{S,(1,i_S)}$	500 mm
Radius, $\rho_{S,(1,i_S)}$	0.75 mm
Azimuth, $\varphi_{S,(1,i_S)}$	0 deg
Elev., $\theta_{S,(1,i_S)}$	~N(0 deg, (4 deg)^2)
Moist. Cont., $m_{S,(1,i_S)}$	0.75

Table 6.1.6 – Canopy Simulation: List of Leaf Parameters

Parameter	**Leaf 1, $t_{L,(1,1)}$**	**Leaf 2, $t_{L,(1,2)}$**	**Leaf 3, $t_{L,(1,3)}$**
Position, $r_{L,(1,i_L)}$	Uniformly distributed along bottom third of stem	Uniformly distributed along center third of stem	Uniformly distributed along top third of stem
Length, $L_{L,(1,i_L)}$	~N(150 mm , (20mm)^2)	~N(150 mm , (20mm)^2)	~N(150 mm , (20mm)^2)
Width, $w_{L,(1,i_L)}$	10 mm	10 mm	10 mm
Thickness, $a_{L,(1,i_L)}$	0.2 mm	0.2 mm	0.2 mm
First-rot. $\alpha_{L,(1,i_L)}$	0 deg	0 deg	0 deg
Azimuth, $\varphi_{L,(1,i_L)}$	Uniformly distributed 0-360 deg	Uniformly distributed 0-360 deg	Uniformly distributed 0-360 deg
Initial Elev, $\theta_{i,L,(1,i_L)}$	~N(90-85 deg, (4 deg)^2)	~N(90-85 deg, (4 deg)^2)	~N(90-85 deg, (4 deg)^2)
Final Elev, $\theta_{f,L,(1,i_L)}$	~N(90+70 deg, (4 deg)^2)	~N(90+70 deg, (4 deg)^2)	~N(90+70 deg, (4 deg)^2)
Rad. of Curv., $R_{L,(1,i_L)}$	55mm	55mm	55mm
Apex Loc., $s_{o,L,(1,i_L)}$	0.6	0.6	0.6
Moisture Cont., $m_{L,(1,i_L)}$	0.75	0.75	0.75

Figure 6.1.15 shows the simulation result for the average range-domain RCS at two different curvature values. The results shows that the amplitude of the RCS is dependent on curvature. The relationship of the RCS amplitude to the leaf curvature is discussed in section 6.2.

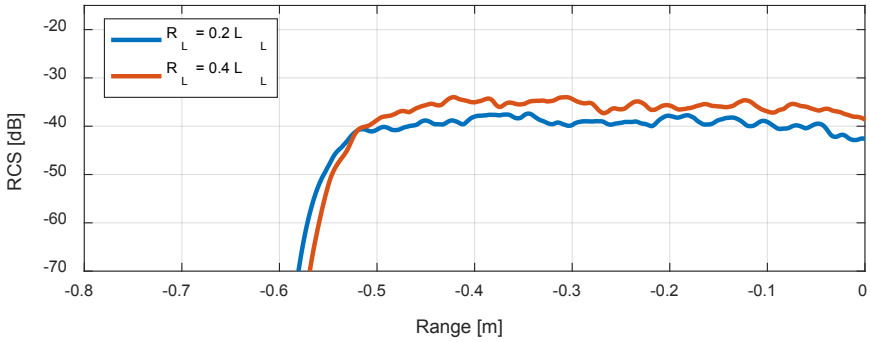

Figure 6.1.15 – Canopy Simulation (Case 2): RCS vs Range

6.1.7. Radar Simulation (Case 3): Curved Leaves (Small Final Inclination Angle)

In this case, we simulated the range-domain RCS due to a wheat canopy with leaves with small final inclination angle. Small final inclination angles are inclination angles that are less than 90 degrees. The stem and leaf parameters used are listed in tables 6.1.7 and 6.1.8, respectively. Figure 6.1.16 and 6.1.17 show the front and perspective view of the geometric model of a single realization of the canopy.

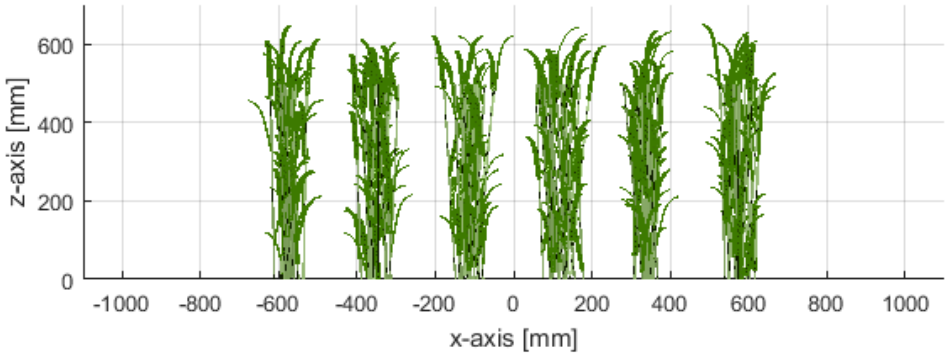

Figure 6.1.16 – Canopy (Case 3): Visualization of Geometric Model. Curved Leaves with Large Final Inclination Angle. Front View.

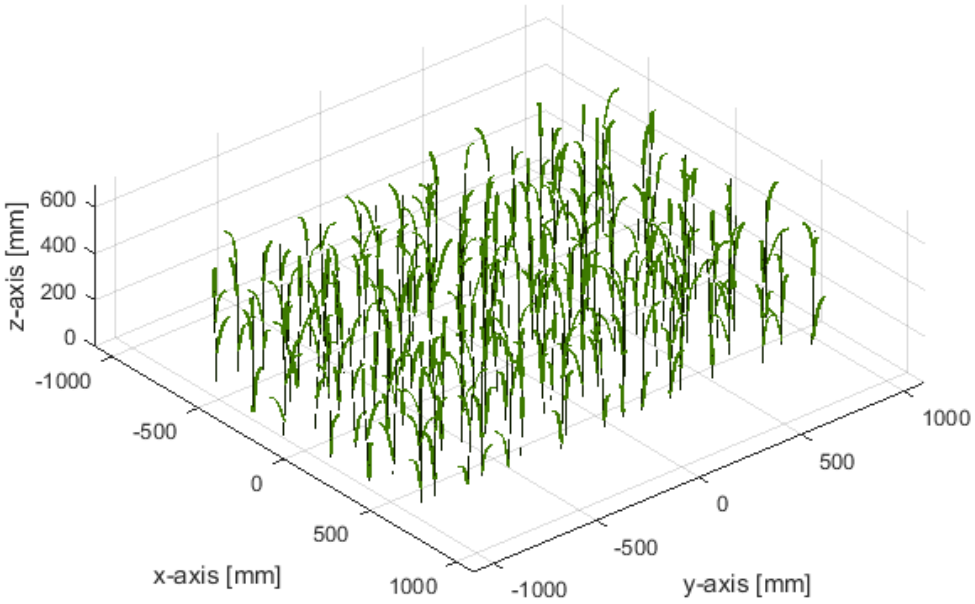

Figure 6.1.17 – Canopy (Case 3): Visualization of Geometric Model. Curved Leaves with Large Final Inclination Angle. Front View.

Table 6.1.7 – Canopy Simulation: List of Stem Parameters

Parameter	**Stem 1, $t_{S,(1,1)}$**
Position, $\mathrm{r}_{S,(1,i_S)}$	$\mathbf{r}_{p,(i_p)}$
Length, $L_{S,(1,i_S)}$	500 mm
Radius, $\rho_{S,(1,i_S)}$	0.75 mm
Azimuth, $\varphi_{S,(1,i_S)}$	Uniformly Dist.
Elev., $\theta_{S,(1,i_S)}$	~N(0 deg, (4 deg)^2)
Moist. Cont., $m_{S,(1,i_S)}$	0.75

Table 6.1.8 – Canopy Simulation: List of Leaf Parameters

Parameter	**Leaf 1, $t_{L,(1,1)}$**	**Leaf 2, $t_{L,(1,2)}$**	**Leaf 3, $t_{L,(1,3)}$**
Position, $r_{L,(1,i_L)}$	Uniformly distributed along bottom third of stem	Uniformly distributed along center third of stem	Uniformly distributed along top third of stem
Length, $L_{L,(1,i_L)}$	~N(150 mm , (20mm)^2)	~N(150 mm , (20mm)^2)	~N(150 mm , (20mm)^2)
Width, $w_{L,(1,i_L)}$	10 mm	10 mm	10 mm
Thickness, $a_{L,(1,i_L)}$	0.2 mm	0.2 mm	0.2 mm
First-rot. $\alpha_{L,(1,i_L)}$	0 deg	0 deg	0 deg
Azimuth, $\varphi_{L,(1,i_L)}$	Uniformly distributed 0-360 deg	Uniformly distributed 0-360 deg	Uniformly distributed 0-360 deg
Initial Elev, $\theta_{i,L,(1,i_L)}$	~N(90-85 deg, (4 deg)^2)	~N(90-85 deg, (4 deg)^2)	~N(90-85 deg, (4 deg)^2)
Final Elev, $\theta_{f,L,(1,i_L)}$	~N(90+0 deg, (4 deg)^2)	~N(90+0 deg, (4 deg)^2)	~N(90+0 deg, (4 deg)^2)
Rad. of Curv., $R_{L,(1,i_L)}$	55mm	55mm	55mm
Apex Loc., $s_{o,L,(1,i_L)}$	0.6	0.6	0.6
Moisture Cont., $m_{L,(1,i_L)}$	0.75	0.75	0.75

Figure 6.1.18 shows the simulation result for the average range-domain RCS for case 3. The simulation was performed for different values of the parameter $s_{o,L}$ that defines the location of the maximum curvature (apex) along the leaf.

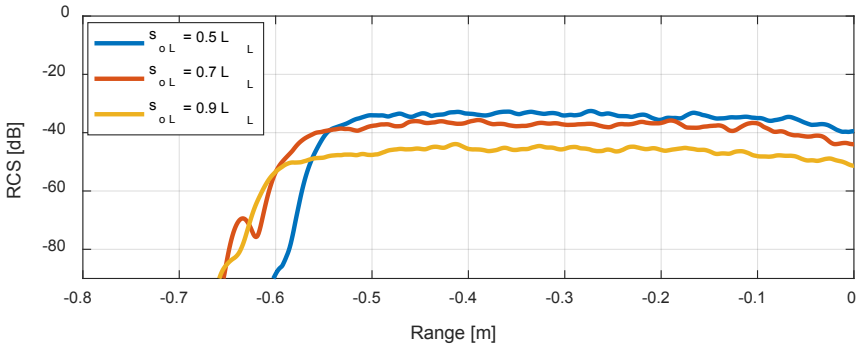

Figure 6.1.18 – Canopy (Case 3): RCS vs Range.

6.2. Canopy Simulations: Simplified Model and Parameter Retrieval

6.2.1. Relationship of Amplitude of RCS to Canopy Parameters

In this section, relationships are found for the amplitude of the RCS waveform to canopy parameters. Only the relationship of leaf parameters to their RCS contributions is considered. This section does not consider propagation losses, since these depend on the depth of the signal into the canopy. Therefore, propagation losses should be taken into account separately, if these relationships are used.

In this section, relationships were found for the amplitude of the range-domain RCS to the plant density, leaf vertical density per plant, leaf volumetric density, leaf thickness, leaf width, leaf water content, leaf minimum radius of curvature, and the projected length of the leaf. The projected length of the leaf is defined below.

For each parameter, these relationships were found by performing Monte Carlo radar simulations of at least 60 realizations. These type of Monte Carlo radar simulations (60 realizations) was repeated for various values of the canopy parameter considered. For instance, the relationship of the plant density to the amplitude of the RCS was found using 11 values of the plant density. In this case, 11x60 radar simulations were performed for wheat canopies.

The number of primitives used for each leaf is 10, which is sufficient to model geometrically typical leaf curvatures and typical leaf lengths of adult plants. The time it takes to compute the RCS waveform for a single leaf primitive, at 64 different frequencies, using an Intel Xeon Central Processing Unit (CPU) with a clock rate of 3.1 GHz, is about 0.05 s. Therefore, computing a canopy with plant density of 40 plants/m^2, an area of 2x1.4 m^2, composed of plants with 3 leaves each, takes 168 seconds. A Monte Carlo simulation consisting of 60 realizations, thus,

takes about 2.8 hours. If the Monte Carlo simulation is computed for 5 different canopy parameters, the simulation time is about 14 hours. In order to improve this simulation time, the simulations are processed in parallel using a 16-core processor, where each realization is processed separately. Since the server with the 16-core processor is a shared machine, we only see an improvement of a factor of about 4.5 to 7. The total time of a set of Monte Carlo radar simulations over 5 different canopy parameters takes about 2 to 3 hours.

Moreover, the set of Monte Carlo simulations were performed for different kinds of leaves to verify that the relationships found are independent of other parameters.

Plant Density

Figure 6.2.1 shows the results from the set of Monte Carlo radar simulations over different values of the plant density. The plot in this figure is given as the average RCS of the canopy with respect to the RCS at a given plant density (40 plants/m^2). The blue curve shows the simulation results and the red stars represent the approximated model. The approximated model relationship between the amplitude of the RCS and the plant density is given by (6.2.1). The RCS is proportional to the plant density, when propagation loss is ignored.

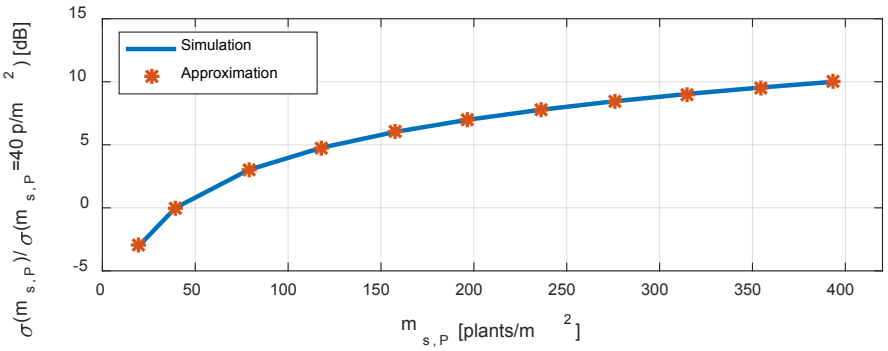

Figure 6.2.1 – RCS vs Plant Density

$$\sigma(m_{s,p}) \propto m_{s,p} \tag{6.2.1}$$

Vertical Leaf Density per Plant

Figure 6.2.2 shows the results for the set of Monte Carlo radar simulations at different vertical leaf densities per plant. The vertical leaf density per plant was modified by changing the number of leaves per plant. The resulting relationship between the amplitude of the RCS and this parameter is given by (6.2.2). The amplitude of the RCS is proportional to the vertical leaf density per plant, when the loss is ignored.

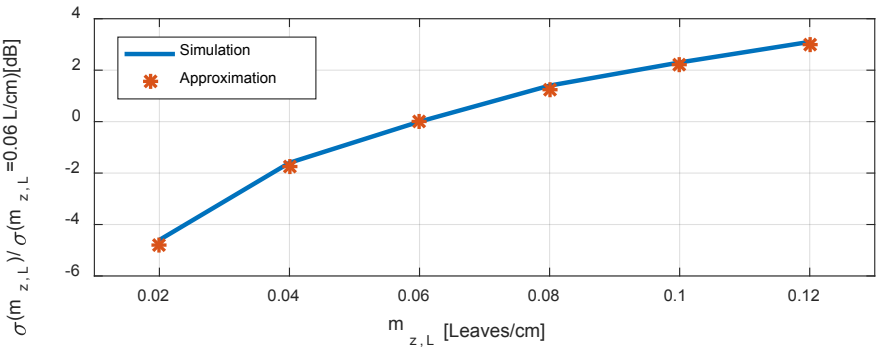

Figure 6.2.2 – RCS vs Vertical Leaf Density per Plant

$$\sigma(m_{z,L}) \propto m_{z,L} \tag{6.2.2}$$

Volumetric Leaf Density

Combining the two previous cases, we find the curve that relates the amplitude of the RCS to the volumetric leaf density. The resulting simulation and approximated curves are shown in figure 6.2.3. Similar to the previous cases, the amplitude of the RCS is proportional to the volumetric leaf density, when loss is ignored.

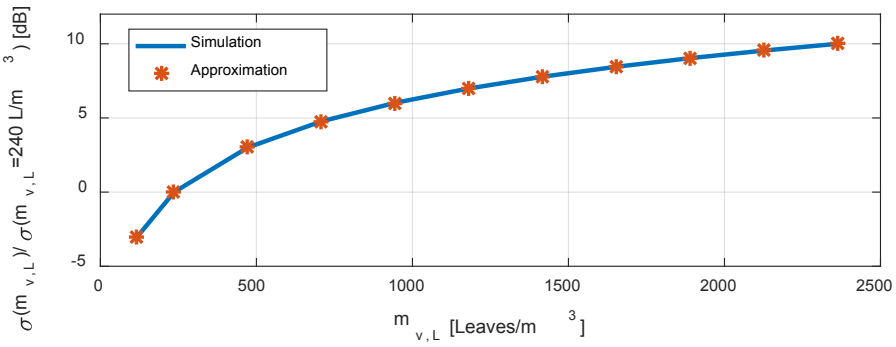

Figure 6.2.3 – RCS vs Volumetric Leaf Density:

$$\sigma(m_{v,L}) \propto m_{v,L} \tag{6.2.3}$$

Leaf Thickness

Figure 6.2.4 shows the result of a set of Monte Carlo radar simulations over different leaf thickness values. The blue curve shows the simulation output and the red stars represents an approximated model of the relationship between the amplitude of the RCS and the leaf thickness. This approximated model is given by (6.2.4). The approximated model indicates that the RCS is proportional to the square of the leaf thickness, when propagation losses are ignored.

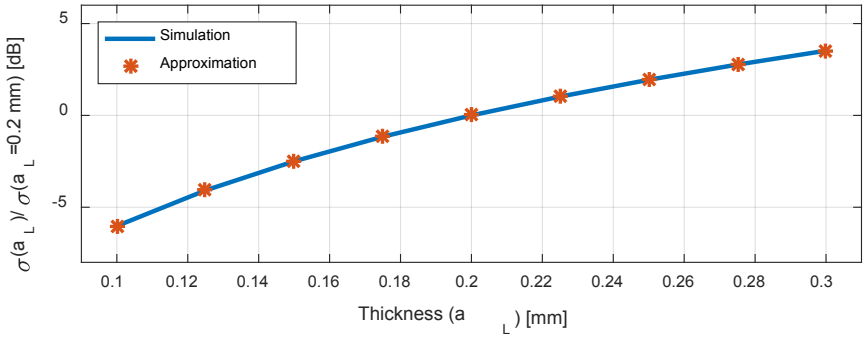

Figure 6.2.4 – Canopy Simulation: Average RCS vs Thickness

$$\sigma(t_L) \propto {a_L}^2 \tag{6.2.4}$$

Leaf Width

Figure 6.2.5 shows the result of a set of Monte Carlo radar simulations over different leaf width values. The blue curve shows the simulation output and the red stars represents an approximated model of the relationship between the amplitude of the RCS and the leaf width. This approximated model is given by (6.2.5). The approximated model indicates that the RCS is proportional to the 1.7 power of the leaf width, when propagation losses are ignored.

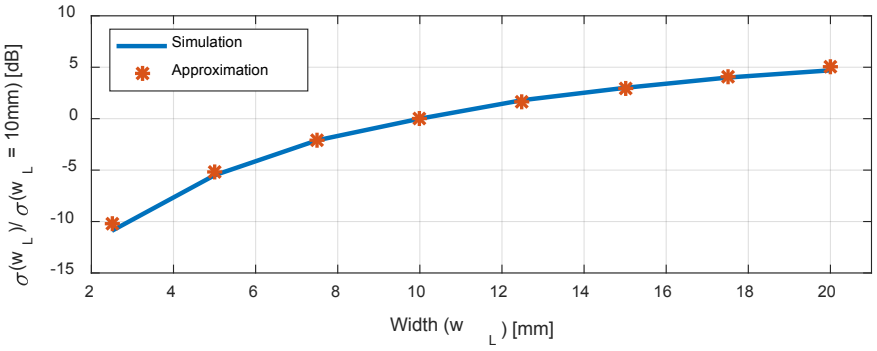

Figure 6.2.5 – Canopy Simulation: Average RCS vs Width (w_L)

$$\sigma(w_L) \propto {w_L}^{1.7} \tag{6.2.5}$$

Leaf Moisture Content

Figure 6.2.6 shows the result of a set of Monte Carlo radar simulations over different values of the leaf moisture content. The blue curve shows the simulation output and the red stars represents an approximated model of the relationship between the amplitude of the RCS and the leaf moisture content. This approximated model is given by (6.2.6). The approximated model indicates that the RCS is proportional to $\left(m_g - 0.19\right)^2$, when propagation losses are ignored.

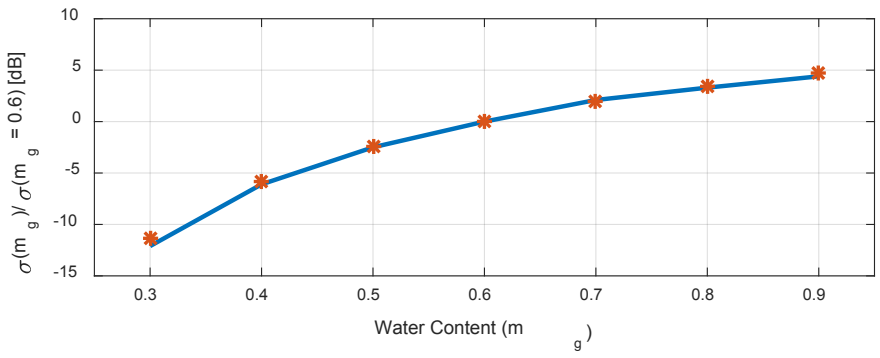

Figure 6.2.6 – Canopy Simulation: Average RCS vs Moisture Content (m_g)

$$\sigma(m_g) \propto \left(m_g - 0.19\right)^2 \tag{6.2.6}$$

Radius of Curvature

A similar procedure was applied to find a relationship between the RCS amplitude and the (minimum) radius of curvature of the leaf. We found that this relationship is only consistent when the initial elevation angle is less than 45 degrees, the final elevation angle is greater than 135 degrees and the apex location parameter $s_{o,L}$ is less than $0.8L_L$. Figure 6.2.7 shows the result of the simulation and the approximated model with a blue curve and red stars, respectively. The relationship between the amplitude of the RCS and the (minimum) radius of curvature of the leaf is given by (6.2.7). This expression indicates that the amplitude of the RCS is proportional to the (minimum) radius of curvature of the leaf, when the propagation losses are ignored. This relationship is only valid over the range of parameters indicated earlier, which are also specified in (6.2.7).

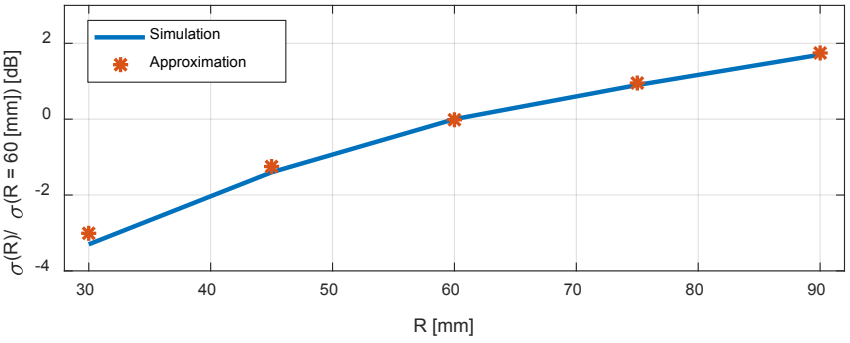

Figure 6.2.7 – Canopy Simulation: Average RCS vs Leaf Radius of Curvature (R_L)

$$\sigma(R_L) \propto R_L \qquad \text{for} \quad s_{o,L} \leq 0.8L_L \; ; \theta_{i,L} < 45 \text{ deg} \; ; \theta_{f,L} > 135 \text{ deg} \qquad (6.2.7)$$

Projected Leaf Area

The previous relationship between the RCS and the minimum radius of curvature was restricted to curved leaves with parameters within those specified in (6.2.7). This restriction limits this relationship to curved leaves that have a large final elevation angles. It does not take into account leaves with small final elevation angles.

The total projected length of the leaf area is the length of the projection of a leaf to a horizontal plane. Furthermore, we restrict the definition of the projected leaf length to those related to the sections of the leaf that form angles less than 40 degrees with the horizontal plane. Figure 6.2.8 shows the result of the set of Monte Carlo simulations for different values of the projected leaf length. The relationship between the amplitude of the RCS and the projected leaf length is given by (6.2.8). This same relationship was found for leaves with large final elevation angles (>90 degrees) and small elevation angles (<90 degrees). This same relationship was also found

for different values of the apex location parameter. Therefore, this expression is more general than the relationship of the RCS to the minimum radius of curvature.

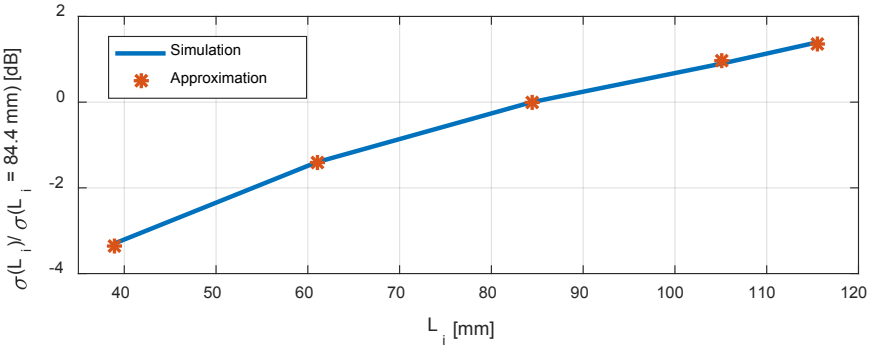

Figure 6.2.8 – Canopy Simulation: Average RCS vs Projected Leaf Length ($L_{i,L}$)

$$\sigma(L_{i,L}) \propto L_{i,L} \qquad \text{for} \quad \theta_{Q,i_Q} < |90 - 40| \text{ deg} \tag{6.2.8}$$

Leaf Elevation Angle of Straight Leaves

Figure 6.2.9 and 6.2.10 show the result of the set of Monte Carlo radar simulations for different values of leaf elevation angle of straight leaves. Figure 6.2.9 shows curves for simulations at different leaf lengths. Figure 6.2.10 shows curves for simulations at different values of the leaf thickness. These plots show that the amplitude of the RCS is dependent to leaf length only for large (~ >50 degrees) elevation angles. The leaf thickness affects the amplitude of the RCS at any elevation angle. The relationship between the RCS amplitude and the leaf thickness was given earlier in (6.2.4).

The RCS of straight leaves with small elevation angles is orders of magnitude smaller than that of curved leaves or leaves with large elevation angles. This includes curved leaves with small final elevation angles. Moreover, it is highly unlikely for all leaves in a canopy to be fully straight and have small elevation angles. Therefore, the contribution from curved leaves and leaves with large elevation angles dominate the radar return. The relationship of the amplitude of the RCS and the projected leaf angle (6.2.8) can be used as a rough approximation of the relationship between the RCS and the leaf elevation angle of straight leaves. The relationship in (6.2.8) is restricted elevation angles greater than 50 degrees.

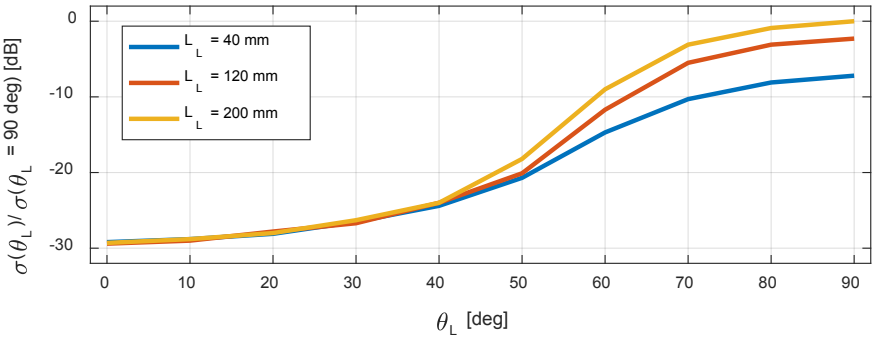

Figure 6.2.9 – Canopy Simulation: Average RCS vs Leaf Inclination Angle. Leaf Length 40 mm. 120 mm and 200 mm.

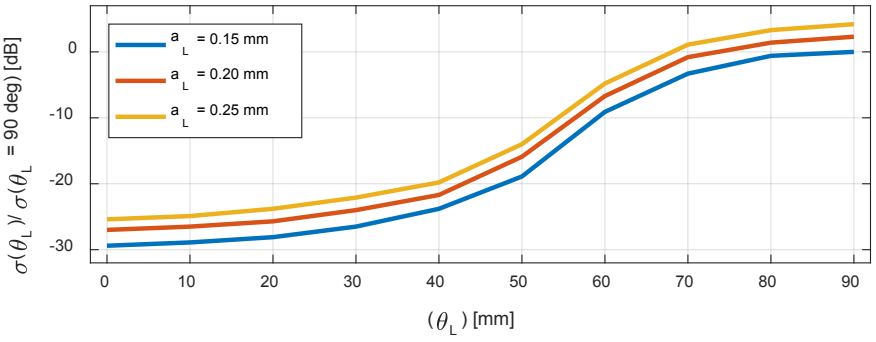

Figure 6.2.10 – Canopy Simulation: Average RCS vs Leaf Inclination Angle. Leaf Thickness 0.15 mm. 0.20 mm and 0.25 mm.

6.2.2. Simplified RCS Model for Wheat Canopy

Combining the expressions found in the previous section for the relationships between the amplitude of the RCS and the canopy parameters results in (6.2.9). Using a reference RCS $\sigma(w_{Lo}, L_{i,Lo}, a_{Lo}, m_{g,Lo}, m_{v,Lo})$ for known canopy parameters, expression (6.2.9) may be re-written as (6.2.10).

$$\sigma(w_L, L_{i,L}, a_L, m_{g,L}, m_{v,L}) \propto m_{v,L}\, L_{L,i}\, {w_L}^{1.7}\, {a_L}^2 \left(m_{g,L} - 0.19\right)^2 \tag{6.2.9}$$

$$\frac{\sigma(w_L, L_{i,L}, a_L, m_{g,L}, m_{v,L})}{\sigma(w_{Lo}, L_{i,Lo}, a_{Lo}, m_{g,Lo}, m_{v,Lo})} = \left(\frac{w_L}{w_{Lo}}\right)^{1.7} \left(\frac{L_{i,L}}{L_{i,Lo}}\right)^1 \left(\frac{a_L}{a_{Lo}}\right)^2 \left(\frac{m_{g,L} - 0.19}{m_{g,Lo} - 0.19}\right)^2 \left(\frac{m_{v,L}}{m_{v,Lo}}\right)^1 \tag{6.2.10}$$

An example of a set of parameters that may be used as a reference are listed in table 6.2.1. If the reference parameters in table 6.2.1 are used with the model of equation (6.2.10), the canopy

parameters used should have the same units as the reference parameters. Moreover, the RCS should be used with linear units (m^2), instead of [dB].

Table 6.2.1 – Reference Canopy Parameters for Approximated Model

Parameter	Value
Reference RCS: $\sigma(w_{Lo}, L_{i,Lo}, a_{Lo}, m_{g,Lo}, m_{v,Lo})$	-35.3 dB
Leaf Width, w_{Lo}	10 mm
Leaf Projected Leaf Length, $L_{i,Lo}$	84.4 mm
Leaf Thickness, a_{Lo}	0.2 mm
Leaf Water Content, $m_{g,Lo}$	0.75 mm
Leaf Volumetric Density, $m_{v,Lo}$	240 leaves/m^3

6.2.3. Retrieval of Canopy Height from RCS Waveform

The canopy height is defined as the average height of the plants of the canopy. The height of a plant is defined as the shortest distance between the ground, where it is rooted, and the highest vegetation point. In a wheat plant, the highest vegetation point may be located at the wheat head or the wheat leaf.

Using the radar simulator, we found an expression to retrieve the height of the wheat canopy from the range-domain RCS. This expression is shown in (6.2.11). In (6.2.11), the terms z_{12} and z_{1m} are defined below.

$$h_{L,P} = -\left[z_{12} + (z_{1m} - z_{12})\, 1.62^{(0.6+0.02/|z_{1m}-z_{12}|)}\right] \tag{6.2.11}$$

Consider the range-domain RCS waveform $\sigma(R)$, where R is the relative-range of the target. This waveform is approximated to the RCS profile $\sigma(z)$, where z is the z-component relative to the scattering center (i.e. the origin). We define $I_\sigma(z)$ in (6.2.12) as the integral of $\sigma(z)$. As expressed by (6.2.13), the term z_{12} is the vertical position at which the integral $I_\sigma(z)$ reaches one third of $I_\sigma(0)$. This vertical position z_{12} corresponds roughly to the limit between the top leaf layer and the second leaf layer.

$$I_\sigma(z) = \int_{-\infty}^{z} \sigma(z')\ dz' \tag{6.2.12}$$

$$I_\sigma(z_{12})/I_\sigma(0) = 1/3 \tag{6.2.13}$$

The vertical position z_{1m} is the weighted average of the RCS within the top layer.

$$z_{1m} = \frac{\int_{-\infty}^{z_1} z'\sigma(z')dz'}{I_\sigma(0)} \tag{6.2.14}$$

The expression in 6.2.11 was tested for a wide range of canopy parameters. Below we show two distinct cases of wheat canopies: wheat canopies with leaves with large final elevation

angles and small final elevation angles. Figure 6.2.11 shows a comparison of the simulated (actual) heights vs the heights approximated (retrieved) with the expression (6.2.11). The comparison of the actual and retrieved heights are shown for five different stem lengths. Figure 6.2.12 shows the same type of plot for a canopy with leaves with small final elevation angles. These plots show the good agreement between the actual heights and the retrieved heights, using expression (6.2.11).

We note that the simulated (actual) heights are found by averaging the maximum z-component of all the geometrically modeled plants in a canopy.

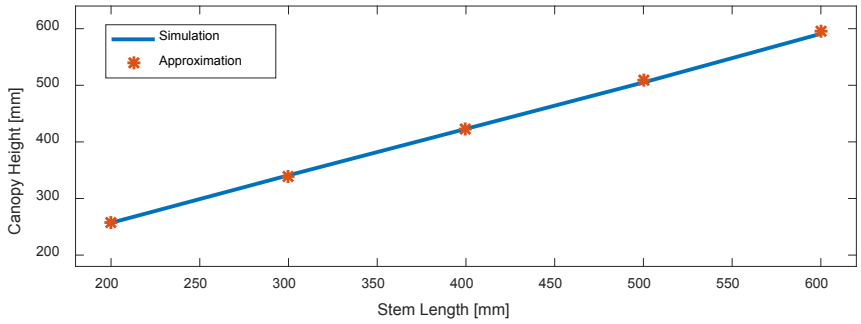

Figure 6.2.11 – Simulated (Actual) Height vs Approximated (Retrieved) Height. Canopy with Curved Leaves with Large Final Elevation Angle

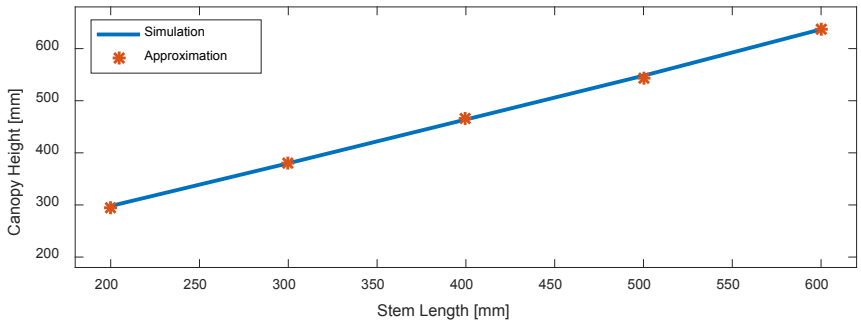

Figure 6.2.12 – Simulated (Actual) Height vs Approximated (Retrieved) Height. Canopy with Straight Leaves with Small Final Elevation Angles

6.2.4. Retrieval of Canopy Projected Leaf Area Density from RCS Waveform

Expression (6.2.10), which approximates the RCS amplitude for a given set of canopy parameters, can be arranged to obtain equation (6.2.15). This expression (6.2.15) can be used to retrieve the product $L_{i,L}\ m_{v,L}$ from a RCS waveform and a given set of canopy parameters.

$$L_{i,L}\ m_{v,L} = L_{i,Lo}\ m_{v,Lo}\ \frac{\sigma(w_L, L_{i,L}, a_L, m_{g,L}, m_{v,L})}{\sigma(w_{Lo}, L_{i,Lo}, a_{Lo}, m_{g,Lo}, m_{v,Lo})}\left(\frac{w_{Lo}}{w_L}\right)^{1.7}\left(\frac{a_{Lo}}{a_L}\right)^{2}\left(\frac{m_{g,Lo}-0.19}{m_{g,L}-0.19}\right)^{2} \tag{6.2.15}$$

The expression (6.2.15) can be re-written as shown in (6.2.16). The equation (6.2.16) can be used to retrieve the product $A_{i,L}m_{v,L}$, if the width does not vary significantly. The term $A_{i,L}$ is the projected leaf area and it is given by (6.2.17) in terms of the projected leaf length and the leaf width.

$$A_{i,L} m_{v,L} = w_L \, L_{i,Lo} \, m_{v,Lo} \, \frac{\sigma(w_L, L_{i,L}, a_L, m_{g,L}, m_{v,L})}{\sigma(w_{Lo}, L_{i,Lo}, a_{Lo}, m_{g,Lo}, m_{v,Lo})} \left(\frac{w_{Lo}}{w_L}\right)^{1.7} \left(\frac{a_{Lo}}{a_L}\right)^2 \left(\frac{m_{g,Lo} - 0.19}{m_{g,L} - 0.19}\right)^2 \quad (6.2.16)$$

$$A_{i,L} = w_L \, L_{i,L} \quad (6.2.17)$$

The product $A_{i,L} m_{v,L}$ expressed by (6.2.16) can also be defined as the Projected Leaf Area Density, as it is equal to the volumetric density of the total projected leaf area $A_{i,T,L}$, where the total projected leaf area is the product of the number of leaves times the projected leaf area of one leaf. If the projected leaf area density is multiplied by the canopy height, we obtain the ratio of the total projected leaf area and the total ground area (6.2.19). This ratio is also known as the projected leaf area index (PLAI).

$$A_{i,L} m_{v,L} h_{P,L} = \frac{A_{i,T,L}}{A_{T,G}} = PLAI \quad (6.2.19)$$

Since the projected leaf area density ($A_{i,L} m_{v,L}$) is the vertical density of the projected leaf area index (PLAI), we also use the term $PLAIz(z)$ to refer to the projected leaf area density. The PLAI over a given vegetation layer may be found by multiplying PLAIz with the layer height.

$$A_{i,L} m_{v,L} = PLAIz(z) \quad (6.2.18)$$

6.3. Field Experiment

6.3.1. Radar Measurements: Data Collection

Radar measurements were taken of 315 wheat canopy plots in nadir mode using the radar system described in chapter 5. The wheat canopy plots measured are part of a Kansas State University (KSU) wheat-breeding program. The wheat plots are located at the Tom Pauli Seed fields in Conway Springs, KS. The geographical location of the wheat field is 37.458046 N, 97.62759 W. The measurements were collected on five different dates: 4/16/2018, 5/7/2018, 5/22/2018, 6/6/2018 and 6/16/2018.

The wheat plots are arranged in 21 rows and there are 15 plots per row. Figure 6.3.1 shows a map of the plots. The horizontal dimension of each plot is 1.4x4.0 meters. Each plots is arranged in 6 rows of plants. Each row of plants is spaced by 9 inches from each other.

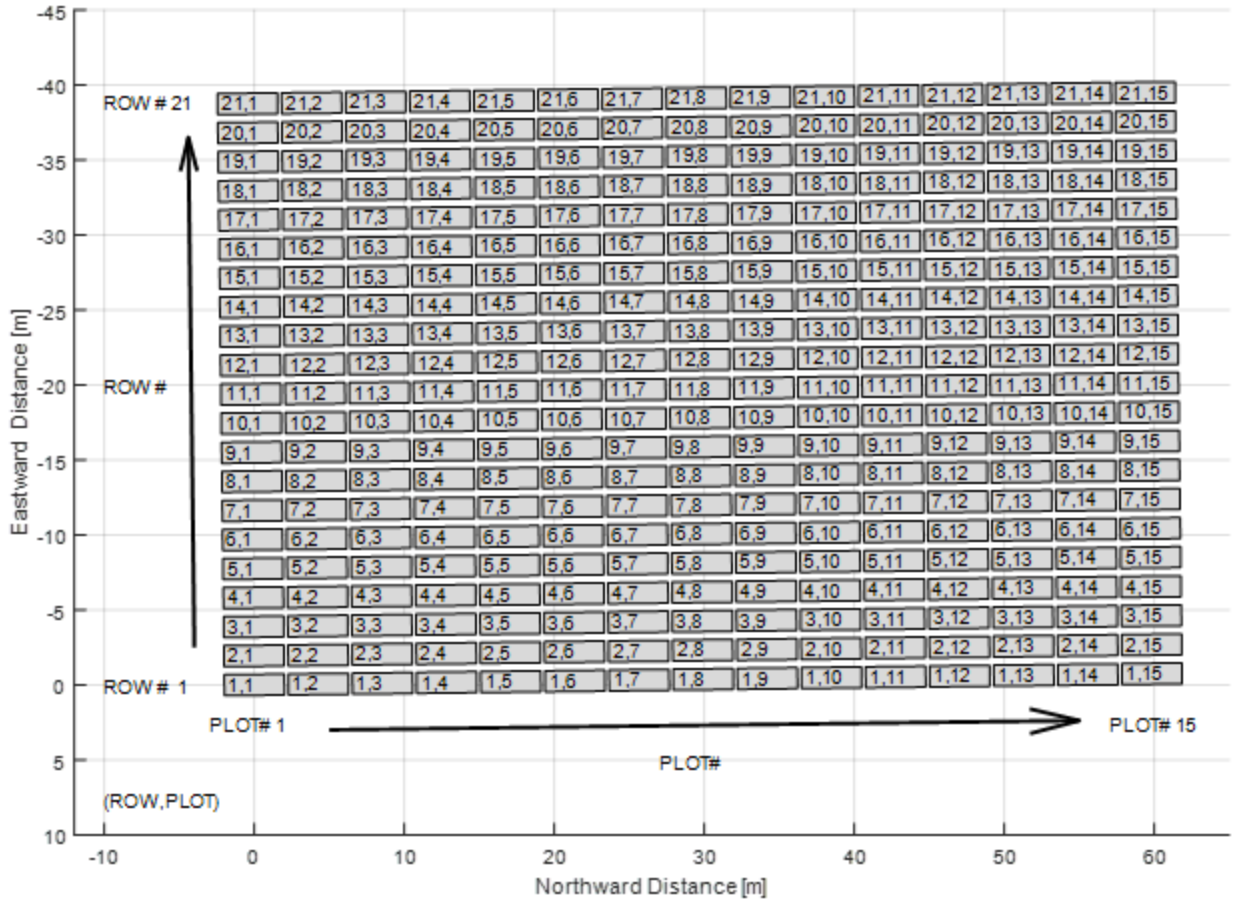

Figure 6.3.1 – Map of Measured Wheat Plots

Before taking radar measurements of the wheat plots, radar measurements are taken of calibration targets. These radar measurements are used to obtain the antenna response, as described in section 5.8.2. The frequency response of the antenna and the rest of the radar sub-systems is used to resolve the frequency-domain RCS during the Level 0 stage of digital signal processing.

After measuring the calibration targets, the radar-mounted cart is transported to the wheat field. A photograph of the radar-mounted cart is shown in figure 5.4.3 in chapter 5. The cart is pushed from one end of each row to the other. The cart was pushed at a rate of one plot length per 8

seconds or 0.5 m/s, approximately. The radar collects measurements at a rate of 500 waveforms per second. This means that about 4000 radar measurements are collected per wheat plot. The data acquisition system stores the radar measurements in 16,000 samples of 16 bits. Thus, it takes about 32,000x4000 B or 122 MB to store the radar measurements of a single plot. The storage size required for 21 rows of 15 plots each amounts to about 38 GB. Table 6.3.1 lists the storage volume collected from radar measurements. These quantities of storage volume accounts for the measurements of the 15 plots of 21 rows, the measurements between plots (gaps) and the repeated measurements.

Table 6.3.1 – Total Data volume collected from radar measurements

Date	**Storage Volume**
5/7/2018	57 GB
5/22/2018	51 GB
6/6/2018	52 GB
6/16/2018	35 GB

After the radar measurements were completed, plant samples were collected from some of the plots. The physical properties relevant to the scattering simulations were measured for each plant collected. A summary of the measurements of the samples is given in section 6.3.3. The values of the measured parameters of the plant samples are given in appendix G.

The radar measurements collected were copied from the radar storage device to a server at the University of Kansas. The stored radar measurements were processed to retrieve the parameters of interest. The processing steps are listed in the section 6.3.2.

6.3.2. Radar Measurements: Digital Signal Processing

6.3.2.1. Level 0: Calibration and Artifact Removal

The objectives of the Level 0 processing stage are to reduce the unnecessary samples, apply radiometric calibration to obtain the RCS waveform in the frequency-domain and remove coherent noise.

Reduce Unnecessary Samples

The measurements are sampled at a sampling rate of 62.5 MHz. The bandwidth of the target's signal and most of the interference signals is less than 5 MHz. This means that the measurement has unnecessary samples. In order to remove the unnecessary samples, the signal is digitally down converted by -1.8531 MHz, low-pass-filtered and decimated by a factor of 16 and. The low-pass-filter step is used to avoid aliasing noise that is out of the band of interest during the decimation step.

Figure 6.3.2 shows the recorded signal in PSD representation. The largest peak (first peak from left to right) correspond to the antenna feed-through. The second largest peak correspond to the ground clutter and canopy targets.

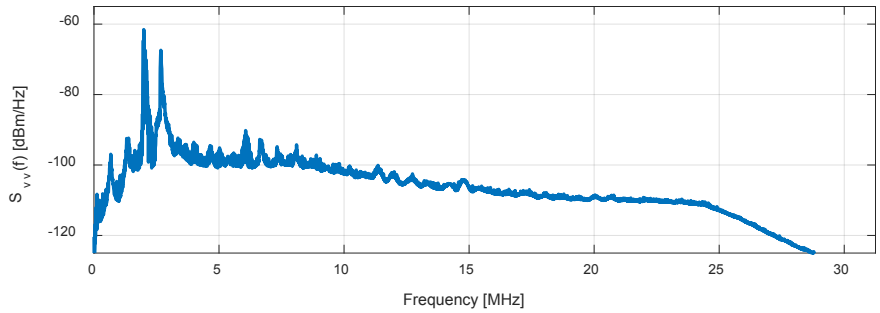

Figure 6.3.2 – PSD of radar output (Incoherent average of a section of row 2)

Figure 6.3.3 shows the PSD representation of the down-converted and decimated signal. The first peak corresponds to the antenna feedthrough. The signal on the right corresponds to the ground and canopy targets.

By removing the unnecessary samples, all the subsequent signal-processing steps are applied to fewer samples, reducing the computation complexity.

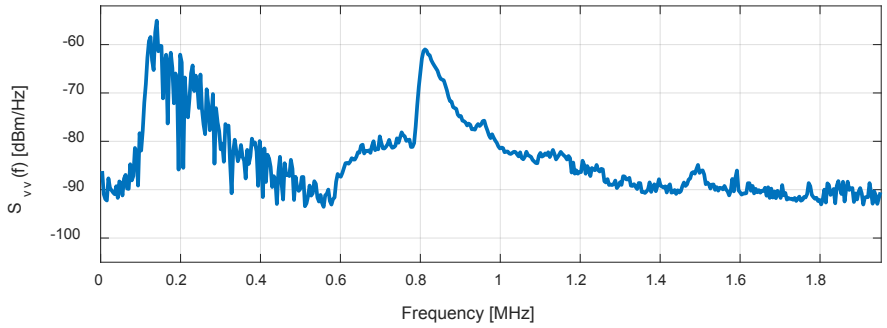

Figure 6.3.3 – PSD of signal after DDC, Filtering and Decimation. (Incoherent average of a section of row 2)

Radar Calibration

The radar calibration step converts the signal from received voltage to the equivalent scattering response in the frequency and time domains. This process is based on the coherent radar equation. It removes the effects due to signal propagation to and from the target, the antenna frequency response and the radar-system frequency response. This coherent process results in the incoherent radiometric calibration and the deconvolution of the signal.

Figure 6.3.4 shows the output of the radar calibration step for the signal shown in figure 6.3.3. This output shows the range-domain RCS waveform, showing the RCS-equivalent antenna feed-through (left) and the range-domain RCS of the ground/canopy target (right).

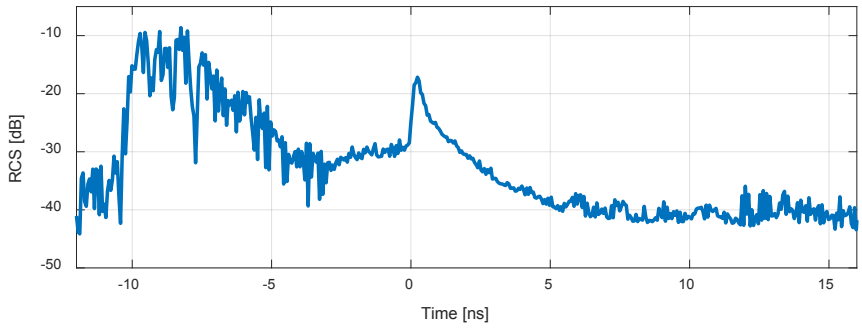

Figure 6.3.4 – Time-domain RCS after deconvolution. (Average of a section of row 2)

Coherent Noise Removal

As mentioned in the chapter 5, the output of the radar contains coherent noise. Additionally, the output of the radar also includes the antenna feedthrough. Both the antenna-feedthrough interference signal and the coherent noise are constant or slow changing from one measurement to the next. The coherent noise and the antenna feedthrough signal are removed by applying a high-pass filter in the slow time.

Figure 6.3.5 shows the output of the coherent-noise removal step for the signal shown in figure 6.3.4. Figure 6.3.5 lacks the antenna feed-through signal, which was present in figure 6.3.4. The remaining signal in figure 6.3.5 is the range-domain RCS waveform due to the ground and canopy.

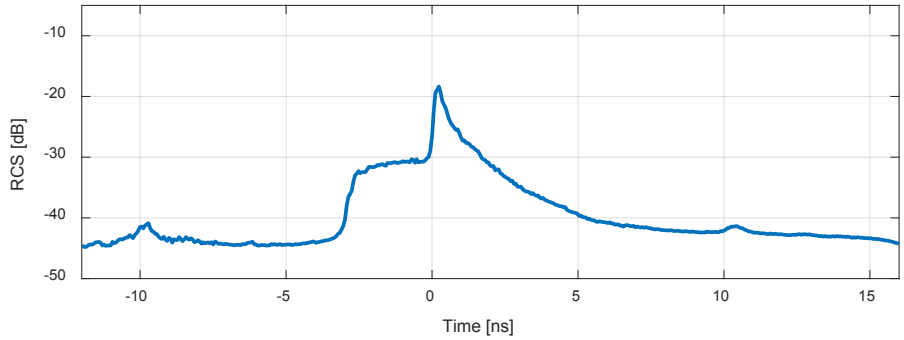

Figure 6.3.5 – Time-domain RCS after Coherent Noise Removal. (Average of a section of row 2)

6.3.2.2. Level 1: Time/Range and Frequency Domain Waveforms

In this step, the measurements are segmented into separate those corresponding to separate plots. Additionally, the ground and canopy contributions to the RCS waveforms are separated.

Before separating the measurements into different plots, the measurements are resampled so that the separation among adjacent measurements in the northing direction is constant. Once this resampling is finished, the measurements corresponding to different plots are separated using the GPS coordinates of the plots.

Once the measurements are separated into different plots, the contributions to the canopy and ground are separated in the time-domain RCS waveform, using time-domain gating. The frequency-domain RCS corresponding to the canopy and ground are found applying the Fourier transform to the time-domain scattering response.

In this step, the signal is also run through a moving weighted average using a Hanning taper of length 16. This averaging is applied coherently to improve the SNR by 8 dB, without modifying the shape of the waveform significantly.

Figure 6.3.6 shows the average range-domain RCS waveform for the wheat plot 1 of row 20, including canopy and ground contributions.

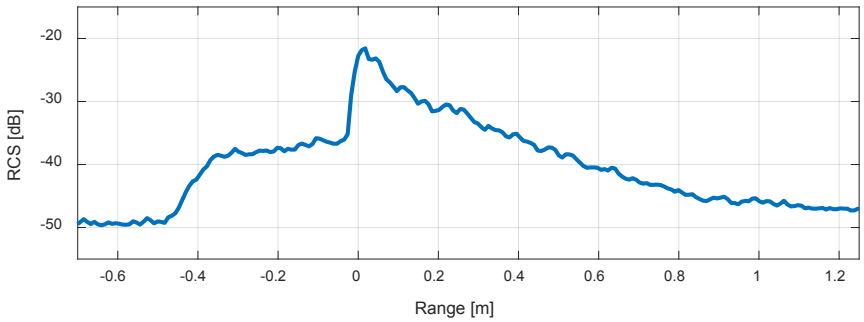

Figure 6.3.6 – Range-domain RCS of canopy and ground. (Average of Row 20; Plot 1)

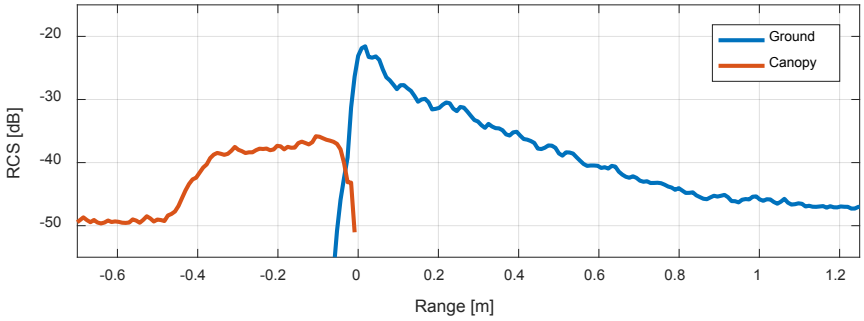

Figure 6.3.7 – Range-domain RCS of canopy and ground separately. (Average of Row 20; Plot 1)

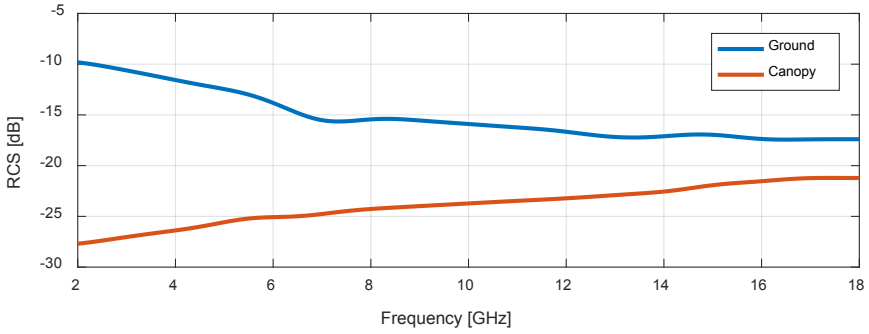

Figure 6.3.8 – Frequency-domain RCS of canopy and ground separately. (Average of Row 20; Plot 1)

Figure 6.3.7 shows the average range-domain RCS waveforms due to the ground and canopy of the wheat plot 1 of row 20, separately.

Figure 6.3.8 shows the average frequency-domain RCS due to the canopy and ground for plot 1 of row 20.

6.3.2.3. Level 2: Biophysical Parameter Retrieval

This processing step using the procedures described in section 6.2 to retrieve the canopy height and the projected leaf area density from the range-domain RCS waveforms of each wheat plot.

Height: $h_{p,L}$

Using the procedure described in section 6.2.3, the height of the canopy is retrieved from the average range-domain RCS waveforms of each canopy plot. Figure 6.3.9 shows the range-domain RCS waveform for plot 1 of row 20. A red line is used in figure 6.3.9 to indicate the range related to the retrieved height. The retrieved height of this canopy 0.41 m.

The results of the retrieved heights for all the plots measured are given graphically in section 6.3.4.

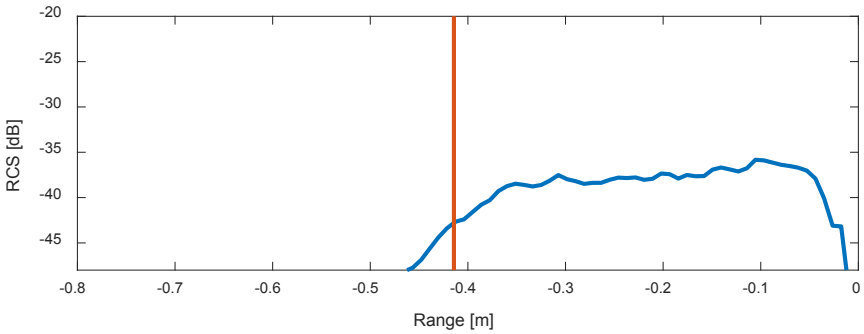

Figure 6.3.9 – Range-domain RCS of canopy (Average of Row 20; Plot 1). Retrieved Average of Top Vegetation (red line).

Projected Leaf Area Density: *PLAIz*

Using the procedure described in section 6.2.4, the PLAIz of the canopy is retrieved from the average range-domain RCS waveforms of each canopy plot. Figure 6.3.10 shows the range-domain RCS waveform for plot 1 of row 20. The red, yellow and purple lines in figure 6.3.10 indicate the average RCS corresponding the top, middle and bottom leaf layer, respectively.

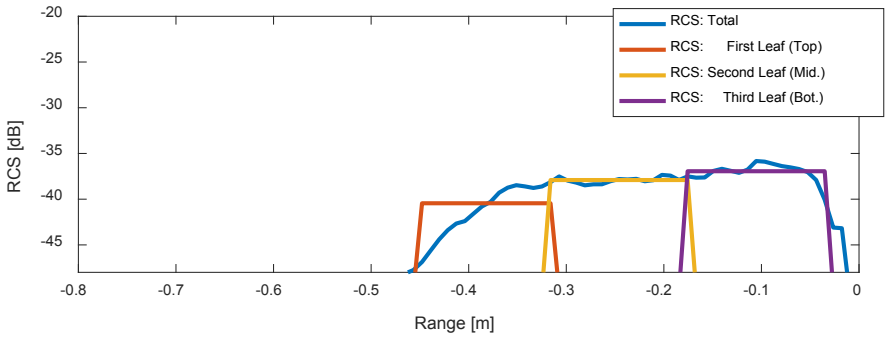

Figure 6.3.10 – Range-domain RCS of canopy (Average of Row 20; Plot 1). Average RCS for top (red), middle (yellow) and bottom (purple) leaf layers.

Figure 6.3.11 shows the retrieved and approximated PLAIz profile. The red, yellow and purple lines in figure 6.3.11 indicate the retrieved average PLAIz for the top, middle and bottom leaf layer, respectively. The results of the retrieved PLAIz for the measured plots that have not headed are given graphically in section 6.3.4.

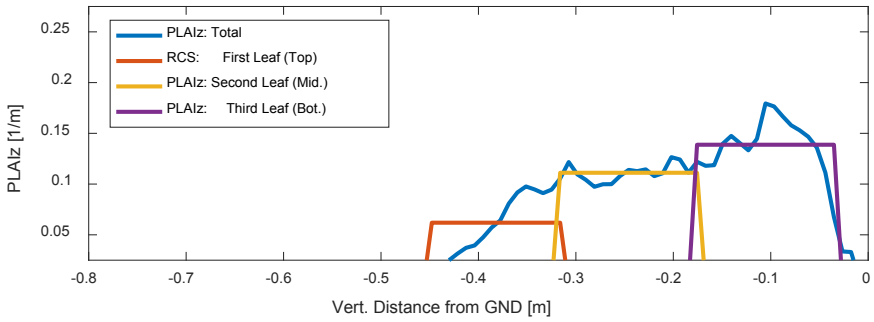

Figure 6.3.11 – Retrieved approximated PLAIz profile. Retrieved PLAIz for top (red), middle (yellow) and bottom (purple) leaf layers.

6.3.3. Manual Measurements

After the radar measurements were collected, plant samples were collected. The physical properties related to scattering analysis were measured manually. Tables 6.3.2, 6.3.3, 6.3.4 and 6.3.5 list the mean and root-mean-square (RMS) of the parameters measured related to the plant height, stem, head and leaves, respectively, collected on 5/7/2018. Likewise, tables 6.3.6, 6.3.7, 6.3.8 and 6.3.9 list the mean and root-mean-square (RMS) of the parameters measured related to the plant height, stem, head and leaves, respectively, collected on 5/7/2018.

The stem length and the plant height were measured with a 36-inch (1-yard) ruler. The stem radius, head radius, head length, leaf length, leaf width and leaf thickness were measured using a micrometer. The leaf's dielectric was measured using a custom-made dielectric probe, which is a parallel-plate transmission line. The water content is derived from the real component of the dielectric constant using the El-Rayes dielectric model of vegetation material, described in chapter 4.

A complete list of the measurements is given in appendix G.

6.3.3.1. Manual Measurements 2018-05-07

Table 6.3.2 – Mean and RMS of Manual Measurements 2018-05-07: Plant Height

	Plant	
	Mean	**RMS**
$H_{H,P}$ [mm]	370.8	13.9
$H_{L,P}$ [mm]	385.7	17.1
H_P [mm]	385.7	17.1

Table 6.3.3 – Mean and RMS of Manual Measurements 2018-05-07: Stem Parameters

	Stem	
	Mean	**RMS**
$r_{z,S}$ [mm]	0	0
L_S [mm]	365.8	13.9
a_S [mm]	1.3	0.1

Table 6.3.4 – Mean and RMS of Manual Measurements 2018-05-07: Head Parameters

	Head	
	Mean	**RMS**
$r_{z,H}$ [mm]	373.6	19.3
L_H [mm]	44	5.5
a_H [mm]	3.2	0.3

Table 6.3.5 – Mean and RMS of Manual Measurements 2018-05-07: Leaf Parameters

	Leaf 1 (Top)		Leaf 2 (Mid.)		Leaf 3 (Bot.)	
	Mean	**RMS**	**Mean**	**RMS**	**Mean**	**RMS**
$r_{z,L}$ [mm]	360.8	13.9	216.0	35.1	74.0	32.1
L_L [mm]	96.0	11.4	132.0	16.4	100.0	28.3
w_L [mm]	11.4	1.3	9.6	0.9	8.4	0.9
a_L [mm]	0.21	0.02	0.20	0.03	0.18	0.01
$\theta_{i,L}$ [deg]	18.0	23.9	17.0	5.7	12.0	4.5
$\theta_{f,L}$ [deg]	54.0	42.8	98.0	36.2	92.0	54.0
R_L [mm]	31.3	4.0	26.6	10.1	33.3	15.0
$s_{o,L}$	0.62	0.25	0.58	0.04	0.58	0.24
$m_{g,L}$	0.70	0.15	0.71	0.15	0.63	0.10

6.3.3.2. Manual Measurements 2018-05-22

Table 6.3.6 – Mean and RMS of Manual Measurements 2018-05-22: Plant Height

	Plant	
	Mean	**RMS**
$H_{H,P}$ [mm]	533.4	36.9
$H_{L,P}$ [mm]	484	33.5
H_P [mm]	536	32.7

Table 6.3.7 – Mean and RMS of Manual Measurements 2018-05-22: Stem Parameters

	Stem	
	Mean	**RMS**
$r_{z,S}$ [mm]	0	0
L_S [mm]	471.9	43.1
a_S [mm]	1.3	0.2

Table 6.3.8 – Mean and RMS of Manual Measurements 2018-05-22: Head Parameters

	Head	
	Mean	**RMS**
$r_{z,H}$ [mm]	471.9	43.1
L_H [mm]	70	6.9
a_H [mm]	5.3	0.7

Table 6.3.9 – Mean and RMS of Manual Measurements 2018-05-22: Leaf Parameters

	Leaf 1 (Top)		Leaf 2 (Mid.)		Leaf 3 (Bot.)	
	Mean	**RMS**	**Mean**	**RMS**	**Mean**	**RMS**
$r_{z,L}$ [mm]	393.8	25.6	213.3	28.4	82.9	23.3
L_L [mm]	129.0	27.5	121.7	20.9	53.8	28.1
w_L [mm]	11.1	1.9	9.0	1.6	6.0	1.8
a_L [mm]	0.23	0.03	0.23	0.04	0.21	0.03
$\theta_{i,L}$ [deg]	34.4	19.1	27.1	9.4	33.8	22.6
$\theta_{f,L}$ [deg]	39.2	21.0	37.3	32.3	40.8	39.7
R_L [mm]	79.2	10.2	59.4	17.8	53.0	11.0
$s_{o,L}$	0.90	0.19	0.90	0.20	0.90	0.20
$m_{g,L}$	0.67	0.09	0.69	0.11	0.41	0.20

6.3.4. Results of Biophysical Parameter Retrievals

6.3.4.1. Plant Height

Using the procedure described in section 6.2.3, the average height of wheat plots were retrieved from the range-domain RCS waveforms.

Figures 6.3.14 and 6.3.15 show maps of the radar-retrieved heights for the wheat plots measured on 5/7/2018 and 5/22/2018, respectively. Table 6.3.10 shows the mean and standard deviation of the radar-derived heights of the wheat plots, measured on 5/7/2018 and 5/22/2018. Figures 6.3.12 and 6.3.13 show the histograms of the radar retrieved heights.

Table 6.3.10 – Mean and standard deviation of radar-retrieved heights of wheat plots

Measurement Date	**Statistical Mean**	**Standard Deviation**
5/7/2018	0.39 m	0.02 m
5/22/2018	0.54 m	0.03 m

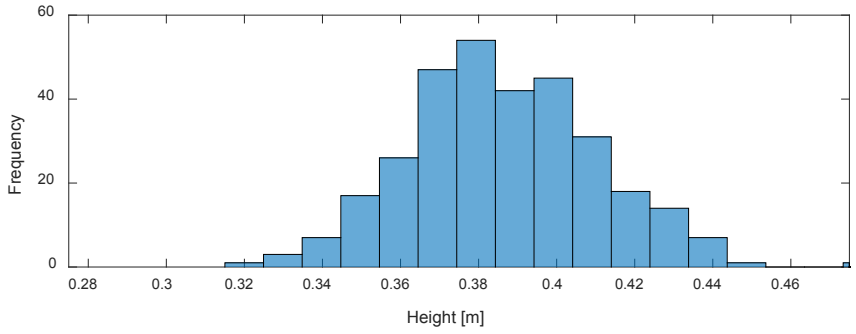

Figure 6.3.12 – Histogram of retrieved height of wheat plots. Measurement date: 5/7/2018

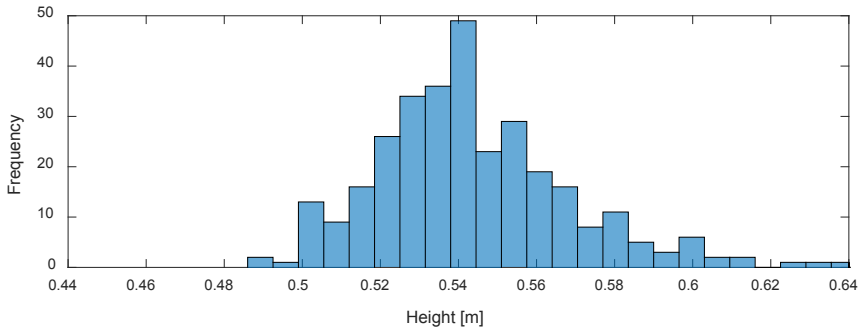

Figure 6.3.13 – Histogram of retrieved height of wheat plots. Measurement date: 5/22/2018

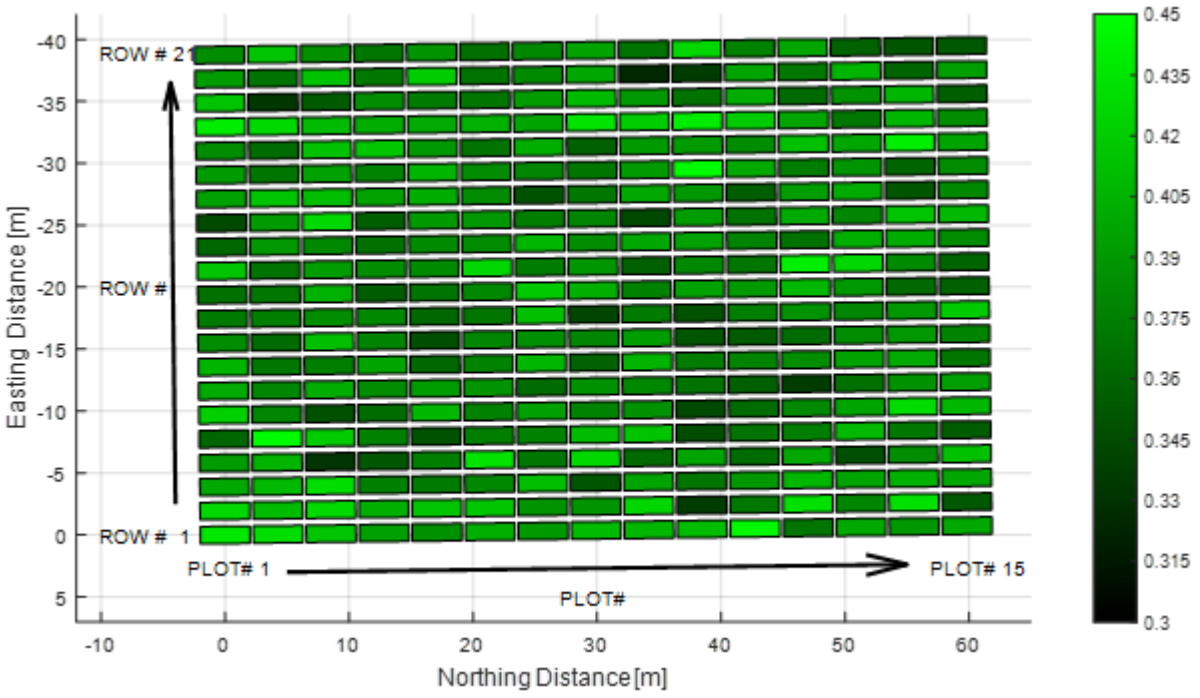

Figure 6.3.14 – Map of Canopy Plots: Height Retrievals (5/7/2018)

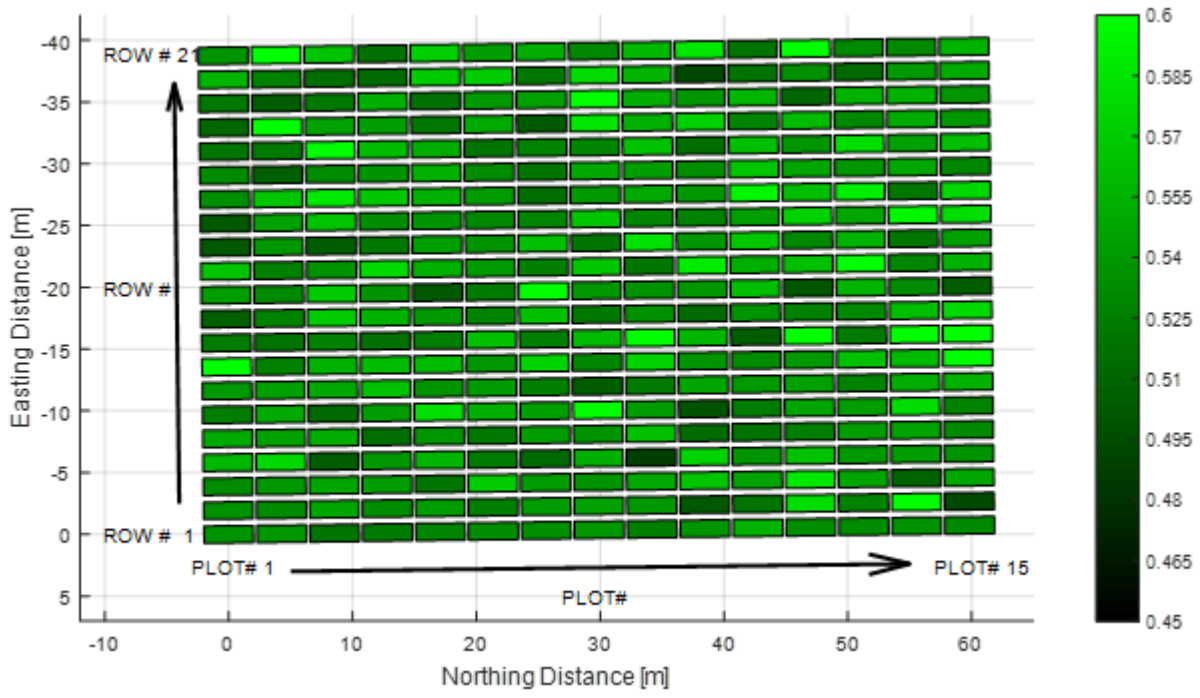

Figure 6.3.15 – Map of Canopy Plots: Height Retrievals (5/22/2018)

The radar-derived heights were also compared against the manual measurements related to both measurement dates. For these comparisons, we use the average values of the heights measured manually.

The blue stars of figures 6.3.16 corresponds to the average of the manually measured heights for wheat plots 8, 10, 12 and 13 of row 1, collected on 5/7/2018. The red stars on this figure corresponds to the radar-derived heights for the same wheat plots.

On average, the radar-retrieved heights are 1.6 cm less than the ruler measurements. The RMS of the difference between the two types of measurements is 3 cm. The average of the offset is within one standard deviation of the manual measurements for row 1.

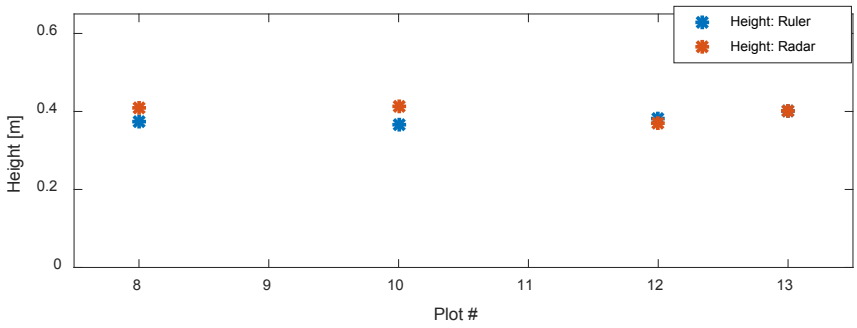

Figure 6.3.16 – Comparison of manually measured height and radar-retrieved height (Date: 5/7/2018; Row: 1; Plots: 8, 10, 12, 13)

Figure 6.3.17 shows the average of the manual measurements and the radar-retrieved heights for plots 1 to 12 of row 1. On average, the offset of the radar-derived heights and the manual measurements is 0.2 cm. The standard deviation of this offset is 2 cm. The average of the offset is within the standard deviation of the manual measurements.

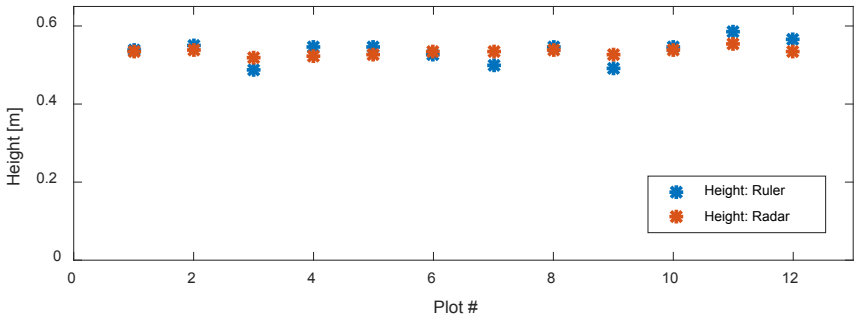

Figure 6.3.17 – Comparison of manually measured height and radar-retrieved height (Date: 5/22/2018; Row: 1; Plots: 1-12)

Figure 6.3.18 shows a scatter plot that compares the average manual measurements and radar-derived heights for both measurement days. The red line corresponds to the ideal correspondence between the two measurements. The correlation coefficient between the radar and manually derived heights is 0.94. The coefficient of determination for the points in the scatter plot and the ideal line is 0.82. Both of these metrics indicate a good agreement between the manual measurements and the radar retrievals.

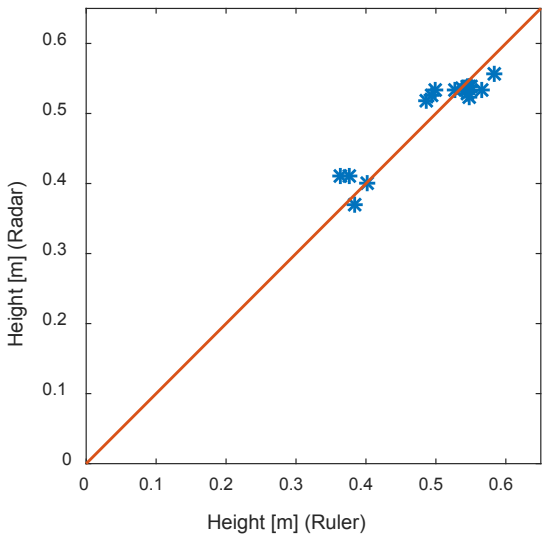

Figure 6.3.18 – Comparison of Height Retrievals: Radar- vs Ruler- based Measurements

6.3.4.2. Projected Leaf Area Density: PLAIz

Retrieval Results

On 5/7/2018, the measured wheat plants were experiencing the “boot” growth stage (Feekes 10.0) or one of the “heading” stages (Feekes 10.1-10.4). Photographs taken with a camera mounted on the mobile platform (cart), were used to identify the plots were the plants were heading. In this experiment, we are interest in the retrievals of PLAIz for plants that have not experienced heading yet. Therefore, the retrieval of PLAIz is only performed on those wheat plots that have not headed yet.

Using the procedure described in section 6.2.4, the average projected leaf area density (PLAIz) of wheat plots was retrieved from the range-domain RCS waveforms.

Figures 6.3.22, 6.3.23, and 6.3.24 show maps of the radar-retrieved PLAIz for the top, middle and bottom leaf layers, respectively, of the wheat plots measured on 5/7/2018. Table 6.3.11 shows the mean and standard deviation of the radar-derived PLAIz of the wheat plots.

Table 6.3.11 – Mean and standard deviation of radar-retrieved PLAIz of wheat plots (5/7/2018)

Measurement Date	**Statistical Mean**	**Standard Deviation**
Top Leaf Layer	0.098	0.070
Middle Leaf Layer	0.206	0.128
Bottom Leaf Layer	0.224	0.094

Figure 6.3.19, 6.3.20 and 6.3.21 show the histograms of the radar-retrieved PLAIz for the top, middle and bottom leaf layers, respectively. These histograms and table 6.3.11 indicate that the average of the PLAIz of the top leaf layer is significantly less than that of bottom two layers. The difference between the average of the PLAIz of the middle and bottom leaf layers is less than one standard deviation. In other words, the middle and bottom leaf layers have about the same leaf area density.

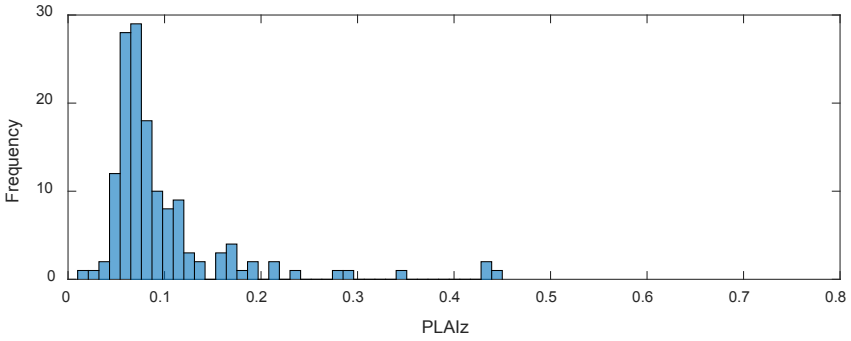

Figure 6.3.19 – Histogram of retrieved PLAIz of wheat plots. Top Layer (Measurement Data: 5/7/2018)

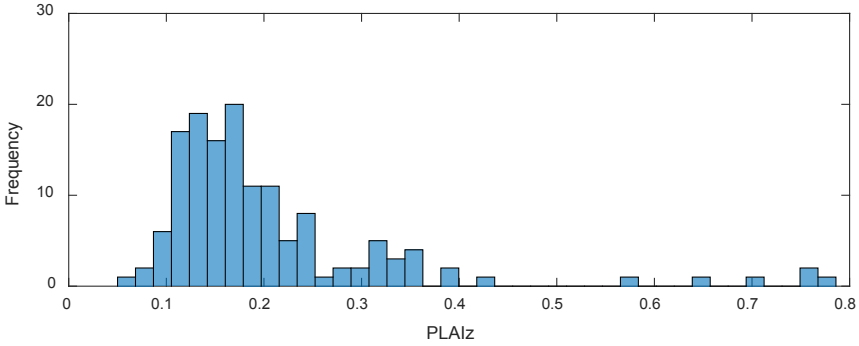

Figure 6.3.20 – Histogram of radar-retrieved PLAIz of wheat plots. Middle Layer (Measurement Data: 5/7/2018)

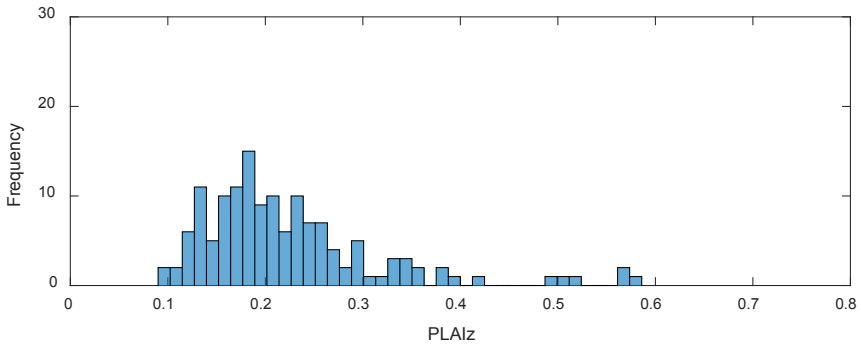

Figure 6.3.21 – Histogram of radar-retrieved PLAIz of wheat plots. Bottom Layer (Measurement Data: 5/7/2018)

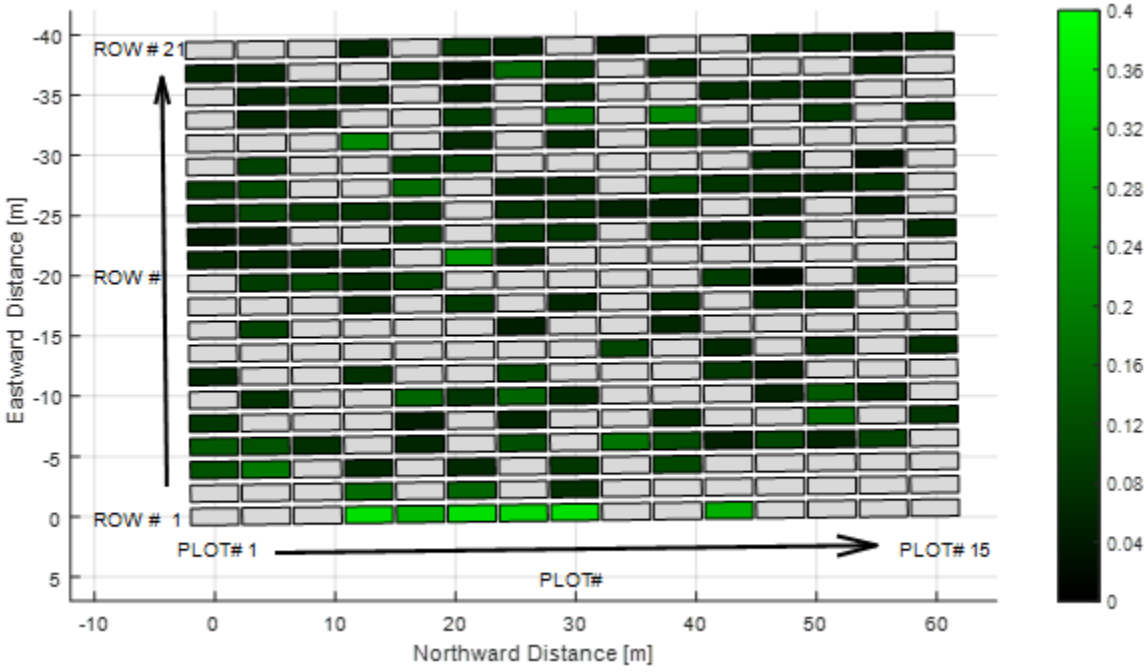

Figure 6.3.22 – Map of Canopy Plots: radar-retrieved PLAIz of top leaf layer (5/7/2018)

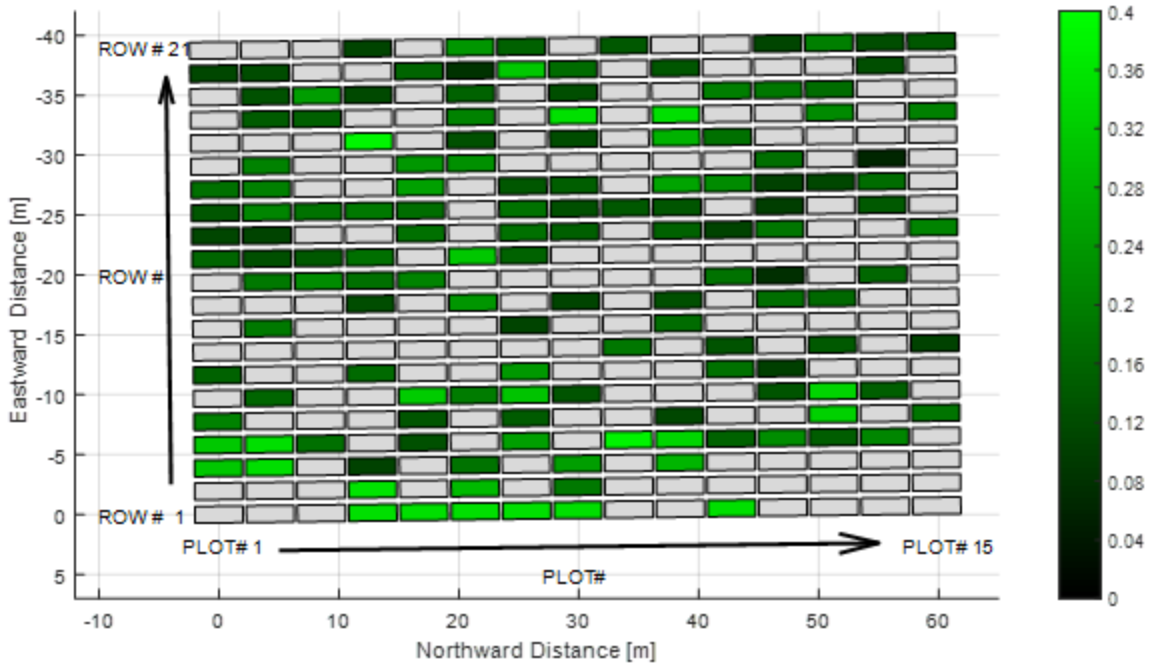

Figure 6.3.23 – Map of Canopy Plots: radar-retrieved PLAIz of middle leaf layer (5/7/2018)

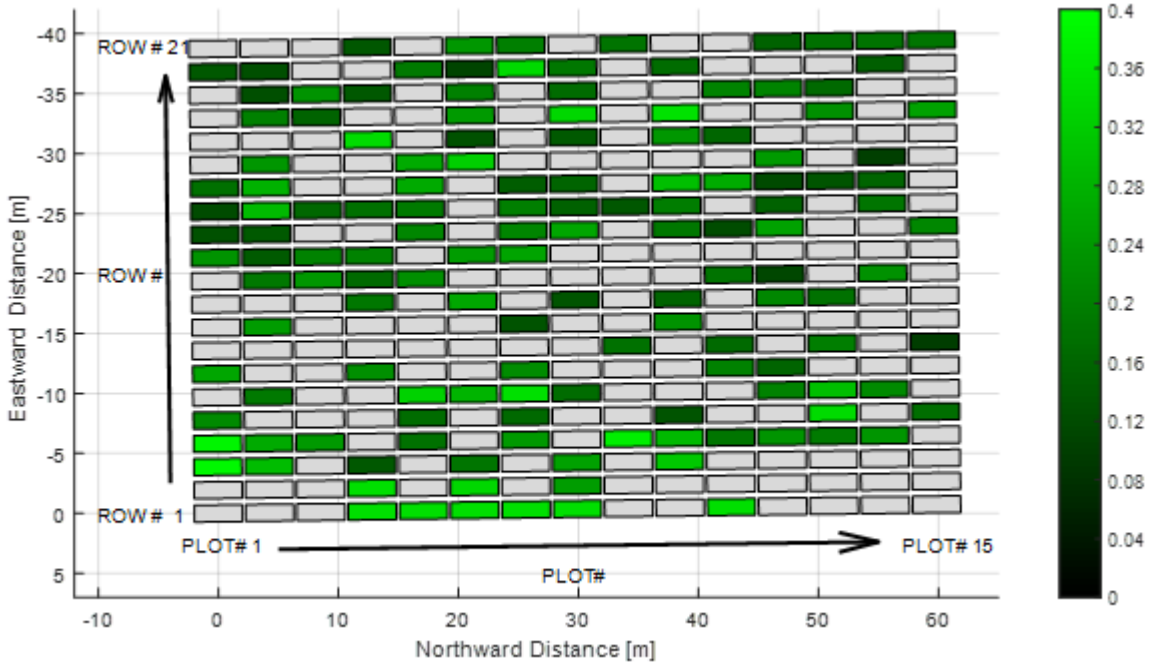

Figure 6.3.24 – Map of Canopy Plots: radar-retrieved PLAIz of bottom leaf layer (5/7/2018)

Comparison of radar- against image- retrieved PLAIz

A camera was mounted on top of the mobile platform used for radar measurements. The camera was used to take top-view photographs of the wheat plots. Using the procedure described in appendix H, the average of the projected leaf area density of the two top layers is retrieved from the images collected.

Figure 6.3.25 shows a comparison a comparison of the average PLAIz of the top layers retrieved using photographs and radar measurements. The abscissa of this figure indicates the number of the plot measured. For this figure, the plots of all rows were appended together. Only the plots of wheat that has not reached the “heading” growth stage are considered. By inspection, figure 6.3.25 show that good agreement exist between the radar- and image-retrieved PLAIz for large values of PLAIz.

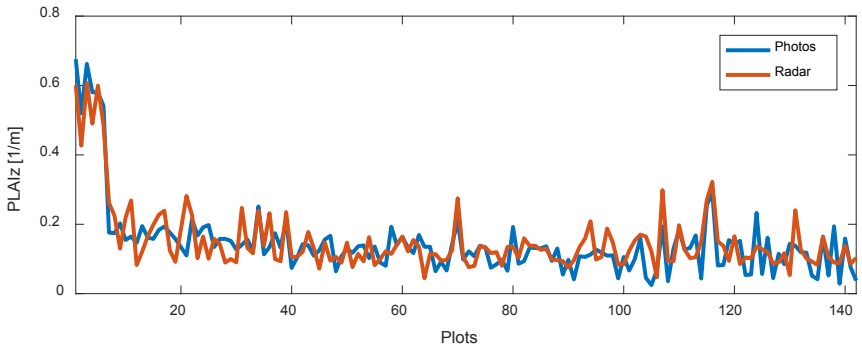

Figure 6.3.25 – Comparison of radar-retrieved PLAIz and photograph-retrieved PLAIz (Date: 5/7/2018)

Figure 6.3.26 shows a scatter plot comparing the radar- and image- retrieved PLAIz. The correlation coefficient of the radar- and the image-based retrievals is 0.86. This indicates a strong linear relationship between each other. The red line in figure 6.3.26 indicates the identity

mapping between radar and image based retrievals. The coefficient of determination (R^2) of the scatter plot in figure 6.3.26 is 0.69, indicating a good agreement between the points in the scatter plot and the model (red line).

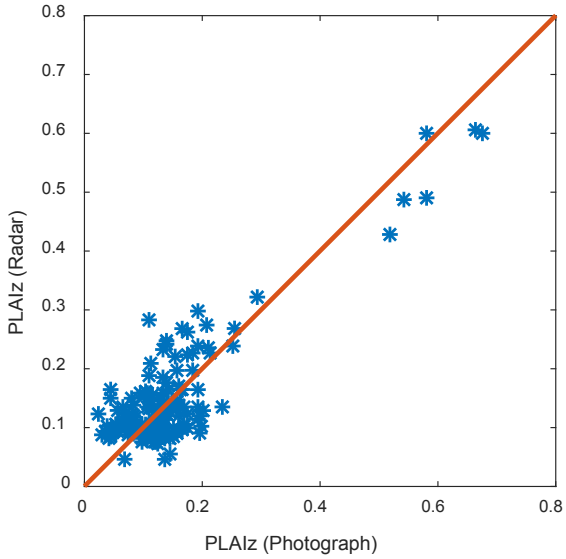

Figure 6.3.26 – Comparison of radar- and image- retrieved PLAIz (Scatter Plot)

Figures 6.3.27 and 6.3.28 are maps that display the radar- and image- retrieved PLAIz, respectively, using a color-coding.

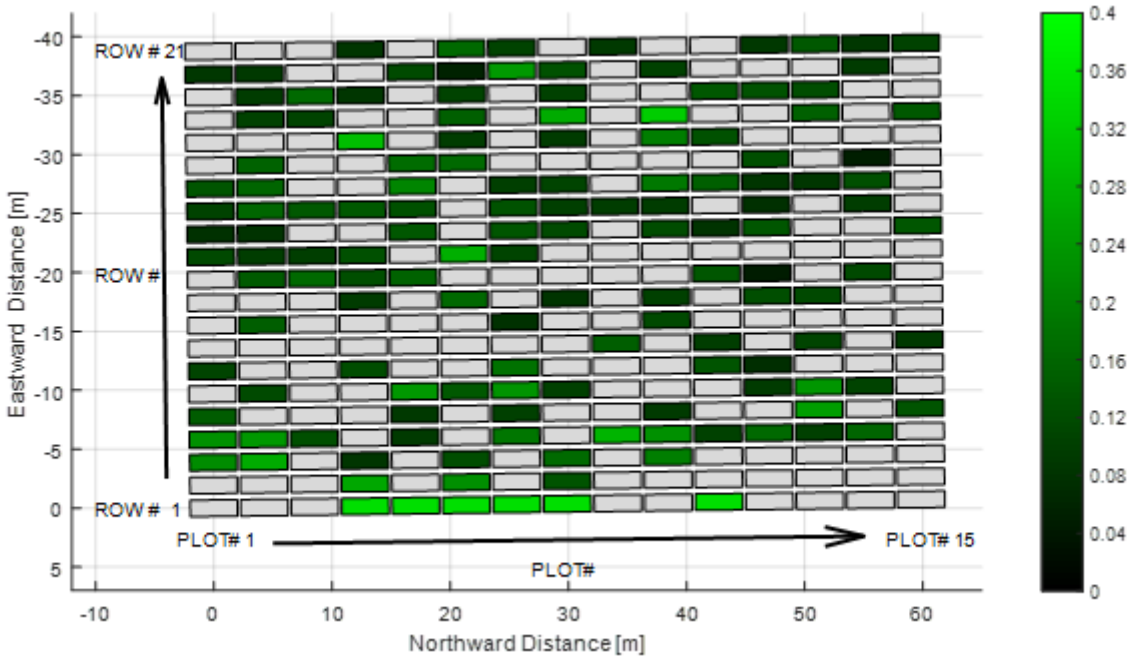

Figure 6.3.27 – Map of Canopy Plots: PLAIz radar retrievals average of top and second layer (5/7/2018)

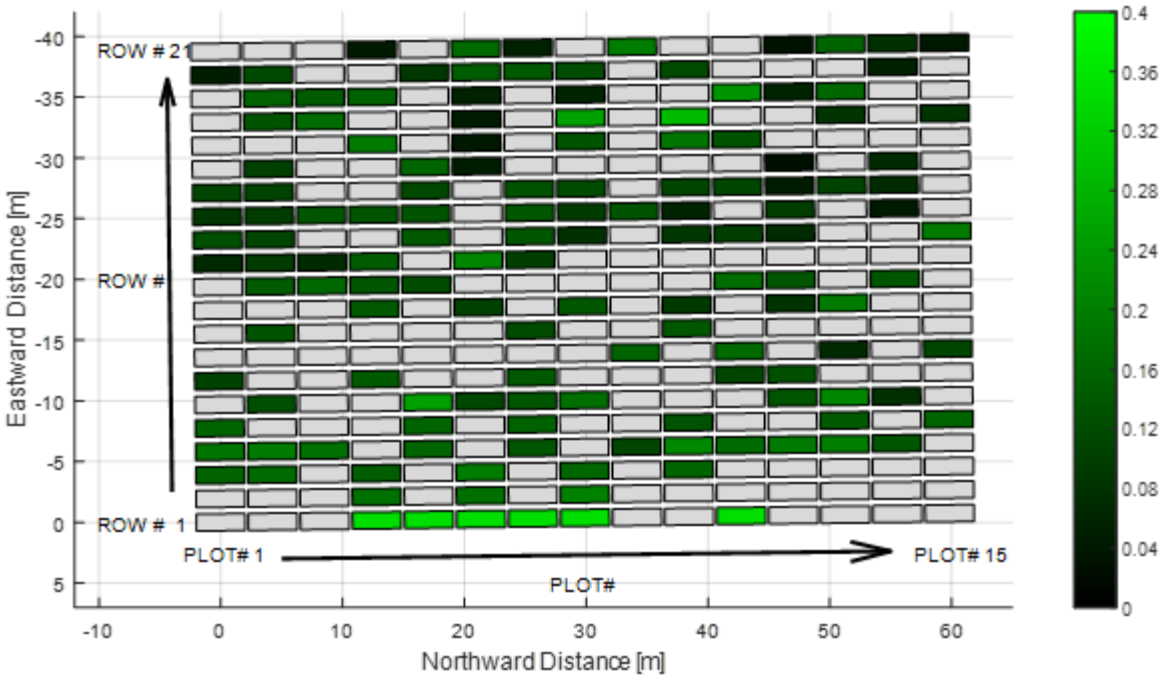

Figure 6.3.28 – Map of Canopy Plots: PLAIz image retrievals average of top and second layer (5/7/2018)

7. Summary

7.1. Summary of Contributions

7.1.1. Radar System and Noise Analysis

In chapter 5, a comprehensive noise analysis of FMCW radar is given. This analysis presents models for the power spectral density due to the different noise sources in an FMCW radar system. The most significant source of noise in FMCW radars is related to the phase noise of the waveform generator and the amplitude of the self-interference signals. This document presents a new model that accurately relates the phase noise of the chirp generator to the power spectral density of the noise at the output signal. This model may be used for the design of FMCW radars to predict and understand how to improve the noise level at the output.

The description and characterization of a new 2-18 GHz FMCW radar prototype is presented. This description includes block diagrams, lists of components and relevant performance plots of each sub-system. The main features of this system are the 2-18 GHz chirp generator and the radar receiver.

A novel chirp-generator design is presented, which is based on a UWB PLL. The chirp generator has a maximum incoherent and coherent phase noise with respect to the carrier of only -45 dBc and -42 dBc, respectively. This is achieved primarily by using a wide loop bandwidth PLL (4.6 MHz), which suppresses the phase noise by 15 dB at 1 MHz from the carrier. A detailed design and characterization of this novel chirp generator is presented.

The receiver has a gain of 47.3 dB and a noise figure of 13 dB. The radar is able to operate transmitting low power (-114 dBm/Hz) and achieve a dynamic range of 56 dB, because of the high pulse-compression gain and the high-gain receiver. Since the noise level of the radar is dominated by phase-noise of interference signals (-96.5 dB), the thermal noise component at the output of the radar (-113.7 dBm/Hz) has little effect on the performance of the radar.

7.1.2. Scattering Analysis of Wheat Canopies

In chapter 3, we present a new method for coherent scattering modeling, the constructive geometric method. This method can be used to model the radar-response and the scattering-response of complex targets. This method is valid for complex targets with no or a small amount of concave surfaces. In chapter 3, improved coherent scattering models for dielectric cylinders and thin sheets are presented.

In chapter 4, the constructive geometric method is used to formulate new and accurate scattering models of wheat leaves with arbitrary curvature and orientation, wheat heads, wheat stems, plants and canopies. Geometric models of the wheat plant constituents, plants and canopies are given. The combined geometric modeler and the solver of the scattering response is refer to as the radar simulator. Using this radar simulator, Monte-Carlo simulations are performed in chapter 6 for the solution of the statistical average of the RCS due to wheat canopies.

The radar simulator, based on the geometric and scattering models, is validated using full-wave simulations and measurements. The radar simulator accurately predicts the radar response due to wheat plant constituents and whole plants.

7.1.3. Canopy Architecture Parameter Retrieval from Radar Measurements

Chapter 6 presents retrieval procedures to infer the canopy architecture parameters: canopy height and the vertical distribution of the projected leaf area density. Monte-Carlo radar simulations were performed to solve for the statistical average of the range-domain RCS waveform for a given set of canopy parameters. These simulations were used to find procedures to retrieve the mentioned canopy architecture parameters. These simulations were also used to find simple relationships between the leaf-related parameters of the wheat canopy and the range-domain RCS waveforms.

In chapter 6, a field experiment is described, in which the radar sensor, described in chapter 5, was used to collect RCS waveform measurements of 315 wheat canopy plots. The mentioned retrieval procedures were used to solve for the canopy architecture parameters (height and projected leaf area density) of the collected radar-measurements. The retrieved heights of wheat plots were compared against measurements made with a ruler. The retrieved projected leaf area densities of the top leaves were compared against retrievals made using a simple image-based procedure.

7.2. Recommendations for Future Studies

7.2.1. Radar System and Noise Analysis

Because the antennas are close to the target, there is a small but noticeable distortion of the measured RCS vertical profile, approximated from the range-domain RCS. This distortion consists of slower rising and falling edges of the impulse response. This distortion may mask small vertical layers adyacent to strong ones. Simulations are used in chapter 6 to show the effect of this type of distortion, which is caused by the wide-beam measurements. The wide-beam antennas used were chosen so that the transmit and receive antenna footprints overlap with each other, while keeping sufficient distance from each other so that the noise associated with antenna coupling is kept low.

In order to reduce this type of distortion while keeping the radar noise level low, the antennas must have high directivity, the antennas footprints must overlap with each other and the antenna feedthrough should be kept low at the same time. Future studies should develop an antenna pair that meets these goals, simultaneously.

7.2.2. Scattering Analysis of Wheat Canopies

Time domain RCS measurements of the wheat heads show different amplitudes for the contributions of the top and bottom of the head. In the modeling of the wheat heads, it was assumed that the effective dielectric was uniform. Measuring the distribution of the dielectric of

the heads would potentially provide a more accurate representation of the model, which would improve the scattering model of the wheat heads.

7.2.3. Canopy Architecture Retrieval from Radar Measurements

The main source of inaccuracies of the retrieved projected leaf area densities could be the vertical distribution of the effective dielectric of leaves. In the retrievals of chapter 6, it was assumed that the vertical distribution of the effective dielectric of leaves was equal to the average of the measurements taken from the first plot. Future studies should consider taking measurements of the water content profiles of all measured wheat plots (canopies).

Appendix A: Morphology of Wheat Plant Constituents

This appendix is used as a reference to the morphology of the wheat plant constituents used throughout the dissertation. The content of this appendix is based on references [1] and [2].

A.1. Wheat Seed

The seed (a.k.a. kernel, grain or berry) is a dry fruit from which the wheat plant grows. This seed is composed of three distinct parts: the bran, the germ or embryo and the endosperm.

The bran is the outer layer of the seed and contains fiber, vitamins and minerals. The endosperm is the place where nutrients, such as protein and carbohydrates are located and stored for consumption by the embryo. Common wheat flower is primarily based of this part of the seed. The embryo or germ is the part of the seed that becomes the plant.

The seeds are attached to the spikelets of the wheat spike (a.k.a. head) through the rachillas. The embryo in a seed is located at the point of attachment to the spikelet. The embryo is composed by the radicle, the plumule and the scutellum. The scutellum is the part of the embryo that absorbs sugars and brakes down the starch form the endosperm. The plumule and the radicle are the regions from which the shoots and roots develop, respectively.

The seminal roots develop from the radicle, which are the first type of roots used by the plant for the absorption of water and nutrients from the soil. The coleoptile emerges from the plumule. The coleoptile is a protective tubular structure, capable to push through the soil and to the surface, which is used by the first shoots (e.g. first leaf) to emerge from the ground.

A.2. Wheat Head

The head or the ear of the plant of an adult specimen is located at the top or vertical superior end. It is attached to the last node by the peduncle. The head is the place where the wheat reproductive system is found and where the seeds develop. The head is composed of two rows of spikelets attached to the central axis or rachis. The glumes and florets, which contain the reproductive system of the wheat, are attached to the spikelets by the rachillas. Each floret in the skilets contains a lemma and a palea that enclose the reproductive organs: the carpel (ovary and stigmas), three stamen and anthers.

A.3. Wheat Leaves

A.3.1. Leaf External Appearance

The leaves of a mature plant are its main organs of the plant used for photosynthesis. They are composed by the leaf blade or lamina, the sheath and the ligule. The leaf sheath is the part that wraps around the main axis of the plant, where the stem or pseudo-stem is located.

The lamina or blade is a planar structure and extends from a point in the main axis of the plant. The angle that the blade makes with the axis of the plant is related to the amount of light absorbed and the photosynthetic rate of that leaf. The distribution of this angle on all leaves of a plant or canopy is called the leaf-angle-distribution (LAD). Plants with leaves that are primarily vertically oriented are said to have erectophile LAD. Plants with leaves that mostly extend horizontally are said to have planophile distribution.

A.3.2. Leaf Anatomy

The anatomy of the leaf can be described by its three main type of structures: the epidermis, the mesophyll and the vascular bundles.

Similar to other monocot plants, the mesophyll and vascular tissue of wheat leaves is arranged in alternating strips that run along parallel to the main axis of the leaf.

The ad and abaxial epidermis are complex cellular structures that protect the internal cells. The stomata, formed by two guard cells, are uniformly distributed across the epidermis.

The mesophyll cells are found between the ad and abaxial epidermis. The mesophyll cells near the epidermis are more elongated than the ones near the center. The arrangement and compactness of mesophyll cells inside the leaf vary from one cultivar type to another.

The vascular bundles contain the xylem and the phloem. They main bundles run parallel to the axis of the leaf. A small percentage of the total bundle length is transverse to the main axis. At the tip of the pointed leaf, the longitudinal bundles connect to each other.

A.4. Wheat Stem

The stem or culm of a mature wheat plant extends along the main axis of the plant. The stem is divided into a number of internodes separated by the nodes.

Before the stem elongation growing stage, the nodes are stacked on top of each other. During its elongation stage, the stem extends along the main axis leaving 4 to 7 nodes distributed along

its length. The part above the stem surrounded only by leaf sheaths is referred as the pseudo-stem. During the stem elongation stage, the head rises through this pseudo-stem.

The part of the culm above the last (top) node, which connects the head to this node, is called the peduncle. Only part of the peduncle is surrounded by the sheath of the flag leaf.

A.4.1. Anatomy of Stem

At the internodes, the stem is shaped as a hollow pipe and it is formed by different cellular structures. At the nodes, the stem is solid or filled. The outermost tissue layer of the stem is the epidermis, where the stomata are located. The epidermis has a thick cuticle surrounding it. The Chlorenchyma is located at the outer part of the stem, composed of cells rich in chloroplasts needed for photosyntehsis. The Schlerenchyma tissue is a thick cellular wall between the Chlorenchyma and the Ground tissue. Small vascular bundles reside among the Chlorenchyma and Schlerenchyma tissue. The rest of the stem is composed of Parenchyma or Ground tissue, where the main vascular bundles are located. Similar to leaves, the vascular bundles are composed by the Xylem and Phloem. At the nodes, the vascular bundles from internodes may diverge to the attached leaves or continue its path to the next internode.

A.5. Wheat Roots

A wheat plant has two types of roots: the seminal roots and the crown or nodal roots. The seminal roots develop from the root primordia within the seed and are the first type of roots to

emerge. Nodal or crown roots emerge from the crown around the same time that tillers start to develop.

A.6. Wheat Tillers

Wheat plants may produce branches called tillers. These tillers may emerge from the axil of the leaves of the main shoot or, more rarely, from the axil of the coleoptile. The former is referred to as a coleoptile tiller. Tillers emerging from the main shoot or the coleoptile are considered primary. Secondary tillers may develop at the axils of leaves of primary tillers. Higher order tillers may also exist. If conditions are favorable, the tiller develops a stem divided by nodes and internodes similar to the main shoot. Additionally, a head may also emerge from a tiller. Tiller stems and leaves are anatomically similar than those belonging to the main shoot.

A.7 References

[1] L. Taiz, E. Zeiger. *Plant Physiology 3rd Edition*. Sunderland, MA: Sinauer Associates, 2002, pp. 111-143.

[2] B. Curtis, S. Rajaram, H. Gomez. *Bread Wheat*. Rome: Food and Agriculture Organization of the United Nations, 2002.

Appendix B: Growth Stages of Wheat

In this section, we briefly describe the different growth stages of wheat from germination to anthesis and grain filling. The content of this appendix is based on reference [1].

B.1. Germination

If the ambient temperature and ambient moisture content are adequate, the seed imbibes water and begins to expand. This is the beginning of germination.

First, the radicle emerges from the embryo. This is the first root of the plant. Subsequently, the coleoptile emerges, which is a tubular sheath that protects the first leaf.

Germination defines the start of the development of the plant and the beginning of its vegetative growth.

B.2. Emergence (Feekes 1.0)

The coleoptile is sufficiently strong to push through the ground. When the coleoptile reaches the surface and encounters light, it stops its development. The first leaf emerges through the coleoptile tip.

During emergence, the seminal roots continue to develop into the first root system of the plant.

After emergence, the sheath of the leaf folds in cylindrical fashion. The coleoptile along with the first leaf sheath and lamina form the first shoot of the plant.

B.3. Tillering Begins (Feekes 2)

In this stage of the plant development, tillers begin to emerge. Tillers emerge from axillary buds located at the axils of the leaves. For this reason, they are also known as axillary shoots or side shoots.

The amount of tillers formed depends on planting dates, environmental factors and genetics. The number of tillers developed by a plant is important because may develop heads and produce grain. However, tillers with insufficient number of leaves will drain resources from the main shoot, potentially reducing the grain weight or number of the main shoot. Additionally, not all tillers will produce heads or grains.

During this stage, the secondary root system begins to develop. This root system is formed above the seed at a node blow the ground called the crown. For this reason it is also known as the nodal or crown root system. This is the main root system of the plant, which provides the water and nutrient intake from the soil. It also serves as the main anchor to the ground. If seeding is not sufficiently deep, nodal roots may develop properly and the plant may be more prone to lodging.

B.4. Completion of Tillering and Double Ridging (Feekes 3)

During this stage, tillering continues. Several primary tillers may develop from the main shoot. If conditions are favorable, secondary and higher order tillers may also develop from the axils of leaves of tillers.

A period of winter dormancy occurs at this time, which is known as vernalization, and is required for the proper development of the wheat plant. Tillering ends shortly before or after vernalization.

After vernalization, the meristem or growing point changes from vegetative to reproductive growth. The meristem stops development of leaves and begins the differentiation of spikelets and florets. This stage of growth is marked by a double ridge at the head, which corresponds to the glumes and skipelet primordia.

The number of florets initiated at this stage determine the potential number of kernels per head.

B.5. Green-Up (Feekes 4 and 5)

During the green-up phase, the plants begins erect growth. The sheaths of the leaves begin to form a pseudo-stem by wrapping themselves in a tubular form. These sheaths strengthen to make the plants stand up right. This stage is known as Feekes 4.

At growing stage Feekes 5, the leaf sheaths are fully elongated. These leaf sheaths form a strong pseudo-stem. The developing head rises up above the ground moving through the pseudo-stem.

The number of spikelets has been fully determined at this growth stage.

B.6. First Node (Feekes 6)

Nodes are regions of active cell division, from which leaves, tillers and adventitious roots may develop. The crown is the first node to develop. Leaves, the main shoot and adventitious roots develop from the crown. However, the label of node #1 or the first node is usually given to the first node above the ground.

Before stem elongation, the nodes are stacked together near the main growing point of the shoot. As the growing point rises and moves through the pseudo-stem, the nodes follow this growing point and remain at different points along the axis of the plant, forming the stem structure. The regions between nodes are called the internodes. Nodes are also referred as joints.

The first node appearance defines the growing stage that marks the beginning of the stem elongation.

B.7. Stem development

During stem elongation, the growing point continues to rise beyond the first node location. Nodes remain at different points along the axis of the plant forming the stem structure. The internal structure of nodes and internodes develops, establishing the vascular bundles, ground tissue and epidermis of the stem. Nodes above the ground have meristems that allow for the

development of leaves. Although up to seven nodes may develop, most plants develop four nodes before the flag leaf. After the emergence of the flag leaf no more nodes will develop.

During stem elongation, the internodes formed continue to grow lengthwise. As indicated in appendix 2.A, the nodes are solid structures and the internodes are hollow.

B.8. Flag Leaf Emergence to Ligule of Flag Leaf Visible (Feekes 8 and 9)

Feekes 8 is marked by the emergence of the flag leaf. The flag leaf, which is the last part of the foliage that emerges before heading. This stage is very important in crop management. The flag leaf accounts for over 50% of the photosynthates used for grain development. It is also the most vulnerable leaf to damage from insects or diseases. Therefore, its identification and proper protection by the use of agronomic inputs helps to ensure that the plant fulfills it yield potential. In most cases, wheat plants develop four nodes, so that the flag leaf arises from the fourth node.

At Feekes 9, the flag leaf has emerged completely and its ligule, which is the membrane that joins the lamina to the sheath, is completely formed. At this stage, the plant is ready to begin heading.

B.9. Boot and Heading (10.0 - 10.1)

Booting (Feekes 10.0) is the stage when the developing head moves through the sheath of the flag leaf. As the developing head reaches the end of the flag leaf sheath, it begins to emerge. The first visible part of the head out of the sheath are the awns of the head (Feekes 10.1.).

During head emergence, the tillers development synchronizes with the main stem, so that the heads may emerge at the same time for all tillers.

During stages Feekes 10.2, 10.3 and 10.4, the head emergence is at 25%, 50% and 75%, respectively. At Feekes 10.5, the head has appeared completely and the peduncle, which is the stem structure between the forth node and the head, continues to elongate.

B.10. Anthesis (Feekes 10.5.1 - 10.5.3)

Anthesis or flowering is the stage that involves the opening of the flowering bud, pollination and fertilization. This stage begins shortly after the head has completely emerged. As the florets open up (Feekes 10.5.1), the anthers extend out of the floret and release pollen. Pollination (Feekes 10.5.2) occurs, when the pollen from the anthers reaches the stigma of the same or a different floret or plant. If the floret is fertile, the ovaries may be fertilized, beginning the development of the grain. Pollination ends at Feekes 10.5.3 and the grains begin to develop.

B.11. Grain Filling (Feekes 11)

The grain is first filled with a clear fluid (Feekes 10.5.4).

In Feekes 11.1, dry matter begins to accumulate in the kernel. At this stage, the grain is filled by a milk-like fluid.

In Feekes 11.2, the grain continues to accumulate biomass becoming a soft doughy material.

At the developing stage Feekes 11.3, the grain has reached its maximum dry weight and it is considered physiologically mature.

Lastly, at Feekes 11.4, the moisture content of the grain decreases to 15%. At this point, the straw is dead and the grains are ready to be harvested.

B.12. References

[1] UW Extension, University of Wisconsin-Madison. *Winter Wheat: Development and Growth Staging*. University of Wisconsin-Madison: Madison, WI.

Appendix C: Dielectric Properties of Pure and Saline Water

Water is one of the main components that affects the dielectric behavior of vegetation and soils. Several studies have been performed in the dielectric properties of water and its dependence on frequency, salinity and temperature [1].

Dielectric Constant of Fresh Water

The frequency dependence of pure water is given by the Debye equation (C.1), Where $\varepsilon_{w\infty}$ is the high frequency dielectric constant, ε_{wo} is the static dielectric constant of pure water, f is the frequency and τ_w is the relaxation constant of water [1][2].

$$\varepsilon_w = \varepsilon_{w\infty} - \frac{\varepsilon_{wo} - \varepsilon_{w\infty}}{1 + j2\pi f \tau_w} \quad \text{(C.1)}$$

The high frequency dielectric constant $\varepsilon_{w\infty}$ has been found to be 4.5 [1]. At microwave frequencies, the static dielectric constant of pure water ε_{wo} was found to follow the polynomial expression in (C.2) [1].

$$\varepsilon_{wo} = 88.045 - 0.4147 \cdot T + 6.295 \times 10^{-4} \cdot T^2 + 1.075 \times 10^{-5} \cdot T^3 \quad \text{(C.2)}$$

The relaxation constant of pure water, at microwave frequencies, is given by (C.3) [1] (C.3).

$$\tau_w = \frac{1}{2\pi}(1.1109 \times 10^{-10} + 3.824 \times 10^{-12} \cdot T + 6.938 \times 10^{-14} \cdot T^2 + 5.096 \times 10^{-16} \cdot T^3) \quad \text{(C.3)}$$

Dielectric Constant of Saline Water

Water content in vegetation and soil bodies usually contain some level of salinity, which affects its effective complex dielectric constant [1]. Salinity is the measure of the amount of salt dissolved in water and it is measured in parts per thousand (ppt or ‰). A Debye-like equation is given by the Klein-Swift dielectric model of saline water (C.4) [1]. In (C.4), ε_{sw}, ε_{swo}, $\varepsilon_{sw\infty}$, τ_{sw}, σ_i are the saline water's complex dielectric constant, static dielectric constant, high frequency dielectric constant, relaxation time and ionic conductivity, respectively [1].

$$\varepsilon_{sw} = \varepsilon_{sw\infty} - \frac{\varepsilon_{swo} - \varepsilon_{sw\infty}}{1 + (j2\pi f \tau_{sw})^{1-\eta}} - i\frac{\sigma_i}{2\pi f \varepsilon_o} \tag{C.4}$$

The high frequency dielectric constant of saline water has no dependence on sanity and it is equal to that of pure water ($\varepsilon_{sw\infty} = \varepsilon_{w\infty}$). The static dielectric constant of saline water depends on both temperature and salinity. This static dielectric constant $\varepsilon_{swo}(T, S_{sw})$ is given by (C.5) [1]. In (C.5), $\varepsilon_{swo}(T, 0)$ and $a(T, S_{sw})$ follow the expressions in (C.6) and (C.7), respectively.

$$\varepsilon_{swo}(T, S_{sw}) = \varepsilon_{swo}(T, 0) \cdot a(T, S_{sw}) \tag{C.5}$$

$$\varepsilon_{swo}(T, 0) = 87.134 - 1.949 \times 10^{-1} \cdot T - 1.276 \times 10^{-2} \cdot T^2 + 2.491 \times 10^{-4} \cdot T^3 \tag{C.6}$$

$$a(T, S_{sw}) = 1.0 + 1.613 \times 10^{-5} \cdot T \cdot S_{sw} - 3.656 \times 10^{-3} \cdot S_{sw} + 3.210 \times 10^{-5} \cdot {S_{sw}}^2 - 4.232 \times 10^{-7} \cdot {S_{sw}}^3 \tag{C.7}$$

The relaxation time of saline water $\tau_{swo}(T, S_{sw})$ at microwave frequencies is given by (C.8) [1]. The terms $\tau_{wo}(T)$ and $b(T, S_{sw})$ are shown in (C.9) and (C.10), respectively.

$$\tau_{swo}(T, S_{sw}) = \tau_{swo}(T, 0) \cdot b(T, S_{sw}) \quad \text{(C.8)}$$

$$\tau_{swo}(T, 0) = \tau_{wo}(T) \quad \text{(C.9)}$$

$$b(T, S_{sw}) = 1.0 + 2.282 \times 10^{-5} \cdot T \cdot S_{sw} - 7.638 \times 10^{-4} \cdot S_{sw} - 7.760 \times 10^{-6} \cdot {S_{sw}}^2 + 1.105 \times 10^{-8} \cdot {S_{sw}}^3 \quad \text{(C.10)}$$

The ionic conductivity $\sigma_i(T, S_{sw})$ is given by (C.11). In (C.11), the ionic conductivity is given in terms of its value at $T = 25°\,\mathrm{C}$, $\sigma_i(25, S_{sw})$, which is given by (C.12). The term φ_i in (C.11) is given by (C.13-C.14).

$$\sigma_i(T, S_{sw}) = \sigma_i(25, S_{sw}) e^{-\varphi_i} \quad \text{(C.11)}$$

$$\sigma_i(25, S_{sw}) = S_{sw}\left(0.18252 - 1.4619 \times 10^{-3} S_{sw} + 2.093 \times 10^{-5} {S_{sw}}^2 - 1.282 \times 10^{-7} {S_{sw}}^3\right) \quad \text{(C.12)}$$

$$\varphi_i = \Delta[2.033 \times 10^{-2} + 1.266 \times 10^{-4}\Delta + 2.464 \times 10^{-6}\Delta^2 - S_{sw}(1.849 \times 10^{-5} - 2.551 \times 10^{-7}\Delta + 2.551 \times 10^{-8}\Delta^2)] \quad \text{(C.13)}$$

$$\Delta = 25°\,\mathrm{C} - T \quad \text{(C.14)}$$

Typically, winter wheat's 5th to 10th Feekes growth stages occur on the months of March to July. Kansas average temperatures on March, April, May, June and July are 7.0° C, 13.5° C, 18.4° C, 23.5° C and 26.0° C, respectively. These temperatures and the room temperature (22° C) are considered in the computation of the dielectric models. Additionally, the typical salinity value of 11 ppt for vegetation material is used.

Figure C.1 shows a comparison of the complex dielectric constant of pure water and saline water over the 1-20 GHz frequency range. For these plots the saline water's salinity and temperature used are $S_{sw} = 11\ ppm$, $T = 18.4°\ \mathrm{C}$ (Kansas average temperature in May), respectively.

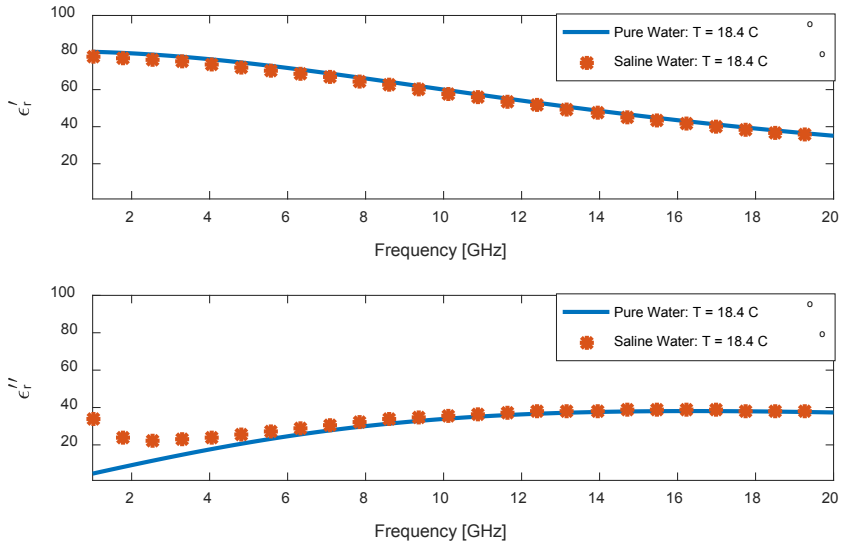

Figure C.1 – Complex Dielectric Constant of Pure and Saline Water at temperature $T = 18.4°\ \mathrm{C}$ and salinity $S_{sw} = 11\ ppm$

Figure C.2 shows a comparison of the complex dielectric constant of saline water at temperatures of $13.5°\ \mathrm{C}$ and $23.5°\ \mathrm{C}$ over the 1-20 GHz frequency range.

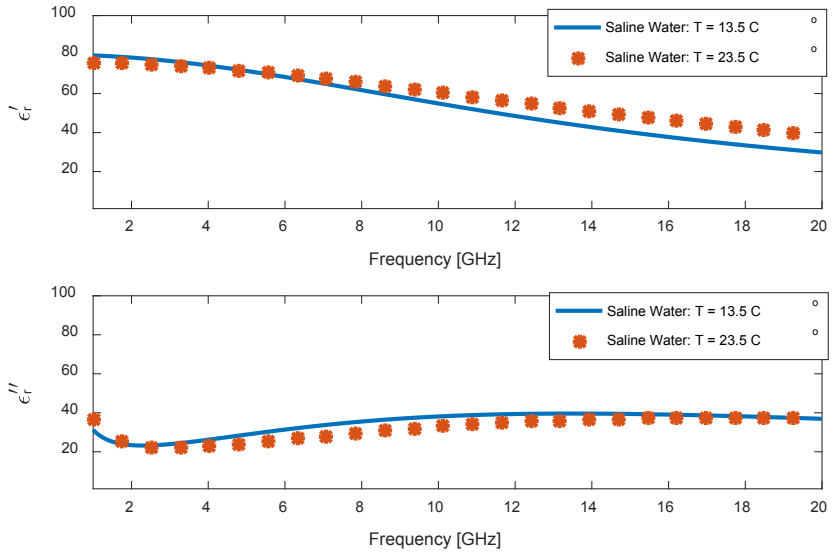

Figure C.2 – Complex Dielectric Constant of Saline Water at salinity $S_{sw} = 11\ ppm$, temperatures $T = 13.5°\ \mathrm{C}$ and $T = 23.5°\ \mathrm{C}$

C.1 References

[1] F. Ulabi, R. K. Moore, A. K. Fung, “Microwave Remote Sensing, Active and Passive”, Volume III, Norwood, MA: Artech House, 1986.

[2] P. Debye, “Polar Molecules,” New York: Dover, 1929.

Appendix D: Dielectric Properties of Vegetation Material

D.1 Moisture Content and Volume Fractions

D.1.1 Gravimetric and Volumetric Moisture of Vegetation Material

The amount of water in vegetation material is usually given using the gravimetric moisture content m_g [2-3]. The gravimetric moisture content or simply "moisture content" is the ratio of the weight of water by the total weight of the vegetation material. This ratio is shown in (D.1). Some dielectric models use the volumetric moisture content. The volumetric moisture content can be found using (D.2), where ρ_{dv} is the density of dry vegetation. A typical value for ρ_{dv} is 0.332.

$$m_g = \frac{W_w}{W_v} = \frac{W_w}{W_w + W_{dv}} \tag{D.1}$$

$$m_v = \frac{m_g\, \rho_{dv}}{1 - m_g(1 - \rho_{dv})} \tag{D.2}$$

D.1.2 Water Volume Fraction: Bound and Free Water

The volumetric moisture content m_v is also referred to as the fractional volume of water v_w. This fractional volume of water can be broken down into the fractional volume of water that is bound

to vegetation material v_{bw} and the fractional volume of water that is free v_{fw} (unbound), as shown in (D.3).

$$m_v = v_w = v_{fw} + v_{bw} \tag{D.3}$$

The fractional volume of bound water has a maximum limit, the maximum fractional volume of bound water $v_{bw,max}$ [3]. If the volumetric water content is larger than $v_{b,max}$, then the fractional volume of bound water is equal to $v_{b,max}$ (D.4). Otherwise, the fractional volume of bound water is equal to the volumetric water content (D.5). Therefore, if the volumetric moisture content is larger than $v_{b,max}$, the fractional volume of free water is zero.

$$v_{bw} = v_{bw,max} \;\; if \;\; m_v \geq v_{b,max} \tag{D.4}$$

$$v_{bw} = m_v \qquad if \;\; m_v < v_{b,max} \tag{D.5}$$

D.1.3 Vegetation Volume Fractions

The fractional volume of solid vegetation v_v can be decomposed into the fractional volume of solid vegetation that binds to water v_{bv} and the rest of solid vegetation v_{rv}, as shown in (D.6) [3].

$$v_v = v_{bv} + v_{rv} \tag{D.6}$$

The fractional volume of solid vegetation that binds to water is proportional to the fractional volume of bound water, as given by (D.7), where x_b is the factor of proportionality.

$$v_{bv} = x_b v_{bw} \tag{D.7}$$

The sum of the fractional volumes due to bound water and the part solid vegetation that binds to water is defined as v_{bm} (D.8).

$$v_{bm} = v_{bw} + v_{bv} \tag{D.8}$$

D.1.4 Air Volume Fraction

The fractional volume of air in vegetation material is the volume fraction that is not related to solid vegetation or water, as shown in (D.9).

$$v_a = 1 - v_v - v_w = 1 - v_v - m_v \tag{D.9}$$

D.1.5 Dielectric Model of Bound Water in Vegetation Materials

In a vegetation material, bound water is the fraction of water for which its molecules are bound to part of the vegetation material [3]. Because the water molecules are bound, the dielectric behavior of this kind of water differs from free (unbound) water.

El-Rayes found that the Cole-Cole formula in (D.10) approximates well the dielectric of bound water [3]. In (D.10), $\varepsilon_{bw\infty}$, ε_{bws}, f_{bw} and α_{bw} are the high frequency dielectric constant, static dielectric constant, relaxation frequency and Cole-Cole relaxation parameter of bound water.

$$\varepsilon_{bw} = \varepsilon_{bw\infty} + \frac{\varepsilon_{bws} - \varepsilon_{bw\infty}}{1 + (jf/f_b)^{1-\alpha_{bw}}} \quad \text{(D.10)}$$

In [3], the values for the parameters $\varepsilon_{bw\infty}$, ε_{bws}, f_{bw} and α_{bw} were found to be 2.9, 57.9, 0.178 GHz and 0.5, respectively.

D.2 Dielectric Models of Vegetation Material

D.2.1 Refractive Model

The simplest dielectric mixing model we consider is the refractive model. This model approximates the refractive index of a mixture as the linear combination of refractive index in the mixture scaled by their volume fraction [1]. Neglecting bound water and air, the refractive model of vegetation material due to free-water and dry-vegetation is given by (D.11).

$$\varepsilon_{rv}{}^{1/2} = m_v \varepsilon_{fw}{}^{1/2} + (1 - m_v)\varepsilon_{dv}{}^{1/2} \quad \text{(D.11)}$$

D.2.2 DeLoor's Model

The deLoor dielectric mixing model is a multi-phase mixing model for a medium with disperse randomly oriented and randomly distributed inclusions [1] [3-6]. This model was proposed by Polder, Van Santan and DeLoor. The formula of the DeLoor mixing model is given by (D.12) [4-6].

$$\varepsilon_m = \varepsilon_h + \sum_{i=1}^{n} \frac{v_i(\varepsilon_i - \varepsilon_h)}{3} \sum_{i=1}^{3} \frac{1}{1 + \left(\frac{\varepsilon_i}{\varepsilon^*}\right) A_i} \quad \text{(D.12)}$$

In (D.12), ε_m, ε_i, ε_h, ε^* are the macroscopic dielectric constant of the medium, the dielectric constant of the inclusions, the dielectric constant of the host and the effective dielectric constant near the inclusion-host boundary, respectively. In (D.12), A_j is the depolarization factor along the main axes of the ellipsoidal inclusions and '*n*' is the number of types of inclusions in the mixture.

El-Rayes used the deLoor model, by considering air as the host medium, water and solid vegetation as the inclusions. The inclusions were assumed disc-shaped and randomly oriented. As noted earlier, free water is only present if the volumetric moisture content is larger than $v_{bw,max}$. The deLoor mixing model for vegetation material for moisture contents below and above $v_{bw,max}$ is given by (D.13-D.14) [3].

$$\varepsilon_{rv} = \frac{\varepsilon_a + \frac{2}{3} v_{bm}(\varepsilon_{bw} - \varepsilon_a) + \frac{2}{3} v_{fw}(\varepsilon_{fw} - \varepsilon_a)}{1 - \frac{1}{3} v_{bm}\left(1 - \frac{\varepsilon_a}{\varepsilon_{bw}}\right) - \frac{1}{3} v_{fw}\left(1 - \frac{\varepsilon_a}{\varepsilon_{fw}}\right)} \quad \text{if } m_v \geq v_{bw,max} \quad \text{(D.13)}$$

$$\varepsilon_{rv} = \frac{\varepsilon_a + \frac{2}{3} v_{bm}(\varepsilon_{bw} - \varepsilon_a) + \frac{2}{3} v_{rv}(\varepsilon_v - \varepsilon_a)}{1 - \frac{1}{3} v_{bm}\left(1 - \frac{\varepsilon_a}{\varepsilon_{bw}}\right) - \frac{1}{3} v_{rv}\left(1 - \frac{\varepsilon_a}{\varepsilon_v}\right)} \quad \text{if } m_v < v_{bw,max} \quad \text{(D.14)}$$

D.2.3 El-Rayes Model

El-Rayes and Ulaby developed a semi-empirical Debye-like model for vegetation material [7-8]. This model approximates the complex dielectric of vegetation material as a linear combination of dielectric constants due to free-water and bound-water, where each term is scaled by its

fractional volume. The model is given by (D.15). The bias term ε_{rv0} and the relation of the fractional volumes (v_{fw} and v_{bw}) to the moisture content m_g were found using regressions.

$$\varepsilon_{rv} = \varepsilon_{rv0} + \varepsilon_{fw} v_{fw} + \varepsilon_{bw} v_{bw} \tag{D.15}$$

$$\varepsilon_{rv0} = 1.7 - 0.74\, m_g + 6.16\, {m_g}^2 \tag{D.16}$$

$$v_{fw} = 0.55\, m_g + 0.0076\, {m_g}^2 \tag{D.17}$$

$$v_{bw} = 4.64/\left({m_g}^2 + 7.36 \right) \tag{D.18}$$

D.2.4 Matzler's Model

Matzler developed a simple semi-empirical model for leaves over the frequency range of 1-100 GHz and moisture content of 0.5-0.9. Matlzer model's equation is show in (D.19) [9].

$$\varepsilon_{rv} = 0.522\big(1 - 1.32(1 - m_v)\big)\varepsilon_{fw} + 0.51 + 3.84(1 - m_v) \tag{D.19}$$

D.2.5 Model Comparison

Figures D.1, D.2 and D.3 show the dielectric constant of vegetation material computed with the various models presented in this section. These dielectric constants were computed using a temperature of $T = 22°C$ and salinity $S_{sw} = 11\, ppt$. The moisture content m_g used in each case is indicated in the caption of each related figure. Both the Matzler and El-Rayes models were

empirically found over the frequency region of interest (2-18 GHz). These two models are used with the simulator, where appropriate.

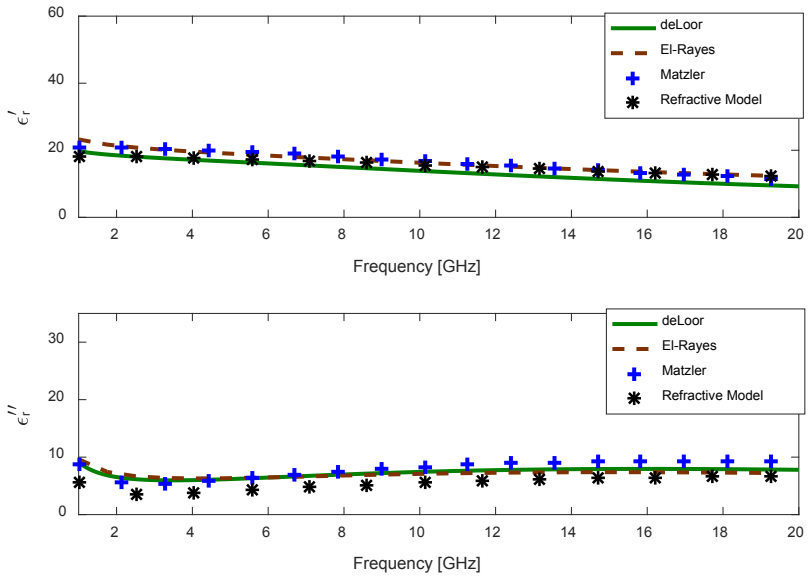

Figure D.1 – Comparison of Dielectric Models of Vegetation Material. $m_g = 0.6$

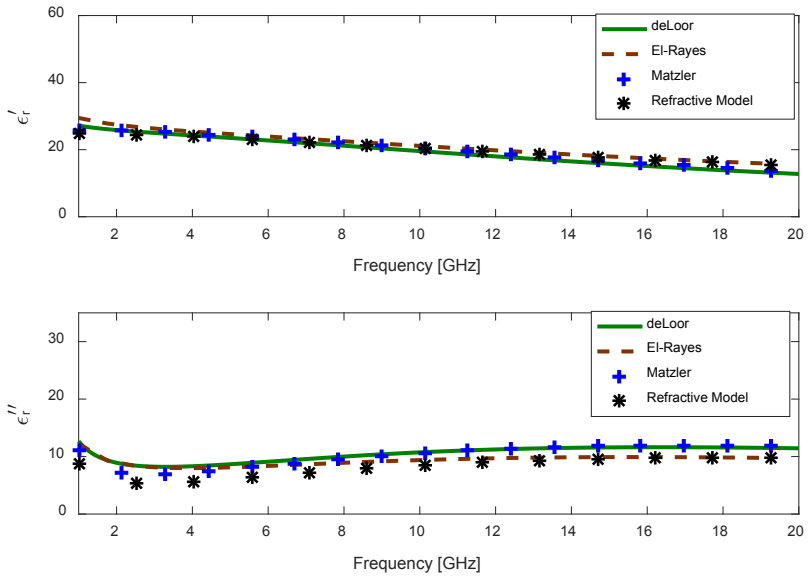

Figure D.2 – Comparison of Dielectric Models of Vegetation Material. $m_g = 0.7$

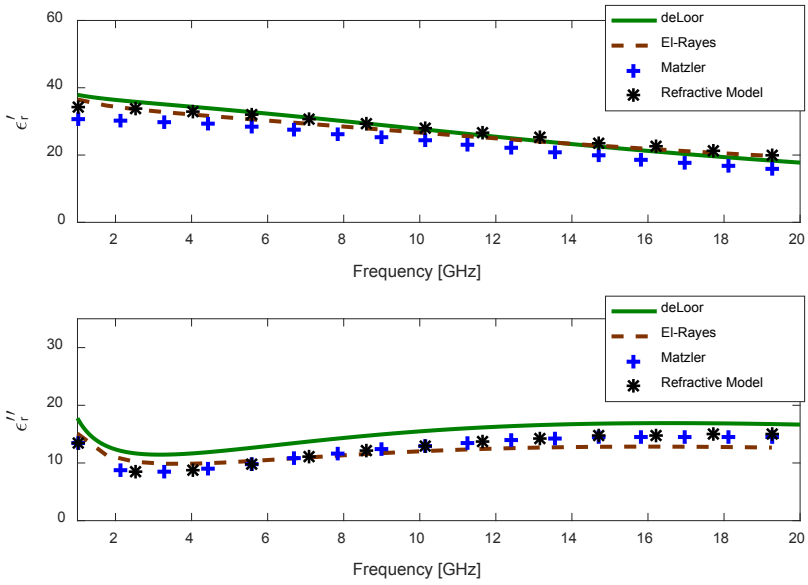

Figure D.3 – Comparison of Dielectric Models of Vegetation Material. $m_g = 0.8$

D.1 References

[1] F. Ulabi, R. K. Moore, A. K. Fung, “Microwave Remote Sensing, Active and Passive”, Volume III, Norwood, MA: Artech House, 1986.

[2] A. Chukhlantsev, “Microwave Radiometry of Vegetation Canopies,” The Netherlands: Springer, 2006.

[3] M. A. El-Rayes, “The Measurement and Modeling of the Dielectric Behavior of Vegetation Materials in the Microwave Region (0.5-20.4 GHz),” Doctoral Dissertation, University of Kansas, 1986.

[4] D. Polder, J. Van Santeen, “The effective permeability of mixture of solids,” Physica, vol. 12, no. 5, pp. 257-271, 1946.

[5] G. P. De Loor, “Dielectric properties of heterogeneous mixtures with a polar constituent,” Applied Scientific Research, Section B, vol. 11, no. 3, pp 310-320, 1964.

[6] G. P. De Loor, “Dielectric Properties of Heterogeneous Mixtures containing water,” Journal of Microwave Power, vol. 3, no. 2, pp. 67-73, 1968.

[7] M. A. El-Rayes and F. T. Ulaby, "Microwave Dielectric Spectrum of Vegetation-Part I: Experimental Observations," in *IEEE Transactions on Geoscience and Remote Sensing*, vol. GE-25, no. 5, pp. 541-549, Sept. 1987.

[8] F. T. Ulaby and M. A. El-Rayes, "Microwave Dielectric Spectrum of Vegetation - Part II: Dual-Dispersion Model," in *IEEE Transactions on Geoscience and Remote Sensing*, vol. GE-25, no. 5, pp. 550-557, 1987.

[9] C. Matzler, "Microwave (1-100 GHz) dielectric model of leaves," in *IEEE Transactions on Geoscience and Remote Sensing*, vol. 32, no. 4, pp. 947-949, Jul 1994.

Appendix E: Propagation in Sparse Inhomogeneous Media

A volume of a sparse inhomogeneous medium can be thought of as a set of targets in a volume of space, where the number density of targets is low. In an inhomogeneous medium, even with a low number density of targets, significant obstruction in the line-of-sight between the antennas to some targets (i.e. shadowing) may occur.

If we attempt to treat this medium as a complex target, its coherent radar equation may be inaccurate if significant shadowing is present. This inaccuracy can be improved by using an effective propagation constant in the propagation function of waves within the inhomogeneous medium. We choose to approximate the effective propagation constant as that of the mean field. This approximation is known as the distorted Born approximation [1-2].

The Foldy-Lax equations are two coupled and recursive equations that fully describe the scattered field due to a volume of targets where multiple scattering occurs. Foldy's approximation (FA) is the truncation in the first hierarchy of the aforementioned equations. FA accounts for single scattering in the propagation and scattering of the medium.

According to FA, the mean field $\langle \mathbf{E} \rangle$ along the propagation direction follows the relationship in (E.1), where $\bar{\bar{\mathbf{K}}}_e$ is the effective propagation dyadic and $\bar{\bar{\mathbf{M}}}$ is the mass function (E.2) [2].

$$\frac{d\langle \mathbf{E} \rangle}{ds} = j\bar{\bar{\mathbf{K}}}_e \cdot \langle \mathbf{E} \rangle = j\left[k_o\left(\bar{\bar{\mathbf{I}}} - \hat{k}\hat{k}\right) - j\bar{\bar{\mathbf{M}}}\right] \cdot \langle \mathbf{E} \rangle \tag{E.1}$$

$$\bar{\bar{\mathbf{M}}} = \frac{jn_o}{2k_o}\langle \bar{\bar{\mathbf{F}}}(\mathbf{k}, \mathbf{k}) \rangle \tag{E.2}$$

The number density is the number of objects per unit volume (E.3). Thus, the mass function can be approximated to the expression in (E.4).

$$n_o = \frac{N}{v} = \frac{N}{A\,h} \tag{E.3}$$

$$\bar{\bar{\mathbf{M}}} \approx \frac{j}{2k_o v} \sum_{\boldsymbol{n}} \bar{\bar{\mathbf{F}}}_{\boldsymbol{n}}(\mathbf{k}, \mathbf{k}) \tag{E.4}$$

If the volume exhibits statistical azimuthal symmetry, cross polarization terms in the mass function are negligible **(**$\hat{h} \cdot \bar{\bar{\mathbf{M}}} \cdot \hat{v} \approx \hat{v} \cdot \bar{\bar{\mathbf{M}}} \cdot \hat{h} \approx 0$**).** In this case, the effective propagation dyadic takes the form in (E.5), and it may be expressed as a vector (E.6). The propagation constant components k_{ev} and k_{eh} are given by (E.7) and (E.8), respectively. The terms k_{ev} and k_{eh} depend on the forward scattering dyad $\bar{\bar{\mathbf{F}}}_{\boldsymbol{n}}(\mathbf{k}, \mathbf{k})$ evaluated in the direction of propagation $\mathbf{k}$**.**

$$\bar{\bar{\mathbf{K}}}_{\boldsymbol{e}} = k_{ev}\hat{v}\hat{v} + k_{eh}\hat{h}\hat{h} \tag{E.5}$$

$$\mathbf{k}_{\boldsymbol{e}} = k_{ev}\hat{v} + k_{eh}\hat{h} \tag{E.6}$$

$$k_{ev} = k_o + \frac{1}{2k_o v} \sum_{n} \hat{v} \cdot \bar{\bar{\mathbf{F}}}_{\boldsymbol{n}}(\mathbf{k}, \mathbf{k}) \cdot \hat{v} \tag{E.7}$$

$$k_{eh} = k_o + \frac{1}{2k_o v} \sum_{n} \hat{h} \cdot \bar{\bar{\mathbf{F}}}_{\boldsymbol{n}}(\mathbf{k}, \mathbf{k}) \cdot \hat{h} \tag{E.8}$$

The segment of distance between the target position and the antenna position that is inside the inhomogeneous medium volume can be determined with trigonometry. The segment related to the transmit antenna and the receive antennas are given by (E.9) and (E.10), respectively.

$$r_{et} = |\mathbf{r_n} - \mathbf{r}_t| \left[1 - \frac{\mathbf{r}_t \cdot \hat{z} - h_c}{(\mathbf{r_t} - \mathbf{r_n}) \cdot \hat{z}}\right] \quad \text{(E.9)}$$

$$r_{er} = |\mathbf{r_r} - \mathbf{r_n}| \left[1 - \frac{\mathbf{r}_r \cdot \hat{z} - h_c}{(\mathbf{r_r} - \mathbf{r_n}) \cdot \hat{z}}\right] \quad \text{(E.10)}$$

Given the distance of the propagation path inside the volume and the effective propagation constant, the coherent radar equation can be adjusted by including the phase correction factor $\Phi_e(\mathbf{r}_n)$ (E.11). The correction function is shown in (E.12), where k_{eq} is the propagation constant for polarization *'q'* (*q = v or h*).

$$V_r(\omega) = jk\eta Z_a V_t(\omega) \sum_{n=1}^{N} \Phi_e(\mathbf{r}_n)\Phi_r(\mathbf{r_r}, \mathbf{r_n})\, \Phi_t(\mathbf{r_n}, \mathbf{r}_t) \left[\, \mathbf{f_r}\left(\hat{\mathbf{k}}_s(\mathbf{r_n})\right) \cdot Rot\left(\bar{\bar{\mathbf{F}}}_n^{\boldsymbol{b}}(\mathbf{k}_s, \mathbf{k}_i), \mathbf{o_n}\right) \cdot \mathbf{f_t}(\hat{\mathbf{k}}_i(\mathbf{r_n}))\right] \quad \text{(E.11)}$$

$$\Phi_e(\mathbf{r}_n) = e^{j(\mathrm{k}_{eq} - k_o)(r_{et} + r_{er})} \quad \text{(E.12)}$$

E.1 References

[1] R. H. Lang, J. S. Sidhu, "Electromagnetic backscattering from a layer of vegetation: a discrete approach," IEEE Transactions on Geoscience and Remote Sensing, vol. GE-21, no. 1, Jan. 1983.

[2] L. Tsang, J. A. Kong, *Scattering of Electromagnetic Waves: Advanced Topics*, New York: Wiley Inter-science, 2000.

Appendix F: Radar System Block Diagram

F.1 - Radar (High-Level)

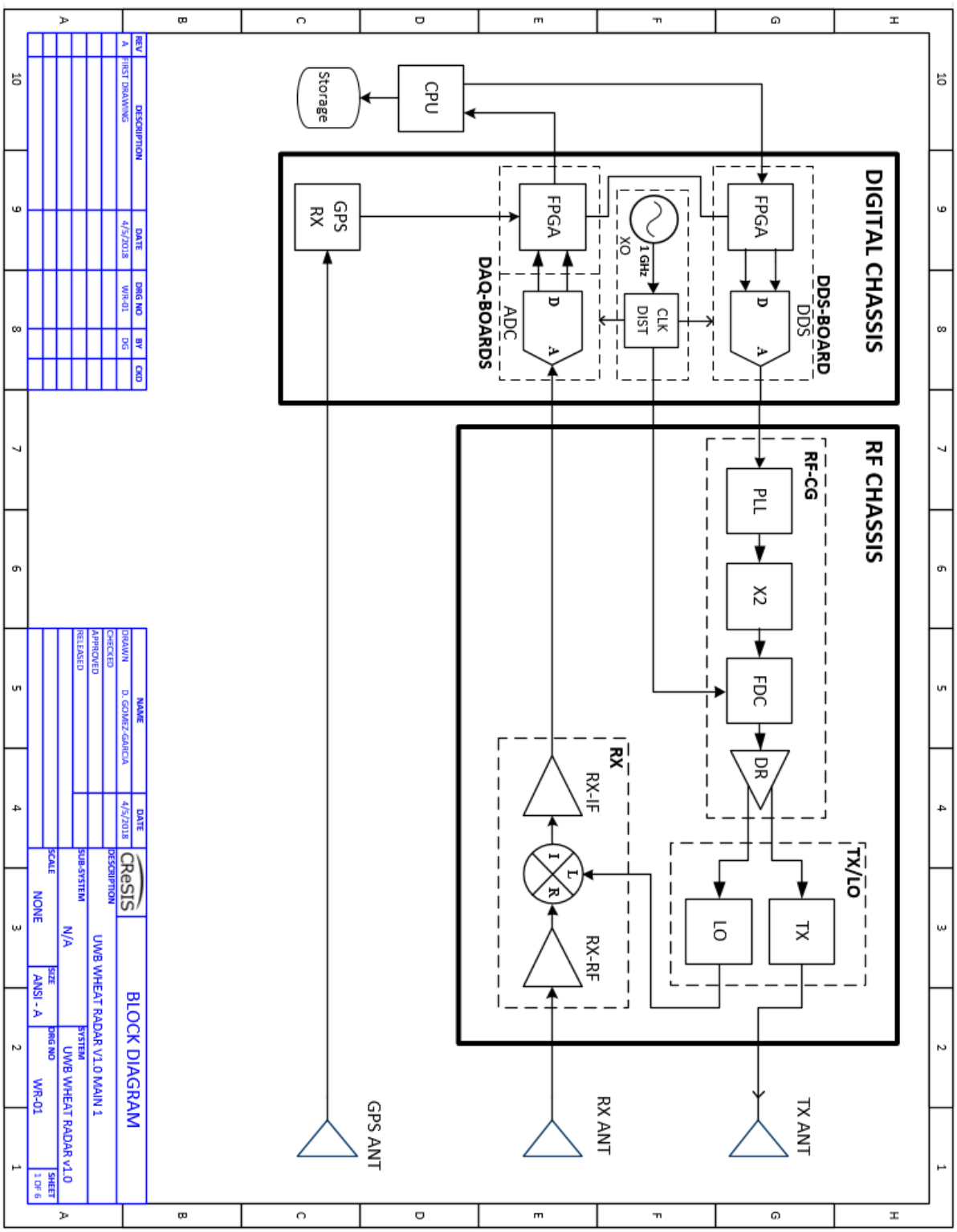

F.2 – CG-RF: PLL

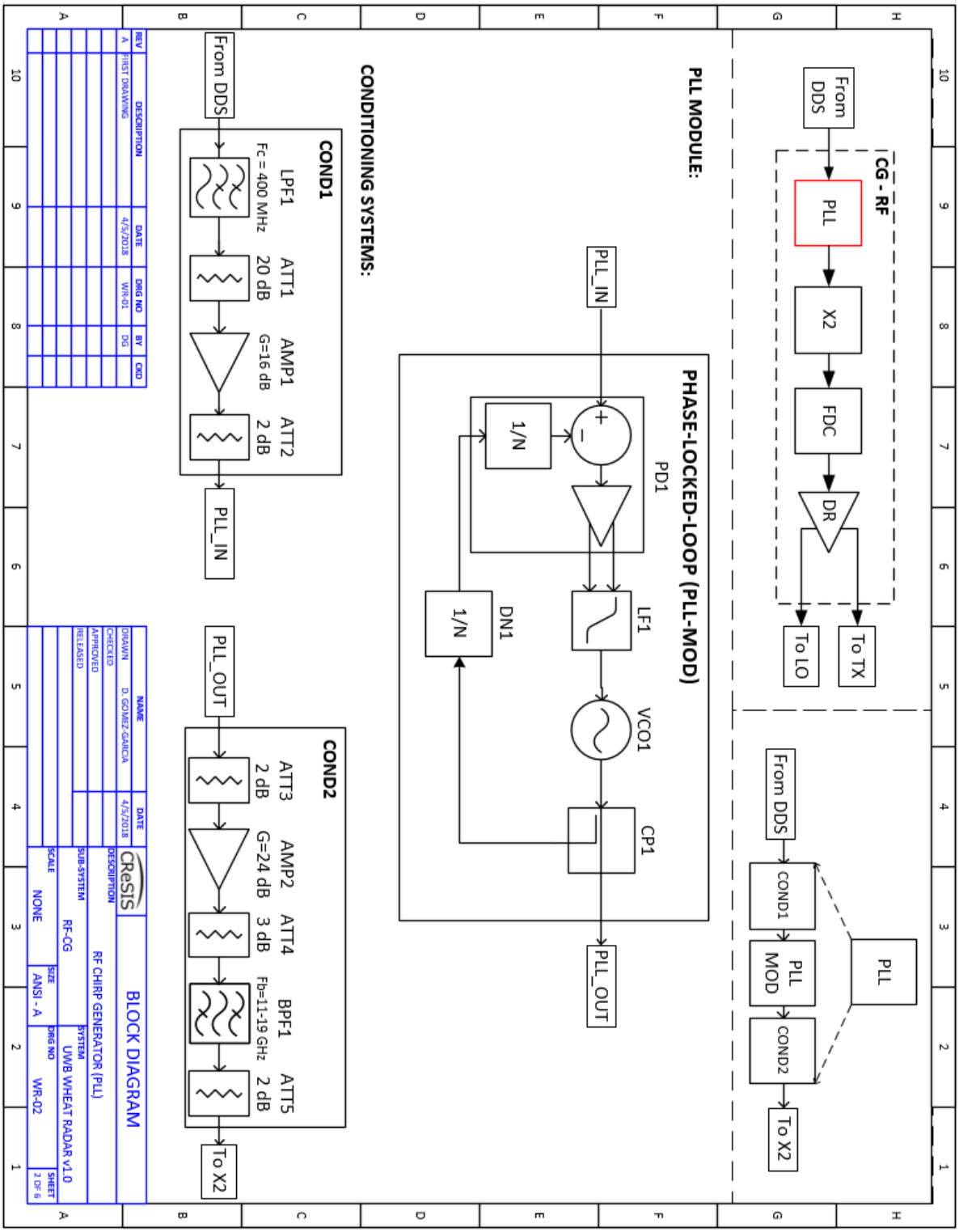
CG - RF
From DDS
PLL
X2
FDC
DR
To LO
To TX
PLL MODULE:
From DDS
COND1
PLL MOD
COND2
To X2
PLL
PHASE-LOCKED-LOOP (PLL-MOD)
PLL_IN
PD1
1/N
LF1
VCO1
CP1
DN1
1/N
PLL_OUT
CONDITIONING SYSTEMS:
COND1
From DDS
LPF1
Fc = 400 MHz
ATT1
20 dB
AMP1
G=16 dB
ATT2
2 dB
PLL_IN
PLL_OUT
COND2
ATT3
2 dB
AMP2
G=24 dB
ATT4
3 dB
BPF1
Fb=11-19 GHz
ATT5
2 dB
To X2
REV
DESCRIPTION
DATE
DRG NO
BY
CKD
A
FIRST DRAWING
4/5/2018
WR-01
DG
NAME
DATE
DRAWN
D. GOMEZ-GARCIA
4/5/2018
CHECKED
APPROVED
RELEASED
CReSIS
BLOCK DIAGRAM
DESCRIPTION
RF CHIRP GENERATOR (PLL)
SUB-SYSTEM
RF-CG
SYSTEM
UWB WHEAT RADAR v1.0
SCALE
NONE
SIZE
ANSI - A
DRG NO
WR-02
SHEET
2 OF 6

F.3 – CG-RF: X2/FDC

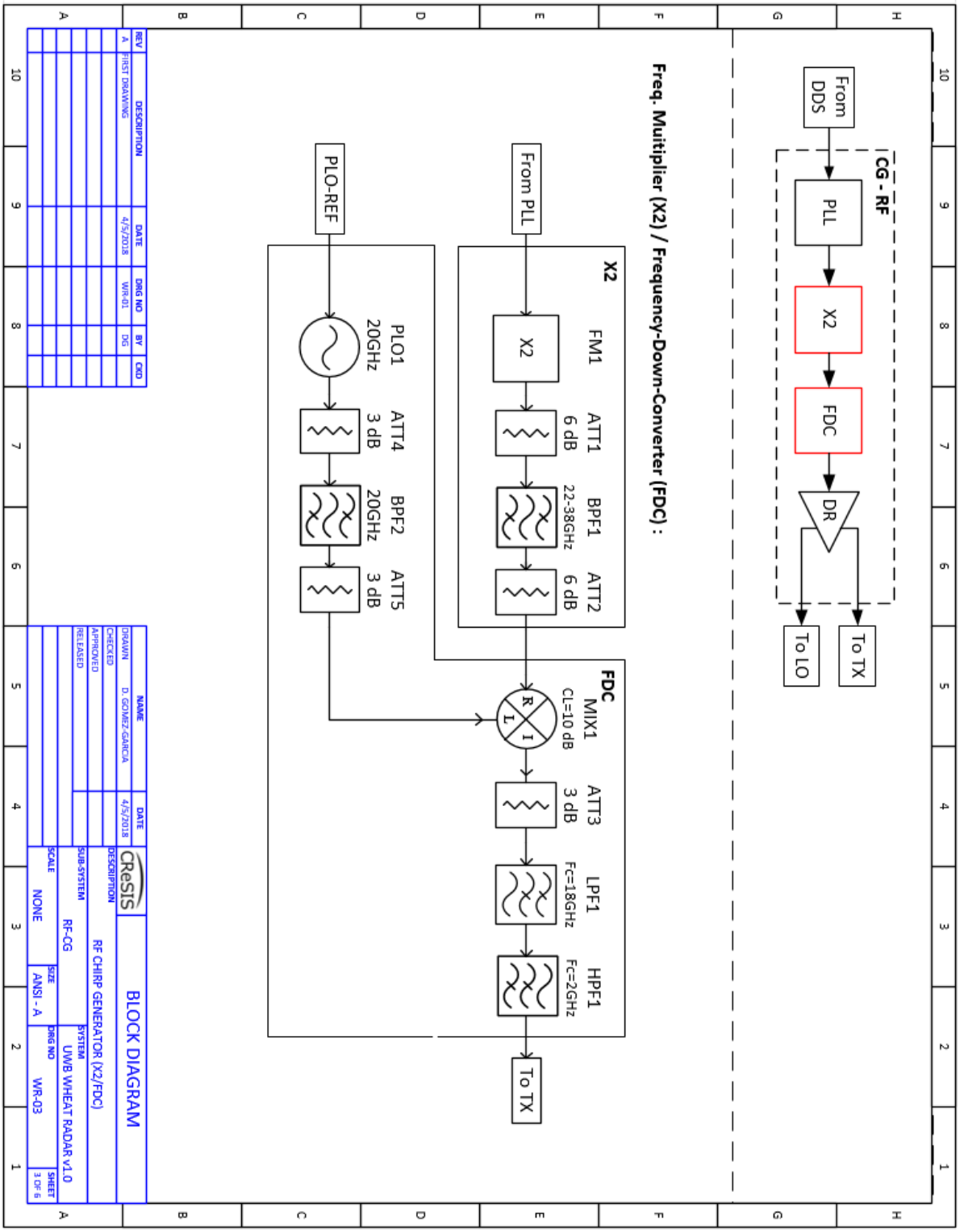

F.4 – CG-RF: DR

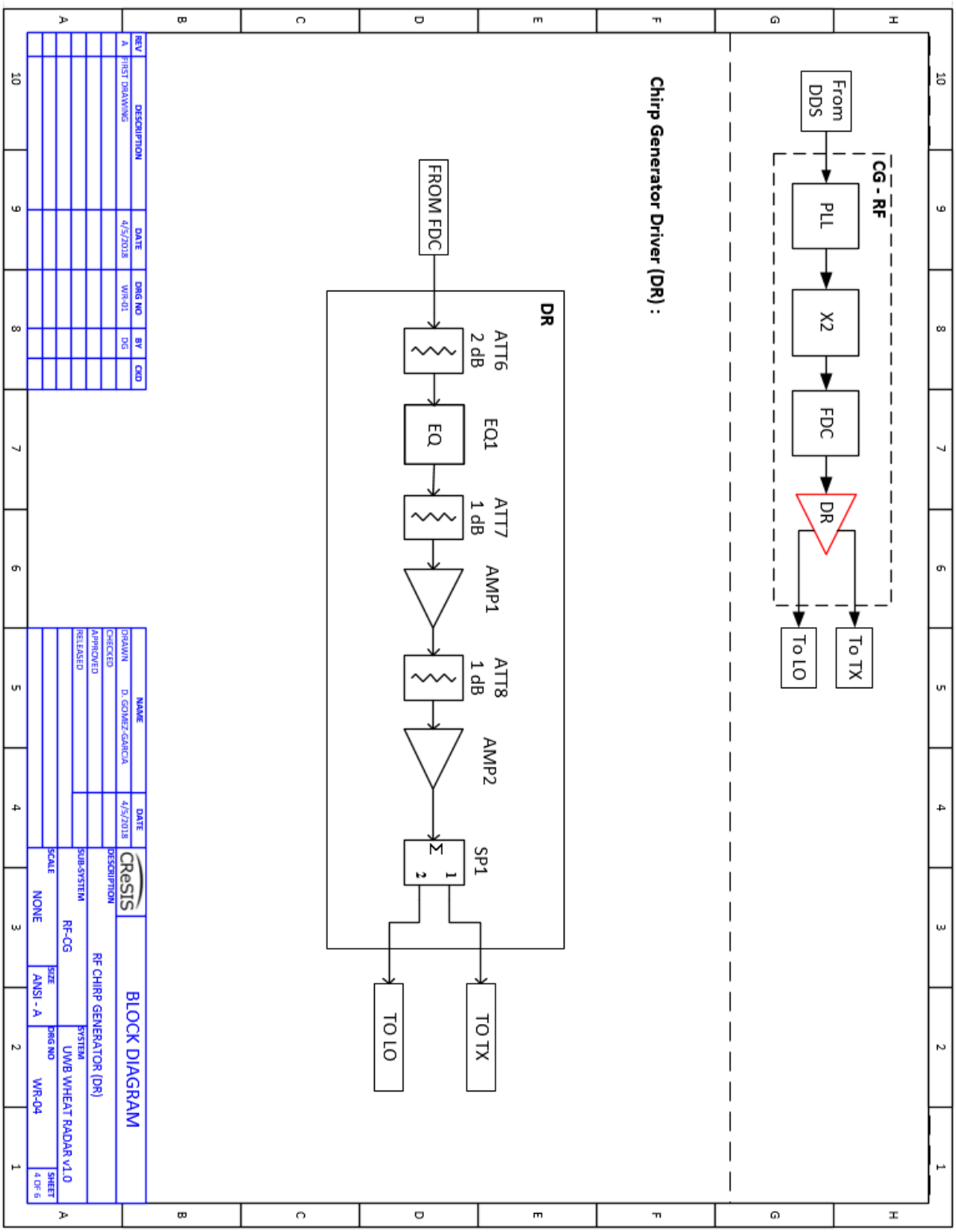
CG - RF
From DDS
PLL
X2
FDC
DR
To TX
To LO
Chirp Generator Driver (DR) :
DR
FROM FDC
ATT6 2 dB
EQ1
EQ
ATT7 1 dB
AMP1
ATT8 1 dB
AMP2
SP1
TO TX
TO LO
REV
DESCRIPTION
DATE
DRG NO
BY
CKD
A
FIRST DRAWING
4/5/2018
WR-01
DG
NAME
DATE
DRAWN
D. GOMEZ-GARCIA
4/5/2018
CHECKED
APPROVED
RELEASED
DESCRIPTION
BLOCK DIAGRAM
RF CHIRP GENERATOR (DR)
SUB-SYSTEM
RF-CG
SYSTEM
UWB WHEAT RADAR v1.0
SCALE
NONE
SIZE
ANSI - A
DRG NO
WR-04
SHEET
4 OF 6

F.5 – TX/LO

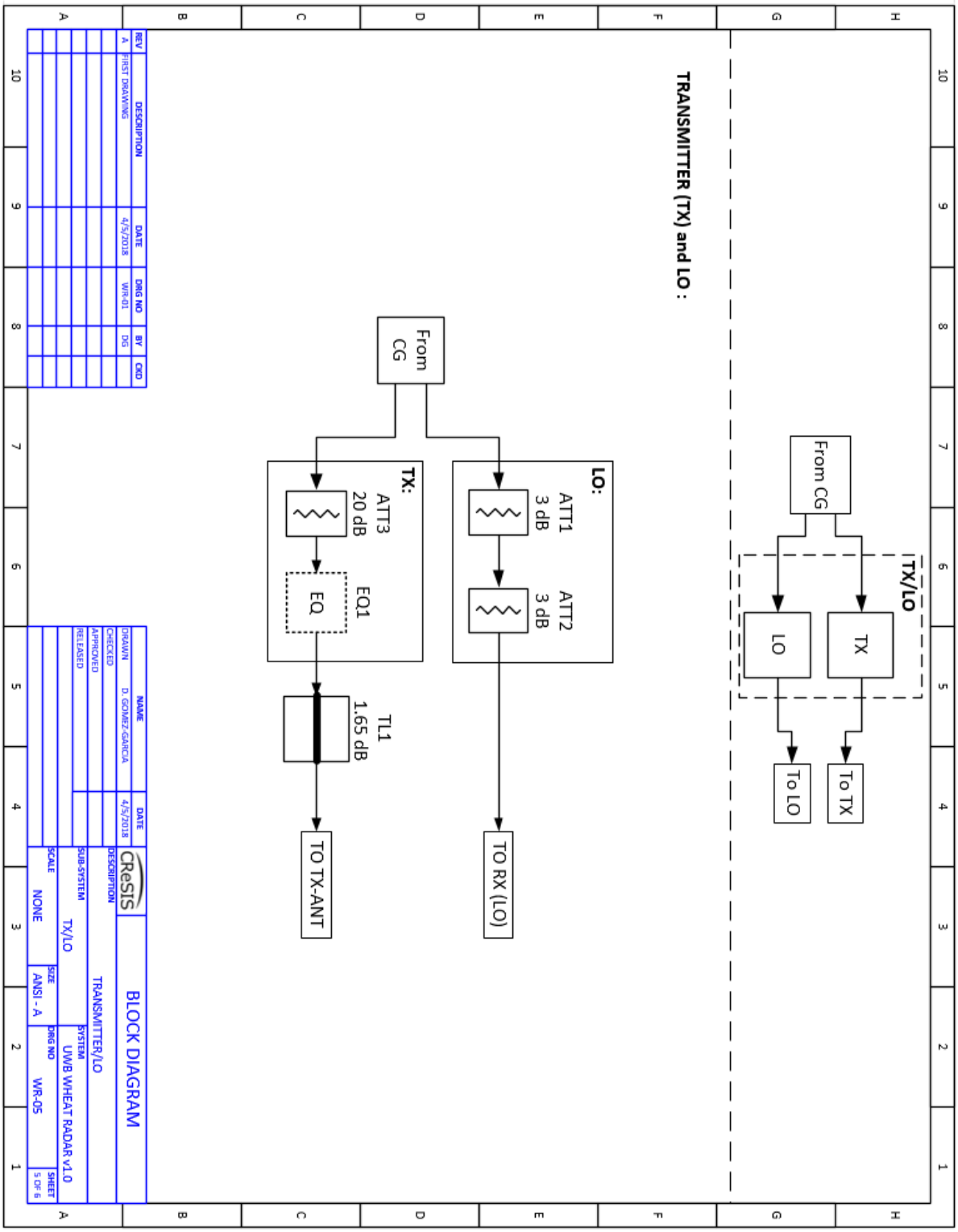
TRANSMITTER (TX) and LO :
From CG
TX/LO
TX
LO
To TX
To LO
From CG
LO:
ATT1
3 dB
ATT2
3 dB
TO RX (LO)
TX:
ATT3
20 dB
EQ1
EQ
TL1
1.65 dB
TO TX-ANT
REV
DESCRIPTION
DATE
DRG NO
BY
CKD
A
FIRST DRAWING
4/5/2018
WR-01
DG
NAME
DATE
DRAWN
D. GOMEZ-GARCIA
4/5/2018
CHECKED
APPROVED
RELEASED
DESCRIPTION
BLOCK DIAGRAM
TRANSMITTER/LO
SUB-SYSTEM
TX/LO
SYSTEM
UWB WHEAT RADAR v1.0
SCALE
NONE
SIZE
ANSI - A
DRG NO
WR-05
SHEET
5 OF 6

F.6 – RX

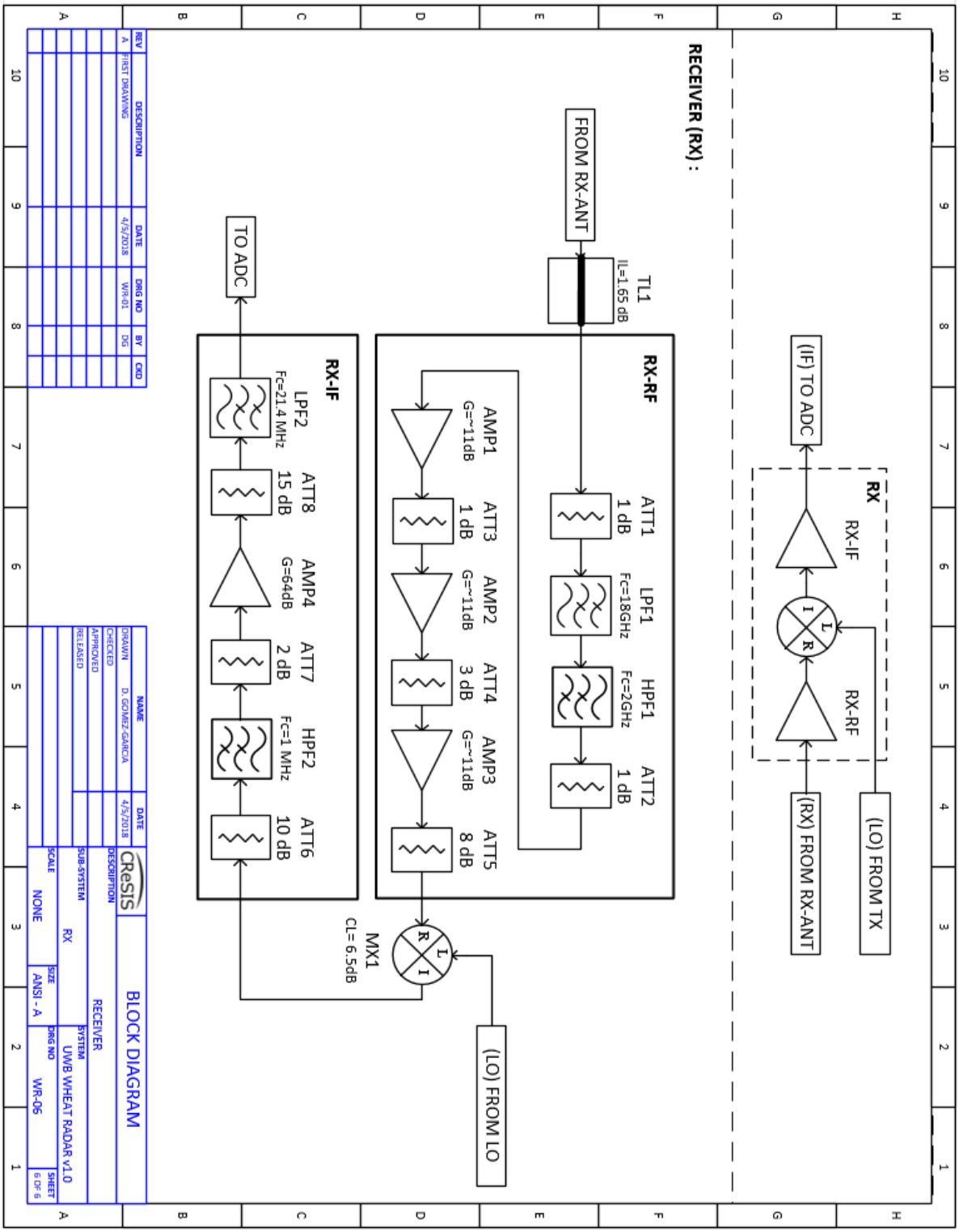
RX
RX-IF
RX-RF
(IF) TO ADC
(RX) FROM RX-ANT
(LO) FROM TX
RECEIVER (RX) :
RX-RF
FROM RX-ANT
TL1
IL=1.65 dB
ATT1 1 dB
LPF1 Fc=18GHz
HPF1 Fc=2GHz
ATT2 1 dB
AMP1 G=~11dB
ATT3 1 dB
AMP2 G=~11dB
ATT4 3 dB
AMP3 G=~11dB
ATT5 8 dB
MX1
CL= 6.5dB
(LO) FROM LO
RX-IF
TO ADC
LPF2 Fc=21.4 MHz
ATT8 15 dB
AMP4 G=64dB
ATT7 2 dB
HPF2 Fc=1 MHz
ATT6 10 dB
REV
DESCRIPTION
DATE
DRG NO
BY
CKD
A
FIRST DRAWING
4/5/2018
WR-01
DG
NAME
DATE
DRAWN
D. GOMEZ-GARCIA
4/5/2018
CHECKED
APPROVED
RELEASED
DESCRIPTION
BLOCK DIAGRAM
RECEIVER
SUB-SYSTEM
RX
SYSTEM
UWB WHEAT RADAR v1.0
SCALE
NONE
SIZE
ANSI - A
DRG NO
WR-05
SHEET
6 OF 6

Appendix G: Measurements of Plant Samples

G.1 Manual Measurements: 2018-05-07

Table G.1 – Manual Measurements 2018-05-07: Plant, Head and Stem

	Plant			Head		Stem	
PLOT#	**$H_{H,P}$ [mm]**	**$H_{L,P}$ [mm]**	**H_P [mm]**	**L_H [mm]**	**a_H [mm]**	**L_S [mm]**	**a_S [mm]**
8	360.0	375.0	375.0	40.0	3.0	355.0	1.5
10	361.0	364.3	364.3	40.0	3.0	356.0	1.3
12	361.0	383.5	383.5	40.0	3.0	356.0	1.3
13	386.0	400.0	400.0	50.0	3.5	381.0	1.3
13	386.0	405.5	405.5	50.0	3.5	381.0	1.3
Mean	370.8	385.7	385.7	44.0	3.2	365.8	1.3
STD	13.9	17.1	17.1	5.5	0.3	13.9	0.1

Table G.2 – Manual Measurements 2018-05-07: Leaf 1 (Top)

	Leaf 1 - Top								
PLOT#	**$r_{Z,L}$ [mm]**	**L_L [mm]**	**w_L [mm]**	**a_L [mm]**	**$\theta_{i,L}$ [deg]**	**$\theta_{f,L}$ [deg]**	**R_L [mm]**	**$s_{o,L}$**	**$m_{g,L}$**
8	350.0	100.0	12.0	0.20	60.0	60.0	inf	1.00	0.72
10	351.0	90.0	10.0	0.24	10.0	100.0	36.0	0.30	0.72
12	351.0	110.0	12.0	0.21	10.0	10.0	inf	0.60	0.93
13	376.0	80.0	10.0	0.22	0.0	90.0	29.0	0.60	0.57
13	376.0	100.0	13.0	0.18	10.0	10.0	29.0	0.60	0.57
Mean	360.8	96.0	11.4	0.21	18.0	54.0	31.3	0.62	0.70
STD	13.9	11.4	1.3	0.02	23.9	42.8	4.0	0.25	0.15

Table G.3 – Manual Measurements 2018-05-07: Leaf 2 (Middle)

	Leaf 2 - Middle								
PLOT#	**$r_{z,L}$ [mm]**	**L_L [mm]**	**w_L [mm]**	**a_L [mm]**	**$\theta i_{,L}$ [deg]**	**$\theta_{f,L}$ [deg]**	**R_L [mm]**	**$s_{o,L}$**	**$m_{g,L}$**
8	190.0	120.0	10.0	0.18	25.0	65.0	36.0	0.60	0.72
10	180.0	140.0	10.0	0.24	20.0	120.0	16.0	0.60	0.95
12	270.0	140.0	8.0	0.20	15.0	85.0	16.0	0.60	0.57
13	220.0	110.0	10.0	0.18	10.0	70.0	29.0	0.50	0.65
13	220.0	150.0	10.0	0.18	15.0	150.0	36.0	0.60	0.65
Mean	216.0	132.0	9.6	0.20	17.0	98.0	26.6	0.58	0.71
STD	35.1	16.4	0.9	0.03	5.7	36.2	10.1	0.04	0.15

Table G.4 – Manual Measurements 2018-05-07: Leaf 3 (Bottom)

	Leaf 3 - Bottom								
PLOT#	**$r_{z,L}$ [mm]**	**L_L [mm]**	**w_L [mm]**	**a_L [mm]**	**$\theta_{i,L}$ [deg]**	**$\theta_{f,L}$ [deg]**	**R_L [mm]**	**$s_{o,L}$**	**$m_{g,L}$**
8	50.0	110.0	10.0	0.20	10.0	70.0	29.0	0.40	0.80
10	70.0	110.0	8.0	0.18	10.0	120.0	52.0	0.50	0.62
12	130.0	50.0	8.0	0.18	10.0	10.0	inf	1.00	0.63
13	60.0	110.0	8.0	0.18	10.0	110.0	16.0	0.50	0.56
13	60.0	120.0	8.0	0.18	20.0	150.0	36.0	0.50	0.56
Mean	74.0	100.0	8.4	0.18	12.0	92.0	33.3	0.58	0.63
STD	32.1	28.3	0.9	0.01	4.5	54.0	15.0	0.24	0.10

G.2 Manual Measurements: 2018-05-22

Table G.5 – Manual Measurements 2018-05-22: Plant, Head, Stem

	Plant			Head		Stem	
PLOT#	**$H_{H,P}$ [mm]**	**$H_{L,P}$ [mm]**	**H_P [mm]**	**L_H [mm]**	**a_H [mm]**	**L_S [mm]**	**a_S [mm]**
1	491	498	498	60	4.5	431	1.2
1	578	470	578	70	5	508	1.15
2	540	490	540	70	6	470	1.5
2	563	560	563	80	6	483	1.3
3	482	493	493	70	5	412	1.3
3	459	481	481	65	5	394	0.9
4	532	455	532	75	5	457	1.25
4	563	490	563	80	6	483	1.25
5	553	421	553	70	5	483	1.35
5	540	524	540	70	5	470	1.2
6	527	501	527	70	6.5	457	1.25
6	527	501	527	70	6.5	457	1.25
7	507	494	507	75	4.5	432	1.4
7	489	484	489	70	4.5	419	1.55
8	559	431	559	80	6	559	1.5
8	533	431	533	80	6	559	1.5
9	497	490	497	65	4.5	450	1.1
9	469	489	489	50	4.5	419	1.15
10	553	435	553	70	5	483	1.2
10	540	542	542	70	5	470	1.15
11	591	461	591	70	5	521	1.5
11	578	481	578	70	6	508	1.25
12	553	488	553	70	6	483	1.4
12	581	507	581	60	4.5	521	1.05
Mean	533.4	484.0	536.0	70.0	5.3	471.9	1.3
RMS	36.9	33.5	32.7	6.9	0.7	43.1	0.2

Table G.6 – Manual Measurements 2018-05-22: Leaf 1 (Top)

Leaf 1 - Top

PLOT#	$r_{z,L}$ [mm]	L_L [mm]	w_L [mm]	a_L [mm]	$\theta_{i,L}$ [deg]	$\theta_{f,L}$ [deg]	R_L [mm]	$s_{o,L}$	$m_{g,L}$
1	380	130	8	0.25	25	25	inf	1	0.57
1	430	95	7	0.27	65	65	inf	1	0.57
2	390	130	12	0.25	40	40	inf	1	0.75
2	430	150	12	0.23	30	30	inf	1	0.75
3	405	170	12	0.20	30	70	65	0.6	0.80
3	340	150	12	0.22	20	20	inf	1	0.80
4	390	115	12	0.25	20	30	90	0.6	0.68
4	390	130	13	0.22	40	40	inf	1	0.68
5	380	90	10	0.22	40	50	90	0.6	0.57
5	430	100	8	0.28	20	20	inf	1	0.57
6	380	140	11	0.26	30	30	inf	1	0.75
6	380	140	11	0.26	30	30	inf	1	0.75
7	390	200	13	0.26	30	30	80	0.6	0.81
7	320	175	15	0.27	20	20	inf	1	0.81
8	400	120	11	0.22	75	75	inf	1	0.68
8	400	120	11	0.22	75	75	inf	1	0.68
9	405	150	10	0.22	20	30	80	0.6	0.68
9	380	120	10	0.18	25	25	inf	1	0.68
10	390	100	8	0.28	25	70	70	0.5	0.68
10	410	140	12	0.20	20	20	inf	1	0.68
11	420	120	12	0.18	70	70	inf	1	0.57
11	410	110	12	0.24	50	50	inf	1	0.57
12	390	100	13	0.18	10	10	inf	1	0.53
12	410	100	11	0.16	15	15	inf	1	0.53
Mean	393.8	129.0	11.1	0.23	34.4	39.2	79.2	0.9	0.67
RMS	25.6	27.5	1.9	0.03	19.1	21.0	10.2	0.19	0.09

Table G.7 – Manual Measurements 2018-05-22: Leaf 2 (Middle)

Leaf 2 - Middle

PLOT#	$r_{z,L}$ [mm]	L_L [mm]	w_L [mm]	a_L [mm]	$\theta_{i,L}$ [deg]	$\theta_{f,L}$ [deg]	R_L [mm]	$s_{o,L}$	$m_{g,L}$
1	280	130	8	0.25	20	120	35	0.6	0.57
1	240	130	11	0.17	40	60	70	0.6	0.57
2	210	130	12	0.23	35	35	inf	1	0.83
2	230	140	11	0.23	40	40	inf	1	0.83
3	230	110	8	0.21	30	30	inf	1	0.68
3	170	90	8	0.22	30	30	inf	1	0.68
4	250	100	10	0.30	45	60	70	0.6	0.83
4	210	120	8	0.27	15	15	inf	1	0.83
5	270	130	10	0.20	30	120	40	0.4	0.90
5	180	110	11	0.24	20	90	90	0.8	0.90
6	220	155	8	0.25	15	5	60	0.6	0.75
6	220	155	8	0.25	15	5	60	0.6	0.75
7	180	150	7	0.26	40	40	inf	1	0.57
7	180	80	9	0.24	40	40	inf	1	0.57
8	200	130	7	0.28	25	25	inf	1	0.65
8	200	130	7	0.28	25	25	inf	1	0.65
9	210	140	8	0.20	20	20	inf	1	0.68
9	210	100	10	0.18	25	25	inf	1	0.68
10	220	110	9	0.28	25	25	inf	1	0.63
10	230	120	7	0.20	30	30	inf	1	0.63
11	210	100	8	0.18	25	-5	50	0.6	0.66
11	180	140	12	0.22	30	30	inf	1	0.66
12	180	130	10	0.19	10	10	inf	1	0.60
12	210	90	10	0.22	20	20	inf	1	0.60
Mean	213.3	121.7	9.0	0.23	27.1	37.3	59.4	0.9	0.69
RMS	28.4	20.9	1.6	0.04	9.4	32.3	17.8	0.2	0.11

Table G.8 – Manual Measurements 2018-05-22: Leaf 3 (Bottom)

Leaf 3 - Bottom

PLOT#	$r_{z,L}$ [mm]	L_L [mm]	w_L [mm]	a_L [mm]	$\theta_{i,L}$ [deg]	$\theta_{f,L}$ [deg]	R_L [mm]	$s_{o,L}$	$m_{g,L}$
1	140	50	7	0.25	20	20	inf	1	0.54
1	110	100	7	0.20	20	140	35	0.5	0.54
2	70	50	5	0.20	30	30	inf	1	0.80
2	100	70	8	0.23	30	30	inf	1	0.80
3	100	60	8	0.20	30	50	60	0.5	0.30
3	60	20	5	0.20	20	20	inf	1	0.30
4	80	60	7	0.22	40	40	inf	1	0.30
4	70	30	6	0.27	30	30	inf	1	0.30
5	150	50	7	0.20	30	140	50	0.6	0.27
5	60	50	6	0.20	20	20	inf	1	0.27
6	80	120	8	0.25	35	-5	60	1	0.68
6	80	120	8	0.25	35	-5	60	1	0.68
7	70	35	6	0.19	30	30	inf	1	0.69
7	70	35	8	0.20	90	90	inf	1	0.69
8	70	50	6	0.20	20	20	inf	1	0.23
8	70	50	6	0.20	20	20	inf	1	0.23
9	90	80	5	0.18	15	15	inf	1	0.23
9	90	40	5	0.18	20	20	inf	1	0.23
10	70	50	5	0.28	30	30	inf	1	0.38
10	80	50	8	0.24	25	25	inf	1	0.38
11	80	40	4	0.18	20	20	inf	1	0.30
11	60	0	0	0.20	90	90	inf	1	0.30
12	60	40	5	0.18	20	20	inf	1	0.27
12	80	40	4	0.20	90	90	inf	1	0.27
Mean	82.9	53.8	6.0	0.21	33.8	40.8	53.0	0.9	0.41
RMS	23.3	28.1	1.8	0.03	22.6	39.7	11.0	0.2	0.20

Appendix H: Photograph-Based Retrieval of Projected Leaf Area Density

Top-view of plants show the projected area of the leaves, for those that are not hidden under other leaves. The density of the leaves in the top layers of a wheat canopy is low. So that, almost all the leaves on the top layers are not hidden in a top view photograph. Therefore, the ratio of the projected leaf area of the top layers to the ground area can be determined, if the leaves of the top layers can be identified in the top-view image.

The light intercepted by the leaves decreases with depth. Thus, the top-layer leaves will shine with a higher intensity than bottom-layer leaves. From a top-illuminated top-view digital photograph, the leaves on the top layer can be identified using a threshold on the intensity of the colors. This threshold would separate the bottom and top layers leaves in a photograph.

If the threshold is high, the top layer is small and a lower number of hidden leaves are ignored. However, if the threshold is too large, the area of leaves detected becomes similar to the area of unrelated pixels (i.e. the false alarm rate is increased). If the threshold is too small, the false alarm rate is decreased, but the number of hidden leaves ignored increases.

Since the leaf area of the top-most layer of the majority of wheat canopies is small, we choose to set the threshold that accounts for the top and middle foliage layers in the canopy. These top two leaf layers occupy the top two thirds of the canopy. Figure H.1 shows a top-view of a leaf on a top layer. Figure H.2 shows the histogram of the sum of the RGB color intensities, where 255 is the maximum value of each color and 765 is the maximum of the sum.

Figure H.1 – Photograph of Curved Leaf

From the histogram in figure H.2, we note that most of sums of the colors that represent the top-layer leaf are above the value of about 500. Similar analysis was performed on other leaves that belong to the two top layers, arriving a similar histogram. We choose the number 500, as the threshold that selects the top two leaf layers.

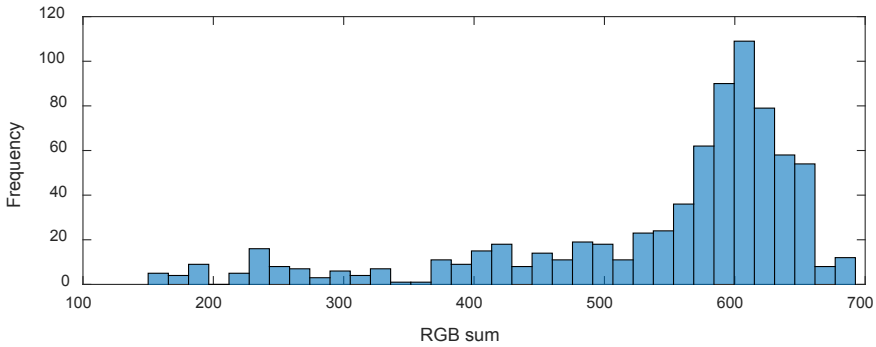

Figure H.2 – Histogram of the sum of the color intensity of a top layer leaf

The selection of the leaves on the top two layers from a top-view image has two steps. The first step is to correct the color and intensity of the image. To do this, the average intensity of the colors of the ground are adjusted to the same values. For this first step, the pixels corresponding to the ground are separated from those related to the vegetation. This separation is done by selecting the pixels that have an intensity value of red greater than an intensity value of green. In the second step, the threshold is applied to the pixels related to the vegetation to select the top two leaf layers.

Figure H.3 – Top View Photograph of Wheat Plot (Row 3; Plot 4)

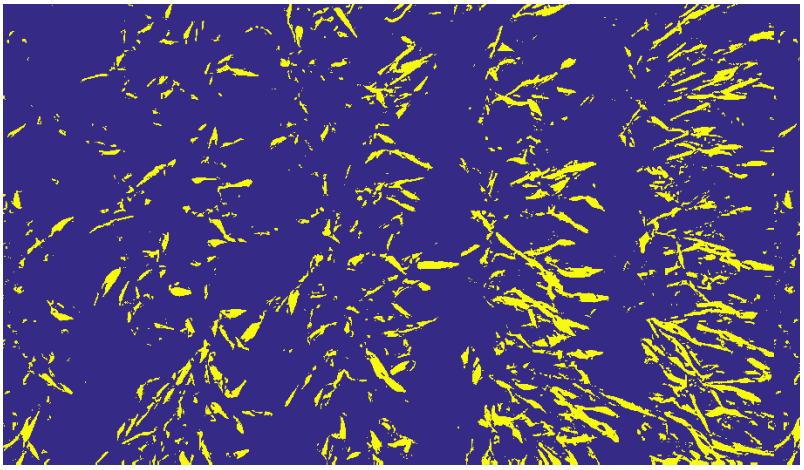

Figure H.3 – Top view of wheat plot showing the selected top two leaf layers (Row 3; Plot 4)

Once the pixels of the top two leaf layers are selected, the total projected leaf area of these layers is divided by the total ground area. This ratio is divided by two thirds of the plot height to obtain the (average) projected leaf area density (PLAIz) of the top two layers, retrieved by this method.

This retrieval method to find the average PLAIz of the top two layers using top-view images is used in chapter 6.